Non-aqueous synthesis of heterometal substituted Lindqvist-type polyoxometalates

Dominic Shiels

A thesis submitted in partial fulfilment of the requirements for the award of

Doctor of Philosophy

School of Natural and Environmental Sciences

Abstract

Mixed metal oxide materials have been successfully applied as active components in environmentally important transformations, *e.g.* ammonia synthesis, water-oxidation or carbon dioxide reduction. To combat rising demands on energy and resources, improvements to these processes, and in turn the active components that drive them, must be made. This requires a fundamental understanding of the relationship between the structure, composition, and activity of these materials.

One way to address this is to develop atomically precise models of these mixed metal oxide materials that can then be systematically modified and the effect of activity noted. This work focuses on the development of a series of such model systems in the form of heterometal-substituted polyoxometalates (POMs)

A robust synthetic approach for the production of heterometal substituted POMs based on the Lindqvist architecture is developed using the reported $(TBA)_7[(Co(II)W_5O_{18}H)_2][X]$ (X = BF_4 or Cl) as a model system. This is then expanded to a range of first row transition metals with evidence of the successful synthesis of magnesium, manganese, iron, nickel, and zinc substituted derivatives presented. The method uses the base degradation of $(TBA)_2[W_6O_{19}]$ to target a "virtual" lacunary species which efficiently reacts with simple metal salts to give the corresponding heterometal containing derivative. A detailed discussion of non-aqueous solution speciation is presented in part to identify the true nature of this "virtual" lacunary species, with combined ^{17}O NMR, ^{183}W NMR and crystallographic studies indicating it is actually a 2:1 mixture of $(TBA)_2[WO_4]$ and a novel isopolytungstate, $(TBA)_5[W_7O_{24}H]$, which is only the third isopolytungstate isolated from non-aqueous solutions.

This synthetic approach was also applied to metal(V) - substituted Lindqvist-type POMs, including new rhenium derivatives, and products were fully characterised by multinuclear NMR and X-ray crystallography where appropriate. The effect of metal substitution on the redox properties is discussed, using cyclic voltammetry and density functional theory calculations to support findings.

Acknowledgements

Firstly, I would like to say a huge thank you to Dr. John Errington for his supervision throughout my PhD. The perfect balance of support and freedom offered, as well as facilitating countless discussions around anything and everything I was curious about, has allowed me to progress greatly as both a chemist and researcher. I am also very greatly for the opportunities he has given me to travel and interact with his extensive professional network which I feel have given me experiences which will prove invaluable as I progress further into research.

I would also like to say a special thank you to Dr. Corinne Wills and Dr. Paul Waddell for their endless support during my studies. Both of them have gone above and beyond to assist me on my journey and I am 100% sure this thesis would look very different without them! My thanks also go out to Dr. Casey Dixon for support with NMR spectroscopy, Dr. Magda Pascual-Borras for support with computational work and Dr. Lee Higham for giving me the opportunity to collaborate on a book chapter and always providing encouraging words.

I am also extremely grateful to all the past and present members of Errington group, as well as the Doherty, Izod and Lu groups. In particular, I would like to thank Magda, Reece, Sam, Fran, Tina, Amar, Nathan, and Aeshah. You have made working in the lab extremely enjoyable over the last few years and I feel very lucky to have been able to share my time here with you.

Finally, I would like to say an enormous thank you to my friends and family for their constant help and encouragement. Whether it be listening to me ramble about my project or allowing me to vent when things were not working, you all made the process a lot easier than it could have been! I would like to say a special thank you to Charlotte who, like my family, has been here since long before I started my PhD and has probably supported me more than anyone else along the way. I hope you know how grateful I am for that!

Table of Contents

List of Figures

List of Tables

Abbreviations

POM: Polyoxometalate

LPOM: Lacunary Polyoxometalate

MOF: Metal Organic Framework

TBA: tetra–n–butylammonium

DCM: Dichloromethane

DMF: Dimethylformamide

THF: Tetrahydrofuran

DMSO: Dimethyl sulfoxide

DCC: N, N'-dicyclohexylcarbodiimide

{TiW$_5$}: (TBA)$_3$[(RO)TiW$_5$O$_{18}$]

{ZrW$_5$}: (TBA)$_6$[(RO)$_2$(ZrW$_5$O$_{18}$)$_2$]

{SnW$_5$}: (TBA)$_3$[(RO)SnW$_5$O$_{18}$]

{TiMo$_5$}: (TBA)$_3$[(RO)TiMo$_5$O$_{18}$]

{W$_6$}: (TBA)$_2$[W$_6$O$_{19}$]

{W$_{10}$}: (TBA)$_4$[W$_{10}$O$_{32}$]

{W$_7$}: (TBA)$_5$[W$_7$O$_{24}$H]

{W$_5$}: Lacunary {W$_5$O$_{18}$} unit of (TBA)$_5$[W$_7$O$_{24}$H]

{W$_2$}: Capping {W$_2$O$_6$} unit of (TBA)$_5$[W$_7$O$_{24}$H]

{VW$_5$}: (TBA)$_3$[VW$_5$O$_{19}$]

{NbW$_5$}: (TBA)$_3$[NbW$_5$O$_{19}$]

{TaW$_5$}: (TBA)$_3$[TaW$_5$O$_{19}$]

{VMo$_5$}: (TBA)$_3$[VMo$_5$O$_{19}$]

{NbMo$_5$}: (TBA)$_3$[NbMo$_5$O$_{19}$]

FTIR: Fourier Transformed Infrared

ATR: Attenuated Total Reflectance

NMR: Nuclear Magnetic Resonance

ppm: Parts per million

FWHM: Full Width at Half Maximum

2D: Two-dimensional

2D-INADEQUATE: Two-dimensional Incredible natural-abundance double-quantum transfer experiment

EXSY: Exchange Spectroscopy

COSY: Correlated Spectroscopy

SCXRD: Single-Crystal X-ray Diffraction

CSD: Cambridge Structural Database

PXRD: Powder X-ray Diffraction

UV-Vis: Ultraviolet and Visible

CHN: Carbon, Hydrogen and Nitrogen

ICP-OES: Inductively Coupled Plasma Optical Emission Spectroscopy

DFT: Density Functional Theory

SQUID: Superconducting Quantum Interference Device

EPR: Electron Paramagnetic Resonance

REDOX: Reduction and Oxidation

Experimental techniques

General considerations

Reactions and manipulations were carried out under dry, oxygen-free nitrogen or argon using standard Schlenk and dry-box techniques unless stated otherwise.[1] Reactions were carried out in screw-top Schlenk flasks fitted with PTFE screw valves (Young's valves). Acetonitrile and dichloromethane were dried with and distilled from calcium hydride and then stored over 3A molecular sieves. Diethyl ether, tetrahydrofuran, hexane and toluene were dried and distilled from sodium benzophenone ketyl and then stored over 3A molecular sieves. Methanol and ethanol were distilled from magnesium activated with a few crystals of iodine and then stored over 3A molecular sieves. Dimethyl sulfoxide, dimethylformamide, ethyl acetate and deuterated solvents were all stored over 3A molecular sieves for at least three days prior to use.

NMR spectroscopy

Samples were prepared in 5 mm (^{1}H, ^{13}C, ^{17}O, ^{51}V, and ^{93}Nb) or 10 mm (^{95}Mo and ^{183}W) screw top NMR tubes. Spectra were recorded on a Bruker AVANCE III 300 MHz spectrometer or a Brucker AVANCE III HD 500 MHz. Chemical shifts are quoted in ppm relative to SiMe$_4$ (^{1}H and ^{13}C), H$_2$O (^{17}O), VOCl$_3$ (^{51}V), (TBA)[NbCl$_6$] (^{93}Nb), Na$_2$MoO$_4$ (*ca.* 2 *M*) (^{95}Mo) or Na$_2$WO$_4$ (*ca.* 2 *M*) (^{183}W). Spectra were recorded at 298 K unless otherwise stated.

Single-crystal X-ray diffraction

Crystal structure data for (BTMA)51.2DMSO were collected on a XtaLAB Synergy, HyPix-Arc 100 diffractometer equipped with a fine-focus sealed X-ray tube (λ Cu Kα = 1.54184 Å) and for (TBA)71.[W6O19] on an Xcalibur, Atlas, Gemini ultra diffractometer using molybdenum radiation (λMo Kα = 0.71073 Å). All data were collected at 150 K using an Oxford Cryosystems CryostreamPlus open-flow N2 cooling device. Cell refinement, data collection and data reduction were undertaken via software CrysAlisPro. Intensities were corrected for absorption analytically using a multifaceted crystal model based on expressions derived by Clark & Reid.[2] The structure was solved using XT[3] and refined by XL[5] using the Olex2 interface.[4] All non-hydrogen atoms were refined anisotropically and hydrogen atoms were positioned with idealised geometry. The displacement parameters of the hydrogen atoms were constrained using a riding model with U(H) set to be an appropriate multiple of the Ueq value of the parent atom. Details of any disorder and how it was modelled are available in the CIF.

Bond valence sums for the oxygen atoms were calculated according to previously reported methods[6,7] using the equations shown below, where z_j (or V) is the oxidation state of the jth atom or ion, s_{ij} is the bond valence contribution from the "bond" between the ith and jth atom/ion, R_0 is a constant that is dependent on the ij pair, r_{ij} is the observed bond length and b is 0.37.

$$z_j = \sum s_{ij}$$

$$s_{ij} = \exp[\frac{R_0 - r_{ij}}{b}]$$

ATR FTIR spectra

FTIR spectra were recorded from powders on a Bruker Alpha FTIR spectrometer fitted with an Platinum ATR attachment.

Computational methods

Specific details of computational methods are given in the experimental section of the chapter in which they are discussed, specifically **Sections 3.7.10** and **5.9.20**. XYZ co-ordinates of optimised structures are given in **Appendix B.**

References

1. R. J. Errington, Advanced Practical Inorganic and MetalorganicChemistry, Blackie Academic & Professional, London,1997.
2. R. C. Clark and J. S. Reid, *Acta Crystallogr*. A, 1995, **51**, 887-897.
3. G. M. Sheldrick, *Acta Crystallogr. A*, 2015, **71**, 3-8.
4. G. M. Sheldrick, *Acta Crystallogr. A*, 2008, **64**, 112-122.
5. O. V. Dolomanov, L. J. Bourhis, R. J. Gildea, J. A. K. Howard and H. Puschmann, *J. Appl. Crystallogr.*, 2009, **42**, 339-341.
6. L. Pauling, *J. Am. Chem. Soc.,* 1929, **51**, 1010-1026.
7. R. M. Wood and G. J. Palenik, *Inorg. Chem.,* 1998, **37**, 16, 4149–4151.

Chapter 1: Introduction to polyoxometalates synthesis

1.1 Chapter outline

This thesis focuses primarily on the development of new synthetic methods targeting the generation of molecular metal oxide materials (also known as polyoxometalates). Therefore, this introduction aims to give the reader an overview of the common synthetic practices employed in both the past, as the field developed, and present, when targeting these materials. The vast majority of synthetic procedures presented in the literature are aqueous based. Hence, these approaches are discussed at length before some of the non-aqueous synthetic methods developed by our group (and others) are outlined. The size of the body of literature discussing synthesis of molecular metal oxide materials prevents an exhaustive discussion of the methodology used. Thus, a series of specific examples are given instead, aiming to guide the reader towards an understanding of the general principles used when designing these procedures.

1.2 Background

Polyoxometalates (POMs) are polynuclear oxoanions classically formed by group five or group six transition metals, in their highest oxidation states.[1] Isopolyoxometalates are those containing a single type of framework metal atom, and can be described using the general formula $[M_xO_y]^{n-}$ where M = V, Nb, Ta, Mo, or W. Heteropolyoxometalates are those which incorporate other main group or transition metal elements into the metal oxide framework and can be described by the general formula $[EM_xO_y]^{n-}$ or $(M_xO_y)E^{n-}$, which exemplifies the fact that these systems are commonly made up of a neutral metal oxide cluster that
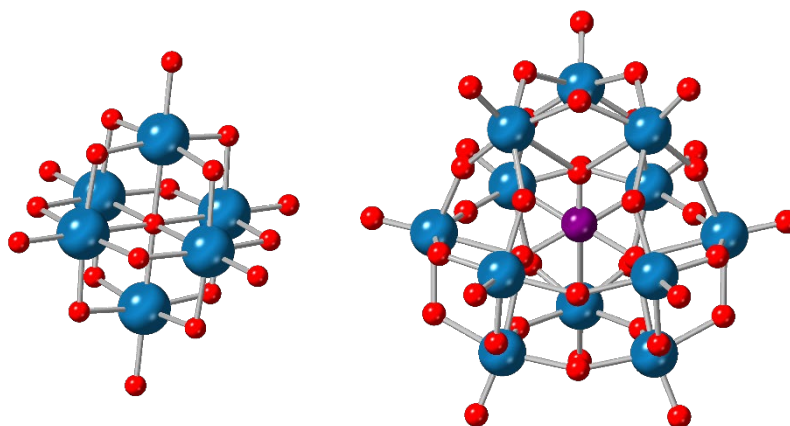
Figure 1.1*:* Left- $[W_6O_{19}]^{2-}$ (Lindqvist) anion is an isopolyoxometalate. Right- $[PW_{12}O_{40}]^{3-}$ (Keggin) anion is a heteropolyoxometalate. W = blue and P = purple.

incorporates anionic atoms or groups.[2] Examples of both iso- and heteropolyoxometalates are given in **Figure 1.1**.

The earliest known example of polyoxometalate chemistry in the literature comes from Berzelius[3] who, in 1826, reacted molybdenum with phosphate and arsenate to form yellow heteropolyanions.[4] Over 100 years would pass until the structure of $[H_3PW_{12}O_{40}].6H_2O$, a now very widely researched system, was solved by Keggin, in 1933.[5] Since then, the development of routinely accessible, high quality, X-ray crystallography, mass spectrometry, ^{17}O NMR spectroscopy, and electrochemical methods have made the characterisation of polyoxometalates both in solution and the solid state a lot more manageable.[4] This has not only resulted in an exponential increase in the number of reported POM structures, but also the development of rational synthetic methodology, some of which will be outlined in **Sections 1.3** and **1.4**.[6,7]

POM structures can, and do, vary massively with structures ranging from a few angstroms to multiple nanometres. They are typically made up of edge- or corner-sharing MO_6 octahedra (face sharing is less common although examples are still seen[8]) with one or two terminal metal oxygen bonds.[2] When two terminal metal-oxo bonds are present, they typically adopt a *cis* geometry[2] (which maximises M-O π-bonding and is an example of the thermodynamic *trans*-effect) apart from in very rare occasions, for example in the case of uranium-based POMs where the linear uranyl (UO_2^{2+}) unit dominates.[9,10] Clusters containing MO_6 octehedra with one terminal oxygen bond and those with two can be split into type I and type II POMs, as they exhibit significantly different redox properties.

Type I structures, e.g. the Keggin anion, have MO_6 units with an idealised local symmetry of C_{4v} (**Figure 1.2**). Qualitative molecular orbital analysis, along with more detailed computational studies, have shown the LUMO in these systems is essentially composed of non-bonding (or slightly anti-bonding) d_{xy} orbitals.[2,12,13] A major consequence of this is that reversible addition of one or two electrons per metal atom leads to minimal structural changes.[2] A recent review by Gumerova and Rompel outlines some of the chemical and electrochemical procedures used to synthesise these highly reduced POMs.[14] This can be paired with a range of theoretical work to give a comprehensive overview of the literature.[13,15a-e]

Type II structures, e.g. $[Mo_7O_{24}]^{6-}$, possess C_{2v} symmetry at each metal centre (**Figure 1.2**).[4] As a consequence, the previously non-bonding d_{xy} character of the LUMO is transformed to a π-
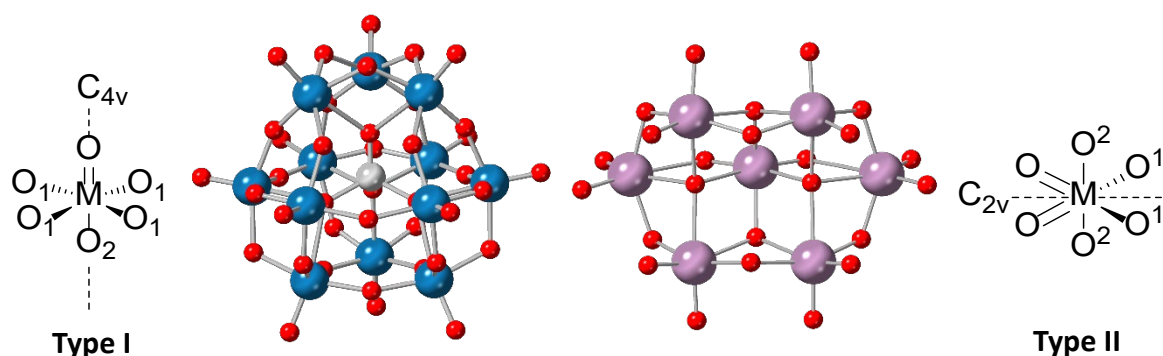
Figure 1.2: Type I POMs, e.g. the Keggin shown, possess localised C_{4v} symmetry at the M atoms. Type II structures, e.g. $[Mo_7O_{24}]^{6-}$ shown, possess metal centres with local C_{2v} symmetry. W = blue, Si = grey, and Mo = pink.

anti-bonding level.[2] This in turn means that reduction of these complexes leads to significant structural changes, for example fragmentation or rearrangement, and is irreverisible.[2]

There are also several type III structures that contain a mixture of type I and type II metal centres, an example being the paratungstate-B anion $[H_2W_{12}O_{42}]^{10-}$.[11]

POMs are versatile reagents that have been previously applied in catalysis[16-18], energy storage[19,20], molecular magnetism[21-23], materials science[24,25], and medicine[26,27]. In recent years, the desire to improve access to sustainable energy sources has fuelled a large increase in research focusing on the use of POMs in water splitting; this is the process of converting water to hydrogen and oxygen using energy, which is usually supplied in the form of electricity from renewable energy sources.[28a-f]

1.3 Aqueous Synthesis

Hervé describes polyoxometalates as, "intermediate species between the mononuclear oxo/hydroxometalates $[MO_x(OH)_y]^{n-}$ and polymeric metallic oxides".[6] It is therefore unsurprising that common synthetic routes used to access polyoxometalates involve either degradation of neutral metal oxides with base (a source of negative charge) or condensation of monometallic precursors with acid.[6,7] This section will explore the typical methods used to synthesise POMs in aqueous media, with an emphasis placed on the synthesis of heterometal containing POMs, which can have application in catalysis.

1.3.1 General Considerations

The solubility of anionic POMs is determined by the nature of the counter cation. Historically, most POM synthesis was done in aqueous media where both the free acids (H^+ as the counter-ion) and alkali metal salts are highly soluble.[6] These small, densely charged, counter ions can

approach close to the POM surface and, along with the high dielectric constant of water, can stabilise highly charged POM species.[7]

Synthesis of simple isopolyoxometalates requires only a source of metal, typically in the form of an metal-oxo species (e.g. $Na_2WO_4.2H_2O$), and acid to allow condensation of terminal M=O bonds into M-O-M bridges (**Equation 1.1**). When using this approach, the POM counter ions come from the monomeric precursor used. If a specific counter ion is required, then neutral metal oxide can be degraded with a specific base (i.e. M*OH) to form $M^*_2[MO_4]$ (assuming M is in group VI) prior to the condensation reaction (shown in **Equation 1.2**).[6]

$$x\,M^*_2[MO_4] + z\,H^+ \rightarrow n\,M^*[M_xO_y] + \frac{z}{2}\,H_2O \qquad (1.1)$$

$$MO_3 + 2\,M^*OH \rightarrow M^*_2[MO_4] + H_2O \qquad (1.2)$$
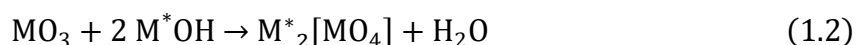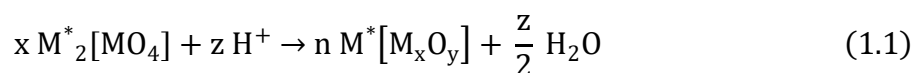
Synthesis of heteropolyoxometalates ($[EM_xO_y]^{n-}$) in aqueous media is very similar, though the addition of a soluble heteroatom/group precursor is also required. These are commonly oxoacids (e.g. H_3PO_4, $B(OH)_3$) or alkaline salts (e.g. Na_2SiO_3), though some oxides (e.g. Sb_2O_3, Nb_2O_5, Ta_2O_5) can be used under specific conditions.[6] In order to selectively form one cluster, in preference of others, a range of experimental factors must be carefully controlled. These include the molar ratio of M and E (i.e. the metal and heteroatom), temperature, pH value, the nature of the solvent (with addition of solvents such as EtOH or MeCN stabilising some structures), and the counter ions.[6] As an example, **Figure 1.3** shows how the dominant POM
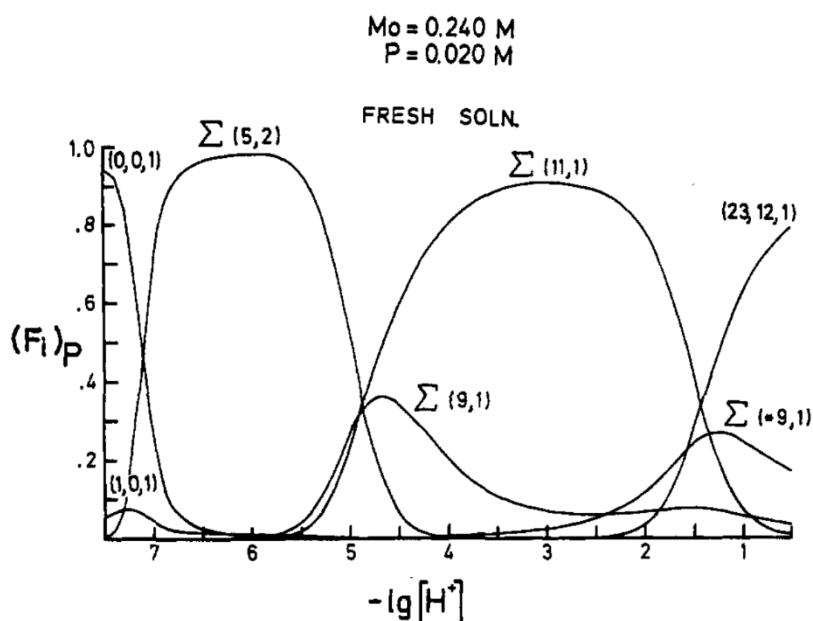
Figure 1.3: Plot showing the relative amounts of POM species present in solution at various pH values. Curves are labelled with the H+:Mo:P ratios or, in the case of species that only differ in the extent of protonation, the sum is given and represented by ∑ Mo:P (produced from ref 29).

structure, in terms of the M:E ratio, varies when the pH of a 12:1 molar ratio solution of $[MoO_4]^{2-}$ and $[HPO_4]^{2-}$ is changed. In this work, Petterson *et al* clearly show how sensitive POM speciation can be to experimental conditions.[4,29] A major benefit of this complex speciation behaviour in solution is that an enormous array of structures can be accessed. The synthesis of a range of POM structures in aqueous media has been outlined by Klemperer.[30]

1.3.2 Lacunary Species

So-called lacunary polyoxometalates (LPOMs) are POMs which have a missing addenda atom or atoms (sometimes referred to as defects).[31] These structures can often be easily related to their parent structures by removal of one or more metal atom, and some of the surrounding oxygen atoms, from the parent species.

A classic example of this is the Keggin structure $[XM_{12}O_{40}]^{n-}$, which is the parent structure for a range of lacunary species. The complete Keggin structure possesses five isomers (sometimes referred to as Baker-Figgis isomers): α-, β-, γ-, δ-, and ε-, formed by a 60° rotation of one, two, three, or all four of the M_3O_{13} triads.[32,33] Subsequently, lacunary species of the parent Keggin anion can also possess a range of isomers, which results in a huge range of individual lacunary species.

Lacunary POMs do not necessarily have to be synthesised by using the parent structure as a starting material. Taking the Keggin structure as an example, Hervé outlined the synthesis of the tri-vacant $Na_{10}[SiW_9O_{34}].18H_2O$, referred to as α-SiW$_9$, from sodium tungstate and sodium silicate in the presence of 6 M HCl.[34] Several other compounds, including β-SiW$_9$, β-GeW$_9$, α-SiW$_{11}$, and β_2-SiW$_{11}$, can be synthesised in the same way.[30,34-36]

In other cases, lacunary species are more conveniently accessed from a pre-formed POM, commonly either the complete (parent) structure or another lacunary species.[7,36] For example, β_1-SiW$_{11}$ can be synthesised from β-SiW$_9$ by adding sodium tungstate and 1 M HCl.[30] It is worth noting that conversion between different lacunary species (or lacunary species and the parent structure) is limited. For the Keggin and its derivatives, synthesis of individual isomers of the same structure requires different approaches. This was conveniently summarised by Hervé and is shown in **Figure 1.4**.[7,36]

Lacunary species are classically employed as precursors for heteroatom substituted POMs as they can act as ligands, where various heteroelements occupy the vacant sites. Lacunary
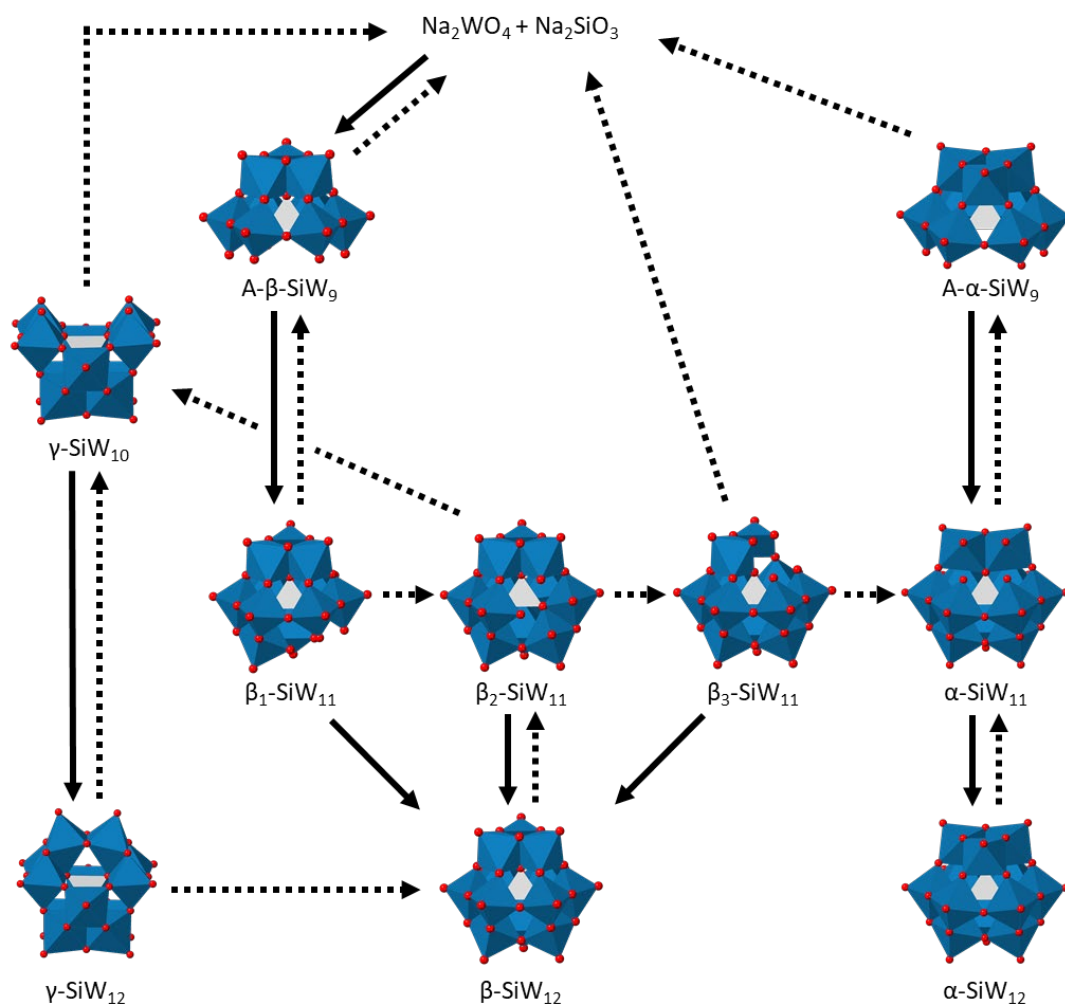
Figure 1.4: Synthesis and structures of tungstosilicates. Reproduced from ref 7 and ref 36. W = blue, and Si = grey.

POMs have also been used as starting materials in the formation of larger framework materials.[31,37,38]

1.3.3 Heterometal Substituted POMs

Both the iso- and heteropolyoxometalates discussed so far only incorporate one type of metal atom. Addition of a second "heterometal" can be used to vastly change the reactivity of the POM, which, in turn, leads to new applications. Numerous heterometals, including a range of transition metals, lanthanides, and actinides, have been successfully incorporated into POM structures.[16,18-24]

There are two main classes of heterometal containing POM structures: Complete (plenary) and defect (lacunary). Complete structures bind metal ions at the surface of the POM via interactions with bridging and terminal oxygen atoms. Defect structures use the heterometal(s) to populate the vacancies present in the structure.[4]
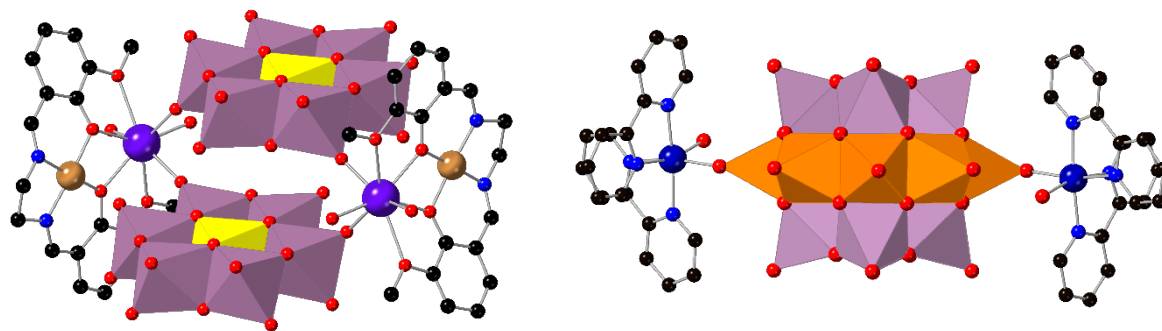
Figure 1.5: Left- [CuTbL(H$_2$O)]$_2$[AlMo$_6$O$_{18}$(OH)$_6$]$_2$ (L = *N,N'*-bis(3-methoxysalicylidene-ethylenediame) (ref 39). Right- [PMo$^{VI}_4$Mo$^V_4$V$^{IV}_8$O$_{44}${Co(2,2'-bipy)$_2$(H$_2$O)}$_2$]$^{3-}$ (ref 40). Mo = lilac, Cu = brown, Tb = purple, V = orange, and Co = blue.

Complete/plenary structures are less common than defect/lacunary structures. They require highly charged POMs in which the external heterometal cation can bind, typically, via more than one oxygen atom.[4] Synthesis of these compounds is also usually done in non-aqueous media, however this is not an absolute requirement.[4] The general procedure for producing complexes of this type involves reaction of a plenary POM and a soluble heterometal precursor, which can be a simple salt or may have been synthesised separately to allow incorporation of specific ligands into the complex.[39,40] For example, Feng *et al* showed that the reaction of [CuTbL(H$_2$O)$_3$Cl$_2$]Cl (L = *N,N'*-bis(3-methoxysalicylidene-ethylenediame) with Anderson-type POMs in water/methanol can yield terbium bound, copper containing, POMs that can act as single-molecule magnets (**Figure 1.5** left).[39] Alternatively, a mixture of the metal-oxo species (e.g. Na$_2$MoO$_4$.2H$_2$O or NH$_4$VO$_3$), heterometal precursor (e.g. CuCl$_2$.2H$_2$O), heteroatom (e.g. H$_3$PO$_3$), and any ligands required, can be used together to build the POM-heterometal complex in-situ. This approach was used by Yuan *et al* during the hydrothermal synthesis of a series of cobalt-bound mixed addenda POMs (**Figure 1.5** right).[40]

Complexes with lacunary/defect structures are far more common. Heterometal containing Keggin[41a-d] and Wells-Dawson[42a-c] structures are the most widely described systems in aqueous media, with numerous reviews present.[31,43-46] These compounds can be synthesised from the parent POM species, lacunary POMs or from the component metal salts in combination with the desired heterometal in the form of an aqueous soluble precursor (**Figure 1.6**).[31] Whether starting from a parent POM or individual metal salts, the lacunary POM may be isolated as an intermediate (as shown in **Figure 1.6**) or generated as a virtual intermediate in-situ. The properties of the resulting complexes are largely dependent on the nature of the heterometal.
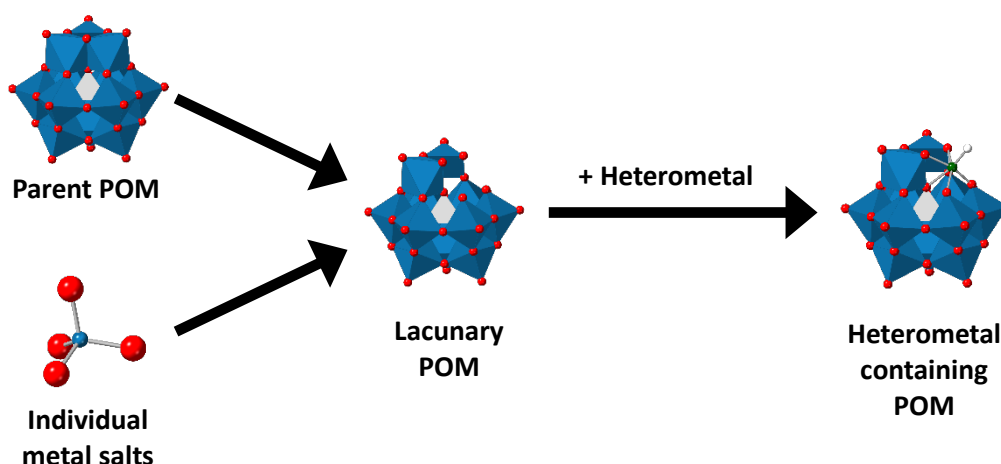
Figure 1.6: Synthesis and isolation of a lacunary POM starting from either a complete POM structure (parent POM) or from individual metal salts. Reproduced from ref 30.

A notable set of heterometal substituted, aqueous soluble, POMs are the Weakley-type POMs. These are sandwich-type clusters in which lacunary POMs serve as inorganic ligands for a central metal ion(s) (**Figure 1.7**).

These compounds are of interest because of their activity as water oxidation catalysts[28a-f], their magnetic properties[47a-e] and the ability to use them in the assembly of useful nanomaterials.[48] Weakley originally synthesised $[Co_4(H_2O)_2(PW_9O_{34})_2]^{10-}$ (often abbreviated to Co_4POM shown in **Figure 1.7b**) by reacting $[(H_2O)Co(PW_{11}O_{39})]^{5-}$ with cobalt ions in aqueous solution.[48] Since then, the synthesis has more commonly involved combination of two di- or trivacant lacunary Keggin units with metal ions (including Co, Ru, Mn, Cu, Fe, Ce, Eu, and Tb), or direct condensation of the monomeric metal-oxo species with the required heteroatoms.[47a-e, 50a,b] Weakley-type sandwich clusters are not limited to the use of lacunary Keggin units as the capping ligands, nor do they have to be symmetrical (i.e. the same capping ligand on both
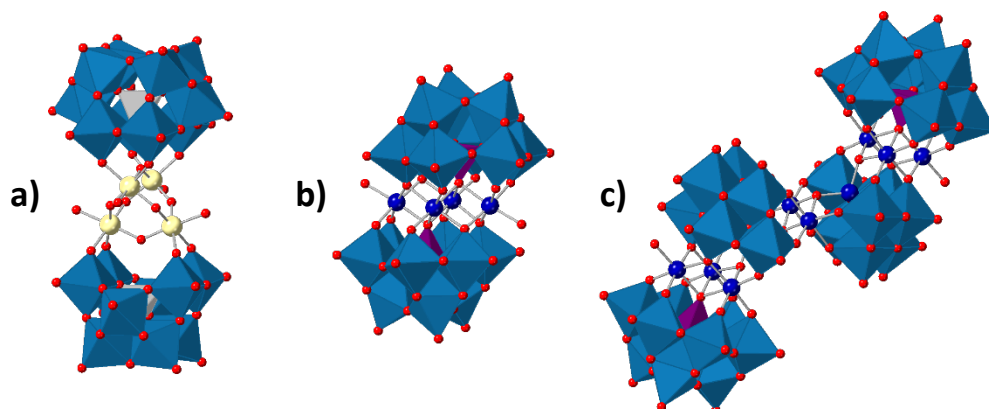
Figure 1.7: Structures of a series of Weakley-type POMs;. **a)** $[\{Ru_4O_4(OH)_2(H_2O)_4\}(\gamma\text{-}SiW_{10}O_{36})_2]^{10-}$ (Ru_4POM) **b)** $[Co_4(H_2O)_2(PW_9O_{34})_2]^{10-}$ (Co_4POM) (ref 49) **c)** $[Co_2\{Co_3(H_2O)(Co(OH)_2W_7O_{26})(PW_9O_{34})\}_2]^{22-}$ (ref 50a). W = dark blue, Ru = pale yellow, and Co = blue.

sides).[50a,51] For example, Duan *et al* reported the synthesis of an asymmetric sandwich-cluster, with the formula $[Co^{II}_4(H_2O)_2(Co^{III}W_9O_{34})(PW_9O_{34})]^{12-}$, and its subsequent reaction with hydrazine, which leads to reduction of the cluster and formation of $[Co^{II}_2\{Co^{II}_3(H_2O)(Co^{II}(OH)_2W_7O_{26})(PW_9O_{34})\}_2]^{22-}$ (**Figure 1.7c**).[50a]

1.3.4 Mixed-addenda POMs

A subset of heterometal containing POMs are mixed-addenda POMs. These structures contain heterometal(s) that can also form POM structures, commonly V, Nb, Ta, Mo, or W. Substitution of one or more framework metal with a different metal can be used to tune properties such as pH stability[52], colour[52], and redox potentials.[53] Several mixed-addenda POMs have been identified as active anti-viral agents[54] and potential energy storage solutions.[55]

Synthesis of mixed-addenda POMs in aqueous media uses either individual metal salts or lacunary POMs as starting materials. Starting from the individual metal salts allows the amounts of each type of addenda to be varied to control the ratio of each metal in the cluster.[52,56] Synthesis starting from a lacunary species is analogous to the synthesis of heterometal-lacunary POM complexes outlined previously. This method gives less flexibility, as the number of heterometal atoms incorporated into the cluster will be dependent on the number of defects present in the lacunary POM, but is more controlled.[57]

1.4 Non-Aqueous Synthesis

So far, the synthetic methods discussed conveniently employ water-soluble, commercially available, precursor materials like $Na_2WO_4.2H_2O$ and Na_2SiO_3, which can be treated with aqueous acid to target a specific pH and produce POMs. Moving to non-aqueous solvents immediately presents problems. Not only are these materials much less soluble in organic solvents but pH control of reactions also becomes much less reliable (as standardisation across different solvents is not simple).[58] It is therefore unsurprising that the methods used for non-aqueous POM synthesis are different, even if the rationale is largely the same.

1.4.1 General Considerations

As previously mentioned, the solubility of POMs is largely dependent on the nature of the counter cations used to balance the negative charge of the POM. To carry out synthesis and reactivity studies on POMs in polar organic solvent, bulky counter cations are required. These are frequently tetraalkylammonium cations with long chains (i.e. tetrabutylammonium (TBA) and longer) that are often abbreviated to Q.[7] The nature of these cations prevents strong anion-cation interactions (the ability of the cation to approach the anion surface is limited by

the size) thus favouring lower charges compared to those commonly observed in the aqueous phase.[7] Large inorganic cations, such as Cs or Ba, also give reduced solubility in aqueous media but tend to lead to completely insoluble materials.[59]

Figure 1.8 shows the structures of $K_4[SiW_{12}O_{40}].9H_2O$ and $(TBA)_3[(^iPrO)TiW_5O_{18}]$ with the counter cations in closest proximity.[60,61] The aqueous soluble Keggin structure (**Figure 1.8a**) is stabilised by K^+ ions, which can approach close to the POM surface. Contrast this with the organic soluble Lindqvist structure (**Figure 1.8b**). The proximity of the counter ions around the structure is limited by the size of the cations, meaning highly charged structures cannot be stabilised by favourable anion-cation interactions. This further illustrates why highly anionic clusters are less common in organic media unless they are protonated (which serves to reduce the overall charge).[7]

The methods used to synthesise organic-soluble POMs are largely the same as those used in aqueous solvents, with the added requirement that bulky cations must be introduced at some point to allow the product POM to be soluble in organic solvents. One way to do this is to use oxo-metalate species with bulky cations as starting materials. These compounds must be synthesised prior to POM synthesis. For example $(TBA)_2WO_4$ can be synthesised from $WO_3.H_2O$ and TBA(OH) in water[62] or methanol.[63] Alternatively, it can be synthesised by salt metathesis using Ag_2WO_4 and $(TBA)Br$[64] or $(TBA)I$.[65] These, and other, designer starting materials can then be combined with the appropriate heteroelements to create the desired POM structure.

A second approach is to synthesise the POM using conventional starting materials and then perform a cation exchange in the work-up of the reaction. For example, $(TBA)_2[W_6O_{19}]$ can be
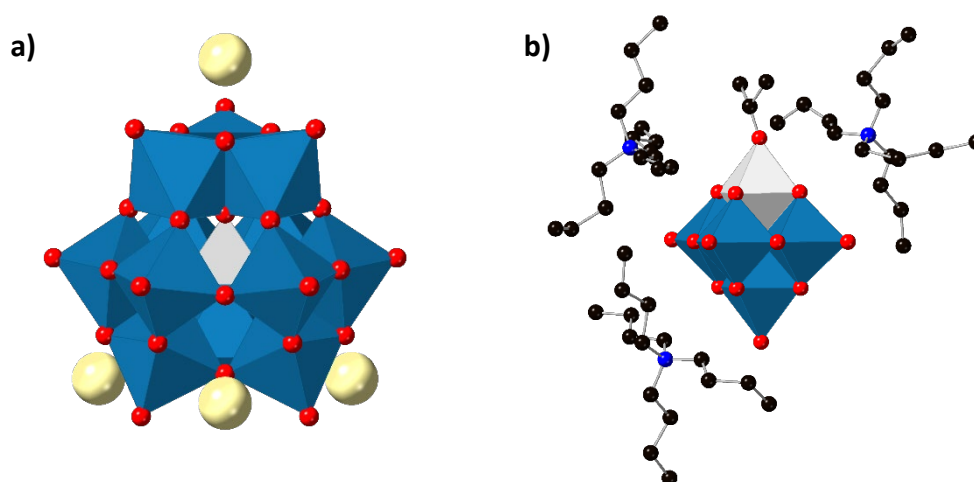
Figure 1.8: **a)** Structure of $K_4[SiW_{12}O_{40}].9H_2O$ with only the closest K^+ ions shown (ref 60). **b)** Structure $(TBA)_3[(^iPrO)TiW_5O_{18}]$ which the TBA ions around the cluster shown (ref 61). W = blue, Si = grey, K = pale yellow, Ti = silver.

synthesised by dissolving Na_2WO_4 in DMF/acetic anhydride, followed by the addition 12 M HCl. The resulting "$Na_2[W_6O_{19}]$" intermediate can then be treated with an excess of (TBA)Br, which causes the POM to precipitate out of solution as the TBA salt, while NaBr remains in solution.[30] This approach is very common as it is a "one-pot" process that typically uses readily available materials. However, it is not always a viable approach as organic salts of more highly negatively charged POMs may still be soluble in aqueous solvents or the polar solvent mixture used above, which leads to difficulties in purficiation.[7]

An advantage of working in organic media is the ability to use reagents that are either not stable or not soluble in aqueous solvents. Relevant examples include numerous metal oxides, metal alkoxides, and metal oxychlorides. These reagents can act as sources of both framework atoms (e.g. $WO(OR)_4$) or heteroelements (e.g. SeO_2)).[7] Jahr and Fuchs gave early examples of how these materials could then be combined to produce POMs.[66a-c] More recently, our group has used $WOCl_4$, along with NH_3/MeOH, to synthesise $WO(OMe)_4$ (which is sensitive to hydrolysis).[67] This in turn was reacted with $[\{Zr(O^iPr)_4(^iPrOH)\}_2]$ and $(TBA)_2[WO_4]$ in the synthesis of $(TBA)_6[\{(MeO)ZrW_5O_{18}\}_2]$ ($\{ZrW_5\}$).[68] This exemplifies the ability to access reaction pathways in organic solvents that are not possible in aqueous solvent.

1.4.2 ^{17}O NMR Spectroscopy

Studying POMs in organic media means there is no oxygen exchange between the POM and solvent water, which allows the use of ^{17}O NMR spectroscopy as a method of analysis and characterisation.[7] From a practical point of view, ^{17}O can be considered as a difficult nucleus to observe.[69] It has a nuclear spin of 5/2 and an electric quadrupole moment of $Q = -2.6 \times 10^{-26}$ cm^2, which leads to rapid quadrupole relaxation. This in turn can give broad signals and a poor signal to noise ratio. Furthermore, the rapid relaxation leads to the use of short delays between radiofrequency pulses, which can cause incomplete spectrometer recovery.[69] However, ^{17}O NMR spectroscopy is still a powerful technique and the resultant NMR spectra can give important insights into solution dynamics and provide structural information. Given that ^{17}O has a natural isotopic abundance of 0.037%, POMs have to be artificially enriched to allow informative spectra to be collected.[69] This can easily be done using ^{17}O enriched water (which can be obtained at a range of enrichment levels). For example, **Equation 1.3** shows how you may produce a partially ^{17}O enriched sample of tetrabutylammonium hexatungstate. If 10% ^{17}O enriched water is used, the product POM contains 5.3% ^{17}O enrichment.

$$(TBA)_2[WO_4] + 5\,WO(OMe)_4 + 10\,H_2O^* \rightarrow (TBA)_2[W_6O^*_{19}] + 20\,MeOH \qquad (1.3)$$
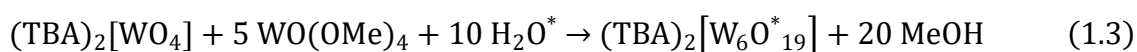
1.4.3 Heterometal Containing Lindqvist Structures

Our group has been interested in the development of rational synthetic methods to produce heterometal containing Lindqvist-type POMs to explore their reactivity and to use them as simple molecular models for extended mixed metal oxides, commonly used in inorganic chemistry.

The synthesis of heterometal substituted Lindqvist-type structures with the general formula $[XM'W_5O_{18}]^{n-}$ (where M' = Ti, Sn, Zr, V, Nb, Ta, and Mo and X = MeO or O) was initially attempted through the hydrolysis of a mixture of $(TBA)_2[WO_4]$, $WO(OMe)_4$ and the corresponding metal alkoxide (e.g. $Ti(OMe)_4$ or $Nb(OMe)_5$) in acetonitrile.[68,70,71] The crystal structure of $(TBA)_3[(MeO)TiW_5O_{18}]$ ({TiW_5}) (**Figure 1.9a**) was obtained, showing the successful incorporation of "$[Ti-OMe]^{3+}$" fragment into the virtual "$[W_5O_{18}]^{6-}$" lacunary species. Furthermore, the hydrolysis of $(TBA)_2[(MeO)NbW_5O_{18}]$ yielded crystals of the dimer $(TBA)_4[(NbW_5O_{18})_2O]$ (**Figure 1.9b**).[70] The use of molybdenum as the framework metal (instead of tungsten) has also been explored, with the group successfully isolating $(TBA)_3[(^iPrO)TiMo_5O_{18}]$ ({TiMo_5}) through the hydrolysis of $(TBA)_2[Mo_2O_7]$, $(TBA)_4[Mo_8O_{26}]$, and $Ti(O^iPr)_4$ in acetonitrile.[72]

The family of heterometal substituted Lindqvist-type structures was extended further in 2009, when our group reported the synthesis of the cobalt substituted Lindqvist-type structures $(TBA)_6[(CoW_5O_{18}H)_2]$ and $(TBA)_3[(Py)CoW_5O_{18}H]$ (Py = pyridine).[73] A slightly different synthetic methodology was employed in which the virtual precursor "$[W_5O_{18}]^{6-}$" was prepared first by reaction of $(TBA)_2[WO_4]$ and $WO(OMe)_4$ (**Equation 1.4**). This virtual precursor was then treated with a solution of cobalt chloride in acetonitrile to give the dimeric anion $(TBA)_6[(CoW_5O_{18}H)_2]$.
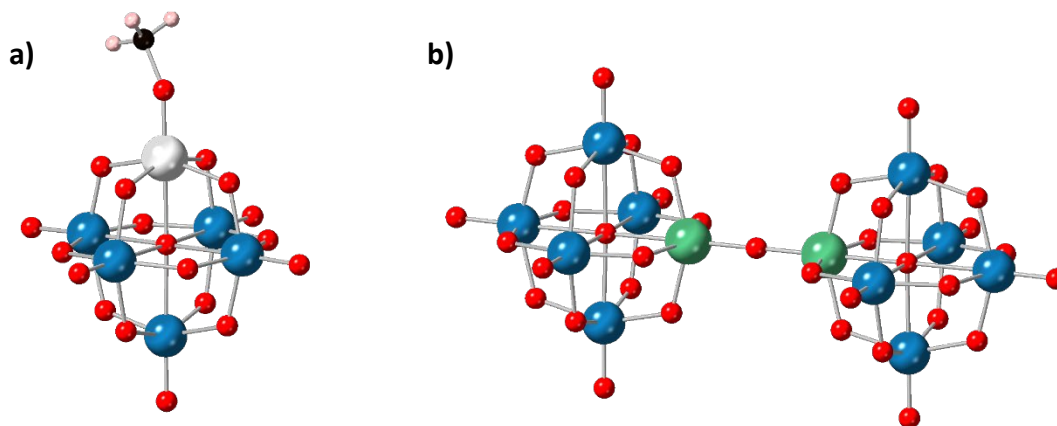
Figure 1.9: Structures of **a)** $(TBA)_3[(MeO)TiW_5O_{18}]$ and **b)** $(TBA)_4[(NbW_5O_{18})_2O]$ (ref 70)

Subsequent treatment with pyridine can be used to isolate the pyridine adduct $(TBA)_3[(Py)CoW_5O_{18}H]$ (**Equations 1.5** and **1.6**).[73]

$$3\ (TBA)_2[WO_4] + 2\ WO(OMe)_4 + 4\ H_2O \rightarrow "(TBA)_6[W_5O_{18}]" + 8\ MeOH \qquad (1.4)$$

$$"(TBA)_6[W_5O_{18}]" + CoCl_2\ (+\ H^+) \rightarrow 0.5\ (TBA)_6[(CoW_5O_{18}H)_2] + 2\ TBA(Cl) \qquad (1.5)$$

$$0.5\ (TBA)_6[(CoW_5O_{18}H)_2] + Pyridine \rightarrow (TBA)_3[(Py)CoW_5O_{18}H] \qquad (1.6)$$
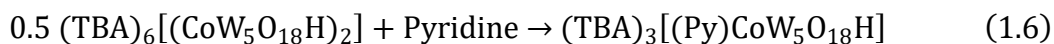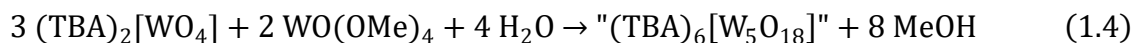
The reactivity of heterometal substituted Lindqvist-type structures has been investigated. Both $(TBA)_3[(MeO)TiW_5O_{18}]$ (ref 74) and $(TBA)_3[(^iPrO)TiMo_5O_{18}]$ (ref 75) were treated with a range of alcohols, and water, to gain insight into ligand exchange reactivity at the heterometal centre. Treatment of $(TBA)_3[(RO)TiM_5O_{18}]$ with aliphatic alcohols R'OH (when M = W, R = Me and R' = Et, ^iPr, ^tBu, when M = Mo, R = ^iPr and R' = Me, ^tBu) allowed exchange of the native MeO or ^iPrO groups for the respective R'O groups. In general, substitution for more sterically demanding R' groups proceeded more slowly. Comparison of the series {TiMo$_5$}, {TiW$_5$}, and {ZrW$_5$} (ref 68) found that the OR group of {TiMo$_5$} was significantly less labile than that of either {TiW$_5$} or {ZrW$_5$}. This is surprising as polyoxomolybdates are often regarded as more labile with respect to oxygen exchange than polyoxotungstates.[74]

A similar study was also carried out with several phenols which behaved similarly to aliphatic alcohols.[74,75] The reaction of $(TBA)_3[(MeO)TiW_5O_{18}]$ with hydroquinone produced a mixture of the monomeric $(TBA)_3[(4-HOC_6H_4O)TiW_5O_{18}]$ and the 1,4-benzenediolate bridged dimer $(TBA)_6[(\mu-OC_6H_4O)(TiW_5O_{18})_2]$. The monomeric species forms hydrogen bonded chains in which the terminal -OH group of one complex interacts with a terminal W=O of another complex, as shown in **Figure 1.10**. The monomeric species can be favoured by dropwise addition of the POM solution (i.e. $(TBA)_3[(MeO)TiW_5O_{18}]$ in MeCN) to a two-fold excess of the phenol in MeCN.[74]
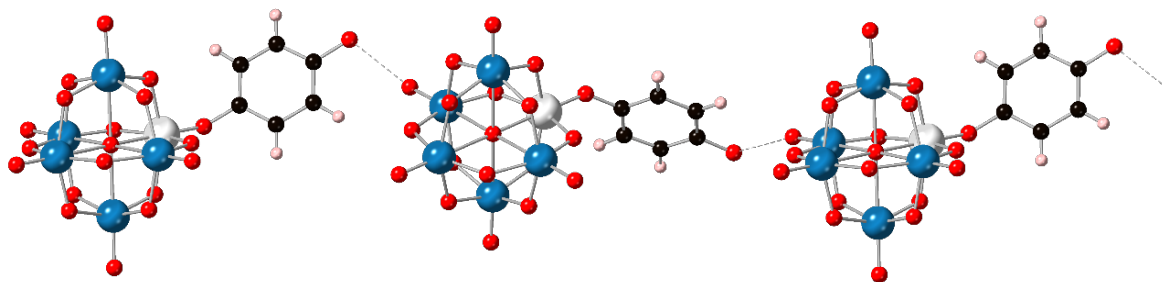
Figure 1.10: Hydrogen bonded chain of $(TBA)_3[(4-HOC_6H_4O)TiW_5O_{18}]$. The distance between the oxygen of the terminal OH of the coordinated quinol and the terminal W=O is 2.72 Å (ref 74).

Treatment of $(TBA)_3[(MeO)TiW_5O_{18}]$ and $(TBA)_3[(^iPrO)TiMo_5O_{18}]$ with water led to the isolation of dimeric $(TBA)_6[(TiM_5O_{18})_2O]$ (M = W or Mo), as opposed to the terminal hydroxide species. Unlike $(TBA)_4[(NbW_5O_{18})_2O]$, which has a linear Nb-O-Nb bond, and the Lindqvist units eclipsed, the Ti-O-Ti bridge is bent for both TiW_5 and $TiMo_5$ (Ti-O-Ti angle is 173.1° for TiW_5 and 173.2 for $TiMo_5$) and the Lindqvist units are not eclipsed.[74,75]

Comparison of the reactivity discussed above with that of $(TBA)_3[(MeO)SnW_5O_{18}]$ ($\{SnW_5\}$) showed that the nature of the Ti-OR and Sn-OR bonds is substantially different.[76] The availability of the lower energy 3d orbitals of Ti allows O→Ti π-bonding, which in turn leads to a higher degree of covalency in the Ti-OR bond compared to that of Sn-OR. This effect appears to dominate over the difference in electronegativity of Ti and Sn (Pauling electronegativities of 1.54 and 1.96 respectively) which may point towards more ionic Ti-OR bond. DFT calculations support a more ionic Sn-OR bond, with calculated electrostatic potentials showing a larger localisation of negative charge on the oxygen of the OR group in $[RO-SnW_5O_{18}]^{3-}$.[76] These differences in the nature of the bonding appear to manifest themselves in the increased hydrolytic sensitivity of the M-OR bond in $\{SnW_5\}$.[76]

1.4.4 Heterometal Containing Keggin Structures

As seen previously, the Keggin structure is extremely common in the POM literature. This popularity has not been limited to the aqueous phase, with heterometal containing Keggin-type POMs being very well documented in organic solvents. Most synthetic routes to heterometal containing Keggin species involve synthesis of the heterometal containing POM in aqueous solvent followed by a phase transfer step. For example, using methods originally outlined by Simmons for the aqueous synthesis of $[(H_2O)CoSiW_{11}O_{39}]^{6-}$ (ref 77 and ref 78), Katsoulis and Pope described the subsequent phase transfer of the cluster into organic solvent by shaking an aqueous solution of the POM and a toluene solution of tetra-*n*-heptylammonium bromide.[79] This process of cation exchange was originally developed by Corigliano and Di Pasquale to acquire IR spectra of polyoxovanadates in non-polar solvents.[80] Interestingly, upon transfer into organic solvent the facile loss of the coordinated H_2O molecule can be observed to produce a suggested penta-coordinated cobalt species (equilibrium shown in **Equation 1.7**).

$$[(H_2O)CoSiW_{11}O_{39}]^{6-} \leftrightharpoons [(\_)CoSiW_{11}O_{39}]^{6-} + H_2O \qquad (1.7)$$
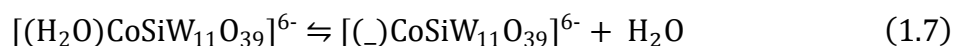
Upon loss of the coordinated water molecule, a colour change from pink/red to green is observed and this equilibrium can be pushed towards the apparent penta-coordinate species

by drying of the solution (e.g. with molecular sieves).[79] The red colour returns upon addition of a donor ligand, like alcohols or pyridine, suggesting the formation of 6-coordinate cobalt species with the form $[(L)CoSiW_{11}O_{39}]^{6-}$.[79] The ease of conversion between the 6-coordinate species (H_2O bound) and the apparent 5-coordinate (anhydrous) species appears to vary with the central atom, and the P-containing analogue ($[(H_2O)CoPW_{11}O_{39}]^{5-}$) remains red (implying it remains 6-coordinate) regardless of how dry the solution is.[79,81] A recent study has implicated the formation of dimers, analogous to the cobalt containing Lindqvist-type species, $[(CoW_5O_{18}H)_2]^{6-}$, mentioned previously, to account for this observation. It is worth noting that upon removal of solvent a green solid forms.[81]

This phase transfer approach to synthesis of heterometal containing POMs with the appropriate cations required to solubilise the cluster in organic solvent has also been used to synthesise Keggin clusters containing manganese[82a], nickel[82b], iron[82c], copper[82d], and rhenium.[82e]

A related strategy was used by Pope to isolate a series of high-valent manganese containing Keggin structures.[83] This route involves electrolytic or chemical oxidation followed by precipitation using a tetraalkylammonium salt. The electrochemical method required dissolution of the potassium salt $K_8[ZnMn(II)(H_2O)W_{11}O_{39}].23H_2O$ in a 0.2 M potassium acetate-acetic acid buffer. It was then electrolysed at 1.05 V vs. SCE (saturated calomel electrode) to produce the corresponding Mn(IV) cluster $K_7[ZnMn(IV)(OH)W_{11}O_{39}].19H_2O$.[83] This cluster could then be precipitated via addition of tetra-*n*-hexylammonium chloride to produce the organic-soluble salt. The compound was purified by dissolution in acetonitrile followed by reprecipitation with water.[83] The analogous reaction was performed by addition $K_2S_2O_8$ (the oxidant) to a solution of $K_8[ZnMn(II)(H_2O)W_{11}O_{39}].23H_2O$ in water, followed by heating to 90°C. The tetraalkylammonium salts can be isolated by precipitation or extraction into hexanes.[83]

1.4.5 Synthesis of Larger Structures

The synthetic procedures required to synthesise other, less common, clusters in organic media largely mirrors those outlined so far, either using specific organic-soluble reagents with the appropriate cations required for synthesis in organic solvent, as discussed in **Sections 1.4.1** and **1.4.3**, or using the techniques outlined in **Section 1.3** for synthesis in aqueous media followed by a phase transfer. The phase transfer approach appears more popular for larger clusters.[84]

A 2013 study by Cronin *et al* illustrates this point.[84] They outline a general strategy for the phase transfer of the water-soluble alkali metal salts of a series POMs (including $K_6[\alpha-P_2W_{18}O_{62}].14H_2O$ (Wells-Dawson), $K_{12.5}Na_{1.5}[NaP_5W_{30}O_{110}].15H_2O$ (Preyssler), and $K_{28}Li_5[H_7P_8W_{48}O_{184}].92H_2O$) into organic solvent.

The process involves dissolution of the alkali metal salt in water and acetonitrile followed by addition of tetrabutylammonium bromide. The solution is then acidified to pH 1.5 through the addition of 4.5 M H_2SO_4, which led to the formation of an oily layer that contains POMs, tetrabutylammonium cations, protons, and acetonitrile. This layer is then separated using a pipette and centrifugation, followed by washing with water and ethanol to remove any remaining acetonitrile.[84] This leads to isolation of the clusters as the tetrabutylammonium salts, though some of the larger clusters can also contain H^+ counter ions. This work is clearly very similar to the earlier work by Katsoulis[79] and Corigliano[80] already discussed.

1.5 Summary

The synthetic procedures commonly used to produce a range of POM clusters in both aqueous and organic solvents have been outlined. It is apparent that the strategies employed are similar regardless of the target structure and interconversion between POM clusters by either degradation in the presence of base or condensation/aggregation in the presence of acid is common. Incorporation of heterometals is typically achieved by taking a lacunary POM, either as an isolated intermediate or virtual precursor, as a template in combination with a heterometal precursor. The analogous organic-soluble clusters are easily isolated either by exchanging the cations of water-soluble POMs, typically Na^+ or K^+, for bulky tetraalkylammonium cations or by using organic-soluble building blocks.

The examples given are far from exhaustive, but it is hoped that the overview given will allow the reader to understand the key factors to consider when attempting to rationally synthesise POM species.

References

1. V. W. Day and W. G. Klemperer, *Science*, 1985, **228**, 533–541.

2. M. T. Pope, *in Polyoxometalate Molecular Science*, Springer Netherlands, Dordrecht, 2003, pp. 3–31.

3. J. J. Berzelius, *Ann. Phys.*, 1826, **82**, 369–392.

4. M. T. Pope and A. Müller, *Angew. Chem. Int. Ed. Engl.*, 1991, **30**, 34–48.

5. J. F. Keggin, *Nature (London)*, 1933, **131**, 908; *Proc. R. Soc. London, Ser. A*, 1934, 144, 75.

6. G. Hervé, A. Tézé and R. Contant, *in Polyoxometalate Molecular Science*, Springer Netherlands, Dordrecht, 2003, pp. 33–54.

7. R. J. Errington, *in Polyoxometalate Molecular Science*, Springer Netherlands, Dordrecht, 2003, pp. 55–78.

8. D. D. Dexter and J. V. Silverton, *J Am. Chem. Soc.*, 1968, **90**, 3589-3590.

9. T. Z. Forbes, J. G. McAlpin, R. Murphy and P. C. Burns, *Angew. Chem. Int. Ed.*, 2008, **47**, 2824–2827.

10. G. E. Sigmon, D. K. Unruh, J. Ling, B. Weaver, M. Ward, L. Pressprich, A. Simonetti and P. C. Burns, *Angew. Chem. Int. Ed.*, 2009, **48**, 2737–2740.

11. M. T. Pope, *Inorg. Chem.*, 1972, **11**, 1973–1974.

12. J. M. Maestre, X. Lopez, C. Bo, J.-M. Poblet and N. Casañ-Pastor, *J. Am. Chem. Soc.*, 2001, **123**, 3749–3758.

13. J. M. Poblet, X. López and C. Bo, *Chem. Soc. Rev.*, 2003, **32**, 297–308.

14. N. I. Gumerova and A. Rompel, *Nat. Rev. Chem.*, 2018, **2**, 112.

15. a) J. M. Maestre, J. M. Poblet, C. Bo, N. Casañ-Pastor and P. Gomez-Romero, *Inorg. Chem.*, 1998, **37**, 3444–3446. b) J. M. Maestre, X. Lopez, C. Bo, J.-M. Poblet and N. Casañ-Pastor, *J. Am. Chem. Soc.*, 2001, **123**, 3749–3758. c) X. López, C. Bo and J. M. Poblet, *J. Am. Chem. Soc.*, 2002, **124**, 12574–12582. d) X. López, C. de Graaf, J. M. Maestre, M. Bénard, M.-M. Rohmer, C. Bo and J. M. Poblet, *J. Chem. Theory Comput.*, 2005, **1**, 856–861. e) Y. Nishimoto, D. Yokogawa, H. Yoshikawa, K. Awaga and S. Irle, *J. Am. Chem. Soc.*, 2014, **136**, 9042–9052.

16. C. L. Hill and C. M. Prosser-McCartha, *Coord. Chem. Rev.*, 1995, **143**, 407–455.

17. A. Proust, R. Thouvenot and P. Gouzerh, *Chem. Commun.*, 2008, 1837–1852.

18. K. Kamata, K. Yonehara, Y. Nakagawa, K. Uehara and N. Mizuno, *Nat. Chem.*, 2010, **2**, 478–483.

19. H. D. Pratt, N. S. Hudak, X. Fang and T. M. Anderson, *J. Power Sources*, 2013, **236**, 259–264.

20. Y. Ji, L. Huang, J. Hu, C. Streb and Y. F. Song, *Energy Environ. Sci.*, 2015, 8, 776–789.

21. J. Lehmann, A. Gaita-Arino, E. Coronado and D. Loss, *Nat. Nanotechnol.*, 2007, **2**, 312–317.

22. B. Botar, A. Ellern, R. Hermann and P. Kögerler, *Angew. Chem. Int. Ed.*, 2009, **48**, 9080–9083.

23. J. M. Clemente-Juan, E. Coronado and A. Gaita-Ariño, *Chem. Soc. Rev.*, 2012, 41, 7464–7478.

24. D. L. Long, E. Burkholder and L. Cronin, *Chem. Soc. Rev.*, 2007, 36, 105–121.

25. A. Proust, R. Thouvenot and P. Gouzerh, *Chem. Commun.*, 2008, 1837–1852.

26. J. Wang, Y. Liu, K. Xu, Y. Qi, J. Zhong, K. Zhang, J. Li, E. Wang, Z. Wu and Z. Kang, *ACS Appl. Mater. Interfaces*, 2014, **6**, 9785–9789.

27. L. Fu, H. Gao, M. Yan, S. Li, X. Li, Z. Dai and S. Liu, *Small*, 2015, **11**, 2938–2945.

28. a) Q. Yin, J. M. Tan, C. Besson, Y. V. Geletii, D. G. Musaev, A. E. Kuznetsov, Z. Luo, K. I. Hardcastle and C. L. Hill, *Science*, 2010, **328**, 342–345. b) S. Goberna-Ferrón, L. Vigara, J. Soriano-López and J. R. Galán-Mascarós, *Inorg. Chem.*, 2012, **51**, 11707–11715. c) S. Goberna-Ferrón, J. Soriano-López and J. Galán-Mascarós, *Inorganics*, 2015, **3**, 332–340. d) Q. Yin and C. L. Hill, *Nat. Chem.*, 2017, 10, 6–7. e) M. Blasco-Ahicart, J. Soriano-López, J. J. Carbó, J. M. Poblet and J. R. Galan-Mascaros, *Nat. Chem.*, 2018, **10**, 24–30. F) K. Azmani, M. Besora, J. Soriano-López, M. Landolsi, A.-L. Teillout, P. de Oliveira, I.-M. Mbomekallé, J. M. Poblet and J.-R. Galán-Mascarós, *Chem. Sci.*, 2021, **12**, 8755-8766.

29. L. Pettersson, I. Andersson, L.-0. Ohman, *Inorg. Chem.*, 1986, **25**, 4726-4733.

30. W. G. Klemperer, *Inorg. Synth.*, 1990, **27**, 71-135.

31. A. Patel, N. Narkhede, S. Singh and S. Pathan, *Catal. Rev.*, 2016, **58**, 337–370.

32. L. C. W. Baker, V. S. Baker, K. Eriks, M. T. Pope, M. S. Orville, W. Rollins, J. H. Fang and L. L. Koh, *J. Am. Chem. Soc.*, 1966, **88**, 2329–2331.

33. L. C. W. Baker and J. S. Figgis, *J. Am. Chem. Soc.*, 1970, **92**, 3794–3797.

34. G. Herve and A. Teze, *Inorg. Chem.*, 1977, **16**, 2115–2117.

35. A. Tézé and G. Hervé, *J. Inorg. Nucl. Chem.*, 1977, **39**, 999–1002.

36. J. Canny, A. Teze, R. Thouvenot and G. Herve, *Inorg. Chem.*, 1986, **25**, 2114–2119.

37. C. Rong and M. T. Pope, *J. Am. Chem. Soc.*, 1992, **114**, 2932–2938.

38. M. Sadakane, M. H. Dickman and M. T. Pope, *Angew. Chem. Int. Ed.*, 2000, **39**, 2914–2916.

39. X. Feng, W. Zhou, Y. Li, H. Ke, J. Tang, R. Clérac, Y. Wang, Z. Su and E. Wang, *Inorg. Chem.*, 2012, **51**, 2722–2724.

40. M. Yuan, Y. Li, E. Wang, C. Tian, L. Wang, C. Hu, N. Hu and H. Jia, *Inorg. Chem.*, 2003, **42**, 3670–3676.

41. a) J.E. Lyons, P.E. Ellis Jr., H.K. Myers Jr., G. Suld and W.A. Langdale, U.S. Patent 4,803,187, Feb. 7, 1989. b) J.E. Lyons, P.E. Ellis, Jr. and V.A. Durante, in R.A. Grasselli and A.W. Sleight (eds.), *Stud. Surf. Sci. Catal.*, Elsevier Scientific, Amsterdam, 1991, p. 99 c) M. Bressan, A. Morvillo and G. Romanello, *J. Mol. Catal.*, 1992, **77**, 283–288. d) M. Sadakane, D. Tsukuma, M. H. Dickman, B. Bassil, U. Kortz, M. Higashijima and W. Ueda, *J. Chem. Soc. Dalton Trans.*, 2006, 4271–4276.

42. a) A. N. Kharat, P. Pendleton, A. Badalyan, M. Abedini and M. M. Amini, *J. Mol. Catal. A Chem.*, 2001, **175**, 277–283. c) S. Vanhaecht, G. Absillis and T. N. Parac-Vogt, *Dalton Trans.*, 2012, **41**, 10028–10034. d) N. Gao, H. Sun, K. Dong, J. Ren, T. Duan, C. Xu and X. Qu, *Nat. Commun.*, 2014, **5**, 1–9.

43. C. L. Hill and C. M. Prosser-McCartha, *Coord. Chem. Rev.*, 1995, **143**, 407–455.

44. L. E. Briand, G. T. Baronetti and H. J. Thomas, *Appl. Catal. A Gen.*, 2003, **256**, 37–50

45. S. T. Zheng and G. Y. Yang, *Chem. Soc. Rev.*, 2012, **41**, 7623–7646.

46. J. W. Zhao, Y. Z. Li, L. J. Chen and G. Y. Yang, *Chem. Commun.*, 2016, **52**, 4418–4445.

47. a) J. Wang, P. Ma, Y. Shen and J. Niu, *Cryst. Growth Des.*, 2008, **8**, 3130–3133. b) Z. Luo, P. Kögerler, R. Cao and C. L. Hill, *Inorg. Chem.*, 2009, **48**, 7812–7817. c) J. Zhao, P. Ma, J. Wang and J. Niu, *J. Clust. Sci.*, 2009, **20**, 671. d) S. Reinoso and J. R. Galán-Mascarós, *Inorg. Chem.*, 2010, **49**, 377–379. e) S. Reinoso, J. R. Galán-Mascarós and L. Lezama, *Inorg. Chem.*, 2011, **50**, 9587–9593.

48. C. Xia, S. Zhang, D. Sun, B. Jiang, W. Wang and X. Xin, *Langmuir*, 2018, **34**, 6367–6375.

49. T. J. R. Weakley, H. T. Evans, J. S. Showell, G. F. Tourné and C. M. Tourné, *J. Chem. Soc., Chem. Commun.*, 1973, 139–140.

50. a) Y. Duan, J. M. Clemente-Juan, J. L. G. Fierro, C. Giménez-Saiz and E. Coronado, *Chem. Commun.*, 2016, **52**, 13245–13248. b) M. Martin-Sabi, J. Soriano-López, R. S. Winter, J. J. Chen, L. Vilà-Nadal, D. L. Long, J. R. Galán-Mascarós and L. Cronin, *Nat. Catal.*, 2018, **1**, 208–213.

51. X. Zhang, T. M. Anderson, Q. Chen and C. L. Hill, *Inorg. Chem.*, 2001, **40**, 418–419.

52. M. Dabbabi and M. Boyer, *J. Inorg. Nucl. Chem.*, 1976, **38**, 1011–1014.

53. X. López, C. Bo and J. M. Poblet, *J. Am. Chem. Soc.*, 2002, **124**, 12574–12582.

54. J. T. Rhule, C. L. Hill, D. A. Judd and R. F. Schinazi, *Chem. Rev.*, 1998, **98**, 327–357.

55. H. D. Pratt and T. M. Anderson, *Dalton Trans.*, 2013, **42**, 15650–15655.

56. M. Martin-Sabi, J. Soriano-López, R. S. Winter, J. J. Chen, L. Vilà-Nadal, D. L. Long, J. R. Galán-Mascarós and L. Cronin, *Nat. Catal.*, 2018, **1**, 208-213.

57. M. K. Harrup, G. S. Kim, H. Zeng, R. P. Johnson, D. Vanderveer and C. L. Hill, *Inorg. Chem.*, 1998, **37**, 5550–5556.

58. S. Rondinini, *Anal. Bioanal. Chem.*, 2002, **374**, 813–816.

59. J. Soriano-López, S. Goberna-Ferrón, L. Vigara, J. J. Carbó, J. M. Poblet and J. R. Galán-Mascarós, *Inorg. Chem.*, 2013, **52**, 4753–4755.

60. K. Y. Matsumoto, A. Kobayashi and Y. Sasaki, *Bull. Chem. Soc. Jpn.*, 1975, **48**, 3146–3151.

61. R. J. Errington, S. S. Petkar, P. S. Middleton, W. McFarlane, W. Clegg, R. A. Coxall and R. W. Harrington, *J. Chem. Soc., Dalton Trans.*, 2006, 5211–5222.

62. T. M. Che, V. W. Day, L. C. Francesconi, M. F. Fredrich, W. G. Klemperer and W. Shum, *Inorg. Chem.*, 1985, **24**, 4055–4062.

63. W. Clegg, R. J. Errington, K. A. Fraser and D. G. Richards, *J. Chem. Soc., Chem. Commun.*, 1993, 1105–1107.

64. R. Calmanti, M. Selva and A. Perosa, *Mol. Catal.*, 2020, **486**, 110854.

65. H. Nakayama, *Bull. Chem. Soc. Jpn.*, 1983, **56**, 877–880.

66. a) K. F. Jahr and J. Fuchs, *Chem. Ber.*, 1963, 96, 2457–2459. b) K. F. Jahr and J. Fuchs, *Angew. Chem., Int. Ed. Engl.*, 1966, **9**, 689–750. C) K. F. Jahr, J. Fuchs and R. Oberhauser, *Chem. Ber.*, 1968, **101**, 477–481.

67. W. Clegg, R. J. Errington, P. Kraxner and C. Redshaw, *J. Chem. Soc., Dalton Trans.*, 1992, 1431–1438.

68. R. J. Errington, S. S. Petkar, P. S. Middleton, W. McFarlane, W. Clegg, R. A. Coxall and R. W. Harrington, *J. Am. Chem. Soc.*, 2007, **129**, 12181–12196.

69. M. Filowitz, R. K. C. Ho, W. G. Klemperer and W. Shum, *Inorg. Chem.*, 1979, **18**, 93–103.

70. W. Clegg, M. R. J. Elsegood, R. J. Errington and J. Havelock, *J. Chem. Soc., Dalton Trans.*, 1996, 681-690.

71. B. Kandasamy, C. Wills, W. McFarlane, W. Clegg, R. W. Harrington, A. Rodríguez-Fortea, J. M. Poblet, P. G. Bruce and R. J. Errington, *Chem. - A Eur. J.*, 2012, **18**, 59–62.

72. R. J. Errington, L. Coyle, P. S. Middleton, C. J. Murphy, W. Clegg and R. W. Harrington, *J. Clust. Sci.*, 2010, **21**, 503–514.

73. R. J. Errington, G. Harle, W. Clegg and R. W. Harrington, *Eur. J. Inorg. Chem.*, 2009, **2009**, 5240–5246.

74. R. J. Errington, S. S. Petkar, P. S. Middleton, W. McFarlane, W. Clegg, R. A. Coxall and R. W. Harrington, *J. Chem. Soc. Dalton Trans.*, 2006, 5211–5222.

75. L. Coyle, P. S. Middleton, C. J. Murphy, W. Clegg, R. W. Harrington and R. J. Errington, *Dalton Trans.*, 2012, **41**, 971–981.

76. B. Kandasamy, P. G. Bruce, W. Clegg, R. W. Harrington, A. Rodríguez-Fortea, M. Pascual-Borrás and R. J. Errington, *Chem. - A Eur. J.*, 2018, **24**, 2750–2757.

77. Simmons, V. E.; Baker, L. C. W. Proc. VII Intl. Conf. Coord. Chem. Stockholm 1962, 195.

78. J. W. Zhao, Y. Z. Li, L. J. Chen and G. Y. Yang, *Chem. Commun.*, 2016, **52**, 4418–4445.

79. D. E. Katsoulis and M. T. Pope, *J. Am. Chem. Soc.*, 1984, **106**, 2737–2738.

80. F. Corigliano and S. Di Pasquale, *Inorg. Chim. Acta*, 1975, **12**, 99–101.

81. A. Dannenhoffer, J. Baker, N. Pantano, J. Stachowski, D. Zemla, W. Swanson, E. Zurek, S. Szczepankiewicz and M. Kozik, *J. Coord. Chem.*, 2014, **67**, 2830–2842.

82. a) D. E. Katsoulis and M. T. Pope, *J. Chem. Soc., Dalton Trans.*, 1989, 1483–1489. b) M. T. Colvin, M. Kozik and S. H. Szczepankiewicz, *J. Phys. Chem. B*, 2006, **110**, 10576–10580. c) F. Zonnevijlle, C. M. Tourne and G. F. Tourne, *Inorg. Chem.*, 1982, **21**, 2751–2757. d) S. H. Szczepankiewicz, C. M. Ippolito, B. P. Santora, T. J. Van de Ven, G. A. Ippolito, L. Fronckowiak, F. Wiatrowski, T. Power and M. Kozik, *Inorg. Chem.*, 1998, **37**, 4344–4352. e) F. Ortega and M. T. Pope, *Inorg. Chem.*, 1984, **23**, 3292–3297.

83. X.-Y. Zhang, M. T. Pope, M. R. Chance and G. B. Jameson, *Polyhedron*, 1995, **14**, 1381–1392.

84. D. Gabb, C. P. Pradeep, T. Boyd, S. G. Mitchell, H. N. Miras, D.-L. Long and L. Cronin, *Polyhedron*, 2013, **52**, 159–164.

Chapter 2: Refining the synthesis of (TBA)$_6$[(CoW$_5$O$_{18}$H)$_2$]

2.1 Introduction

After previously reporting non-aqueous synthetic routes to a series of early transition metal containing Lindqvist-type POMs, namely those containing Ti, Zr, V, and Nb[1-3], our group set out to extend the family of heterometal containing Lindqvist-type POMs to the later first-row transition metals. Later transition metal containing POMs can act as molecular models for important metal oxide materials which are commonly applied in heterogeneous catalysis.[4-6] These relatively small molecular models are more readily characterised using solution-state spectroscopy, e.g. NMR spectroscopy, and have well-defined "active sites" which can be efficiently modelled using computational methods (in particular density functional (DFT) theory calculations), with relatively low computational cost.

Numerous cobalt substituted POMs are known and, importantly, have shown potential as highly active water-oxidation catalysts.[7-12] Most of these POMs contain multiple cobalt centres in the +2 or +3 (d^7 or d^6 respectively) oxidation state bound to multiple bridging metal-oxo groups (and sometimes water). In this weak field ligand environment the cobalt centres tend to be high-spin (this can be experimentally verified using magnetic measurements or NMR spectroscopy)[12] and therefore each possesses multiple unpaired electrons. The potential for interaction between these unpaired electrons makes the modelling of these systems with DFT difficult. Given this challenge, a system containing one or two, well defined, cobalt centres incorporated into a small POM structure would serve as a more manageable system to model both the catalytic activity of cobalt containing POMs, and more generally of cobalt-containing metal oxide materials. With this in mind our group targeted the synthesis of a cobalt substituted Lindqvist-type POM with the general formula [(L)Co(II)W$_5$O$_{18}$]$^{4-}$, where L = a neutral donor.

When synthesising early transition metal containing Lindqvist-type structures (focusing on the polyoxotungstates), our group used an approach based on the hydrolysis of WO(OMe)$_4$ and the heterometal alkoxide in the presence of (TBA)$_2$[WO$_4$] (TBA = tetrabutylammonium), as shown in **Equation 2.1** for titanium.[2]

$$3 \text{ (TBA)}_2[\text{WO}_4] + 7 \text{ WO(OMe)}_4 + 2 \text{ Ti(OMe)}_4 + 17 \text{ H}_2\text{O} \rightarrow$$
$$2 \text{ (TBA)}_3[\text{(MeO)TiW}_5\text{O}_{18}] + 34 \text{ MeOH} \qquad (2.1)$$
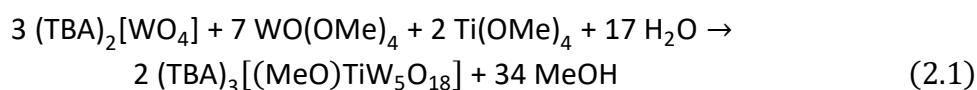
This methodology can be rationalised in terms of generating a "virtual" lacunary $\{W_5O_{18}\}$ unit that is poised to accept a "Ti-OMe" fragment to fill the vacancy and return the complete Lindqvist structure (as shown in **Equations 2.2** and **2.3**). The reaction likely proceeds via a complex mixture of intermediates in equilibrium and the stability of the complete Lindqvist structure gives a thermodynamic driving force which pushes the reaction to completion.

$$3\ (TBA)_2[WO_4] + 7\ WO(OMe)_4 + 17\ H_2O \rightarrow 2\ "(TBA)_3[W_5O_{18}H_3]" + 28\ MeOH \qquad (2.2)$$

$$"(TBA)_3[W_5O_{18}H_3]" + Ti(OMe)_4 \rightarrow (TBA)_3[(MeO)TiW_5O_{18}] + 3\ MeOH \qquad (2.3)$$
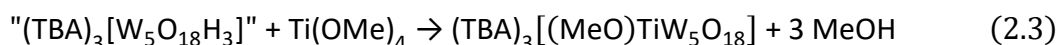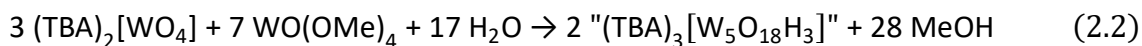
A similar approach, involving the generation of a "virtual" lacunary precursor was used in the synthesis of $(TBA)_7[(CoW_5O_{18}H)_2][X]$ (where X = BF_4 or Cl).[14] In this example, $WO(OMe)_4$ was hydrolysed in the presence of tetrabutylammonium tungstate and the product was isolated. This product was then subsequently reacted with a cobalt salt, either $[Co(MeCN)_4(H_2O)_2](BF_4)_2$ or $CoCl_2$, to generate the cobalt containing Lindqvist structure (as shown in **Equations 2.4** and **2.5**). It should be noted that X-ray crystallographic studies, FTIR spectroscopy and elemental analysis all supported the formula $(TBA)_7[(CoW_5O_{18}H)_2][X]$ and no effort was made to remove the additional TBA(X) salt.

$$3\ (TBA)_2[WO_4] + 2\ WO(OMe)_4 + 4\ H_2O \rightarrow "(TBA)_6[W_5O_{18}]" + 8\ MeOH \qquad (2.4)$$

$$2\ "(TBA)_6[W_5O_{18}]" + 2\ CoX_2\ (+\ 2\ H^+) \rightarrow (TBA)_6[(CoW_5O_{18}H)_2] + 4\ TBA(X)\ (+\ 2\ TBA^+) \qquad (2.5)$$
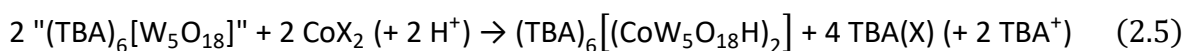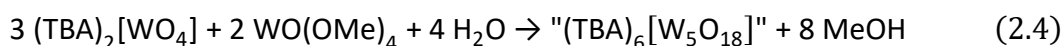
The routes outlined above, used to synthesise heterometal containing Lindqvist-type structures, all exploit the hydrolysis of $WO(OMe)_4$. Though this route has proved effective, the use of the tungsten alkoxide is not ideal. Firstly, it is highly moisture sensitive and can easily decompose into insoluble tungsten oxide if mishandled. Secondly, the synthesis of $WO(OMe)_4$ (synthesis outlined in **Chapter 3**) uses toxic reagents. The synthesis of $WOCl_4$, a precursor, requires the use of large quantities of thionyl chloride and the conversion of the oxychloride to the alkoxide requires the use of gaseous ammonia, neither of which are considered environmentally friendly. It would therefore be beneficial to have a more user-friendly approach to the synthesis of heterometal containing Lindqvist-type POMs.

2.2 Chapter outline

This chapter describes an alternative approach for the synthesis of first-row transition metal substituted Lindqvist-type POMs. The synthesis of $(TBA)_7[(CoW_5O_{18}H)_2][X]$ was used as a

model system as the previously obtained characterisation data could be used comparatively as an indicator of success.

Once evidence of the formation of the crude product was obtained, the synthetic approach was optimised in terms of simplicity and the purity of the final product, with a particular focus on whether removal/minimisation of the additional TBA(X) present in the previously reported product is possible.

The ability to access large quantities (i.e. tens of grams) of the dimeric product then allowed preliminary reactivity studies to be carried out. Initially, this focused on adduct formation, as the ability to access the cobalt centre is a key criterion for heterometal centred reactivity.

2.3 A degradative reassembly approach

A common approach used in the synthesis of heterometal substituted POMs is to first treat the unsubstituted parent POM with base to produce the lacunary species (which has one or more vacancies).[15] This is then reacted with a simple heterometal salt which essentially plugs the vacancies and reforms the stable parent structure but now with one or more heterometals present in the framework.[16] This approach has been used by our group to produce $(TBA)_5[CoPW_{11}O_{39}]$ from the parent $Na_3[PW_{12}O_{40}]$ via treatment with TBA(OH) and then $CoCl_2$, as shown in **Equations 2.6** and **2.7**.[15]

$$Na_3[PW_{12}O_{40}] + 6\ TBA(OH) \rightarrow (TBA)_6[NaPW_{11}O_{39}] + Na_2WO_4 + 3\ H_2O \qquad (2.6)$$

$$TBA_6[NaPW_{11}O_{39}] + CoCl_2 \rightarrow (TBA)_5[CoPW_{11}O_{39}] + NaCl + TBA(Cl) \qquad (2.7)$$

These methods commonly involve isolation and characterisation of the intermediate lacunary species, although this is not a requirement. Rather than isolating the lacunary species, a "virtual" lacunary species can be generated and used directly in subsequent reactions without isolation. This may be advantageous if isolation (and characterisation) of the lacunary species in question proves difficult, or in the development of one-pot procedures.

It was therefore theorised that treatment of $[W_6O_{19}]^{2-}$ (the parent Lindqvist anion) with base could be used to produce the "virtual" lacunary species "$[W_5O_{18}H]^{5-}$" for direct reaction with a cobalt salt to produce the cobalt containing Lindqvist-type POM (**Equations 2.8** and **2.9**).

$$5\ (TBA)_2[W_6O_{19}] + 20\ TBA(OH) \rightarrow 6\ "(TBA)_5[W_5O_{18}H]" + 7\ H_2O \qquad (2.8)$$

$$2\ "(TBA)_5[W_5O_{18}H]" + 2\ Co(NO_3)_2.6H_2O \rightarrow (TBA)_6[(CoW_5O_{18}H)_2] + 4\ TBA(NO_3) \qquad (2.9)$$
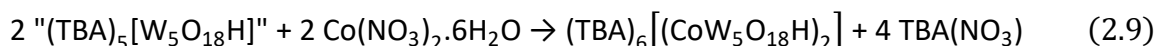
2.3.1 Synthesis

Experimentally, this process involves suspending $(TBA)_2[W_6O_{19}]$ in acetonitrile and then adding a solution of four equivalents of TBA(OH) in acetonitrile. Stirring the resulting mixture at room temperature slowly led to the complete dissolution of the $(TBA)_2[W_6O_{19}]$ as it reacted with the base and produced more highly charged species. Once the mixture was homogenous, cobalt(II) nitrate hexahydrate was added (the nitrate was used as it provides a characteristic peak in the infrared spectrum to check for the presence of nitrate in the product), upon which the reaction mixture slowly turned dark blue/purple. The reaction was also attempted with cobalt chloride, cobalt bromide and cobalt acetate with no change in outcome. The crude product was isolated by removal of the solvent under dynamic vacuum, which led to the formation of a thick blue oil. This oil was triturated with ethyl acetate and diethyl ether and dried further under vacuum to give a free flowing dark purple/blue powder.

Attempts to precipitate the product directly from the reaction mixture as a powder, via addition of an excess of anti-solvents (either diethyl ether of ethyl acetate), were unsuccessful and only led to the formation of viscous oils. The crude product can be precipitated by removing the reaction solvent, dissolving the thick oil obtained in the minimum amount of acetonitrile or dichloromethane, and then adding the solution dropwise to a large excess of ethyl acetate. This is the work-up of choice for large-scale preparations, where trituration of the oil can take a long time.

2.3.2 Infrared spectroscopy

To determine if the reaction was successful, the infrared spectrum of the crude product was recorded and compared to the previously reported spectrum of $(TBA)_7[(CoW_5O_{18}H)_2][BF_4]$. The results are shown in **Figure 2.1**. The spectra both show intense $v_{W=O}$ bands at 933 cm^{-1}, which is significantly different from that of $(TBA)_2[W_6O_{19}]$ ($v_{W=O}$ = 977 cm^{-1}). They both also show bands at 806, 759, 699 and 666 cm^{-1} which can be assigned to vibrations of the bridging oxygens. The complex bridging region was originally attributed to the protonation of the product which leads to a lower level of symmetry than would be expected for a simple $\{LMW_5O_{18}\}$-type structure.[14] These results suggest that the crude product isolated using this degradative approach is the same as the compound previously reported.
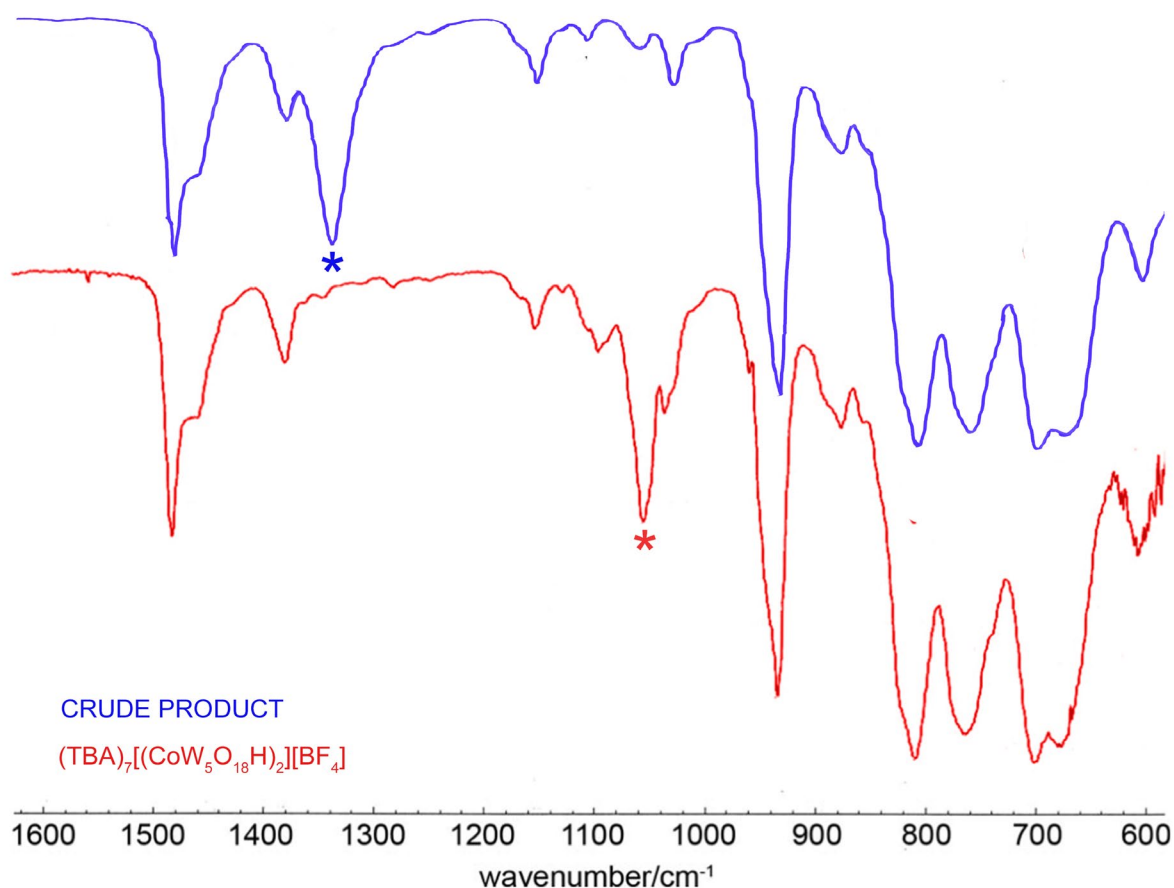
Figure 2.1: ATR FTIR transmittance spectra of the crude product from reaction of $(TBA)_2[W_6O_{19}]$ with TBA(OH) and $Co(NO_3)_2.6H_2O$ (blue), and the previously reported (and characterised) $(TBA)_7[(CoW_5O_{18}H)_2][BF_4]$. (ref 14)

The main differences in the two spectra appear to be a result of the cobalt salts used in the procedure. The previously characterised $(TBA)_7[(CoW_5O_{18}H)_2][BF_4]$ has a peak at 1055 cm^{-1} (marked with a red asterisk) attributed a to B-F stretching vibration. On the other hand, the crude product obtained from this preparation instead has a peak at 1337 cm^{-1} (marked with a blue asterisk). This can be attributed to the N-O stretch of NO_3^-. This supports the presence of $TBA(NO_3)$ in the crude product which perhaps is not surprising given that the previously reported cobalt dimer was not separated from one equivalent of $TBA(BF_4)$.

2.3.3 X-ray diffraction

To further confirm the formation of $(TBA)_6[(CoW_5O_{18}H)_2]$, the crude product was successfully recrystallized, though in very low yields, by slow evaporation of a saturated solution of the product in dichloromethane/toluene. The obtained structure is shown in **Figure 2.2**.

Six tetrabutylammonium cations are associated with the anion shown in **Figure 2.2**, consistent with the formation of the doubly protonated $[(Co(II)W_5O_{18}H)_2]^{6-}$. Further evidence for the protonation of the cage was provided by bond valence sum (BVS) calculations, which suggest these protons are localised on O6 ($V_{O6} = 1.41$) and O25 ($V_{O25} = 1.34$), though these protons are

26
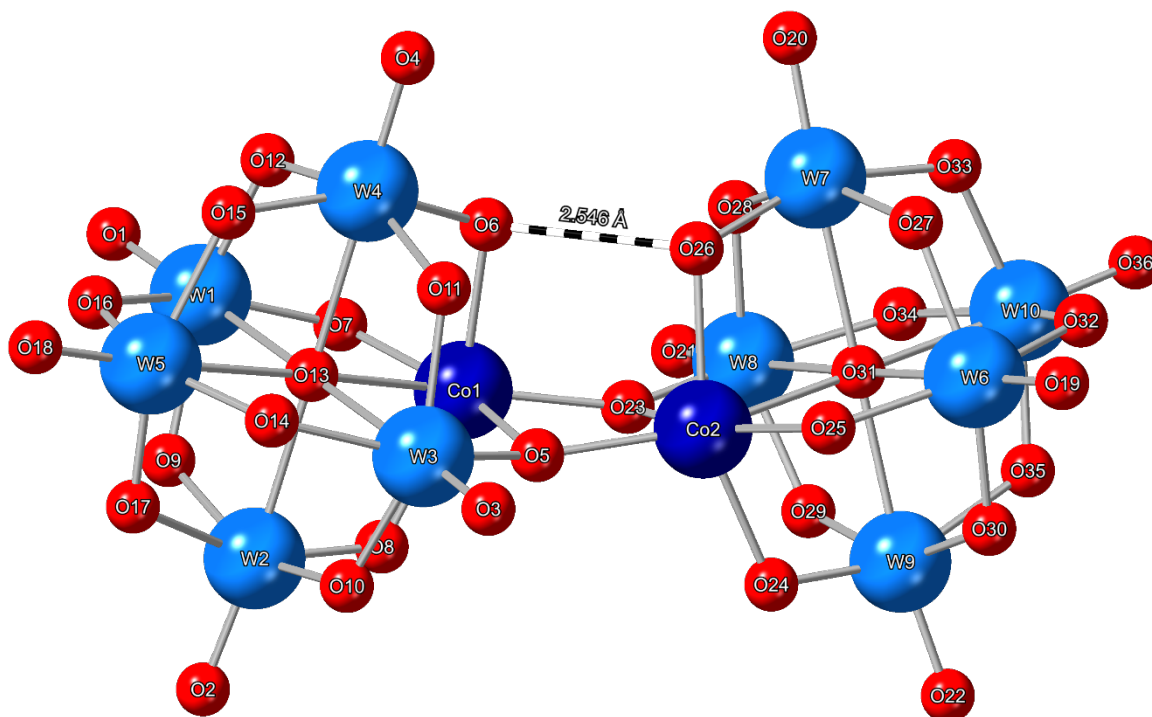
Figure 2.2: Single-crystal X-ray diffraction structure of the $[(CoW_5O_{18}H)_2]^{6-}$ anion, showing the presence of a hydrogen bond between O6 and O26. The atomic radii are set to the CSD covalent radii. Cations are omitted for clarity.

somewhat delocalised across the corresponding oxygens on the other half of the dimer (i.e. O7 (V_{O7} = 1.49) and O26 (V_{O26} = 1.46)). The protonation of O6/O26 leads to a short interatomic distance of ca. 2.55 Å. This is consistent with the formation of a hydrogen bonding interacting which leads to a bend in the dimeric unit. The localisation of a proton on O7/O25 does not lead to any further hydrogen bonding interactions.

The average Co-O bond length, excluding the bond to the central μ_6-oxo, was found to be ca. 2.09 Å. This is significantly longer than the average W-O distance of ca. 1.94 Å. This bond lengthening is likely a consequence of the reduced π-donation from the filled p orbitals of oxygen to now partially filled d-orbitals of cobalt (vs. W^{6+}, d^0), as well as the reduced charge density of cobalt(II) versus tungsten(VI). This relatively long average Co-O bond length is paired with a contraction of the W-O bonds that complete the Co-O-W bridges, which are substantially shorter than the average W-O bond distance at ca. 1.84 Å. This may indicate that the lack of competition for oxygen π-electron density from cobalt leads to increased π-bonding to tungsten in these bridges, and a concomitant shortening of these bonds. Intriguingly, the Co-O bonds between the halves of the dimer (i.e. Co1-O23 and Co2-O5) are shorter, at 2.04(1) Å and 2.02(1) Å respectively, than some of the other internal (i.e. within the Lindqvist unit) Co-O bonds. The longest Co-O bonds are actually between Co1-O5, at 2.19(1) Å, and Co2-O23, at

2.20(2) Å. This may suggest these bonds are weaker and that any chemistry that requires access to the cobalt centre may involve the neighbouring oxygen atoms.

No evidence of nitrate (or an additional TBA cation) was observed in the obtained X-ray structure suggesting either that the nitrate was removed during crystallisation or that it is highly disordered and therefore hard to observe in X-ray diffraction experiments. In order to determine whether the nitrate was still present, the infrared spectrum of the crystalline material was recorded. The infrared spectrum still shows a peak at 1337 cm^{-1}, consistent with the presence of nitrate.

To further prove isolation of the target compound, and assess the bulk purity, the experimental powder X-ray diffraction pattern was obtained and compared to the simulated pattern obtained from the single-crystal X-ray diffraction structure.

Single-crystal X-ray diffraction gives unparalleled structural insight. However, this only gives information about the nature of the recrystallized solid (strictly just the crystal that was picked) and not the bulk material. Given the difficulty of recrystallizing large amounts of the crude compound, powder X-ray diffraction was used to analyse the crude material. The obtained powder pattern is shown in **Figure 2.3** compared to the simulated pattern obtained from the diffraction data reported in reference 14.

Unit Cell Parameters	Obtained from SCXRD	Refined from PXRD
a [Å]	24.3778(3)	24.386(4)
b [Å]	17.0185(2)	17.011(3)
c [Å]	18.1359(3)	18.132(3)
Alpha [°]	90	90
Beta [°]	90	90
Gamma [°]	90	90
Volume [Å^3]	7524.106	7521.73
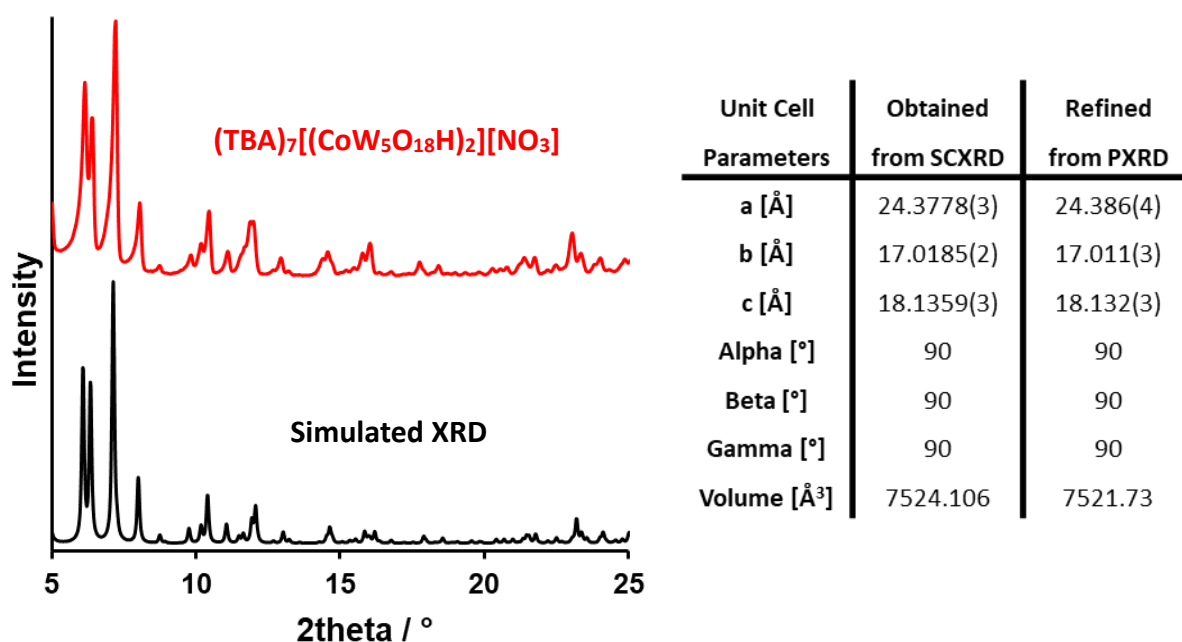
Figure 2.3: PXRD pattern of the crude product obtained from the reaction of $(TBA)_2[W_6O_{19}]$ with TBA(OH), and $Co(NO_3)_2.6H_2O$ compared to the simulated pattern obtained from SCXRD experiments on $(TBA)_7[(CoW_5O_{18}H)_2][BF_4]$. The unit cell parameters obtained from refinement of the experimental PXRD pattern and the SCXRD pattern are also shown.

An initial visual inspection shows that the two patterns match up well, with no obvious additional peaks observed in the experimental powder pattern that may be attributed to impurity. A Rietveld refinement was performed on the obtained powder pattern to obtain the unit cell parameters. These are shown in **Figure 2.3** with a comparison with those obtained from SCXRD. The values are in good agreement, which indicates that the structure of the bulk material and the recrystallized solid are likely to be the same. The fact that the crystal structure used to simulate the powder pattern in **Figure 2.3** incorporates one equivalent of TBA(BF$_4$) further supports the presence of one equivalent of TBA(NO$_3$) in samples prepared from Co(NO$_3$)$_2$.6H$_2$O, and that the nature of the tetrabutylammonium salt present does not have a large impact on the structure.

2.4 Attempts to remove TBA(X)

Initial attempts to synthesise (TBA)$_6$[(CoW$_5$O$_{18}$H)$_2$] appear to suggest that removal of the TBA(X) by-product is difficult and the salt will still be present even after recrystallization. For most applications this will not be an issue as the synthesis is robust in terms of the CoX$_2$ salt used and therefore it can be modified to produce a (TBA)$_7$[(CoW$_5$O$_{18}$H)$_2$][X] salt in which X$^-$ is inert in the context of the desired application. However, this is not ideal. For example, heterometal containing POMs have been shown to be active catalysts for the production of cyclic carbonates from epoxides and CO$_2$ but simple tetrabutylammonium salts are also known to enhance reactivity.[17] This could be viewed as advantageous as our compound contains both a catalyst and co-catalyst for this process. However, understanding the catalytic activity will be difficult without the ability to separate the two. This section will explore various options to attempt to remove/avoid contamination of (TBA)$_6$[(CoW$_5$O$_{18}$H)$_2$] with TBA(X).

2.4.1 Trituration/scratching

Simple tetrabutylammonium salts are soluble in a range of organic solvents such as dichloromethane, alcohols and toluene.[18,19] Therefore, if a suitable solvent can be found that dissolves simple TBA salts, like TBA(NO$_3$), but does not dissolve the target POM (i.e. (TBA)$_6$[(CoW$_5$O$_{18}$H)$_2$]) then it should be possible to separate the TBA(X) by-product from the target compound simply by trituration.

In order to explore this, the solubility of the crude product from reaction of (TBA)$_2$[W$_6$O$_{19}$] with TBA(OH) and Co(NO$_3$)$_2$.6H$_2$O, outlined in **Section 2.3.1**, was first tested in a range of organic solvents including toluene, dimethoxyethane, 1,4-dioxane, tetrahydrofuran and ethyl acetate. (TBA)$_6$[(CoW$_5$O$_{18}$H)$_2$] was found to be insoluble in all of these solvents and therefore trituration

with these solvents, followed by diethyl ether to remove residual solvent, was attempted. The product, after drying under vacuum, was then analysed by infrared spectroscopy to check for the presence of tetrabutylammonium nitrate as evidenced by the characteristic peak at 1337 cm^{-1}. Unfortunately, nitrate was still present after trituration with organic solvents. Given that some of these solvents are known to dissolve TBA(NO$_3$), it is clear that removal of this by-product is not simple and that it is "sticking" to the product.

2.4.2 Starting with Co(OMe)$_2$

An ideal strategy to avoid contamination of (TBA)$_6$[(CoW$_5$O$_{18}$H)$_2$] with TBA(X) would be to modify the procedure in such a way that reaction does not lead to the formation of TBA(X) salts. This can be achieved by using a cobalt based starting material (CoX$_2$) in which the cobalt(II) ion can be separated from X by protonolysis rather than salt metathesis, thereby giving HX as a by-product, as opposed to TBA(X). One such starting material is Co(OMe)$_2$. Theoretically, reaction of Co(OMe)$_2$ with a "virtual" lacunary species which was protonated would allow for the reaction to proceed with the formation of MeOH as the only by-product, as shown in **Equations 2.10-2.12**.

$$5\ (TBA)_2[W_6O_{19}] + 8\ TBA(OH) + 5\ H_2O \rightarrow 6\ "(TBA)_3[W_5O_{18}H_3]" \tag{2.10}$$

$$2\ "(TBA)_3[W_5O_{18}H_3]" + 2\ Co(OMe)_2 \rightarrow (TBA)_6\big[(CoW_5O_{18}H)_2\big] + 4\ MeOH \tag{2.11}$$

OR

$$"(TBA)_3[W_5O_{18}H_3]" + Co(OMe)_2 \rightarrow (TBA)_3\big[(MeOH)CoW_5O_{18}H\big] + MeOH \tag{2.12}$$
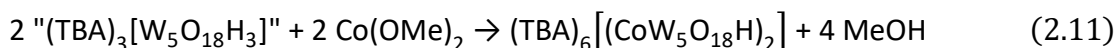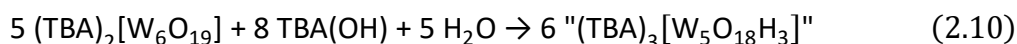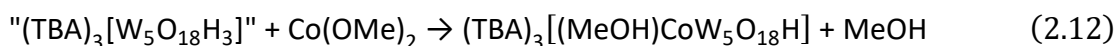
This reaction was attempted by suspending (TBA)$_2$[W$_6$O$_{19}$] in acetonitrile and reacting it with the appropriate amount of TBA(OH) and water to give a homogenous solution of "(TBA)$_3$[W$_5$O$_{18}$H$_3$]". This was then added to a suspension of Co(OMe)$_2$ in acetonitrile. The resulting suspension was stirred at room temperature for three hours and then at 70 °C overnight with no real change. The lack of solubility of Co(OMe)$_2$ (which has a polymeric structure) in organic solvents appears to prevent it from interacting with the basic degradation mixture. Further heating at reflux led to the formation of a cloudy black/brown solution however, isolation of products from this mixture proved difficult. Preliminary characterisation of the species obtained using infrared spectroscopy showed the presence of bands at 932-935 cm^{-1}, consistent with the terminal W=O stretch of (TBA)$_6$[(CoW$_5$O$_{18}$H)$_2$], though these were often lower intensity and accompanied by numerous additional bands when compared to previous spectra of (TBA)$_7$[(CoW$_5$O$_{18}$H)$_2$][X]. These results suggest that reaction of the "virtual"

lacunary precursor with Co(OMe)$_2$ in acetonitrile does not offer an efficient path to (TBA)$_6$[(CoW$_5$O$_{18}$H)$_2$].

2.4.3 Starting with {Co[N(SiMe$_3$)$_2$]$_2$}$_2$

An alternative approach is to use cobalt bis(bis(trimethylsilyl)amide). This strategy also attempts to exploit the presence of groups that will undergo protonolysis, giving only neutral by-products (in this case hexamethyldisilazane) as shown in **Equations 2.13-2.15**. The advantage of this approach over the previous method using Co(OMe)$_2$ is the increased solubility of cobalt bis(bis(trimethylsilyl)amide) in organic solvents compared with Co(OMe)$_2$, which should hopefully overcome the issues previously seen.

$$5\ (TBA)_2[W_6O_{19}] + 8\ TBA(OH) + 5\ H_2O \rightarrow 6\ "(TBA)_3[W_5O_{18}H_3]" \tag{2.13}$$

$$2\ "(TBA)_3[W_5O_{18}H_3]" + \{Co[N(SiMe_3)_2]_2\}_2 \rightarrow$$
$$(TBA)_6[(CoW_5O_{18}H)_2] + 4\ HN(SiMe_3)_2 \tag{2.14}$$

OR

$$2\ "(TBA)_3[W_5O_{18}H_3]" + \{Co[N(SiMe_3)_2]_2\}_2 \rightarrow$$
$$2\ (TBA)_3[\{(Me_3Si)_2NH\}CoW_5O_{18}H)_2] + 2\ HN(SiMe_3)_2 \tag{2.15}$$
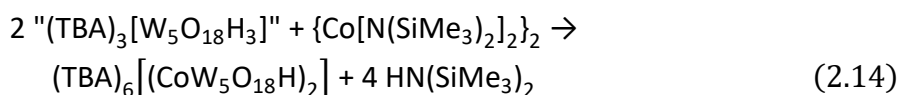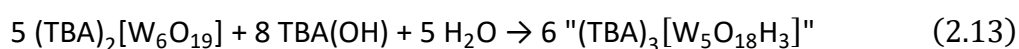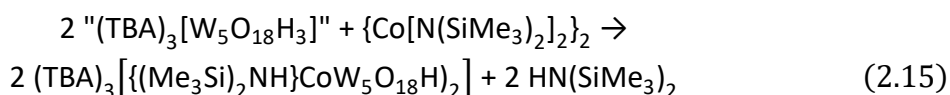
Firstly, (TBA)$_2$[W$_6$O$_{19}$] was suspended in acetonitrile and reacted with TBA(OH) and water to target the "virtual" precursor. This was then transferred via cannula onto the solid {Co[N(SiMe$_3$)$_2$]$_2$}$_2$. This led to the formation of a black/purple solution that slowly turned red overtime. A small amount of solid was removed by filtration. After removal of solvent and trituration with ethyl acetate/diethyl ether, a red solid was obtained. The infrared spectrum of this solid was recorded and is shown in **Figure 2.4**.

The spectrum is similar to that of the dimeric product shown in **Figure 2.1**. Peaks at 934, 802, 760, 677 and 601 cm^{-1} are very close to those previously observed and therefore very much indicative of the successful incorporation of cobalt into the Lindqvist unit.

However, there are some additional peaks, most notably at 1036 (a peak is previously seen here but it is much less intense) and 1250 cm^{-1}. Both of these stretches are in regions characteristic for trimethylsilyl (TMS) groups. Though not shown in **Figure 2.4**, there are no peaks in the 3000-3500 cm^{-1} region. The lack of any N-H stretches means that the presence of TMS stretches in the infrared spectrum cannot be assigned to the presence of bis(trimethylsilyl)amine (the expected by-product of this reaction). It therefore may suggest binding of a TMS group to the POM cluster. This could happen either at a bridging oxygen
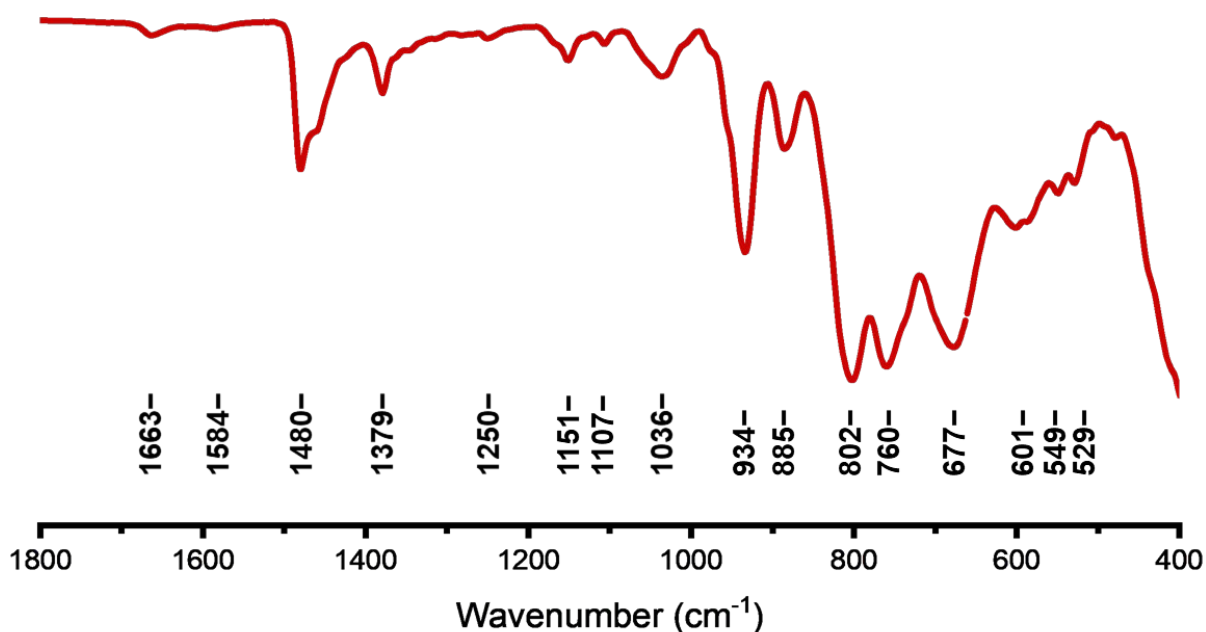
Figure 2.4: ATR FTIR transmittance spectrum of the crude product obtained from the reaction of $(TBA)_2[W_6O_{19}]$ with TBA(OH), and $\{Co[N(SiMe_3)_2]_2\}_2$.

position (with the TMS group acting as a proton mimic) or at the cobalt centre (mostly likely as part of a Co-N(TMS)$_2$ or Co-O(TMS) unit). The red colour of the reaction product (which is sensitive to the co-ordination environment at cobalt) may be evidence of the latter.

In order to gain precise structural information about the nature of the product, attempts were made to crystallise the compound. This was done by slow diffusion of diethyl ether into a saturated solution of the compound in acetonitrile. However, during the attempted recrystallization, a series of colour changes were noted. The solution first changed from red to purple. This may be consistent with loss of a ligand at the cobalt centre and reformation of the dimeric unit. Soon after, the solution changed from purple to green. This is indicative of oxidation of the cobalt from Co(II) to Co(III). Unfortunately, single crystals could not be isolated from this solution and therefore the exact nature of the reactivity present could not be confirmed.

Overall, it appears that use of cobalt bis(bis(trimethylsilyl)amide) as the source of cobalt for the synthesis of $(TBA)_6[(CoW_5O_{18}H)_2]$ provides a pathway to the crude product without the presence of additional TBA(X) by-products. However, the colour of the sample, the infrared spectrum, and the observations during recrystallization all provide evidence that the silyl amide ligands are not innocent, both appearing to change the nature of the crude product and causing additional reactivity during recrystallization. When these factors are considered in combination with the fact that cobalt bis(bis(trimethylsilyl)amide) has to be independently

32

synthesised (and has to be very carefully handled to avoid decomposition), it seems this approach is arguably more problematic than the original approaches using simple cobalt salts. Therefore, further characterisation of the products of this reaction or refinement of this method was not pursued.

2.5 Isolation of (TBA)$_3$[(Py)CoW$_5$O$_{18}$H]

Our group have previously shown that (TBA)$_7$[(CoW$_5$O$_{18}$H)$_2$][BF$_4$] will react with pyridine to form the monomeric adduct (TBA)$_3$[(pyridine)CoW$_5$O$_{18}$H].[14] Given the difficulty in obtaining the dimeric (TBA)$_6$[(CoW$_5$O$_{18}$H)$_2$] without additional TBA(X) impurity, it was postulated that isolation of the pyridine adduct may allow for removal of the additional salt. This could then act as a well-defined, compositionally pure, starting point for reactivity studies assuming the pyridine is sufficiently labile to allow further reactivity at the cobalt centre.

2.5.1 Synthesis and characterisation

In order to synthesise the pyridine adduct, crude (TBA)$_7$[(CoW$_5$O$_{18}$H)$_2$][NO$_3$] (synthesised using methods discussed in **Section 2.3.1**) was dissolved in pyridine. This led to an immediate colour change from dark blue/purple to dark pink, presumably associated with the cleaving of the dimeric unit and formation of the pyridine adduct (TBA)$_3$[(Py)CoW$_5$O$_{18}$H]. The product was precipitated from solution as a free-flowing pink powder by the addition of excess ethyl acetate. The mixture was then filtered and the solid was washed with diethyl ether before drying under vacuum.

The infrared spectrum obtained is shown below in **Figure 2.5**. The spectrum is similar to that of (TBA)$_7$[(CoW$_5$O$_{18}$H)$_2$][NO$_3$]. The major differences are the presence of a low intensity peak at 1600 cm^{-1}, due to the bound pyridine ligand, and the lack of a peak at 606 cm^{-1}, which is attributed to the Co$_2$O$_2$ core of the dimeric anion.[14] These differences are in-line with successful formation of (TBA)$_3$[(Py)CoW$_5$O$_{18}$H].

The infrared spectrum of crude, dimeric, (TBA)$_7$[(CoW$_5$O$_{18}$H)$_2$][NO$_3$] contains an intense peak at 1337 cm^{-1} (**Figure 2.1**). The spectrum of the pyridine adduct shown in **Figure 2.5** contains a much smaller peak at 1341 cm^{-1}. This may either indicate that most of the TBA(NO$_3$) has been removed but there is a small amount still present or, that removal of all the TBA(NO$_3$) allows visualisation of a new peak that was hidden by the intense nitrate band. To verify this, a control experiment in which the cobalt containing Lindqvist-type dimer was synthesised from CoCl$_2$, was carried out. The infrared spectrum of the crude product obtained by applying the methodology from **Section 2.3.1** with CoCl$_2$ instead of Co(NO$_3$)$_2$.6H$_2$O was almost identical to
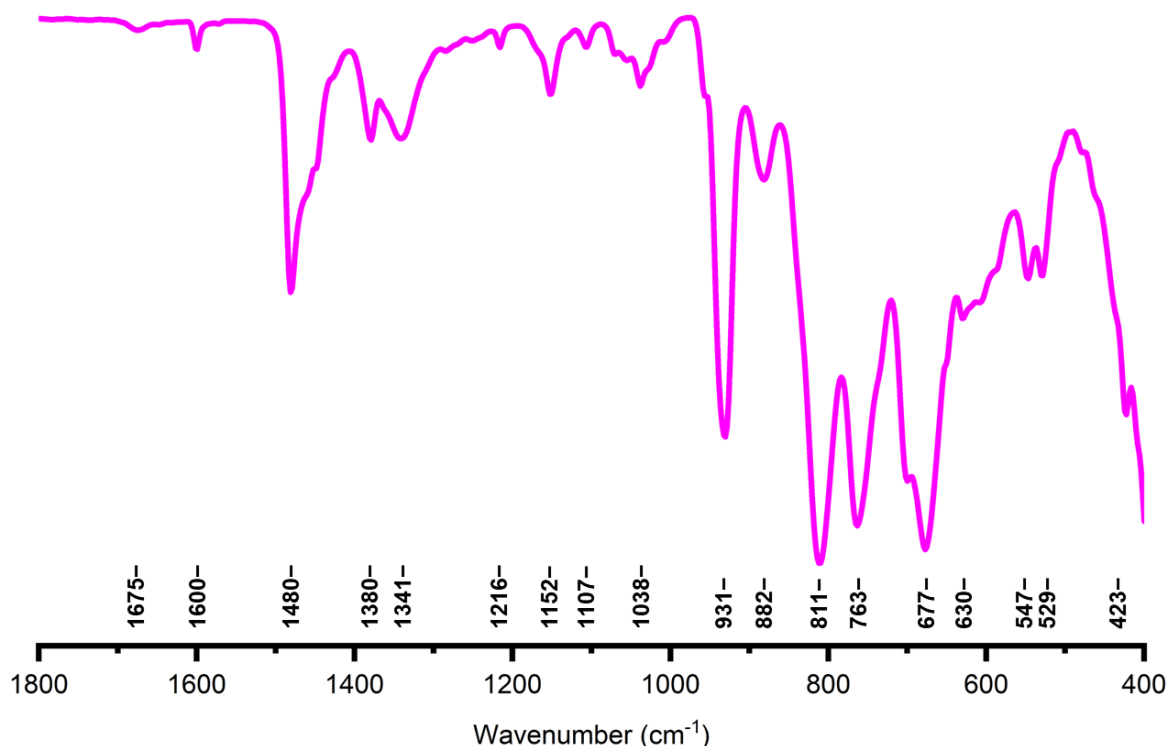
Figure 2.5: ATR FTIR transmittance spectrum of the crude product obtained from the reaction of $(TBA)_7[(CoW_5O_{18}H)_2]$ with pyridine.

that shown in **Figure 2.1** however, it lacks any peaks in the 1335-1350 cm^{-1} region. This suggests that both the sharp peak at 1337 cm^{-1} and the smaller peak at 1341 cm^{-1} are caused by nitrate (pyridine is not expected to give any major peaks in this region).

Our group previously reported the X-ray structure of $(TBA)_3[(Py)CoW_5O_{18}H]$. The crude product was recrystallized by slow evaporation of a concentrated solution of the product in dichloromethane under a stream of nitrogen. This led to high quality crystals, but the yield is presumed to be low as it was not reported. In this work, it was found that the pyridine adduct can be efficiently recrystallized in high yields directly from cooled solutions of the compound in pyridine, saturated via the addition of diethyl ether. This not only led to a higher quantity of the recrystallized compound but also gave crystals suitable for single-crystal X-ray diffraction. The structure obtained is shown in **Figure 2.6** along with the infrared spectrum of the obtained crystals.

The X-ray structure showed the presence of three tetrabutylammonium cations per Lindqvist unit, which is consistent with mono protonation of the cage. This proton was located from a peak in the Fourier difference map and was found to be localised on O2. This was further supported using BVS calculations (V_{O2} = 1.10). Interestingly, the crystal lattice was found to contain one water molecule closely associated with each $[(Py)CoW_5O_{18}H]^{3-}$ anion. The water
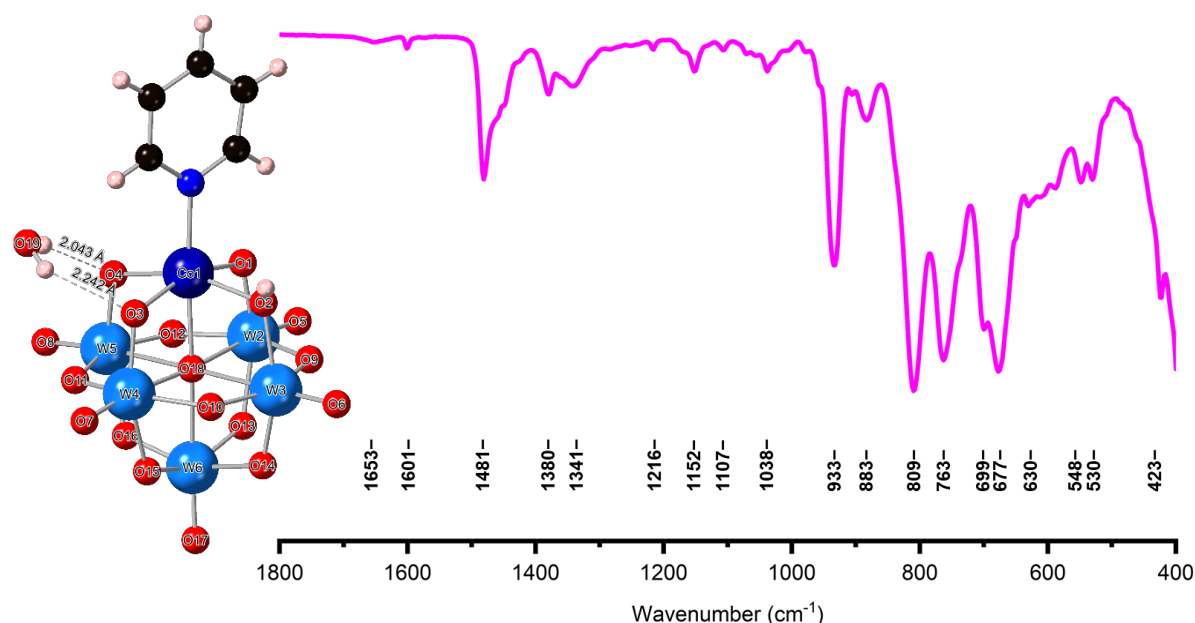
Figure 2.6: X-ray structure of $(TBA)_3[(Py)CoW_5O_{18}H].H_2O$ showing the shortest distances between the hydrogen atoms of the associated water molecule and the oxygens of the cage. The infrared spectrum of the same sample is also given.

molecule shows hydrogen-bonding interactions between both its protons and two oxygens of the POM cage, with interatomic distances of ca. 2.04 Å and ca. 2.24 Å respectively. The fact that the water appears to preferentially interact with W-O-Co bridging oxygens indicates the high basicity of these oxygen atoms (seemingly the most basic in the cluster). This is important in the context of water oxidation catalysis as it shows the ability of the basic oxygens adjacent to the cobalt centre to guide water molecules close to the active metal centre. This leaves the water molecule poised for transformation.

The infrared spectrum of the obtained crystals is almost identical to that of the crude product. In particular, there is still a small peak at 1341 cm^{-1} perhaps indicating the presence of some $TBA(NO_3)$ after recrystallization. It should be noted though that no nitrate was located in X-ray diffraction analysis. Accurate elemental analysis is currently being performed in collaboration with Professor Masahiro Sadakane at Hiroshima University but the data are not yet available to be presented here.

Given the spontaneous formation of $(TBA)_3[(Py)CoW_5O_{18}H]$ from $(TBA)_7[(CoW_5O_{18}H)_2][NO_3]$ in pyridine, it follows that performing the degradation of $(TBA)_2[W_6O_{19}]$ with TBA(OH) in pyridine, followed by treatment with $Co(NO_3)_2.6H_2O$ should allow for direct synthesis of $(TBA)_3[(Py)CoW_5O_{18}H]$, as shown in **Equations 2.16** and **2.17**.

$$5\ (TBA)_2[W_6O_{19}] + 20\ TBA(OH) \rightarrow 6\ "(TBA)_5[W_5O_{18}H]" + 7\ H_2O \qquad (2.16)$$

$$\text{"(TBA)}_5[\text{W}_5\text{O}_{18}\text{H}]\text{"} + \text{Co(NO}_3)_2.6\text{H}_2\text{O} \rightarrow \text{(TBA)}_3[\text{(Py)CoW}_5\text{O}_{18}\text{H}] + 2\text{ TBA(NO}_3) \qquad (2.17)$$
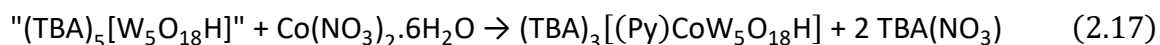
To verify this, $(TBA)_2[W_6O_{19}]$ was suspended in pyridine. A solution of TBA(OH) in pyridine was slowly added which very quickly led to complete dissolution of the starting material and formation of a pale red/brown solution. To this solution, solid $Co(NO_3)_2.6H_2O$ was added. This quickly dissolved and led to the formation of a dark pink solution, consistent with the formation of $(TBA)_3[(Py)CoW_5O_{18}H]$. The product can be directly precipitated from solution by addition of an excess of ethyl acetate, giving a free-flowing pink powder. This is a lot simpler than the trituration process (or precipitation by dropwise addition of a saturated solution of the product in dichloromethane or acetonitrile to an excess of ethyl acetate) required to obtain a free-flowing powder of $(TBA)_7[(CoW_5O_{18}H)_2][NO_3]$. After drying under vacuum, the infrared spectrum of the crude product was obtained, and it was found to be identical to that shown in **Figure 2.5**. As before, the crude product can be recrystallized from saturated pyridine solutions after cooling to −30 °C. This confirms that performing the degradation and reassembly steps in the presence of a strong ligand can be used to directly access monomeric adducts of $[CoW_5O_{18}H]^{3-}$.

2.5.2 Reformation of the dimer

Direct synthesis of $(TBA)_3[(Py)CoW_5O_{18}H]$ is useful as it allows us to minimise the issues in removal of $TBA(NO_3)$ from $(TBA)_7[(CoW_5O_{18}H)_2][NO_3]$. However, if the pyridine ligand is not sufficiently labile, then it will prevent further reactivity at the cobalt centre. This may give opportunities for interesting chemistry if functionalised N-heterocycles can be bound to the POM but it will ultimately limit the opportunities to explore further reactivity at the cobalt centre. It was therefore important to determine whether the pyridine ligand can be removed and, in the absence of any other potential donors, dimeric $(TBA)_6[(CoW_5O_{18}H)_2]$ can be reformed.

Observations obtained during the synthesis suggest that the pyridine ligand of $(TBA)_3[(Py)CoW_5O_{18}H]$ is stable with respect to removal after prolonged periods under vacuum at relatively low temperatures (50 °C and below). Placing samples of $(TBA)_3[(Py)CoW_5O_{18}H]$ under vacuum at 130 °C led to a gradual colour change from pink to blue over the course of a few hours. This is consistent with the removal of the pyridine ligand and formation of the dimeric species. This result is promising and suggests that thermal treatment of the adduct under vacuum is enough to remove the pyridine ligand. However, the rate of heat transfer is limited when heating the neat solid and therefore long periods of heating are required to

ensure complete removal of the ligand. This problem is also likely to be exacerbated when scaling up.

To simplify this procedure and eliminate these issues, an alternative approach was developed. It was found that suspending $(TBA)_3[(Py)CoW_5O_{18}H]$ in boiling toluene leads to the same colour change of dark pink to blue but after only 15 minutes of heating. The stirring can then be stopped, and the toluene solution can be decanted (this was repeated at least once with fresh toluene to ensure complete removal of the pyridine). The blue powder was then washed with ethyl acetate and diethyl ether.

After drying under vacuum, the infrared spectrum was recorded and is shown in **Figure 2.7** (red) with a comparison to the crude $(TBA)_7[(CoW_5O_{18}H)_2][NO_3]$ (blue) obtained using the methods outlined in **Section 2.3.1** and crude $(TBA)_3[(Py)CoW_5O_{18}H]$ (pink). Analysis of the spectrum shows the successful removal of the pyridine, evidenced by the absence of a peak at 1601 cm^{-1}. The reappearance of a peak at around 601 cm^{-1} is consistent with the formation of the Co_2O_2 core unit, indicating reformation of the dimer, which is in line with the visual observations during the experiment. Compared to the crude dimer (blue), which contains an intense stretch at 1337 cm^{-1} due to the presence of nitrate impurity, there is only now a small stretch at 1346 cm^{-1} in this region for the product (red). This may still indicate the presence of
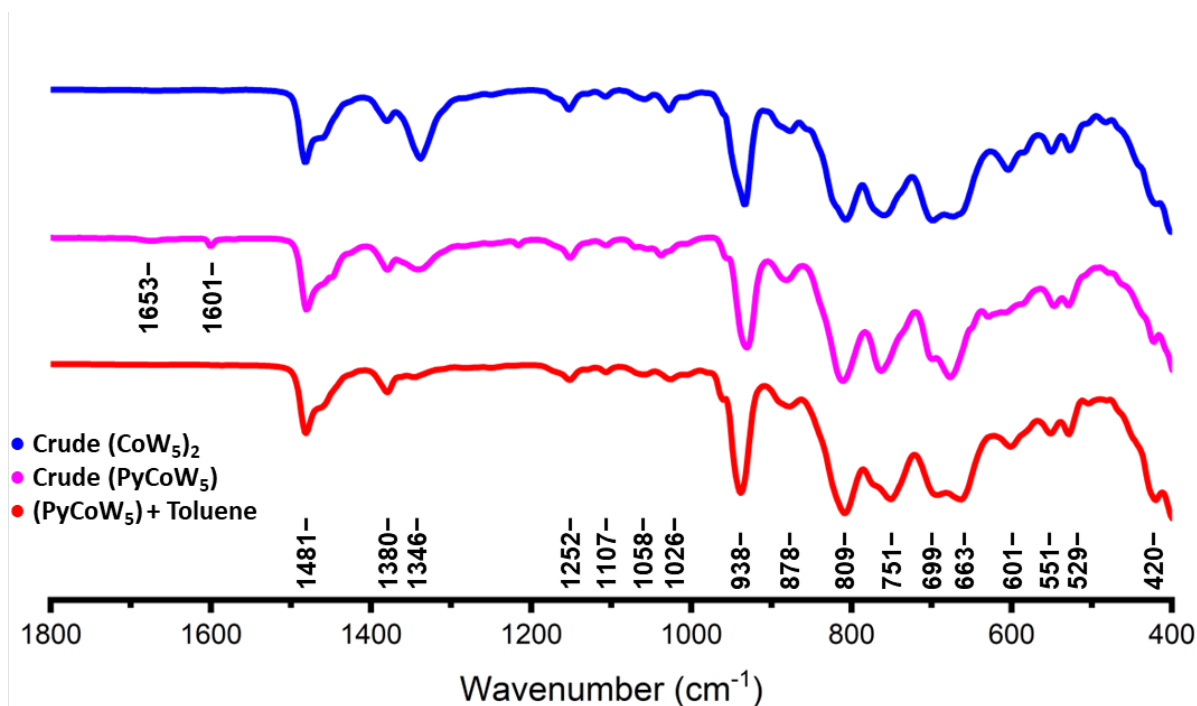
Figure 2.7: ATR FTIR trnasmittance spectrum of the product obtained after refluxing $(TBA)_3[(Py)CoW_5O_{18}H]$ in toluene (red). The spectra of crude dimeric $(TBA)_7[(CoW_5O_{18}H)_2][NO_3]$ (blue) and $(TBA)_3[(Py)CoW_5O_{18}H]$ (pink) are also shown.

some TBA(NO$_3$) in the product, but not to the same degree as in the crude material. Therefore, formation of the pyridine adduct followed by removal of the ligand and reformation of the dimer could act as a method of purification for the crude material. This is very useful as (TBA)$_6$[(CoW$_5$O$_{18}$H)$_2$] is not easily recrystallized on a large scale.

Interestingly, the terminal W=O stretching frequency is shifted slightly, appearing at 938 cm^{-1} after heating in toluene as opposed to 933 cm^{-1} in both crude samples of the dimer and pyridine adduct. Typically, changes in this stretch are associated with changes in the charge of the cluster. Given how similar the infrared spectra of the crude dimer (blue) and the compound obtained after heating in toluene (red) are, it is unlikely that there is any major structural change to the cluster, however the change in the terminal W=O oxygen stretching frequency may be indicative of a change in the protonation state of the cluster. If formation of the pyridine adduct followed by reformation of the dimer was to be applied as a method of purification for this compound, then further characterisation is required to determine the exact nature of the product after heating in toluene.

2.6 Forming other adducts of [CoW$_5$O$_{18}$H]$^{3-}$

The ease by which (TBA)$_7$[(CoW$_5$O$_{18}$H)$_2$][NO$_3$] is converted to its monomeric pyridine adduct is encouraging in the context of producing heterometal containing POMs decorated with highly functionalised organic fragments. This may allow pairing of the unique reactivity of the cobalt containing cluster with further functionality for designer reactivity.

To explore the tolerance of this chemistry to donors with different steric profiles and functional groups, (TBA)$_7$[(CoW$_5$O$_{18}$H)$_2$] was treated with a series of substrates containing a N-heterocycle, i.e. quinoline (which is more sterically demanding than pyridine), 4-aminopyridine (which has a free –NH$_2$), and 4,4'-bipyridine (which contains two N donor atoms). This was done either by directly dissolving the crude cobalt containing dimer in the donor molecule (in the case of quinoline) or by adding the donor molecule to a saturated dichloromethane solution of the dimer (an excess of 4-aminopyrdine was used but the reaction with 4,4'-bipyridine was done at 1.5:1 L:POM). Successful reaction typically resulted in a colour change, which was dependent on the ligand present. The crude products could be precipitated from solution by the addition of an excess of ethyl acetate. The solids were then washed with diethyl ether and dried under vacuum before the infrared spectrum was recorded. The resulting spectra are shown in **Figure 2.8** with a comparison to crude (TBA)$_7$[(CoW$_5$O$_{18}$H)$_2$][NO$_3$].
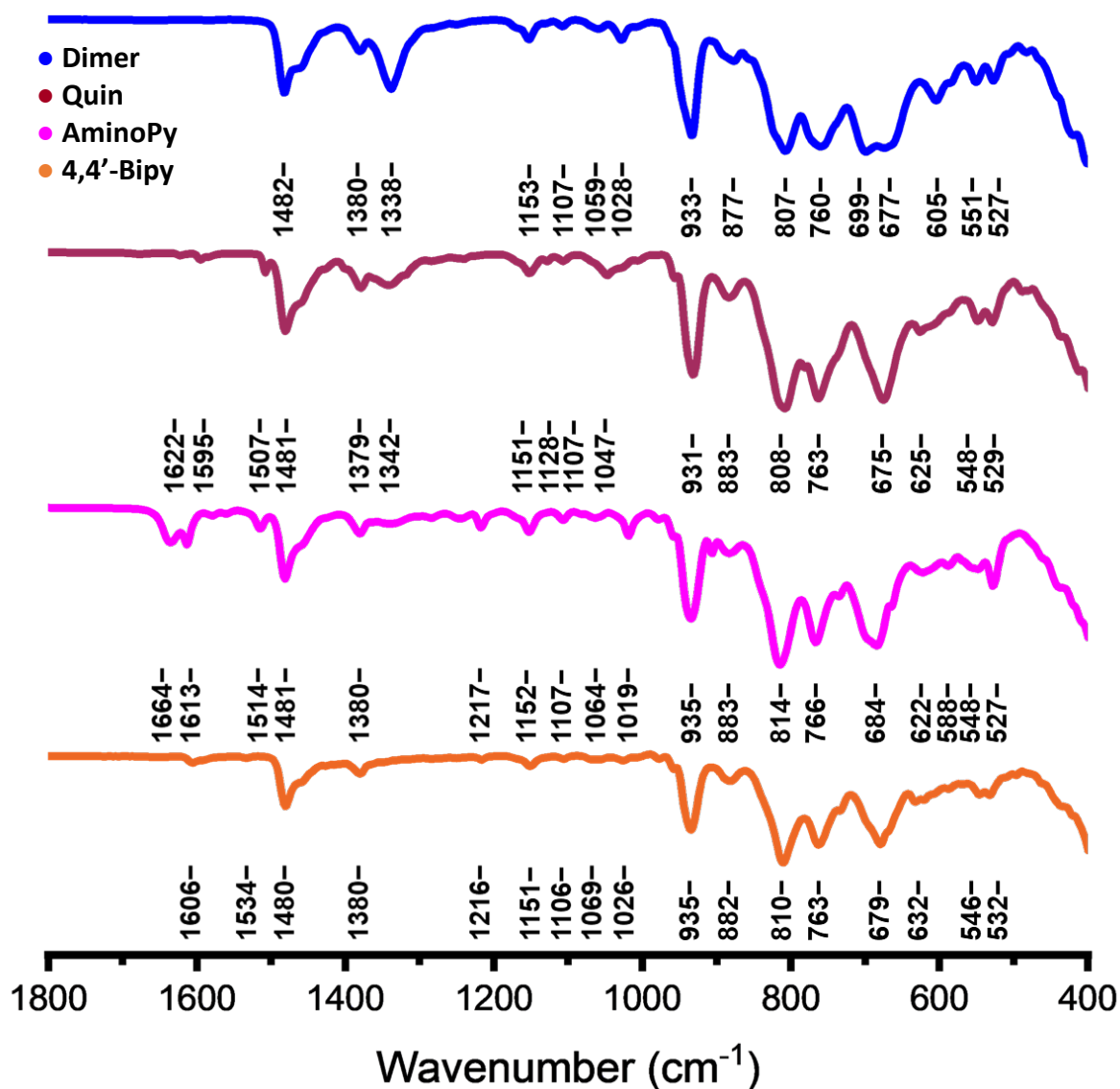
Figure 2.8: ATR FTIR transmittance spectrum of the crude product obtained from the reaction of $(TBA)_7[(CoW_5O_{18}H)_2]$ with an excess of quinoline (red), 4-aminopyridine (pink), and 4,4'-bipyridine (orange).

The infrared spectra of the adducts contain a small peak around 1600 cm^{-1} which can be attributed to a C=N stretch of the bound ligand. In some cases, there is also a broader peak at a slightly higher wavenumber (approximately 1660 cm^{-1}) that is likely caused by the same stretch in the free ligand. This implies that in some cases more thorough washing steps should added (for example washing with toluene) to ensure complete removal of the free ligands. The terminal W=O stretch, observed at 933 cm^{-1} in the crude dimer, is relatively unchanged after reaction with all of the N-donor molecules. This indicates that the charge on the cluster, and therefore the protonation state, is unchanged, meaning none of the ligands are basic enough to deprotonate the cage. Simplification of the bridging region, with the loss of peaks at 699 and 605 cm^{-1} compared to the dimer, may provide further support for the formation of N-bound clusters.

In order to further establish the nature of the adducts, single crystals of the respective adducts were grown and were analysed by single-crystal X-ray diffraction. These were grown either by vapour diffusion of diethyl ether into a saturated solution of the dimer dissolved in the ligand (for quinoline) or vapour diffusion of the same solvent into saturated solutions of the dimer in acetonitrile, in the presence of the ligand.

The obtained X-ray structures are shown in **Figure 2.9** and **2.10**. The structures of (TBA)$_3$[(Quin)CoW$_5$O$_{18}$H] and (TBA)$_3$[(AminoPy)CoW$_5$O$_{18}$H] (both shown in **Figure 2.9**) are very similar to that of (TBA)$_3$[(Py)CoW$_5$O$_{18}$H]. As for the pyridine adduct, they both feature a localised proton, present on one of the Co-O-W bridges. BVS analysis shows that this proton is localised on O2 (V_{O2} = 1.05) for (TBA)$_3$[(Quin)CoW$_5$O$_{18}$H] and O3 (V_{O3} = 0.97) for (TBA)$_3$[(AminoPy)CoW$_5$O$_{18}$H]. The bond lengths are very similar for all the adducts shown. The structure formed when (TBA)$_7$[(CoW$_5$O$_{18}$H)$_2$][NO$_3$] is reacted with an slight excess of 4,4'-bipyrdine is shown in **Figure 2.10**. It can be seen that the 4,4'-bipyridine has reacted in a 1:1 fashion, bridging between the two cobalt atoms. This could be considered an insertion of 4,4'-bipyridine into the [(CoW$_5$O$_{18}$H)$_2$]$^{6-}$ dimer. The torsion angle between the two aromatic rings of the 4,4'-bipyridine is ca. 41.5 ° which suggests the two halves of the compound are electronically separated (i.e. the π-system does not connect between the two halves of the dimer). Again, the bonding within the POM cage is relatively unchanged, with the average
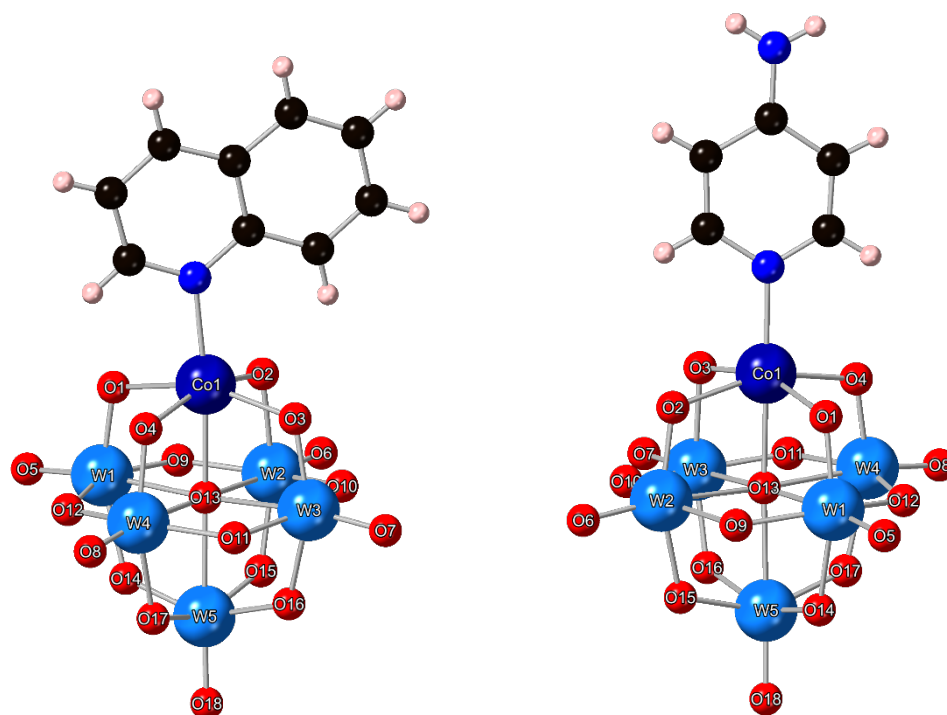
Figure 2.9: Single-crystal X-ray diffraction structures of the (TBA)$_3$[(Quin)CoW$_5$O$_{18}$H] and (TBA)$_3$[(AminoPy)CoW$_5$O$_{18}$H]. The atomic radii are set to the CSD covalent radii. Cations are omitted for clarity.
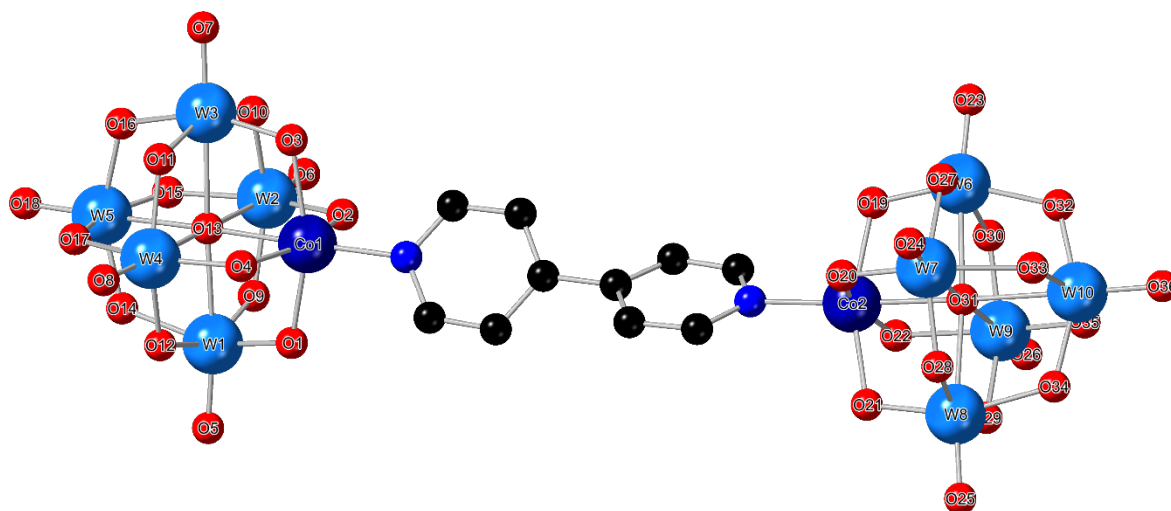
Figure 2.10: Single-crystal X-ray diffraction structure of $(TBA)_6[(4,4'-Bipy)(CoW_5O_{18}H)_2]$. The atomic radii are set to the CSD covalent radii. Cations are omitted for clarity.

bond lengths in line with the other adducts characterised. BVS analysis suggests localisation of protons primarily on O3 (V_{O3} = 1.34) and O22 (V_{O22} = 1.05). This analysis also suggests that cobalt remains in the 2+ oxidation state throughout these experiments.

A number of other nitrogen donor ligands were also tested for their ability to form adducts with $[CoW_5O_{18}H]^{3-}$. These include 2,6-lutidine, 4-hydroxypyridine, triethylamine, *tert*-butylamine, piperidine and ammonia. Generally, reactions with these compounds yielded no colour change on addition of the ligand, perhaps indicating a lack of interaction with the cobalt centre. Furthermore, addition of excess ethyl acetate failed to precipitate the products as a powder and instead yielded thick oils. The reaction with ammonia did appear to give an initial colour change to red/purple, however this faded over time. The exact reason these ligands failed to efficiently form adducts is still unclear.

In order to determine whether the formation of adducts of $[CoW_5O_{18}H]^{3-}$ is possible with anything other than nitrogen donors, attempts were made to isolate an alcohol adduct. Upon dissolving crude $(TBA)_7[(CoW_5O_{18}H)_2][NO_3]$ (which is dark blue/purple) in methanol or ethanol, a red/purple solution is formed along with some colourless solid. The mixture was filtered to separate the solid, which was found to be $(TBA)_2[W_6O_{19}]$ (by infrared spectroscopy).

Attempts to precipitate alcohol adducts directly from solutions by adding an excess of ethyl acetate or diethyl ether failed, usually giving oils or diluted solutions. When these solutions (i.e. alcohol + anti-solvent) were allowed to evaporate, the solutions slowly turned dark purple and some amorphous solid formed. Infrared spectroscopy performed on this solid showed the characteristic spectrum of the cobalt containing dimer. However, when solutions of the dimer

in only ethanol were allowed evaporate at room temperature, a small crop of red crystals formed over a couple of weeks. Analysis of these crystals by single-crystal X-ray diffraction gave the structure shown in **Figure 2.11**.

The crystal structure clearly showed the formation of an ethanol adduct with the formula $(TBA)_3[(EtOH)CoW_5O_{18}H]$. There are also two other molecules of ethanol close to the cage which seem to form a localised hydrogen bonded network which also incorporates one of the oxygen atoms of the POM cage (O2). These additional ethanol molecules (containing O20 and O21) are only 50% occupied. This may imply the presence of only a single additional solvent molecule at any one time, or gradual loss of solvent from the crystals. Given the independent molecules appear to arrange well, with O-O distances of ca. 2.6-2.7 Å, into a chain of hydrogen bonded solvent molecules, solvent loss from the crystals after removal from the mother liquor appears likely.

The terminal Co-O(H)-Et bond is 2.107(12) Å, which is very similar to the N-bound adducts previously synthesised, which have an average Co-N bond length of ca. 2.07 Å. However, there is a significant deviation in the average Co-O bond length compared to the other adducts
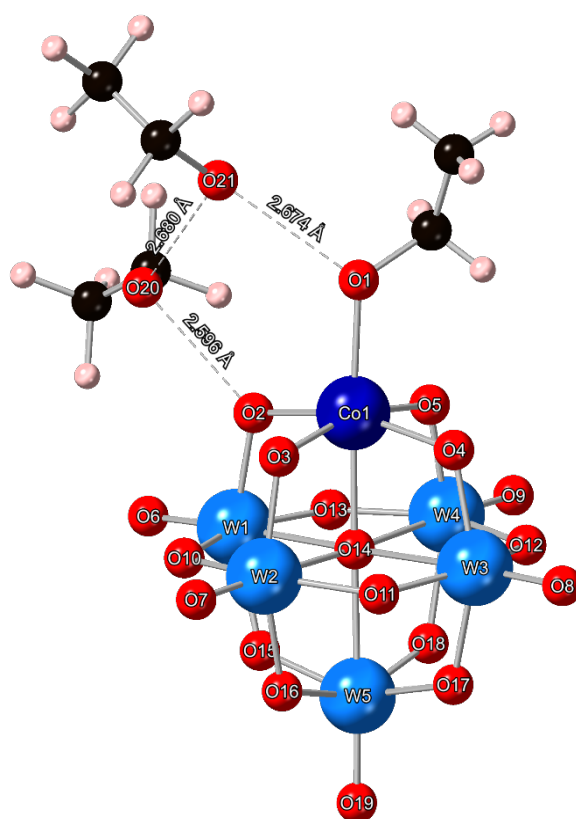
Figure 2.11: Single-crystal X-ray diffraction structure of $(TBA)_3[(EtOH)CoW_5O_{18}H]$. Two EtOH solvent molecules are shown but only have approx. 0.5 occupancy. The atomic radii are set to the CSD covalent radii. Cations are omitted for clarity.

present. In $(TBA)_3[(EtOH)CoW_5O_{18}H]$, the average Co-O bond length is ca. 1.95 Å (not including the bond to the central μ_6-oxo), whereas in the other adducts the average bond length is ca. 2.08 Å (average of ca. 2.09 Å for the dimer). The sizeable contraction in the Co-O bond length may be a result of a relatively weak interaction between cobalt and ethanol compared to the corresponding interactions in the other adducts (and dimer). This can be rationalised in terms of the decreased basicity of ethanol compared to the N-heterocycles.

The apparent reformation of the dimer when the ethanol solution is evaporated in the presence of an anti-solvent or when placed under vacuum, appears to support this hypothesis. This weak bonding interaction could be "compensated for" by an increase in π-donation from the oxygens in the Co-O-W bridges to the cobalt centre (causing the decrease in bond length).

Bond valence sum (BVS) analysis of the cluster implies delocalisation of the proton across all four Co-O-W bridges ($V_{O2} = 1.51$, $V_{O3} = 1.61$, $V_{O4} = 1.69$, and $V_{O5} = 1.64$), which different to the other adducts, where the proton appears to be localised in a single position. This delocalisation could be promoted by the formation of hydrogen bonding interactions with residual solvent (some of which may have been lost during X-ray analysis) which provides a low energy pathway for proton migration.

Attempts to crystallise the corresponding methanol adduct have been unsuccessful so far and *iso*-propanol/*tert*-butanol appear to be unreactive (and the dimer does not dissolve in these solvents).

2.7 Cation exchange experiments

All the reactions targeting cobalt containing Lindqvist-type POMs discussed so far have utilized tetrabutylammonium cations to allow dissolution of the reactants and products in polar organic solvents. The main reason for this is that the Lindqvist structure exists primarily in non-aqueous solution and therefore it is rational, when attempting to isolate functionalised derivatives, to stay in a non-aqueous environment.

However, after successfully accessing $(TBA)_7[(CoW_5O_{18}H)_2][NO_3]$ using the methods outlined in **Section 2.3.1**, we were interested to know whether the solubility can be altered by moving away from tetrabutylammonium (for example to other quaternary ammonium cations or alkali metal cations), and whether the structure is retained in aqueous solution. In order to probe this, a number of cation exchange experiments were explored and some of the products were characterised using single-crystal X-ray diffraction.

2.7.1 Ammonium cations

Reducing the chain length of a quaternary ammonium cation will result in reduced solubility of salts of that cation in organic solvents but will lead to increased solubility in aqueous media. When a methanol solution of $(TBA)_7[(CoW_5O_{18}H)_2][NO_3]$ was treated with an excess of ammonium chloride (NH_4Cl added as a methanol solution), a blue precipitate rapidly formed. This precipitate was separated from the solution by centrifugation and washed with large amounts of acetonitrile and methanol to remove any remaining tetrabutylammonium salts.

Attempts to dissolve the resulting compound in water led to partial dissolution and formation of a blue solution. Heating the solution allows for complete dissolution of the compound and caused the solution to turn pink. Allowing the solution to cool slowly led to the formation of pink crystals. Analysis of these crystals by X-ray diffraction gave the structure shown in **Figure 2.12**.

It seems that cation exchange and dissolution in water leads to huge structural changes in the compound. There is a conversion of the cobalt containing Lindqvist unit to paratungstate B (i.e. $[H_2W_{12}O_{40}]^{10-}$) and the cobalt centres are no longer part of the POM framework, they instead bridge between POM units. There are four cobalt ions per POM (one of the Co centres in **Figure 2.12** is disordered over two positions) suggesting a tentative formulation of $H_2Co_4[H_2W_{12}O_{42}].26.4H_2O$ (the number of waters based on the number of oxygens located in
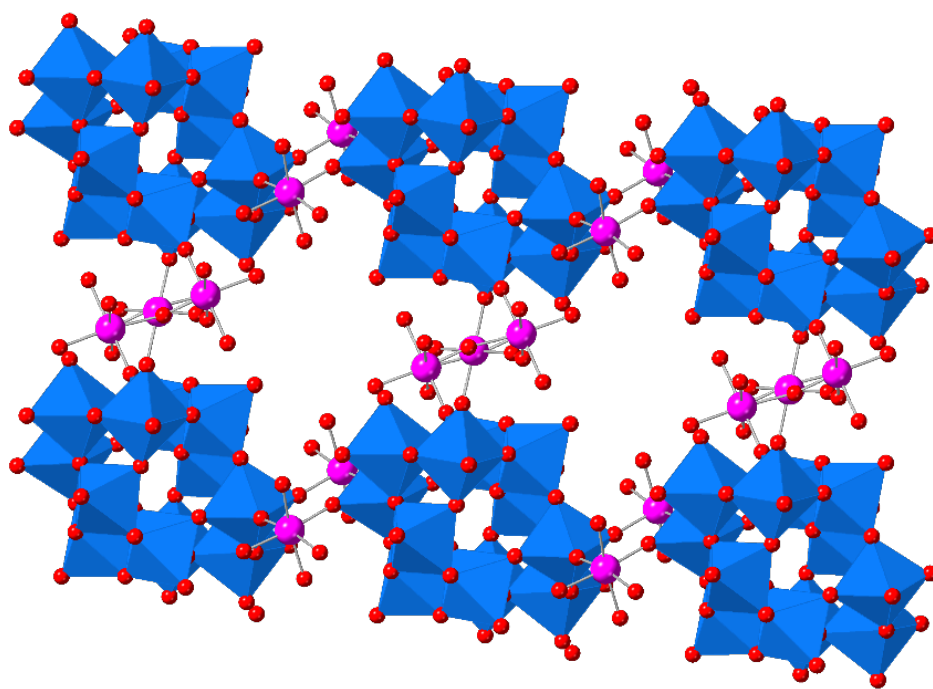
Figure 2.12: Single-crystal X-ray diffraction structure of $H_2Co_4[H_2W_{12}O_{42}].26.4H_2O$. Unbound/disordered solvent molecules are omitted for clarity. Co^{2+} shown in pink. One of the Co^{2+} centres is disordered over two positions. The atomic radii are set to the CSD covalent radii.

the structure). Protons are required to balance the charge, as there appear to be no ammonium cations present in the structure, though neither the protons known to sit inside the $\{W_{12}O_{42}\}$ unit or the suggested counter ions have been located. Some of the cobalt centres form bridges between POM units creating 2D layers. The inner co-ordination spheres of the cobalt centres are completed by water ligands. Similar structures to this are present in the literature but are prepared via aqueous methods and tend to incorporate additional alkali metal cations.[20,21]

It is likely that the process of dissolving (and heating) in water led to the formation of free cobalt ions and the isopolytungstate species $[H_2W_{12}O_{42}]^{10-}$ (and potentially others). The nature of the crystalline solid analysed suggests that as the mixture is cooled, the species that crystallises most readily utilises cobalt ions as the primary cation (perhaps indicating a lower solubility than ammonium salts of $[H_2W_{12}O_{42}]^{10-}$). This leads to a higher cobalt to tungsten ratio in the product (1:3) than in the starting material (1:5), meaning the reaction solution still contains POM species, likely present as ammonium or mixed ammonium/Co^{2+} salts.

2.7.2 Sodium cations

Reactions with ammonium chloride appear to show the lability of the Lindqvist structure either during the process of cation exchange or after dissolution in water. However, one factor to consider is that ammonium cations do also provide access to protons. These protons can facilitate hydrolysis and condensation processes that can, in turn, drive the rearrangement of POM structures. To further investigate the stability of the cobalt substituted Lindqvist-type structure, a cation exchange experiment which avoids the presence of potentially labile protons was investigated.

Instead, $(TBA)_7[(CoW_5O_{18}H)_2][NO_3]$ was dissolved in acetonitrile and treated with an excess of NaOTf (as a saturated acetonitrile solution). Again, a blue precipitate forms immediately which can be separated from the reaction mixture by centrifugation. The product was then washed with acetonitrile to remove any tetrabutylammonium salts and dried under vacuum. The solid was then re-dissolved in DMSO (with a few drops of water) with gentle heating to form a dark blue solution. This solution was used as the stock solution in a series of nanodrop encapsulation crystallisation experiments performed by Alexandra Longcake (Indicatrix Crystallography). These experiments involve encapsulation of a droplet of the stock solution containing the compound within an oil droplet. This allows for a controlled rate of solvent loss, helping to promote the formation of crystals (typical experiments will probe a range of
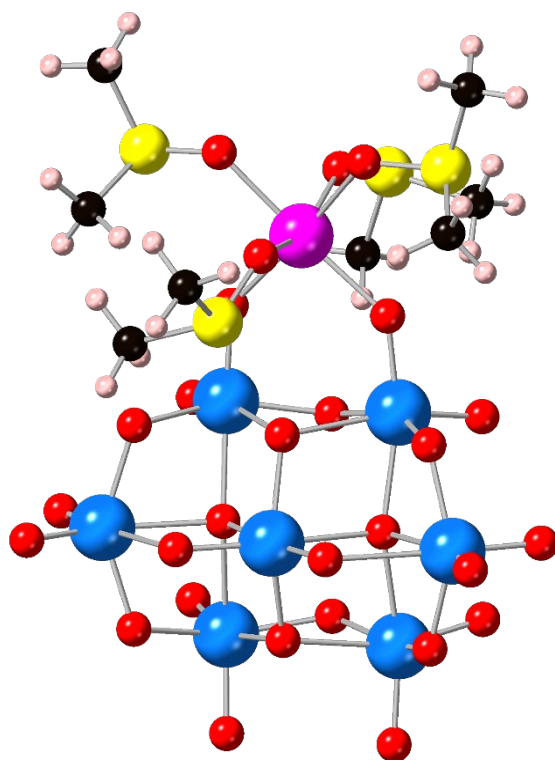
Figure 2.13: Single-crystal X-ray diffraction structure of a {(DMSO)$_4$CoW$_7$O$_{24}$}-type structure. Sodium cations and disorder in the DMSO ligands has been omitted for clarity. Co (pink), S (yellow) and C (black). The atomic radii are set to the CSD covalent radii.

solvent/oil combinations). Specific experimental details are given in **Section 2.10.16**. Crystals were obtained using this method and the structure is shown in **Figure 2.13**.

The structure consists of a paratungstate A (i.e. [W$_7$O$_{26}$]$^{6-}$) unit with a cobalt ion bound to the surface via two Co-O-W bridges. The co-ordination sphere of the cobalt ion is then filled by four DMSO molecules. There are then a number of sodium counter cations occupying space in between the POM units, though there was considerable disorder and therefore attempts to determine the exact formula/stoichiometry were not made.

The obtained structure suggests that, even when water is not the primary solvent and proton sources are avoided for both the cation exchange step and recrystallization step, the cobalt containing Lindqvist-type POM is still labile, with the respect to loss of the cobalt centre from the POM framework and rearrangement, when the cations are changed.

Interestingly, when the amount of water (and temperature) is changed, another structure can be isolated. Dissolving the crude solid obtained after cation exchange in a mixture of hot water/DMSO leads to the formation of a pink solution. Allowing the solution to cool to room temperature and stand for 2 days gave a crop of pink crystals. Analysis of the crystals by single-crystal X-ray diffraction gave the structure shown in **Figure 2.14**.
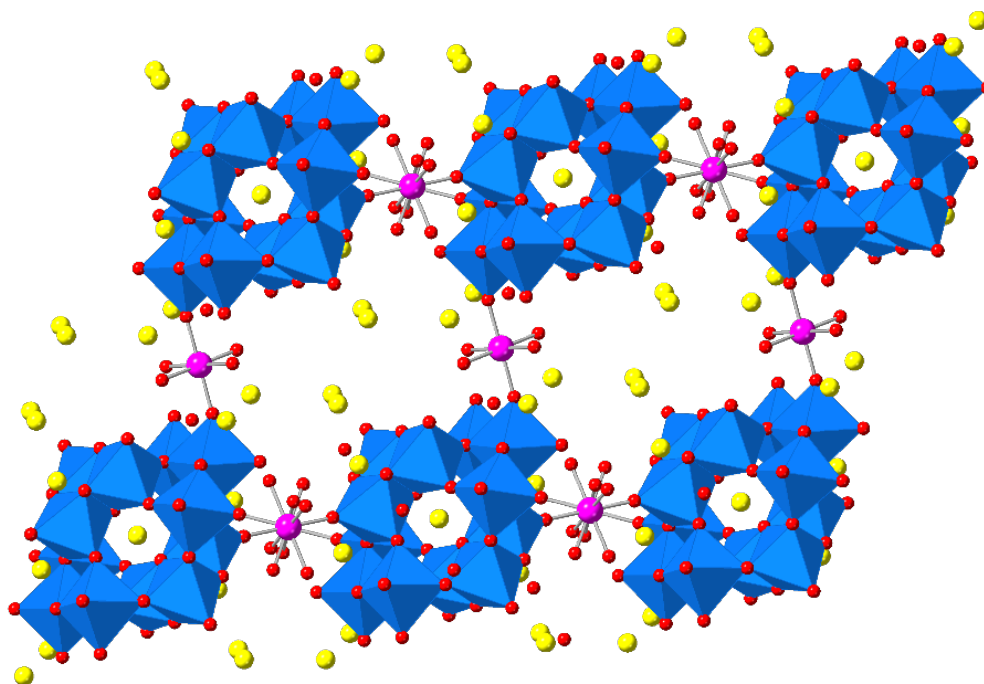
Figure 2.14: Single-crystal X-ray diffraction structure obtained when the crude product from the reaction of $(TBA)_7[(CoW_5O_{18}H)_2][NO_3]$ with excess NaOTf is recrystallized from hot water/DMSO. Additional solvent molecules are omitted for clarity. Co^{2+} shown in pink and Na^+ in yellow. The atomic radii are set to the CSD covalent radii.

The obtained structure is very similar to that shown in **Figure 2.12**, containing paratungstate B units bridged by $[Co(H_2O)_4]^{2+}$ ions. The cobalt centres bridge the POM units both within each layer and between layers, creating a 3D network of interconnected POMs. As well as cobalt ions, there are a significant number of water-solvated sodium ions occupying the cavities between the POM units. Again, there is a significant amount of disorder and therefore attempts to determine the exact number of sodium cations per POM have not been made.

The significant difference in the structures of the materials obtained when changing the method of recrystallization shows the sensitivity of the compound to the solvent conditions used. The fact that the Lindqvist structure is lost in all cases, however, shows how labile the structure is when the cations are exchanged and/or when the compound is exposed to even small quantities of water. This may be beneficial in some cases whereby these low energy pathways can be utilised to make interesting solid-state materials.

2.8 Conclusion

An efficient pathway for the synthesis of $(TBA)_7[(CoW_5O_{18}H)_2][NO_3]$ directly from $(TBA)_2[W_6O_{19}]$ has been developed. This involves treatment of the parent hexametalate with four equivalents of TBA(OH) to target a virtual "$(TBA)_5[W_5O_{18}H]$" lacunary species in-situ. The

mixture can then be directly treated with simple cobalt salts (like $Co(NO_3)_2.6H_2O$) to generate the dimeric $[(CoW_5O_{18}H)_2]^{6-}$ Lindqvist-type POM. The crude product of this reaction is contaminated with the tetrabutylammonium salt that is produced as a by-product in the reaction.

Given preparative scale recrystallization of the product has proved difficult, a number of alternative methods for removal of the excess TBA salt have been explored, including trituration of the crude product and the use of alternative cobalt sources. However, the most effective method for removal of the impurity involved the formation of a monomeric pyridine adduct. This adduct is simple to synthesise and purify when compared to the dimer. Spectroscopic analysis of the isolated adduct shows that the majority of the TBA salt impurity is lost during the reaction. Heating the adduct in toluene allows for removal of the pyridine ligand and reformation of the dimeric POM. Therefore, conversion of crude dimer to the corresponding pyridine adduct, followed by reformation of the dimer can provide an effective method of purification. This process can be made even more efficient by directly synthesising the pyridine adduct from $(TBA)_2[W_6O_{19}]$ by performing the initial synthesis in pyridine instead of acetonitrile.

Preliminary investigations into the formation of other adducts of $[CoW_5O_{18}H]^{3-}$ showed that more complex N-heterocycles can also efficiently form adducts. Aliphatic amines were generally found to be unreactive. Reactions with alcohols appear to illustrate the formation of labile adducts in which the ligand is lost very easily and that sterics may be important, with *iso*-propanol and *tert*-butanol giving no indication of adduct formation.

Cation exchange experiments have begun to indicate that the substituted Lindqvist dimer is very susceptible to rearrangement when the tetrabutylammonium cations are replaced. Evidence of rearrangement to multiple structures depending on the cation and solvents used has been obtained.

2.9 Future work

The synthetic methods described in this chapter represent a very efficient route to the $[(CoW_5O_{18}H)_2]^{6-}$ anion. However, more detailed characterisation, in the form of elemental analysis and inductively coupled plasma optical emission spectroscopy (ICP-OES), is required to verify the purity of crude samples of the dimeric product obtained from reactions of $(TBA)_2[W_6O_{19}]$ with TBA(OH), and $Co(NO_3)_2.6H_2O$. This should then be compared to the purity of samples obtained after formation of the corresponding pyridine adduct and reformation of

the dimer to give a clearer idea of how effective this method of purification is. This will give a solid basis for further reactivity studies as an exact appreciation of the nature of the starting material is required for any fundamental reactivity study.

Further efforts are also required to understand the key factors underpinning adduct formation. Several aliphatic amines, triphenylphosphine, and other neutral oxygen donors like THF were all found to be unreactive towards the dimer. These are very typical ligands but they appear to fail to form strong enough interactions with the dimer (and cobalt centre) to allow the formation of monomers. It may be that the presence of a π-system, for the aromatic N-donor ligands, and access to hydrogen bonding, for alcohols, are key factors but it is hard to say without further studies.

Finally, oxidation studies are required in order to determine the accessibility of higher cobalt oxidation states within the Lindqvist structure. Electrochemical studies could provide preliminary insight, giving an idea of the redox potentials. This could be followed by chemical oxidation studies, in which the dimer is exposed to sufficiently strong oxidising agents (e.g. iodosylbenzene, nitrous oxide, or tetrabutylammonium tribromide) to allow the isolation of oxidised products. This is important in the context of water oxidation catalysis, where higher oxidation state cobalt species are implicated as the active components.

2.10 Experimental

__2.10.1 Synthesis of (TBA)$_2$[W$_6$O$_{19}$] (ref 22)__

Sodium tungstate dihydrate (33 g, 100 mmol) was added to a conical flask along with acetic anhydride (40 mL) and dimethylformamide (30 mL). The mixture was heated to 100 °C and stirred for 3 hours. While keeping the white suspension at 100 °C, a solution of 12 M HCl (18 mL) in acetic anhydride (20 mL) and DMF (50 mL) was carefully added. The mixture was stirred for 10 minutes and then allowed to cool. The reaction mixture was vacuum filtered, and the white solid was washed with methanol (50 mL). The filtrate was the transferred to a conical flask. With vigorous stirring, a solution of TBA(Br) (15 g, 47 mmol) in methanol (50 mL) was added. A white precipitate forms immediately. The mixture was stirred for 5 minutes and then filtered to isolate a white solid that was washed with methanol (20 mL) and diethyl ether (50 mL). The crude product (20.46 g, 65% yield) can be recrystallized from boiling MeCN.

ATR FTIR: $\tilde{\nu}$ = 2963 (CH), 2936 (CH), 2876 (CH), 1462, 1381, 966 (s), 889, 873, 801 (s), 736 (s), 669, 584 (s).

__2.10.2 Synthesis of (TBA)$_7$[(Co(II)W$_5$O$_{18}$H)$_2$][NO$_3$]__

In a Schlenk flask, (TBA)$_2$[W$_6$O$_{19}$] (2.45 g, 1.29 mmol) was suspended in MeCN (10 mL). To a separate flask, TBA(OH) (5.30 mL, 5.18 mmol, 0.98 M in MeOH) was added and pumped dry. The golden oil was re-dissolved in MeCN (5 mL). The solvent was removed under reduced pressure. This process was repeated twice to ensure complete removal of MeOH. The TBA(OH) was dissolved in MeCN (5 mL) and transferred via cannula to the suspension of (TBA)$_2$[W$_6$O$_{19}$]. The mixture was stirred for 15 minutes or until all the solid dissolved. The colourless solution was transferred via cannula to a Schlenk flask containing Co(NO$_3$)$_2$.6H$_2$O (0.45 g, 1.55 mmol) suspended in MeCN (5 mL). The mixture was stirred and gradually turns dark purple/blue. The solution was stirred for one hour after which the solvent was removed under reduced pressure to leave a purple/blue oil. The oil was triturated with ethyl acetate (4 x 10 mL) and diethyl ether (4 x15 mL) and dried under vacuum to leave a free-flowing dark purple powder (2.56 g, 79% yield).

Small quantities of single-crystal X-ray diffraction quality crystals were grown by either:

- Slow evaporation of a saturated solution of (TBA)$_7$[(CoW$_5$O$_{18}$H)$_2$][NO$_3$] in DCM/toluene.
- Layering of ethyl acetate onto a saturated solution of (TBA)$_7$[(CoW$_5$O$_{18}$H)$_2$][NO$_3$] in DCM.

ATR FTIR: $\tilde{v}$ = 2956 (CH), 2924 (CH), 2871 (CH), 1482, 1380, 1338 (NO_3), 1153, 1028, 933 (s), 877, 807 (s), 760 (s), 699 (s), 675 (s), 606 cm^{-1}

2.10.3 Large scale preparation of (TBA)$_7$[(Co(II)W$_5$O$_{18}$H)$_2$][NO$_3$]

TBA(OH) (15.73 mL, 15.73 mmol, 1 M in MeOH) was added to a Schlenk flask and pumped dry. The golden oil was re-dissolved in MeCN (20 mL). The solvent was removed under reduced pressure. This process was repeated twice to ensure complete removal of MeOH. The TBA(OH) was dissolved in MeCN (30 mL) and (TBA)$_2$[W$_6$O$_{19}$] (7.44 g, 3.93 mmol) was added to form a white suspension. The mixture was stirred until all the solid was dissolved. To the colourless solution, Co(NO$_3$)$_2$.6H$_2$O (1.37 g, 4.72 mmol) was added. The red solid gradually dissolved and a dark purple/blue solution formed. The mixture was stirred overnight, after which the solvent was removed under reduced pressure to leave a purple/blue oil. The oil was dissolved in the minimum amount of DCM (ca. 10 mL) and transferred dropwise, via pipette, to a beaker containing ethyl acetate (150 mL) with vigorous stirring. A pale purple powder formed. To obtain the highest yield (and to avoid reformation of an oil) the ethyl acetate/DCM mixture was decanted and replaced with fresh ethyl acetate (150 mL) after every 2-3 mL portion of the DCM solution was added. After adding all the DCM solution, the mixture can be vacuum filtered. The purple solid was washed with ethyl acetate (100 mL) and diethyl ether (3 x 100 mL). The solid was dried on the filter paper followed by further drying in a vacuum oven (50 °C) overnight. This gave a dark purple/blue free flowing powder (8.97 g, 89% yield).

2.10.4 Synthesis of Li(OMe)

n-BuLi (26.3 mL, 2.5 M in hexanes, 66 mmol, 1 eq)) was added to a Schlenk flask. The flask was cooled to 0 °C and then MeOH (3.2 mL, 71 mmol, 1.2 eq) was added EXTREMELY SLOWLY (large amounts of butane gas are given off during the addition which can lead to over pressurisation if the addition is too quick). A white precipitate forms and, after all the MeOH is added, the solution was allowed to warm to room temperature and stirred for a further 30 minutes. A small amount of MeOH (ca. 0.3 mL) was added at this point to check for unreacted n-BuLi. If gas is given off, keep adding small portions of MeOH until no more gas is evolved. The suspension was filtered and the white powder obtained was washed with hexane (20 mL). The product was dried under vacuum (2.34 g, 93% yield).

2.10.5 Drying CoCl₂.xH₂O

Glassware was assembled as shown in the schematic adjacent. A KOH trap is a Dreschel flask filled with KOH pellets.
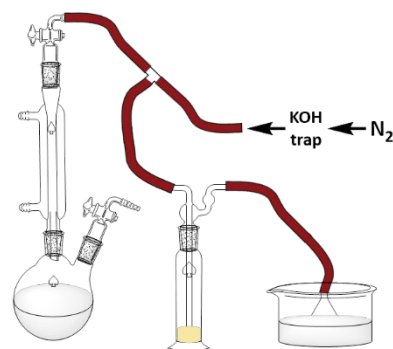
CoCl₂.xH₂O was added (19.52 g, 82 mmol based on hexahydrate) was added to a 100 mL round-bottom flask (rbf) with a sidearm/tap. The rbf and condenser were purged for 10 minutes with nitrogen by opening the sidearm/tap. $SOCl_2$ (50 ml, excess) was added slowly via the sidearm/tap. The sidearm/tap was closed, and the purple suspension was heated at reflux for 4 hours. During this time the purple suspension turned dark blue. The mixture was allowed to cool to room temperature before the condenser was removed and replaced with a stopper/screw cap. The volatiles were removed under reduced pressure and the collected thionyl chloride was stored for recycling. The remaining blue powder was washed with DCM (40 mL) and Et_2O (3 x 20 mL). The fine blue powder was dried under vacuum (10.21 g, 96% yield based on hexahydrate).

2.10.6 Synthesis of Co(OMe)₂

Anhydrous $CoCl_2$ (2 g, 15.4 mmol, 1 eq)) was added to a Schlenk flask and dissolved in MeOH (40 mL). In a separate Schlenk flask, Li(OMe) (1.17 g, 30.8 mmol, 2 eq) was dissolved in MeOH (20 mL). The Li(OMe) solution was transferred via cannula to the $CoCl_2$ solution. A dark purple solution formed immediately which was stirred for 30 minutes. The suspension was transferred via cannula onto a filter frit and the dark purple solid was washed with MeOH (5 x 10 mL) and diethyl ether (2 x 10 mL). The solid was dried under vacuum to obtain a free flowing dark purple powder (1.74 g, 94% yield).

2.10.7 Attempted synthesis of (TBA)₆[(Co(II)W₅O₁₈H)₂] from Co(OMe)₂ in MeCN

In a Schlenk flask, $(TBA)_2[W_6O_{19}]$ (1.65 g, 0.87 mmol) was suspended in MeCN (10 mL). To a separate flask, TBA(OH) (1.4 mL, 1.4 mmol, 1 M in MeOH) was added and pumped dry. The golden oil was re-dissolved in MeCN (2-3 mL). The solvent was removed under reduced pressure. This process was repeated twice to ensure complete removal of MeOH. The TBA(OH) was dissolved in MeCN (5 mL) and transferred via cannula to the suspension of $(TBA)_2[W_6O_{19}]$. The mixture was stirred for 45 minutes or until all the solid dissolved. H_2O (16 µL, 0.87 mmol) was added and the solution was stirred at room temperature overnight. The colourless solution was transferred via cannula to a Schlenk flask containing a purple suspension of

Co(OMe)$_2$ (0.13 g, 1.03 mmol) in MeCN (5 mL). There was no obvious change after stirring at room temperature for three hours or after heating at 70 °C overnight. Refluxing the mixture for a further 18 hours led to the formation of a dark brown/red suspension. After cooling to room temperature, the mixture was passed through a filter stick, leading to the isolation of a small amount of grey/black solid. The filtrate (still cloudy) was pumped dry giving a sticky solid. Trituration with ethyl acetate and diethyl ether gave no change. The crude solid was dissolved in minimum amount of DCM and cooled to −30 °C to attempt to crystallise the product, however only amorphous grey solid formed. Filtration of the mixture, followed by removal of the solvent gave a tacky purple solid (Infrared spectrum was taken and is shown below).
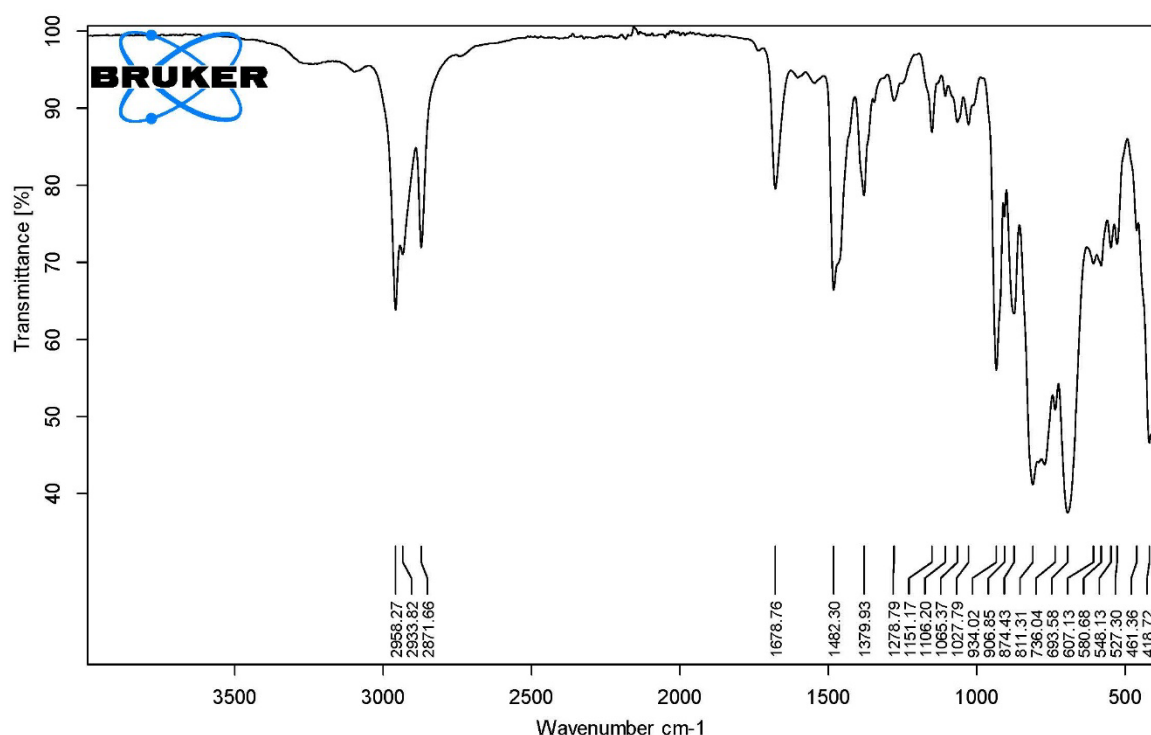
2.10.8 Synthesis of {Co[N(SiMe$_3$)$_2$]$_2$}$_2$ (ref 23)

Anhydrous CoCl$_2$ (0.65 g, 5 mmol, 1 eq) was added to a Schlenk flask and suspended in degassed THF (10 mL). LiN(SiMe$_3$)$_2$ (1.67 g, 10 mmol, 2 eq) was added to a separate Schlenk and dissolved in degassed THF (20 mL). Both solutions were cooled to 0 °C before the solution of LiN(SiMe$_3$)$_2$ in THF was added dropwise by cannula to the CoCl$_2$ solution. The resulting mixture was stirred for 30 minutes during which time it turned from dark blue to green. The mixture was left to stir overnight at room temperature before the solvent was removed under reduced pressure. The dark green residue was extracted into hexane (30 mL) and then pumped dry. The sticky oil was dissolved in the minimum amount of hexane and transferred (in the glove box) to a sublimation flask (this is a wide necked Schlenk flask which can accommodate

a cold finger). The cold finger was filled with dry ice/acetone. The flask was heated to 120 °C under vacuum to induce sublimation of the crude material onto the cold finger. Note if larger quantities of crude material are sublimed then material may begin to fall off the cold finger. The flask was taken into a glove box, the cold finger removed, and the sublimed green crystals were scraped off the cold finger (0.76 g, 40% yield)

2.10.9 Synthesis of (TBA)$_6$[(Co(II)W$_5$O$_{18}$H)$_2$] from {Co[N(SiMe$_3$)$_2$]$_2$}$_2$

In a Schlenk flask, (TBA)$_2$[W$_6$O$_{19}$] (1.09 g, 0.58 mmol) was suspended in MeCN (5 mL). To a separate flask, TBA(OH) (0.92 mL, 0.92 mmol, 1 M in MeOH) was added and pumped dry. The golden oil was redissolved in MeCN (2 mL). The solvent was removed under reduced pressure. This process was repeated twice to ensure complete removal of MeOH. The TBA(OH) is dissolved in MeCN (5 mL) and transferred via cannula to the suspension of (TBA)$_2$[W$_6$O$_{19}$]. The mixture was stirred for 45 minutes or until all the solid dissolved. H$_2$O (10 µL, 0.58 mmol) was added and the solution was stirred at room temperature overnight. The colourless solution was transferred via cannula to a Schlenk flask containing solid {Co[N(SiMe$_3$)$_2$]$_2$}$_2$ (0.26 g, 0.35 mmol). The mixture immediately turned dark purple/black but slowly turned red/brown after approximately 30 minutes. Stirring at room temperature for 2 days gave a dark red solution (slightly cloudy). The mixture was filtered and the volatiles were removed. The dark red/purple solid was triturated with ether to give a free flowing solid. The infrared spectrum was taken (shown below) before attempting to recrystallize by vapour diffusion of ether into a saturated MeCN solution of the crude solid.

54
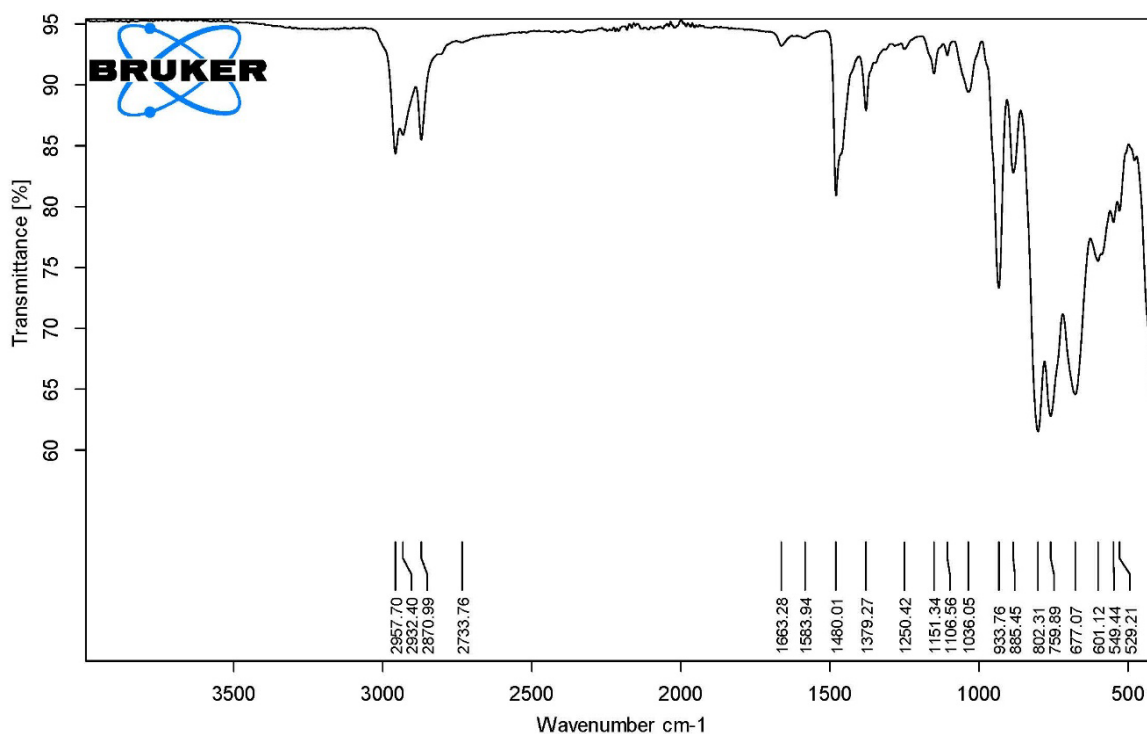
2.10.10 Synthesis of (TBA)$_3$[(Py)Co(II)W$_5$O$_{18}$H] from (TBA)$_7$[(Co(II)W$_5$O$_{18}$H)$_2$][NO$_3$]

(TBA)$_7$[(Co(II)W$_5$O$_{18}$H)$_2$][NO$_3$] (2 g, 0.47 mmol) was added to a Schlenk flask along with pyridine (5 mL). This leads to the formation of a dark pink solution which was stirred at room temperature for 15 minutes. With vigorous stirring, ethyl acetate (30 mL) was quickly added which leads to instant precipitation of a fine pink powder. The suspension was stirred for a further 5 minutes before vacuum filtering. The pink solid was washed with ethyl acetate (10 mL) and diethyl ether (2 x 10 mL) and allowed to dry on the filter paper. The solid was either transferred back to a Schlenk flask and dried under high vacuum (note the solid is very fine when dried and can easily be pulled out of the flask) or dried in the vacuum oven (50 °C) overnight. The crude product (1.63 g, 86%) was recrystallized by adding diethyl ether dropwise to a saturated solution of the compound in pyridine (2-3 mL). The solution was then either filtered to remove insoluble material or a couple of drops of pyridine were added to re-dissolve the solid. The resulting solution was cooled to −40 °C. Crystals formed within 24-72 hours and were isolated from the mother liquor by cannula filtration and washed with small amounts of cold *iso*-propanol. Drying under vacuum (or washing with anti-solvents like Et$_2$O or EtOAc) led to loss of crystallinity and the formation of a pink powder (0.76 g, 40%).

ATR FTIR: ṽ = 2958 (CH), 2924 (CH), 2871 (CH), 1653, 1601 (CN), 1481, 1380, 1341, 1151 , 1038, 933 (s), 883, 809 (s), 763 (s), 699 (s), 677 (s) cm^{-1}

2.10.11 Direct synthesis of (TBA)$_3$[(Py)CoW$_5$O$_{18}$H]

In a Schlenk flask, (TBA)$_2$[W$_6$O$_{19}$] (2.15 g, 1.14 mmol) was suspended in Pyridine (4 mL). To a separate flask, TBA(OH) (4.7 mL, 4.54 mmol, 0.98 M in MeOH) was added and pumped dry. The golden oil was re-dissolved in MeCN (5 mL). The solvent was removed under reduced pressure. This process was repeated twice to ensure complete removal of MeOH. The TBA(OH) was dissolved in pyridine (4 mL) and transferred via cannula to the suspension of (TBA)$_2$[W$_6$O$_{19}$]. The mixture was stirred for 5 minutes or until all the solid dissolved and a pale brown solution forms. Solid Co(NO$_3$)$_2$.6H$_2$O (0.40 g, 1.36 mmol) was added directly to reaction mixture. The solution was stirred at room temperature and gradually turns dark pink as the solid dissolves. The solution was stirred for one hour. With vigorous stirring, ethyl acetate (40 mL) was quickly added to the Schlenk flask immediately precipitating a fine pink powder. The solution was stirred for a further 5 minutes before vacuum filtering. The pink solid was washed with ethyl acetate (10 mL) and diethyl ether (2 x 10 mL) and allowed to dry on the filter paper. The solid is then either transferred back to a Schlenk flask and dried under high vacuum (note

the solid is very fine when dried and can easily be pulled out of the flask) or dried in the vacuum oven (50 °C) overnight. A free-flowing pink solid was isolated (2.22 g, 81%). The product can be recrystallized using the methods previously described.

2.10.12 Synthesis of (TBA)$_3$[(Quin)CoW$_5$O$_{18}$H]

In a 10 mL screw-top sample tube, (TBA)$_7$[(Co(II)W$_5$O$_{18}$H)$_2$][NO$_3$] (0.25 g, 0.06 mmol) was dissolved in the minimum amount of quinoline forming a dark red solution. EtOAc (6 mL) was added and the tube was sealed. The tube was shaken for 30 seconds forming a red/orange suspension. The suspension was allowed to settle before the pale orange supernatant was decanted. The solid was washed with EtOAc (2 x 6 mL) and Et$_2$O (2 x 8 mL). The solid was dried in a vacuum oven at 50 °C overnight (0.21 g, 85% yield). Crystalline samples of (TBA)$_3$[(Quin)CoW$_5$O$_{18}$H] can be obtained by vapour diffusion of Et$_2$O into saturated solutions of (TBA)$_7$[(Co(II)W$_5$O$_{18}$H)$_2$][NO$_3$] dissolved in quinoline.

ATR FTIR: ṽ = 3053 (CH), 2958 (CH), 2924 (CH), 2871 (CH), 2734, 1677, 1622, 1595, 1507, 1481, 1379, 1342, 1152, 1128, 1107, 1047, 956, 932 (s), 883, 808 (s), 763 (s), 676 (s), 626 (s), 548, 529, 488 cm^{-1}

2.10.13 Synthesis of (TBA)$_3$[(AminoPy)CoW$_5$O$_{18}$H]

In a 10 mL screw-top sample tube, (TBA)$_7$[(Co(II)W$_5$O$_{18}$H)$_2$][NO$_3$] (0.25 g, 0.06 mmol) and 4-aminopyridine (60 mg, 0.64 mmol) were dissolved in DCM (1-2 mL). Note 4-aminopyridine is not very soluble in DCM and therefore most of it remains undissolved. The pink solution was stirred for 5 minutes before passing through a PTFE syringe filter into a 10 mL screw-top sample tube. EtOAc (6 mL) was added and the tube was sealed. The tube was shaken for 30 seconds forming a pink suspension. The suspension was allowed to settle before the pale pink supernatant was decanted. The solid was washed with EtOAc (2 x 6 mL) and Et$_2$O (2 x 8 mL). The solid was dried in a vacuum oven at 50 °C overnight (0.17 g, 70% yield). Crystalline samples of (TBA)$_3$[(AminoPy)CoW$_5$O$_{18}$H] can be obtained by vapour diffusion of Et$_2$O into saturated solutions of (TBA)$_7$[(Co(II)W$_5$O$_{18}$H)$_2$][NO$_3$] and excess 4-aminopyridine dissolved in MeCN.

ATR FTIR: ṽ = 3585, 3478, 3312, 3181, 2959 (CH), 2872 (CH), 1636, 1613, 1579, 1514, 1481, 1380, 1246, 1217, 1152, 1107, 1064, 1019, 935 (s), 906, 883, 815 (s), 766 (s), 684 (s), 622, 588, 548, 529 cm^{-1}

2.10.14 Synthesis of (TBA)$_6$[(4,4'-Bipy)(CoW$_5$O$_{18}$H)$_2$]

In a 20 mL screw-top sample tube, (TBA)$_7$[(Co(II)W$_5$O$_{18}$H)$_2$][NO$_3$] (1.67 g, 0.39 mmol) and 4,4'-bipyridine (90 mg, 0.58 mmol) were dissolved in MeCN (4 mL). A dark red/orange solution formed which was stirred overnight. The mixture was precipitated by the addition of an excess of ethyl acetate (approx. 15 mL). The pale orange supernatant was decanted. The solid was washed with EtOAc (2 x 15 mL) and Et$_2$O (2 x 15 mL). The solid was dried in a vacuum oven at 50 °C overnight (1.45 g, 90% yield). Crystalline samples of (TBA)$_6$[(4,4'-Bipy)(CoW$_5$O$_{18}$H)$_2$] can be obtained by vapour diffusion of Et$_2$O into saturated solutions of (TBA)$_7$[(Co(II)W$_5$O$_{18}$H)$_2$][NO$_3$] and a slight excess of 4,4'-bipyridine dissolved in MeCN.

ATR FTIR: $\tilde{v}$ = 2957 (CH), 2871 (CH), 1606, 1534, 1481, 1380, 1216, 1151, 1106, 1069, 1026, 977, 958, 935 (s), 881, 810 (s), 763 (s), 679 (s), 632, 546, 523 cm^{-1}

2.10.15 Attempted Cation exchange with ammonium chloride

In a 20 mL screw-top sample tube, (TBA)$_7$[(Co(II)W$_5$O$_{18}$H)$_2$][NO$_3$] (1.0 g, 0.23 mmol) was dissolved in MeOH (5 mL). A pink/red solution formed along with a small amount of white solid (found to be (TBA)$_2$[W$_6$O$_{19}$]). The solution was filtered through either a small celite pipette plug or a PTFE syringe filter to separate the solid. The pink/red solution was treated with a solution of ammonium chloride (0.25 g, 4.67 mmol) in MeOH (1-2 mL) with stirring. This lead to the precipitation of a blue solid. The solid can be isolated from supernatant by centrifugation (6000 rpm, 5 minutes). The supernatant was decanted and the solid was washed with MeOH (2 x 10 mL), MeCN (2 x 10 mL) and diethyl ether (2 x 10 mL). Each time the solid was separated by centrifugation. The isolated solid was dried under vacuum overnight. The solid was dissolved in the minimum amount of boiling water giving a pale pink solution (slightly cloudy). The solution was filtered through a PTFE syringe filter while hot before allowing to cool to room temperature and stand for 3 days. During this time, pink crystals formed which were analysed by single-crystal X-ray diffraction.

2.10.16 Attempted Cation exchange with sodium triflate

Crystallization using nanodrop encapsulation methodology performed by Dr. Alexandra Longcake.

In a 20 mL screw-top sample tube, (TBA)$_7$[(Co(II)W$_5$O$_{18}$H)$_2$][NO$_3$] (0.5 g, 0.12 mmol) was dissolved in the minimum amount of MeCN (around 2 mL) leading to the formation of a blue solution. This solution was treated with a saturated solution of NaOTf (0.40 g, 2.33 mmol) in MeCN with stirring. A blue precipitate forms immediately. The solid can be isolated from

supernatant by centrifugation (6000 rpm, 5 minutes). The supernatant was decanted and the solid was washed with MeCN (2 x 10 mL) and diethyl ether (2 x 10 mL). Each time the solid was separated by centrifugation. The isolated solid was dried under vacuum overnight.

Solutions of the solid in DMSO and DMSO with a few drops of water were made for attempted crystallisation using encapsulated nanodroplet crystallisation (ENaCt) protocols.[24] The stock solutions was dispensed in 50 nL portions via an SPT Labtech Mosquito liquid handling robot into 96-well glass plates (SWISSCI LCP Modular, 100 mm spacer) containing either an appropriate crystallisation oil (200 nL) or no oil. For wells containing oil, the oil was dispensed prior to injection of the stock solution into the oil droplet. The plate was sealed with a glass cover slip and allowed to stand undisturbed at room temperature in the dark. After 14 days, the crystallisation wells were assessed visually and by cross-polarized light microscopy for crystal growth. A single crystal of the compound was grown from DMSO/water (50 ηL) encased in a 200 ηL droplet of Fomblin-Y.

Wells were opened with use of a tungsten carbide scriber to remove a small portion of the glass cover slide, and the crystal manipulated using MiTeGen Kapton microtools. Crystals were transferred to a glass slide and extracted under oil (Fomblin YR-1800) and mounted onto a 35 μm MiTeGen Kapton loop before being flash-cooled to 150 K under N2 using an Oxford Cryosystems cryostream before the collection. SCXRD data was collected on a Rigaku XtaLAB Synergy PhotonJet micro-focus sealed X-ray tube diffractometer (Cu-Kα radiation, λ = 1.54184 Å, 4-circle goniometer, HyPix Arc-100 Detector).

Alongside this, a pink solution of the crude solid in a mixture hot water/DMSO was allowed to slowly cool to room temperature and stand for 3 days. This lead to the formation of a crop of pink crystals that were characterised using single-crystal X-ray diffraction.

2.11 References

1. W. Clegg, M. R. J. Elsegood, R. J. Errington and J. Havelock, *J. Chem. Soc., Dalton Trans.*, 1996, 681–690.

2. R. J. Errington, S. S. Petkar, P. S. Middleton, W. McFarlane, W. Clegg, R. A. Coxall and R. W. Harrington, *J. Chem. Soc., Dalton Trans.*, 2006, 5211–5222.

3. R. J. Errington, S. S. Petkar, P. S. Middleton, W. McFarlane, W. Clegg, R. A. Coxall and R. W. Harrington, *J. Am. Chem. Soc.*, 2007, **129**, 12181–12196.

4. X. Deng and H. Tüysüz, *ACS Catal.*, 2014, **4**, 3701–3714.

5. J. C. Védrine, *ChemSusChem*, 2019, **12**, 577–588.

6. Y. V. Geletii, B. Botar, P. Kögerler, D. A. Hillesheim, D. G. Musaev and C. L. Hill, *Angew. Chem. Int. Ed.*, 2008, **47**, 3896–3899.

7. Q. Yin, J. M. Tan, C. Besson, Y. V. Geletii, D. G. Musaev, A. E. Kuznetsov, Z. Luo, K. I. Hardcastle and C. L. Hill, *Science*, 2010, **328**, 342–345.

8. M. Natali, S. Berardi, A. Sartorel, M. Bonchio, S. Campagna and F. Scandola, *Chem. Commun.*, 2012, **48**, 8808.

9. S. Goberna-Ferrón, L. Vigara, J. Soriano-López and J. R. Galán-Mascarós, *Inorg. Chem.*, 2012, **51**, 11707–11715.

10. G. Zhu, Y. V. Geletii, P. Kögerler, H. Schilder, J. Song, S. Lense, C. Zhao, K. I. Hardcastle, D. G. Musaev and C. L. Hill, *Dalton Trans.*, 2012, **41**, 2084–2090.

11. D. Barats-Damatov, L. J. W. Shimon, L. Weiner, R. E. Schreiber, P. Jiménez-Lozano, J. M. Poblet, C. De Graaf and R. Neumann, *Inorg. Chem.*, 2014, **53**, 1779–1787.

12. J. Soriano-López, S. Goberna-Ferrón, J. J. Carbó, J. M. Poblet and J. R. Galán-Mascarós, in *Advances in Inorganic Chemistry*, Academic Press Inc., 2017, vol. 69, pp. 155–179.

13. D. F. Evans, *J. Chem. Soc.*, 1959, 2003–2005.

14. R. J. Errington, G. Harle, W. Clegg and R. W. Harrington, *Eur. J. Inorg. Chem.*, 2009, **2009**, 5240–5246.

15. T. Izuagie, PhD thesis, Newcastle University, 2017.

16. C. M. Tourné, G. F. Tourné, S. A. Malik and T. J. R. Weakley, *J. Inorg. Nucl. Chem.*, 1970, **32**, 3875–3890.

17. R. Calmanti, M. Selva and A. Perosa, *Mol. Catal.*, 2020, **486**, 110854.

18. A. B. Charette, in *Encyclopedia of Reagents for Organic Synthesis (EROS)*, 2001.

19. S. Dharuman and Y. D. Vankar, in *Encyclopedia of Reagents for Organic Synthesis (EROS)*, 2014, 1–8.

20. C. Gimenez-Saiz, J. R. Galan-Mascaros, S. Triki, E. Coronado and L. Ouahab, *Inorg. Chem.*, 1995, **34**, 524–526.

21. Z. Žák, J. Perůtka, J. Havel, I. Císařová and G. Giester, *J. Alloys Compd.*, 1998, **281**, 169–174.

22. W. G. Klemperer, *Inorg. Synth.*, 1990, **27**, 71-135.

23. A. M. Bryan, G. J. Long, F. Grandjean and P. P. Power, *Inorg. Chem.*, 2013, **52**, 12152–12160.

24. A. R. Tyler, R. Ragbirsingh, C. J. McMonagle, P. G. Waddell, S. E. Heaps, J. W. Steed, P. Thaw, M. J. Hall and M. R. Probert, *Chem.*, 2020, **6**, 1755–1765.

Chapter 3: Non-aqueous polyoxometalate solution speciation

3.1 Introduction

The assembly of polyoxotungstates by the acidification of monometallic $[WO_4]^{2-}$ in aqueous solution is well established.[1a-c] Analysis of the products obtained from such reactions is often done using single-crystal X-ray diffraction experiments. This gives unparalleled solid-state structural information but does not provide information regarding the species in solution. Instead, crystallographic studies give insight into which structures crystallise most readily. In order to gain information about the compounds present in solution, or the solution speciation, other techniques are required. The primary tool used in this regard is NMR spectroscopy.

Aqueous polyoxotungstate solutions have been well studied using ^{17}O and ^{183}W NMR spectroscopy by Maksimovskaya[2] and Howarth[3] (and co-workers). Their results showed that the acidification of various tungstate sources first leads to the formation of paratungstates A ($[W_7O_{24}]^{6-}$) and B ($[H_2W_{12}O_{42}]^{10-}$). Interestingly, freshly prepared solutions of $[H_2W_{12}O_{42}]^{10-}$ slowly convert into $[W_7O_{24}]^{6-}$ when held at 330 K. However, if the solution is cooled to room temperature, $[H_2W_{12}O_{42}]^{10-}$ crystallises out of the solution, leaving only $[W_7O_{24}]^{6-}$ in solution. This shows how the complimentary nature of both solid and solution state characterisation can provide a full picture of reactivity. Further acidification leads to various metatungstate species, $[H_2W_{12}O_{40}]^{6-}$, which adopt known Keggin structures. Potential pathways for the conversion of para- and metatungstates are also discussed. Similar studies in aqueous media have extended this understanding to different addenda atoms (Mo and V), mixed metal systems and heteropolyoxometalates.[4a-h] More recently, Falaise and co-workers have investigated the effects of supramolecular interactions on aqueous isopolytungstate speciation in the presence of γ-cyclodextrin.[5]

Solution speciation studies have been augmented in recent years by the development of a body of computational work from the group of Bo aimed at developing an understanding of aqueous POM systems.[6a-c] This group uses known POM structures and simple hydrolysis, condensation, and protonation processes to create a network of proposed building blocks for POMs in aqueous media. These building blocks then form the basis of millions of potential speciation models. The number of possible models is significantly reduced by applying constraints, such as only considering condensation/hydrolysis reactions in which one of the reactants is a monomer. This, combined with the application of a linear correction for the

formation constants predicted by the DFT methods applied (using experimentally determined formation constants for known species), leads to a final simulated speciation model which, generally, agrees well with experiment results. The group have applied this method (the so called POMSimulator) to aqueous Mo, W, V, Nb and Ta isopolyoxometalate systems.[6a-c]

Solution speciation in non-aqueous media is far less studied, particularly for polyoxotungstates, and hence the role of solvent of in the formation and stability of polyoxometalates is poorly understood. Various organic-soluble tetraalkylammonium salts of isopolytungstates (which are soluble in non-aqueous media) have been characterised by solution state ^{183}W and ^{17}O NMR spectroscopy.[1a-c] These are generally prepared by cation exchange from aqueous solutions and give very little insight into how the assembly process changes when moving away from aqueous systems. A significant exception is the seminal work by Jahr and co-workers on the formation of polyoxometalates by basic hydrolysis of metal alkoxides in organic solvents, including the synthesis of $[W_6O_{19}]^{2-}$ from oxoalkoxides $WO(OR)_4$ (R = Me, Et).[7a-c]

3.2 Chapter outline

This chapter describes an exploration of non-aqueous polyoxometalate speciation, using multinuclear NMR spectroscopy to identify the species present in solution. These studies were combined, where possible, with single-crystal X-ray diffraction experiments to give structural information about previously unknown species.

The first part of the chapter focuses on the nature of reaction mixtures targeting "(TBA)$_5$[W$_5$O$_{18}$H]" which, when combined with Co(NO$_3$)$_2$.6H$_2$O, were used to generate cobalt-containing Lindqvist-type POMs in the previous chapter, providing insight into the true nature of the intermediate solution.

This is followed by a more general examination of non-aqueous polyoxotungstate speciation, using ^{17}O and ^{183}W NMR spectroscopy to identify the products of the reaction of (TBA)$_2$[W$_6$O$_{19}$] with different amounts of TBA(OH) (as a source of charge). This can be considered analogous to examining the solution speciation at different pH in aqueous solutions.

*Note: Results from Section 3.3.1 to 3.3.5 were recently published - **Chem. Commun.**, 2023, **59**, 7919-7922.*

3.3 "(TBA)$_5$[W$_5$O$_{18}$H]" – What is in solution?

In the previous chapter, the degradation of (TBA)$_2$[W$_6$O$_{19}$] with four equivalents of base was used to target the virtual lacunary species "(TBA)$_5$[W$_5$O$_{18}$H]" as a precursor for the synthesis of heterometal containing Lindqvist-type POMs. Although this reaction proceeds as intended, the exact nature of the intermediate species is unknown.

3.3.1 ^{17}O NMR spectrum of the reaction mixture

To gain some insight into the nature of the reaction intermediate, the degradation mixture was probed by ^{17}O NMR spectroscopy.

The ^{17}O NMR spectrum of the starting (TBA)$_2$[W$_6$O$_{19}$] is shown in **Figure 3.1** for reference and shows the expected peaks for the central μ_6-O at −77 ppm (expected 1 O), bridging W-O-W at 415 ppm (expected 12 O), and terminal W=O at 776 ppm (expected 6 O).[8] During initial attempts to record this spectrum, the central μ_6-O peak was not observed. These attempts employed a delay time (D1) of 0.1 seconds between pulses. Only when increasing the delay time was the central peak observed and the spectrum shown in **Figure 3.1** (which appears to have a reasonably accurate integration) was recorded using a delay time of 500 seconds. The T1 time for the central oxygen was determined using an inverse recovery sequence. A relaxation delay of 600 seconds was used to allow for complete relaxation between pulses
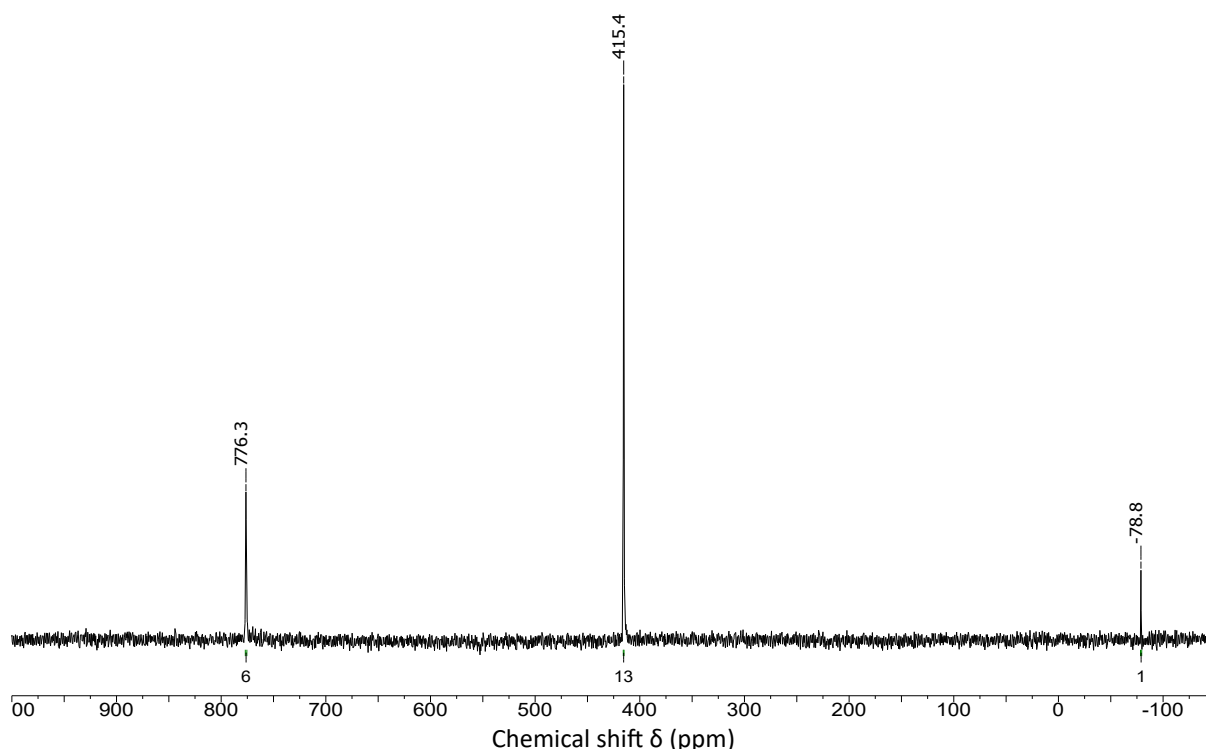
Figure 3.1: ^{17}O NMR spectrum of (TBA)$_2$[W$_6$O$_{19}$] in CD$_3$CN recorded with a 500 second relaxation delay between pulses.

and τ_{null} was found to be approximately 38 seconds, which corresponds to a T1 of approximately 55s, as given by the equation $\tau_{null} = T1 \times \ln 2$. This extremely long T1 for oxygen is due to the highly symmetrical nature of the octahedral environment for the μ_6-O which means there is no electric field gradient and therefore no efficient relaxation mechanism of relaxation for the quadrupolar ^{17}O nucleus.

The ^{17}O NMR spectrum presented in **Figure 3.2**, shows the product of reaction of (TBA)$_2$[W$_6$O$_{19}$] with four equivalents of TBA(OH). This is after stirring for one day at room temperature and removal of the volatiles to prepare the NMR sample. The absence of peaks at 776 ppm and 415 ppm is consistent with complete degradation of (TBA)$_2$[W$_6$O$_{19}$] into other metal-oxo species. The most prominent feature is a sharp peak at 437 ppm which can be assigned to [WO$_4$]$^{2-}$. Mono-tungstate clearly forms an important part of the mixture but, without knowing the exact nature of the other species in solution, we cannot be sure how dominant it is. The broad peak at −2 ppm is indicative of the formation of water, which is the expected by-product of POM hydrolysis with base. The rest of the spectrum consists of a series of broad peaks in the terminal W=O and bridging W-O-W regions. This may suggest the presence of several species, or a single low symmetry species (with many inequivalent oxygen
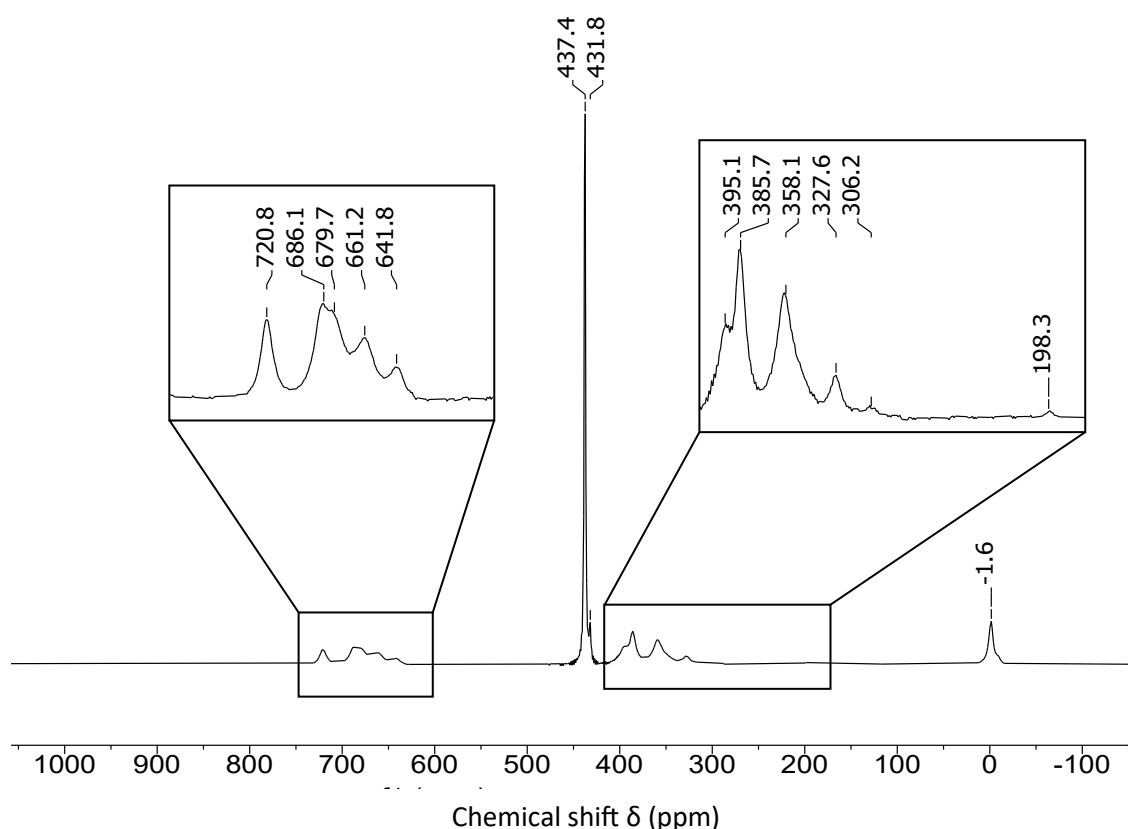
Figure 3.2: ^{17}O NMR spectrum of the reaction of (TBA)$_2$[W$_6$O$_{19}$] with 4 eq. of TBA(OH) after stirring at room temperature for one day and removal of the solvent. Acquired in CD$_3$CN.

environments), but unambiguous assignments are not possible without any structural information. The broad nature of the peaks could be indicative of exchange between oxygen environments on the NMR timescale, or could suggest the presence of large species, as relaxation times, and in turn line widths, are known to depend on the cube molecular radius (a), as described in **Equation 3.1** and **3.2**: where n is the electric field gradient asymmetry parameter, ($e^2Qq/\hbar$) is the quadrupole constant, and τ_c is the correlation time (i.e. tumbling rate). Correlation time is dependent on solvent viscosity (η), molecular radius (a), and temperature (T).[8]

$$\frac{1}{T_1} = \frac{1}{T_2} = \frac{3}{125}\left(1 + \frac{n^2}{3}\right)\left(\frac{e^2Qq}{\hbar}\right)^2 \tau_c \tag{3.1}$$

$$\tau_c = \frac{4\pi\eta a^3}{3kT} \tag{3.2}$$

3.3.2 ^{183}W NMR spectrum of the reaction mixture

Although some useful information was obtained from ^{17}O NMR spectroscopy of the reaction of (TBA)$_2$[W$_6$O$_{19}$] with four equivalents of TBA(OH), it is hard to determine the number of species present and their structure in solution from ^{17}O NMR spectroscopy alone. ^{183}W NMR spectroscopy can be employed as a complimentary technique. In particular, line widths tend to be very narrow and exchange processes are often slow for tungsten. This leads to well-defined peaks, which should make it easier to verify the number of individual metal environments, and compare the relative integrals to assign groups of peaks to the same species.

The relative insensitivity of ^{183}W NMR spectroscopy compared to more typically used NMR active nuclei means that ^{183}W NMR experiments are slightly different from conventional NMR spectroscopy methods. Firstly, significantly larger quantities of material are required (ca. 0.5-2 g). This means experiments use a 10 mm diameter tube as opposed to 5 mm tubes used for standard experiments. Secondly, a huge number of scans (10000-50000 for ^{183}W compared to 128-1024 for a typical ^{13}C experiment) are required to compensate for the low gyromagnetic ratio and relative abundance (14.3%).[9] This leads to very long acquisition times ranging from a few hours to a few days depending on the sample.

To probe the exact nature of the proposed "(TBA)$_5$[W$_5$O$_{18}$H]" intermediate by ^{183}W NMR spectroscopy, approximately two grams of (TBA)$_2$[W$_6$O$_{19}$] was reacted with four equivalents of TBA(OH) in acetonitrile. After stirring for one day at room temperature, the solvent was removed to leave a viscous oil. This was then taken up in a 2-3 mL mixture of deuterated and
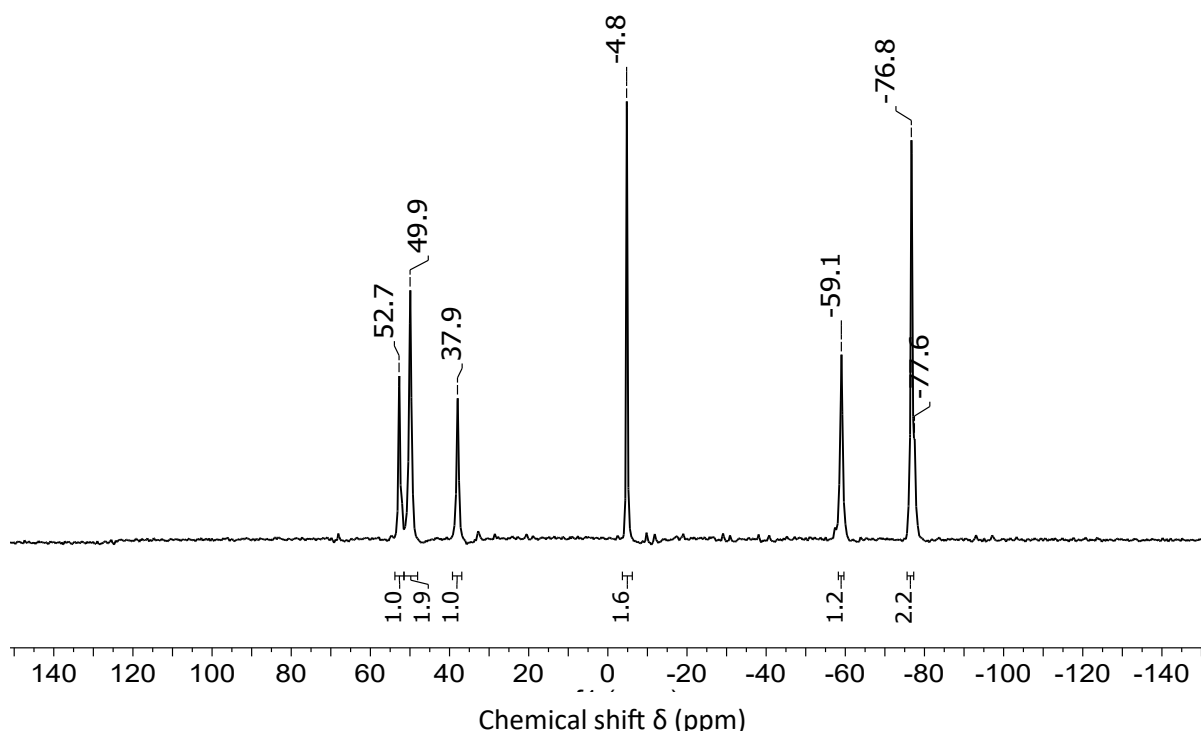
Figure 3.3: ^{183}W NMR spectrum of the reaction of (TBA)$_2$[W$_6$O$_{19}$] with 4 eq. of TBA(OH) after stirring at room temperature for one day and removal of volatiles. The spectrum is recorded in 1:1 CH$_3$CN:CD$_3$CN.

non-deuterated acetonitrile (at least 50% CD$_3$CN to ensure a solvent lock during the ^{183}W NMR experiment). Doing this gives an NMR solution that is approximately 0.35 M based on (TBA)$_2$[W$_6$O$_{19}$]. The ^{183}W NMR spectrum was then recorded over three days. The resulting ^{183}W NMR spectrum is shown In **Figure 3.3**.

The spectrum shows six signals. The central peak at −5 ppm can be assigned to [WO$_4$]$^{2-}$, which is consistent with the ^{17}O NMR spectrum and suggests that monomeric tungstate is a key component of the reaction mixture. The other five lines, at −77, −58, 38, 50 and 53 ppm respectively, appear in a 1:2:1:1:2 ratio. This is consistent with the presence of an isopolytungstate containing 7n tungsten atoms in five unique environments. Interestingly, compared to the ^{17}O NMR spectrum, the spectrum is relatively simple and may imply that this 7n isopolytungstate has a range of unique terminal W=O and bridging W-O-W environments to account for the complex ^{17}O NMR spectrum.

Previously, a similar spectrum was obtained during our group's efforts to produce [W$_2$O$_7$]$^{2-}$.[10] The experiments performed are summarised in **Scheme 3.1**. These can all be considered as different methods of targeting a ratio of negative charge to tungsten of 1, either by the addition of negative charge to isopolytungstates/tungsten oxide, introduction of a neutral tungsten source to "dilute" the charge, or the addition of electrophiles to reduce the charge
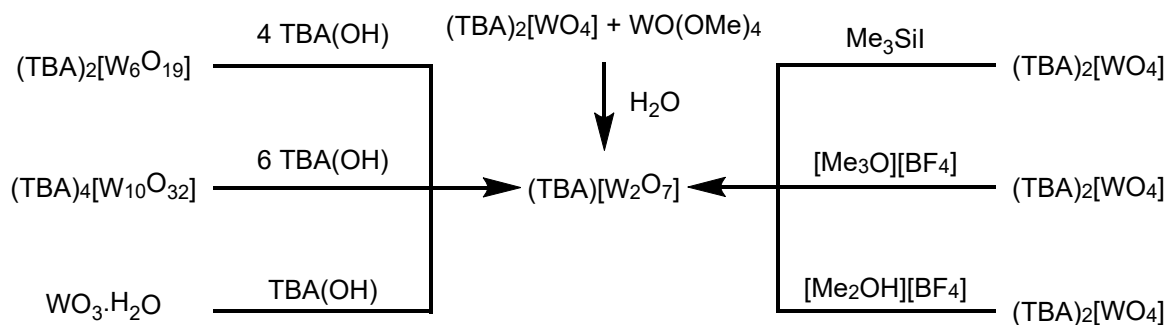
Scheme 3.1: General scheme summarising numerous methods used to target $[W_2O_7]^{2-}$

per tungsten atom. The spectrum obtained in ref 10 is the same as that shown in **Figure 3.3** except the peaks are shifted upfield by approximately 9 ppm.

The striking resemblance between the 5-line pattern shown in **Figure 3.3** and that shown in ref 10 (and the fact that one of the reactions in the previous study was also the degradation of $(TBA)_2[W_6O_{19}]$ with four equivalents of TBA(OH)) suggests that the same species may be responsible, regardless of the difference in chemical shifts.

In order to verify the chemical shifts obtained from the degradation of $(TBA)_2[W_6O_{19}]$ with four equivalents of base, the reaction was repeated and the [183]W NMR spectrum was re-acquired with a capillary insert containing 2 M $Na_2WO_4.2H_2O$ in D_2O as an internal standard. The resulting spectrum is shown in **Figure 3.4**. The Na_2WO_4 reference appears at 0.5 ppm. The 5-
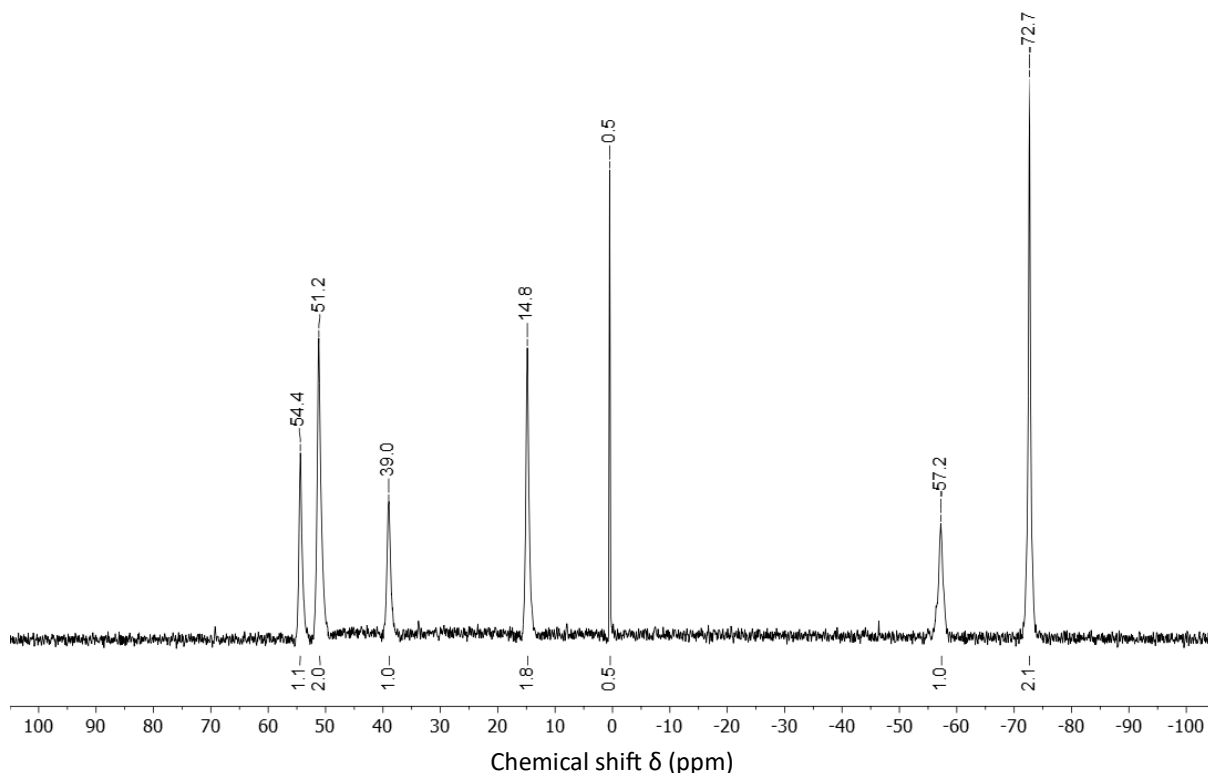
Figure 3.4: [183]W NMR spectrum of the reaction of $(TBA)_2[W_6O_{19}]$ with four equivalents of TBA(OH) with a coaxial insert containing 2 M $Na_2WO_4.2H_2O$ as a reference. The reference peak appears at 0.5 ppm.

lines of the degradation product appear at −73, −57, 15, 51, and 54 ppm respectively. These chemical shifts are in good agreement with those shown in **Figure 3.3** though are not perfectly reproduced (there is an average downfield shift of ca. 2 ppm). The peak previously observed at -77 ppm displays the largest difference of ca. 4 ppm.

Interestingly, the most striking difference between the two spectra is the ca. 20 ppm downfield shift of the peak assigned to $[WO_4]^{2-}$ to 14.8 ppm. In an attempt to rationalise this observation, the effects of both concentration and the presence of water on the chemical shift of $[WO_4]^{2-}$ were investigated.

Firstly, 2 M and 1 M solutions $(TBA)_2[WO_4]$ in MeCN were prepared and the ^{183}W NMR spectra of the samples were recorded with the same capillary insert containing 2 M $Na_2WO_4.2H_2O$ in D_2O as a reference. The resulting spectra are shown in **Figure 3.5b** and **3.5c**. There is an upfield shift of 2 ppm upon halving the concentration of $[WO_4]^{2-}$ (i.e. moving from 2 M to 1 M). This shows that the chemical shift of $[WO_4]^{2-}$ may have a concentration dependence, however, given the relatively small change in chemical shift upon halving the concentration of $[WO_4]^{2-}$ and the fact that the concentration of $[WO_4]^{2-}$ is unlikely to vary much between individual degradation reactions (the relative integrals of $[WO_4]^{2-}$ shown in **Figure 3.3** and **Figure 3.4** are 1.6 and 1.8 respectively) suggests concentration dependence is unlikely to be responsible for the observed 20 ppm difference.
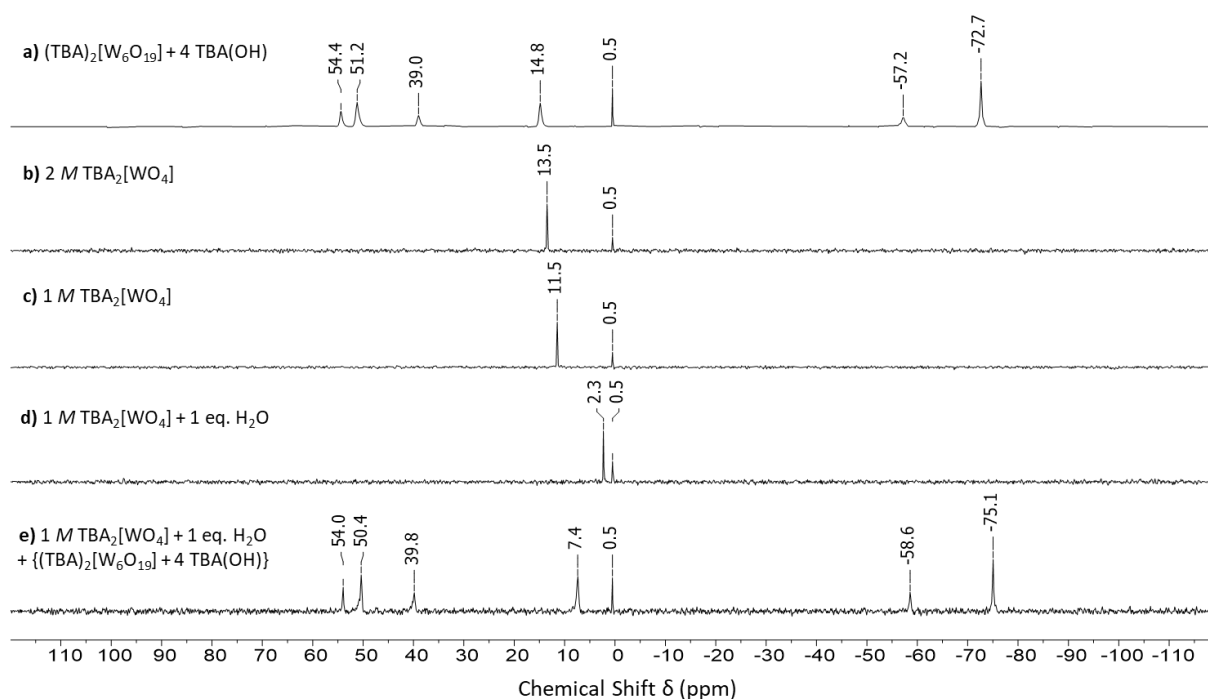
Figure 3.5: ^{183}W NMR spectra showing the effect of concentration and water on the observed chemical shift for $[WO_4]^{2-}$ and relative line widths of the $[WO_4]^{2-}$ peak in the presence/absence of the 5-line species.

Secondly, the influence of water was investigated. The ^{183}W NMR sample of 1 M TBA$_2$[WO$_4$] responsible for the spectrum shown in **Figure 3.5c** was treated with one equivalent water and the ^{183}W NMR spectrum was re-acquired. This produced a substantial change in the [WO$_4$]$^{2-}$ chemical shift, with the peak moving 9.2 ppm upfield. Given that the basic degradation of (TBA)$_2$[W$_6$O$_{19}$] produces water as a by-product, it is likely that the presence of water is the cause of the variation in the [WO$_4$]$^{2-}$ peak position. This should not be surprising in view of the high basicity of the [WO$_4$]$^{2-}$ anion, as exemplified by the hydrogen-bonding to water in the crystal structure of hydrated (Me$_3$BnN)$_2$[WO$_4$].H$_2$O.[11] Therefore, the removal of volatiles after the base degradation appears to be a key step in determining where the [WO$_4$]$^{2-}$ peak appears. Since steps were not taken to ensure all water was removed after the reactions responsible for the ^{183}W NMR spectra shown in **Figure 3.3** and **3.4**, it is reasonable to expect the amount of water present in each solution, and in turn, the position of the [WO$_4$]$^{2-}$, to vary significantly.

During experiments to rationalise the position of the [WO$_4$]$^{2-}$ peak, it became apparent that there is also a significant difference between the line widths of independently synthesised samples of (TBA)$_2$[WO$_4$] (**Figures 3.5b**, **3.5c**, and **3.5d**) and [WO$_4$]$^{2-}$ generated during the basic degradation of (TBA)$_2$[W$_6$O$_{19}$] (**Figures 3.3**, **3.4** and **3.5a**). The full width at half maximum (FWHM) increases from ca. 2.5 Hz in samples of independently synthesised TBA$_2$[WO$_4$] to a maximum of 13.0 Hz in solutions produced by basic degradation of (TBA)$_2$[W$_6$O$_{19}$] (as shown in **Figure 3.6**), although there is considerable variation from spectrum to spectrum with values from 6-13 Hz observed.

The broadening of the [WO$_4$]$^{2-}$ peak in the presence of the "5-line" species was verified by combining the product of degradation of (TBA)$_2$[W$_6$O$_{19}$] with four equivalents of TBA(OH) (responsible for the ^{183}W NMR spectrum shown in **Figure 3.4** and reproduced in **Figure 3.5a**) with a solution of 1 M TBA$_2$[WO$_4$] and 1 equivalent of water. The [WO$_4$]$^{2-}$ peak in the resulting

a) 11.5 FWHM = 2.4 Hz

b) 14.9 FWHM = 13.0 Hz
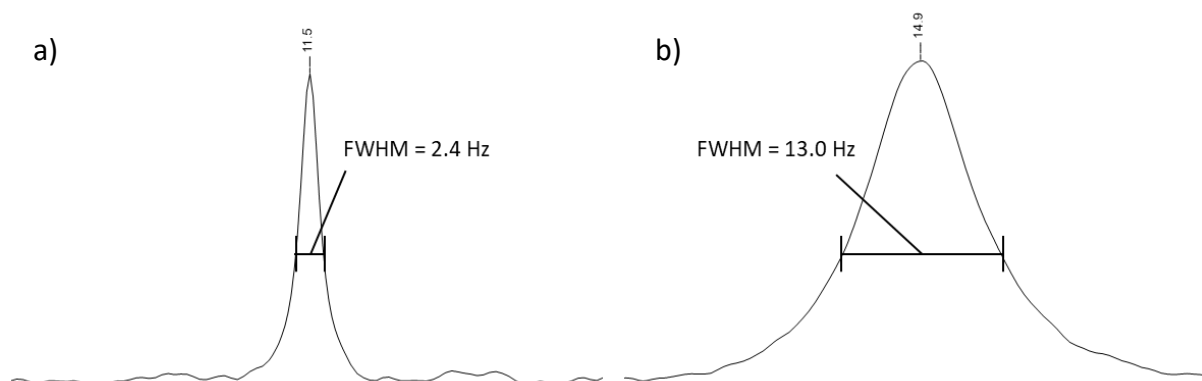
Figure 3.6: The position of and line width of the ^{183}W NMR signal of [WO$_4$]$^{2-}$ from a) 1 M solution of TBA$_2$[WO$_4$] in CH$_3$CN/CD$_3$CN and b) the degradation of (TBA)$_2$[W$_6$O$_{19}$] with four equivalents of base in CH$_3$CN/CD$_3$CN .

^{183}W NMR spectrum, shown in **Figure 3.5e**, appears to show an average of the effects produced. The peak appears at 7.4 ppm which is approximately halfway in between the corresponding peaks in the starting solutions (at 14.8 and 2.3 ppm respectively). This is likely to be a manifestation of the change in the ratio of $[WO_4]^{2-}$ to water. The peak is also notably broadened compared to the solution of $(TBA)_2[WO_4]$ alone, with a FWHM of 8.9 Hz. This may suggest chemical exchange between $[WO_4]^{2-}$ and the species responsible for the 5-line pattern.

In previous studies,[10] the peaks in ^{183}W NMR spectra were notably narrower than those observed in these current studies, and J_{WW} coupling between the two larger peaks in the 5-line spectrum of 22.6 Hz could be resolved. The broader peak observed in the spectra shown in **Figure 3.3**, **3.4**, and **3.5a** may be a result of the chemical exchange just discussed. The ^{183}W NMR spectrum shown in ref 10 does not contain any appreciable peak from $[WO_4]^{2-}$ which may seem odd, as the reactions summarised in **Scheme 3.1** target the same charge to tungsten ratio (Z/W) as those in this study. However, it is possible that the tungstate may have been removed during work-up as $(TBA)_2[WO_4]$ is very soluble (and hygroscopic) and may be removed with residual solvent, during trituration for example. The absence of tungstate will inhibit any broadening due to chemical exchange and therefore likely limit line widths. Furthermore, the ^{183}W NMR spectra shown in the original work were recorded with a dedicated ^{183}W probe and a 7.05 T magnet, whereas the spectra in this work were obtained using a low-gamma broad-band probe and 11.7 T magnet. Line broadening due to chemical shift anisotropy is more problematic at higher field strengths and therefore will likely compound the exchange effects, giving broad peaks and loss of the resolution of coupling constants.

3.3.3 Crystallographic studies

Detailed ^{17}O and ^{183}W NMR spectroscopy studies gave some insight into the true nature of the reaction mixture targeting the virtual "$(TBA)_5[W_5O_{18}H]$" lacunary species. So far, the results suggest the solution contains a mixture, made up of $[WO_4]^{2-}$ and a $7n$ isopolytungstate with five unique tungsten environments, which hosts a range of unique terminal and bridging oxygen environments. However, we cannot extract precise structural information based on the NMR spectroscopy alone.

Numerous attempts have been made to obtain single crystals from reactions targeting "$(TBA)_5[W_5O_{18}H]$". Crystallisation by slow evaporation of acetonitrile solutions or slow

diffusion of anti-solvents (such as diethyl ether or hexane) into saturated solutions results in oils. This mirrors the results reported in ref. 10, where the group were unable to isolate anything crystalline from reaction mixtures.

In order to try to overcome this issue, the effect of changing the quantity of base was investigated. Given the solubility of POMs in non-aqueous solution (with quaternary ammonium salt cations) increases with charge, it is reasonable to suggest that the addition of less charge (i.e. less base) to reaction mixtures will produce species with low enough solubility that they may crystallise. The effect changing the quantity of base has on solution speciation, studied by ^{17}O and ^{183}W NMR spectroscopy, will be discussed in **Section 3.4**.

Treatment of $(TBA)_2[W_6O_{19}]$ with one equivalent of TBA(OH) produces a white suspension. This suspension can be stirred overnight with slight warming (60 °C) to bring most of the solid into solution. The mixture was filtered, and diethyl ether was slowly added by vapour diffusion over the course of several weeks. This eventually produced colourless crystals which were shown to be 1:1 co-crystals of $(TBA)_2[W_6O_{19}]$ and the new isopolytungstate $(TBA)_5[W_7O_{24}H]$, shown in **Figure 3.7**. The seven cations per $[W_6O_{19}]^{2-}$ and $\{W_7O_{24}H\}$ indicates the charge is 5− and hence, the given formula includes one proton which is not located by the diffraction experiment. The structure is distinctly different from the known $[W_7O_{24}]^{6-}$ structure (shown in **Figure 3.8** for comparison) isolated from aqueous solutions. $[W_7O_{24}H]^{5-}$ can be regarded as a combination of a lacunary pentatungstate $\{W_5O_{18}\}$ and ditungstate $\{W_2O_7\}$, neither of which have been isolated independently.
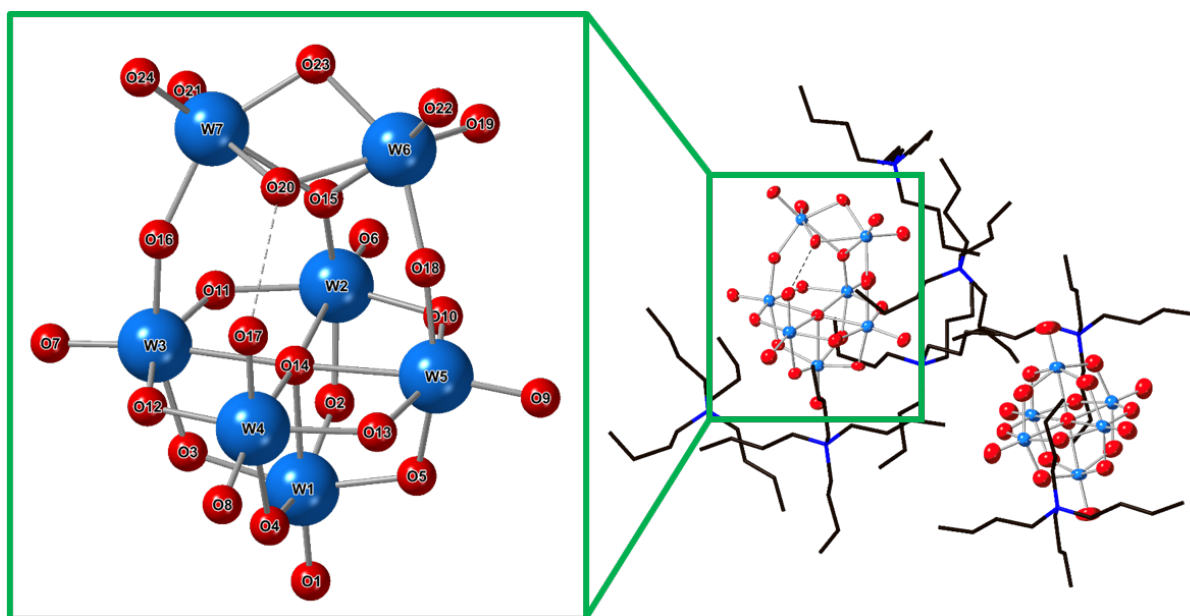
Figure 3.7: Single-crystal X-ray diffraction structure of $(TBA)_7[W_7O_{24}H].[W_6O_{19}].3MeCN$ with probability ellipsoids at 50% level for the anions. The cations are shown in skeletal form for clarity. An enlarged view of $[W_7O_{24}H]^{5-}$ is also given.
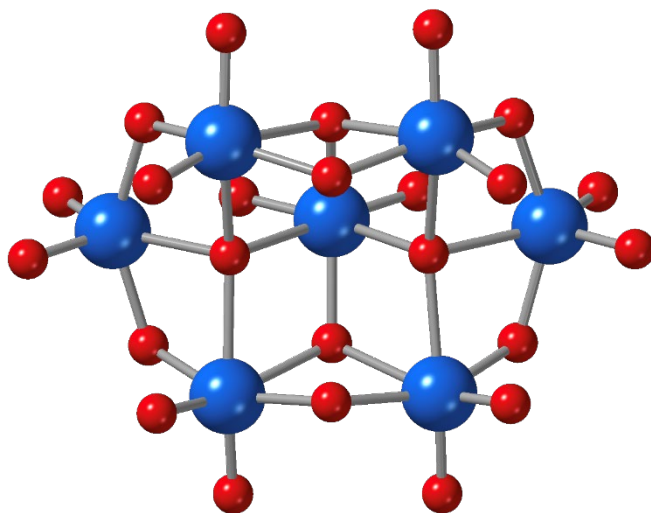
Figure 3.8: Single-crystal X-ray diffraction structure of $Na_6[W_7O_{24}].14H_2O$ reported in ref 13. The cations and co-crystallized solvent are omitted for clarity.

Using Pope's classification of POMs, $(TBA)_5[W_7O_{24}H]$ can be described as a type III POM as it contains addenda atoms with both one or two terminal M=O bonds.[12] Analysis of the terminal W=O bond lengths for the W atoms which make up the $\{W_5\}$ unit (i.e. W1-W4), show an average bond length of ca. 1.73 Å. This is significantly longer than those of the $[W_6O_{19}]^{2-}$ found in the co-crystal (ca. 1.69 Å), which is a manifestation of the higher charge associated with $\{W_7O_{24}H\}$.

The bridging W-O bond lengths of $[W_7O_{24}H]^{5-}$ show sizeable distortions versus those in $[W_6O_{19}]^{2-}$ (average bridging W-O of ca. 1.92 Å). There is a compression in the W-O bonds linking the $\{W_5\}$ unit and the capping $\{W_2\}$ unit (I.e. W2-O15, W3-O16 and W5-O18) with an average bond length of ca. 1.88 Å. This is paired with a lengthening of axial W-O bonds of the W_5 unit (i.e. W2-O2, W3-O3, W4-O4 and W5-O5) with an average bond length of ca. 1.99 Å, consistent with an associated trans effect. Any bridging W-O bonds lying in the equatorial plane of the $\{W_5\}$ unit (including all of those from W1) are a lot closer in length to those observed in $[W_6O_{19}]^{2-}$, with an average of ca. 1.92 Å.

The short O-O distance between O17 and O20 is consistent with a hydrogen bond between these atoms and suggests that the proton of $[W_7O_{24}H]^{5-}$ is localised, rather than disordered over multiple sites. Bond valence sum analysis indicates localisation of the proton on O20 rather than on O17 ($V_{O20} = 1.18$ vs. $V_{O17} = 1.58$). This, along with the short W4-O17 bond length of 1.750(7) Å, means the presence of a second terminal W=O on W4, which is hydrogen bonding to a proton localised on O20, is an appropriate description of the bonding, as opposed

to a formal W-OH. The "capping" $\{W_2\}$ unit contains *cis*-WO_2 fragments with an average W=O bond length of ca. 1.74 Å, which is very similar to the other present in the structure.

There are three oxygens bridging W6 and W7, however, the W6-O23-W7 bridge contains considerably shorter W-O bonds (1.940(7) and 1.949(7) Å respectively) compared to the other two bridges, which have an average W-O bond length of ca. 2.20 Å. This is likely because O15 is bridging three W atoms (μ_3-O) and O20 can be considered as a bridging hydroxide (μ_2-OH), whereas O23 can be deemed a genuine μ_2-O.

Importantly, the C_s symmetry of $[W_7O_{24}H]^{5-}$, which is a result of the tilted $\{W_2\}$ capping group, gives rise to five unique tungsten environments for the seven tungsten atoms. The two tungsten's of the ditungstate unit (W6 and W7) and two of the four atoms in the equatorial plane of the pentatungstate unit (W3 and W5) are chemically equivalent. This should produce a ^{183}W NMR spectrum with five peaks in a 1:2:1:1:2 ratio, which is exactly what is observed in **Figures 3.3**, **3.4** and **3.5a**. This suggests the new isopolytungstate $[W_7O_{24}H]^{5-}$, only the third to be isolated from non-aqueous solutions after $[W_6O_{19}]^{2-}$ and $[W_{10}O_{32}]^{4-}$, is the other major component of degradation reactions targeting "$(TBA)_5[W_5O_{18}H]$" and previous studies targeting ditungstate.[10]

The formation of a mixture of $(TBA)_5[W_7O_{24}H]$ and $(TBA)_2[WO_4]$ from reactions targeting "$(TBA)_5[W_5O_{18}H]$" or "$(TBA)_2[W_2O_7]$" (Z/W =1) can be rationalised using **Equation 3.3** and **3.4**.

$$9 \text{ "}(TBA)_5[W_5O_{18}H]" \rightarrow 5 \text{ } (TBA)_5[W_7O_{24}H] + 10 \text{ } (TBA)_2[WO_4] + 2 \text{ } H_2O \qquad (3.3)$$

$$3 \text{ } (TBA)_2[W_6O_{19}] + 12 \text{ } (TBA)[OH] \rightarrow 2 \text{ } (TBA)_5[W_7O_{24}H] + 4 \text{ } (TBA)_2[WO_4] + 5 \text{ } H_2O \qquad (3.4)$$
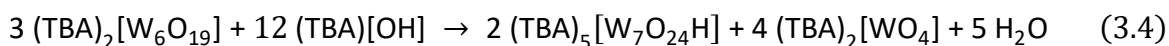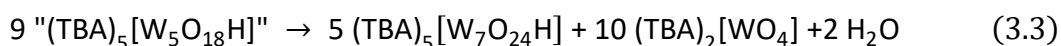
A 1:2 ratio of $[W_7O_{24}H]^{5-}$ and $[WO_4]^{2-}$ also has a Z/W ratio of 1. Experimentally, we see integrals for the $[WO_4]^{2-}$ peak in ^{183}W NMR spectra in region of 1.6-1.8 per $[W_7O_{24}H]^{5-}$. This is close to the proposed 2:1 ratio and suggests this mixture is preferred over any lacunary species or lower nuclearity isopolytungstates. Furthermore, this mixture must be labile with respect to rearrangement as the addition of metal salts, such as the cobalt salts discussed in **Chapter 2**, to this mixture led to facile generation of the heterometal containing Lindqvist-type polyoxometalate.

3.3.4 NMR spectroscopy simulations

*The simulations discussed in this section were performed by Dr Magda Pascual-Borras. Experimental details are given in **Section 3.7.10**.*
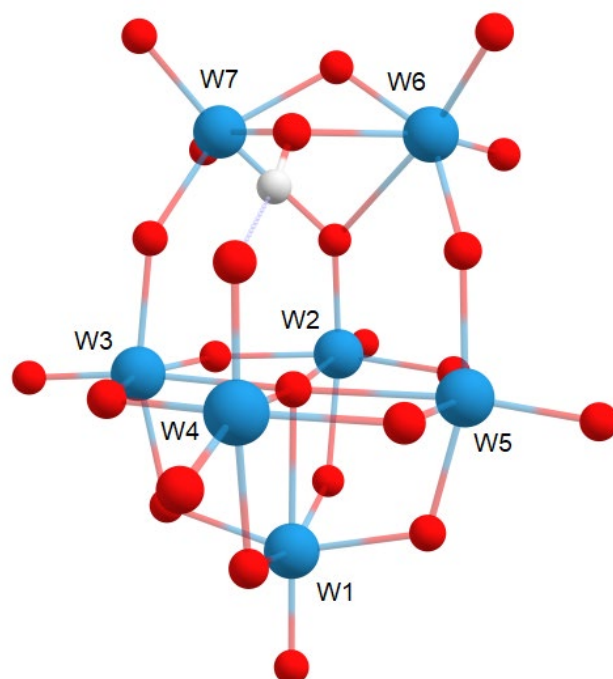
Figure 3.9: Optimised structure of $[W_7O_{24}H]^{5-}$, obtained using the OPBE functional and TZ2P basis set.

In order to further confirm the assignment of the 5-line pattern observed upon degradation of $(TBA)_2[W_6O_{19}]$ with four equivalents of TBA(OH), Density Functional Theory calculations were used to simulate the ^{183}W and ^{17}O NMR spectra of $[W_7O_{24}H]^{5-}$. Firstly, the structure was optimised using a range of functionals and basis sets. The optimised structure using the OPBE functional and TZ2P basis set is shown in **Figure 3.9**. It shows good agreement with the experimental structure, in particular showing that a bridging μ_2-OH between W6 and W7 is more energetically favourable than a terminal W4-OH. From the optimised structure, single-point NMR calculations are performed to obtain average isotropic shielding values for the nuclei of the target compound (σ_x). This process was also done for a reference compound (σ_{ref}), $[WO_4]^{2-}$ for tungsten NMR spectroscopy and H_2O for oxygen NMR spectroscopy. The calculated chemical shifts were obtained using **Equation 3.5**.

$$\delta_{cal} = \sigma_{ref} - \sigma_x \tag{3.5}$$

Computational procedure (NMR//OPT)	W_1	W_4	$W_{3/5}$	W_2	$W_{6/7}$	MAE	J_{WW}
PBE/TZP//PBE86/TZ2P	-44	138	152	118	-38	64	22.6
OPBE/TZP//PBE/TZ2P	-98	93	105	70	-80	34	22.8
PBE/TZP//OPBE/TZ2P	-66	94	126	87	-60	38	22.8
BP86/TZP//BP86/QZ4P	-51	135	146	112	-46	58	23.0
This work	-58	53	50	38	-77	-	22.6[a]

[a] Value taken from ref 10.

Table 3.1: Computed and experimental ^{183}W NMR chemical shifts (in ppm) and coupling constant (in Hz) for anion $[W_7O_{24}H]^{5-}$ using several methodologies.

The calculated [183]W NMR chemical shifts obtained from a range of functionals and basis sets are summarised in **Table 3.1**. All of the methods employed reproduce the experimentally observed 1:2:1:1:2 pattern for $[W_7O_{24}H]^{5-}$. Deviations of the computed chemical shifts from the experimental values obtained in this study were given as Mean Absolute Errors (MAEs). The best methodology for reproducing the experimental [183]W NMR spectrum of $[W_7O_{24}H]^{5-}$ was OPBE/TZP//PBE/TZ2P, with a MAE of 34 ppm compared to the values given in **Figure 3.3**. These simulations also allowed us to tentatively assign the peaks of the experimental spectrum to the tungsten atoms responsible for them, as shown in **Figure 3.10**. The simulations suggest that the peaks at −77 and −58 ppm are from the tungsten atoms of the {W$_2$} capping unit (red) and the bottom tungsten atom of the {W$_5$} unit (blue) respectively. The remaining peaks at 38, 50 and 53 ppm can be assigned to the four equatorial tungstens of the {W$_5$} unit (purple, green and yellow). These three peaks are fairly similar in chemical shift and may imply that the chemical enviroments for these tungsten atoms are equally similar. Coupling constants are also obtained during the NMR calculation and, from **Table 3.1**, it is apparent that the experimentally obtained coupling constant from ref. 10 is extremely well reproduced regardless of the method used.
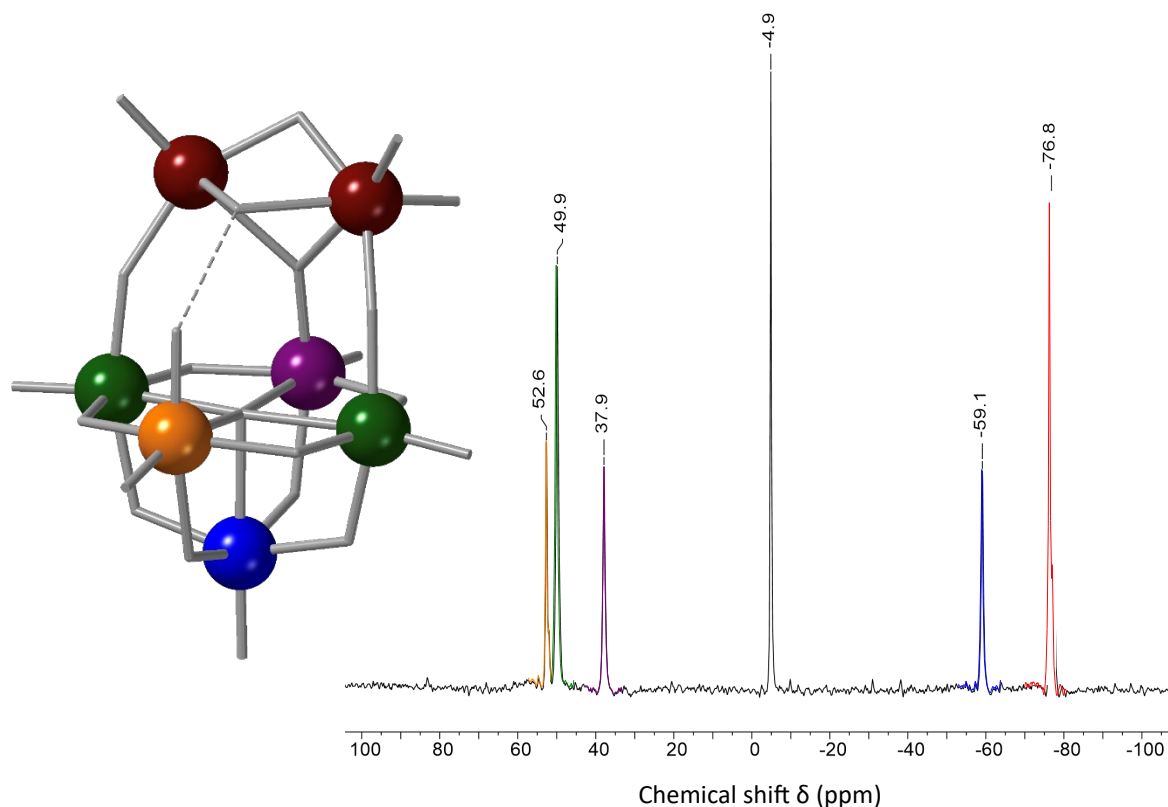
Figure 3.10: Experimental [183]W NMR spectrum obtained from the reaction of (TBA)$_2$[W$_6$O$_{19}$] and 4 eq. of TBA(OH) with assignments to $[W_7O_{24}H]^{5-}$ based on computational findings.

The computed ^{17}O NMR shifts of $[W_7O_{24}H]^{5-}$ were also obtained using the best perfoming functional and basis set (OPBE/TZP//PBE/TZ2P) identified from the ^{183}W NMR simulations. A full list of the obtained chemical shifts is given in **Section 3.7.10** and a qualitative view of the results is given in **Figure 3.11**, with a comparison to the experimentally obtained ^{17}O NMR spectrum from the reaction of $(TBA)_2[W_6O_{19}]$ with four equivalents of base. It should be noted that standard NMR calculations give information about chemical shifts but give no information about linewidths and therefore, purely for the purpose of comparison with the experimental spectrum, the linewidths have been arbitrarily set to 300 Hz, which is similar to those observed in the experimental spectrum.

Immediately, we can see that the simulated NMR spectrum of $[W_7O_{24}H]^{5-}$ (**Figure 3.11b**) is in good agreement with the experimental NMR spectrum (**Figure 3.11a**). In particular, the obtained chemical shifts and pattern for the terminal W=O region of the spectrum (800-600 ppm) are very similar. Both show a separate peak around 720 ppm. The calculations assign this peak to O7/O9 (see **Figure 3.7**), which lie in the plane of the $\{W_5\}$ unit. The calculations then suggest that the chemical shifts of O1, O6, O19 and O21 are all extremely similar. This may be used to help explain the cluster of intensity in the experimental spectrum between 680-690 ppm. The remaining three terminal W=O units (O17, O22 and O24) are predicted to give two
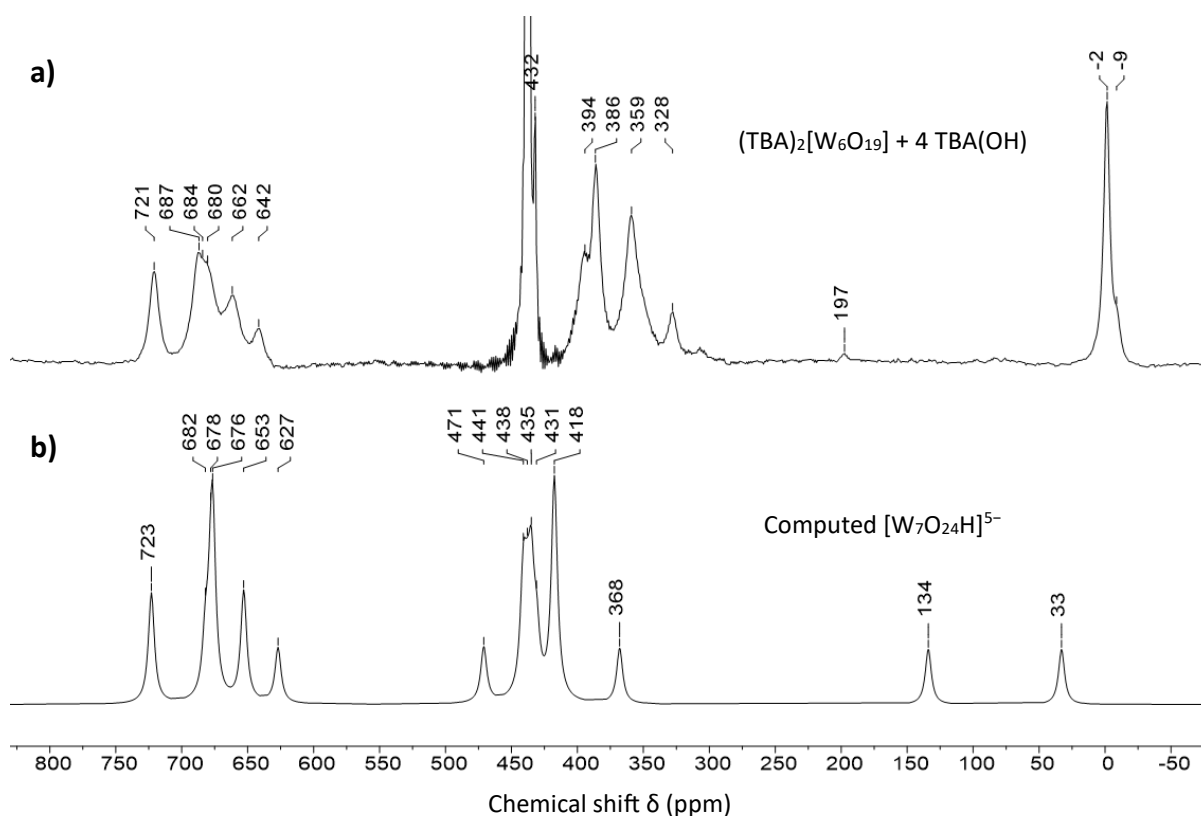
Figure 3.11: Experimental ^{17}O NMR spectrum for the reaction of $(TBA)_2[W_6O_{19}]$ with 4 eq. of TBA(OH) and the simulated ^{17}O NMR spectrum of $[W_7O_{24}H]^{5-}$. The linewidths in the simulated spectrum are arbitrarily set to 300 Hz.

peaks (O22 and O24 are chemically equivalent) that are more upfield than the rest, which may be attributed to their close proximity to the localised proton of $[W_7O_{24}H]^{5-}$ on O20.

The pattern observed for the bridging W-O-W region (300-500 ppm) is also somewhat similar to the experimental spectrum, however, the chemical shifts appear to be systematically overestimated (i.e. values are too positive). This observation is consistent with and was discussed by Pascual-Borràs and co-workers, who claim that the errors may come from solvent effects, rovibrational effects and other methodological limitations.[14] In order to improve the fit between experimental results and the computed chemical shifts, the group used a set of known polyoxometalates and their experimentally determined ^{17}O NMR chemical shifts to find a linear relation between the computed isotropic shieldings (σ_{calc}) and the reported chemical shifts. This gave **Equation 3.6**, where δ = experimental chemical shift. A second linear regression was performed by the authors using only data for the bridging W-O-W chemical shifts and isotropic shields and these were found to have higher average errors than other oxygen environments. This gave **Equation 3.7**.

$$\delta = -1.079\sigma + 313.0 \tag{3.6}$$

$$\delta = -1.157\sigma + 271.1 \tag{3.7}$$

The effects of linear scaling on the computed ^{17}O NMR shifts of $[W_7O_{24}H]^{5-}$ are summarised in **Figure 3.12**. Linear scaling does very little to improve the fit between computed and experimental values for the terminal W=O peaks, and in fact, the original computed values tend to agree more with the experimental results. Where the scaling really helps is with the bridging W-O-W region. Before scaling, the shifts obtained for this region were between 368-471 ppm, compared with 328-432 ppm for the experimental spectrum. Scaling with **Equation 3.6** (shown in Figure **3.12e**) led to a reduction in the error associated with these peaks, which now appear between 347-457 ppm. An interesting application of this scaling also moves the computed chemical shift for the central μ_5-O to −15 ppm, which is now close to the experimentally observed, and very broad, water peak at −2 ppm. This may explain why no distinct peaks are observed in the central oxygen region in the experimental spectrum.

The effect of applying the linear scaling equation derived just from bridging W-O-W values is shown in **Figure 3.12d**. As we may expect, this leads to a further improvement in the errors associated with the peaks in the bridging region, now occurring between 308-426 ppm. This could now be considered in very good agreement with the experimental spectrum. Obviously,
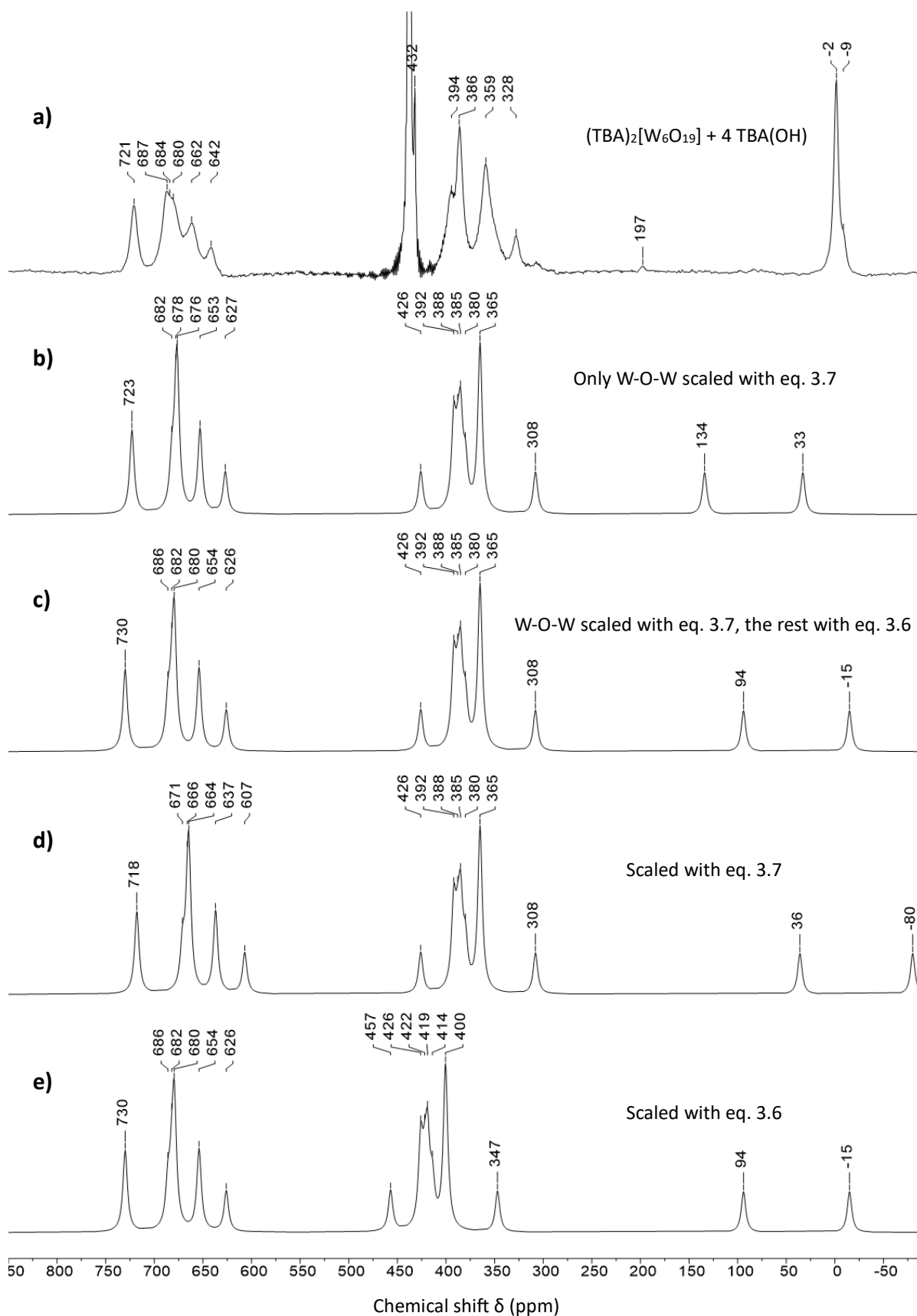
Figure 3.12: The experimental ^{17}O NMR spectrum obtained from the reaction of $(TBA)_2[W_6O_{19}]$ with 4 eq. of base (a) and a series of simulated ^{17}O NMR spectra obtained by applying the linear scaling **Equations 3.6** and **3.7** in various ways to the computed ^{17}O NMR shifts of $[W_7O_{24}H]^{5-}$. Again, the linewidths in the simulations have been arbitrarily set to 300 Hz.

the very large peak at 437 ppm in the experimental spectrum which is caused by the presence of $[WO_4]^{2-}$ is not present in the simulations. The peak assigned to the bridging μ_2-OH (O20), originally computed at 134 ppm and tentatively assigned to the very low intensity peak at 197 ppm in the experimental spectrum, does not benefit from linear scaling as it is underestimated in the original calculations.

The simulation shown in **Figure 3.12c** shows the effect of applying **Equation 3.7** to only the bridging W-O-W peaks and **Equation 3.6** to the remaining oxygens. This offers a compromise in which we can see a significant improvement in the accuracy of the bridging W-O-W chemical shifts without moving the bridging μ_2-OH (O20) to 36 ppm (representing an error of 161 ppm if the experimental assignment is correct). However, this effect is also achieved by only scaling the bridging W-O-W shifts and leaving the remaining computed shifts unchanged, as shown in **Figure 3.12b**. This appears to give the best fit between the experimental data and the calculated chemical shifts.

It is important to note that the original linear scaling relations reported by Pascual-Borràs and co-workers were obtained using the same functional and basis set used in this study to obtain the computed ^{17}O NMR chemical shifts of $[W_7O_{24}H]^{5-}$. If the methods were different then it would be appropriate to either recalculate the ^{17}O NMR chemical shifts using the same methods used to produce the linear scaling equations, or to produce new scaling equations with the new method. The group did use the ADF2010 software package, as opposed to the ADF2019 package used in this study. The two packages likely use different convergence threshold values and therefore, calculation outputs will be marginally different. These differences are likely to be small and therefore the qualitative observations and conclusions presented here should still be valid. To obtain the most reliable results, the ^{17}O NMR chemical shifts of $[W_7O_{24}H]^{5-}$ should be recalculated using ADF2010, however, we do not have access to this software package anymore.

3.3.5 Isolation of $[W_7O_{24}H]^{5-}$ by cation exchange

The high solubility in organic solvents of the proposed $(TBA)_5[W_7O_{24}H]$ obtained from the reaction of $(TBA)_2[W_6O_{19}]$ with four equivalents of TBA(OH) has prevented its crystallisation as a single compound and therefore, its separation from $(TBA)_2[WO_4]$ has proved difficult.

In order to isolate $[W_7O_{24}H]^{5-}$ as a single compound, the use of an alternative cation which should impart lower solubility in organic solvents was explored. Performing the same degradation reaction of $(TBA)_2[W_6O_{19}]$ with four equivalents of benzyltrimethylammonium
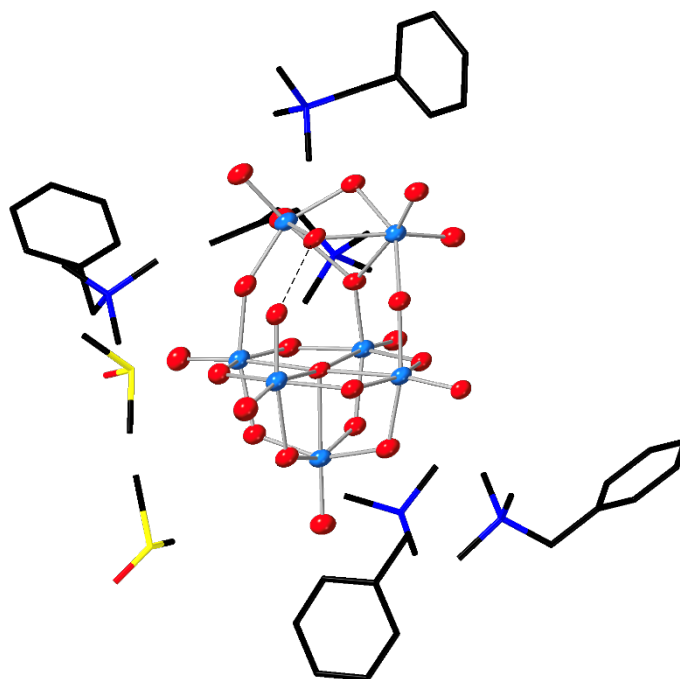
Figure 3.13: Single-crystal X-ray diffraction structure of $(BMTA)_5[W_7O_{24}H].2DMSO$ with probability ellipsoids at 50% level. Cations and solvent shown in wire form for clarity.
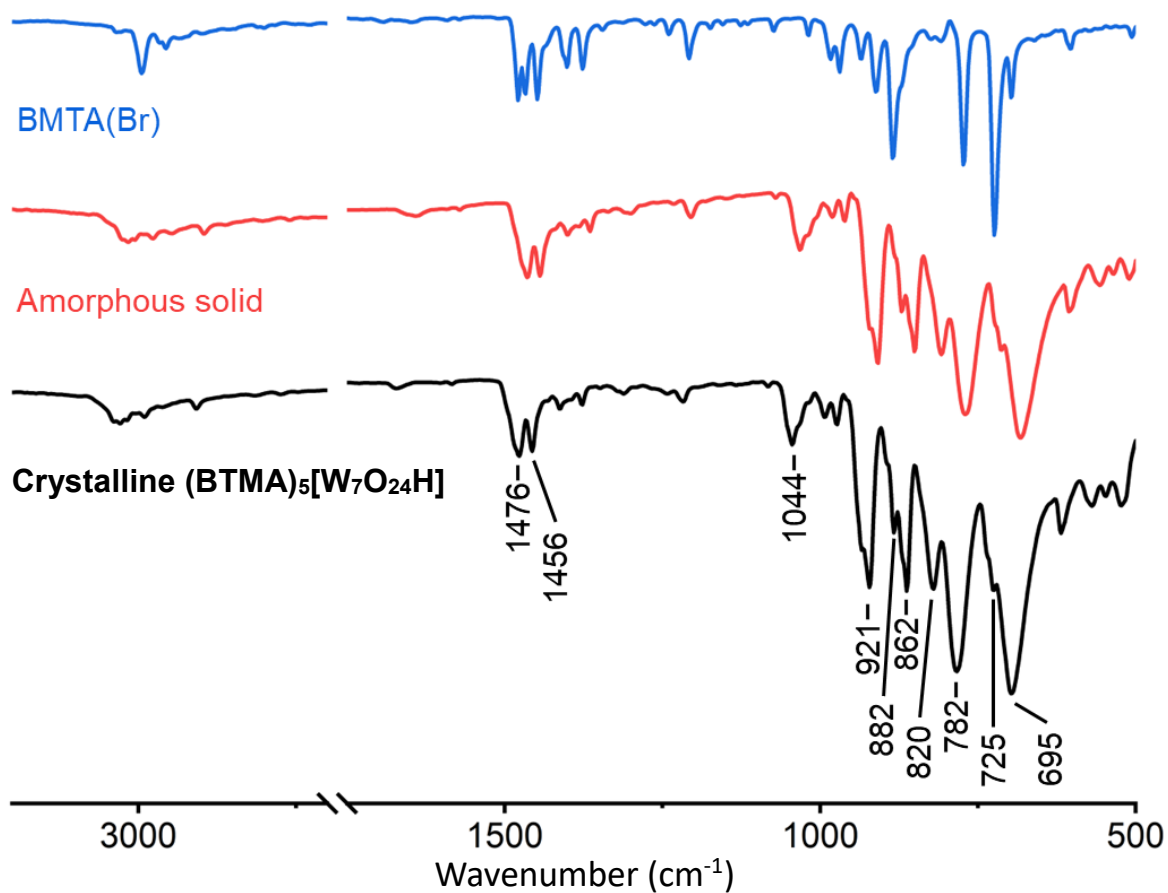
Figure 3.14: ATR FTIR transmittance spectrum of BTMA(Br) (blue), the amorphous solid obtained the recrystallization of the crude product from treatment of $(TBA)_2[W_6O_{19}]$ with 4 equivalents of (BTMA)OH from DMSO/DMF (red) and crystalline $(BTMA)_5[W_7O_{24}H]^{5-}$ (black).

hydroxide BMTA(OH) in a mixture of acetonitrile and methanol produced a white precipitate, after stirring at room temperature overnight. The solid was separated by centrifugation and washed with acetonitrile and methanol to ensure complete removal of starting materials. At this point, the solid may still contain a mixture of tetrabutylammonium and benzyltrimethylammonium cations as little is known about the solubility of mixed organic cation POMs.

The resulting solid was then recrystallized from boiling DMSO/DMF which produced a mixture of amorphous white solid and colourless crystals. Single-crystal X-ray diffraction experiments showed that the crystalline material was that of $(BTMA)_5[W_7O_{24}H].2DMSO$, shown in **Figure 3.13**. The structure of $[W_7O_{24}H]^{5-}$ in $(BMTA)_5[W_7O_{24}H].2DMSO$ and $(TBA)_7[W_7O_{24}H].[W_6O_{19}].3MeCN$ is very similar, suggesting that the nature of the cation and solvent used in the crystallization has no real impact on the POM structure.

In order to determine if the amorphous solid produced during the recrystallization is also $(BTMA)_5[W_7O_{24}H]$, the infrared spectra of both the amorphous solid and crystals of $(BTMA)_5[W_7O_{24}H].2DMSO$, after drying under vacuum, were recorded. The resulting spectra, along with the infrared spectrum of BMTA(Br) are shown in **Figure 3.14**. The IR spectra of the amorphous solid (red) and the crystalline $(BTMA)_5[W_7O_{24}H]$ (black) are extremely similar, implying that the amorphous solid is also $(BTMA)_5[W_7O_{24}H]$. It may be that the incredibly low solubility of $(BTMA)_5[W_7O_{24}H]$ in organic solvents leads to rapid precipitation of amorphous $(BTMA)_5[W_7O_{24}H]$ from the hot DMSO/DMF solutions as they cool. Only then is this followed by the slower formation of crystalline material from the saturated solution at room temperature.

The infrared spectrum of crystalline $(BTMA)_5[W_7O_{24}H]$ contains numerous peaks below 1000 cm^{-1}, the region in which M-O stretches are found. The intense peak at 921 cm^{-1} can be assigned to a terminal W=O stretch. This peak also appears to have a shoulder which could be indicative of several symmetry inequivalent W=O stretches, which is consistent with the structure of $[W_7O_{24}H]^{5-}$ that contains tungsten atoms with both one and two terminal W=O bonds. Furthermore, the presence of numerous intense peaks in the region of 880-650 cm^{-1} could be a result of the C_s symmetry of $[W_7O_{24}H]^{5-}$, which in turn, produces a large number of unique bridging W-O-W stretches. It is worth noting that the infrared spectrum of BTMA(Br) also shows a series of sharp stretches in this region and therefore some of this complexity could be a result of the counter ion. The low intensity stretches at approximately 1450 cm^{-1}

and 3000 cm^{-1} can be assigned to various deformations of C-H, C-C and C-N bonds present in the benzyltrimethylammonium cation. These regions appear significantly different from samples of tetrabutylammonium salts, showing that the presence of sp^2 carbons and a lack of aliphatic C-C bonds in BTMA produces a major difference in the spectrum. This could be used, alongside ^{1}H and ^{13}C NMR spectroscopy, to confirm the absence of TBA in these samples.

Together with the degradation of (TBA)$_2$[W$_6$O$_{19}$] with four equivalents of BTMA(OH), a simple cation exchange procedure was explored. In this case, (TBA)$_2$[W$_6$O$_{19}$] was reacted with four equivalents of TBA(OH) in acetonitrile to produce the same reaction mixture previously discussed (^{183}W NMR spectrum shown in **Figure 3.15**). The solvent was then removed, and the resulting viscous oil was re-dissolved in a small amount of DMSO. The ^{183}W NMR spectrum of the mixture in DMSO was also recorded to ensure there was no chemical change upon changing the solvent. The resulting spectrum is shown in **Figure 3.16**. There are some minor impurities, but the mixture appears largely the same. This mixture of tetrabutylammonium salts was then treated with an excess of benzyltrimethylammonium bromide in DMSO, which led to the immediate precipitation of a white solid. Washing with acetonitrile/methanol and recrystallization from hot DMSO/DMF again led to a mixture of colourless amorphous and crystalline solids. Single-crystal X-ray diffraction was used to check the unit cell parameters of
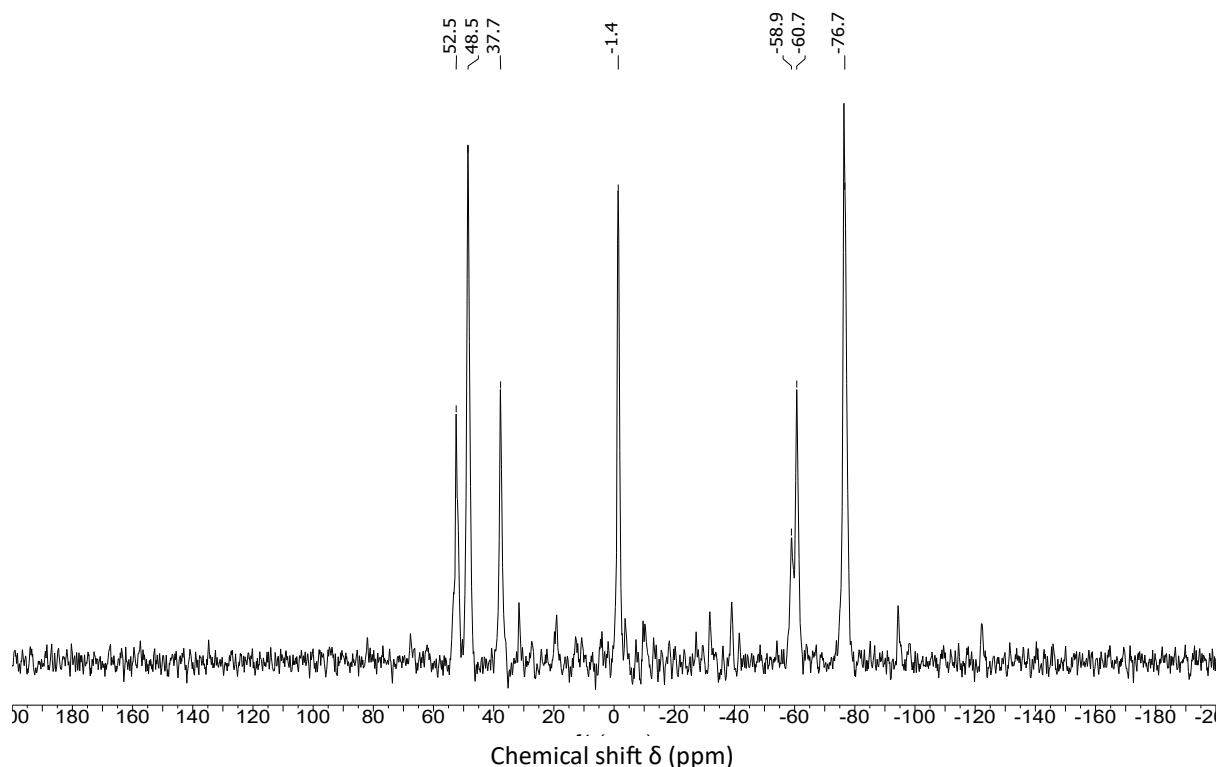
Figure 3.15: ^{182}W NMR spectrum of the reaction between (TBA)$_2$[W$_6$O$_{19}$] and 4 eq. of (TBA)OH in CH$_3$CN/CD$_3$CN.
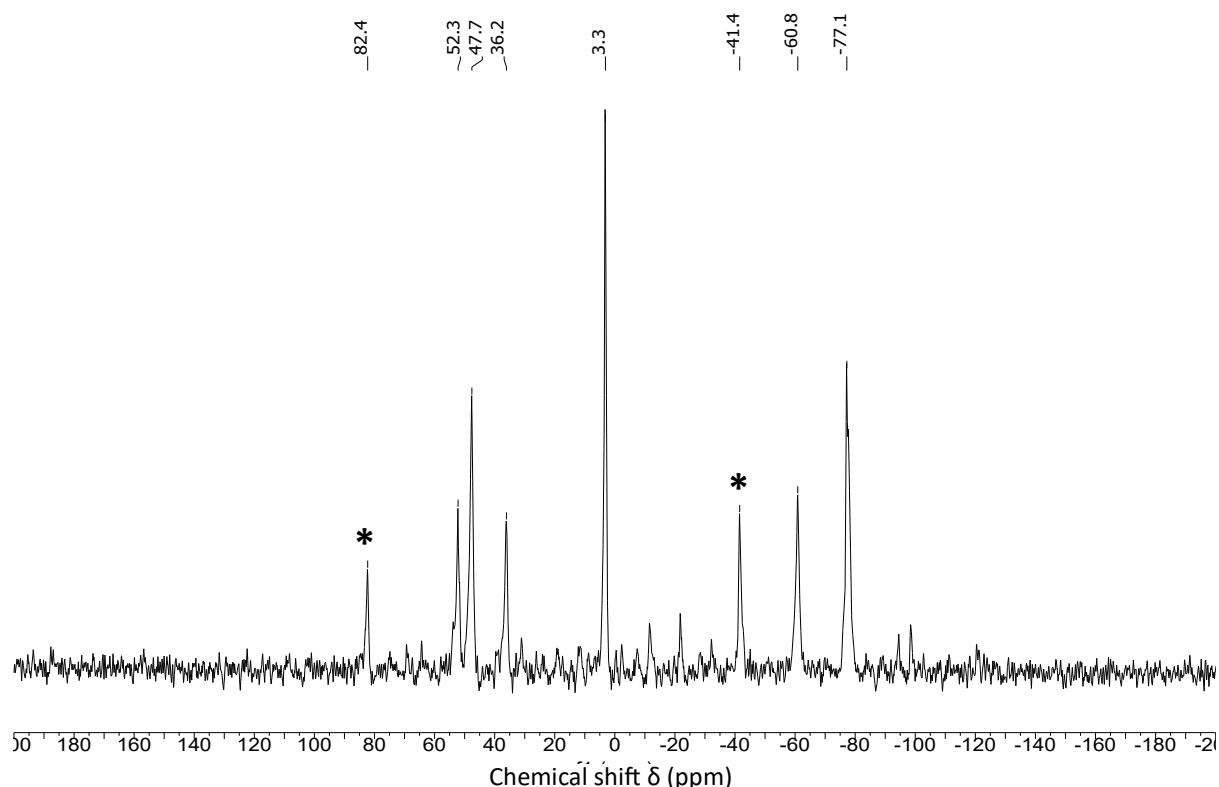
Figure 3.16: ^{183}W NMR spectrum of the reaction between (TBA)$_2$[W$_6$O$_{19}$] and 4 eq. of TBA(OH) in d_6-DMSO. Peaks marked with asterisks are likely due to the presence of additional degradation products.

the crystalline material and they were found to be identical to those of (BTMA)$_5$[W$_7$O$_{24}$H].2DMSO and are given in **Section A.2.2**. This shows that the incredibly low solubility of (BTMA)$_5$[W$_7$O$_{24}$H] in organic solvents allows for its simple separation from (BTMA)$_2$[WO$_4$] (and other TBA salts), which are much more soluble. Unfortunately, the solubility of (BTMA)$_5$[W$_7$O$_{24}$H] is too low for ^{183}W NMR spectroscopy.

3.3.6 Targeting [W$_7$O$_{24}$H]$^{5-}$

Now knowing that [W$_7$O$_{24}$H]$^{5-}$ is a major component of degradation reactions of (TBA)$_2$[W$_6$O$_{19}$], we can look to directly target [W$_7$O$_{24}$H]$^{5-}$ by changing the ratio of {W$_6$} to base used in the degradation reaction. As shown in **Equation 3.8**, approximately 2.3 equivalents of TBA(OH) per (TBA)$_2$[W$_6$O$_{19}$] are theoretically required to target [W$_7$O$_{24}$H]$^{5-}$. This represents a charge/tungsten (Z/W) ratio of 0.71, which is significantly lower than those previously discussed (they target Z/W = 1). Alternatively, the controlled hydrolysis of the appropriate ratio of (TBA)$_2$[WO$_4$] and WO(OMe)$_4$ can also be used to target [W$_7$O$_{24}$H]$^{5-}$. This route is described in **Equation 3.9** and is analogous to methods previously used by our group during the synthesis of heterometal containing Lindqvist-type POMs.

83

$$7 \, (\text{TBA})_2[\text{W}_6\text{O}_{19}] + 16 \, \text{TBA(OH)} \rightarrow 6 \, (\text{TBA})_5[\text{W}_7\text{O}_{24}\text{H}] + 5 \, \text{H}_2\text{O} \qquad (3.8)$$

$$5 \, (\text{TBA})_2[\text{WO}_4] + 9 \, \text{WO(OMe)}_4 + 19 \, \text{H}_2\text{O} \rightarrow 2 \, (\text{TBA})_5[\text{W}_7\text{O}_{24}\text{H}] + 36 \, \text{MeOH} \qquad (3.9)$$
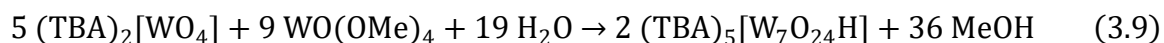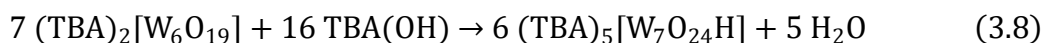
As before, these reactions are most readily monitored using [183]W NMR spectroscopy. Firstly, the hydrolysis of WO(OMe)$_4$ with water in the presence of (TBA)$_2$[WO$_4$] was studied. The two tungsten-based reagents were dissolved in acetonitrile and allowed to stir for approximately one hour. The water was then added to the solution to drive the hydrolysis of metal alkoxide bonds and, in turn, the condensation reactions required to form isopolytungstates. After stirring overnight, the solvent was removed and the resulting viscous oil was dissolved in 2-3 mL of a 1:1 mixture of CH$_3$CN and CD$_3$CN. The [183]W NMR spectrum was recorded and the resulting spectrum is shown in **Figure 3.17a**. Analysis of this spectrum shows that a fairly complex mixture has formed, with more species present than was previously observed for reactions targeting the higher charge to tungsten ratio of 1. The peaks highlighted in blue at −78, −62, 38, 48 and 52 ppm respectively can be assigned to [W$_7$O$_{24}$H]$^{5-}$ as they occur with very similar chemical shift to those seen previously and in the distinctive 1:2:1:1:2 pattern. In addition to these, the peaks highlighted in orange at −162 and −20 ppm respectively occur in a 1:4 ratio and are consistent with the formation of [W$_{10}$O$_{32}$]$^{4-}$, one of the few isopolytungstates known to form in non-aqueous solutions.

The remaining signals are not readily assignable to any known isopolytungstate. Some of the peaks have been assigned to the same species based on inspection of the relative integrals since peaks from the same species should have integrals which can be related by multiplication by whole numbers. These assignments have largely been made by inspection of a lot of individual [183]W NMR spectra, in which it becomes more apparent which peaks are related as they always appear in the same ratio, regardless of how prominent they are in the reaction mixture. This will become clearer in **Section 3.4.2** where [183]W NMR studies of reactions at a range of charge to tungsten ratios are presented. From this inspection, the presence of at least two more isopolytungstate species is suggested. The eight peaks in red appear in a 1:1:1:1:1:1:1:1 ratio and therefore imply the presence of an *8n* isopolytungstate with eight unique tungsten environments. Again, this does not fit with the reported structure of any known POM we have seen. The peaks highlighted in purple occur in a 1:1:2:2:1:1:1:4:1 ratio which is consistent with the presence of a *14n* isopolytungstate. Unfortunately, the inability to crystallise these species out of reaction mixtures, at this time, severely limits the ability to discuss the nature of these species. This also makes analysis with other techniques like [17]O
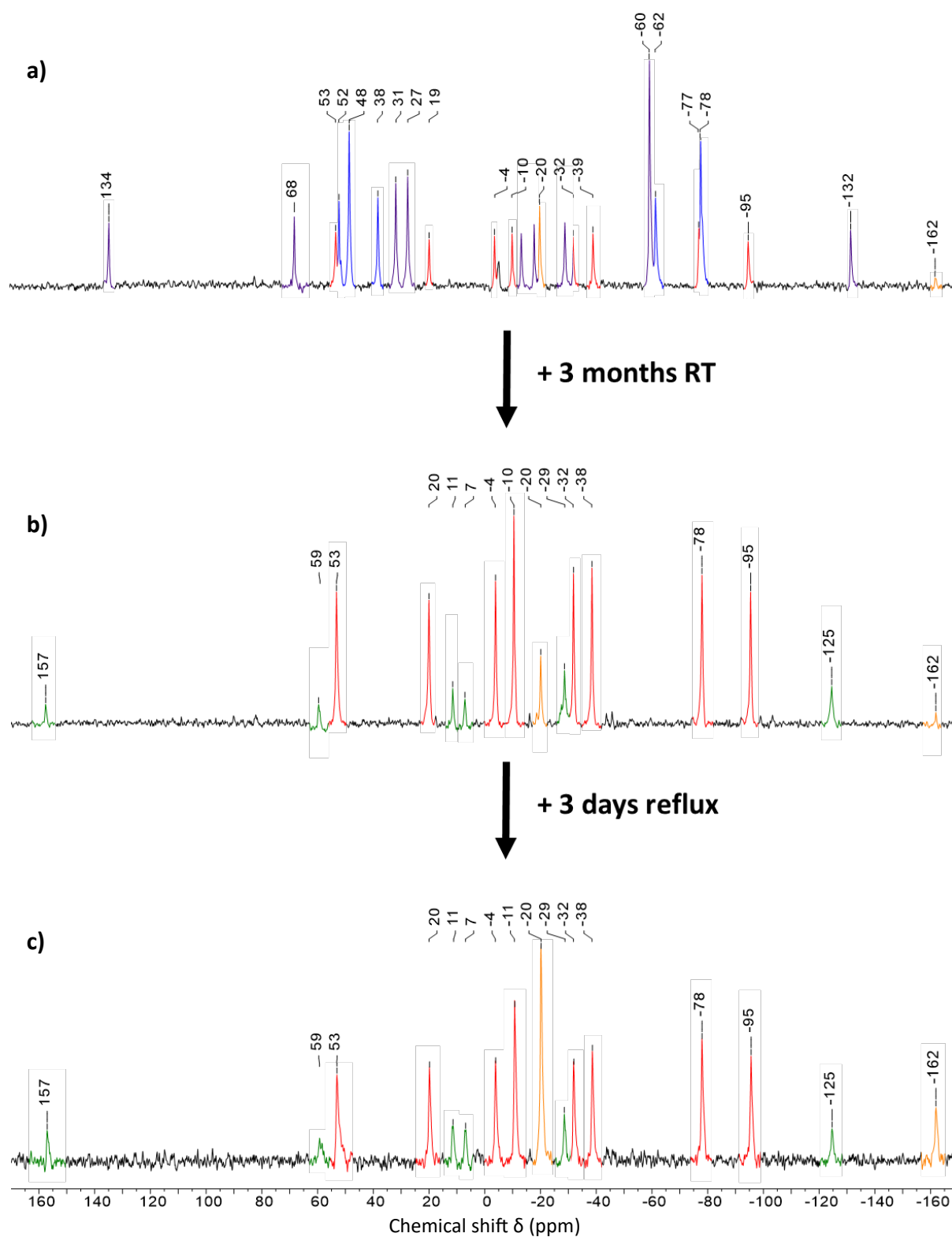
Figure 3.17: [183]W NMR spectra of the hydrolysis of WO(OMe)$_4$ in the presence of (TBA)$_2$[WO$_4$] after (a) 1 day, (b) 3 months and (c) after stirring for 3 months and then refluxing for 3 days. The spectra were acquired in a mixture of CH$_3$CN and CD$_3$CN.

NMR spectroscopy difficult, as these spectra are likely to be extremely complicated. Furthermore, the fact that they exist in a complex mixture which is likely to be made up of species with similar solubilities, separation of this mixture is extremely difficult. The peaks left

in black could not be assigned with any confidence as of yet, but that does not necessarily mean that one or more of these does not belong to the same species.

These insights suggest that directly targeting $[W_7O_{24}H]^{5-}$ from monomeric starting materials is difficult. However, given that $[W_7O_{24}H]^{5-}$ forms part of the product mixture, and that the kinetics of isopolytungstate assembly may be quite slow, it is worthwhile to extend the reaction time to ensure that what we see in the ^{183}W NMR spectrum is the equilibrium state of the reaction. Allowing the reaction mixture that produced the spectrum shown in **Figure 3.17a** to stir for three months at room temperature gave the spectrum shown in **Figure 3.17b**. The spectrum is substantially different to the one acquired after just one day and does verify the idea that isopolytungstate formation, interconversion and therefore equilibration is quite slow. What is immediately apparent is that any $[W_7O_{24}H]^{5-}$ that was present initially is no longer present and therefore, at this charge to tungsten ratio (Z/W = 0.71), it can be considered a kinetic product of the reaction. It is clear that, over the course of three months, a series of hydrolysis and condensation reactions have converted $[W_7O_{24}H]^{5-}$ into other species present in the mixture. This is also true for the "purple species", which is completely absent from the reaction mixture after three months. Notably, the relative amount of the "red species" has massively increased to the point where it now appears to dominate the reaction mixture. This may imply that it is the most stable species accessible under these conditions. Interestingly, the amount of $[W_{10}O_{32}]^{4-}$ appears to have changed very little. This may suggest a larger energetic barrier to its formation, perhaps associated with the formation of four approximately linear W-O-W bridges.

In addition to the previously discussed species, there now appears to be a small amount of another component. There are six peaks highlighted in green which occur in a 1:1:1:1:1:1 pattern. There also appears to be an increase in the intensity of the peak highlighted in red at −10 ppm. Analysis of the integrals of some of the red and green peaks from **Figure 3.17b** and **3.17c** is shown in **Figure 3.18**. This shows that the intensity of the peak at −10 ppm is approximately the sum of the intensity of one red peak and one green peak suggesting that there are two overlapping peaks, one from each species, occurring at −10 ppm. This can be seen as a slight shoulder on the side of the peak and is consistently observed whenever both species are present. Therefore, the "green species" actually contains seven unique tungsten environments (*7n*) equally populated (i.e. 1:1:1:1:1:1:1).
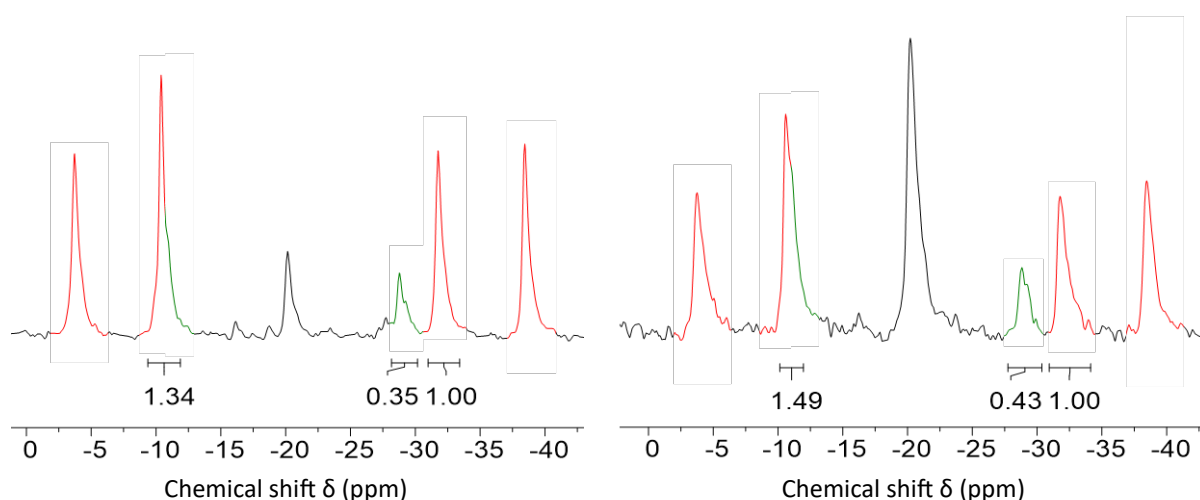
Figure 3.18: Sections of the [183]W NMR spectra shown in **Figure 3.17b** and **3.17c** showing the relative integrals of the red and green peaks.

To verify the stability of this mixture and whether any other species are accessible at a higher temperature, the reaction mixture was then refluxed for three days. The solution was then allowed to cool to room temperature and the [183]W NMR spectrum of the reaction mixture was recorded. The resulting [183]W NMR spectrum is shown in **Figure 3.17c**. The observed changes to the spectrum are minimal. The most striking difference is the large increase in the amount of $[W_{10}O_{32}]^{4-}$ present in the reaction mixture. The higher reaction temperature appears to drive the equilibrium towards $\{W_{10}\}$ implying that it is likely to be the most stable of the accessible species at this charge to tungsten ratio (Z/W = 0.71), but that the energy barriers associated with its formation are high enough that it is not rapidly formed at room temperature. The rise in the amount of $\{W_{10}\}$ seems to be accompanied by a reduction in the intensity of the peaks assigned to the "red species", perhaps indicating a mechanism of interconversion between the two species. On the other hand, the relative amount of the "green species" seems stable even after heating at reflux for three days. It is worth pointing out that without precise structural information about the species present in solution, and therefore knowledge of how many tungsten nuclei are responsible for each peak, it is not possible to know the exact proportion of each species in the mixture.

Following these results, the same charge to tungsten ratio theoretically required to target $[W_7O_{24}H]^{5-}$ (Z/W = 0.71) was targeted using the degradation of $(TBA)_2[W_6O_{19}]$ with approximately 2.3 equivalents of TBA(OH), as described in **Equation 3.8**. Our group has used both the hydrolysis of $WO(OMe)_4$ in the presence of $TBA_2[WO_4]$ and basic degradation of $(TBA)_2[W_6O_{19}]$ interchangeably to target virtual lacunary species and therefore we expect

targeting the same charge to tungsten ratio to give similar results, regardless of the method used.

To test this, $(TBA)_2[W_6O_{19}]$ was treated with 2.3 equivalents of TBA(OH) in acetonitrile. The solution was stirred at room temperature for one week (the experiment was longer due to limited availability of spectrometer time for [183]W NMR spectroscopy). The volatiles were then removed, and the resulting viscous oil was taken up in CH_3CN/CD_3CN and the [183]W NMR
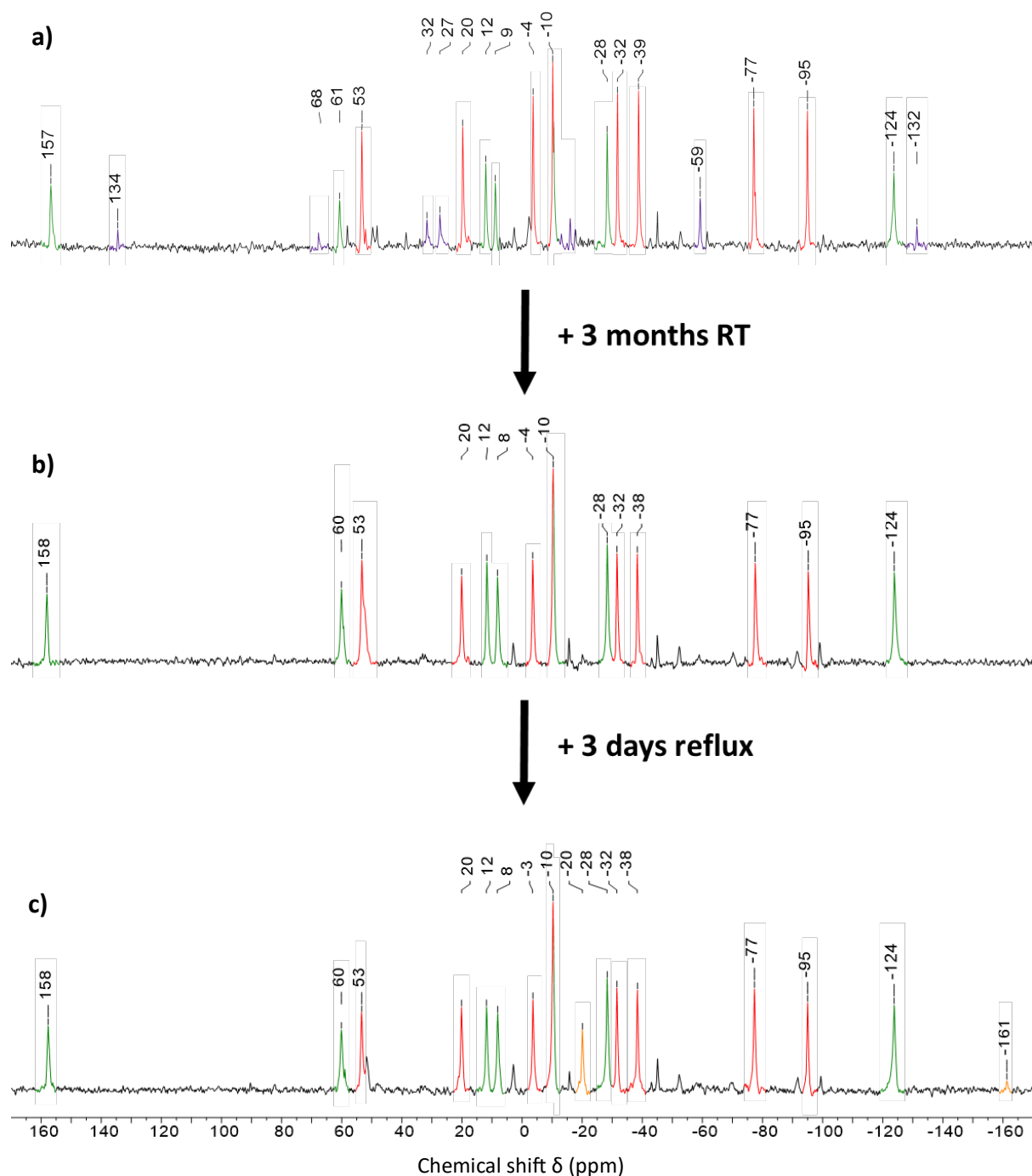
Figure 3.19: [183]W NMR spectra of the degradation of $(TBA)_2[W_6O_{19}]$ with 2.3 equivalents of TBA(OH) after (a) 1 week, (b) 3 months and (c) after stirring for 3 months and then refluxing for 3 days. The spectra were acquired in a mixture of CH_3CN and CD_3CN.

spectrum was recorded. The resulting spectrum is shown in **Figure 3.19a**. The mixture produced is largely similar to those shown in **Figure 3.17b** and **3.17c**. The major peaks observed are the eight peaks assigned to the "red species" and the seven peaks assigned to the "green species". There also appear to be low intensity peaks in the same positions as those previously assigned to the "purple species", indicating it may be a minor component of the reaction mixture.

As done previously, this mixture was left to stir at room temperature for three months to attempt to allow the mixture to equilibrate. The ^{183}W NMR spectrum recorded after three months at room temperature is shown in **Figure 3.19b**. In this case, there was very little change during this time. There appears to be a small increase in the relative intensity of the peaks assigned to the "green species" relative to those of the "red species". Furthermore, any peaks associated with the "purple species" seem to have diminished. This leads to an overall simplification of the reaction mixture, which is now seemingly dominated by two currently unknown species. This appears to indicate good solution stability for these two species, at least at room temperature. Unfortunately, without knowing the nature of either of these species it is hard to know how to separate the two compounds, or how to bias the mixture towards either of them. It is also worth noting in this case that there is no $[W_{10}O_{32}]^{4-}$ observable in the mixture even after three months. This may suggest that there is a mechanism for its formation at room temperature during the hydrolysis of $WO(OMe)_4$ in the presence of $TBA_2[WO_4]$ (as it is present in the spectra shown in **Figure 3.17a** and **3.17b**) that is not readily accessible during basic degradation. Also, the fact that it doesn't grow into reaction mixtures over time, again supports the notion that there may be a large energetic barrier associated with its formation in these reaction mixtures.

The high temperature solution stability of this mixture was tested by refluxing the reaction mixture for three days. The ^{183}W NMR spectrum was then re-recorded and is shown in **Figure 3.19c**. At this point, the formation of $\{W_{10}\}$ is observed and is evidenced by the new peaks at −20 (8W) and −161 ppm (2W) highlighted in orange. This indicates that giving the reaction mixture more energy allows the formation of $\{W_{10}\}$ as previously discussed. The formation of $\{W_{10}\}$ appears to be accompanied by a slight decrease in the intensity of the other peaks in the reaction mixture, which makes sense as the total amount of tungsten in the mixture must be conserved. It is obvious when comparing the ^{183}W NMR spectra shown in **Figure 3.17c** and **3.19c** that the relative amount of $\{W_{10}\}$ formed during the basic degradation of $(TBA)_2[W_6O_{19}]$

is lower than the corresponding WO(OMe)$_4$ hydrolysis reaction targeting the same charge to tungsten ratio (Z/W = 0.71).

The exact reason for this is unknown, but it is worth considering that the mechanisms of isopolytungstate formation are likely to be slightly different, with reactions of WO(OMe)$_4$ and (TBA)$_2$[WO$_4$] involving assembly from monomeric/dimeric units. Conversely, reactions with (TBA)$_2$[W$_6$O$_{19}$] immediately have access to higher nuclearity fragments. This, along with the presence of methanol in reactions involving WO(OMe)$_4$, may allow for slight differences in solution speciation even when all other factors are equal.

Interestingly, there are no peaks that can be assigned to [W$_7$O$_{24}$H]$^{5-}$ in any of the ^{183}W NMR spectra shown in **Figure 3.19**. This was observed after leaving the previously discussed reaction mixture to stir at room temperature for three months (**Figure 3.17b**). This may provide support for the earlier postulated idea that [W$_7$O$_{24}$H]$^{5-}$ may form as a kinetic product but undergoes slow interconversion into other species soon after. In this case, it would imply that leaving the degradation mixture stirring at room temperature for one week was enough time for complete loss of any [W$_7$O$_{24}$H]$^{5-}$ that may have formed. To verify if [W$_7$O$_{24}$H]$^{5-}$ does indeed form initially during the degradation of (TBA)$_2$[W$_6$O$_{19}$] with 2.3 equivalents of TBA(OH), the reaction was repeated but in this case the spectrum was acquired after stirring overnight. The ^{183}W NMR spectrum obtained is shown in **Figure 3.20**.

Acquiring the spectrum after much less time results in a huge change. The peaks at −77, −60, 38, 49 and 52 ppm respectively, highlighted in blue, show the characteristic 1:2:1:1:2 pattern of [W$_7$O$_{24}$H]$^{5-}$. This suggests that after much shorter reaction times [W$_7$O$_{24}$H]$^{5-}$ is a major component of reactions targeting a charge to tungsten ratio of 0.71. However, under these conditions [W$_7$O$_{24}$H]$^{5-}$ is only metastable, and appears to undergo conversion into other isopolytungstate species over the course of a few days. Several other species are also present at this time, with familiar peaks highlighted in red and purple. There is also some indication of the formation of peaks previously assigned to the "green species", however they are too low intensity at this point to make a confident assignment.

Given that [W$_7$O$_{24}$H]$^{5-}$ dominates reaction mixtures targeting a charge to tungsten ratio of 1, and that it is a prominent feature initially in reactions targeting a charge to tungsten ratio of 0.71, it may be reasonable to suggest that formation of [W$_7$O$_{24}$H]$^{5-}$ is, at the very least, kinetically favoured and in turn, that there are no particularly high energy transition states involved in its assembly. In the absence of other more thermodynamically stable species it may
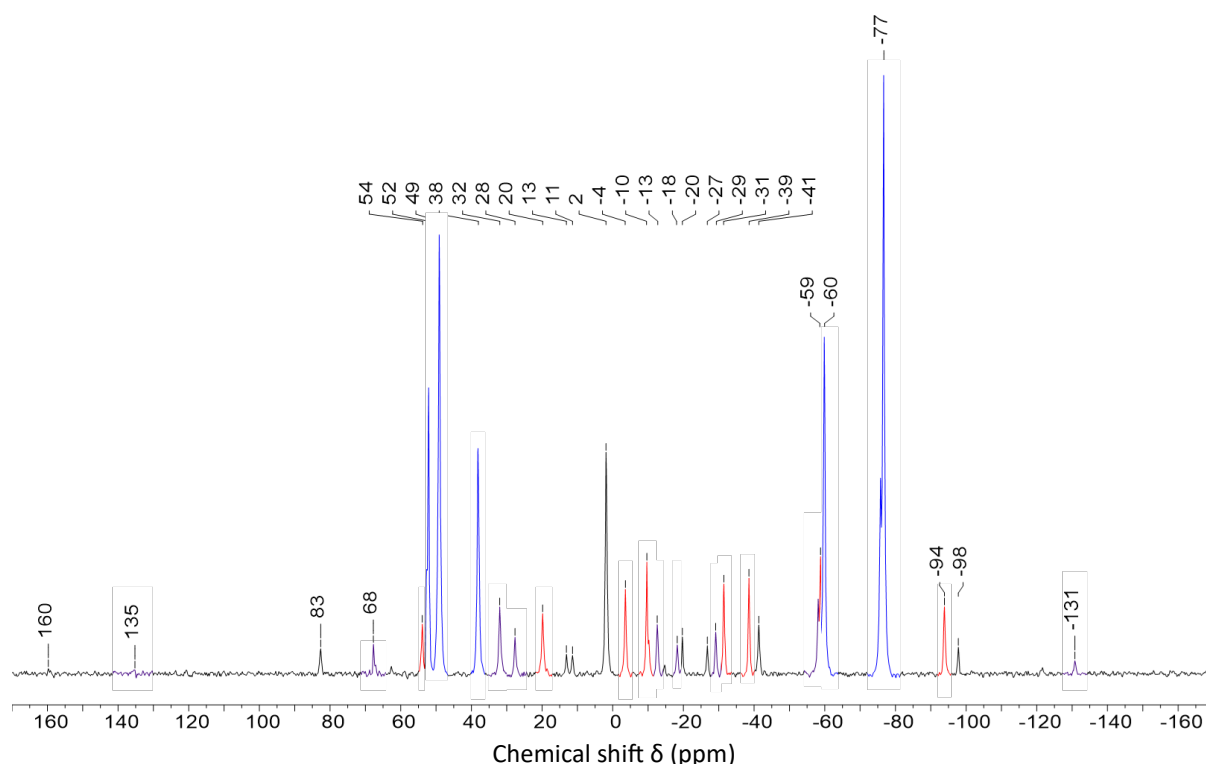
Figure 3.20: ^{183}W NMR spectrum of the degradation of (TBA)$_2$[W$_6$O$_{19}$] with 2.3 equivalents of TBA(OH) after stirring overnight. The spectrum was recorded in a mixture of CH$_3$CN and CD$_3$CN.

persist in solution for extended periods, which may be the case at higher charge to tungsten ratios where, so far, none of the other species observed in **Figure 3.17** or **3.19** have been seen. However, at the lower charge to tungsten ratio of 0.71 discussed here, there appears to be a number of other species present in the reaction mixture. All the findings so far support the idea that [W$_7$O$_{24}$H]$^{5-}$ is unstable with respect to conversion into one or more of these species.

In order to try to get some structural information about the species present in these reaction mixtures, numerous attempts to grow crystals from the ^{183}W NMR solutions were made. To date, any attempts to crystallise tetrabutylammonium salts by slow evaporation of reaction mixtures or diffusion of anti-solvents have only given (TBA)$_2$[W$_6$O$_{19}$] or (TBA)$_4$[W$_{10}$O$_{32}$]. Use of cation exchange with benzyltrimethylammonium was very successful in acquiring a structure of [W$_7$O$_{24}$H]$^{5-}$ and therefore we thought it may also be useful in characterisation of the unknown species observed in these ^{183}W NMR studies. However, treatment of the mixtures with an excess of BTMA(Br) followed by recrystallization from DMSO/DMF only ever gave (BTMA)$_5$[W$_7$O$_{24}$H].2DMSO.

It may be that the conditions used for the recrystallization are favouring the formation of [W$_7$O$_{24}$H]$^{5-}$, however, given the extremely limited solubility of benzyltrimethylammonium

91

salts, there are very few options in terms of solvent combinations, and high temperatures tend to be required to get any appreciable amount of the crude product to dissolve.

The selective formation of $[W_7O_{24}H]^{5-}$ from crystallization studies is very intriguing in the context of the previous discussion in which ^{183}W NMR studies imply that $[W_7O_{24}H]^{5-}$ disappears from solutions over time. This could be considered analogous to the observations of Maksimovskaya in aqueous solution, where NMR studies showed $[H_2W_{12}O_{42}]^{10-}$ slowly converts to $[W_7O_{24}]^{6-}$ in solution. However, although $[W_7O_{24}]^{6-}$ dominates solutions, the only species that crystallises out of these solutions is $[H_2W_{12}O_{42}]^{10-}$. This is strikingly similar to our system where apparent solution instability of $[W_7O_{24}H]^{5-}$ with respect to interconversion to another isopolytungstate is simultaneously paired with preferential formation in the solid state. This may imply a somewhat flat potential energy surface in which isopolytungstate species, such as $[W_7O_{24}H]^{5-}$ and the numerous unknown species discussed in this section, can interconvert reversibly to respond to small changes in conditions (e.g. reaction concentration, temperature, solvent polarity etc.).

3.4 Expanding the scope

So far, this chapter has focused on attempting to understand the non-aqueous reaction between $(TBA)_2[W_6O_{19}]$ and four equivalents of TBA(OH) in order to target a solution with a charge to tungsten ratio of 1. This led to the discovery of the new isopolytungstate $[W_7O_{24}H]^{5-}$, which was found to exist in a 1:2 ratio with $(TBA)_2[WO_4]$ in these solutions. Directly targeting $[W_7O_{24}H]^{5-}$ by changing the equivalents of TBA(OH) used in the reaction, to target a solution with a Z/W of 0.71, gave evidence of several isopolytungstate species that are not known in the literature. This exemplifies how little is known about non-aqueous isopolytungstate speciation.

All known (and theorised) isopolytungstate species can be described in terms of a charge to tungsten ratio simply by dividing the overall charge of the anion by the number of metal atoms in the structure. The values of Z/W can range from zero for neutral tungsten oxide, to two for monomeric tungstate. Isopolytungstate species fall somewhere between these two extremes and six known structures are shown on a scale of charge to tungsten ratio in **Figure 3.21**, along with some of the "virtual" species our group has targeted during previous studies. In general, the few isopolytungstate species already obtained from non-aqueous media ($[W_6O_{19}]^{2-}$ and $[W_{10}O_{32}]^{4-}$) have lower charge, and Z/W, than those isolated from aqueous media ($[W_7O_{24}]^{6-}$
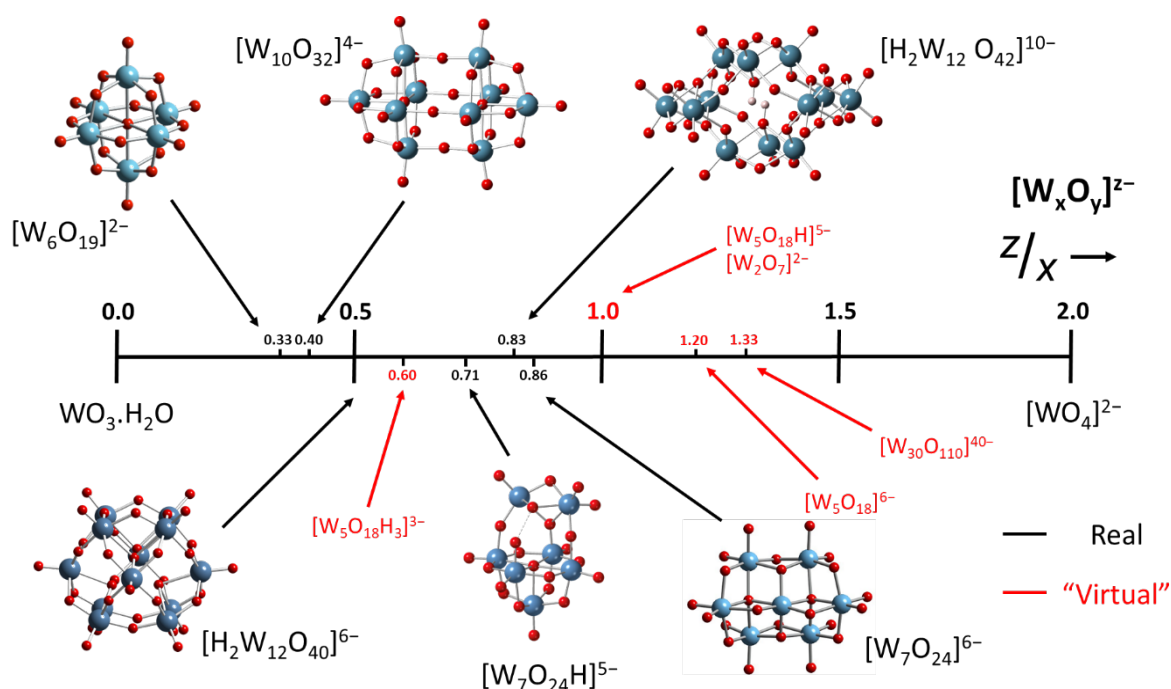
Figure 3.21: Isopolytungstate species, both real and "virtual" placed on a scale in terms of their charge to tungsten ratio.

and $[H_2W_{12}O_{42}]^{10-}$). This is consequence of the lower polarity of non-aqueous solvents compared to water, which makes them less able to stabilise highly charged species.

In order to gain more insight into non-aqueous isopolytungstate speciation we examined the nature of solutions at a range of Z/W ratios using solution state NMR spectroscopy, as we have already done for Z/W = 1 and 0.71. These solutions can be readily prepared by reacting $(TBA)_2[W_6O_{19}]$ (Z/W = 0.33) with varying amounts of TBA(OH) to move right on the scale shown in **Figure 3.21**. As shown already, these solutions are readily ^{17}O-enriched by degrading pre-enriched $(TBA)_2[W_6O_{19}]$. These may also be obtained by hydrolysing varying ratios of $(TBA)_2[WO_4]$ and $WO(OMe)_4$ as was already done for Z/W= 0.71. However, given ^{183}W NMR studies require large amounts of material, this would require the synthesis of large amounts of $WO(OMe)_4$ which is not ideal as discussed in **Chapter 2**. Therefore, this section will rely solely on the degradation of $(TBA)_2[W_6O_{19}]$ with base to access solutions with various charge to tungsten ratios.

3.4.1 ^{17}O NMR spectroscopy

^{17}O NMR studies were useful in **Section 3.3.1** in giving some preliminary insight into the complexity of the reaction mixture and for identifying known species, like monomeric tungstate. NMR scale reactions of ^{17}O-enriched $(TBA)_2[W_6O_{19}]$ with between 0.4 and 10

equivalents of TBA(OH) were performed in deuterated acetonitrile. The resulting ^{17}O NMR spectra are shown in **Figures 3.22-3.27**.

The first reaction between (TBA)$_2$[W$_6$O$_{19}$] and 0.4 equivalents of TBA(OH) targets a Z/W ratio of 0.4. This is the charge to tungsten ratio theoretically required to target [W$_{10}$O$_{32}$]$^{4-}$. The limited amount of base used in this reaction led to large amounts of solid left in the reaction after several days, which presumably is unreacted (TBA)$_2$[W$_6$O$_{19}$]. The solution was warmed to 60 °C for 2-3 hours which led to a sizable decrease in the amount of solid remaining after the mixture returned to room temperature.

The reported ^{17}O NMR chemical shifts of [W$_{10}$O$_{32}$]$^{4-}$ are 762 (10 O), 430/416 (20 O), and -6 (2 O) ppm respectively.[15] **Figure 3.22** shows peaks at 765, 432 and 416 ppm which may be tentatively assigned to {W$_{10}$}, though integration is not possible given the number of other peaks in close proximity. Furthermore, the broad peak at −5 ppm, which is likely to be a result of the formation of water during hydrolysis of (TBA)$_2$[W$_6$O$_{19}$], prevents visualisation of the reported peak at −6 ppm. The ^{17}O NMR spectrum of (TBA)$_2$[W$_6$O$_{19}$], shown in **Figure 3.1**, has peaks at 776 (6 O), 415 (12 O) and −77 (1 O) ppm respectively. While we would not expect to resolve the peak at −77 ppm, due to the exceptionally long relaxation time of this central oxygen, the peak at 777 ppm in **Figure 3.22** confirms the presence of some unreacted {W$_6$}
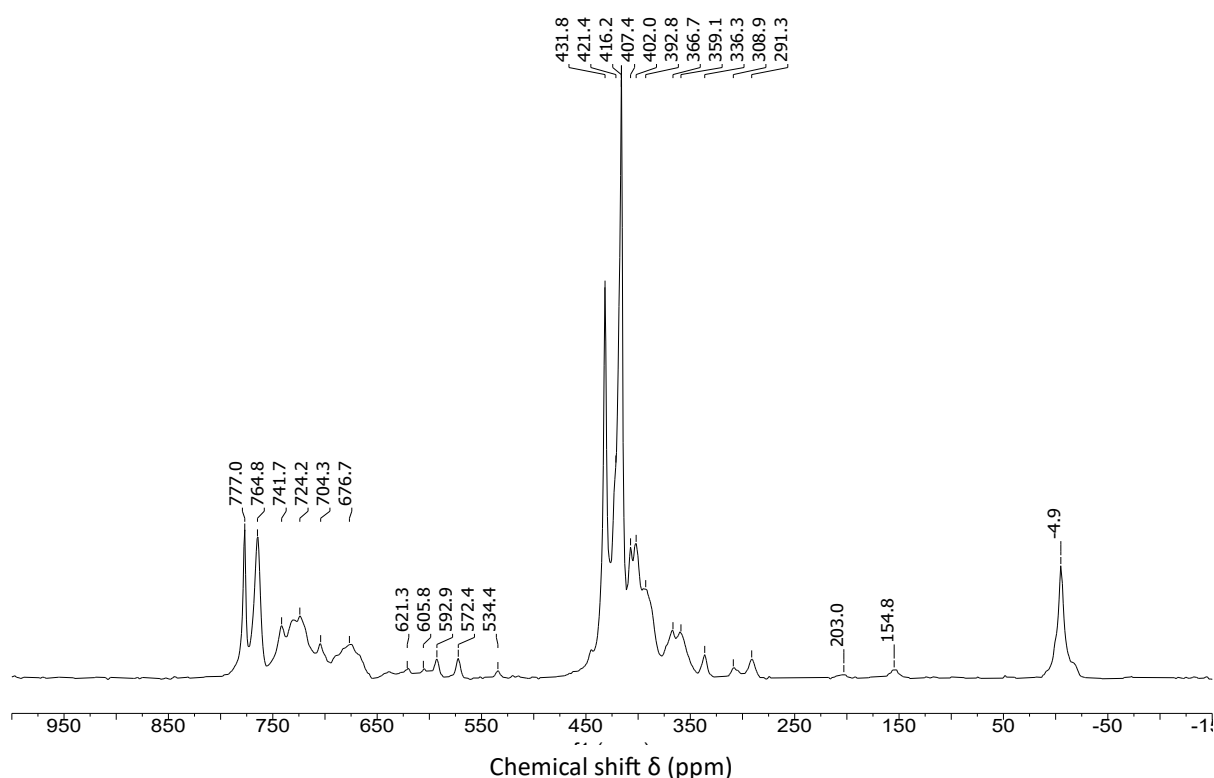
Figure 3.22: ^{17}O NMR spectrum of the reaction between (TBA)$_2$[W$_6$O$_{19}$] and 0.4 eq. of (TBA)OH in CD$_3$CN.

and in turn that the intense peak at 416 ppm is likely caused by the bridging W-O-W oxygens of both {W_6} and {W_{10}}.

Along with the signals that can be assigned to {W_{10}}, {W_6} and H_2O, there are several other lower intensity signals. There are a series of broad features in the terminal W=O region between 742-676 ppm. These are paired with a set of equally broad peaks in the bridging W-O-W region between 407-291 ppm. This complex pattern may suggest several species present in solution and/or species with low symmetry which have a large number of unique oxygen environments. Additionally, there are a cluster of peaks between 621-534 ppm. These are on the low end for terminal W=O peaks but shifts between 650-590 ppm have been observed for structures with tungsten atoms bearing *cis*-dioxo functionality.[16] The two low intensity peaks at 203 and 155 ppm respectively could indicate the presence of bridging hydroxides, caused by protonation of isopolytungstate species. This may be expected to occur at lower charge to tungsten ratios.

Increasing the amount of TBA(OH) used to one equivalent per (TBA)$_2$[W_6O_{19}], to give a solution with a Z/W = 0.5, leads to a significant change in the ^{17}O NMR spectrum (shown in **Figure 3.23**). Firstly, any observable peaks associated with the presence of unreacted (TBA)$_2$[W_6O_{19}] are now gone. There are still peaks at 764, 432 and, 417 ppm respectively that can be assigned to {W_{10}}. The intensity of the peaks at 764 and 417 ppm appears significantly reduced, while the peak
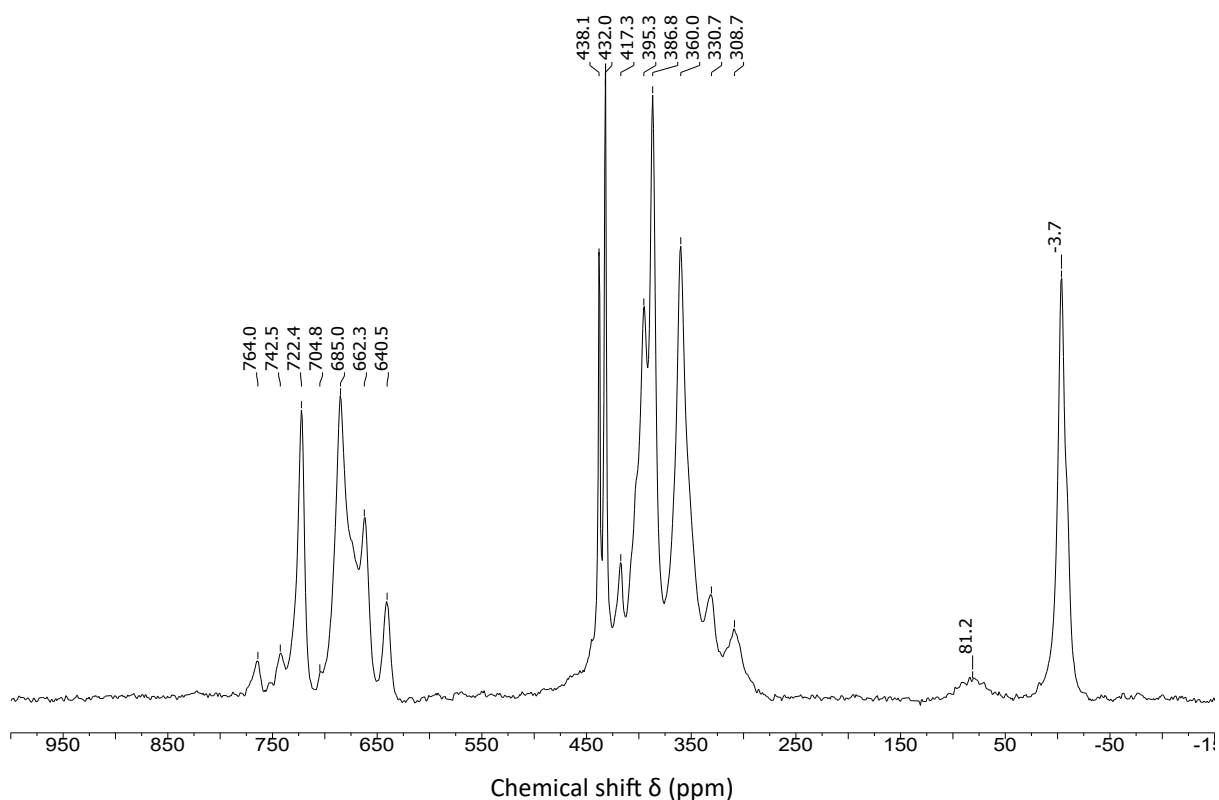
Figure 3.23: ^{17}O NMR spectrum of the reaction between (TBA)$_2$[W_6O_{19}] and 1 eq. of TBA(OH) in CD$_3$CN.

at 432 ppm is still very intense, implying that this peak may be caused by multiple unique oxygen nuclei in very similar chemical environments, and therefore its intensity is disproportional to the other peaks of {W_{10}}. The chemical shifts of the clusters of peaks in the terminal W=O region (743-640 ppm) and the bridging W-O-W region (432-308 ppm) are very similar to those in **Figure 3.22**, but these peaks are now quite intense. This could indicate that degradation of the previously unreacted (TBA)$_2$[W_6O_{19}] has led to an increase in the amount of the degradation products observed in **Figure 3.22**.

There is now also a sharp peak at 438 ppm. This peak was previously observed in **Figure 3.2** and is characteristic of the formation of [WO_4]$^{2-}$. This could be considered quite surprising as [WO_4]$^{2-}$ has the highest charge to tungsten ratio possible and therefore we may have expected to form isopolytungstate species with an increasing Z/W ratio as base is added, and only form the most charge dense monomeric tungstate when large quantities of base have been added. Instead, [WO_4]$^{2-}$ already forms in solution at Z/W = 0.5. This may imply the other isopolytungstate species in this mixture have a low Z/W ratio and formation of [WO_4]$^{2-}$ is required to "mop up" the extra charge in the mixture. This behaviour has already been observed in solutions with Z/W = 1, which exist as an approximately 1:2 mixture of [$W_7O_{24}H$]$^{5-}$ (Z/W = 0.71) and [WO_4]$^{2-}$ rather than a mixture species with charge to tungsten ratios closer to 1.

While there are no peaks between 150-250 ppm in **Figure 3.23**, there is now a very broad feature centred at 81 ppm. This is in the region suggested for [OH]$^-$ or [OH]$^-$/H_2O clusters.[17] This could be evidence of unreacted TBA(OH) or could be due to the interaction of the water produced in the hydrolysis of {W_6} with the basic oxygens of tungstate leading to polarisation of the O-H bonds of water.

Changing from 1 to 1.6 equivalents of TBA(OH) per (TBA)$_2$[W_6O_{19}] gives Z/W = 0.6, and is the charge to tungsten ratio previously targeted by our group during the synthesis of M(IV)-containing Lindqvist-type polyoxometalates.[18] The ^{17}O NMR spectrum at this charge to tungsten ratio is shown in **Figure 3.24**. This spectrum has not changed drastically upon the addition of the extra 0.6 equivalents of base. Most notably, the size of the tungstate peak, at 440 ppm in this spectrum, is more intense compared to the broad features in the terminal W=O region (740-640 ppm) and bridging W-O-W region (432-308 ppm). This indicates that as charge is added to the mixture the amount of the highly charged [WO_4]$^{2-}$ increases, while the amount of the other isopolytungstate species decreases. This further supports the idea that
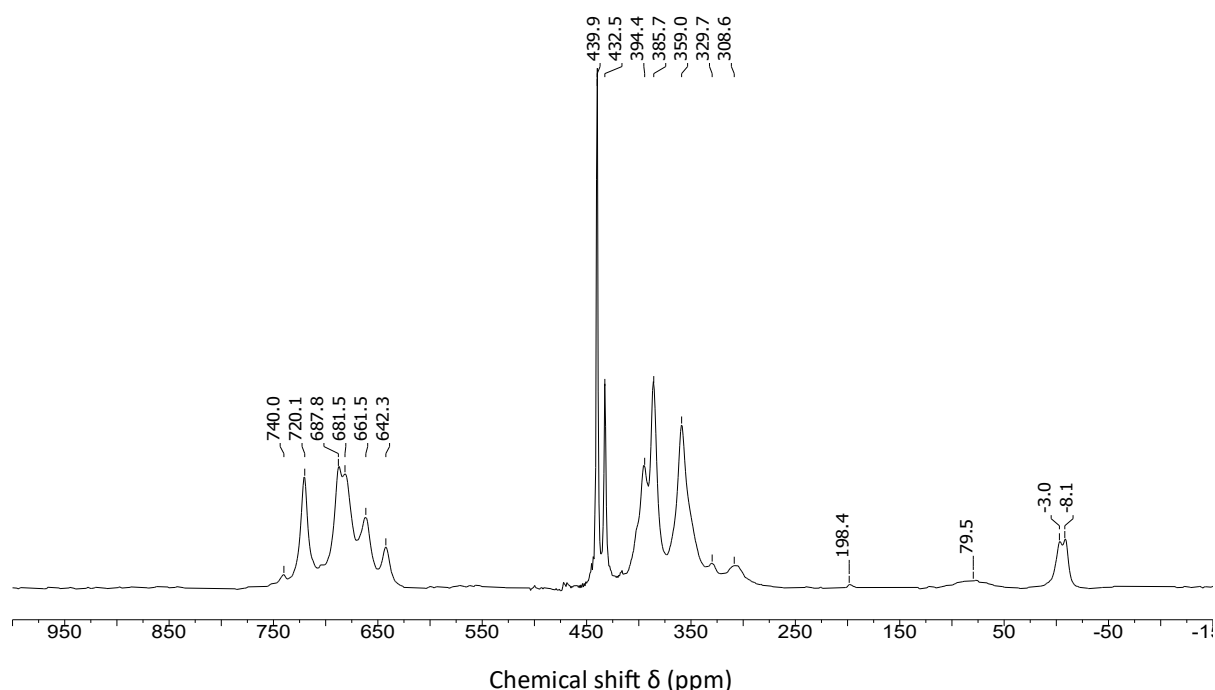
Figure 3.24: ^{17}O NMR spectrum of the reaction between $(TBA)_2[W_6O_{19}]$ and 1.6 eq. of TBA(OH) in CD_3CN.

formation of monomeric tungstate is important in "mopping up" the additional charge added to the mixture. The small peaks observed at 764 and 417 ppm in **Figure 3.24**, previously assigned to $\{W_{10}\}$, are no longer visible, while a significant peak at 432 ppm remains, reinforcing the fact that this sharp peak cannot only be assigned to $\{W_{10}\}$.

Figures 3.25, **3.26** and **3.27** show the ^{17}O NMR spectra after treatment of $(TBA)_2[W_6O_{19}]$ with 2.3, 3 and 5.2 equivalents of TBA(OH) respectively. These spectra show a continuation of the trends beginning to emerge in **Figure 3.24**. As more TBA(OH) is added, the size of the peak at 438 ppm grows as the features in the terminal W=O and bridging W-O-W regions appear to decrease. From this we can infer that the reaction mixtures are increasingly dominated by $[WO_4]^{2-}$ as charge is added. Interestingly, there are no obvious changes in the terminal W=O or bridging W-O-W regions, perhaps implying that the same/similar isopolytungstate species are present in solution, they just make up an ever-decreasing part of the mixture.

To verify if the mixture tends towards solely consisting of monomeric $[WO_4]^{2-}$, the reaction of $(TBA)_2[W_6O_{19}]$ with ten equivalents of TBA(OH) was performed. The resulting spectrum contains only a large peak at 437 ppm and two very small peaks at 285 ppm and 198 ppm. This confirms that targeting a solution with Z/W = 2 contains almost exclusively monomeric tungstate.
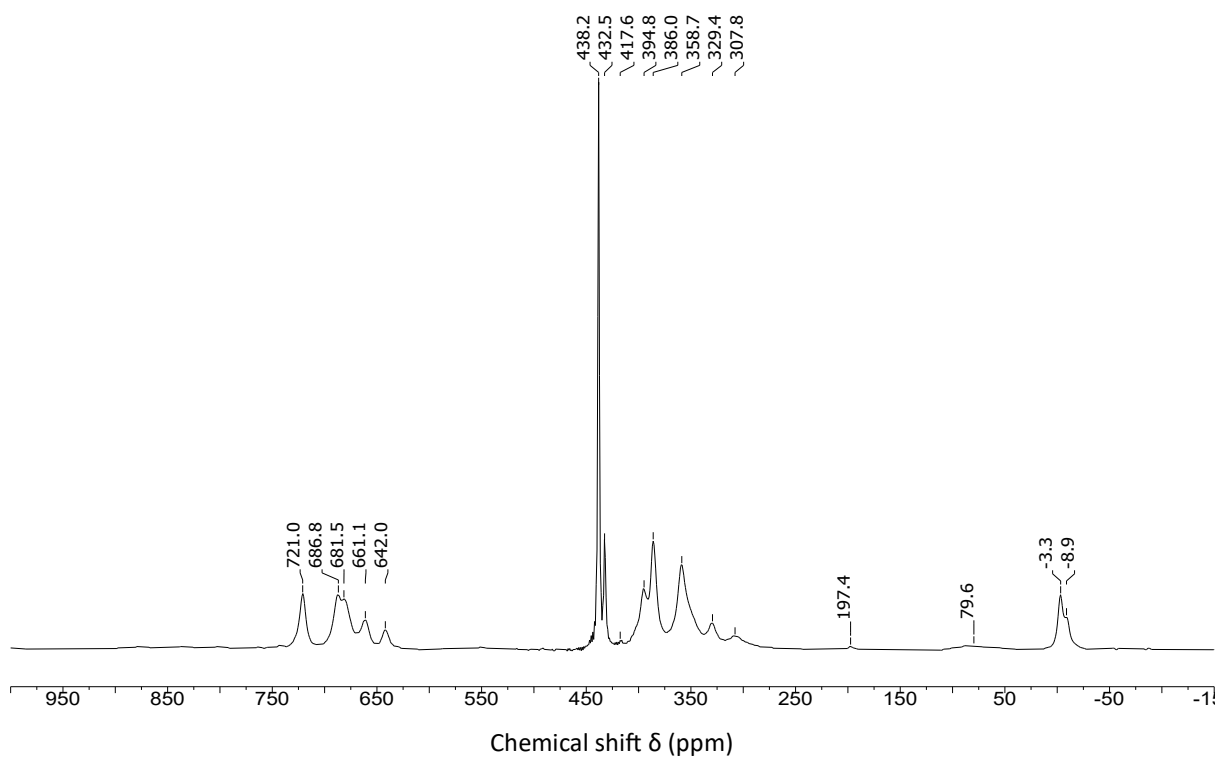
Figure 3.25: ^{17}O NMR spectrum of the reaction between $(TBA)_2[W_6O_{19}]$ and 2.3 eq. of TBA(OH) in CD_3CN.
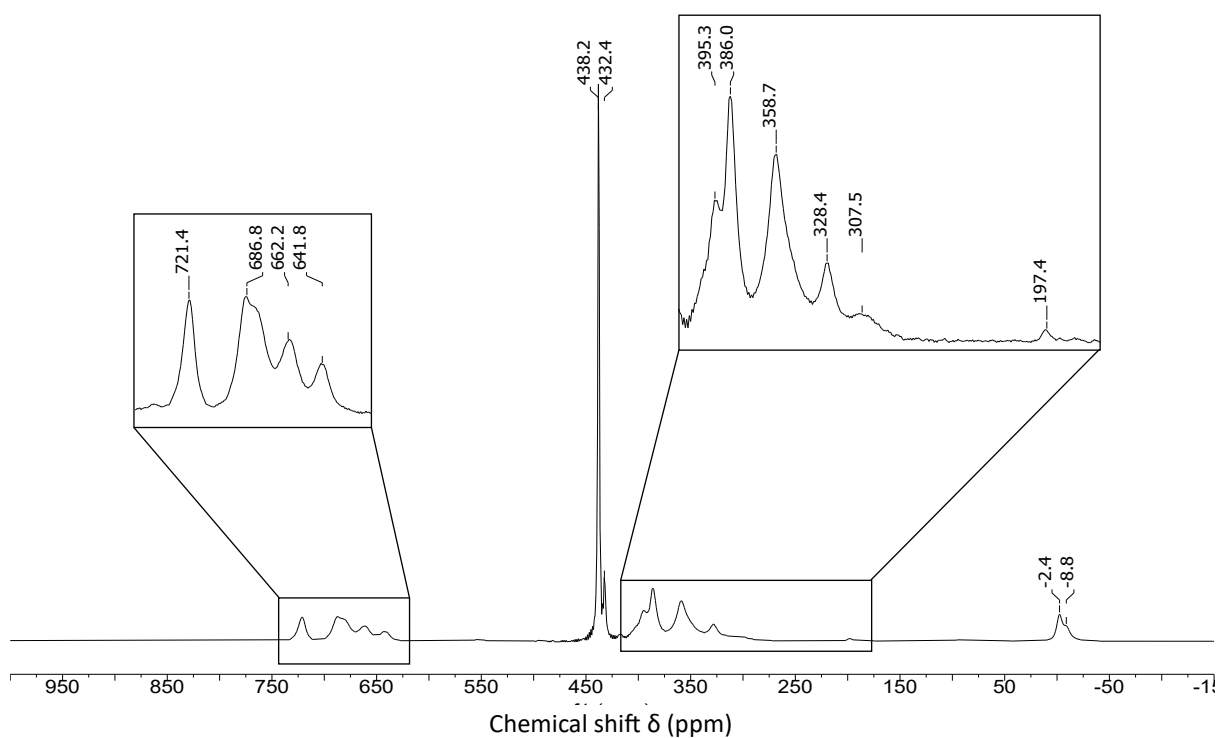
Figure 3.26: ^{17}O NMR spectrum of the reaction between $(TBA)_2[W_6O_{19}]$ and 3 eq. of (TBA)OH in CD_3CN.
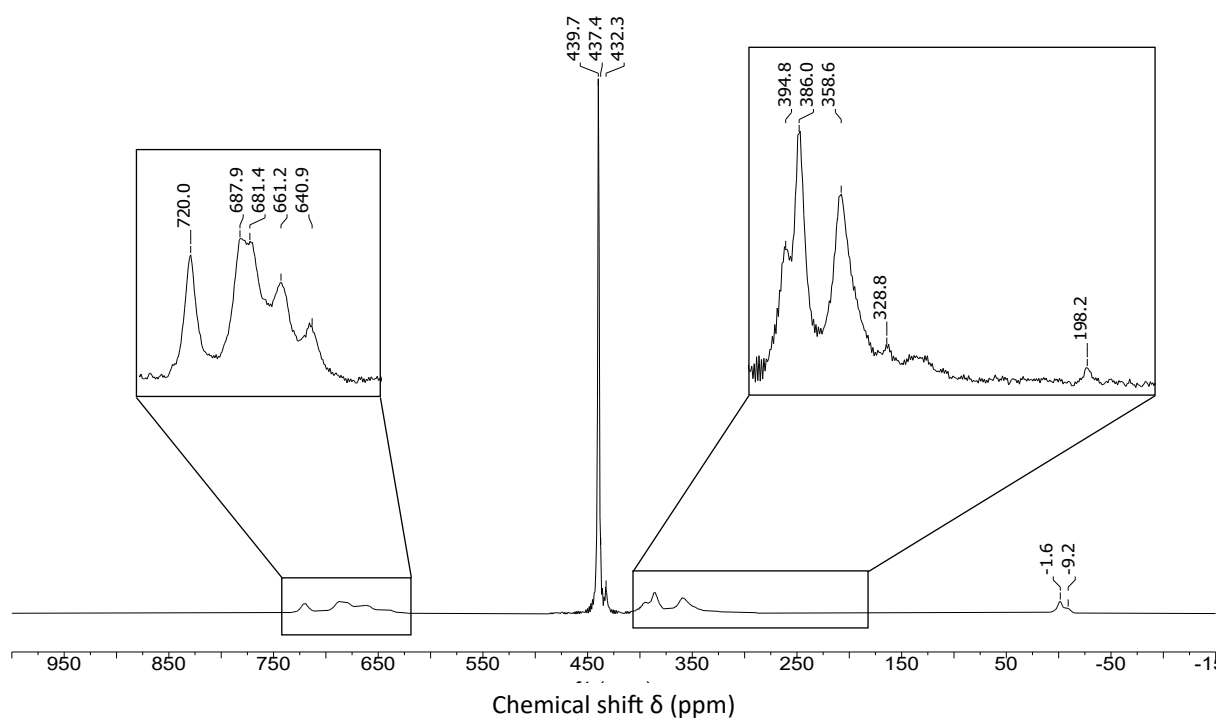
Figure 3.27: ^{17}O NMR spectrum of the reaction between $(TBA)_2[W_6O_{19}]$ and 5.2 eq. of (TBA)OH in CD_3CN.

3.4.2 ^{183}W NMR spectroscopy

Preliminary characterisation of reaction mixtures with a range of charge to tungsten ratios using ^{17}O NMR spectroscopy has started to give some insight into the nature of these solutions. The data suggest that known isopolytungstate species, like $[W_6O_{19}]^{2-}$ and $[W_{10}O_{32}]^{4-}$, exist in solutions with low Z/W ratios. However, these species quickly give way to several broad peaks that cannot be assigned to any isopolytungstate species known in the literature, implying the presence of one or more unknown species present in these solutions. As the amount of base (and charge) in the reaction mixture is increased, monomeric tungstate makes up an ever-increasing portion of the mixture until eventually, it is all that remains.

In order to get a better understanding of the nature of these reaction mixtures, particularly at Z/W = 0.5-1.2 where the broad unassigned features are observed, complimentary ^{183}W NMR spectroscopy experiments were performed.

Firstly, a single sample of $(TBA)_2[W_6O_{19}]$ was treated with portions of TBA(OH) allowing the ^{183}W NMR spectrum of a single reaction mixture to be recorded as the charge to tungsten ratio was increased. To do this, $(TBA)_2[W_6O_{19}]$ was dissolved in acetonitrile and one equivalent of TBA(OH) was added. The solution was allowed to stir at room temperature for one week before the solvent was removed and the resulting oil was dissolved in a 1:1 mixture of $CH_3CN:CD_3CN$. The ^{183}W NMR spectrum was then recorded. The sample was then transferred back to a

Schlenk flask, and the solution was diluted before the addition of another portion of TBA(OH). The solution was again allowed to stir at room temperature for one week and this was repeated to allow for the acquisition of ^{183}W NMR spectra at Z/W = 0.5, 0.8, 1 and 1.2. The resulting spectra are shown in **Figure 3.28**.

Straight away we can see a somewhat familiar picture when bearing in mind what we observed in **Figure 3.19** (Z/W = 0.71). The reaction mixture produced from treatment of $(TBA)_2[W_6O_{19}]$ with one equivalent of TBA(OH) (Z/W = 0.5 shown in **Figure 3.28a**) appears fairly simple. The ^{183}W NMR spectrum shows the mixture is primarily made up of $[W_{10}O_{32}]^{4-}$ (peaks highlighted in orange) and the same *8n* (1:1:1:1:1:1:1:1) isopolytungstate previously observed (highlighted in red). Unlike in **Figure 3.19**, this "red species" appears to be the only major unknown component of this reaction mixture, suggesting that perhaps it is preferred over any of the other previously observed species at low charge to tungsten ratios. The observation of $\{W_{10}\}$ in the ^{183}W NMR spectrum at Z/W = 0.5 is consistent with the ^{17}O NMR studies, which showed characteristic peaks of $\{W_{10}\}$ at 764, 432 and 417 ppm respectively. The additional peak at 59 ppm indicates the presence of some unreacted $[W_6O_{19}]^{2-}$.[19]

After the addition of 1.3 equivalents of TBA(OH), taking the charge to tungsten ratio to 0.8, the spectrum gets substantially more complicated, shown in **Figure 3.28b**. The relative amount of the "red species" appears to decrease drastically and gives way to the formation of other species. The peaks highlighted in blue appear in a now familiar pattern and are easily assigned to $[W_7O_{24}H]^{5-}$. The seven peaks highlighted in green were also previously observed in **Figure 3.17** and **3.19** (Z/W = 0.71), however in this case, the relative intensity of the peaks highlighted in green far outweighs those in red. This may suggest that the isopolytungstate species responsible for these peaks in red is readily transformed into other species as TBA(OH) is added.

Curiously, the peaks at −20 and −162 ppm, assigned to $\{W_{10}\}$ are still very prominent in this ^{183}W NMR spectrum. This contrasts the results of the ^{17}O NMR study, where solutions with a Z/W > 0.5 showed no evidence of $\{W_{10}\}$. This could indicate that $\{W_{10}\}$ possesses some kinetic stability with respect to conversion to other isopolytungstate species as base is added, which in turn means that the solution speciation observed is not only a consequence of the charge to tungsten ratio targeted, but also the nature of the solution upon which charge is added. This could have a drastic impact on the observed solution speciation as the ability to reach a "true" equilibrium state (i.e. observation of the most stable products at that Z/W) would be
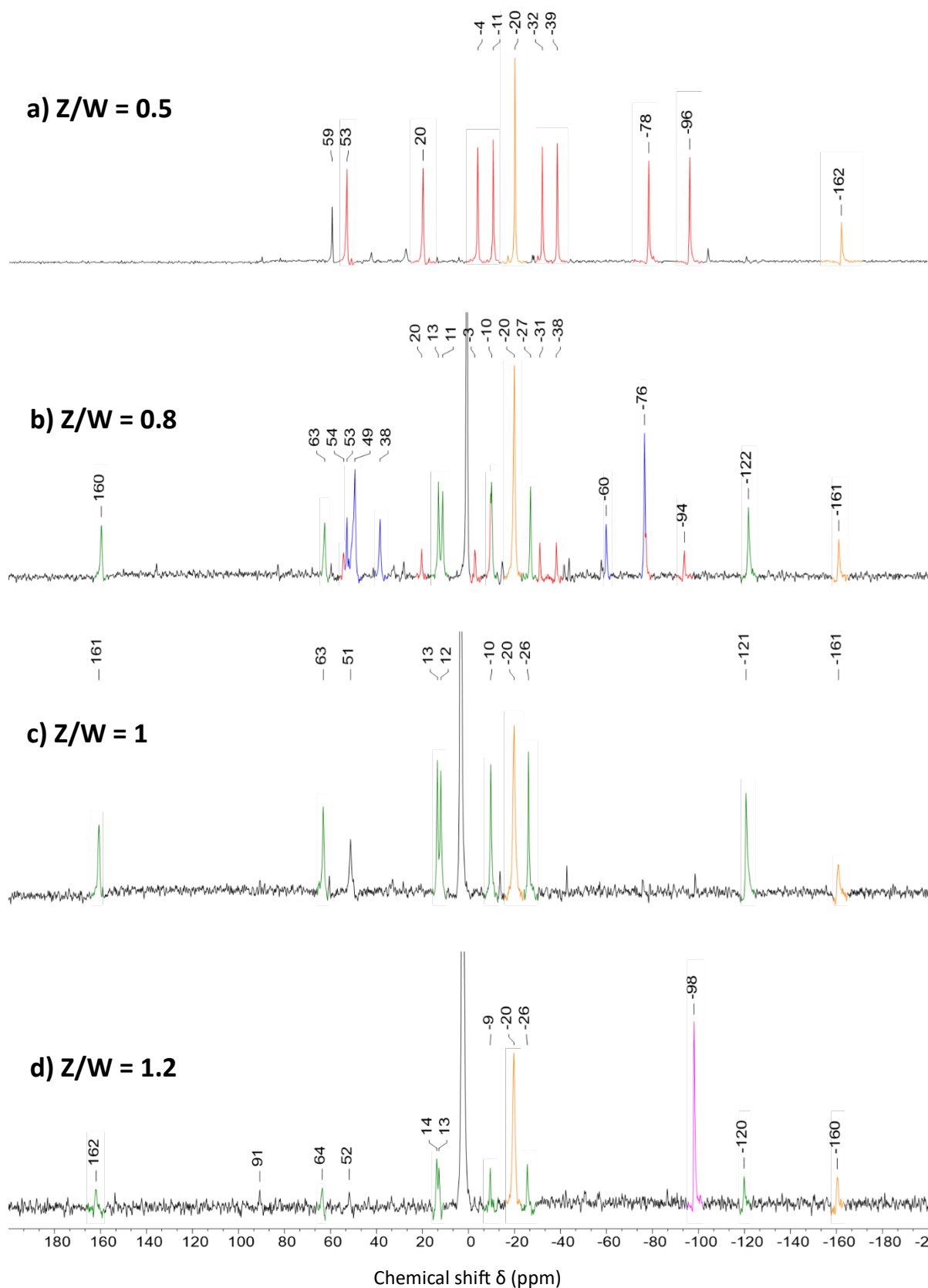
Figure 3.28: ^{183}W NMR spectra of the portion wise addition of TBA(OH) to $(TBA)_2[W_6O_{19}]$. The spectra were recorded after addition of a) 1 eq. (Z/W = 0.5), b) 2.3 eq. (Z/W = 0.8), c) 4 eq. (Z/W = 1), and d) 5.2 eq. (Z/W = 1.2) of base. The spectra were recorded in a 1:1 mixture of CH_3CN and CD_3CN.

dependent on the ability to overcome any kinetic barriers allowing interconversion of isopolytungstate species. This may also help to explain why monomeric tungstate is observed at such low charge to tungsten ratios in non-aqueous solutions. If significant quantities of tungsten are locked up in kinetically stable species, then the base added is likely to act on the remaining (labile) isopolytungstate species, causing their conversion to highly charged tungstate. A large peak for $[WO_4]^{2-}$ is seen at the centre of **Figure 3.28b** at 1 ppm.

This trend continues as the charge to tungsten ratio is increased to 1. The spectrum shown in **Figure 3.28c** is obtained after the addition of four equivalents of TBA(OH) to $(TBA)_2[W_6O_{19}]$, the exact same conditions used to produce **Figure 3.3** which was shown to be an approximate 1:2 mixture of $[W_7O_{24}H]^{5-}$ and $[WO_4]^{2-}$. We can see that the two spectra are completely different. Both spectra contain a large peak that can be assigned to $[WO_4]^{2-}$, observed at 3 ppm in **Figure 3.28c**, but the spectrum obtained after portion wise addition of base to reach Z/W = 1 contains no $[W_7O_{24}H]^{5-}$. Any $[W_7O_{24}H]^{5-}$ that was present in **Figure 3.28b** appears to have been converted into tungstate and/or the "green species". The peaks assigned to $\{W_{10}\}$ highlighted in orange are still present.

Further basification of the reaction mixture to give a Z/W = 1.2 leads to almost complete conversion of everything in the reaction mixture into monomeric tungstate (**Figure 3.28d**). The peaks highlighted in green and orange both drop in intensity with respect to the tungstate peak. This is more clearly shown in **Figure 3.29**, which gives a better representation of how big the central tungstate peak (observed at 1-3 ppm) is compared to the other peaks in the reaction mixture and in turn how the relative amount of everything else in the reaction mixture is decreasing with respect to the amount of tungstate. There is a new peak present in **Figure 3.28d** at −98 ppm, which may be tentatively assigned to $[H_2W_{12}O_{40}]^{6-}$, which has been reported at −113 ppm as a sodium salt in aqueous conditions.[20]

Z/W = 0.8   **Z/W = 1**   **Z/W = 1.2**
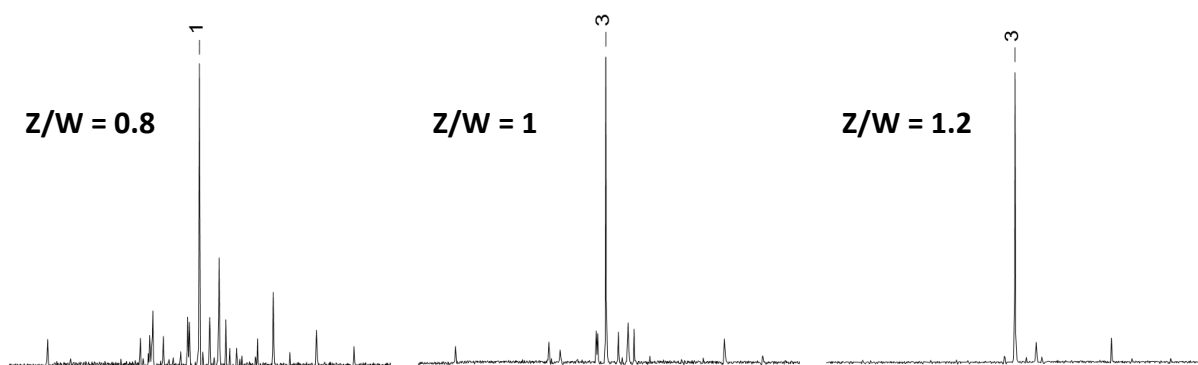
Figure 3.29: Comparison of the intensity of the tungstate peak compared to the rest of the reaction mixture in the ^{183}W NMR spectra obtained from the reaction of $(TBA)_2[W_6O_{19}]$ with increasing quantities of TBA(OH).

In order to determine the extent to which the observed solution speciation at a given charge to tungsten ratio is affected by the nature of the starting solution, a similar set of experiments were performed. In this case, separate samples of $(TBA)_2[W_6O_{19}]$ were treated with the required amount of TBA(OH) to reach charge to tungsten ratios between 0.5-1.2. This means that the starting point for every reaction is the same. The resulting spectra are shown in **Figure 3.30**. It should be noted that the spectra shown in Figure **3.30a**, **3.30c** and **3.30e** have already been discussed in this chapter but as they were prepared by treatment of $(TBA)_2[W_6O_{19}]$ with the appropriate amount of base to reach the target Z/W, added in one portion, it is suitable to discuss them here.

The spectrum shown in **Figure 3.30a**, obtained at Z/W = 0.5 was discussed above, and appears to simply contain a mixture of $\{W_{10}\}$ and the "red species". However, things quickly get more complicated. Treatment of $(TBA)_2[W_6O_{19}]$ with 1.6 equivalents of TBA(OH), targeting Z/W = 0.6, produces a much more complex mixture. Peaks at 59, −20 and −162 ppm can be assigned to $\{W_6\}$ and $\{W_{10}\}$. In contrast to the study using portion wise addition of base, the relative amount of $\{W_{10}\}$ in the mixture already appears to be much lower, with signals appearing much less intense than those in **Figure 3.28**. This is in keeping with the idea that $\{W_{10}\}$ may be a thermodynamically favourable reaction product at lower Z/W ratios, but kinetic stability is the main cause of its persistence after further basification. Careful analysis of the remaining chemical shifts gives evidence for the previously assigned "red species", "purple species" and $[W_7O_{24}H]^{5-}$. The complexity of this mixture is evidence that there is very limited preference for a single species at this charge to tungsten ratio, and therefore we can infer that the solution stability of these species (under these conditions) is similar.

Interestingly, in this spectrum, the observed signals are sufficiently narrow to reveal some W-W coupling. Peaks at 31, 27 and −59 ppm respectively, all of which are assigned to the purple species in a 2:2:4 ratio, have observable tungsten-tungsten coupling. **Figure 3.31** highlights this. The observed coupling constants (i.e. J_{WW}) are 25.4 Hz for the peak at 31 ppm and 24.5 Hz for the two peaks at 27 and −59 ppm respectively. This indicates that the tungsten nuclei responsible for the peaks at 27 and −59 ppm are coupled to one another as the coupling constants are identical. There are no other peaks either assigned to the purple species, or in the spectrum as a whole, which have a coupling constant of 25.4 Hz. This is initially confusing as every observed homonuclear coupling constant must appear twice in the spectrum, once for each environment coupled to each other. However, it may be in this case that the tungsten

a) Z/W = 0.5
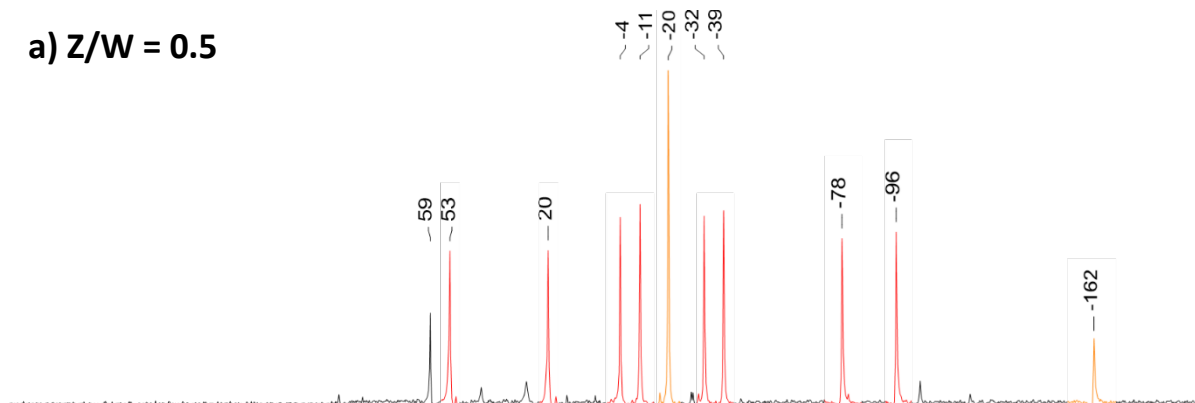
b) Z/W = 0.6

c) Z/W = 0.71

d) Z/W = 0.8

Chemical shift δ (ppm)

104
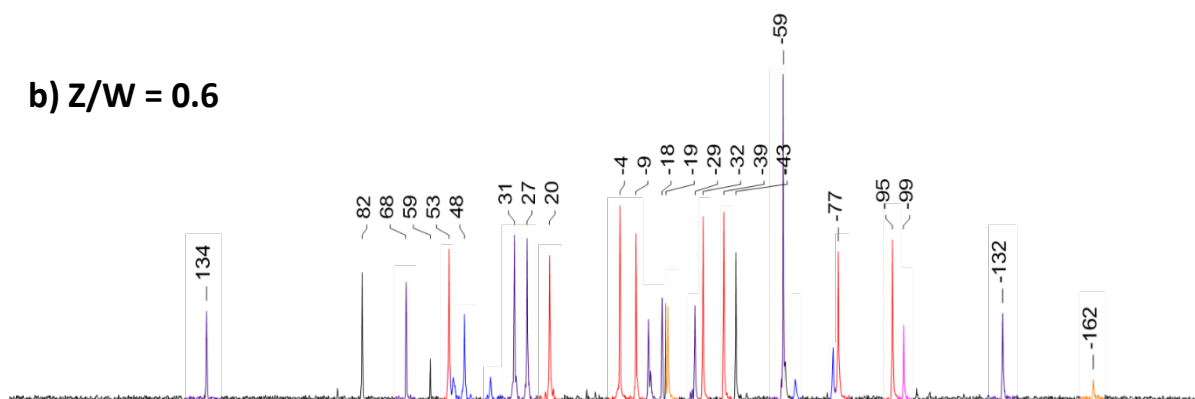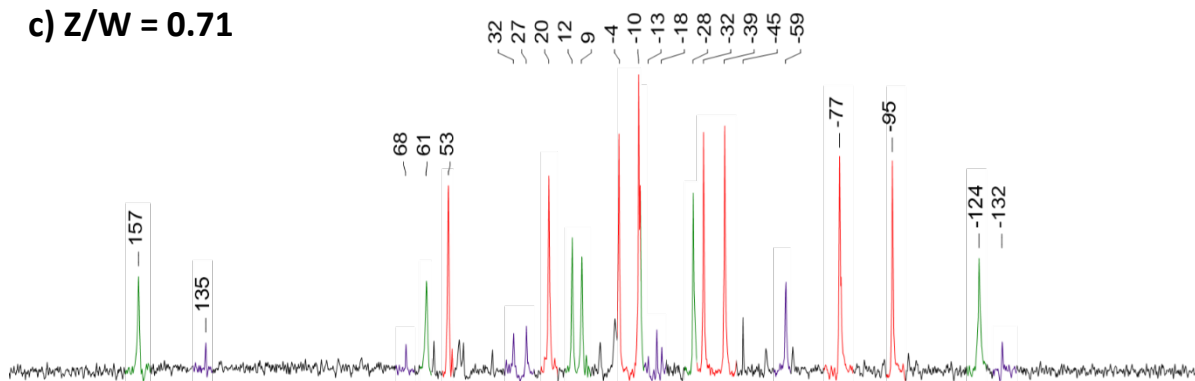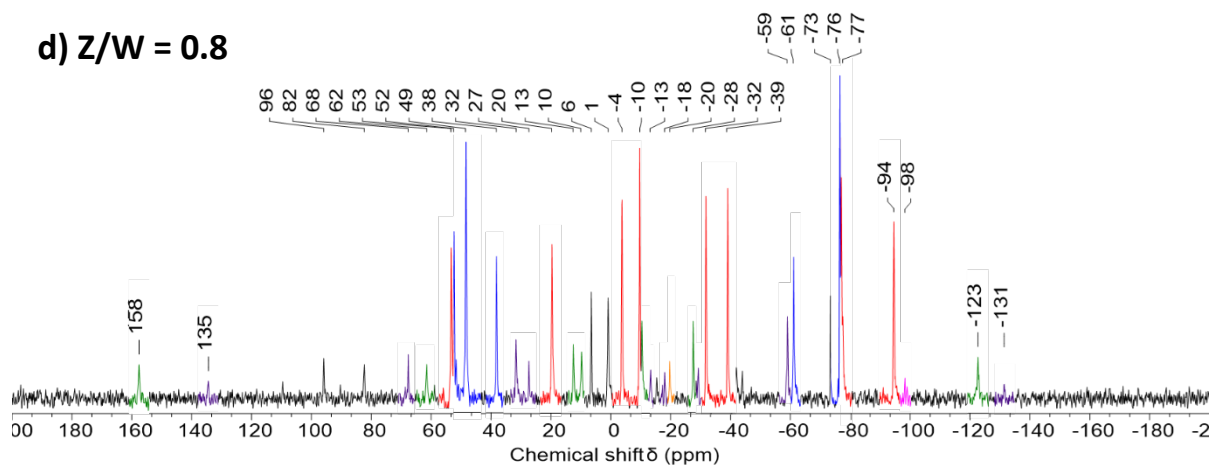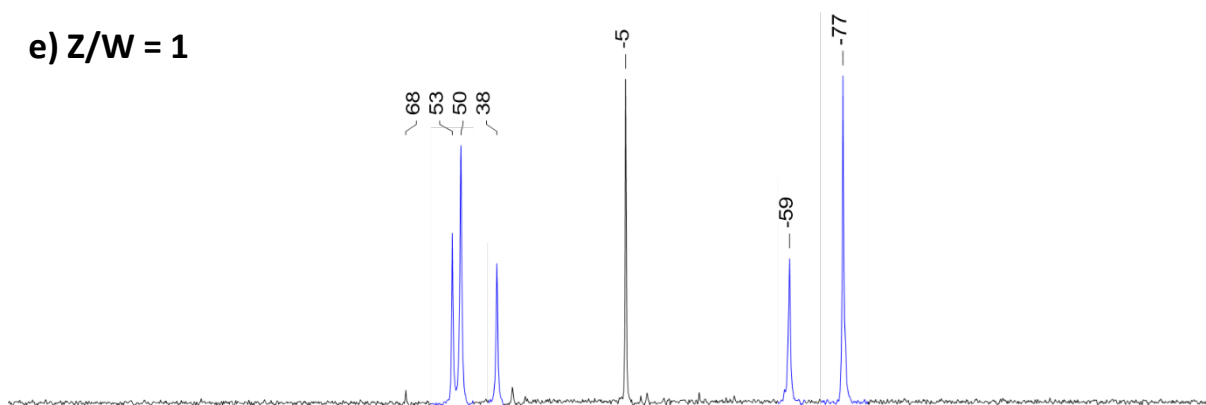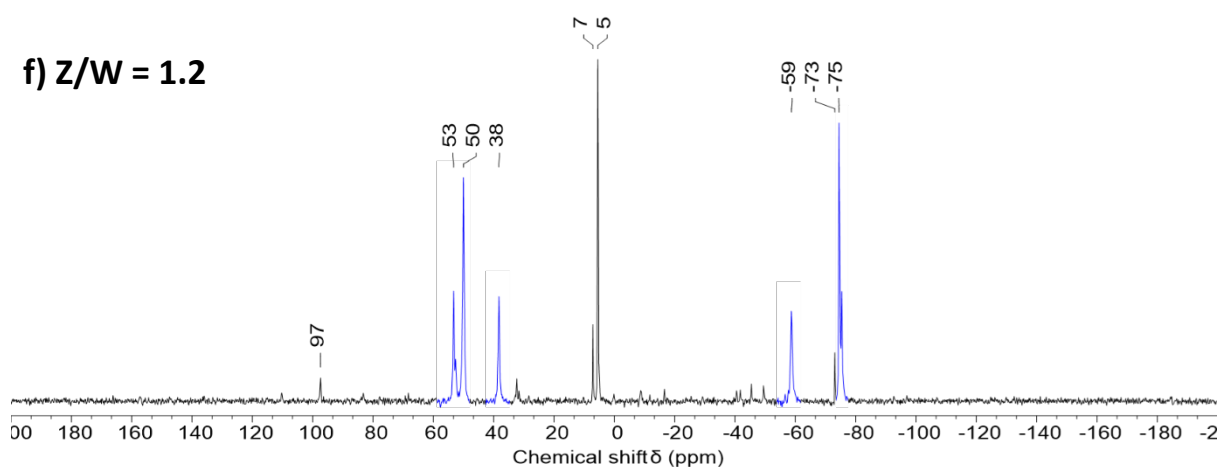
Figure 3.30: ^{183}W NMR spectra of the reaction of $(TBA)_2[W_6O_{19}]$ with a) 1eq. Z/W = 0.5, b) 1.6 eq. Z/W = 0.5, c) 2.3 eq. Z/W = 0.71, d) 2.8 eq., Z/W = 0.8, e) 4 eq., Z/W = 1 and, f) 5.2 eq. Z/W = 1.2 of TBA(OH). The spectra were recorded in a 1:1 mixture of $CH_3CN:CD_3CN$.

nuclei responsible for the peak at 31 ppm are coupled with the nuclei responsible for one the peaks at 27 or −59 ppm. The relative abundance of ^{183}W is 14.3% and therefore the intensity of a doublet of doublets (that is to say when an NMR active ^{183}W nucleus is coupled simultaneously to two chemically unique NMR active ^{183}W nuclei) would be 2% of the main
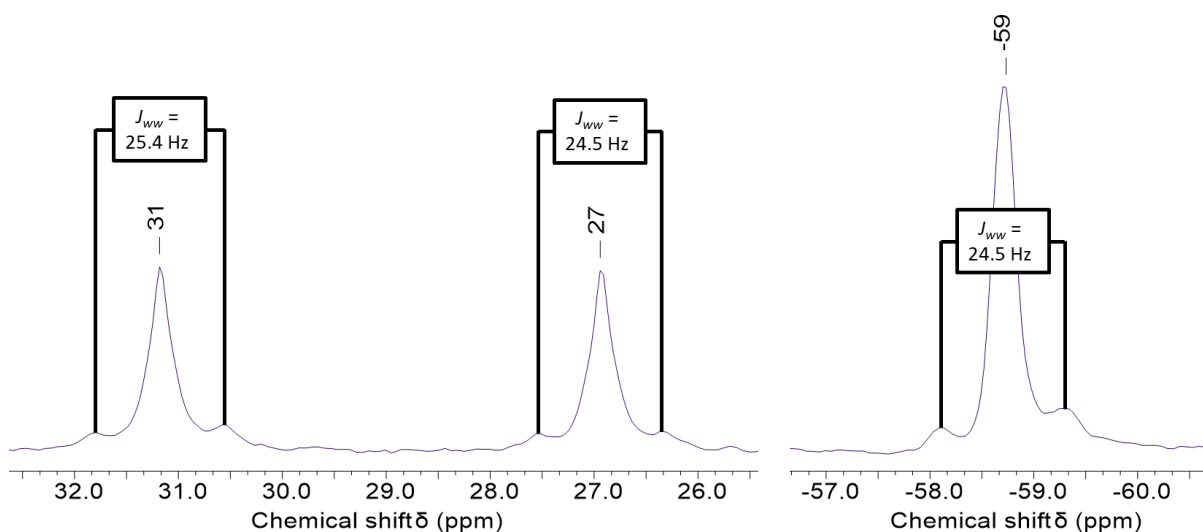
Figure 3.31: Observed J_{WW} couplings for the "purple species" in the ^{183}W NMR spectrum of the reaction of $(TBA)_2[W_6O_{19}]$ with 1.6 eq. of TBA(OH), giving Z/W = 0.6.

105

peak (split into the 4 peaks of a dd at 0.5% intensity). This would be very difficult to observe and what is far more likely is to only observe a single coupling at any given time. If this were the case, we would expect two observed couplings, one of 24.5 Hz and one of 25.4 Hz, which would likely be impossible to separate. Each peak of the doublets would have 7.15% intensity compared to the main peak (85.7%), meaning that we would expect the observed satellites to be 14.3% of the intensity of the main peak (2 x 7.15%). This appears to be the most logical description in this case.

The J_{WW} coupling constant for coupling between W3/W5 and W6/W7 of $[W_7O_{24}H]^{5-}$ was reported 25.6 Hz.[10] This was observed for W-O-W bridges with large bond angles of ca. 146 °. Observation of coupling constants of very similar magnitude for the "purple species" is indicative of it also containing similarly "linear" W-O-W bridges and we may speculate that the "purple species" and $[W_7O_{24}H]^{5-}$ could share some structural similarity.

Further analysis of the ^{183}W NMR spectrum shown in **Figure 3.30b** also shows several sets of observable satellites, caused by tungsten-tungsten coupling, around peaks previously assigned to the "red species" (shown in **Figure 3.32**). These couplings have not been observed in previous spectra. The peaks at 53 and −77 ppm couple to each other with a coupling constant of 17.9 Hz, and the peaks at 20 and −9 ppm couple to each other with a coupling constant of 20.7 Hz. Both of these coupling constants are slightly smaller than those observed for the "purple species" and $[W_7O_{24}H]^{5-}$.

$^2J_{WW}$ values in polyoxometalates are reported to depend both on the W-O-W bond angle and the bond lengths of the bridge, with larger bond angles and shorter bonds leading to larger coupling constants.[21] These factors may be used to infer that the slightly smaller coupling
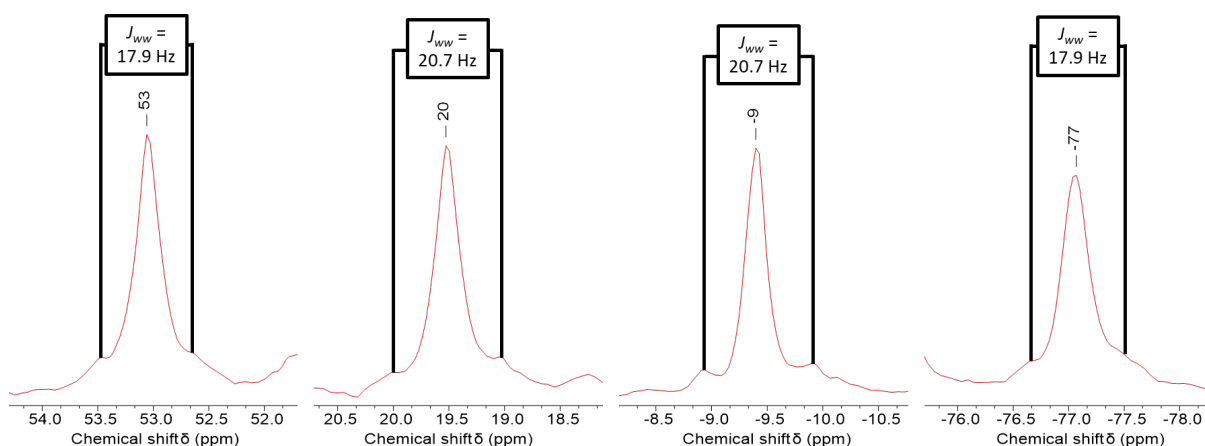
Figure 3.32: Observed J_{WW} couplings for the "red species" in the ^{183}W NMR spectrum of the reaction of (TBA)$_2$[W$_6$O$_{19}$] with 1.6 eq. of TBA(OH), giving Z/W = 0.6.

constants observed for the "red species", compared to $[W_7O_{24}H]^{5-}$ or the "purple species", are consistent with either slightly longer bonds or smaller bond angles than the W-O-W bridges responsible for the observed W-W couplings in $[W_7O_{24}H]^{5-}$ or the "purple species". Values of 17.9 and 20.7 Hz are still very much in the range consistent with 140-150° W-O-W bond angles.[21]

Moving to Z/W = 0.71, via the reaction of $(TBA)_2[W_6O_{19}]$ with 2.3 equivalents of TBA(OH), leads to a slight simplification in the mixture. In particular, all resonances assignable to $\{W_6\}$ and $\{W_{10}\}$ are either unobservable or very small, consistent with the loss of these low charge density species (Z/W = 0.33 and 0.4 respectively) as more charge is added to the mixture. The relative amount of the "purple species" has decreased drastically, apparently giving way to the "green species" which consistently appears at this charge to tungsten ratio, as discussed in more detail in **Section 3.3.6**. The "red species" remains a major component of the mixture.

Increasing the charge to tungsten ratio to 0.8, requiring the use of 2.8 equivalents of TBA(OH) per $\{W_6\}$ leads to some minor changes, though the major features are largely the same. Like at Z/W = 0.71, the peaks assigned to the "red", "purple" and "green species" are all present with the "red species" holding its dominance in the mixture with respect to the others. Interestingly, as we approach Z/W = 1, the ratio at which we know $[W_7O_{24}H]^{5-}$ is a major component, the amount of $[W_7O_{24}H]^{5-}$ in the mixture significantly increases. This only appears to happen once the charge to tungsten ratio of $[W_7O_{24}H]^{5-}$ (0.71) is surpassed and may be evidence for its stability in the presence of excess base. One of the two unassigned peaks at 6 and 10 ppm respectively may correspond to tungstate. This is consistent with ^{17}O NMR experiments in which $[WO_4]^{2-}$ is also observed. Tungstate is a much more prominent component of the mixture in the ^{183}W NMR spectrum shown in **Figure 3.28b**, also recorded at Z/W = 0.8. The difference between this and **Figure 3.30d** further exemplifies the effect the nature of the starting solution has on the observed speciation, with the results from the series of experiments in which the TBA(OH) was added portion wise deviating from the rest.

The final two ^{183}W NMR spectra, shown in **Figure 3.30e** and **3.30f**, correspond to the reaction of $(TBA)_2[W_6O_{19}]$ with 4 and 5.2 equivalents of TBA(OH) respectively, targeting charge to tungsten ratios of 1 and 1.2. The spectrum shown in **Figure 3.30e** has already been extensively discussed in **Section 3.3.2**. The addition of an extra 1.2 equivalents of TBA(OH) does little to change this spectrum. There are a few extra, low intensity, peaks present, with the most prominent at 97, 7 and −73 ppm respectively. The relative amounts of $[W_7O_{24}H]^{5-}$ and $[WO_4]^{2-}$

present in the mixture do not change much with the addition of the extra 1.2 equivalents of base, although ^{17}O NMR studies suggest that this mixture will eventually tend towards containing only tungstate.

3.5 Conclusion

The nature of the reaction mixture targeting the virtual lacunary species "(TBA)$_5$[W$_5$O$_{18}$H]" has been probed in depth. Combining solution NMR methods and single-crystal X-ray diffraction methods led to the discovery of a new isopolytungstate, [W$_7$O$_{24}$H]$^{5-}$. This new structure was found to be a major component of the reaction mixtures previously targeting "(TBA)$_5$[W$_5$O$_{18}$H]". Instead of this virtual species, we now know that our precursor solutions used in the synthesis of [(CoW$_5$O$_{18}$H)$_2$]$^{6-}$ consist of approximately a 1:2 mixture of [W$_7$O$_{24}$H]$^{5-}$ and monomeric tungstate.

Reactions directly targeting [W$_7$O$_{24}$H]$^{5-}$, by changing the ratio of TBA(OH) to (TBA)$_2$[W$_6$O$_{19}$] used, did not allow clean formation of [W$_7$O$_{24}$H]$^{5-}$. Instead, they gave evidence for the formation of a several other previously unknown isopolytungstate species, exemplifying that little is currently known about isopolytungstate speciation in non-aqueous solution.

This led us to explore how solution speciation changes as the charge to tungsten ratio was varied (which can be considered analogous to changing pH in aqueous solutions). Reactions of (TBA)$_2${W$_6$O$_{19}$] with varying amounts of TBA(OH) were used to produce reaction mixtures with a range of charge to tungsten ratios. ^{17}O and ^{183}W NMR spectroscopy have been employed to give an insight into non-aqueous isopolytungstate solution speciation. The key findings are:

1. The species known in the literature (i.e. {W$_6$} and {W$_{10}$}) are present in non-aqueous solutions but mostly in solutions with low charge to tungsten ratios. In particular, {W$_{10}$} seems to only be readily accessible when mixtures are heated, but once present, it persists.

2. Non-aqueous solutions with Z/W = 0.5-1 show evidence for several isopolytungstate species currently unknown in the literature. The characteristic peaks of these species are consistently observed in varying ratios in these solutions.

3. Solutions with Z/W = 1-1.2 are shown to contain a mixture of monomeric tungstate and the new isopolytungstate [W$_7$O$_{24}$H]$^{5-}$, which is fully characterized in this chapter and represents only the third isopolytungstate to be isolated from non-aqueous media.

4. As large amounts of base are added to non-aqueous solutions, the mixture tends towards monomeric tungstate, mirroring what is observed in aqueous solution.

5. Experiments looking at the step wise basification of a single solution of $(TBA)_2[W_6O_{19}]$ indicate that the observed isopolytungstate speciation is not only dependant on the charge to tungsten ratio, but the nature of the solution prior to addition of base, demonstrating that the kinetic barriers associated with the interconversion of isopolytungstate species are extremely important.

3.6 Future work

These investigations into non-aqueous isopolytungstate speciation have highlighted that there are number of species which constitute a large proportion of the chemical space, which are currently uncharacterised. The main goal of any future work in this area would be to combine these solution investigations with solid state structural characterisation to give a clear understanding of non-aqueous isopolytungstate speciation. This would primarily involve extensive screening to attempt to grow crystals of these structures. This initially could involve screening of solvent combinations and crystallization methods. This could then be built upon with further experiments exploring cation exchange. Swapping TBA cations for things like benzyltrimethylammonium or tetraphenylphosphonium may impart intermediate different solubility properties that in turn may allow isolation of currently elusive species.

Another very interesting avenue would be to explore how the solution speciation varies with the introduction of stoichiometric quantities of metal cations. Isolation of $[W_7O_{24}H]^{5-}$ in this work gives some indication that structures incorporating a $\{W_5O_{18}\}$-fragment are present in organic media. Introduction of metals, e.g. NaOMe, KO^{t}Bu or Mg(OMe)$_2$, could act as a way to stabilise this fragment and allow isolation of a true lacunary $\{W_5\}$ compound. This in turn would be a very useful precursor for the synthesis of other heterometal containing Lindqvist-type POMs.

Finally, it would also be desirable to expand this work to explore the non-aqueous solution speciation of isopolymolybdates and isopolyvanadates. Like isopolytungstates, the non-aqueous chemistry of these framework metals is not fully understood. This would also provide a comparison of the behaviour of the respective metals and would give insight into how the nature of the framework metal affects the structures, and stabilities, of species observed in solution.

3.7 Experimental

3.7.1 Synthesis of WO₃.H₂O (H₂WO₄)

Sodium tungstate dihydrate (60 g, 182 mmol) was added to a conical flask and dissolved in water (340 mL). The mixture was heated to 90 °C with stirring. Once at 90 °C, hydrochloric acid (212 mL, 6M, 1.3 moles, 7 eq) was added slowly. A yellow suspension quickly formed. The mixture was stirred for 30 minutes and then cooled to room temperature. The mixture was then filtered with suction (note: this filtration can be very slow and some of the fine yellow solid may pass through the filter). The solid was then washed with water (50 mL) and ethanol (100 mL) before allowing to dry overnight. Grinding with a pestle and mortar gave a fine yellow/green powder (38.4 g, 84% yield).

3.7.2 Purification of SOCl₂

Previously used thionyl chloride can be purified by successively distilling over quinoline and then over linseed oil.

The apparatus used is shown adjacent. $SOCl_2$ (500 mL) was placed in a 1 L round bottom flask connected to a distillation head, with a flow of N_2 and a water trap. For the first distillation, quinoline (100 mL) was added and the solution was slowly brought up to the boil. Any liquid collected before the thermometer in the still head read 70 °C was discarded. The temperature remained at around 70 °C for the remainder of the distillation, during which time approx. 450 mL of liquid was collected. After cleaning the apparatus, the resulting distillate was added to a 1 L rbf along with linseed oil (50 mL). The process then repeated to obtain freshly distilled $SOCl_2$ as a colourless liquid. This can be stored in screw top glass bottles until use.

3.7.3 Synthesis of WOCl₄

Glassware was assembled as shown in the schematic adjacent. A KOH trap is a Dreschel flask filled with KOH pellets.

$WO_3.H_2O$ (20.8 g, 83.2 mmol) was added to a 500 mL two neck round bottom flask. The flask was then charged with thionyl chloride (200 mL). Some HCl was produced upon addition so this step was done cautiously. The reaction mixture was then heated to 85 °C and stirred

overnight. During the reaction the initial yellow suspension became an orange solution and all the solid dissolved. The solution was cooled to room temperature. The remaining thionyl chloride was removed under vacuum and collected in a cold trap for recycling (a KOH trap should also be placed between the cold trap and vacuum to neutralise any HCl gas), leaving an orange solid. This solid was then transferred to a sublimation flask. The crude product was purified by irradiating it with infrared light under vacuum to induce sublimation (setup shown adjacent). Dark red needles of WOCl$_4$ were produced (22.5 g, 79% yield).
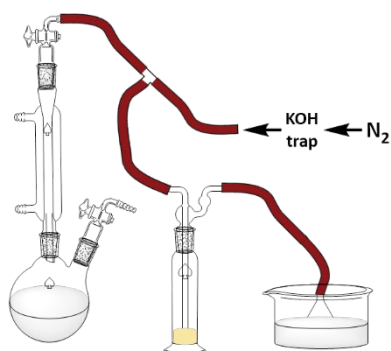
3.7.4 Synthesis of WO(OMe)$_4$

WOCl$_4$ (10.8 g, 31.6 mmol) was added to a round bottom flask under N$_2$. The flask was then cooled to −30 °C using a dry ice/MeCN bath. The solid was then dissolved in THF (250 mL). MeOH (7.7 mL, 190 mmol, 6 eq) was added slowly and the solution was allowed to warm to room temperature, during which time the solution turned pale yellow. The supply of N$_2$ was then swapped for a supply of NH$_3$. The solution was then bubbled steadily with NH$_3$ for 30 minutes which caused the exothermic formation of a white precipitate. The gas supply was then swapped back to N$_2$ and the solution was bubbled with N$_2$ for 10 minutes. The mixture was filtered through a glass filter frit and the separated solid was washed with THF (2 x 50 mL). (Note: the pale-yellow filtrate may need to be filtered again to remove any fine precipitate). The volume of the filtrate was reduced under vacuum until precipitate started to form. At this point, the solution was placed under N$_2$ and then warmed to re-dissolve any solid. The solution was cooled to −30 °C in the freezer and white crystalline WO(OMe)$_4$ formed. The the resulting solid was washed with a toluene (5-10 mL) and dried under vacuum (8.4 g, 82% yield).

3.7.5 Synthesis of ^{17}O enriched

(TBA)$_2$[W$_6$O$_{19}$]WO(OMe)$_4$ (1.97 g, 6.06 mmol) and (TBA)$_2$[WO$_4$] (0.89 g, 1.23 mmol) were placed in a Schlenk flask under N$_2$. Acetonitrile (30 mL) was added, and the mixture was stirred

at 80 °C for 30 minutes. ^{17}O-enriched water (219 μL, 10.2 mmol, 40% enriched) was added and the solution was stirred for a further 3 hours. The solution was then cooled to room temperature and the solvent was removed under reduced pressure. The solid was then re-dissolved in the minimum amount of hot acetonitrile. The solution was allowed to cool to room temperature and then cooled further in the freezer. Large white crystals of (TBA)$_2$[W$_6$O$_{19}$] fomed during this time. The crystals were isolated by cannula filtration and then dried under vacuum (yield).

^{17}**O NMR** (67.8 MHz, CD$_3$CN) δ (ppm) = −76.8 (μ$_6$-O, 1 O), 415.4 (W-O-W, 12 O), 776.3 (W=O, 6 O). ^{183}**W NMR** (20.8 MHz, CD$_3$CN) δ (ppm) = 58.9 ppm. ^{1}**H NMR** (300 MHz, CD$_3$CN) δ (ppm) = 0.98 (24 H, t, CH$_3$), 1.37 (16 H, sext, CH$_2$), 1.60 (16 H, qu, CH$_2$), 3.11 (16H, m, CH$_2$). ^{13}**C NMR** (75.5 MHz, CD$_3$CN) δ (ppm) = 13.8, 20.3, 24.3, 59.3. v_{max}/**cm^{-1}** = 2963 (CH), 2936 (CH), 2876 (CH), 1461, 1381, 1172, 1109, 1068, 1035, 966 (vs), 889, 873, 801 (vs), 736, 669, 584, 437 (vs).

3.7.6 Synthesis of TBA$_2$[WO$_4$]

WO$_3$.H$_2$O (15.0 g, 60 mmol) was added to a 250 mL two neck round bottom flask. The flask was evacuated and backfilled three times with N$_2$. TBA(OH) (120 mL, 120 mmol, 1M in MeOH) was added and the yellow suspension was left to stir for 30 minutes at room temperature during which time, the yellow colour faded. MeCN (40 mL) was added, and the solution was left to stir overnight. Most of the solid had dissolved at this point, but the mixture was filtered to remove any remaining solid. The solvent was removed under vacuum to leave a white sticky solid. The solid was triturated with diethyl ether and dried under high vacuum to give a free-flowing white powder (37.2 g, 85% yield). Note the solid is extremely hygroscopic and should be handled under inert atmosphere.

3.7.7 ^{17}O-enriched reaction targeting "[W$_5$O$_{18}$H]$^{5-}$"

^{17}O enriched (TBA)$_2$[W$_6$O$_{19}$] (50 mg, 0.026 mmol) was added to a Schlenk flask and suspended in MeCN (1 mL). The appropriate amount of (TBA)OH (0.42 mL, 0.11 mmol, 0.25 M in MeCN) was added to the flask. The total volume of the reaction mixture was made up to approx. 3 mL. The solution was stirred at room temperature for 3 days. The solvent was removed, and the residual oil was dissolved in CD$_3$CN (0.5 mL). The mixture was transferred to a 5 mm screw top NMR tube for ^{17}O NMR spectroscopy.

3.7.8 Reaction targeting "[W$_5$O$_{18}$H]$^{5-}$" for ^{183}W NMR spectroscopy

TBA(OH) (5.3 mL, 5.3 mmol, 1 M in MeOH) was added to a Schlenk flask. The solvent was removed, and the colourless oil was re-dissolved in MeCN (5 mL). This process was repeated

twice more to ensure complete removal of the MeOH. The oil was then dissolved in MeCN (10 mL) and $(TBA)_2[W_6O_{19}]$ (2.50 g, 1.3 mmol) was added to give a white suspension that cleared slowly as the solid dissolved over 15-30 minutes. The solution was stirred at room temperature for up to one week. The solution was then pumped dry and the residue was dissolved in a mixture of $MeCN/CD_3CN$ (1 mL/1 mL). The solution was transferred to a 10 mm screw top NMR tube and the [183]W NMR spectrum was recorded. The [183]W NMR spectrum of the degradation reaction was recorded both with and without an internal standard of 2 M Na_2WO_4 in D_2O, in a 10 mm coaxial insert, in order to assess chemical shift variations.

3.7.9 Reactions between [17]O-enriched $(TBA)_2[W_6O_{19}]$ and (TBA)OH

[17]O enriched $(TBA)_2[W_6O_{19}]$ (50 mg, 0.03 mmol) was added to a Schlenk flask and suspended in MeCN (1 mL). The appropriate amount of (TBA)OH (0.25 *M* in MeCN) was added to the flask. The total volume of the reaction mixture was made up to approx. 3 mL. The solution was stirred at room temperature for 3 days. The solvent was removed and the residual oil was dissolved in CD_3CN (0.5 mL). The mixture was transferred to a 5 mm screw top NMR tube for ^{17}O NMR spectroscopy. Following analysis by ^{17}O NMR spectroscopy, solutions were transferred to vials and Et_2O was added by vapour diffusion in an attempt to induce crystallization.

Note: When 0.4 eq of (TBA)OH per $(TBA)_2[W_6O_{19}]$ was used, the solid remaining after stirring the reaction mixture at room temperature for 3 days was dissolved by warming to 60 °C for 2 hours.

3.7.10 NMR simulations

The simulations discussed in this section were performed by Dr Magda Pascual-Borras.

Density functional theory (DFT) calculations were performed using the ADF2019 package.[22-24] The process for obtaining the [183]W NMR chemical shifts consists of (i) a geometry optimization step and (ii) a single-point NMR calculation, a procedure expressed throughout the text as FunctionalNMR/BasisNMR//FunctionalOPT/BasisOPT.

The geometries were optimised with Slater- type all-electron basis sets with the GGA-type PBE,[25] OPBE,[26] and BP86[27] functionals. For NMR calculations, we used a Slater- type all-electron basis set and PBE, OPBE, BP86 with spin–orbit (SO) corrections. The basis sets utilized were all-electron of triple-ζ+ polarization (TZP) or triple-ζ+ double polarization (TZ2P) quality for all atoms with scalar relativistic corrections to the electrons via the zeroth-order regular

approximation (ZORA).[28-30] The performance of a large QZ4P basis set was also tested as it was reported to be the best methodology to reproduce ^{183}W NMR chemical shifts for polyoxometalates.[31] Since were dealing with anionic species in solution, we applied the effects of solvent and counter ions as a continuum *via* the conductor-like screening model (COSMO), with a given dielectric constant (ε) that induces charge polarization on a surface around the molecule.[32,33] Taking the optimized geometries, NMR single-point calculations were carried out for the target and reference (WO_4^{2-}) anions, introducing spin-orbit (SO) corrections and the GIAO method.[34-36] The calculated chemical shift was determined as $\delta_{cal} = \sigma_{ref} - \sigma_x$, where σ_x and σ_{ref} are the isotropic average shielding for the nucleus of the target and the reference compounds, respectively.

The quality of a given calculation was referred to the mean absolute error (MAE) either per site or as an average of them. The reported MAE values have been obtained as:

$$MAE = \frac{1}{N}\sum \delta_{cal,i} - \delta_{exp,i \, i}$$

where $\delta_{cal,i}$ and $\delta_{exp,i}$ are the calculated and experimental chemical shifts, respectively. The coupling constants (J_{WW}) were calculated with the same methodologies stated above.

Table 3.2: ^{17}O NMR chemical shits (in ppm) for $[W_7O_{24}H]^{5-}$ with OPBE/TZP//PBE/TZ2P.

Oxygen type	Atom	Chemical Shift
Central	O_{14}	33
Bridging	O_{15}	431
	O_{23}	368
	O_4	471
	O_{12} or O_{13}	417
	O_{16} or O_{18}	418
	O_{20}	134
	O_2	438
	O_3 or O_5	435
	O_{10} or O_{11}	441
Terminal	O_8	682
	O_{17}	627
	O_{22} or O_{24}	653
	O_1	677
	O_6	678
	O_7 or O_9	723
	O_{19} or O_{21}	676

3.7.11 Preparation of (BTMA)$_5$[W$_7$O$_{24}$H] by treatment of (TBA)$_2$[W$_6$O$_{19}$] with (BTMA)OH.

(TBA)$_2$[W$_6$O$_{19}$] (1.0 g, 0.5 mmol) was suspended in a mixture of MeCN (20 mL) and MeOH (20 mL). Benzyltrimethylammonium hydroxide (40 wt% in MeOH, 0.95 mL, 2.1 mmol) was added. The slightly cloudy solution was stirred overnight, after which a white precipitate formed. The mixture was centrifuged, and the supernatant was decanted. The solid was then washed with MeOH (10 mL), MeCN (10 mL) and Et$_2$O (10 mL) (centrifugation was used after each wash to separate the solid) and dried under vacuum. The crude material (0.8 g) was recrystallized by dissolving in DMSO at 100 °C, followed by dropwise addition of DMF to until saturated (i.e. cloudiness persists). The solution was heated to 160 °C and then cooled slowly on a hot plate. The solution was allowed to stand for two days, after which a mixture of crystalline and amorphous solids had formed (0.29 g, 34%).

3.7.12 Preparation of (BTMA)$_5$[W$_7$O$_{24}$H] by cation exchange.

(TBA)$_2$[W$_6$O$_{19}$] (2.5 g, 1.3 mmol) was treated with (TBA)OH (5.3 mL, 5.3 mmol) following the procedure described above. After stirring at room temperature for 3 days, the solvent was removed, the residue dissolved in DMSO (3 mL) and a solution of (BTMA)Br (3.0 g, 13.2 mmol) in DMSO (5 mL) was added with vigorous stirring. The white suspension which formed was centrifuged, and the supernatant was decanted. The solid was then washed with MeOH (2 x 10 mL), MeCN (2 x 10 mL), and Et$_2$O (2 x 10 mL) (centrifugation was used after each wash to separate the solid). The solid product (1.9 g) was dried under vacuum and recrystallized from hot DMSO/DMF as described above (0.82 g, 38%). Crystals for elemental microanalysis were dried in vacuo after the unit cell had been determined by XRD. CHN: Found: C, 24.6; H, 3.4; N, 2.6 %. Calculated for C$_{50}$H$_{81}$N$_5$O$_{24}$W$_7$: C, 24.8; H, 3.4; N, 2.9 %.

3.7.13 ^{183}W NMR experiment targeting (TBA)$_5$[W$_7$O$_{24}$H] from (TBA)[WO$_4$] and WO(OMe)$_4$

(TBA)$_2$[WO$_4$] (2.07 g, 2.8 mmol) and WO(OMe)$_4$ (1.65 g, 5.1 mmol) were added to a Schlenk flask and dissolved in MeCN (10 mL). The mixture was stirred at room temperature for one hour. H$_2$O (0.19 mL, 10.8 mmol) was added and the reaction mixture was stirred at room temperature overnight. The solvent was then removed under reduced pressure to give a viscous oil. The oil was taken up in a mixture of MeCN (1 mL) and CD$_3$CN (1 mL) and then transferred to a 10 mm screw top NMR tube for ^{183}W NMR spectroscopy. The NMR solution was aged for three months and then the ^{183}W NMR spectrum was reacquired. Finally, the solution was transferred back to a Schlenk flask and stirred at reflux for three days. The solution

turned golden/brown over this period. The mixture was transferred to a 10 mm screw top NMR tube and the ^{183}W NMR spectrum was recorded.

3.7.14 ^{183}W NMR experiment targeting (TBA)$_5$[W$_7$O$_{24}$H] from (TBA)$_2$[W$_6$O$_{19}$]

TBA(OH) (3.0 mL, 3.0 mmol, 1 M in MeOH) was added to a Schlenk flask. The solvent was removed, and the colourless oil was re-dissolved in MeCN (5 mL). This process was repeated twice more to ensure complete removal of MeOH. The oil was then dissolved in MeCN (10 mL) and (TBA)$_2$[W$_6$O$_{19}$] (2.50 g, 1.3 mmol) was added to give a white suspension that cleared slowly as the solid dissolved over 15-30 minutes. The solution was stirred at room temperature for one week. The solution was pumped dry and the residue dissolved in a mixture of MeCN/CD$_3$CN (1 mL/1 mL). The solution was transferred to a 10 mm screw top NMR tube and the ^{183}W NMR spectrum was recorded. The NMR solution was aged for three months and then the ^{183}W NMR spectrum was reacquired. Finally, the solution was transferred back to a Schlenk flask and stirred at reflux for three days. The solution turned golden/brown over this period. The mixture was transferred to a 10 mm screw top NMR tube and the ^{183}W NMR spectrum was recorded.

3.7.15 ^{183}W NMR studies of reactions between (TBA)$_2$[W$_6$O$_{19}$] and (TBA)OH

TBA(OH) (Required vol., 1 M in MeOH) was added to a Schlenk flask. The solvent was removed, and the colourless oil was re-dissolved in MeCN (5 mL). This process was repeated twice more to ensure complete removal of MeOH. The oil was then dissolved in MeCN (10 mL) and (TBA)$_2$[W$_6$O$_{19}$] (2.50 g, 1.3 mmol) was added to give a white suspension that cleared slowly as the solid dissolved over 15-30 minutes. The solution was stirred at room temperature for up to one week. The solution was pumped dry and the residue dissolved in a mixture of MeCN/CD$_3$CN (1 mL/1 mL). The solution was transferred to a 10 mm screw top NMR tube and the ^{183}W NMR spectrum recorded.

References

1. a) M. T. Pope, Heteropoly and Isopoly Oxometalates, Springer-Verlag, Berlin, 1983; b) W.G. Klemperer, Early transition metal polyoxoanions, in A.P. Ginsberg (ed.), *Inorganic Syntheses*, John Wiley & Sons, **27**, 1990, 71-135; c) G. Hervé, A. Tézé and R. Contant, *in Polyoxometalate Molecular Science*, Springer Netherlands, Dordrecht, 2003, 33–54.

2. R. I. Maksimovskaya and K. G. Burtseva, *Polyhedron*, 1985, **4**, 1559–1562.

3. J. J. Hastings and O. W. Howarth, *J. Chem. Soc., Dalton Trans.*, 1992, 209–215.

4. a) R. I. Maksimovskaya, A. K. Il'yasova, D. U. Begalieva, D. F. Takezhanova and A. K. Akhmetova, *Bull. Acad. Sci. USSR, Div. Chem. Sci. 1985 3310*, 1984, **33**, 1977–1982. b) R. I. Maksimovskaya and N. N. Chumachenko, *Polyhedron*, 1987, **6**, 1813–1821. c) O. W. Howarth, P. Kelly and L. Pettersson, *J. Chem. Soc., Dalton Trans.*, 1990, 81–84. d) L. Pettersson, *Mol. Eng. 1993 31*, 1993, **3**, 29–42. e) I. Andersson, J. J. Hastings, O. W. Howarth and L. Pettersson, *J. Chem. Soc., Dalton Trans.*, 1994, 1061–1066. f) I. Andersson, J. J. Hastings, O. W. Howarth and L. Pettersson, *J. Chem. Soc., Dalton Trans.*, 1996, 2705–2711. g) B. J. Smith and V. A. Patrick, *Aust. J. Chem.*, 2004, **57**, 261–268. h) R. I. Maksimovskaya and G. M. Maksimov, *Inorg. Chem.*, 2007, **46**, 3688–3695.

5. C. Falaise, M. A. Moussawi, S. Floquet, P. A. Abramov, M. N. Sokolov, M. Haouas and E. Cadot, *J. Am. Chem. Soc.*, 2018, **140**, 11198–11201.

6. a) E. Petrus, M. Segado and C. Bo, *Chem. Sci.*, 2020, **11**, 8448–8456. b) E. Petrus and C. Bo, *J. Phys. Chem. A*, 2021, **125**, 5212–5219. c) E. Petrus, M. Segado-Centellas and C. Bo, *Inorg. Chem.*, 2022, **18**, 12.

7. a) K. F. Jahr and J. Fuchs, *Angew. Chem. Int. Ed.* 1996, **9**, 689-750; b) K. F. Jahr and J. Fuchs, *Chem. Ber.*, 1963, **96**, 2457–2459; c) K. F. Jahr, J. Fuchs and R. Oberhauser, *Chem. Ber.*, 1968, **101**, 477–481.

8. M. Filowitz, R. K. C. Ho, W. G. Klemperer and W. Shum, *Inorg. Chem.*, 1979, **18**, 93–103.

9. (^{183}W) Tungsten NMR, https://chem.ch.huji.ac.il/nmr/techniques/1d/row6/w.html (accessed September 2023).

10. R. J. Errington, M. D. Kerlogue and D. G. Richards, *J. Chem. Soc., Chem. Commun.*, 1993, 649–651.

11. W. Clegg, R. J. Errington, K. A. Fraser and D. G. Richards, *J. Chem. Soc. Chem. Commun.*, 1993, 1105–1107.

12. a) M. T. Pope and A. Müller, *Angew. Chem. Int. Ed. Engl.*, 1991, **30**, 34–48. b) M. T. Pope, *in Polyoxometalate Molecular Science*, Springer Netherlands, Dordrecht, 2003, pp. 3–31.

13. E.O.Tolkacheva, V.S.Sergienko, A.B.Ilyukhin, S.V.Meshkov, Zh. *Neorg. Khim.,* 1997, **42**, 752.

14. M. Pascual-Borràs, X. López, A. Rodríguez-Fortea, R. J. Errington and J. M. Poblet, *Chem. Sci.*, 2014, **5**, 2031–2042.

15. Y. Martinetto, B. Pégot, C. Roch-Marchal, M. Haouas, B. Cottyn-Boitte, F. Camerel, J. Jeftic, D. Morineau, E. Magnier and S. Floquet, *New J. Chem.*, 2021, **45**, 9751–9755.

16. M. A. Fedotov and R. I. Maksimovskaya, *J. Struct. Chem.*, 2006, **47**, 952–978.

17. V. Mäemets and I. Koppel, *J. Chem. Soc., Faraday Trans.*, 1997, **93**, 1539–1542.

18. W. Clegg, M. R. J. Elsegood, R. J. Errington and J. Havelock, *J. Chem. Soc, Dalton Trans.*, 1996, 681–690.

19. A. Bagno, M. Bonchio and J. Autschbach, *Chem. – A Eur. J.*, 2006, **12**, 8460–8471.

20. R. Acerete, C. F. Hammer and L. C. W. Baker, *J. Am. Chem. Soc.*, 1982, **104**, 5384–5390.

21. A. Bagno and M. Bonchio, *Angew. Chem. Int. Ed.*, 2005, **44**, 2023–2026.

22. G. te Velde, F. M. Bickelhaupt, E. J. Baerends, C. Fonseca Guerra, S. J. A. van Gisbergen, J. G. Snijders and T. Ziegler, *J. Comput. Chem.*, 2001, **22**, 931–967.

23. C. Fonseca Guerra, J. G. Snijders, G. te Velde and E. J. Baerends, *Theor. Chem. Acc.*, 1998, **99**, 391–403.

24. ADF2019, SCM, Theoretical chemistry, Vrije Universiteit, Amsterdam, The Netherlands, https:// www.scm.com.

25. J. P. Perdew, K. Burke and M. Ernzerhof, *Phys. Rev. Lett.*, 1996, **77**, 3865–3868.

26. M. Swart, A. W. Ehlers and K. Lammertsma, *Mol. Phys.*, 2004, **102**, 2467–2474.

27. a) A. D. Becke, *Phys. Rev. A: At., Mol., Opt. Phys.*, 1988, **38**, 3098– 3100. b) J. P. Perdew and W. Yue, *Phys. Rev. B*, 1986, **33**, 8800–8802.

28. E. V. Lenthe, E. J. Baerends and J. G. Snijders, *J. Chem. Phys.*, 1993, **99**, 4597–4610.

29. E. V. Lenthe, E. J. Baerends and J. G. Snijders, *J. Chem. Phys.*, 1994, **101**, 9783–9792.

30. E. V. Lenthe, A. Ehlers and E. J. Baerends, *J. Chem. Phys*., 1999, **110**, 8943–8953.

31. L. Vilà-Nadal, J. P. Sarasa, A. Rodríguez-Fortea, J. Igual, L. P. Kazansky and J. M. Poblet, *Chem. -Asian J*., 2010, **5**, 97–104.

32. A. Klamt, *J. Phys. Chem*., 1995, **99**, 2224–2235.

33. A. Klamt, V. Jonas, T. Bürger and J. C. W. Lohrenz, *J. Phys. Chem. A*, 1998, **102**, 5074–5085.

34. R. Ditchfield, *Mol. Phys*., 1974, **27**, 789–807.

35. K. Wolinski, J. F. Hinton and P. Pulay, *J. Am. Chem. Soc*., 1990, **112**, 8251–8260.

36. G. Schreckenbach and T. Ziegler, *J. Phys. Chem*., 1995, **99**, 606–611.

Chapter 4: Synthesis of first-row transition metal containing Lindqvist-type polyoxometalates

4.1 Introduction

Desires to avoid the negative impacts of climate change are driving a move away from carbon intensive industrial processes and towards greener practices.[1] This has led a surge of research focused on the development of new catalytic materials that can make large industrial processes more efficient, with a lot of attention being placed on the use of earth abundant first-row transition metal-based materials to avoid a reliance on the ever-dwindling supplies of precious metals like platinum and palladium.[2-4] Simultaneously, a desire to reduce carbon dioxide emissions and adopt renewable sources of energy has led to a huge amount of interest in the development of processes that can aid these goals. The production of new catalyst materials for processes like CO_2 reduction[5,6] (which can be used in combination with carbon capture and storage to attempt to create a more circular carbon economy) and water oxidation[7,8] (which facilitates the storage of electricity produced from renewable technology as hydrogen fuel) have come to the forefront of research focus. Again, there is a focus on the use of earth abundant materials, both to mimic what is seen in nature and to lower costs.

A significant number of the first-row transition metal-based materials used are solid-state metal oxide materials.[9,10] There are numerous examples of the use of manganese[11,12], cobalt[13,14], and nickel[15,16] oxide materials in the development of artificial photosynthesis systems. To make rational improvements to these catalytic systems, the nature of the active site (i.e. the site that performs the rate-determining step) must be understood. This can then allow systematic modifications to the system to be made while the effect on activity is measured, which subsequently provides well-understood structure activity relations. One issue with this is that often understanding the true nature of heterogeneous catalyst materials can be difficult, with many having very irregular surfaces with numerous defects that create unique atomic environments.[17] This can be partially combatted by the use of computational simulation[18] but without a clear experimental understanding of the active site, it is still very difficult to gain a concrete grasp of the catalytic activity.

A promising strategy that can be used to gain insight into the key factors determining the activity of a catalyst is to build a model of the active site.[19] This model can then be methodically probed or modified and then the information acquired can be (theoretically) translated back

to the heterogeneous metal oxide material. One method of creating such a model is to create well-defined, spatially separated, metal sites on a support material. Copéret, who has used surface organometallic chemistry to immobilize a range of transition metals on supports and probe their catalytic activity, has employed this strategy with great success.[20-23] An alternative approach is to isolate a catalytically active metal within an atomically precise molecular metal oxide, also known as a heterometal substituted polyoxometalate.

There are numerous examples of polyoxometalates that incorporate one or more first-row transition metals into their framework.[24-26] Some examples of cobalt containing POMs, and their use as water oxidation catalysts, were mentioned at the start of **Chapter 2**. Similar studies have been performed with structures incorporating transition metals from across the first-row, looking at activity in alkene epoxidation[27,28], CO_2 activation[29], water oxidation[30,31], and medicinal applications[32] (among others). The vast majority of the compounds studied are based on the Keggin structure and its derivatives (i.e. Weakley-type sandwich structures of various lacunary species).

Conversely, there are very few examples of Lindqvist-type structures incorporating first-row transition metals. Alongside our group's report on the synthesis of $(TBA)_7[(CoW_5O_{18}H)_2][X]$ (X = Cl, BF_4), the other main example comes group the group of Matson, who successfully incorporated iron into an all vanadium Lindqvist oxoalkoxide structure.[33] They subsequently examined both the redox properties and reactivity towards nitric oxide.[34-36] Other examples of Lindqvist-type systems include a handful of all first-row transition metal based structures[37-40] and numerous examples of first-row transition metals bound to the surface of complete Lindqvist structures.[41-45]

The Lindqvist unit is a good potential starting point for the development of a model of a transition metal oxide catalyst active site. The ability to incorporate a single metal into the hexametalate gives both a well-defined site and a computationally inexpensive system when compared to the larger POMs (which incorporate multiple heterometals) common in the literature. It is therefore very desirable to pursue the generation of a series of Lindqvist-type POMs that contain a single transition metal from across the first-row.

4.2 Chapter outline

The chapter builds upon our "2nd generation" approach for the synthesis of heterometal substituted Lindqvist-type POMs outlined and refined in **Chapter 2** using the synthesis of $(TBA)_7[(CoW_5O_{18}H)_2][NO_3]$ as a model system. The new method uses $(TBA)_2[W_6O_{19}]$ and

TBA(OH) to generate a "virtual" lacunary precursor, "(TBA)$_5$[W$_5$O$_{18}$H]", which was then reacted with Co(NO$_3$)$_2$.6H$_2$O. The use of a range of simple first-row transition metal salts, in the +2 and +3 oxidation sate, in place of Co(NO$_3$)$_2$.6H$_2$O was explored in this chapter, with the aim of producing a series of the transition metal substituted Lindqvist-type POMs with the general formula [(MW$_5$O$_{18}$H)$_2$]$^{6-}$.

Products were initially characterised using infrared spectroscopy, using data obtained for the cobalt containing system as a reference for success. Attempts to crystallize the crude products, and in turn provide more precise structural characterisation in the form of X-ray structures, were then made. This was followed by ^{17}O and ^{183}W NMR spectroscopy experiments probing the incorporation of diamagnetic zinc into the framework, with this system providing the ability to gain some insight into how the degradation mixture (which was characterised in **Chapter 3**) changes upon addition of the metal cation.

Finally, preliminary work exploring the development of a "3rd generation" approach to the synthesis of transition metal substituted Lindqvist-type POMs is discussed. It was postulated that metal ion exchange reactions could provide a simple entry point for the synthesis of a range of heterometal containing Lindqvist-type POMs from a single precursor. With this in mind, the synthesis of a magnesium substituted Lindqvist-type POM, which was characterised by infrared spectroscopy, single-crystal X-ray diffraction, and multinuclear NMR spectroscopy, from magnesium methoxide was examined.

4.3 Synthetic approach

Chapter 2 explored the synthesis of (TBA)$_6$[(CoW$_5$O$_{18}$H)$_2$] and the corresponding pyridine adduct which can be viewed as a model system for the incorporation of lower oxidation state M(II) atoms into the Lindqvist framework. The results presented in **Chapter 2** suggest that the degradative reassembly approach, involving the generation of a "virtual" lacunary species from (TBA)$_2$[W$_6$O$_{19}$] and TBA(OH), represents a viable method for the general synthesis of (TBA)$_6$[(M(II)W$_5$O$_{18}$H)$_2$]-type compounds.

To explore this, the original method used for the synthesis of (TBA)$_7$[(CoW$_5$O$_{18}$H)$_2$][NO$_3$], details given in **Section 2.3.1** and described in **Equations 4.1** and **4.2**, was used as a template for a general procedure targeting M(II) substituted Lindqvist-type POMs.

$$5 \text{ (TBA)}_2[\text{W}_6\text{O}_{19}] + 20 \text{ (TBA)[OH]} \rightarrow 6 \text{ (TBA)}_5[\text{W}_5\text{O}_{18}\text{H}] + 7 \text{ H}_2\text{O} \qquad (4.1)$$

$$2 \text{ (TBA)}_5[\text{W}_5\text{O}_{18}\text{H}] + \text{MX}_2 \rightarrow \text{ (TBA)}_6\big[(\text{MW}_5\text{O}_{18}\text{H})_2\big] + 4 \text{ TBA(X)} \qquad (4.2)$$
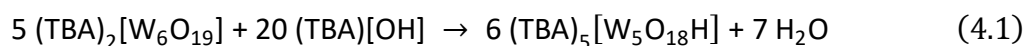
Following this method, $(TBA)_2[W_6O_{19}]$ was first treated with four equivalents of TBA(OH) in acetonitrile giving what we now know to be approximately a 1:2 mixture of $(TBA)_5[W_7O_{24}H]$ and $(TBA)_2[WO_4]$. This mixture was reacted with a series of simple M(II) salts dissolved or suspended in acetonitrile (including $CrCl_2$, $Mn(NO_3)_2.4H_2O$, $FeCl_2$, $NiCl_2$, $CuCl_2$ and $Zn(NO_3)_2.6H_2O$). After combination of the solutions, any remaining solid quickly dissolved and in some cases there was a colour change, presumably associated with a change in the inner co-ordination sphere of the respective M(II) ion. The reaction mixtures were allowed to stir at room temperature overnight before the volatiles were removed, typically leaving viscous oils. The oils were triturated with ethyl acetate and diethyl ether (and hexane where required) to attempt to remove tetrabutylammonium salt by-products and residual solvent, leaving the crude product as a free-flowing powder which was characterised initially by infrared spectroscopy (discussed in **Section 4.4**).

Reactions involving chromium, manganese, and iron appeared visibly to be extremely sensitive to the presence of oxygen. When solvent was not degassed, the reaction mixtures would gradually change colour from blue, yellow, and black, to green, purple, and orange respectively over the course of a few hours. This is likely associated with the oxidation of the starting M(II) to M(III). Similar observations were not present for reactions using cobalt, nickel, copper and zinc. This is in line with the known trends in redox properties across the group, with +2 oxidation state becoming more stable with respect to the +3 oxidation state as you move across the period.

To verify these observations, analogous reactions with M(III) salts of chromium, manganese and iron were attempted. The synthetic method was adapted to target the appropriate precursor mixture for reaction with MX_3 salts, as shown in **Equations 4.3** and **4.4**.

$$5\ (TBA)_2[W_6O_{19}] + 26\ (TBA)[OH] \rightarrow 6\ "(TBA)_6[W_5O_{18}]" + 13\ H_2O \qquad (4.3)$$

$$2\ "(TBA)_6[W_5O_{18}]" + 2\ MX_3 \rightarrow (TBA)_6[(MW_5O_{18})_2] + 6\ TBA(X) \qquad (4.4)$$
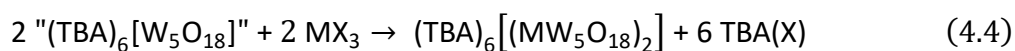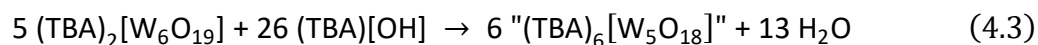
Other than these modifications, the same procedure was followed; the degradation mixture produced from the reaction of {W_6} and the appropriate quantity of base being directly added to an acetonitrile solution of the MX_3 salts, namely $Cr(NO_3)_3.9H_2O$, $Mn(OAc)_3$, and $FeCl_3$. As expected, the reaction mixtures immediately turned green, purple and orange respectively, providing further support to the idea that the reactions utilising the M(II) salts of chromium, iron, and manganese are very sensitive to the presence of oxygen. The crude reaction mixtures

were worked up in the same manner as described for reaction involving M(II) salts, allowing isolation of a free-flowing powder of the crude product which was initially characterised by infrared spectroscopy.

4.4 Infrared spectroscopy

Infrared spectroscopy is a powerful technique in polyoxometalate chemistry as it can give insight into both the structure and charge of a compound. The infrared spectrum of $(TBA)_7[(Co(II)W_5O_{18}H)_2][NO_3]$ was presented and discussed in **Chapter 2**. If the reactions using other M(II) salts lead to analogous bent dimeric structures, then the infrared spectra of the crude compounds should be very similar to that obtained for cobalt.

After obtaining free-flowing powders of the crude products from reactions of the degradation mixture with M(II) salts from Cr-Zn, the ATR FTIR transmittance spectra of the compounds were obtained, and a stack of the spectra is shown in **Figure 4.1**.

The previously discussed spectrum of $(TBA)_7[(Co(II)W_5O_{18}H)_2][NO_3]$ is shown in blue for reference. It is immediately apparent that the spectra produced from reactions with Mn-Zn bear a lot of resemblance to the previously obtained spectrum of the Co analogue. A peak at 1338 cm^{-1} was observed in the spectra of reactions which employed a nitrate salt as the source of the heterometal. This indicates the presence of TBA(NO$_3$) in the crude product which is consistent with observations from the synthesis of $(TBA)_7[(Co(II)W_5O_{18}H)_2][NO_3]$ where removal of TBA(X) from the product proved difficult. Spectra that do not contain this peak likely still contain additional TBA(Cl), however chloride is infrared silent and therefore cannot be identified by infrared spectroscopy.

The most intense feature in the spectra is an intense peak at around 930-933 cm^{-1} (labelled at 932 cm^{-1} for Zn). This peak can be assigned to the terminal $\nu_{W=O}$ stretch. The fact that this peak appears consistently, within a few wavenumbers across the series, implies that the crude products likely all possess the same charge. The series of intense peaks between 809 and 666 cm^{-1} can be assigned to bridging W-O-W stretches. The nature of this region (i.e. number and position of peaks) is strongly related to the structure of the polyoxometalate and therefore the consistency seen across the series in this region suggests that products are structurally alike. Given the structure of $[(CoW_5O_{18}H)_2]^{6-}$ is known to exist as a bent dimer, it is likely the crude products in this series occupy the same structure.
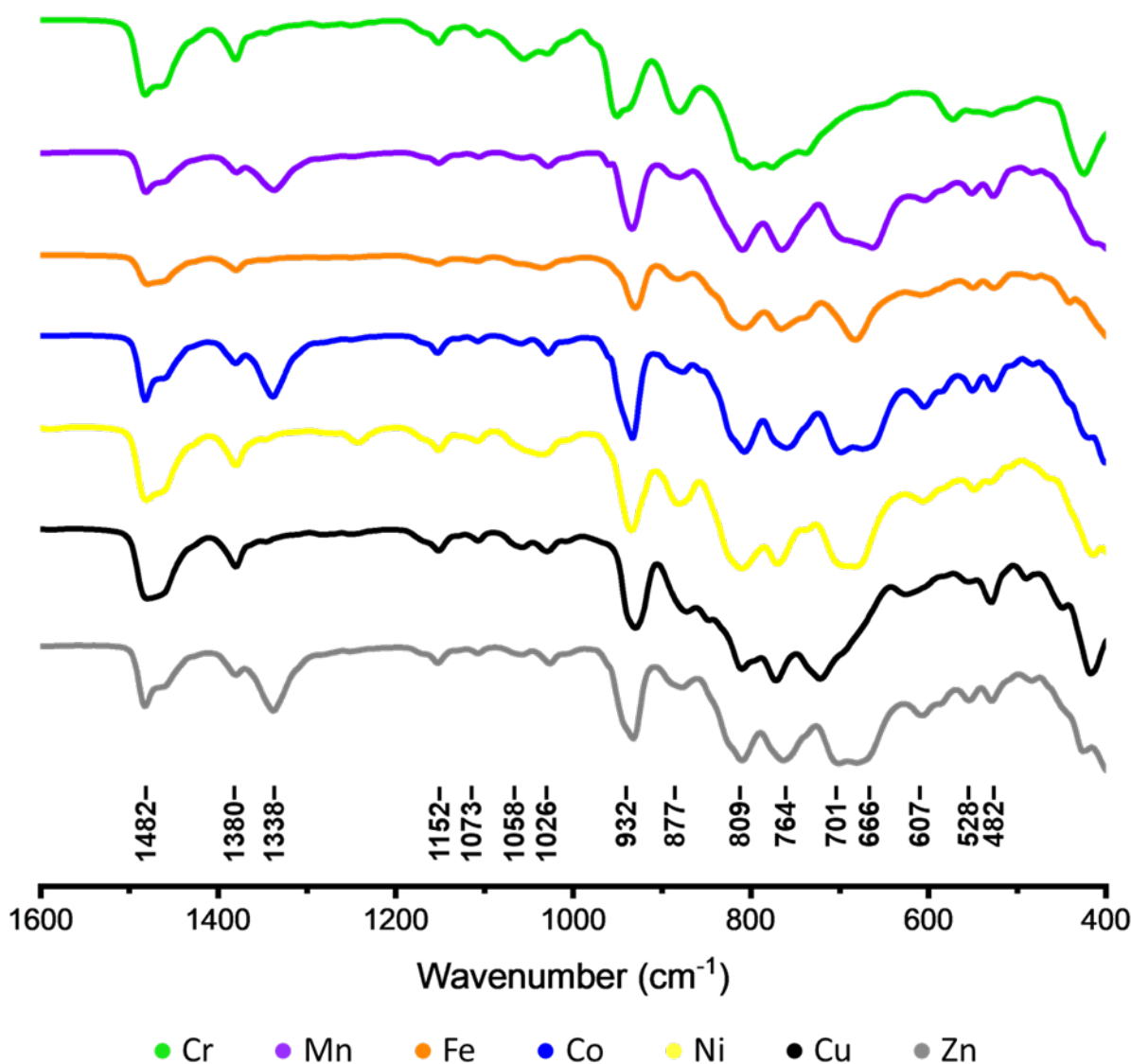
Figure 4.1: ATR FTIR transmittance spectra of the crude products from reaction of $(TBA)_2[W_6O_{19}]$ with TBA(OH) and the simple M(II) salts $CrCl_2$, $Mn(NO_3)_2 \cdot 4H_2O$, $FeCl_2$, $Co(NO_3)_2 \cdot 6H_2O$, $NiCl_2$, $CuCl_2$, and $Zn(NO_3)_2 \cdot 6H_2O$.

The spectrum obtained from the reaction of the degradation mixture with $CrCl_2$ (shown in green) differs substantially from the rest. Firstly, the terminal $\nu_{W=O}$ stretch appears at 951 cm^{-1}, which may indicate a lower charge on the POM cage (or be a consequence of a change in structure/size). Secondly, the bridging region is very different with peaks at 797 and 776 cm^{-1} extending out of an overall broad feature. The deviation in the pattern observed compared to rest of the series could be indicative of a change in structure. For example, Cr(II) (d^4) often prefers a square planar geometry which could lead to a change in the framework structure to incorporate that geometry.

Infrared spectra obtained from the direct reaction of the degradation mixture, targeting "$(TBA)_6[W_5O_{18}]$", with M(III) salts are shown in **Figure 4.2**. The bridging regions (800-600 cm^{-1}) for reactions with $Mn(OAc)_3$ and $FeCl_3$ (shown in purple and orange) differ significantly from
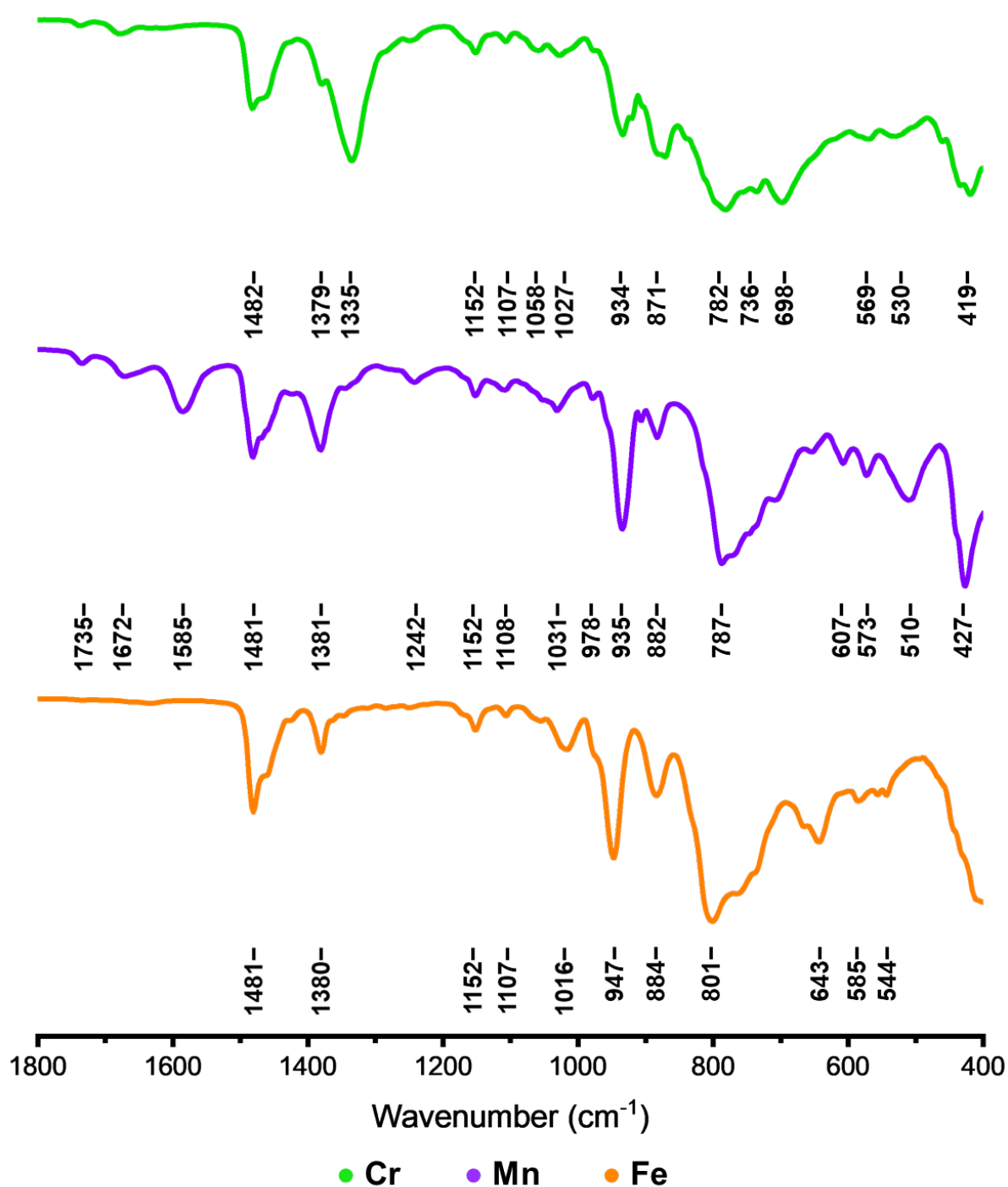
Figure 4.2: ATR FTIR transmittance spectra of the crude products from reaction of $(TBA)_2[W_6O_{19}]$ with TBA(OH) and the simple M(III) salts $Cr(NO_3)_3 \cdot 9H_2O$, $Mn(OAc)_3$, and $FeCl_3$.

the consistent pattern observed across the series of products from reactions with M(II) salts. The reduced number of peaks in this region may be indicative of formation of monomeric species, which have higher symmetry and therefore fewer unique bridging oxygen stretches. This may be a consequence of the increased Lewis acidity of the metal centre in the 3+ oxidation state which has a higher affinity for X^-. Holding onto this X^- ligand would prevent formation of the dimeric unit. The spectra of the product produced from reaction of the

degradation mixture with $Cr(NO)_3.9H_2O$ has more features in the bridging oxygen region and is more similar to the patterns observed from reactions with M(II) salts. This could indicate formation of dimeric $[(CrW_5O_{18})_2]^{6-}$. In this case the nitrate may not interact strongly enough with Cr(III) to prevent dimer formation.

The terminal $v_{W=O}$ of the products from reaction with Cr, Mn, and Fe are 934, 935 and 947 cm^{-1} respectively. The fact that $v_{W=O}$ of the reaction with iron is around 12 cm^{-1} higher than the others, and those observed for reactions with M(II) salts, could indicate a lower charge for the product incorporating iron. This is consistent with unpublished work from our group in which methylation of bridging oxygens of the Lindqvist framework is observed for structures incorporating iron.[46] This leads to structures with a 2− charge per {FeW_5} unit, rather than the 3− charge associated with {CoW_5} units.

4.5 Single-Crystal X-ray diffraction

Preliminary characterisation of crude products using infrared spectroscopy is very useful for giving an indication of the potential structure of the product, especially with data for the characterised $(TBA)_7[(CoW_5O_{18}H)_2][NO_3]$ in hand as a reference. However, in order to give conclusive evidence for the formation of first-row transition metal substituted Lindqvist-type POMs, attempts were made to grow crystals of the crude products. This in turn allows for characterisation by single-crystal X-ray diffraction which can be used to definitively prove the incorporation of a heterometal into the Lindqvist framework.

4.5.1 Manganese containing Lindqvist structures

During work focused on the synthesis of $(TBA)_3[(Py)CoW_5O_{18}H]$ discussed in **Chapter 2**, it was found that crystals of the pyridine adduct of the Co substituted Lindqvist-type POM were far more readily obtained than crystals of the corresponding dimer. Therefore, it was reasoned that the easiest way to obtain conclusive evidence of incorporation of the heterometal, in this case manganese, into the Lindqvist structure, would be to treat the crude product with pyridine. This would theoretically cleave the dimer and produce the corresponding pyridine adduct, which should be easy to crystallize by vapour diffusion of diethyl ether into this solution.

When this was done for cobalt, an immediate colour change was observed from blue/purple to pink as the inner co-ordination sphere around cobalt changed. However, interestingly when the crude pale yellow product obtained from reactions between the "virtual" lacunary mixture and $Mn(NO_3)_2.6H_2O$ was dissolved in pyridine there was no notable colour change. Vapour

diffusion of diethyl ether into this solution led to the formation of pale-yellow crystals. The single-crystal X-ray diffraction structure obtained from these crystals is shown in **Figure 4.3a**.

Surprisingly, the crystals obtained were those of a dimeric manganese substituted Lindqvist-type POM, suggesting that the binding of pyridine to the manganese(II) centre does not provide a sufficient thermodynamic (or entropic) driving force to lead to formation of the corresponding pyridine adduct. This is likely an illustration of the general stabilities of M(II) complexes described by the Irving-Williams series.[47] The authors original work compares the relative stabilisation energies for exchange of aqua ligands with other ligands for divalent first-row transition metal cations. They found that complexes of Mn(II) are the least stable, with respect to the hexa-aqua complex, which is attributed to the lack of crystal field stabilisation energy (high-spin d^5, CFSE = 0) and low Lewis acidity, which increases across the period as ionic radius decreases.

The structure shows the presence of seven tetrabutylammonium cations per dimer, which are omitted from **Figure 4.3a**. This could imply that the dimer is mono-protonated with the formula $(TBA)_7[(Mn(II)W_5O_{18}H)(Mn(II)W_5O_{18})]$. However, bond valence sum (BVS) analysis (**Appendix A Section A.3.1**) supports protonation of both O3 and O20 (V_{O3} = 1.31 and V_{O20} = 1.21) which is consistent with a doubly protonated POM with the formula $(TBA)_6[(Mn(II)W_5O_{18-}H)_2]$, analogous to the structure obtained for cobalt. Further to this, infrared spectroscopy performed on the crystalline sample still indicates the presence of nitrate, allowing the assignment of the seventh tetrabutylammonium cation to the presence of one equivalent of $TBA(NO_3)$ in the structure (though the nitrate anion is not located in the crystallographic
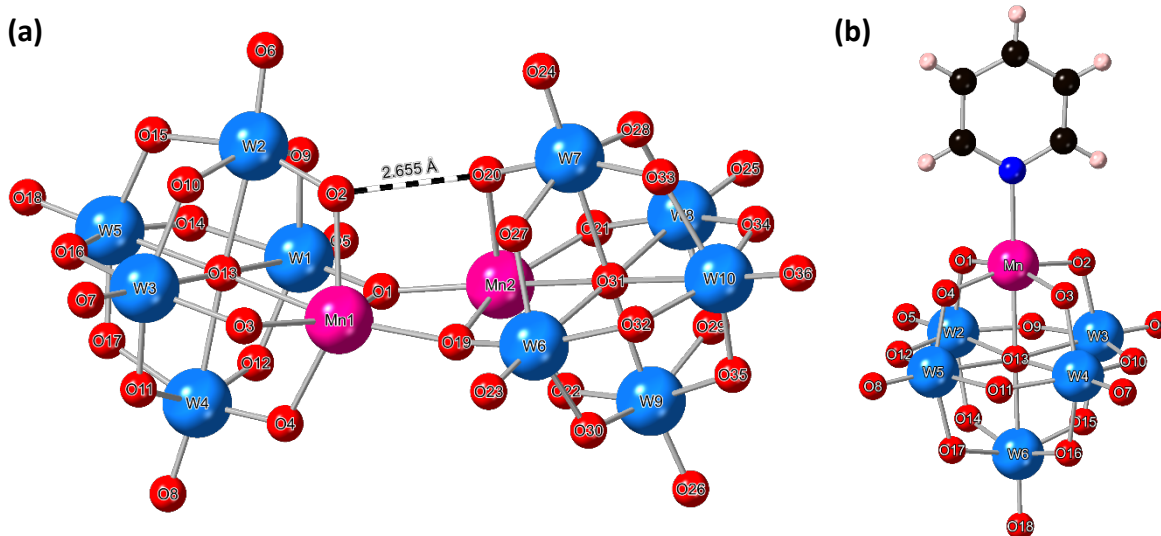
Figure 4.3: Single-crystal X-ray diffraction structures of $(TBA)_7[(MnW_5O_{18}H)_2][NO_3]$ **(a)** and $(TBA)_3[(Py)MnW_5O_{18}]$ **(b)**. Cations and solvent are omitted for clarity. The atomic radii are set to the CSD covalent radii.

experiments). During the refinement, some extremely disordered electron density was masked and it is plausible, given the evidence supporting the presence of nitrate, that this electron density contains a disordered nitrate anion and therefore the actual formula is $(TBA)_7[(MnW_5O_{18}H)_2][NO_3]$.

The dimeric unit itself displays the same bent arrangement observed for $[(CoW_5O_{18}H)_2]^{6-}$, with a short interatomic distance of ca. 2.66 Å between O2 and O20. This distance is consistent with the formation of a hydrogen bond between O2 and O20 and consequently (along with bond valence sum analysis) localisation of a proton on O20.

Analysis of the bond distances around manganese shows an average Mn-O bond length of ca. 2.16 Å (excluding the bond to the central μ_6-O). These bonds are significantly longer than the bridging W-O bonds in the structure, which are on average ca. 1.92 Å. The increased bond length is likely a consequence of reduced π-bonding between filled orbitals on oxygen and the partially filled d-orbitals of manganese. This results in a significant increase in the Lewis basicity of the oxygens surrounding manganese, which explains why BVS analysis indicates protonation of O3 and O20, both of which are oxygens directly adjacent to manganese. The W-O bonds that complete the W-O-Mn bridges (i.e. W1-O1, W2-O2, etc.) are also considerably shorter than the average for the rest of the structure, at ca. 1.83 Å, which could indicate increased π-bonding to tungsten due to the lack of competition for electron density from manganese. This is not the case for the W-O bonds between W1-O3 and W7-O20 which are longer at 1.930(9) and 1.976(8) Å respectively. Localisation of protons on these oxygens, meaning these positions could be described as W-O(H)-Mn bridges, is the likely cause of this lengthening.

Interestingly, the Mn-O bonds between the two halves of the dimer are not the longest Mn-O bonds, being shorter than the average Mn-O bond length (ca. 2.16 Å) at 2.107(7) and 2.060(8) Å respectively. This goes some way to indicate the stability of the dimeric unit and may imply that reactivity around the heterometal will involve the neighbouring oxygen atoms within each $[MnW_5O_{18}H]^{3-}$ unit.

Leaving pale-yellow solutions of the dimeric Mn-containing POM dissolved in pyridine open to air led to a gradual colour change, with the solution eventually turning dark red. Vapour diffusion of diethyl ether into this solution led to the formation of single crystals. Single-crystal X-ray diffraction experiments revealed the formation of the pyridine adduct shown in **Figure 4.3b**. The crystal structure shows the presence of three tetrabutylammonium cations per POM

which, along with BVS analysis shown in **Appendix A Section A.3.2**, suggests oxidation of manganese and loss of any protons to give the formula $(TBA)_3[(Py)Mn(III)W_5O_{18}]$.

Further evidence for the oxidation of Mn(II) to Mn(III) is provided by the decrease in the average Mn-O bond length, which reduces from ca. 2.16 Å for the dimer to ca. 1.93 Å, due to the increase in Lewis acidity at the metal centre. This is also likely to be the primary reason why the pyridine adduct is now preferred over the dimer. There is very little structural change to the rest of the Lindqvist unit, with the average W-O bond lengths remaining at ca. 1.92 Å, while the W-O bonds of the W-O-Mn bridges remain shorter at ca. 1.84 Å.

4.5.2 Iron containing Lindqvist structures

The same strategy of attempting to form the pyridine adduct was used to gain crystallographic evidence for the formation of incorporation of iron into the Lindqvist framework. This time, when the crude black/brown product from the reaction of the degradation mixture with $FeCl_2$ was dissolved in pyridine, the solution turned dark red. Slow diffusion of diethyl ether into this solution led to the formation of dark red crystals. The single-crystal X-ray diffraction structure obtained from these crystals is shown in **Figure 4.4a**. The pyridine group shows disorder over multiple orientations and therefore only the nitrogen atom is shown. The TBA cations are also extremely disordered, inhibiting a strict assignment of three cations per POM. BVS analysis supports an oxidation state of +2 at iron and the protonation of O16 (V_{O16} = 1.27) which may allow the tentative formula of $(TBA)_3[(Py)FeW_5O_{18}H]$ to be assigned. This is comparable to the corresponding cobalt compound.
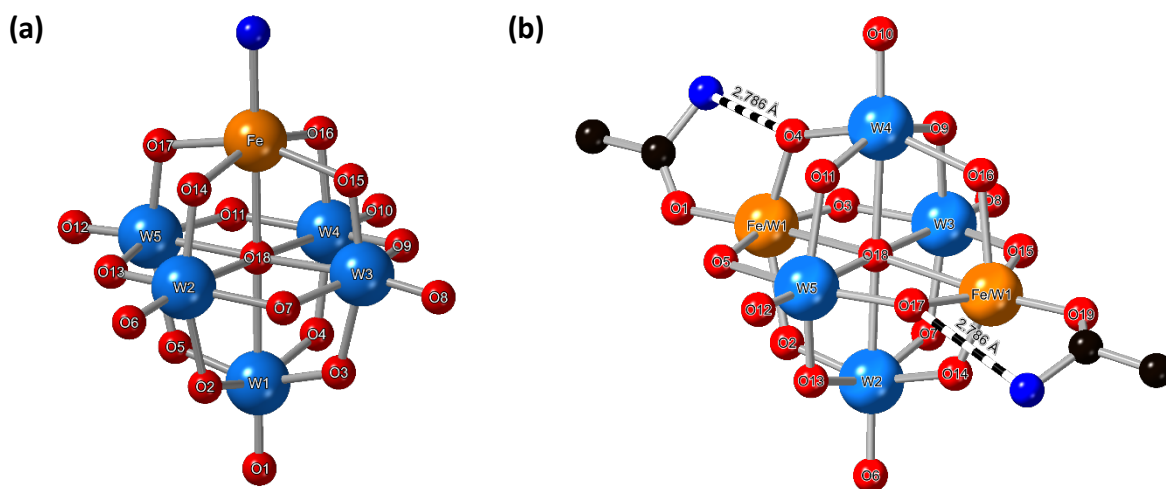
Figure 4.4: Single-crystal X-ray diffraction structures of **(a)** $(TBA)_3[(Py)FeW_5O_{18}H]$ (pyridine was disordered and therefore only the nitrogen is shown) and **(b)** $(TBA)_3[(CH_3CONH_2)FeW_5O_{18}]$, in which the Fe-acetamide group is disordered over two positions of the Lindqvist unit. Cations and solvent omitted for clarity. The atomic radii are set to the CSD covalent radii.

These results show how moving from Mn(II) to Fe(II) leads to a complete change in structure from a dimer to a monomeric adduct when exposed to an excess of pyridine. This again is in line with the trends observed in the Irving-Williams series. In our case the dimer, which involves iron forming a dative bond with an oxygen atom of a Fe-O-W bridge, is comparable to the aqua complex. Moving to iron leads to an increase in CSFE (d^6, high spin, CSFE = 0.4 Δ_{oct}) and a decrease in ionic radius (increasing Lewis acidity) when compared to manganese. This in turn leads to an increased stabilisation energy of the pyridine adduct over the corresponding dimer (analogous to the aqua complex).

In the absence of any strong ligands, a dimeric structure is predicted based on observations from work with cobalt and manganese. Slow diffusion of diethyl ether into saturated acetonitrile solutions of the crude iron product (in air), performed by Amar Mohammed, gave such a structure after analysis by single-crystal X-ray diffraction.[46] The partial structure, which will be reported in his thesis, is not shown here but is consistent with the previously obtained dimeric structures incorporating Co(II) and Mn(II). It features the same bent geometry, with hydrogen bond of ca. 2.62 Å between the two halves of the dimer. BVS analysis supports the presence of two Fe(III) centres which is consistent with the observations discussed in **Section 4.3** of this chapter, in which reactions with FeCl$_2$ quickly oxidised when the solvent was not degassed. The analysis also indicates, that along with a proton bridging between the two halves of the dimer, there is also evidence for the protonation of a terminal W=O bond. This would give a possible formula of (TBA)$_4$[(Fe(III)W$_5$O$_{18}$H)$_2$], though a better structure and elemental analysis are required to confirm this. Efforts to crystallize a dimeric structure without oxidation of the iron centres are ongoing.

The direct reaction between the degradation mixture produced by treatment of (TBA)$_2$[W$_6$O$_{19}$] with 5.2 equivalents of TBA(OH) and FeCl$_3$, discussed in **Section 4.3**, may theoretically provide access to the same [(Fe(III)W$_5$O$_{18}$H)$_2$]$^{4-}$ dimer. However, when the crude product of that reaction was recrystallized by vapour diffusion of diethyl ether into a saturated acetonitrile
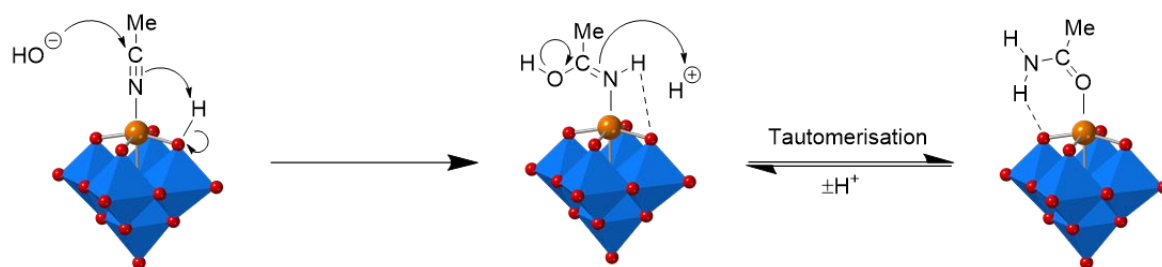
Figure 4.5: Potential mechanism for the formation of acetamide from MeCN and TBA(OH) mediated by [Fe(III)W$_5$O$_{18}$H]$^{2-}$.

solution of the product, crystals with the structure shown in **Figure 4.4b** were obtained. This partial structure contains an acetamide bound iron centre incorporated into Lindqvist structure with *trans* disorder (i.e. 50% occupancy of two positions in the Lindqvist unit) with three tetrabutylammonium cations per POM giving a formula of $(TBA)_3[(CH_3CONH_2)FeW_5O_{18}]$. The presence of this compound implies that the mixture of $(TBA)_2[W_6O_{19}]$, TBA(OH), and $FeCl_3$ is sufficiently reactive to cause activation of the solvent. It is difficult to know if the iron substituted Lindqvist species is responsible for reactivity but one possible mechanism for this reactivity could involve the reversible formation of an acetonitrile bound adduct of $[FeW_5O_{18}H]^{2-}$. This may subsequently undergo attack by hydroxide, leading to an intermediate iron bound imine species, which tautomerises to give acetamide. This postulated mechanism is outlined in **Figure 4.5**. This mechanism suggests transfer of a proton from the POM cage to generate acetamide and may explain the 3– charge on the POM cage (and therefore lack of protonation).

4.5.3 Nickel containing Lindqvist structures

Crystals of the crude product from the reaction of $(TBA)_2[W_6O_{19}]$ with TBA(OH) and $NiCl_2$ were difficult to obtain. A range of solvent (acetonitrile, benzonitrile, dichloromethane, chloroform, difluorobenzene, trimethylphosphate, and quinoline) and anti-solvent (diethyl ether, ethyl acetate, toluene, and hexane) combinations were tried with no success. Eventually, crystals of high enough quality for single-crystal X-ray diffraction were obtained by vapour diffusion of diethyl ether into a concentrated dimethylformamide solution of the crude product. The pale-yellow crystals gave a partial structure of the dimer shown in **Figure 4.6a**.
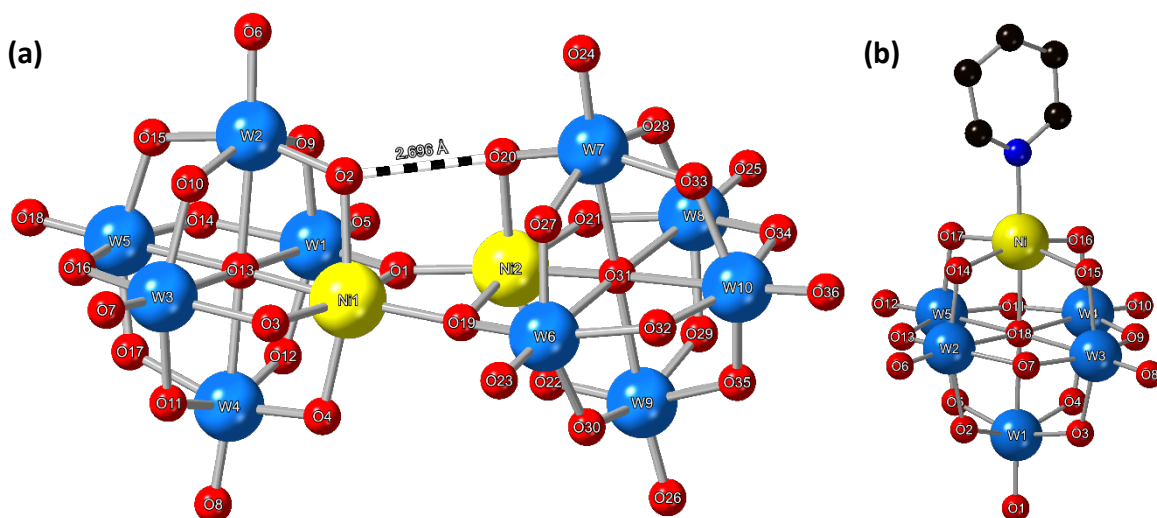
Figure 4.6: Single-crystal X-ray diffraction structures of $[(NiW_5O_{18}H)_2]^{6-}$ **(a)** and $(TBA)_3[(Py)NiW_5O_{18}H]$ **(b)**. Cations and solvent are omitted for clarity. The atomic radii are set to the CSD covalent radii.

The structure obtained is consistent with the others obtained so far (Mn to Co), with the dimer showing a bent structure resulting in a short interatomic distance of ca. 2.70 Å between O2 and O20. As for previous structures, this is caused by the presence of a hydrogen bond between the two halves of the dimer caused by localisation of a proton between the two oxygen atoms. As the two halves of the dimer are related by a C_2 axis, it is impossible to say on which of the two oxygens the proton lies but BVS analysis does support protonation at this position ($V_{O2/20}$ = 1.42). Further, analysis of the bond valence sums suggests the most likely position for the second protonation is O3/O21 ($V_{O3/21}$ = 1.18). No information about cations was obtainable from the diffraction data as they were too severely disordered, but based on the structure and BVS analysis a likely formula is $(TBA)_6[(NiW_5O_{18}H)_2]$.

In line with observations for the series, the average Ni-O bond length (ca. 2.09 Å) is considerably longer than the average W-O bond length (ca. 1.93 Å), which again is a consequence of reduced π-bonding between filled orbitals on oxygen and the partially filled d-orbitals of nickel(II) (d^8). This is paired with the same contraction of the W-O bonds of the Ni-O-W bridges (average bond length of ca. 1.87 Å).

Dissolution of the crude yellow product in pyridine led to an immediate colour change to green. Slow diffusion of diethyl ether into this solution led to the formation of light green crystals. The single-crystal X-ray diffraction structure obtained from these crystals is shown in **Figure 4.6b**. The structure contains three tetrabutylammonium cations per POM, consistent with mono-protonation of the cage. BVS analysis indicated that this proton may lie on O15 (V_{O15} = 1.36) or O17 (V_{O17} = 1.39) and therefore it is reasonable to suggest it is disordered over these two sites. It is worth noting that both these oxygens are neighbouring the Ni(II), which indicates the increased basicity of these positions compared to the other bridging W-O-W positons.

4.5.4 Zinc containing Lindqvist structures

The infrared spectrum of the crude product from the reaction of $(TBA)_2[W_6O_{19}]$ with TBA(OH) and $Zn(NO_3)_2.6H_2O$ was almost identical to the analogous reaction using $Co(NO_3)_2.6H_2O$, suggesting the structures are closely related. To verify this, single crystals of the product of the reaction of "$(TBA)_5[W_5O_{18}H]$" and $Zn(NO_3)_2.6H_2O$ were obtained by slow diffusion of diethyl ether into a saturated solution of the crude product dissolved in acetonitirle. A partial structure was obtained from these crystals and is shown in **Figure 4.7a**.
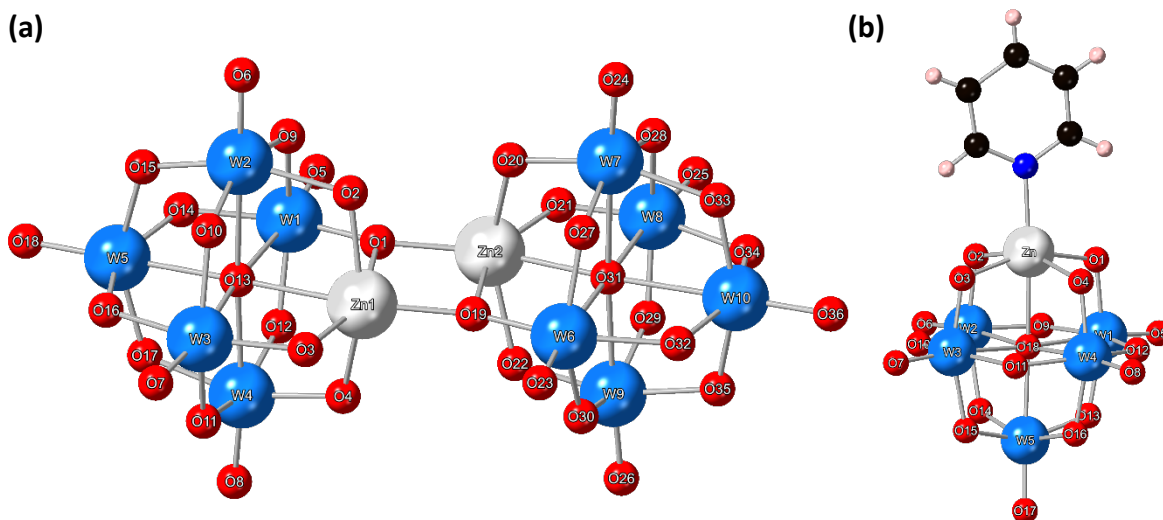
Figure 4.7: Single-crystal X-ray diffraction structures of $[(ZnW_5O_{18}H)_2]^{6-}$ **(a)** and $(TBA)_3[(Py)ZnW_5O_{18}H]$ **(b)**. Cations and solvent are omitted for clarity. The atomic radii are set to the CSD covalent radii.

The tetrabutylammonium cations present in the structure were severely disordered, though the data supports the presence of six cations per POM. In line with the other dimers obtained, this suggests a formula of $(TBA)_6[(ZnW_5O_{18}H)_2]$. Interestingly, the dimer does not show any bend/kink like the others in the series. This is very surprising given that all other structures show localisation of a proton on a M-O-W bridge which leads to the formation of a hydrogen bond between the two halves of structure.

BVS analysis indicates protonation of both O2 (V_{O2} = 1.00) and O4 (V_{O4} = 1.37). Relatively low bond valence sums of O20 (V_{O20} = 1.43) and O22 (V_{O22} = 1.45) may also imply partial delocalisation of the protons present onto these positons. All of these oxygens are directly bound to zinc and are in appropriate positions to form the same hydrogen bond formed between the two halves of the cages in other structures.

One key difference between the structure incorporating zinc and the other dimeric structures discussed is that the BVS analysis suggest that both protons lie in positions where they could form hydrogen bonds between the two halves of the cage. For the other structures, BVS analysis typically suggests that the second proton lies in the equatorial plane containing the heterometal (i.e. on O3 or O21 in **Figure 4.7a**). Protonation of this position does not lead to any hydrogen bonding interaction and therefore the dimer can bend to one side to maximise the stabilisation caused by hydrogen bond formation on one side of the dimer. When both protons are in positions in which hydrogen bonds can form (i.e. O3 and O4) then a linear dimer allows the formation of, albeit weaker, hydrogen bonding interactions on both sides of the dimer. The interatomic distances between O3-O20 and O4-O22 are ca. 3.16 Å and ca. 3.34 Å

respectively, which is significantly longer than the hydrogen bonding distances observed for the other dimers (ca. 2.55-2.70 Å), but still within the upper limit of hydrogen bonding interactions (approx. 3.5 Å).[48] The stabilisation energy afforded by formation of these two weaker interactions must be larger than the single "strong" interaction offered by a bent configuration. This effect may be compounded by additional lattice stabilisation energy contributions in the solid-state, which add to the preference for the linear arrangement.

Comparison of the average Zn-O bond length (ca. 2.09 Å), W-O bond length (ca. 1.92 Å), and the Zn-Zn distance (ca. 3.02 Å, 2.96-3.16 Å for the other dimers) to the other $[(MW_5O_{18}H)_2]^{6-}$ structures showed no obvious differences. Therefore, the preferential protonation of O3 and O4, and in turn the lack of formation of a bent dimeric structure, cannot be attributed to deviations in bond lengths within the structure.

Dissolution of this dimer in pyridine, followed by vapour diffusion of diethyl ether into the solution, led to the formation of colourless crystals. Analysis of these crystals by single-crystal X-ray diffraction gives the expected structure of the pyridine adduct shown in **Figure 4.7b**. The structure shows the presence of three TBA cations per POM and BVS analysis indicates the presence of a proton on O1 (V_{O1} = 1.36), giving the molecular formula of $(TBA)_3[(Py)ZnW_5O_{18}H]$ that is consistent with the rest of the M(II) pyridine adducts.

4.5.5 Conclusion

These studies represent conclusive evidence of our ability to incorporate first-row, divalent, transition metals into the Lindqvist framework using the degradative reassembly approach first used for the synthesis of $[(CoW_5O_{18}H)_2]^{6-}$. Crystallographic studies show the tendency of {M(II)W_5}-type POMs to dimerise in the absence of strong ligands, with the general formula $(TBA)_6[(MW_5O_{18}H)_2]$. The presence of protons on the Lindqvist framework has a major influence on the solid-state structure. These protons appear to sit preferentially on oxygens adjacent to the heterometal centre, with these oxygen atoms being the most basic in the structure. One consequence of this is the formation of internal hydrogen bonds between the two halves of the dimers. Formation of a single hydrogen bond on one side of the dimer leads to a bend in the structure, whereas formation of hydrogen bonding interactions on both sides of the dimer leads to a more symmetrical linear dimer, as is the case for zinc.

In the presence of an excess of pyridine (a strong ligand), the dimers are generally cleaved to give the corresponding pyridine adduct, with the general formula $(TBA)_3[(Py)MW_5O_{18}H]$. The manganese substituted system represents a notable exception to this observation whereby a

combination of the low Lewis acidity (compared to the other M(II) ions), and a lack of crystal field stabilisation energy, appears to destabilise the pyridine adduct with respect to the dimer. Therefore, in this case, even in the presence of an excess of the ligand, the dimer persists. Oxidation of Mn(II) to Mn(III) is enough to tip the balance back into the favour of the adduct, with $(TBA)_3[(Py)Mn(III)W_5O_{18}]$ readily forming in an excess of pyridine.

4.6 ^{17}O and ^{183}W NMR of $[(ZnW_5O_{18}H)_2]^{6-}$

Solid-state characterisation methods like single-crystal X-ray diffraction and infrared spectroscopy have provided convincing evidence for the formation of M(II) containing Lindqvist-type POMs. However, these methods provide no insight into the preference for these structures in solution. For this, chemists typically rely on NMR spectroscopy, which can be used to determine both the prevalence and stability of species in solution.

One issue with the series of $[(M(II)W_5O_{18}H)_2]^{6-}$ compounds targeted in this chapter is that most of them aim to incorporate a paramagnetic metal centre. These nuclei have unpaired electrons, which can couple to nuclear spins and provide rapid relaxation pathways. One major consequence of this, alongside major changes in typical chemical shifts, is detrimental signal broadening that is often so severe that signals cannot be resolved. This can make it near impossible to extract meaningful insight from NMR spectroscopy experiments, as peaks can be both lost and difficult to assign.

Fortunately, Zn(II) (d^{10}) is diamagnetic and therefore does not cause any of these issues. This means the synthesis of $[(Zn(II)W_5O_{18}H)_2]^{6-}$ can be followed by both ^{17}O and ^{183}W NMR spectroscopy and in theory, these methods can provide insight into the prevalence of the dimeric unit in solution. Due to the structural similarities in the series of $[(M(II)W_5O_{18}H)_2]^{6-}$ anions, this can then act as a model system for the compounds that contain paramagnetic metal centres which cannot be probed directly.

4.6.1 ^{17}O NMR studies

In order to follow the synthesis of $[(Zn(II)W_5O_{18}H)_2]^{6-}$ by ^{17}O NMR spectroscopy, ^{17}O enriched $(TBA)_2[W_6O_{19}]$ was first treated with four equivalents of TBA(OH) in acetonitrile. This reaction was discussed in **Chapter 3** and the spectrum was shown in **Section 3.3.1**. The mixture was then transferred via cannula onto a solution of $Zn(NO_3)_2.6H_2O$ dissolved in acetonitrile. The solution was allowed to stir overnight before the volatiles were removed and the resulting thick oil was taken up in the minimum amount of CD_3CN (approx. 0.5 mL). ^{17}O NMR spectra

were then obtained at a range of temperatures between 253-343 K (−20 °C to 70 °C). The resulting spectra are shown in **Figure 4.8**.

The spectra are very complicated with many broad and sharp peaks observed across the temperature range. A broad feature is observed at 253 K (**Figure 4.8a**) between 670-720 ppm that sharpens significantly as the temperature is increased to give several individual peaks. This is in the region characteristic for terminal W=O environments but these peaks are slightly
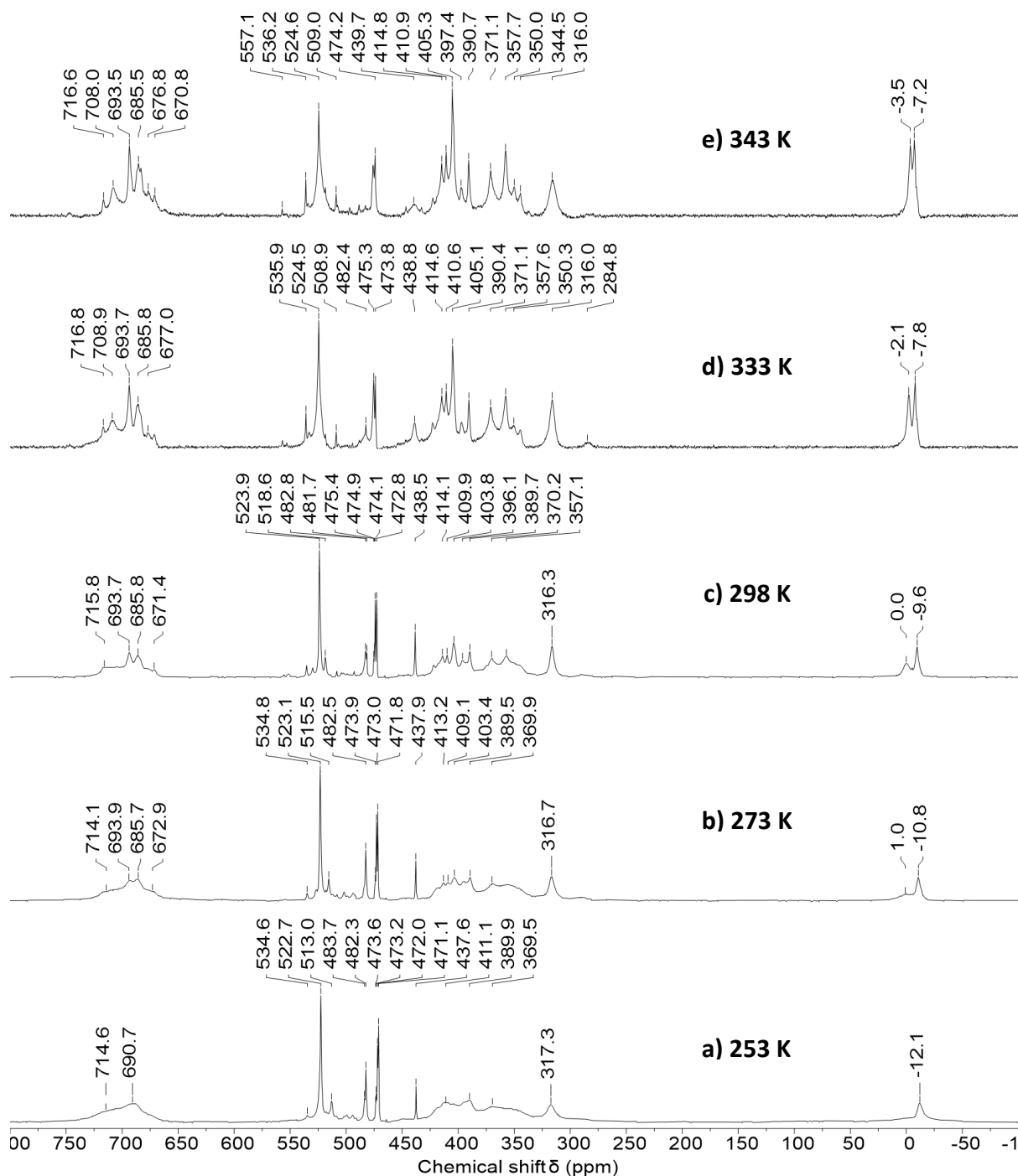
Figure 4.8: ^{17}O NMR spectra obtained from the reaction of (TBA)$_2$[W$_6$O$_{19}$] with TBA(OH), and Zn(NO$_3$)$_2$.6H$_2$O in CD$_3$CN at **a)** 253 K, **b)** 273 K, **c)** 298 K, **d)** 333 K, and **e)** 343 K.

more downfield than previously observed for 3– {MW$_5$}-type POMs (see **Chapter 5**). This may indicate an equilibrium with the deprotonated 4– species.

This behaviour is mirrored by the very broad feature between 320-430 ppm, typical for bridging W-O-W environments, which also grows into several sharp peaks with similar chemical shifts as the temperature is increased. Interestingly, the reverse behaviour is also observed. The peaks at 438 (characteristic for [WO$_4$]$^{2-}$), 482, and 523 ppm broaden as temperature is increased.

The presence of different types of variable temperature behaviour indicates the presence of multiple dynamic processes, which are changing the number of unique oxygen environments resolved on the NMR timescale. The sharpening of peaks as temperature increases is indicative of a process which is relatively slow at room temperature (meaning multiple unique but exchanging environments are resolved) which becomes rapid at higher temperatures. This leads to fast exchange and therefore the multiple environments are instead observed as a single average peak whose linewidth depends on the rate of exchange. On the other hand, the broadening of peaks as temperature increases is indicative of a dynamic process that is inaccessible at room temperature (activation barrier is too high) and therefore multiple (non-exchanging) environments are observed. As temperature is increased, this dynamic process is "switched on" and exchange between the environments is possible. This leads to broadening of the individual peaks. Eventually, these individual peaks would coalesce into a single "average" peak but this is not observed over the temperature range studied.

These observations indicate that [(Zn(II)W$_5$O$_{18}$H)$_2$]$^{6-}$ forms a part of multiple equilibria in solution which leads to very complex ^{17}O NMR spectra. These equilibria may include proton migration (i.e. protonation of different oxygens of the cage), protonation/deprotonation or monomer/dimer formation. The complexity may be further added to if we consider the possibility that some of these peaks (and the corresponding dynamic behaviour) may belong to by-products.

In an attempt to simplify the observed spectra, the volatiles were removed from the sample and the crude product was re-dissolved in pyridine. As shown crystallographically, this should convert [(Zn(II)W$_5$O$_{18}$H)$_2$]$^{6-}$ to [(Py)Zn(II)W$_5$O$_{18}$H]$^{3-}$ and therefore remove any issues with a monomer/dimer equilibrium (the presence of an excess of pyridine should push the equilibrium to the monomer). The ^{17}O NMR spectra obtained in pyridine at 298 K and 343 K are shown in **Figure 4.9**. It should be noted that ^{17}O NMR spectra obtained in pyridine are

naturally broader than those obtained in acetonitrile due to the increased viscosity of pyridine (0.88 cP) compared to acetonitrile (0.34 cP).[49]

The NMR spectra immediately appear simpler. The terminal W=O region consists of a single broad feature (with a shoulder) at ca. 700 ppm at 298 K. This then sharpens up revealing two peaks at 700 and 664 ppm respectively at 343 K. Two peaks in 4:1 ratio would be expected for $[(Py)Zn(II)W_5O_{18}H]^{3-}$ if the proton is delocalised across the four Zn-O-W bridges. The observation of a broad feature that is beginning to sharpen into two peaks as the temperature increases may indicate that the rate of proton migration is initially slow, but is increasing with temperature. Again, the peaks appear further downfield than is typical for terminal W=O peaks of 3− {MW$_5$}-type POMs (ca. 700-800 ppm) and may indicate formation of the deprotonated 4− form in solution (perhaps aided by the presence of pyridine, a Brønsted base).

There are significantly fewer peaks in the bridging region (320-430 ppm) with only three broad peaks at 362, 396, and 409 ppm at 298 K. These peaks appear to sharpen somewhat upon heating to 343 K. Theoretically, there could be up to five unique bridging W-O-W environments if the proton on the cage was completely static, but this would reduce to two if the proton was delocalised over all of the bridging Zn-O-W positions. The two larger peaks at 361 and 409 ppm at 343 K may be assignable to these two W-O-W environments, assuming that proton migration is fast at this temperature.

There are a collection of peaks between 470-560 ppm. One or more of these peaks could plausibly be assigned to the bridging Zn-O-W environments of $[(Py)Zn(II)W_5O_{18}H]^{3-}$, with these
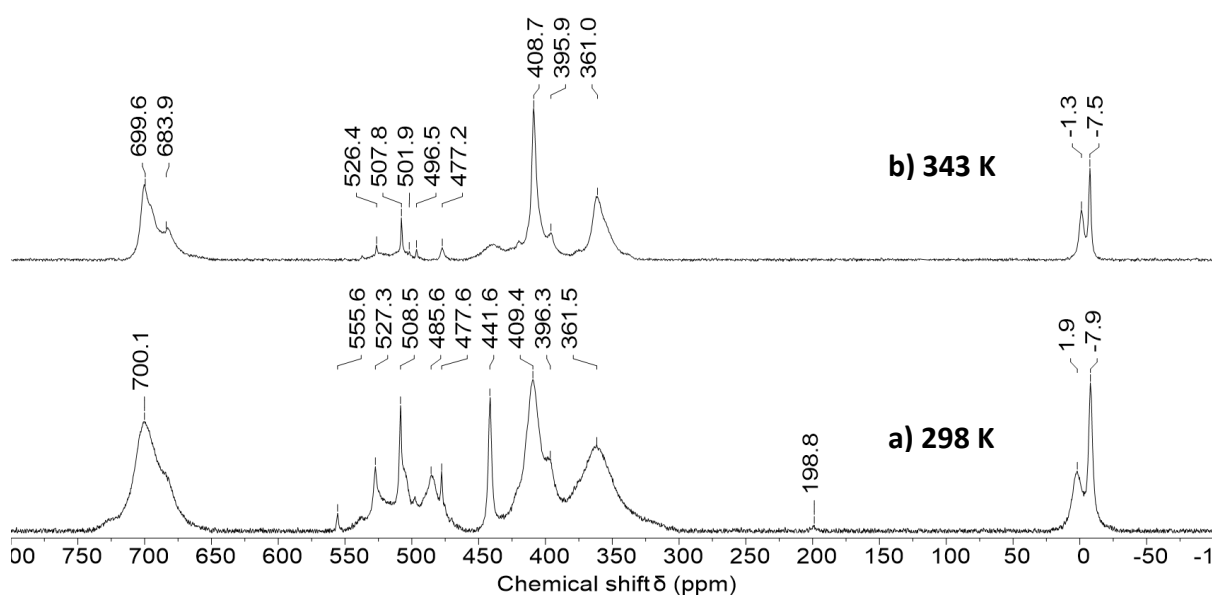
Figure 4.9: ^{17}O NMR spectra obtained from the reaction of (TBA)$_2$[W$_6$O$_{19}$] with TBA(OH), and Zn(NO$_3$)$_2$.6H$_2$O in pyridine at **a)** 298 K, and **b)** 343 K.

peaks falling in the region of other M-O-W bridging oxygens in Lindqvist-type POMs (see **Chapter 5**). Again, the number of peaks expected depends on the extent of delocalisation of the proton on the cage and/or the prevalence of the deprotonated form. The intensities of these peaks appears to drop as temperature increases. There is also a drop in intensity of the peak observed at 438 ppm which appears to broaden. The chemical shift of this peak is characteristic of monomeric tungstate. The fact that all these peaks drop in intensity/broaden, may indicate chemical exchange between tungstate and the {ZnW$_5$} species at higher temperatures.

4.6.2 ^{183}W NMR studies

To gain further insight into the nature of solutions containing [(ZnW$_5$O$_{18}$H)$_2$]$^{6-}$, ^{183}W NMR was performed. The spectrum of crude (TBA)$_6$[(ZnW$_5$O$_{18}$H)$_2$] dissolved in CD$_3$CN was recorded and is shown in **Figure 4.10**. There is a significant number of environments observed in the spectrum. If [(ZnW$_5$O$_{18}$H)$_2$]$^{6-}$ is stable in solution, then the number of tungsten environments present in the ^{183}W NMR would depend only on the symmetry of the species. With the lowest possible symmetry, 10 equal intensity peaks would be expected (one for each tungsten of the dimeric unit). There are 17 obvious peaks in the spectrum shown in **Figure 4.10**. This suggests that more than one species is present in solution. This could include a mixture of dimeric species, monomeric species, or even species that have undergone rearrangement and lost the zinc cation into solution (as well as possible by-products formed in the synthesis).

Analysis of the observed chemical shifts gives no real evidence for any known isopolytungstates apart from potentially the formation of some (TBA)$_2$[W$_6$O$_{19}$] evidenced by the presence of a peak at 59.6 ppm. Furthermore, comparison of the spectrum with those
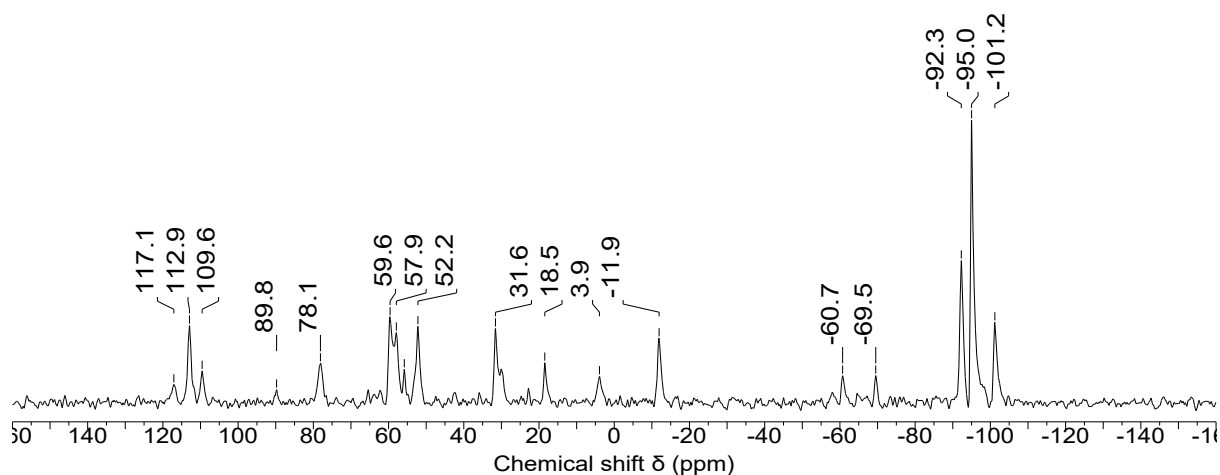
Figure 4.10: ^{183}W NMR spectrum of the crude product obtained from the reaction of (TBA)$_2$[W$_6$O$_{19}$] with TBA(OH), and Zn(NO$_3$)$_2$.6H$_2$O. Recorded in CD$_3$CN at 298 K.

discussed in **Section 3.4.2** gives no suggestion of formation of any of the known or unknown degradation products from reaction of $(TBA)_2[W_6O_{19}]$ with base.

There are two clusters of peaks in **Figure 4.10** at −92.3 to −101.2 ppm and 109.6 to 117.1 ppm respectively. Integration of these peaks shows that these groups occur in a 4:1 ratio. This is very characteristic of the four equatorial tungstens and one axial tungsten present in a $\{MW_5\}$ unit. Furthermore, integration of the separate peaks shows that each of the peaks in the smaller cluster (i.e. 109.6 to 117.1 ppm) is accompanied by a peak in the larger cluster (i.e. −92.3 to −101.2) that is approximately four times the size. This may be indicative of a set of three similar $\{ZnW_5\}$-type species present in solution. It should be noted that these could be either monomers (i.e. 4:1 ratio of tungsten atoms) or dimers (i.e. 8:2 ratio of tungsten atoms).

The remaining peaks in the spectrum span a broad chemical shift range from −69.5 to 89.8 ppm. Given they are not assignable to any known isopolytungstate species, and the indication of formation of $\{W_6\}$, it may be plausible that they are the result of the rearrangement of $[(ZnW_5O_{18}H)_2]^{6-}$ into various heteropolytungstate species which incorporate zinc. For example, a zinc centred Keggin anion with formula $[ZnW_{12}O_{40}]^{6-}$ has been isolated using aqueous methods.[50]

When studying the ^{17}O NMR spectra of $[(ZnW_5O_{18}H)_2]^{6-}$, it was postulated that re-acquiring spectra in pyridine could simplify things by potentially supressing any monomer/dimer interconversions (i.e. pushing any equilibria towards the monomeric pyridine adduct). Indeed, some changes were observed after re-acquiring the ^{17}O NMR spectrum in pyridine.

In order to probe the affect this has on the observed ^{183}W NMR spectrum, the solvent was removed from the sample and the obtained oil was re-dissolved in d_5-pyridine. The ^{183}W NMR spectrum was then collected and is shown in **Figure 4.11**.

As in the ^{17}O NMR spectra, there are some notable changes in the observed ^{183}W NMR spectrum. Firstly, instead of a cluster of peaks at −92.3 to −101.2 ppm, there is now a pair of peaks at −71.6 and −79.3 ppm respectively. It is difficult to know if a subset of the species responsible for the cluster observed between −92.3 to −101.2 ppm in **Figure 4.10** are also responsible for the pair of peaks in **Figure 4.11**, however the significant downfield shift can be attributed to the change in solvent from acetonitrile (dielectric constant = 37.5) to pyridine (dielectric constant = 12.4).[49] Typically, downfield shifts of 5-20 ppm are observed for POMs (with the magnitude of the change showing a dependence on the charge of the POM) when
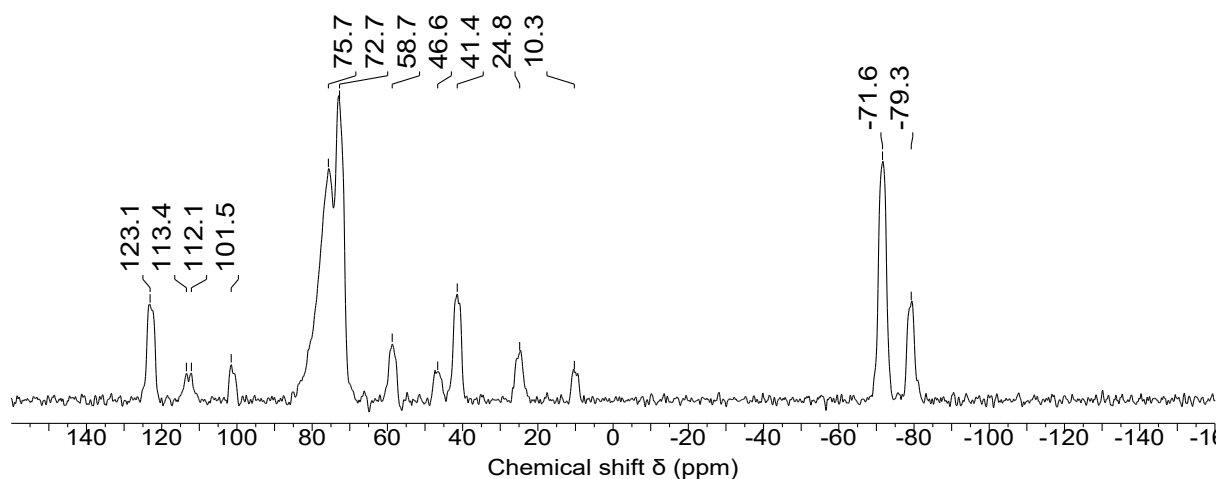
Figure 4.11: ^{183}W NMR spectrum of the crude product obtained from the reaction of (TBA)$_2$[W$_6$O$_{19}$] with TBA(OH), and Zn(NO$_3$)$_2$.6H$_2$O. Recorded in C$_5$D$_5$N at 298 K.

reducing the dielectric constant of the solvent (typically studied when going from H$_2$O to DMF). A computational study by Vilà-Nadal and co-workers suggested that these shifts can be attributed to a slight increase in W-O bond lengths upon dissolution in lower dielectric constant solvents.[51] Their work did not expand to lower polarity solvents, nor did it examine the dependence of the degree of chemical shift change on the original chemical shift (i.e. would a peak originally observed at 100 ppm shift to the same degree as a peak originally observed at −100 ppm) and therefore the magnitude of chemical shift changes expected in the current study is unknown.

The simplification of the cluster of peaks at −92.3 to −101.2 ppm is paired with a similar simplification of the cluster observed at 109.6 to 117.1 ppm in **Figure 4.10**. Instead, there is now a larger peak at 123.1 ppm and a smaller feature at 112.1-113.4 ppm (which appears to be two overlapping peaks). As discussed previously for **Figure 4.10**, these peaks are significantly smaller than those at −71.6 and −79.3 ppm and therefore may plausibly be assigned to the equatorial (4 W) and axial (1 W) of a {ZnW$_5$} unit. Furthermore, the simplification of both regions may be consistent with pushing the mixture towards a monomeric pyridine adduct (removing complexity associated with the presence of dimeric species).

The space between peaks discussed so far has simplified somewhat with eight obvious signals in this region, the most significant of these being the pair of peaks at 72.7 and 75.7 ppm. It is very difficult to assign any of these peaks as there is no literature data for ^{183}W NMR chemical shifts of POMs in pyridine. Given what we have observed previously, it is very possible that

peaks corresponding to monomeric $(TBA)_2[WO_4]$ and $(TBA)_2[W_6O_{19}]$ may be present in this region.

4.7 Laying the foundation for a third-generation approach

The degradative reassembly approach presented in this chapter and in **Chapter 2** represents a substantial step forward over the original methodology involving the controlled hydrolysis of $WO(OMe)_4$ in the presence of $(TBA)_2[WO_4]$. Moving away from the use of $WO(OMe)_4$ removes the need to synthesise this compound, which avoids the use of substantial quantities of thionyl chloride during the synthesis of the $WOCl_4$ precursor and ammonia gas during its conversion to the oxoalkoxide.

However, the new method is not without its limitations when applied to the synthesis of M(II) containing Lindqvist-type POMs. In particular, as alluded to in **Chapter 2**, the required use of four equivalents of TBA(OH) per $\{W_6\}$ during the generation of the precursor mixtures leads to the formation of 2.4 equivalents of TBA(X) after reaction with MX_2. These tetrabutylammonium salts are difficult to separate from the product as evidenced by infrared studies when using $M(NO_3)_2.XH_2O$ salts that show the persistence of nitrate even after work up. Recrystallization may have offered a solution to this issue but, as of yet, recrystallization of large quantities of the crude product has proved challenging. Therefore, an ideal approach would avoid the generation of any TBA(X) by-products during the synthesis.

One way to achieve this may be through metal-ion exchange. Theoretically, if a lacunary $\{W_5O_{18}\}$-type species could be stabilised by a metal(II) cation (M), this could act as a precursor for the compounds targeted in this chapter. This metal cation would then have to be readily displaced upon treatment with a divalent first-row transition metal (M'). This would produce only MX_2 as a by-product which, if this salt was insoluble in the reaction solvent, could easily be separated from the product and drive the reaction forward, as shown in **Equation 4.5**.

$$(TBA)_6[(MW_5O_{18}H)_2] + 2\ M'X_2 \rightarrow (TBA)_6[(M'W_5O_{18}H)_2] + 2\ MX_2 \downarrow \qquad (4.5)$$
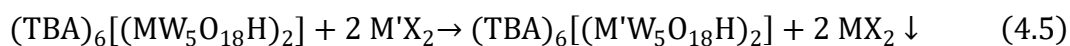
This route only offers improvement if the starting $(TBA)_6[(M(II)W_5O_{18}H)_2]$ material can be produced cleanly, without any additional TBA(X) salts. One way to do this is to use a M(II) alkoxide as the starting material, as the synthesis of the corresponding $(TBA)_6[(M(II)W_5O_{18}H)_2]$ material only requires the use of 1.6 equivalents of base per $\{W_6\}$ and produces only the alcohol as the by-product (**Equations 4.6** and **4.7**). This route was trialled during attempts to

refine the synthesis of $(TBA)_6[(Co(II)W_5O_{18}H)_2]$ but the low solubility of the first-row transition metal alkoxides was an issue.

$$5\ (TBA)_2[W_6O_{19}] + 8\ (TBA)[OH] + 5\ H_2O \rightarrow 6\ (TBA)_3[W_5O_{18}H_3] \qquad (4.6)$$

$$2\ (TBA)_3[W_5O_{18}H_3] + 2\ M(OR)_2 \rightarrow (TBA)_6[(M'W_5O_{18}H)_2] + 4\ ROH \qquad (4.7)$$
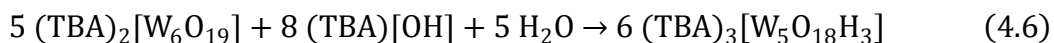
Therefore, we require an element that has a M(II) alkoxide that is soluble in polar solvents (e.g. acetonitrile, dichloromethane, methanol etc.) and relatively insoluble MX_2 salts in similar solvents. One metal that fits these criteria is magnesium. Magnesium methoxide is soluble in methanol, while salts like magnesium chloride possess little to no solubility in solvents like acetonitrile or dichloromethane. Therefore, we set out to see if we could synthesise $(TBA)_6[(MgW_5O_{18}H)_2]$ as a theoretical starting material for other $(TBA)_6[(MW_5O_{18}H)_2]$ systems if magnesium can be readily replaced by other first-row transition metals.

4.6.1 Synthesis of a magnesium containing Lindqvist structure

First, magnesium methoxide was synthesised in-situ by refluxing finely divided magnesium metal (obtained by ball milling) in anhydrous methanol overnight.[52] This led to the dissolution of the magnesium and gave a slightly cloudy solution. In a separate flask, {W_6} was degraded with 1.6 equivalents of TBA(OH) at room temperature in acetonitrile (with one equivalent of water). The degradation mixture was then transferred directly onto the methanol solution of $Mg(OMe)_2$ via cannula. The colourless, slightly cloudy, solution was allowed to stir overnight before passing through a PTFE syringe filter and removing the solvent. A thick oil was obtained which was triturated with diethyl ether, to give a free-flowing white powder. The infrared spectrum of the crude material was obtained and is shown in **Figure 4.12**.

The spectrum is somewhat similar to that previously obtained for $(TBA)_7[(CoW_5O_{18}H)_2][NO_3]$, also shown in **Figure 4.12**. The spectrum contains several peaks in the bridging W-O-W region. As for cobalt, this could be indicative of a dimeric structure, as monomeric POMs tend to feature a simpler bridging region. The terminal W=O is observed at 940 cm^{-1} for the reaction involving magnesium. This is higher than what was observed for the series of M(II) substituted Lindqvist-type POMs synthesised in this chapter (approx. 930-935 cm^{-1}). This may indicate some electronic differences in the products, perhaps stemming from the fact that magnesium is not a d-block element, and therefore has no electrons in d-orbitals, and is in the third period rather than the fourth as is the case for all other elements discussed. This could change the
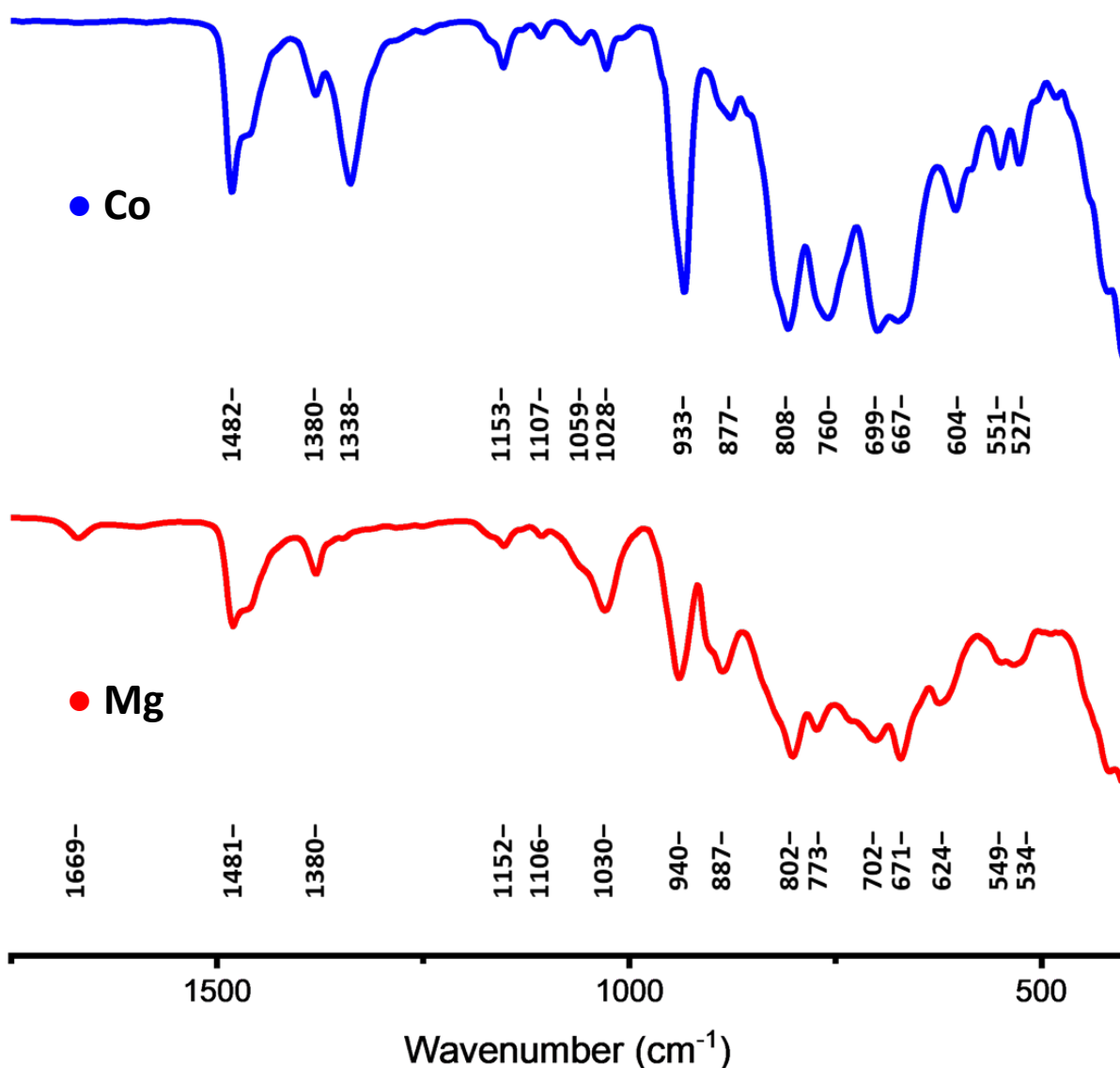
Figure 4.12: ATR FTIR transmittance spectra of the crude products from reaction of $(TBA)_2[W_6O_{19}]$ with TBA(OH), and $Co(NO_3)_2.6H_2O$ (blue) or $Mg(OMe)_2$ (red).

way the charge is distributed within the POM cage and in turn, change the W=O stretching frequency.

The presence of extra peaks at 1030 and 1669 cm^{-1} for the reaction involving magnesium may be attributed to residual $Mg(OMe)_2$ (perhaps interacting with the POM).[53]

In order to gain more conclusive evidence for the incorporation of magnesium into the Lindqvist framework, crystals of the crude material were grown by vapour diffusion of methyl *tert*-butylether into a saturated solution of the crude product dissolved in pyridine. The obtained colourless crystals were analysed by single-crystal X-ray diffraction, giving the structure shown in **Figure 4.13**.

The structural similarities between the magnesium containing dimer shown in **Figure 4.13** and the other structures presented in this chapter is immediately apparent. The dimer is
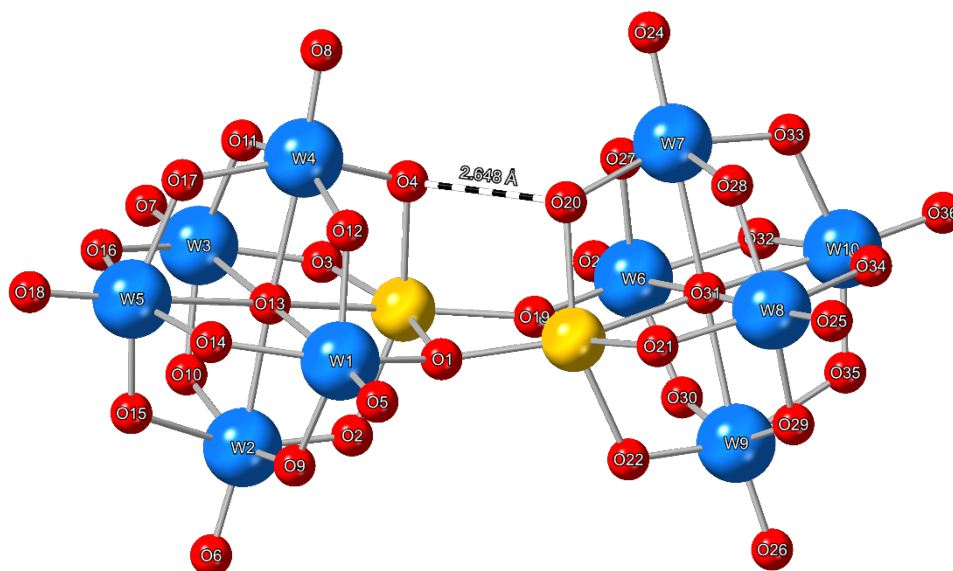
Figure 4.13: Single-crystal X-ray diffraction structures of $(TBA)_6[(MgW_5O_{18}H)_2]$. Cations and solvent are omitted for clarity. The atomic radii are set to the CSD covalent radii.

surrounded by six tetrabutylammonium ions, implying the presence of two protons on the cage and the formula $(TBA)_6[(MgW_5O_{18}H)_2]$. BVS analysis indicates localisation of the two protons on O3 (V_{O3} = 1.26) and O20 (V_{O3} = 1.29). The dimeric unit is bent to one side with an interatomic distance between O4 and O20 of ca. 2.65 Å, consistent with the formation of a hydrogen bond between the two halves of the dimer. Unlike for the analogous Zn compound, the second proton is in a position that cannot take part in hydrogen bonding. Comparison of the bond lengths of $[(MgW_5O_{18}H)_2]^{6-}$ with the other structures in the series shows many similarities. The average Mg-O bond length (ca. 2.07 Å) is significantly longer than the W-O bond length in the W-O-W bridges (ca. 1.94 Å). As seen previously, the comparatively long Mg-O bonds of the Mg-O-W bridges are paired with a short W-O distance of ca. 1.86 Å, perhaps indicative of increased W-O π-bonding in these bridges. The terminal W=O bond lengths are in line with other Linqdvist-type POMs discussed in this thesis, with an average length of ca. 1.72 Å.

4.7.2 ^{17}O NMR studies

To gain some insight into what is present in non-aqueous solutions of $(TBA)_6[(MgW_5O_{18}H)_2]$, ^{17}O NMR spectroscopy studies were carried out. A small-scale procedure, analogous to that discussed in **Section 4.7.1**, was performed using ^{17}O enriched $(TBA)_2[W_6O_{19}]$. The obtained product was then dissolved in CD_3CN and ^{17}O NMR spectra were recorded at 298 and 343 K. The resulting spectra are shown in **Figure 4.14**.
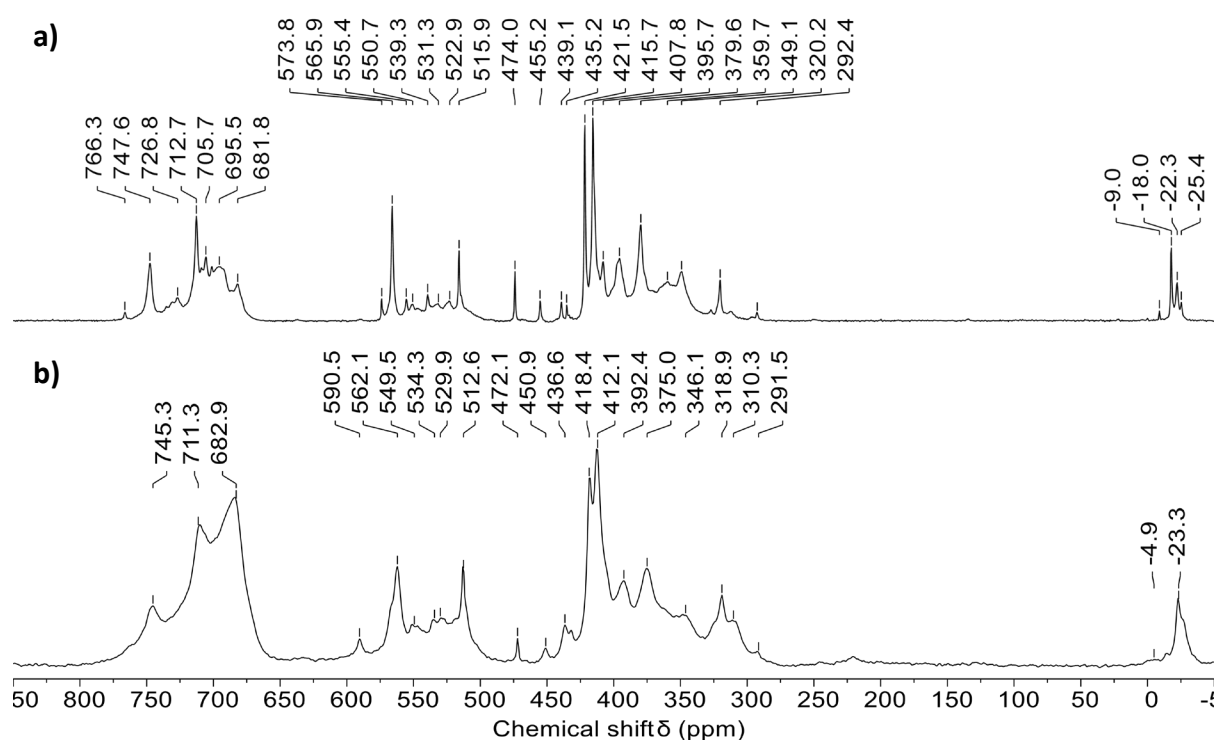
Figure 4.14: ^{17}O NMR spectra of the crude product obtained from the reaction of (TBA)$_2$[W$_6$O$_{19}$] with TBA(OH), H$_2$O, and Mg(OMe)$_2$ in CD$_3$CN at a) 298 K, and b) 343 K.

As was the case when studying acetonitrile solutions of (TBA)$_7$[(ZnW$_5$O$_{18}$H)$_2$][NO$_3$], the obtained NMR spectra are very complicated. There are many peaks in both the typical bridging and terminal oxygen regions. At 298 K, the obtained spectrum contains mostly broad peaks. Both the number of peaks and the sharpness of these peaks increases significantly upon heating the solution to 343 K (**Figure 4.14b**). Correlation time, which is related to relaxation time and line width, is expected to decrease as temperature increases and therefore the sharpening of signals should occur naturally. However, signal sharpening can also be indicative of increasing the rate of a dynamic process. The increase in the number of observed peaks may either be a consequence of the lower linewidths, allowing the resolution of multiple signals with very similar chemical shifts, or may be evidence of the presence of new peaks due to dynamic processes that are inaccessible at room temperature.

The observed peaks can be split into three major groups. Firstly, those occurring in the terminal W=O region, observed between 682 and 766 ppm. The number of peaks expected in this region depends on the symmetry of the species present in solution. If we assume the dimeric unit is retained, then the number of terminal W=O signals depends both on whether the bent structure persists in solution and whether the second proton on the cage is localised. If this is the case, then there is complete asymmetry (i.e. C_s symmetry) and therefore ten unique terminal W=O environments that give ten signals in the ^{17}O NMR spectrum would be expected.

147

Obviously, some of these would likely have very similar chemical shifts and therefore they might not all be resolved separately. If the protons on the cage are delocalised and the bent structure is not retained, then only four unique terminal environments are expected; if the dimer splits into monomers, then as few as two terminal W=O environments would be observed. With only the NMR spectroscopy presented in **Figure 4.14**, it is impossible to tell which situation we have. The true situation may involve a combination of these scenarios, along with the possibility of loss of protons or the magnesium centre.

A similar discussion could be had around the number of peaks occurring in the bridging W-O-W region, between 310 and 474 ppm. It may be reasonable to suggest that the two larger peaks at 412.1 and 418.4 ppm respectively, at 298 K (415.7 and 421.5 ppm at 343 K) correspond to the two bridging W-O-W environments of a $\{(L)MgW_5O_{18}\}$-type POM, which are expected to occur in a 1:1 ratio. The other smaller, more upfield, peaks could then be assigned to bridging W-O-W environments in lower symmetry species.

The third group of peaks occurs in between the two previously discussed groups, between 512 and 590 ppm. It is typical that M-O-W bridges in substituted Lindqvist-type POMs occur more downfield than the W-O-W environments. Therefore, this group could be assigned to the Mg-O-W bridging oxygen environment. There are two major signals at 512.6 and 562.1 ppm at 298 K (515.9 and 565.9 ppm at 343 K) which dominate this region. The relative size and chemical shifts of these two peaks may allow them to sensibly be assigned to bridging Mg-O-W and Mg-O(H)-W environments of a Lindqvist-type POM. The peak for the bridging hydroxide (assigned to the peak at 512.6 ppm) would be expected to be both less intense (as only 2 of the 8 bridging Mg-O-W's can be protonated), and more upfield than the corresponding bridging metal-oxo (assigned to the peak at 562.1 ppm), which is what is observed.[54] The other smaller peaks are likely a result of a range of Mg-O-W and Mg-O(H)-W environments in other lower symmetry species.

Finally, there are also several peaks in the central μ_6-O region which is indicative of more than one individual POM species present (and/or a dimer in which the two halves of the dimer are completely inequivalent). This is in line with the complexity of the system and how sensitive ^{17}O NMR spectroscopy is to the symmetry of the species present in solution. When studying $(TBA)_7[(ZnW_5O_{18}H)_2][NO_3]$, the spectrum was recorded in pyridine to attempt maximise the formation of monomeric $(TBA)_3[(Py)ZnW_5O_{18}H]$ in solution and to simplify the ^{17}O NMR spectrum. However, given that $(TBA)_6[(MgW_5O_{18}H)_2]$ can be crystallized from pyridine, we

know that the addition of simple neutral ligands is unlikely to cleave the dimeric unit. Therefore, similar studies were not pursued for $(TBA)_6[(MgW_5O_{18}H)_2]$.

4.7.3 ^{183}W NMR studies

The complexity of the ^{17}O NMR spectra obtained from acetonitrile solutions of $(TBA)_6[(MgW_5O_{18}H)_2]$ makes interpretation of the results difficult. Analysis of the same solutions with ^{183}W NMR spectroscopy should simplify the results as there are fewer tungsten nuclei than oxygen, which limits the possible number of unique environments. As before, the crude product from the reaction of $(TBA)_2[W_6O_{19}]$ with TBA(OH), H_2O, and $Mg(OMe)_2$ was dissolved in CD_3CN. The ^{183}W NMR was recorded at 298 and 343 K. The resulting spectra are shown in **Figure 4.15**.

Five major peaks were observed. At 298 K (**Figure 4.15a**) these were seen at −115.6, 1.0, 36.4, 88.7, and 99.8 ppm respectively. These peaks shifted downfield by an average of ca. 4 ppm when the sample was heated, which is expected as ^{183}W NMR chemical shifts are known to be sensitive to changes in temperature.[55] The peaks at 1.0 and 88.7 ppm in **Figure 4.15a** are approximately equal intensity regardless of temperature, while the same is true for the peaks at −111.3 and 36.4 ppm. However, these pairs of peaks cannot be related by an integer scale factor at either temperature, and therefore cannot be easily assigned to the same molecule. The peaks at −111.3, 36.4 and 99.8 ppm increased in intensity with respect to the peaks at 1.0
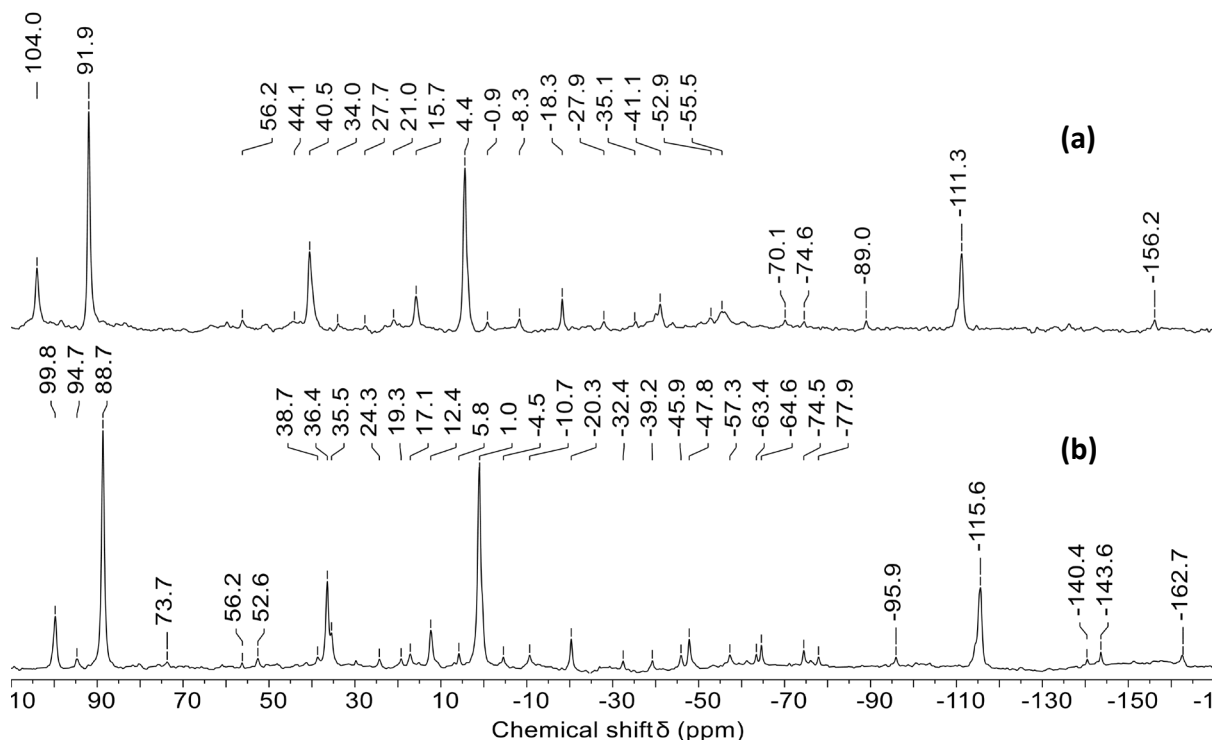
Figure 4.15: ^{183}W NMR spectrum obtained when the crude product from reaction of $(TBA)_2[W_6O_{19}]$ with TBA(OH), H_2O, and $Mg(OMe)_2$ was dissolved in CD_3CN at **(a)** 298 K and **(b)** 343 K.

and 88.7 ppm as the temperature was increased. There is no obvious way to assign these peaks to any Lindqvist-type POM.

The central peak occurring at 1.0 ppm is in the region characteristic of monomeric tungstate (i.e. $[WO_4]^{2-}$) and therefore this may be a plausible assignment. However, the ^{17}O NMR spectra, shown in **Figure 4.14**, did not contain a large peak around 437 ppm, which is typical for tungstate. It may be reasonable to suggest that if the tungstate present in solution was forming strong interactions with free Mg^{2+} then this could cause the peak in the ^{17}O NMR spectrum to be shifted upfield. This would mean that one of the larger peaks at 412.1 or 418.4 ppm could potentially be assigned to tungstate. Unfortunately, when relying only on ^{17}O and ^{183}W NMR spectroscopy, it is difficult to make a conclusive assignment and therefore the possibility that this peak is caused by another species cannot be ruled out.

The two peaks observed at −20.3 and −162.7 ppm at 298 K (−18.3 and −156.2 ppm at 343 K) can be assigned to $(TBA)_4[W_{10}O_{32}]$. These peaks were observed in **Chapter 3** (**Section 3.4.2**) when $(TBA)_2[W_6O_{19}]$ was reacted with ≤1.6 equivalents of TBA(OH). Given the reaction used to produce $(TBA)_6[(MgW_5O_{18}H)_2]$ employed 1.6 equivalents of TBA(OH) per $\{W_6\}$ it is likely that this $\{W_{10}\}$ formed during the degradation and small amounts were left unreacted after the addition of $Mg(OMe)_2$. It should be possible to separate residual $\{W_{10}\}$ by recrystallization, however efficient conditions for quantitative recrystallization of $(TBA)_6[(MgW_5O_{18}H)_2]$ are yet to be found.

Analysis of the smaller features in **Figure 4.15a** showed some familiar peaks. The eight peaks observed at −95.9, −77.9, −39.2, −32.4, −10.7, −4.5, 19.3, and 52.6 ppm respectively appear consistently during the ^{183}W NMR spectroscopy studies of the reaction of $(TBA)_2[W_6O_{19}]$ with varying quantities of TBA(OH), outlined in **Section 3.4.2**. These peaks occur in a 1:1:1:1:1:1:1:1 ratio and in **Chapter 3** were assigned to the unknown "red species". Though the presence of these peaks in this spectrum does not give any further insight into the true nature of this species, it does add to the growing body of ^{183}W NMR evidence that this species is a major component of non-aqueous isopolytungstate solutions, particularly at lower charge to metal ratios (analogous to lower pH's in an aqueous system). Upon heating the solution to 70 °C (343 K shown in **Figure 4.15b**) these peaks seem to disappear. This may indicate that this "red species" is labile with respect to rearrangement to other structures given enough energy. None of the other peaks observed are readily assignable to known isopolytungstates or the "new" species observed in **Chapter 3**. This may mean they represent new isopolytungstates or, more

likely, that the presence of magnesium leads to structures containing one or more heterometals.

4.8 Conclusion

Access to a number of first-row transition metal(II) containing Lindqvist-type POMs, and their pyridine adducts has been demonstrated. Characterisation by infrared spectroscopy and single-crystal X-ray diffraction showed the structural similarity of the compounds, all giving dimeric structures in the absence of strong ligands. The exact nature of the dimer was somewhat variable with the zinc containing analogue adopting a linear structure, while all others were bent due to the presence of a single hydrogen bonding interaction. The ability of the compounds to bind ligands was similarly variable, with the manganese derivative persisting as a dimer while dissolved in pyridine. This behaviour was attributed to trends observed in the Irving-Williams series, where the reduced Lewis acidity of Mn(II) (and lack of CFSE) leads to weaker interactions with donor ligands. When oxidised to Mn(III), the pyridine adduct was found to form rapidly. Unfortunately, this variability in ligand binding has prevented use of the process of converting the dimers to the pyridine adduct and back to the dimers as a method of purification for the full series of compounds.

Studying the formation of the diamagnetic $[(ZnW_5O_{18}H)_2]^{6-}$ by ^{17}O NMR spectroscopy showed very complex reaction mixtures which were difficult to interpret. This was attributed to the presence of one or more dynamic processes that were investigated using variable temperature NMR spectroscopy, but the possibility that the reaction just creates several unwanted by-products cannot be ruled out. Further characterisation of the crude product by ^{183}W NMR gave a similarly complex picture. Unfortunately, without access to an efficient method of recrystallization, it is difficult to determine whether the additional peaks in the NMR spectra are due to solution dynamics or the presence of impurities.

Finally, the synthesis of a magnesium containing Lindqvist-type POM was discussed. This methodology utilised $Mg(OMe)_2$ as the magnesium precursor meaning the procedure could be adapted to use fewer equivalents of TBA(OH) in the degradation step, and in turn, avoid the generation of unwanted tetrabutylammonium salts which are difficult to remove. Solution-state NMR spectroscopy painted an equally complex picture for this system as was observed for the zinc analogue. Unfortunately, time limitations prevented the investigation of exchange reactions in which first-row transition metals attempt to displace magnesium, offering a convenient avenue for the production of the other compounds discussed in this chapter.

4.9 Future work

Though preliminary characterisation has been collected for Mn, Fe, Ni, Zn, and Mg containing Lindqvist-type POMs, further work is required to fully gauge the purity of the products. Elemental analysis and ICP-OES should give a lot of insight into the presence of excess TBA salts and/or the presence of POM based impurities (which will also aid with the interpretation of the ^{17}O and ^{183}W NMR spectra obtained here). Electrochemical characterisation of the compounds using cyclic voltammetry is also relevant. Along with giving insight into compound purity, it is very important to understand the redox properties of these clusters, in particular for the manganese and iron containing clusters that have shown reactivity towards air.

Once the purity of the compounds is established, reactivity studies focusing on oxidation chemistry would be desirable in the context of potential application in water oxidation catalysis. Chemical oxidation using reagents such as bromine, di-*tert*-butyl peroxide, or iodosylbenzene will give valuable insight into the nature of the oxidised products (i.e. ligands bound to the metal centre, protonation of the POM cluster etc.). This could then be followed by electrochemical water oxidation studies.

Alongside this, further work is required to explore the use of $(TBA)_6[(MgW_5O_{18}H)_2]$ as a starting material for the synthesis of first-row transition metal containing Lindqvist-type POMs. With preliminary characterisation in hand, the magnesium containing species should be treated with simple M(II) halides, like $FeCl_2$ for example, in acetonitrile or dichloromethane. A successful reaction should lead to exchange of the magnesium for the other transition metals, which in turn leads to the formation of insoluble $MgCl_2$, which can be separated by filtration. If this is successful, then the purity of the products should be investigated using ICP-OES to determine the amount of magnesium remaining in the samples after workup. This procedure could then be theoretically expanded beyond the first-row to metals spanning the d-block.

4.10 Experimental

4.10.1 Attempted synthesis of "(TBA)$_6$[(Cr(II)W$_5$O$_{18}$H)$_2$]"

In a Schlenk flask, (TBA)$_2$[W$_6$O$_{19}$] (2.0 g, 1.1 mmol) was suspended in MeCN (10 mL). To a separate flask, TBA(OH) (4.2 mL, 4.2 mmol, 1 M in MeOH) was added and pumped dry. The resulting golden oil was then re-dissolved in MeCN (5 mL). The solvent was removed under reduced pressure. This process was repeated twice to ensure complete removal of MeOH. The TBA(OH) was then dissolved in MeCN (5 mL) and transferred via cannula to the suspension of (TBA)$_2$[W$_6$O$_{19}$]. The mixture was stirred for 15 minutes or until all the solid dissolved. The colourless solution was degassed by bubbling with argon for 15-20 minutes and was then transferred via cannula to a Schlenk flask containing CrCl$_2$ (0.16 g, 1.3 mmol) dissolved in MeCN (5 mL). The resulting dark blue mixture was stirred overnight, after which the solvent was removed under reduced pressure to leave a dark blue oil. The oil was triturated in alternation with ethyl acetate (10 mL) and diethyl ether (15 mL), until a free-flowing blue powder was obtained (2.0 g, 79% yield based on target). The ATR FTIR transmittance spectrum was recorded. Crystallization by vapour diffusion of diethyl ether into saturated solutions of the crude product in MeCN and pyridine was attempted, but only amorphous green solid formed.

v_{max}/cm^{-1} = 2958 (CH), 2934 (CH), 2872 (CH), 1670, 1482, 1380, 1152, 1106, 1056, 951 (s), 881 (s), 798 (vs), 776 (vs), 572, 529, 425 (vs).

4.10.2 Attempted synthesis of "(TBA)$_6$[(Cr(III)W$_5$O$_{18}$)$_2$]"

In a Schlenk flask, (TBA)$_2$[W$_6$O$_{19}$] (2.0 g, 1.1 mmol) was suspended in MeCN (10 mL). To a separate flask, TBA(OH) (5.5 mL, 5.5 mmol, 1 M in MeOH) was added and pumped dry. The resulting golden oil was then re-dissolved in MeCN (5 mL). The solvent was removed under reduced pressure. This process was repeated twice to ensure complete removal of MeOH. The TBA(OH) was then dissolved in MeCN (5 mL) and transferred via cannula to the suspension of (TBA)$_2$[W$_6$O$_{19}$]. The mixture was stirred for 15 minutes or until all the solid dissolved. The mixture was then transferred via cannula to a Schlenk flask containing Cr(NO$_3$)$_3$.9H$_2$O (0.51 g, 1.3 mmol) dissolved in MeCN (5 mL). A dark green solution formed which was stirred overnight. The solvent was removed under reduced pressure to leave a dark green oil. The oil was triturated in alternation with ethyl acetate (10 mL) and diethyl ether (15 mL), until a free-flowing green powder was obtained (1.8 g, 71% yield based on target). The infrared spectrum was recorded. Crystallization by vapour diffusion of diethyl ether into saturated solutions of

the crude product in MeCN and pyridine was attempted, but only amorphous green solid formed.

v_{max}/cm^{-1} = 2959 (CH), 2934 (CH), 2872 (CH), 1738, 1679, 1482, 1379 (vs), 1335, 1152, 1197, 1958, 1027, 934 (s), 872 (vs), 782 (vs), 736 (s), 698 (vs), 569, 530, 419 (vs)

4.10.3 Synthesis of (TBA)$_6$[(Mn(II)W$_5$O$_{18}$H)$_2$]

In a Schlenk flask, (TBA)$_2$[W$_6$O$_{19}$] (2.0 g, 1.1 mmol) was suspended in MeCN (10 mL). To a separate flask, TBA(OH) (4.2 mL, 4.2 mmol, 1 M in MeOH) was added and pumped dry. The resulting golden oil was re-dissolved in MeCN (5 mL). The solvent was removed under reduced pressure. This process was repeated twice to ensure complete removal of MeOH. The TBA(OH) was then dissolved in MeCN (5 mL) and transferred via cannula to the suspension of (TBA)$_2$[W$_6$O$_{19}$]. The mixture was stirred for 15 minutes or until all the solid dissolved. The colourless solution was degassed by bubbling with argon for 15-20 minutes and the mixture was then transferred via cannula to a Schlenk flask containing Mn(NO$_3$)$_2$.4H$_2$O (0.32 g, 1.3 mmol) dissolved in MeCN (5 mL). The mixture was stirred and gradually turned from pale purple to pale yellow. The solution was stirred overnight, after which the solvent was removed under reduced pressure to leave a golden oil. The oil was triturated in alternation with ethyl acetate (10 mL) and diethyl ether (15 mL), until a free-flowing sandy yellow powder was obtained (1.9 g, 75% yield). The infrared spectrum was recorded. Small quantities of crystals could be obtained by vapour diffusion of diethyl ether into a saturated pyridine solution of the crude product (must be under inert conditions to prevent oxidation).

v_{max}/cm^{-1} = 2957 (CH), 2931 (CH), 2870 (CH), 1481, 1379, 1337, 1151, 1106, 1057, 1028, 960, 934 (vs), 881, 810 (vs), 765 (vs), 663 (vs), 605, 551, 527, 483.

4.10.4 Synthesis of (TBA)$_3$[(Py)Mn(III)W$_5$O$_{18}$]

(TBA)$_6$[(Mn(II)W$_5$O$_{18}$H)$_2$] (2 g, 0.5 mmol) was dissolved in pyridine (10 mL) to give a pale-yellow solution. The mixture was stirred in air overnight during which time the mixture slowly turned dark red. An excess of ethyl acetate (30 mL) was added to the mixture, which led to the immediate precipitation of a red powder. The reaction solution was decanted away from the solid and the solid was washed with ethyl acetate (10 mL) and diethyl ether (3 x 10 mL). The solid was dried under vacuum to give a free-flowing red powder (1.9 g, 91% yield). The crude product was crystallized by the addition of diethyl ether to a pyridine solution of the crude compound until precipitate began to form. At this step, the solid was re-dissolved by the addition of the minimum amount of pyridine (dropwise) and then the solution was cooled to

-30 °C. Crystals formed after two days. The crystals were separated from the mother liquor and washed with small amounts of cold ^{i}PrOH or dry lutidine (adducts are not very soluble in lutidine if it is dry). The crystals were then dried under vacuum (1.4 g, 67% yield).

v_{max}/cm^{-1} = 2957 (CH), 2871 (CH), 1598, 1578, 1480, 1446, 1379, 1215, 1150, 1106, 1070, 1033, 1009, 961, 936 (vs), 884, 783 (vs), 750 (vs), 701 (vs), 625, 599, 575, 511, 442, 425 (vs).

4.10.5 Attempted synthesis of "(TBA)$_6$[(Mn(III)W$_5$O$_{18}$)$_2$]"

In a Schlenk flask, (TBA)$_2$[W$_6$O$_{19}$] (2.0 g, 1.1 mmol) was suspended in MeCN (10 mL). To a separate flask, TBA(OH) (5.5 mL, 5.5 mmol, 1 M in MeOH) was added and pumped dry. The golden oil was then re-dissolved in MeCN (5 mL). The solvent was then removed under reduced pressure. This process was repeated twice to ensure complete removal of MeOH. The TBA(OH) was then dissolved in MeCN (5 mL) and transferred via cannula to the suspension of (TBA)$_2$[W$_6$O$_{19}$]. The mixture was stirred for 15 minutes or until all the solid dissolved. The mixture was then transferred via cannula to a Schlenk flask containing Mn(OAc)$_3$ (0.22 g, 1.3 mmol) dissolved in MeCN (5 mL). A dark purple solution formed which was stirred overnight. The solvent was removed under reduced pressure to leave a purple oil. The oil was scratched in alternation with ethyl acetate (10 mL) and diethyl ether (15 mL) until a free-flowing orange powder was obtained (1.9 g, 75% yield based on target). The infrared spectrum was recorded. Crystallization by vapour diffusion of diethyl ether into saturated solutions of the crude product in MeCN and pyridine was attempted, but only amorphous purple solid formed.

v_{max}/cm^{-1} = 3381 (br), 2958 (CH), 2873 (CH), 1735, 1672, 1585, 1481, 1381, 1242, 1152, 1108, 1031, 978, 935 (vs), 907, 883, 787 (vs), 607, 573, 510, 427 (vs).

4.10.6 Synthesis of (TBA)$_6$[(Fe(II)W$_5$O$_{18}$H)$_2$]

In a Schlenk flask, (TBA)$_2$[W$_6$O$_{19}$] (2.0 g, 1.1 mmol) was suspended in MeCN (10 mL). To a separate flask, TBA(OH) (4.2 mL, 4.2 mmol, 1 M in MeOH) was added and pumped dry. The golden oil was then re-dissolved in MeCN (5 mL). The solvent was then removed under reduced pressure. This process was repeated twice to ensure complete removal of MeOH. The TBA(OH) was then dissolved in MeCN (5 mL) and transferred via cannula to the suspension of (TBA)$_2$[W$_6$O$_{19}$]. The mixture was stirred for 15 minutes, or until all the solid dissolved. The colourless solution was degassed by bubbling with argon for 15-20 minutes and the mixture was transferred via cannula to a Schlenk flask containing FeCl$_2$ (0.16 g, 1.3 mmol) dissolved in MeCN (5 mL). The mixture was stirred overnight resulting in a dark black/brown solution. The solvent was removed under reduced pressure to leave tacky brown/black solid. The solid was

triturated in alternation with ethyl acetate (10 mL) and diethyl ether (15 mL) (hexane can also be used if the solid remains sticky after a prolonged period of scratching) until a free-flowing brown powder was obtained (1.7 g, 67% yield). The infrared spectrum was recorded.

v_{max}/cm^{-1} = 2958 (CH), 2871 (CH), 1479, 1380. 1152, 1108, 1035, 930 (vs), 882, 808 (vs), 766 (vs), 682 (vs), 609, 549, 526, 481, 441.

4.10.7 Synthesis of (TBA)$_3$[(Py)Fe(II)W$_5$O$_{18}$H]

(TBA)$_6$[(Fe(II)W$_5$O$_{18}$H)$_2$] (2 g, 0.5 mmol) was dissolved in degassed pyridine (10 mL) to give a dark red solution. The mixture was stirred for 30 minutes before an excess of degassed ethyl acetate (30 mL) was added to the mixture leading to immediate precipitation of a red powder. The supernatant was decanted away from the solid and then the solid was washed with ethyl acetate (10 mL) and diethyl ether (3 x 10 mL). The solid was then dried under vacuum to give a free-flowing red powder (1.9 g, 91% yield). Crystals were obtained by vapour diffusion of diethyl ether into a saturated solution of the crude product in pyridine. The crystals were separated from the mother liquor and were washed with small amounts of cold ^{i}PrOH or dry lutidine (adducts are not very soluble in lutidine if it is dry). The crystals were then dried under vacuum (0.8 g, 38% yield).

v_{max}/cm^{-1} = 3059 (CH), 2957 (CH), 2933 (CH), 2871 (CH), 2799, 1597, 1481 (s), 1445, 1378, 1250, 1151, 1106, 1043, 955, 931 (vs), 881, 841, 811 (vs), 763 (vs), 704, 673 (vs), 647, 606, 548, 531, 482, 455, 423 (vs).

4.10.8 Attempted synthesis of "(TBA)$_6$[(Fe(III)W$_5$O$_{18}$)$_2$]"

In a Schlenk flask, (TBA)$_2$[W$_6$O$_{19}$] (2.0 g, 1.1 mmol) was suspended in MeCN (10 mL). To a separate flask, TBA(OH) (5.5 mL, 5.5 mmol, 1 M in MeOH) was added and pumped dry. The golden oil was then re-dissolved in MeCN (5 mL). The solvent was then removed under reduced pressure. This process was repeated twice to ensure complete removal of MeOH. The TBA(OH) was dissolved in MeCN (5 mL) and transferred via cannula to the suspension of (TBA)$_2$[W$_6$O$_{19}$]. The mixture was stirred for 15 minutes or until all the solid dissolved. The mixture was transferred via cannula to a Schlenk flask containing FeCl$_3$ (0.21 g, 1.3 mmol) dissolved in MeCN (5 mL). A yellow/orange solution formed which was stirred overnight. The solvent was removed under reduced pressure to leave an orange oil. The oil was triturated in alternation with ethyl acetate (10 mL) and diethyl ether (15 mL) until a free-flowing orange powder was obtained (2.1 g, 83% yield based on target). The infrared spectrum was recorded.

Crystallization by vapour diffusion of diethyl ether into saturated solutions of the crude product in MeCN and pyridine was attempted, but only orange oil formed.

v_{max}/cm^{-1} = 2959 (CH), 2934 (CH), 2873 (CH), 1481, 1380, 1152, 1107, 1016, 948 (vs), 884, 801 (vs), 643, 585, 556, 544.

4.10.9 Synthesis of (TBA)$_6$[(Ni(II)W$_5$O$_{18}$H)$_2$]

In a Schlenk flask, (TBA)$_2$[W$_6$O$_{19}$] (2.0 g, 1.1 mmol) was suspended in MeCN (10 mL). To a separate flask, TBA(OH) (4.2 mL, 4.2 mmol, 1 M in MeOH) was added and pumped dry. The golden oil was then re-dissolved in MeCN (5 mL). The solvent was then removed under reduced pressure. This process was repeated twice to ensure complete removal of MeOH. The TBA(OH) was then dissolved in MeCN (5 mL) and transferred via cannula to the suspension of (TBA)$_2$[W$_6$O$_{19}$]. The mixture was stirred for 15 minutes or until all the solid dissolved. The mixture was then transferred via cannula to a Schlenk flask containing a green solution of NiCl$_2$.6H$_2$O (0.30 g, 1.3 mmol) dissolved in MeCN (5 mL). The mixture was stirred overnight and gradually turned pale yellow during this time. The solvent was removed under reduced pressure to leave a yellow oil. The oil was triturated in alternation with ethyl acetate (10 mL) and diethyl ether (15 mL), until a free-flowing sandy yellow powder was obtained (2.2 g, 87% yield). The infrared spectrum was recorded. Small quantities of crystals were obtained by vapour diffusion of diethyl ether into a saturated DMF solution of the crude product.

v_{max}/cm^{-1} = 2598 (CH), 2934 (CH), 2871 (CH), 1667, 1480, 1380, 1152, 1107, 2036, 935 (vs), 909, 885, 810 (vs), 769 (vs), 678 (vs), 605, 549, 413 (vs).

4.10.10 Synthesis of (TBA)$_3$[(Py)Ni(II)W$_5$O$_{18}$H]

(TBA)$_6$[(Ni(II)W$_5$O$_{18}$H)$_2$] (2 g, 0.5 mmol) was dissolved in degassed pyridine (10 mL) to give a green solution. The mixture was stirred for 30 minutes before an excess of degassed ethyl acetate (30 mL) was added to the mixture which led to the immediate precipitation of a pale green powder. The reaction solution was decanted away from the solid and then the solid was washed with ethyl acetate (10 mL) and diethyl ether (3 x 10 mL). The solid was then dried under vacuum to give a free-flowing pale green powder (1.8 g, 86% yield). Crystals were be obtained by vapour diffusion of diethyl ether into a saturated solution of the crude product in pyridine. The crystals were separated from the mother liquor and were washed with small amounts of cold ^{i}PrOH or dry lutidine (adducts are not very soluble in lutidine if it is dry). The crystals were then dried under vacuum (0.6 g, 29% yield).

ν_{max}/cm^{-1} = 2958 (CH), 2872 (CH), 1736, 1669, 1602, 1481, 1380, 1241, 1216, 1151, 1107, 1041, 933 (vs), 882, 813 (vs), 770 (vs), 701 (vs), 683 (vs), 634, 546, 427 (vs).

4.10.11 Attempted synthesis of (TBA)$_6$[(Cu(II)W$_5$O$_{18}$H)$_2$]

In a Schlenk flask, (TBA)$_2$[W$_6$O$_{19}$] (2.0 g, 1.1 mmol) was suspended in MeCN (10 mL). To a separate flask, TBA(OH) (4.2 mL, 4.2 mmol, 1 M in MeOH) was added and pumped dry. The golden oil was then re-dissolved in MeCN (5 mL). The solvent was then removed under reduced pressure. This process was repeated twice to ensure complete removal of MeOH. The TBA(OH) was then dissolved in MeCN (5 mL) and transferred via cannula to the suspension of (TBA)$_2$[W$_6$O$_{19}$]. The mixture was stirred for 15 minutes or until all the solid dissolved. The mixture was then transferred via cannula to a Schlenk flask containing a green solution of Cu(acac)$_2$ (0.33 g, 1.3 mmol) dissolved in MeCN (5 mL). The mixture was stirred overnight and gradually turned from dark blue to dark green. The solvent was removed leaving a yellow/brown oil. The oil was scratched in alternation with ethyl acetate (10 mL) and diethyl ether (15 mL) (hexane could also be used if the solid remains sticky after a prolonged period of scratching) until a free-flowing brown powder was obtained (2.0 g, 87% yield).

ν_{max}/cm^{-1} = 2958 (CH), 2934 (CH), 2871 (CH), 1670, 1480, 1380, 1152, 1107, 1057, 1029, 930 (vs), 872, 810 (vs), 772 (vs), 722 (vs), 626, 529, 490, 449, 417 (vs).

4.10.12 Synthesis of (TBA)$_6$[(Zn(II)W$_5$O$_{18}$H)$_2$]

In a Schlenk flask, (TBA)$_2$[W$_6$O$_{19}$] (2.0 g, 1.1 mmol) was suspended in MeCN (10 mL). To a separate flask, TBA(OH) (4.2 mL, 4.2 mmol, 1 M in MeOH) was added and pumped dry. The golden oil was then re-dissolved in MeCN (5 mL). The solvent was then removed under reduced pressure. This process was repeated twice to ensure complete removal of MeOH. The TBA(OH) was then dissolved in MeCN (5 mL) and transferred via cannula to the suspension of (TBA)$_2$[W$_6$O$_{19}$]. The mixture was stirred for 15 minutes or until all the solid dissolved. The mixture was then transferred via cannula to a Schlenk flask containing a green solution of Zn(NO$_3$)$_2$.6H$_2$O (0.38 g, 1.3 mmol) dissolved in MeCN (5 mL). The colourless solution was stirred overnight. The solvent was removed under reduced pressure to leave a colourless oil. The oil was triturated in alternation with ethyl acetate (10 mL) and diethyl ether (15 mL) until a free-flowing white powder was obtained (2.0 g, 79% yield). The infrared spectrum was recorded. Small quantities of crystals were obtained by vapour diffusion of diethyl ether into a saturated MeCN solution of the crude product.

v_{max}/cm^{-1} = 2956 (CH), 2871 (CH), 1482, 1380, 1152, 1107, 1058, 1026, 932 (vs), 877, 809 (vs), 764 (vs), 701 (vs), 697, 554, 529, 483, 425 (vs).

4.10.13 Synthesis of $(TBA)_3[(Py)Zn(II)W_5O_{18}H]$

$(TBA)_6[(Zn(II)W_5O_{18}H)_2]$ (2 g, 0.5 mmol) was dissolved in degassed pyridine (10 mL) to give a colourless solution. The mixture was stirred for 30 minutes before an excess of degassed ethyl acetate (30 mL) was added to the mixture leading to immediate precipitation of a white powder. The reaction solution was decanted and the resulting solid was washed with ethyl acetate (10 mL) and diethyl ether (3 x 10 mL). The solid was then dried under vacuum to give a free-flowing white powder (1.7 g, 82% yield). Crystals can be obtained by vapour diffusion of diethyl ether into a saturated solution of the crude product in pyridine. The crystals were separated from the mother liquor and can be washed with small amounts of cold ^{i}PrOH or dry lutidine (adducts are not very soluble in lutidine if it is dry). The crystals were then dried under vacuum (1.0 g, 48% yield).

v_{max}/cm^{-1} = 2958 (CH), 2934 (CH), 2871 (CH), 1669, 1479 (s), 1380, 1152, 1107, 1036, 929 (vs), 880, 826 (vs), 810 (vs), 771 (vs), 686 (vs), 611, 552, 528, 482, 441, 441 (vs).

4.10.14 Preparation of finely divided magnesium metal

Two stainless steel jars (with O-ring and screw seal) were each filled with magnesium turnings (2 g, 83 mmol) in an argon filled glovebox. Two 10 mm stainless steel balls were added to each jar and the jars were sealed before removing from the glove box. The mixtures were ball milled at 30 Hz for two one-hour periods (allowing the jars to cool to room temperature in between). The jars were then returned to the glovebox before opening. The finely divided magnesium metal was transferred to a screw top vial and stored in the glovebox (3.9 g, 98% yield).

4.10.15 Synthesis of $(TBA)_6[(MgW_5O_{18}H)_2]$ from magnesium metal

In a Schlenk flask, $(TBA)_2[W_6O_{19}]$ (2.0 g, 1.1 mmol) was suspended in MeCN (10 mL). To a separate flask, TBA(OH) (1.7 mL, 1.7 mmol, 1 M in MeOH) was added and pumped dry. The golden oil was re-dissolved in MeCN (2-3 mL). The solvent was removed under reduced pressure. This process was repeated twice to ensure complete removal of MeOH. The TBA(OH) was then dissolved in MeCN (5 mL) and transferred via cannula to the suspension of $(TBA)_2[W_6O_{19}]$. The mixture was stirred for one hour or until all the solid dissolved. H_2O (19.1 μL, 1.1 mmol) was added and the solution was stirred at room temperature overnight.

In a separate Schlenk flask, finely divided magnesium metal (31 mg, 1.3 mmol) was suspended in MeOH (5 mL). The flask was heated to reflux and then sealed after 15 minutes. The mixture was refluxed overnight. The mixture was allowed to cool to room temperature before the previously prepared degradation mixture was added via cannula to the solution. The colourless, but slightly cloudy, solution was stirred at room temperature overnight. The solution was passed through a PTFE syringe filter before the solvent was removed under reduced pressure to leave a colourless oil. The oil was scratched with diethyl ether (3 x 15 mL), giving a free-flowing white powder (2.0 g, 80% yield). The infrared spectrum was recorded. Small quantities of crystals were obtained by vapour diffusion of methyl *tert*-butyl ether into a saturated pyridine solution of the crude product.

v_{max}/cm^{-1} = 3670, 2958 (CH), 2933 (CH), 2872 (CH), 1669, 1481, 1380, 1152, 1106, 1030, 940 (s), 887 (s), 802 (vs), 773, 702, 671, 625 (vs).

4.10.16 Synthesis of (TBA)$_6$[(MgW$_5$O$_{18}$H)$_2$] from Mg(OMe)$_2$

In a Schlenk flask, (TBA)$_2$[W$_6$O$_{19}$] (4.0 g, 2.1 mmol) was suspended in MeCN (15 mL). To a separate flask, TBA(OH) (3.4 mL, 3.4 mmol, 1 M in MeOH) was added and pumped dry. The golden oil was re-dissolved in MeCN (5 mL). The solvent was removed under reduced pressure. This process was repeated twice to ensure complete removal of MeOH. The TBA(OH) was then dissolved in MeCN (5 mL) and transferred via cannula to the suspension of (TBA)$_2$[W$_6$O$_{19}$]. The mixture was stirred for one hour or until all the solid dissolved. H$_2$O (38.1 μL, 2.1 mmol) was added and the solution was stirred at room temperature overnight. The mixture was then added via cannula to a solution of Mg(OMe)$_2$ (0.22 g, 2.5 mmol) in MeOH (20 mL) with stirring. The resulting colourless solution was allowed to stir at room temperature overnight. A small amount of colourless solid formed during this time. The mixture was filtered through Celite and the solvent was removed. The resulting colourless oil was triturated with diethyl ether (3 x 20 mL). This gave a free-flowing white powder that was dried under vacuum (3.9 g, 79% yield).

v_{max}/cm^{-1} = 3674, 2958 (CH), 2933 (CH), 2872 (CH), 1668, 1608, 1480 (vs), 1380, 1152, 1106, 1033, 935 (vs), 883 (s), 804 (vs), 771 (vs), 702 (vs), 674 (vs), 625, 568, 552, 528, 490, 445 (vs).

4.11 References

1. X. Hu and A. C. K. Yip, *Front. Catal.*, 2021, doi.org/10.3389/fctls.2021.667675

2. B. Su, Z.-C. Cao and Z.-J. Shi, *Acc. Chem. Res.*, 2015, 48, 886–896.

3. J. V Obligacion and P. J. Chirik, *Nat. Rev. Chem.*, 2018, 2, 15–34.

4. M. D. Kärkäs and B. Åkermark, *Dalt. Trans.*, 2016, 45, 14421–14461.

5. C. Costentin, M. Robert and J.-M. Savéant, *Chem. Soc. Rev.*, 2013, 42, 2423–2436.

6. K. A. Grice, *Coord. Chem. Rev.*, 2017, 336, 78–95.

7. A. R. Parent and K. Sakai, *ChemSusChem*, 2014, 7, 2070–2080.

8. B. M. Hunter, H. B. Gray and A. M. Müller, *Chem. Rev.*, 2016, 116, 14120–14136.

9. J. C. Védrine, *Catalysts*, 2017, 7, 341.

10. J. C. Védrine, *ChemSusChem*, 2019, 12, 577–588.

11. M. Huynh, C. Shi, S. J. L. Billinge and D. G. Nocera, *J. Am. Chem. Soc.*, 2015, 137, 14887.

12. M. Huynh, D. K. Bediako and D. G. Nocera, *J. Am. Chem. Soc.*, 2014, 136, 6002–6010.

13. M. W. Kanan and D. G. Nocera, *Science*, 2008, 321, 1072–1075.

14. A. M. Ullman, C. N. Brodsky, N. Li, S. L. Zheng and D. G. Nocera, *J. Am. Chem. Soc.*, 2016, 138, 4229–4236.

15. A. Singh, S. L. Y. Chang, R. K. Hocking, U. Bach and L. Spiccia, *Energy Environ. Sci.*, 2013, 6, 579–586.

16. D. K. Bediako, B. Lassalle-Kaiser, Y. Surendranath, J. Yano, V. K. Yachandra and D. G. Nocera, *J. Am. Chem. Soc.*, 2012, 134, 6801–6809.

17. J. Jia, C. Qian, Y. Dong, Y. F. Li, H. Wang, M. Ghoussoub, K. T. Butler, A. Walsh and G. A. Ozin, *Chem. Soc. Rev.*, 2017, 46, 4631–4644.

18. J. Soriano-López, W. Schmitt and M. García-Melchor, *Curr. Opin. Electrochem.*, 2018, 7.

19. J. Sauer and H.-J. Freund, *Catal. Letters*, 2015, 145, 109–125.

20. C. Copéret, M. Chabanas, R. Petroff Saint-Arroman and J.-M. Basset, *Angew. Chem. Int. Ed.*, 2003, 42, 156–181.

21. C. Coperet, *Chem. Rev.*, 2010, 110, 656–680.

22. C. Copéret, A. Comas-Vives, M. P. Conley, D. P. Estes, A. Fedorov, V. Mougel, H. Nagae, F. Núñez-Zarur and P. A. Zhizhko, *Chem. Rev.*, 2016, 116, 323–421.

23. K. Larmier, W.-C. Liao, S. Tada, E. Lam, R. Verel, A. Bansode, A. Urakawa, A. Comas-Vives and C. Copéret, *Angew. Chem. Int. Ed.*, 2017, 56, 2318–2323.

24. S. T. Zheng and G. Y. Yang, *Chem. Soc. Rev.*, 2012, 41, 7623–7646.

25. X.-Y. Zhang, M. T. Pope, M. R. Chance and G. B. Jameson, *Polyhedron*, 1995, 14, 1381–1392.

26. C. M. Tourné, G. F. Tourné, S. A. Malik and T. J. R. Weakley, *J. Inorg. Nucl. Chem.*, 1970, 32, 3875–3890.

27. C. L. Hill and C. M. Prosser-McCartha, *Coord. Chem. Rev.*, 1995, 143, 407–455.

28. L. E. Briand, G. T. Baronetti and H. J. Thomas, *Appl. Catal. A Gen.*, 2003, 256, 37–50.

29. Y. Cao, Q. Chen, C. Shen and L. He, *Molecules*, 2019, 24.

30. G. Maayan, N. Gluz and G. Christou, *Nat. Catal.*, 2018, 1, 48–54.

31. K. Azmani, M. Besora, J. Soriano-López, M. Landolsi, A.-L. Teillout, P. de Oliveira, I.-M. Mbomekallé, J. M. Poblet and J.-R. Galán-Mascarós, *Chem. Sci.*, 2021, 12, 8755-8766.

32. N. Gao, H. Sun, K. Dong, J. Ren, T. Duan, C. Xu and X. Qu, *Nat. Commun.*, 2014, 5, 1–9.

33. F. Li, L. E. VanGelder, W. W. Brennessel and E. M. Matson, *Inorg. Chem.*, 2016, 55, 7332–7334.

34. F. Li, S. H. Carpenter, R. F. Higgins, M. G. Hitt, W. W. Brennessel, M. G. Ferrier, S. K. Cary, J. S. Lezama-Pacheco, J. T. Wright, B. W. Stein, M. P. Shores, M. L. Neidig, S. A. Kozimor and E. M. Matson, *Inorg. Chem.*, 2017, 56, 7065–7080.

35. F. Li, R. L. Meyer, S. H. Carpenter, L. E. VanGelder, A. W. Nichols, C. W. Machan, M. L. Neidig and E. M. Matson, *Chem. Sci.*, 2018, 9, 6379–6389.

36. R. L. Meyer, M. H. Anjass, B. E. Petel, W. W. Brennessel, C. Streb and E. M. Matson, *Chem. – A Eur. J.*, 2020, 26, 9905–9914.

37. L. J. Batchelor, R. Shaw, S. J. Markey, M. Helliwell and E. J. L. McInnes, *Chem. – A Eur. J.*, 2010, 16, 5554–5557.

38. O. Nachtigall, M. Kusserow, R. Clérac, W. Wernsdorfer, M. Menzel, F. Renz, J. Mrozinski and J. Spandl, *Angew. Chem. Int. Ed.*, 2015, 54, 10361–10364.

39. H. Kara, E. Gungor, M. B. Coban and Y. Acar, *Inorg. Chem. Commun.*, 2019, 107, 107466.

40. S. Liu, Y. Deng and F. Xu, *Chem. Commun.*, 2020, 56, 6066–6069.

41. R. P. Bontchev, E. L. Venturini and M. Nyman, *Inorg. Chem.*, 2007, 46, 4483–4491.

42. P. T. Ma, G. Chen, G. Wang and J. P. Wang, Russ. *J. Coord. Chem.*, 2011, 37, 772–775.

43. J. H. Son, C. A. Ohlin and W. H. Casey, *Dalton Trans.*, 2012, 41, 12674–12677.

44. Z. Liang, D. Zhang, Q. Liu, P. Ma, J. Niu and J. Wang, *Inorg. Chem. Commun.*, 2015, 54, 19–20.

45. X.-X. Li, L.-J. Zhang, C.-Y. Cui, R.-H. Wang and G.-Y. Yang, *Inorg. Chem.*, 2018, 57, 10323–10330.

46. A. Mohammed, unpublished work.

47. H. Irving and R. J. P. Williams, *J. Chem. Soc.*, 1953, 3192–3210.

48. K. P. Tan, K. Singh, A. Hazra and M. S. Madhusudhan, *Curr. Res. Struct. Biol.*, 2021, **3**, 1–8.

49. Properties of Solvents Used in Organic Chemistry, http://murov.info/orgsolvents.htm (accessed September 2023).

50. K.-K. Guo, M. Xu, Y. Zheng, X.-X. Wang, F.-Y. Li, W.-J. Xu and L. Xu, *Inorg. Chem.*, 2021, **60**, 9097–9109.

51. L. Vilà-Nadal, J. P. Sarasa, A. Rodríguez-Fortea, J. Igual, L. P. Kazansky and J. M. Poblet, *Chem. – An Asian J.*, 2010, **5**, 97–104.

52. O. Yamaguchi, K. Kawabe and K. Shimizu, *J. Chem. Soc., Dalton Trans.*, 1983, 2139–2141.

53. H. S. Jung, J.-K. Lee, J.-Y. Kim and K. S. Hong, *J. Colloid Interface Sci.*, 2003, **259**, 127–132.

54. M. Pascual-Borràs, X. López, A. Rodríguez-Fortea, R. J. Errington and J. M. Poblet, *Chem. Sci.*, 2014, **5**, 2031–2042.

55. J. Banck and A. Schwenk, *Z. Phys. B Condens. Matter*, 1975, **20**, 75–80.

Chapter 5: Moving away from M(II) – Synthesis of M(V) containing hexametalates

5.1 Introduction

The metal(V) oxides are widely studied materials. Vanadium pentoxide is a key component in catalyst materials used industrially for the oxidation of sulphur dioxide to sulphur trioxide during the synthesis of sulfuric acid, and for the conversion of naphthalene to phthalic anhydride.[1-3] Heterogeneous materials, based on the dispersion of V_2O_5 on supports, such as titanium dioxide or aluminium oxide, creating so-called vanadium oxide monolayer catalysts have been extensively investigated and reviewed.[2]

The comparatively lower reactivity of niobium and tantalum pentoxides, with lower mobility (due to higher melting points) and reducibility than V_2O_5, has somewhat limited their application in catalysis. However, there are still multiple examples of systems incorporating niobium[5] and tantalum[6,7] oxides into catalytically active materials. Instead, the oxides of niobium and tantalum have seen more widespread application as solid electrolytic capacitors, photochromic devices and transparent conductive oxides for use in electronic devices.[8,9]

The interest in group V oxide materials, in particular their use as monolayer catalysts on other metal oxide supports, means that a greater understanding of these materials and what factors affect their performance is very desirable. One way to probe these systems is to create a molecular model, in which an atomically precise active site is isolated. The reactivity of this site could then be probed and the impact of systematic changes to the model can be monitored. This could be achieved by incorporating a single group V metal into a polyoxometalate, which acts as a molecular model for a metal oxide support. Some of these systems, based on the Lindqvist structure, have been isolated.

The earliest examples of such structures came from Flynn and Pope who isolated a range of $[V_2W_4O_{19}]^{4-}$ and $[VW_5O_{19}]^{3-}$ salts by acidification of aqueous mixtures of $[WO_4]^{2-}$ and $[VO_3]^{-}$.[10] Simple sodium and potassium salts were obtained by applying the corresponding alkali metal salts of the starting material to the synthesis, whereas quaternary ammonium salts were typically obtained by subsequent ion exchange reactions. Similar methods have been used since by other groups to isolate these compounds and an analogous approach was also used in the isolation of the vanadium substituted Lindqvist-type polyoxomolybdate $(TBA)_3[VMo_5O_{19}]$.[11,12]

Alternatively, Klemperer reported a non-aqueous synthesis of both (TBA)$_3$[VW$_5$O$_{19}$] and (TBA)$_3$[VMo$_5$O$_{19}$].[13] His route first used basic degradation of vanadium pentoxide with tetrabutylammonium hydroxide in acetonitrile to generate a soluble vanadium precursor mixture. This was followed by treatment with either (TBA)$_4$[W$_{10}$O$_{32}$] or (TBA)$_4$[α-Mo$_8$O$_{26}$]. The mixture was refluxed for six hours before cooling and recrystallization. Stirring {W$_{10}$} or {Mo$_8$} with ^{17}O enriched water in acetonitrile prior to addition to the vanadium oxide mixture can be used to conveniently introduce ^{17}O enrichment into the product. This approach is very reminiscent of the basic degradation approach discussed in **Chapters 2-4**.

Access to [NbW$_5$O$_{19}$]$^{3-}$ was first achieved by Dabbabi and Boyer who used a similar acidification approach to those originally used to access [VW$_5$O$_{19}$]$^{3-}$.[14] A key difference was the use of a Lindqvist-type hexaniobate, K$_8$[Nb$_6$O$_{19}$], as a soluble source of niobium.[15,16] Again, the use of a parent hexametalate as a starting component in the synthesis of a bimetallic cluster is similar to methodology that underlines this thesis.

The tantalum derivative, [TaW$_5$O$_{19}$]$^{3-}$, is more commonly accessed using a non-aqueous approach.[17] The reaction involves the dissolution of Ta(OC$_2$H$_5$)$_5$ in acetonitrile followed by acidification with trichloroacetic acid. This solution is then added dropwise to a solution of (TBA)$_2$[WO$_4$] in acetonitrile. The crude product precipitates from the reaction mixture upon addition of diethyl ether. As for the non-aqueous approach to produce (TBA)$_3$[VW$_5$O$_{19}$], the product can be readily ^{17}O enriched by adding ^{17}O enriched water to the solution of (TBA)$_2$[WO$_4$] in acetonitrile. Replacement of Ta(OC$_2$H$_5$)$_5$ with Nb(OC$_2$H$_5$)$_5$ can be used to access (TBA)$_3$[NbW$_5$O$_{19}$]. It should be noted that access to the corresponding compounds using molybdenum as the framework metal, i.e. (TBA)$_3$[NbMo$_5$O$_{19}$] and (TBA)$_3$[TaMo$_5$O$_{19}$], has not been reported.

Some of these group V containing polyoxometalates have been studied for their catalytic properties in their own right. (TBA)$_3$[VW$_5$O$_{19}$] has been used as catalyst for the conversion of cyclooctene to cyclooctene oxide by hydrogen peroxide.[18] On the other hand niobium containing Lindqvist-type polyoxotungstates were used as precursors for hydrodesulfurization catalysts which promote the isomerisation of cyclohexane into methane cyclopentane.[19] Photocatalytic and optical properties have also been explored.[20,21]

5.2 Chapter outline

This chapter describes the application of the generic degradative reassembly approach applied in **Chapters 2** and **4** for the synthesis of [M(II)W$_5$O$_{18}$]$^{3-}$ Lindqvist-type POMs to the synthesis of

analogous M(V) containing species, firstly targeting the known heteropolytungstates (TBA)$_3$[VW$_5$O$_{19}$], (TBA)$_3$[NbW$_5$O$_{19}$], and (TBA)$_3$[TaW$_5$O$_{19}$]. Given the corresponding heteropolymolybdate (TBA)$_3$[VMo$_5$O$_{19}$] is also reported in the literature, the use of the degradative reassembly approach was also applied to target (TBA)$_3$[VMo$_5$O$_{19}$], and the previously unreported POMs (TBA)$_3$[NbMo$_5$O$_{19}$] and (TBA)$_3$[TaMo$_5$O$_{19}$].

The targets were fully characterised using multinuclear NMR spectroscopy (^{51}V, ^{93}Nb, ^{183}W, ^{96}Mo, and ^{17}O) and the redox properties of the series were investigated using cyclic voltammetry to see how the introduction of the group V heterometal alters the redox chemistry of the series with respect to the parent hexametalates, (TBA)$_2$[W$_6$O$_{19}$] and (TBA)$_2$[Mo$_6$O$_{19}$]. Density functional theory calculations are used to support the interpretation of the experimental findings.

Finally, the series of M(V) containing Lindqvist-type POMs was expanded to rhenium. Appropriate rhenium(V) precursors were synthesised by adapting literature methods and they were applied in a similar manner to target (TBA)$_3$[ReW$_5$O$_{19}$] and (TBA)$_3$[ReMo$_5$O$_{19}$], which can be viewed as a model system for the potential incorporation of radioactive technetium into the Lindqvist unit. Preliminary investigations into the redox properties of the POMs and the reactivity of the Re=O unit are presented.

5.3 Synthesis of [M(V)W$_5$O$_{19}$]$^{3-}$ Lindqvist-type POMs

During **Chapter 2** and **4**, a synthetic approach to the synthesis of M(II) substituted Lindqvist-type POMs was outlined. The method, successfully used to incorporate a range of heterometals, involved the degradation of (TBA)$_2$[W$_6$O$_{19}$] with four equivalents of TBA(OH) to target a precursor solution that is theoretically poised to react with simple metal(II) salts, as shown in **Equations 5.1** and **5.2**.

$$5 \ (TBA)_2[W_6O_{19}] + 20 \ (TBA)[OH] \ \rightarrow \ 6 \ (TBA)_5[W_5O_{18}H] + 7 \ H_2O \qquad (5.1)$$

$$2 \ (TBA)_5[W_5O_{18}H] + MX_2 \rightarrow \ (TBA)_6[(MW_5O_{18}H)_2] + 4 \ TBA(X) \qquad (5.2)$$
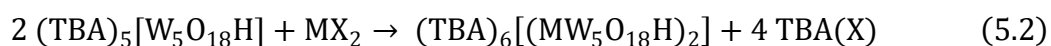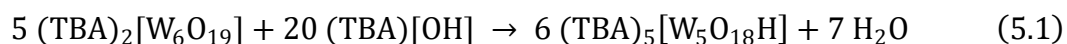
The same rationale can be used to develop a sensible approach for the synthesis of metal(V) containing Lindqvist-type POMs. Again, treatment of the parent hexatungstate with base can be used to generate precursor solutions, however the ratios of (TBA)$_2$[W$_6$O$_{19}$] to base used can be adjusted depending on the source of the heterometal. For example, treatment of (TBA)$_2$[W$_6$O$_{19}$] with 1.6 equivalents of TBA(OH), as shown in **Equation 5.3**, gives the appropriate charge to tungsten ratio required to produce [M(V)W$_5$O$_{19}$]$^{3-}$ by direct reaction

with the corresponding metal oxo-alkoxide, as described in **Equation 5.4**. This approach is advantageous as the free alcohol is the only by-product, and therefore issues associated with removal of tetrabutylammonium salts are mitigated.

$$5 \ (TBA)_2[W_6O_{19}] + 8 \ (TBA)[OH] + 5 \ H_2O \rightarrow \ 6 \ (TBA)_3[W_5O_{18}H_3] \qquad (5.3)$$

$$(TBA)_3[W_5O_{18}H_3] + MO(OR)_3 \rightarrow \ (TBA)_3[MW_5O_{19}] + 3 \ ROH \qquad (5.4)$$
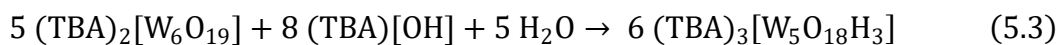
Alternatively, treatment of $(TBA)_2[W_6O_{19}]$ with 5.2 equivalents of base (**Equation 5.5**) gives a more highly charged precursor solution. Theoretically, treatment of this mixture with metal(V) oxo-chlorides provides an alternative pathway to $[M(V)W_5O_{19}]^{3-}$, instead producing three equivalents of TBA(X) as the by-product, **Equation 5.6**. On the surface this is a less desirable approach as the high oxidation state metal chlorides are sensitive to water and therefore additional steps to remove the water produced in the degradation would be required.

$$5 \ (TBA)_2[W_6O_{19}] + 26 \ (TBA)[OH] \ \rightarrow \ 6 \ (TBA)_6[W_5O_{18}] + 13 \ H_2O \qquad (5.5)$$

$$(TBA)_6[W_5O_{18}] + MOX_3 \rightarrow \ (TBA)_3[MW_5O_{19}] + 3 \ TBA(X) \qquad (5.6)$$
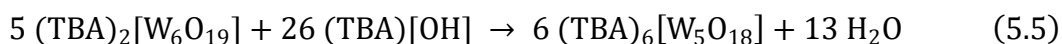
Overall, it is easy to see how the synthetic methods developed in **Chapters 2** and **4** can be adapted to suit several metal(V) precursors and in turn produce the corresponding $\{M(V)W_5\}$ POM. This section will explore this approach using $(TBA)_3[VW_5O_{19}]$, $(TBA)_3[NbW_5O_{19}]$, and $(TBA)_3[TaW_5O_{19}]$ as model systems as multinuclear NMR data is readily available and can be used to confirm the formation of the target compounds. Specifically for vanadium, several heterometal sources are investigated in order to evaluate the pros and cons of each and make some judgement about the optimal approach.

5.3.1 Synthesis of (TBA)₃[VW₅O₁₉]

Our group has previously reported attempts to synthesise $(TBA)_3[VW_5O_{19}]$ by hydrolysis of $VO(OMe)_3/WO(OMe)_4$ in the presence of $(TBA)_2[WO_4]$. The ^{17}O and ^{51}V NMR spectroscopy presented was consistent with the formation of the desired $\{VW_5\}$ POM, however formation of $\{W_6\}$ and other vanadate species was also reported.[22] This result, as well as our groups successful use of M(IV) alkoxides as the heterometal source in the synthesis of $[(MeO)TiW_5O_{18}]^{3-}$ and $[(MeO)SnW_5O_{18}]^{3-}$,[23,24] makes the use of a vanadium oxo-alkoxide as the heterometal source a sensible starting point for these studies.

$VO(OMe)_3$ is commonly prepared simply by stirring $VO(O^tBu)_3$ in methanol, followed by precipitation and recrystallization.[25] Rather than go through this step, $VO(O^tBu)_3$ was chosen

as a suitable reagent for this study as it should behave the same as VO(OMe)$_3$ in these reactions, producing ^{t}BuOH as a by-product instead of MeOH (**Equation 5.7**). VO(O^{t}Bu)$_3$ was prepared by refluxing vanadium(V) pentoxide in *tert*-butanol for five days (**Equation 5.8**). Residual *tert*-butanol was removed by distillation and the crude vandium oxytritertbutoxide was purified by vacuum distillation. The product was identified by a characteristic peak at −672 ppm in the ^{51}V NMR spectrum and 1.44 ppm in the ^{1}H NMR spectrum (from the ^{t}Bu groups). The second fraction collected from the vacuum distillation also contained a small peak at −659 ppm in ^{51}V NMR spectrum and at 1.52 ppm in the ^{1}H NMR spectrum. This may indicate the presence of another vanadium oxo-alkoxide species perhaps formed by hydrolysis of VO(O^{t}Bu)$_3$, however the integrals of the impurity peaks with respect to product were extremely low and therefore the fraction was still considered pure enough for use.

$$(TBA)_3[W_5O_{18}H_3] + VO(O^tBu)_3 \rightarrow (TBA)_3[VW_5O_{19}] + 3\ ^tBuOH \qquad (5.7)$$

$$V_2O_5 + 6\ ^tBuOH \rightarrow 2\ VO(O^tBu)_3 + 3\ H_2O \qquad (5.8)$$
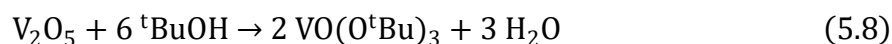
With VO(O^{t}Bu)$_3$ in hand, a small-scale reaction with degraded ^{17}O enriched (TBA)$_2$[W$_6$O$_{19}$*] ({W$_6$*}) was carried out. Addition of a mixture of {W$_6$*} and 1.6 equivalents of TBA(OH) to a solution of VO(O^{t}Bu)$_3$ in acetonitrile led to the immediate formation of a yellow solution, consistent with the formation of (TBA)$_3$[VW$_5$O$_{19}$]. After stirring overnight at room temperature, the solvent was removed, and the crude solid was analysed by ^{17}O NMR spectroscopy. The resulting spectrum, shown in **Figure 5.1**, shows clean formation of (TBA)$_3$[VW$_5$O$_{19}$] with only very small impurity peaks present. The peaks at 1219.8 ppm and 565.8 ppm can be assigned
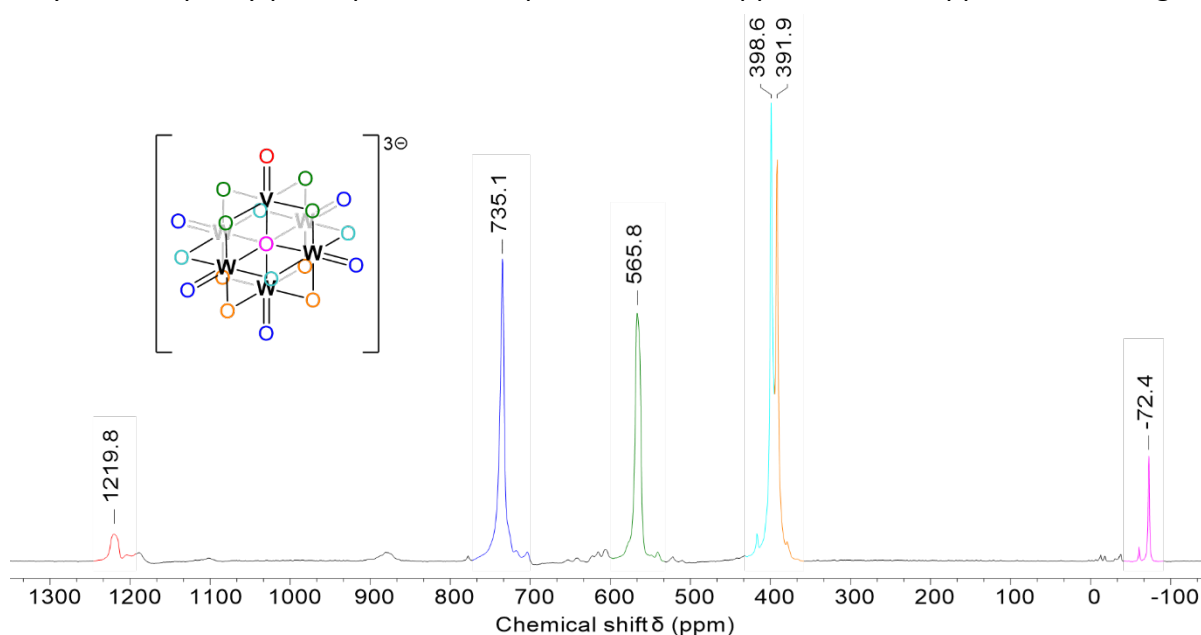
Figure 5.1: ^{17}O NMR spectrum of the crude product after treatment of ^{17}O enriched (TBA)$_2$[W$_6$O$_{19}$] with 1.6 eq. of TBA(OH), followed by reaction with VO(O^{t}Bu)$_3$, recorded in CD$_3$CN.

to the terminal V=O and V-O-W bridges respectively. These peaks are significantly broadened compared to others in the spectrum due to spin-spin coupling to the quadrupolar ^{51}V nucleus (I = 7/2). The sharper peaks at 735.1, 398.6, 391.9 and, −72.4 ppm can be assigned to the remaining oxygens of $[VW_5O_{19}]^{3-}$, as shown in **Figure 5.1**.

Given the encouraging results of the small-scale reaction, a larger (multigram) scale reaction was attempted. The same procedure was employed and the crude solid obtained was readily recrystallized from acetonitrile. The obtained yellow crystals were analysed by ^{51}V NMR spectroscopy and ^{183}W NMR spectroscopy (spectra shown in **Figure 5.2**). The ^{51}V NMR spectrum shows a single peak at -508 ppm, which is characteristic of $(TBA)_3[VW_5O_{19}]$ and suggests that a single recrystallization is adequate to remove any vanadium containing impurities.[11] The ^{183}W NMR spectrum contains a broad feature that appears to contain two peaks, at 78.4 ppm and 79.6 ppm respectively. It is hard to compare the relative intensities of the signals due to the broadness and very similar chemical shift, but these peaks have previously been assigned to the two tungsten environments of $(TBA)_3[VW_5O_{19}]$ (as shown in **Figure 5.2b**) based on previous reports.[11,26] It should be noted that typical chemical shift differences between the axial (blue) and equatorial (red) tungsten environments, for example compared to those reported in this chapter, are significantly bigger than the 1.2 ppm difference reported here.
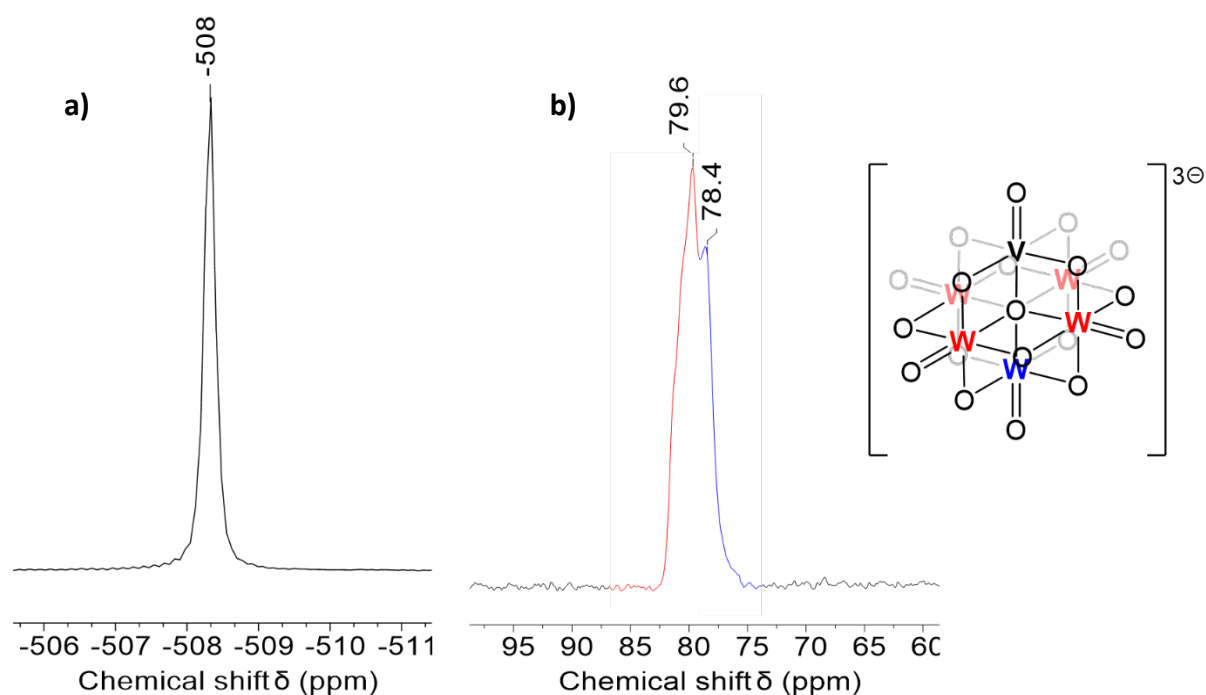
Figure 5.2: ^{51}V (a) and ^{183}W (b) NMR spectra of $(TBA)_3[VW_5O_{19}]$. The ^{51}V NMR spectrum was recorded in CD_3CN and the ^{183}W NMR spectrum was recorded in d_6-DMSO.

These results collectively show that our degradative approach can be applied to the synthesis of $(TBA)_3[VW_5O_{19}]$, using $VO(O^tBu)_3$ as the source of vanadium. However, the use of a hydrolytically sensitive oxo-alkoxide, which has to be synthesised and distilled prior to use, is less than ideal. Because of this, the use of alternative sources of vanadium were explored.

Firstly, the replacement of $VO(O^tBu)_3$ with $VOCl_3$ was examined. Vanadium oxychloride is also very moisture sensitive but it is commercially available and therefore can be used directly in the synthesis. The procedure used above was adapted appropriately to ensure compatibility with $VOCl_3$. Instead of 1.6 equivalents, $(TBA)_2[W_6O_{19}]$ was degraded with 5.2 equivalents of TBA(OH) in acetonitrile to produce a colourless solution. The stoichiometry used in this degradation should lead to the formation of 2.6 equivalents of water relative to $\{W_6\}$, as shown in **Equation 5.5**. This water may be expected to hydrolyse $VOCl_3$, ultimately producing insoluble vanadium oxide (or hydroxides) and releasing acid, which would lower the effective charge to tungsten ratio in the solution and could in turn lead to reformation of $\{W_6\}$. To avoid this, efforts were made to remove any water present in the reaction mixture.

After the water was removed, vanadium oxychloride was slowly added directly to the degradation mixture. Initially, the $VOCl_3$ turns red on contact with the solution. After stirring for approximately 15 minutes, a brown/green solution forms which may indicate the formation of some vanadium(IV) species. The green colour can be removed by adding 1-2 crystals of iodine, further indicating that some vanadium(IV) species are formed that can be re-oxidised via the addition of an oxidising agent. After stirring overnight, the volatiles were removed, and crude yellow/brown oil was recrystallized from the minimum amount of hot acetonitrile. Washing the crystals with small amounts of dichloromethane appears to remove the brown products, leaving the characteristic bright yellow solid. The ^{51}V NMR spectrum showed that the dominant product of the reaction was the target compound $(TBA)_3[VW_5O_{19}]$, evidenced by a large peak at −508 ppm. However, there were two additional small signals at −364 and −510 ppm respectively, indicating the presence of additional vanadium containing products even after recrystallization. These were efficiently removed by a second recrystallization.

Synthesis of $(TBA)_3[VW_5O_{19}]$ from $VOCl_3$ represents an improvement in terms of simplicity over the procedure requiring $VO(O^tBu)_3$. However, $VOCl_3$ is still very moisture sensitive and reactions proceed less cleanly than when employing the metal oxoalkoxide. An ideal approach would employ an air and moisture stable source of vanadium which still gives efficient conversion to $(TBA)_3[VW_5O_{19}]$. With this in mind, the synthesis of $(TBA)_3[VW_5O_{19}]$ was

attempted using vanadium oxide as the source of heterometal, following **Equation 5.9**. V_2O_5 is completely air and moisture stable.

$$2\ (TBA)_3[W_5O_{18}H_3] + V_2O_5 \rightarrow 2\ (TBA)_3[VW_5O_{19}] + 3\ H_2O \quad\quad (5.9)$$

Treatment of $(TBA)_2\{W_6O_{19}*\}$ with 1.6 equivalents of TBA(OH) in pyridine leads to the formation of a colourless solution of the precursor mixture. Solid vanadium pentoxide can then be directly added to the reaction mixture forming a green/brown suspension. Given the extremely low solubility of the V_2O_5, the reaction was heated at reflux and the reaction time was extended to two days to attempt to ensure reaction goes to completion. This is also why pyridine was adopted as the solvent, as previous work by our group has found that heating basic mixtures in acetonitrile can lead to the formation of acetamide as a by-product (which consumes base in the process).

After two days the brown suspension was filtered through celite leaving the characteristic yellow solution seen in previous reactions targeting $(TBA)_3[VW_5O_{19}]$. The volatiles were removed under reduced pressure and the crude solid was recrystallized from hot acetonitrile. The ^{17}O NMR spectrum of the recrystallized material is shown in **Figure 5.3**. The spectrum contains the same characteristic pattern that was shown in **Figure 5.1** and described above. The spectrum is remarkably clean and therefore suggests a single recrystallization is enough to remove any other minor POM products. The ^{51}V NMR spectrum also shows a single peak at −508 ppm, suggesting removal of any other vanadium containing species. Unfortunately, the yield of $(TBA)_3[VW_5O_{19}]$ was slightly lower starting from vanadium pentoxide (63% yield when
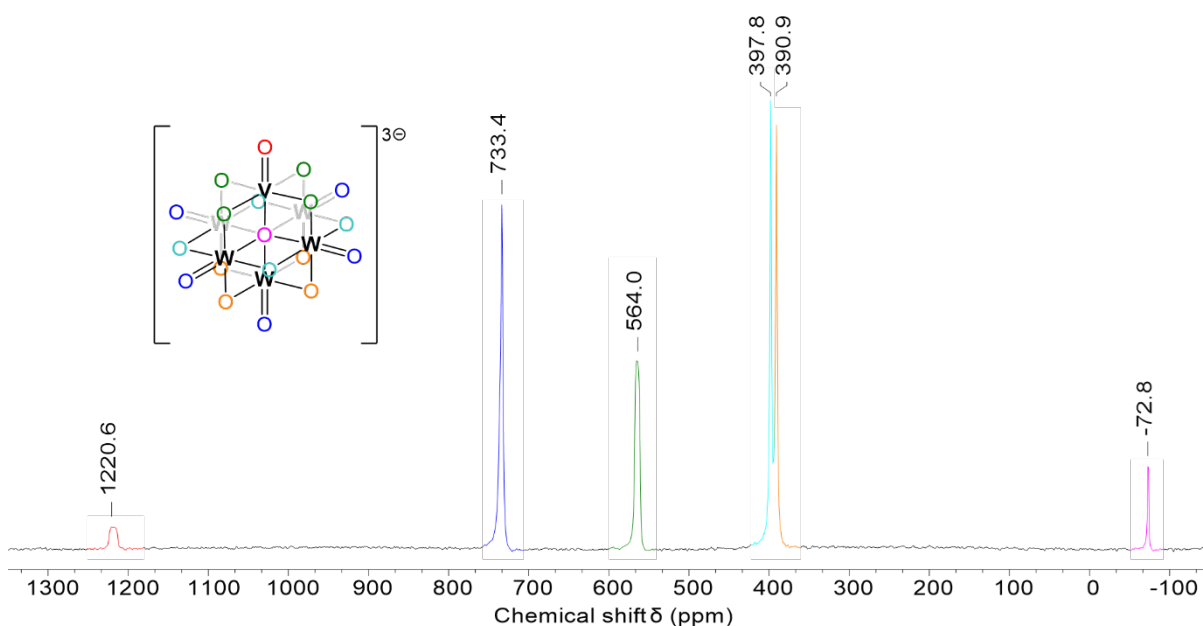
Figure 5.3: ^{17}O NMR spectrum of recrystallized $(TBA)_3[VW_5O_{19}]$ obtained from the reaction of $(TBA)_2[W_6O_{19}]$, TBA(OH) and V_2O_5. The spectrum was recorded in CD_3CN.

using V_2O_5 vs. 83% when using $VO(O^tBu)_3$). This may be attributed to the lower solubility and reactivity of the oxide compared to the oxoalkoxide. Therefore, there is trade-off between the simplicity of using the air and moisture stable oxide as the source of vanadium versus the final yield of the product.

To take it one step further, the synthesis of $(TBA)_3[VW_5O_{19}]$ from both metal oxides was attempted (**Equation 5.10**). In this case hydrated tungsten oxide was used to build the tungsten framework as opposed to $(TBA)_2[W_6O_{19}]$. The appropriate quantity of TBA(OH) in pyridine was added to a Schlenk flask along with $WO_3.H_2O$ and V_2O_5 in a 10:1 ratio. The mixture was then refluxed for three days. A green/brown suspension was obtained which was very similar in appearance to the reaction mixture obtained from the reaction of $\{W_6\}$ and V_2O_5. The suspension was filtered through celite, and the volatiles were removed to leave a crude yellow solid. As previously discussed, this solid could be recrystallized from hot acetonitrile to give bright yellow crystals of $(TBA)_3[VW_5O_{19}]$, confirmed by a single peak in the ^{51}V NMR spectrum at −507 ppm. The yield drops further to only 53% when using both metal oxides as starting materials. This, along with the extended reaction times required, represents a trade-off between the simplicity of the reaction and the efficiency of product formation.

$$10\,WO_3.H_2O + V_2O_5 + 6\,TBA(OH) \rightarrow 2\,(TBA)_3[VW_5O_{19}] +\ 13\,H_2O \qquad (5.10)$$
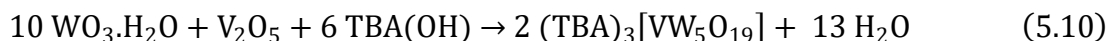
To summarise, this section shows that the degradative reassembly approach developed in **Chapters 2** and **4** is very much applicable to the synthesis of $(TBA)_3[VW_5O_{19}]$. The procedure can be modified to tolerate a range of sources of the heterometal, showing that the approach is very robust and therefore very appealing as a potential platform for the synthesis of a range of metal(V) substituted Lindqvist-type POMs. When comparing the sources of heterometal, it appears that the solubility of the material is important in giving efficient conversion to product. Furthermore, where possible the use of less base is advantageous (as in the case when using $VO(O^tBu)_3$ or V_2O_5) as it leads to the formation of easy to remove by-products, like alcohols or water, as opposed to tetrabutylammonium salts. This is not a major issue for $\{VW_5\}$ as it crystallizes readily, but it may be more important for novel species which are more difficult to recrystallize.

5.3.2 Synthesis of $(TBA)_3[NbW_5O_{19}]$

After successfully synthesising $(TBA)_3[VW_5O_{19}]$ using the degradative reassembly approach with several sources of vanadium, expansion of the methodology to target $(TBA)_3[NbW_5O_{19}]$ was a logical step.

(TBA)₃[NbW₅O₁₉] was synthesised by Klemperer and co-workers by acidification of a mixture of tetrabutylammonium tungstate and niobium ethoxide with trichloroacetic acid.[17] Though this method was effective for producing large quantities of ^{17}O enriched product, the reported yield was only 30-40% (based on W) and therefore there is significant room for improvement. Given the successful use of $VO(O^tBu)_3$ in the synthesis of (TBA)₃[VW₅O₁₉], commercially available niobium ethoxide was a sensible choice as a source of heterometal. $Nb(OEt)_5$ is a liquid under ambient conditions which readily dissolves in acetonitrile and can be applied as shown in **Equation 5.11**.

$$(TBA)_3[W_5O_{18}H_3] + Nb(OEt)_5 + H_2O \rightarrow (TBA)_3[NbW_5O_{19}] + 5\ EtOH \qquad (5.11)$$
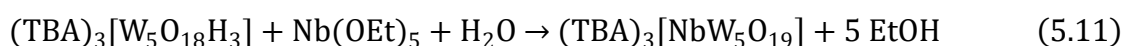
Treatment of (TBA)₂[W₆O₁₉] with 1.6 equivalents of TBA(OH) (and 2.2 eq. of H_2O) was used to generate the precursor solution. This solution was then treated with $Nb(OEt)_5$ and stirred overnight. The volatiles were then removed leaving a crude white solid which was readily recrystallized from hot acetonitrile. The ^{17}O NMR spectrum, shown in **Figure 5.4**, of the resulting white crystals was similar to that obtained during the synthesis of (TBA)₃[VW₅O₁₉]. Large peaks at 734.2 and 393.9 ppm can be assigned to the terminal W=O and W-O-W environments. Though there are two unique W=O environments and two unique W-O-W bridging environments present in (TBA)₃[NbW₅O₁₉], only a single peak is observed for each. This is likely a result of spin-spin coupling between the oxygen nuclei and quadrupolar niobium
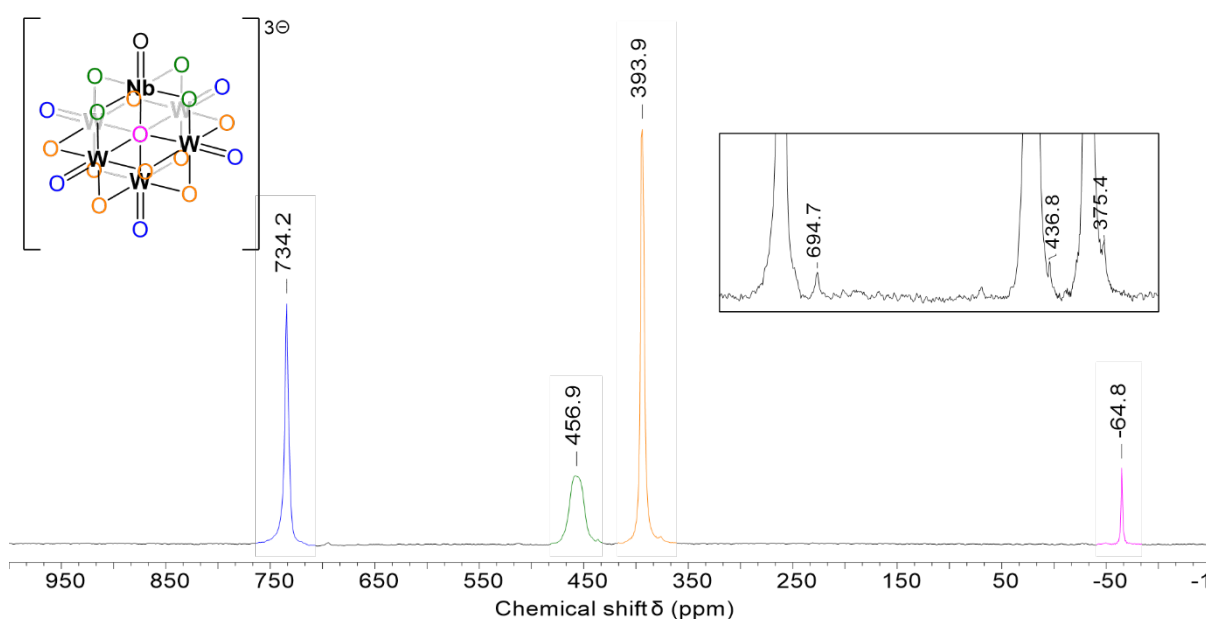
Figure 5.4: ^{17}O NMR spectrum of (TBA)₃[NbW₅O₁₉] obtained from the reaction of (TBA)₂[W₆O₁₉] with TBA(OH) and $Nb(OEt)_5$. The insert in the top right shows a portion of the spectrum providing evidence of the formation of (TBA)₄[Nb₂W₄O₁₉] as a minor product. Spectrum recorded in CD_3CN.

(I = 9/2). This leads to signal broadening and therefore the individual peaks produced by oxygen nuclei in each environment, which have very similar chemical shifts, are not resolved.

The observed signal broadening is even more pronounced for the peak at 456.9 ppm, which can be assigned to the oxygen nuclei of the Nb-O-W bridges, as these nuclei are in closer proximity to the quadrupolar niobium centre. The same effect leads to the lack of observation of peak corresponding to the oxygen of the terminal Nb=O unit. Klemperer, similarly, reported an inability to see this peak in non-niobium decoupled experiments, however the peak is readily observed at 799 ppm when niobium decoupling is employed.[17]

The insert shown in **Figure 5.4**, shows a series of very small peaks observed in the ^{17}O NMR spectrum on top of those assignable to $(TBA)_3[NbW_5O_{19}]$. These peaks are reported to correspond to $(TBA)_4[Nb_2W_4O_{19}]$.[17] The very low intensity of these peaks suggests that a simple recrystallization is sufficient to remove the majority of this impurity, however, a second recrystallization could be used to obtain a purer sample of $(TBA)_3[NbW_5O_{19}]$. The presence of these peaks also implies that adjustment of the amount of TBA(OH) and $Nb(OEt)_5$ used in the reaction may allow direct targeting of $(TBA)_4[Nb_2W_4O_{19}]$ if desired. It should be noted that no evidence of $(TBA)_4[V_2W_4O_{19}]$ was observed during all the efforts to prepare the mono-substituted derivative.

The product was further characterized by [93]Nb and [183]W NMR spectroscopy. The spectra are shown in **Figure 5.5**. The [93]Nb NMR spectrum shows a single broad peak (FWHM = 2700 Hz) at −883 ppm when recorded in d_6-DMSO. This is consistent with the reported value of −888 ppm obtained in acetonitrile (FWHM = 600-800 Hz).[17] The line width obtained in this study is significantly larger but that may be attributed to the change in solvent and the difference in concentrations used (the sample prepared here was approximately an order of magnitude higher in concentration). The [183]W NMR spectrum (**Figure 5.5b**) shows three signals, two at 29.4 and 74.5 ppm respectively (in a 1:4 ratio) which can be assigned to $(TBA)_3[NbW_5O_{19}]$, and a smaller peak at 59.2 ppm which can be attributed to $\{W_6\}$. Analysis of the integrals shows the sample contains about 6.5% $\{W_6\}$ after a single recrystallization. Further recrystallization may allow removal of this contaminant. It is worth mentioning that $\{W_6\}$ impurity was not observed in the ^{17}O NMR spectrum shown in **Figure 5.4**.

The obtained yield of $(TBA)_3[NbW_5O_{19}]$, after recrystallization, of 77% was much higher than the procedure reported by Klemperer. This shows the utility of the synthetic approach outlined
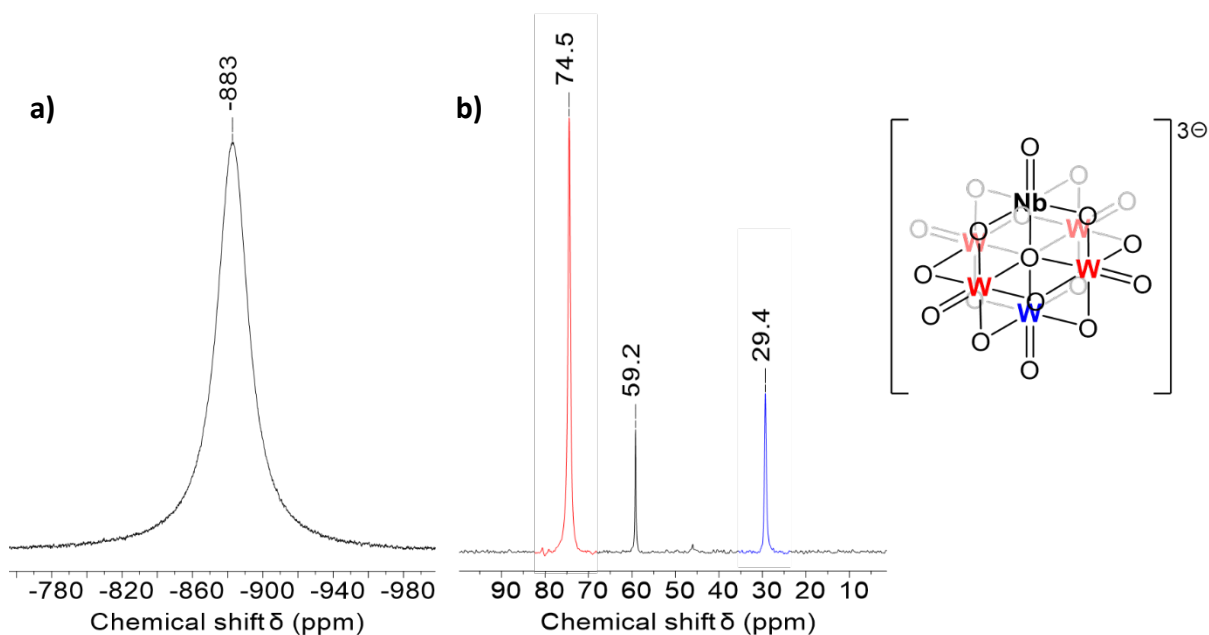
Figure 5.5: ^{93}Nb (a) and ^{183}W (b) NMR spectra of (TBA)$_3$[NbW$_5$O$_{19}$]. Both spectra were recorded in *d*$_6$-DMSO.

here, which is not only tolerant to a range of heterometals in various oxidation states, but also gives good yields of target compounds.

After the successful synthesis of (TBA)$_3$[NbW$_5$O$_{19}$] from Nb(OEt)$_5$, the robustness of the synthetic approach was tested by exploring if the target compound was also accessible from niobium oxychloride, as was the case with vanadium oxychloride.

In order to investigate this, niobium pentachloride was first prepared from hydrated niobium oxide by reaction with thionyl chloride at room temperature, outlined in **Equation 5.12** for the anhydrous oxide (the water of the hydrated oxide also reacts with SOCl$_2$ to give SO$_2$ and HCl).[27] During this time the suspension of the colourless oxide slowly turns into a yellow solution of NbCl$_5$. The volatiles were then removed to leave the crude material which was purified by vacuum sublimation. The obtained niobium pentachloride is then converted to niobium oxychloride by reaction with hexamethyldisiloxane, as shown in **Equation 5.13**.[28] Performing this reaction in acetonitrile led to the formation of the acetonitrile adduct of niobium oxychloride, NbOCl$_3$(MeCN)$_2$, which was readily crystallized directly from the reaction mixture after concentrating.

$$Nb_2O_5 + 5\ SOCl_2 \rightarrow 2\ NbCl_5 + 5\ SO_2 \tag{5.12}$$

$$NbCl_5 + (Me_3Si)_2O + 2\ MeCN \rightarrow NbOCl_3(MeCN)_2 + 2\ Me_3SiCl \tag{5.13}$$
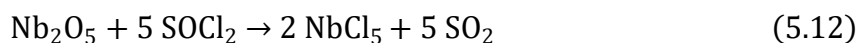
The degradation of $(TBA)_2[W_6O_{19}]$ with 5.2 equivalents of TBA(OH) targeting "$(TBA)_6[W_5O_{18}]$" was performed to prepare an appropriate precursor solution for reaction with niobium oxychloride, which is outlined in **Equation 5.14**.

$$"(TBA)_6[W_5O_{18}]" + NbOCl_3(MeCN)_2 \rightarrow (TBA)_3[NbW_5O_{19}] + 3\ TBA(Cl) + 2\ MeCN \quad (5.14)$$

As was the case when using $VOCl_3$, care was taken to remove the water produced in the degradation step to prevent decomposition of the $NbOCl_3(MeCN)_2$ into insoluble niobium oxide. Additionally, the reaction mixture was also ^{17}O enriched to allow easy monitoring of the reaction progress. This meant that after removal of the water produced in the degradation, ^{17}O enriched water was added to allow statistical enrichment of the degradation products simply by stirring at room temperature overnight. The volatiles, including residual water, were then removed under reduced pressure leaving a thick oil. This oil was then re-dissolved in dry pyridine and the solid $NbOCl_3(MeCN)_2$ was added. The colourless solution was then stirred overnight before removal of the volatiles and recrystallization of the crude product from hot acetonitrile.

The ^{17}O NMR spectrum of the recrystallized product is shown in **Figure 5.6**. The spectrum is very similar to that shown in **Figure 5.4** and shows very efficient formation of $(TBA)_3[NbW_5O_{19}]$ from $NbOCl_3(MeCN)_2$. This adds to the successful formation of $(TBA)_3[VW_5O_{19}]$ from $VOCl_3$ and indicates that metal(V) oxychlorides are viable sources of the heterometal in the synthesis of substituted Lindqvist-type POMs. Small peaks at 415.2 and 776.9 ppm respectively show the
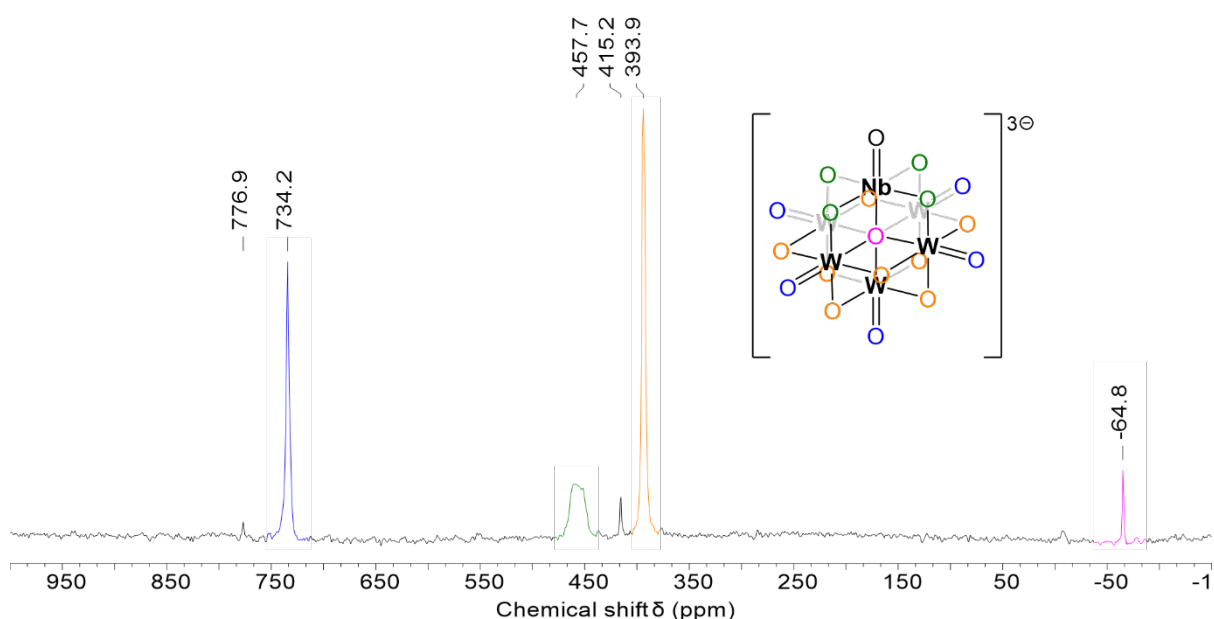
Figure 5.6: ^{17}O NMR spectrum of $(TBA)_3[NbW_5O_{19}]$ obtained from the reaction of $(TBA)_2[W_6O_{19}]$ with TBA(OH) and $NbOCl_3(MeCN)_2$. Spectrum recorded in CD_3CN.

presence of a small amount of $(TBA)_2[W_6O_{19}]$ (approximately 50:1 {NbW_5}:{W_6}) after recrystallization. This may be a result of a small amount hydrolysis of $NbOCl_3(MeCN)_2$ (likely due to residual moisture) during the reaction, which would lead to the release of HCl into the mixture. This acid can then act to effectively lower the charge to tungsten ratio of the mixture and drive to the reformation of {W_6} (i.e. the reverse of the degradation step) as shown in **Equation 5.15** and **5.16**.

$$2\ NbOCl_3(MeCN)_2 + 3\ H_2O \rightarrow Nb_2O_5 + 6\ HCl + 4\ MeCN \qquad (5.15)$$

$$6\ (TBA)_6[W_5O_{18}] + 26\ HCl \rightarrow 5\ (TBA)_2[W_6O_{19}] + 26\ TBA(Cl) \qquad (5.16)$$
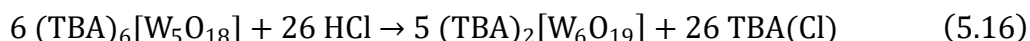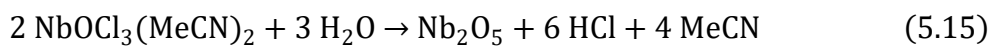
Given the very low intensity of these peaks with respect to the product, this must be only a minor process compared to the assembly of $(TBA)_3[NbW_5O_{19}]$. There was no evidence of {W_6} formation when using $Nb(OEt)_5$ as the source of heterometal. This makes sense as, although $Nb(OEt)_5$ is moisture sensitive, it degrades to give Nb_2O_5 and EtOH, which will not drive the formation of {W_6}. Interestingly, the ^{17}O NMR spectrum obtained when using $NbOCl_3(MeCN)_2$ shows no evidence of formation of $(TBA)_4[Nb_2W_4O_{19}]$. Clearly different processes are competing when using $NbOCl_3(MeCN)_2$ as a source of the heterometal when compared to $Nb(OEt)_5$, which may be a result of different mechanisms of assembly.

5.3.3 Synthesis of $(TBA)_3[TaW_5O_{19}]$

After successfully synthesising both $(TBA)_3[VW_5O_{19}]$ and $(TBA)_3[NbW_5O_{19}]$ using adapted versions of the degradative reassembly approach developed in **Chapters 2** and **4**, attention was turned to the synthesis of $(TBA)_3[TaW_5O_{19}]$, to complete the series of group V substituted Lindqvist-type polyoxotungstates. As for the niobium derivative, $(TBA)_3[TaW_5O_{19}]$ has previously been prepared by acidification of a mixture of tetrabutylammonium tungstate and tantalum ethoxide with trichloroacetic acid in acetonitrile. The reported yield after recrystallization, was comparable to the niobium derivative at around 40%.[17]

Using an approach completely analogous to that used to synthesise $(TBA)_3[NbW_5O_{19}]$ from niobium ethoxide (shown in **Equation 5.17**), tantalum ethoxide can be reacted with the product of degradation of {W_6} with 1.6 equivalents of TBA(OH). Direct addition of $Ta(OEt)_5$ to this solution gives a colourless solution which was stirred overnight. The volatiles were then removed to leave a colourless tacky solid, which can be recrystallized from hot acetonitrile to give large colourless crystals.

$$(TBA)_3[W_5O_{18}H_3] + Ta(OEt)_5 + H_2O \rightarrow (TBA)_3[TaW_5O_{19}] + 5\ EtOH \qquad (5.17)$$
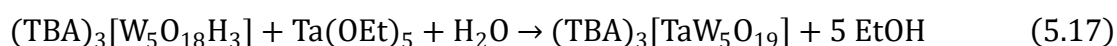
The ^{17}O NMR spectrum of the obtained crystalline solid is shown in **Figure 5.7**. The pattern observed is very reminiscent of that observed for (TBA)$_3$[VW$_5$O$_{19}$] and (TBA)$_3$[NbW$_5$O$_{19}$], and is therefore consistent with the formation of the target (TBA)$_3$[TaW$_5$O$_{19}$]. The large peak at 736.3 ppm can be assigned to the oxygen nuclei of the terminal W=O units. As seen for the other {M(V)W$_5$}-type POMs discussed so far, separate peaks for the two unique W=O environments (which should appear is a 4:1 ratio) are not observed and instead a single peak is detected.

The peaks at 421.6 and 395.0 ppm, which appear in a 1:2 ratio, can be assigned to the oxygen nuclei of the bridging Ta-O-W and W-O-W groups respectively. The peak assigned to the bridging oxygen nuclei directly adjacent to tantalum (green) is substantially narrower in {TaW$_5$} when compared to {NbW$_5$} or {VW$_5$}. Though tantalum is also quadrupolar (I = 7/2), it's quadrupole moment (Q = 3 b) is significantly larger than that of vanadium (Q = −0.05 b) or niobium (Q = −0.2 b). This leads to rapid metal quadrupole relaxation which in turn serves to decouple the metal spins from the oxygen spins.[17] The lack of interaction between the oxygen and metal nuclei means there is no broadening effect.

Given this, it may be expected that a sharp peak for the oxygen of the Ta=O should be resolved. However, we do not observe it, which must imply that the oxygen of the terminal Ta=O is not readily enriched during the reaction. Non-statistical enrichment was also observed by Klemperer and co-workers in their ^{17}O NMR studies.[17] The central μ_6-oxygen nucleus of (TBA)$_3$[TaW$_5$O$_{19}$] produced a peak at −72.7 ppm.
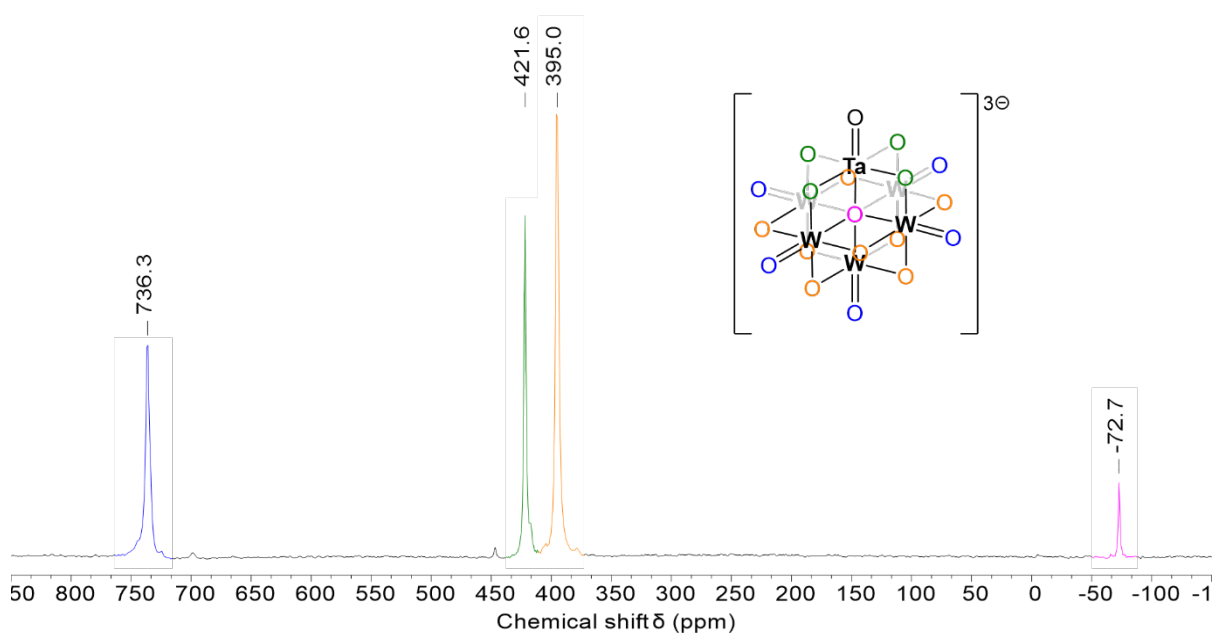
Figure 5.7: ^{17}O NMR spectrum of (TBA)$_3$[TaW$_5$O$_{19}$] obtained from the reaction of (TBA)$_2$[W$_6$O$_{19}$] with TBA(OH) and Ta(OEt)$_5$. Spectrum recorded in CD$_3$CN.
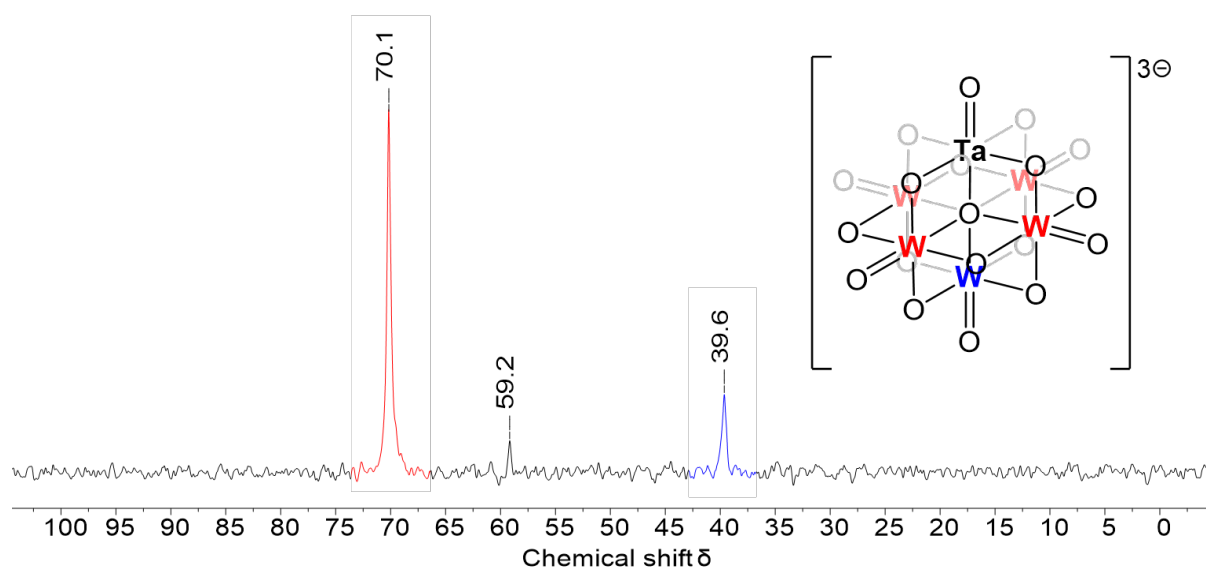
Figure 5.8: ^{183}W NMR spectrum of (TBA)$_3$[TaW$_5$O$_{19}$] recorded in d_6-DMSO. Small peak at 59.2 ppm due to (TBA)$_2$[W$_6$O$_{19}$] impurity.

The ^{183}W NMR spectrum was also recorded and is shown in **Figure 5.8**. It is very similar to that of (TBA)$_3$[NbW$_5$O$_{19}$], showing two peaks in a 4:1 ratio at 70.1 and 39.6 ppm respectively. There is also a small peak at 59.2 ppm which can be assigned to {W$_6$}. As with the niobium analogue, evidence of {W$_6$} was not observed in ^{17}O experiments but is seen in the ^{183}W NMR spectrum, perhaps implying that the higher solubility in DMSO allows resolution of the impurity. Again, it may be that a second recrystallization is required to remove this residual {W$_6$}.

Given the successful isolation of (TBA)$_3$[TaW$_5$O$_{19}$] from Ta(OEt)$_5$, and the time constraints of the project, alternative sources of tantalum were not investigated. An obvious alternative is TaOCl$_3$ which theoretically should behave very similar to VOCl$_3$ and NbOCl$_3$(MeCN)$_2$, which have been applied here.

To conclude this section, it has been shown that the degradative reassembly approach, discussed in **Chapters 2** and **4** for the synthesis of M(II) containing Lindqvist-type polyoxotungstates, can be efficiently modified and applied to produce the group V containing analogues. Metal alkoxides, metal oxychlorides and simple metal oxides have all been investigated as sources of the heterometal and have all proven to be viable starting materials. The choice of starting materials comes down to a trade-off between sensitivity (and therefore difficulty to handle), reactivity, and efficiency of product formation.

5.4 Synthesis of $[M(V)Mo_5O_{19}]^{3-}$ Lindqvist-type POMs

The methods outlined in **Chapter 2**, **4**, and the beginning of this chapter have shown the efficient use of a degradative reassembly approach, based on treatment of tetrabutylammonium hexatungstate with varying amounts of tetrabutylammonium hydroxide, to access several heterometal containing Lindqvist-type heteropolytungstates. This work built off previous work of our group investigating the use of controlled alkoxide hydrolysis, in the presence of tetrabutylammonium tungstate, to access analogous species.[22]

Similarly, our group has previously used the hydrolysis of mixtures of $(TBA)_2[Mo_2O_7]$, $(TBA)_4[Mo_8O_{26}]$, and titanium alkoxides to produce titanium substituted Lindqvist-type polyoxomolybdates (i.e. $(TBA)_3[(RO)TiMo_5O_{18}]$ where R = ^iPr or ^iBu), as shown in **Equation 5.18**. The group subsequently investigated the reactivity of the Ti-OR group towards a range of alcohols and water.[29]

$$(TBA)_2[Mo_2O_7] + (TBA)_4[Mo_8O_{26}] + 2\,Ti(OR)_4 + 3\,H_2O \rightarrow$$
$$2\,(TBA)_3[(RO)TiW_5O_{18}] + 6\,ROH \qquad (5.18)$$
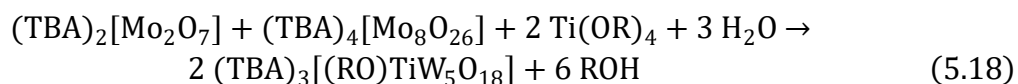
Like $(TBA)_3[VW_5O_{19}]$, $(TBA)_3[VMo_5O_{19}]$ is already known in the literature.[11,12] It has been synthesised both using aqueous and non-aqueous methods. The aqueous route involves acidification of a solution of monomeric sodium orthovanadate (Na_3VO_4) and sodium molybdate $(Na_2MoO_4.2H_2O)$ with HCl. This is followed by addition of a simple tetrabutylammonium salt to precipitate $(TBA)_3[VMo_5O_{19}]$.[12] The non-aqueous method involves the reaction of V_2O_5 with TBA(OH) (likely forming an intermediate mono- or polyoxovanadate species) followed by the addition of $(TBA)_4[Mo_8O_{26}]$ and refluxing for six hours.[13] This method is somewhat like the degradative approach developed in these studies.

These results together suggest that the synthetic methodology outlined in **Section 5.3** may be extended to the analogous polyoxomolybdates. Unlike for the tungsten derivatives, $(TBA)_3[NbMo_5O_{19}]$ and $(TBA)_3[TaMo_5O_{19}]$ are not reported in the literature. Extension of the series of M(V) containing Lindqvist-type polyoxometalates to complete the series (i.e all tungsten and molybdenum derivatives) is desirable. This would allow precise control of the redox properties of the system by providing the ability to vary both the heterometal and framework metal.

This section starts by briefly exploring non-aqueous isopolymolybdate speciation using ^{17}O NMR spectroscopy in order to give some insight into the nature of reaction intermediates for the molybdenum system (as was done in detail in **Chapter 3** for tungsten). Attention then turns

to applying our method to the synthesis of the known compound $(TBA)_3[VMo_5O_{19}]$. Finally, attempts were made to extend the series of metal(V) containing Lindqvist-type heteropolymolybdates to the niobium and tantalum derivatives.

5.4.1 Non-aqueous isopolymolybdate speciation

Treatment of $(TBA)_2[W_6O_{19}]$ with TBA(OH) has been used to increase the charge to tungsten ratio present in reaction mixtures and in turn lead to the conversion of hexatungstate into a number of other isopolytungstate species. Detailed ^{183}W and ^{17}O NMR studies were presented in **Chapter 3** and showed that mixtures consisted primarily of $[WO_4]^{2-}$, $[W_{10}O_{32}]^{4-}$, $[W_7O_{24}H]^{5-}$, and three currently unidentified species. Similarly, treatment of $(TBA)_2[Mo_6O_{19}]$ with varying amounts of TBA(OH) should predictably lead to the conversion of hexamolybdate into other isopolymolybdate species. However, the known isopolymolybdate structures differ from those of tungsten, with $[Mo_2O_7]^{2-}$ and $[Mo_8O_{26}]^{4-}$ known but the analogous decamolybdate "$[Mo_{10}O_{32}]^{4-}$" is not seen, and therefore we may expect the non-aqueous solution speciation to differ significantly.

Unlike ^{183}W, quadrupolar ^{95}Mo ($I = 5/2$) is known to give very broad signals (hundreds to thousands of hertz) for lower symmetry species like those containing multiple unique Mo environments.[30] This means ^{95}Mo NMR spectroscopy is a far less useful tool for understanding complex mixtures of molybdenum containing species when compared to using ^{183}W NMR spectroscopy to analyse the analogous tungsten-based systems. Instead, ^{17}O NMR spectroscopy will be the primary tool used to analyse these mixtures.

^{17}O enriched $(TBA)_2[Mo_6O_{19}]$ was previously obtained by Klemperer by stirring a solution of $(TBA)_4[\alpha-Mo_8O_{26}]$ with ^{17}O enriched water followed by careful acidification to drive the rearrangement to $(TBA)_2[Mo_6O_{19}]$. In this study, an alternative, solvent-free, approach was used. It was found that $(TBA)_2[Mo_6O_{19}]$ can readily be statistically enriched by ball-milling with stoichiometric amounts of 40% ^{17}O enriched water for two hours at 30 Hz. The obtained pale-yellow powder can be dried in a vacuum oven to remove residual water. The ^{17}O NMR spectrum of the resulting solid, without recrystallization, is shown in **Figure 5.9**. The spectrum shows clean enrichment at all positions without any conversion to other isopolymolybdate species. Characteristic peaks for the terminal Mo=O nuclei and bridging Mo-O-Mo nuclei are observed at 937.3 ppm and 555.5 ppm respectively. The signal at −25.4 ppm can be assigned to the central μ_6-oxo. Like for $(TBA)_2[W_6O_{19}]$, the relaxation time (T1) of this oxygen is expected to be very long due to the highly symmetrical environment and was determined using an
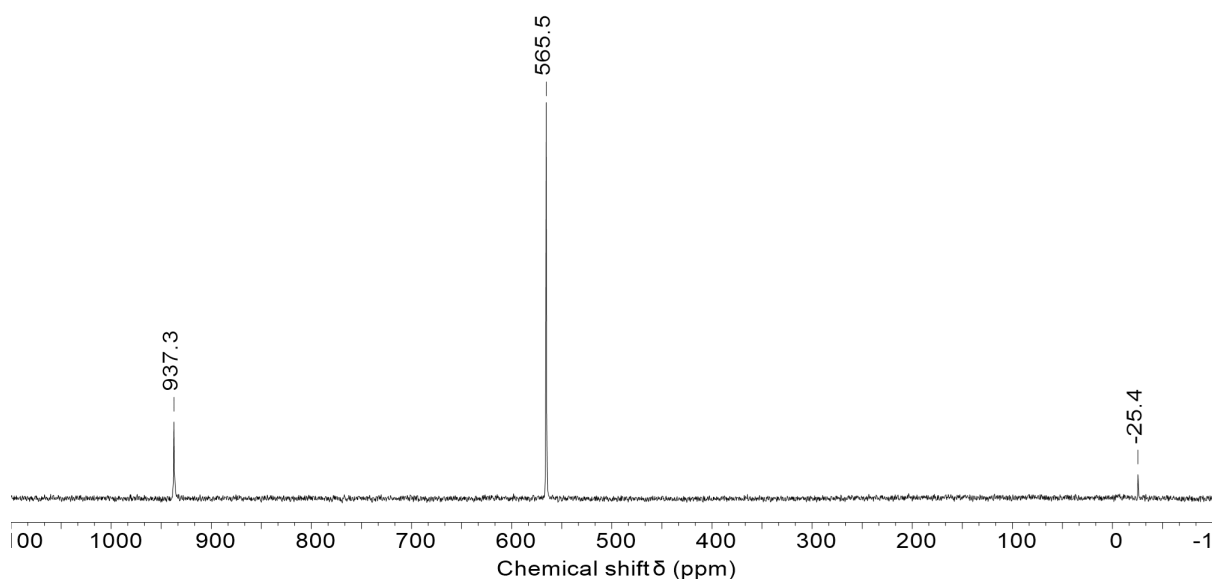
Figure 5.9: The ^{17}O NMR spectrum of enriched $(TBA)_2[Mo_6O_{19}]$ in CD_3CN. Spectrum recorded with a delay time of 10 seconds.

inverse recovery sequence. T1 was found to be approximately 51($\pm$2) seconds. A relaxation delay of 10 seconds was used to acquire the spectrum in **Figure 5.9** which is not sufficient to allow complete relation of the central oxygen nucleus and explains the apparent sub-statistical enrichment of the central oxygen. Repeating the experiment with a delay time of around 500 seconds could be used to give a more accurate intensity for the signal.

The obtained ^{17}O enriched $(TBA)_2[Mo_6O_{19}]$ was then treated with varying amounts of TBA(OH) to study the resulting non-aqueous solution speciation at charge to molybdenum ratios between 0.4 and 2. Experiments were carried out at room temperature in acetonitrile and reactions were given at least 24 hours to equilibrate. The ^{17}O NMR spectra were then recorded and the resulting spectra are shown in **Figure 5.10**. Peaks that can be assigned to known isopolymolybdates are highlighted in various colours and a key is given below.[13]

The addition of 0.4 equivalents of TBA(OH) per {Mo_6} was used to target a Z/Mo ratio of 0.4. The ^{17}O NMR spectrum obtained at this ratio is shown in **Figure 5.10a**. Immediately, it can be seen that the characteristic peaks of {Mo_6} are still visible at 997.3 and 555.2 ppm respectively (highlighted in orange). This shows that there is incomplete conversion of {Mo_6} into other species at this ratio. The {Mo_6} that has undergone reaction appears to have primarily converted into isomers of $[Mo_8O_{26}]^{4-}$. The major product is the α-isomer, evidenced by broad peaks at 868.4, 782.7, 499.9 and, 400.6 ppm respectively (highlighted in blue). Traces of the β-isomer are also present, as shown by small peaks at 896.3, 746.2, 421.2, 300.9, and 60.1 ppm (highlighted in pink). The mixture of {Mo_6} and {Mo_8} obtained at this ratio appears sensible

a) Z/Mo = 0.4

937.3
909.2
896.3
868.4
565.2
782.7
746.2
499.9
421.2
400.6
300.9
60.1
-5.7

b) Z/Mo = 0.5

885.5
868.4
819.2
784.7
746.2
717.1
553.9
499.8
414.5
400.6
301.4
252.0
61.8
44.3
-6.6

c) Z/Mo = 0.6

716.9
909.2
885.5
869.3
818.9
784.9
553.8
499.0
438.9
423.2
417.1
398.1
301.1
252.1
61.8
-5.1

d) Z/Mo = 0.7

716.1
884.3
870.4
818.7
784.7
553.9
499.9
439.4
424.0
396.0
253.7
61.8
-5.3

Chemical shift δ (ppm)

● $[Mo_6O_{19}]^{2-}$ ● α-$[Mo_8O_{26}]^{4-}$ ● β-$[Mo_8O_{26}]^{4-}$ ● $[Mo_2O_7]^{2-}$ ● $[MoO_4]^{2-}$

183

e) Z/Mo = 0.8
870.0
715.3
554.2
390.0
253.4
-4.8

f) Z/Mo = 0.9
715.3
252.6
-5.6

g) Z/Mo = 1.0
716.1
540.8
254.2
-4.0

h) Z/Mo = 1.2
716.1
540.8
254.2
-4.6
-27.7

Chemical shift δ (ppm)

● $[Mo_6O_{19}]^{2-}$ ● α-$[Mo_8O_{26}]^{4-}$ ● β-$[Mo_8O_{26}]^{4-}$ ● $[Mo_2O_7]^{2-}$ ● $[MoO_4]^{2-}$

Figure 5.10: ^{17}O NMR spectra obtained from the reaction of $(TBA)_2[Mo_6O_{19}]$ with between 0.4 and 10 equivalents of TBA(OH). The reactions were stirred for at least 24 hours at room temperature. Spectra recorded in acetonitrile.

as these are the two isopolymolybdate species known to exist in organic media with the lowest Z/Mo ratios ({Mo_6} = 0.33 and {Mo_8} = 0.5). The broad peak at −5.7 ppm can be assigned to water.

Increasing the Z/Mo ratio of the solution to 0.5 leads to complete consumption of all hexamolybdate (**Figure 5.10b**). This in turn increases the proportion of $\alpha\text{-}[Mo_8O_{26}]^{4-}$ significantly, while the *β*-isomer remains as only a minor product. There are now also peaks at 717.1 and 252.0 ppm (highlighted in red), which indicate the presence of $[Mo_2O_7]^{2-}$. This could be considered surprising as the Z/Mo ratio of {Mo_2} = 1, and therefore it may have been expected to be present only after the addition of larger quantities of base. However, its formation after the addition of just one equivalent of base (required to reach Z/Mo = 0.5) suggests that it is stable even in fairly low charge mixtures.

The spectra shown in **Figures 5.10c-f** show the result of gradually increasing the Z/Mo ratio from 0.6 to 0.9. They show a gradual decrease in the amount of {Mo_8} (both isomers) and the corresponding increase in the proportion of {Mo_2} present in the mixture. This finally settles

at Z/Mo = 0.9, where the solution appears to solely consist of {Mo$_2$}. This represents a stark contrast with the tungsten-based system which was dominated by numerous unknown species in this region. This may be largely attributed to the stability of dimolybdate (i.e. [Mo$_2$O$_7$]$^{2-}$) and the apparent instability of ditungstate in non-aqueous solution. Access to a stable species with a high Z/M ratio provides a convenient sink for the charge being added to the mixture and consequently leads to very fairly simple mixtures for molybdenum, which consist of varying ratios of {Mo$_8$} and {Mo$_2$}.

This agrees nicely with the experimental work previously done by our group targeting (TBA)$_3$[(RO)TiMo$_5$O$_{18}$]. In this work, rather than targeting a "[Mo$_5$O$_{18}$H$_3$]$^{3-}$" precursor (Z/Mo = 0.6) by degrading {Mo$_6$}, they used a mixture of {Mo$_2$} and {Mo$_8$} as shown in **Equation 5.19**. Similarly, rather than targeting "[Mo$_5$O$_{18}$H$_3$]" we can express the degradation of {Mo$_6$} with 1.6 equivalents (Z/Mo = 0.6) as targeting a 1:1 mixture of {Mo$_8$} and {Mo$_2$}, as shown in **Equation 5.20**. The obtained ^{17}O NMR spectrum at Z/Mo = 0.6 (**Figure 5.10c**) shows we do indeed obtain a mixture of {Mo$_8$} and {Mo$_2$} and therefore suggests that degradation of {Mo$_6$} with TBA(OH) should be an appropriate method of accessing reactive solutions which can go on to form [MMo$_5$O$_{19}$]$^{3-}$-type POMs.

$$(TBA)_2[Mo_2O_7] + (TBA)_4[Mo_8O_{26}] + 3\,H_2O \rightarrow\ 6\,(TBA)_3[Mo_5O_{18}H_3] \qquad (5.19)$$

$$5\,(TBA)_2[Mo_6O_{19}] + 8\,TBA(OH) \rightarrow$$
$$3\,(TBA)_2[Mo_2O_7] + 3\,(TBA)_4[Mo_8O_{26}] + 4\,H_2O \qquad (5.20)$$
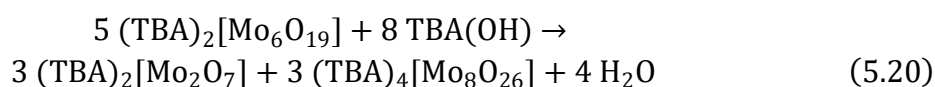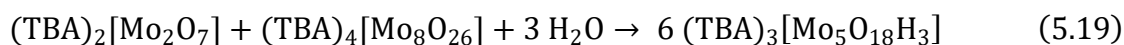
It should also be noted that there are several small peaks at 819, 785, and 554 ppm which appear in **Figures 5.10c-e** which have not been assigned and may correspond to a currently unidentified species.

When increasing the Z/Mo ratio further (shown in **Figures 5.10g-j**) a large peak at 540.8 ppm is observed which indicates the formation of monomeric [MoO$_4$]$^{2-}$. The relative amount of {Mo$_2$} gradually decreases over this period, eventually just leaving monomeric molybdate at Z/Mo = 2. The formation of monomeric tungstate was observed at much lower Z/M ratios, which again is likely to be a consequence of the lack of access to stable isopolytungstate species with higher M/Z ratios. The access to {Mo$_2$} in non-aqueous polyoxomolybdate speciation allows the charge added to the mixture to be effectively "stored" as dimolybdate and only when going beyond the Z/M ratio of {Mo$_2$} (Z/Mo = 1) is the formation of monomeric molybdate observed. The more highly charged mixtures also contain an additional peak at ca. −27 ppm. This is significantly more upfield than for water (which is consistently observed

between -2 and -7 ppm) and may be caused by the interaction of water (or hydroxide) with the highly basic POMs present.

Overall, when compared to non-aqueous isopolytungstate speciation, the molybdenum case is far easier to follow, with mixtures largely consisting of the known α- and β-$[Mo_8O_{26}]^{4-}$, $[Mo_2O_7]^{2-}$, and $[MoO_4]^{2-}$ in different ratios to compensate for charge present in the mixture. Thus, alongside the degradation of {Mo$_6$} with TBA(OH), combinations of these known species could be used as precursors for accessing heterometal substituted species. This may be attractive as these materials can be readily ^{17}O enriched by simply stirring acetonitrile solutions of the compound with ^{17}O enriched water.

5.4.2 Synthesis of (TBA)$_3$[VMo$_5$O$_{19}$]

After investigating non-aqueous isopolymolybdate speciation, it is apparent that the synthetic approach used to target (TBA)$_3$[VMo$_5$O$_{19}$] could vary. The evidence presented in the previous section suggests that rather than using the degradation of {Mo$_6$} with TBA(OH), using a one-to-one mixture of {Mo$_8$}/{Mo$_2$} would be a viable method to prepare the precursor mixture required to react with the heterometal source. This may be advantageous as the highly soluble molybdenum precursors could be combined with the heterometal source prior to addition of water. This could allow the species to interact before hydrolysis and limit unwanted side reactions with the heterometal source (e.g. hydrolysis to insoluble metal oxides).

However, given the consistent success of the degradative reassembly approach presented throughout this thesis, and the ease of preparation of the starting materials, this approach will remain as the focus of this work. Also, considering the results obtained from the use of a variety of vanadium sources in **Section 5.3.1**, V$_2$O$_5$ was chosen as the source of heterometal as it gave reasonable yields while also being air and moisture stable.

With this in mind, the synthesis of (TBA)$_3$[VMo$_5$O$_{19}$] was carried out. Firstly, (TBA)$_2$[Mo$_6$O$_{19}$] was reacted with 1.6 equivalents of TBA(OH) and one equivalent of water in pyridine. This led to the formation of a pale brown solution. This was then treated with solid V$_2$O$_5$, forming a brown suspension which was refluxed for two days. Filtration of this mixture gave a bright yellow solution reminiscent of those obtained during the synthesis of (TBA)$_3$[VW$_5$O$_{19}$]. After removal of the solvent and recrystallization from hot MeCN, the ^{17}O NMR spectrum was recorded and is shown in **Figure 5.11**.
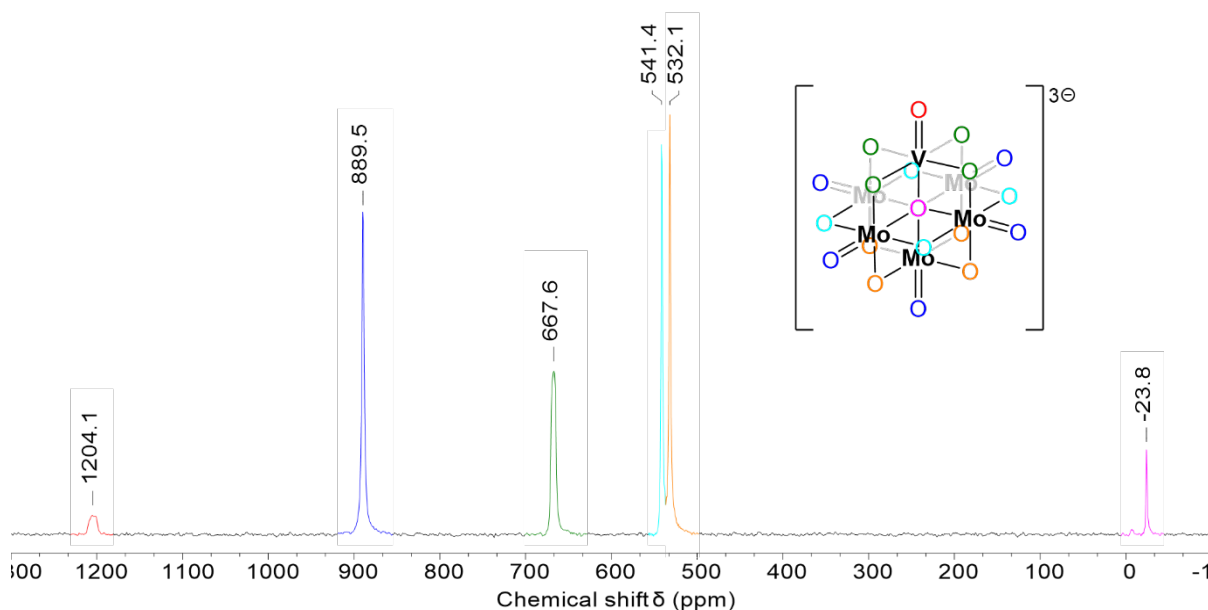
Figure 5.11: ^{17}O NMR spectrum of $(TBA)_3[VMo_5O_{19}]$ obtained from the reaction of $(TBA)_2[Mo_6O_{19}]$ with TBA(OH) and V_2O_5. Spectrum recorded in CD_3CN.

The spectrum obtained is very similar to that of $(TBA)_3[VW_5O_{19}]$. The broad peak at 1204.1 ppm can be assigned to the terminal V=O unit and is just 16 ppm away from the peak observed in the corresponding tungsten compound. This peak is broad due to ^{51}V-^{17}O coupling. The peak at 889.5 ppm can be assigned to the five terminal Mo=O groups. Though there should be two peaks in a 4:1 ratio for these oxygen nuclei, the individual environments are not resolved. The peak at 667.6 ppm corresponds to the bridging V-O-Mo nuclei, and again is broadened by coupling to quadrupolar vanadium. The two peaks at 541.4 and 532.1 ppm are assignable to the two Mo-O-Mo environments present in the structure. Though they have been colour coded for clarity in **Figure 5.11**, the allocation given is arbitrary as a definite assignment is not possible. Finally, the sharp peak at −23.8 ppm corresponds to the central μ_6-oxo unit.

The ^{51}V and ^{95}Mo NMR spectra of the product were also recorded and are shown in **Figure 5.12**. The ^{51}V NMR spectrum contains a single peak at −488 ppm. This is in a very similar position to the tungsten analogue and therefore further supports successful incorporation of a single vanadium centre into the Lindqvist framework. The ^{95}Mo NMR spectrum shows three peaks at 144.9, 15.0 and −6.7 ppm respectively. The broad peak at 144.9 ppm has been assigned to the four molybdenum nuclei in the equatorial plane of the structure. This peak is in a similar position to that of the parent compound $(TBA)_2[Mo_6O_{19}]$, which appears at 122 ppm.[26] The sharp peat at −6.7 ppm was assigned to molybdenum nucleus trans to the vanadium centre. This peak is presumably sharper due to the increased symmetry at this position (C_{4v}) when compared to the equatorial positions (C_1). The additional peak at 15.0 ppm
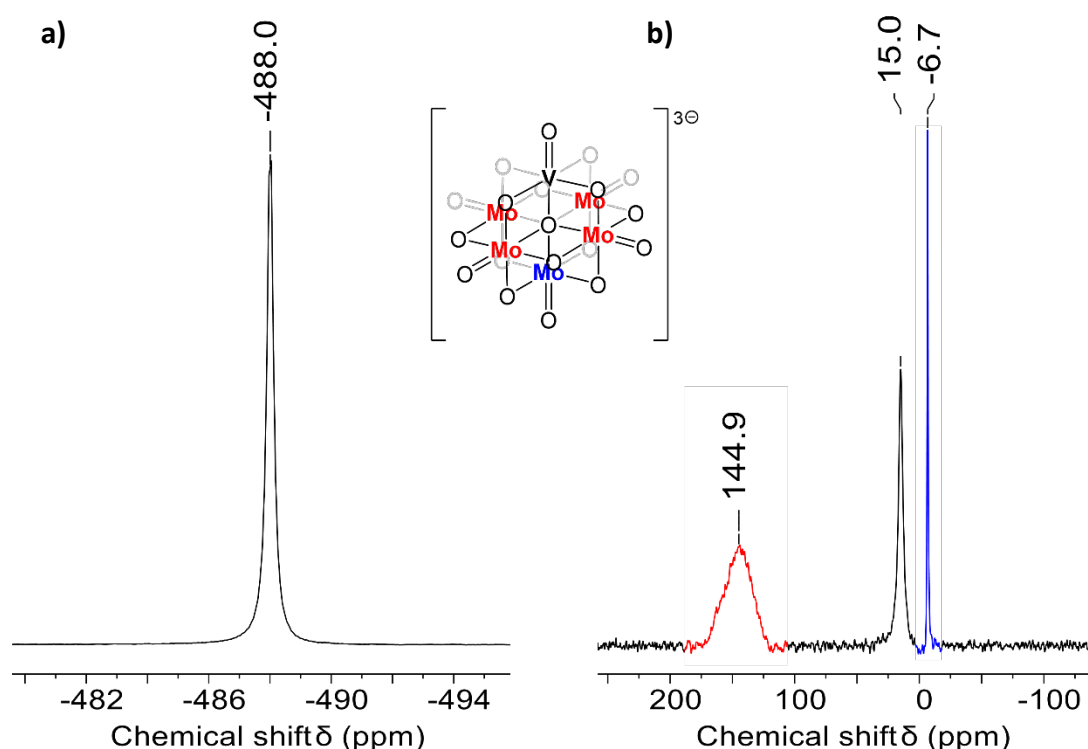
Figure 5.12: a) ^{51}V NMR spectrum of (TBA)$_3$[VMo$_5$O$_{19}$] recorded in CD$_3$CN. **b)** ^{95}Mo NMR spectrum of (TBA)$_3$[VMo$_5$O$_{19}$] recorded in DMSO.

was assigned to α-[Mo$_8$O$_{26}$]$^{4-}$ which is reported to appear at 16 ppm.[26] This was verified by leaving the NMR solution used to record the ^{95}Mo spectrum shown in **Figure 5.12b** to stand for two weeks, during which time a colourless solid crystallized out. The solid was verified to be (TBA)$_4$[Mo$_8$O$_{26}$] by infrared spectroscopy. The ^{95}Mo spectrum of the mother liquor was re-recorded and the intensity of the signal at 15.0 ppm had decreased significantly with respect to the other signals.

As well as characterisation by multinuclear NMR spectroscopy, single-crystal X-ray diffraction quality crystals were obtained by slow evaporation of a saturated solution of (TBA)$_3$[VMo$_5$O$_{19}$] in DCM. The obtained structure is shown in **Figure 5.13**. Though the structure of (TBA)$_3$[VMo$_5$O$_{19}$] is already known, the obtained structure is a previously unknown DCM solvate. The vanadium atom present in the structure is completely disordered over the positions of the Lindqvist unit and therefore the presence of three cations per POM are shown in **Figure 5.13**, consistent with the formation of (TBA)$_3$[VMo$_5$O$_{19}$]. As you would expect, the bond angles and distances present in the anion agree well with the previously obtained structures.[31]

After successfully synthesising (TBA)$_3$[VMo$_5$O$_{19}$] from {Mo$_6$} and TBA(OH), the synthesis from the combination of the metal oxides (i.e. MoO$_3$ and V$_2$O$_5$) was attempted following **Equation**
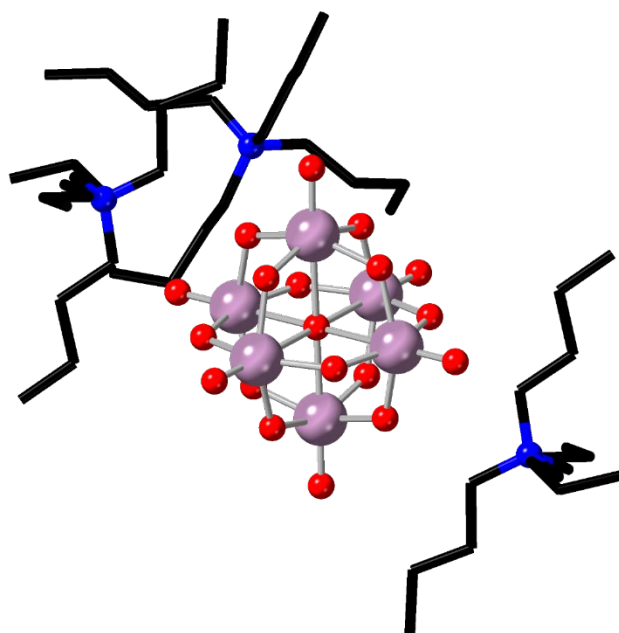
Figure 5.13: Single-crystal X-ray diffraction of (TBA)$_3$[VMo$_5$O$_{19}$]. Mo atoms in lilac, V not shown as it is disordered over all metal positions. Cations are shown in skeletal form for clarity and solvent molecules are not shown. Atomic radii set to CSD covalent radii.

5.21. This approach was successful for the tungsten analogue and represents a very atom efficient approach to the synthesis of (TBA)$_3$[VMo$_5$O$_{19}$], as well as using simple commercially available precursors. Furthermore, unlike the analogous tungsten reaction, the anhydrous oxide can be used which allows statistical ^{17}O enrichment of the reaction mixture without having to worry about loss of the ^{17}O label due to the extra water present in the reaction mixture.

$$10\ MoO_3 + V_2O_5 + 6\ TBA(OH) \rightarrow 2\ (TBA)_3[VMo_5O_{19}] + 3\ H_2O \qquad (5.21)$$

The reaction was performed by adding a 10:1 ratio of MoO$_3$/V$_2$O$_5$ directly to a pyridine solution containing the appropriate quantity of TBA(OH). The resulting suspension was then refluxed for 3 days before filtering through celite. Again, a bright yellow solution was obtained and the crude material (after removal of volatiles) could be recrystallized from hot MeCN. The formation of (TBA)$_3$[VMo$_5$O$_{19}$] was confirmed by ^{51}V NMR spectroscopy, which contained a single peak at −488 ppm. The yield of (TBA)$_3$[VMo$_5$O$_{19}$] obtained when using this route is considerably lower than the previous reaction employing (TBA)$_2$[Mo$_6$O$_{19}$] as the source of molybdenum, which is likely due to the highly insoluble nature of the starting metal oxides. However, given the simplicity, cost, and atom efficiency of this route, it could still be considered a useful approach, particularly for fast, large-scale preparations, where synthesis of large quantities of (TBA)$_2$[Mo$_6$O$_{19}$] can be avoided.

These results show that, like the tungsten analogue, $(TBA)_3[VMo_5O_{19}]$ can be efficiently synthesised from the parent hexamolybdate using a degradative reassembly approach, as well as from the extended metal oxides.

5.4.3 Synthesis of $(TBA)_3[NbMo_5O_{19}]$

Unlike for the vanadium substituted Lindqvist-type POMs, the corresponding niobium substituted polyoxomolybdate is not reported in the literature. In order to determine if it is accessible using our methods, the degradative reassembly approach developed in this work was applied, this time using $Nb(OEt)_5$ as the source of heterometal.

The precursor solution was prepared as before, by treating $(TBA)_2[Mo_6O_{19}]$ with 1.6 equivalents of TBA(OH) and 2.2 equivalents of water. The resulting solution was then reacted directly with neat $Nb(OEt)_5$ at room temperature, following **Equation 5.22**. After stirring overnight, the yellow/brown solution was pumped dry, and the crude material obtained was recrystallized from hot acetonitrile. The ^{17}O NMR spectrum of the obtained material is shown in **Figure 5.14**.

$$(TBA)_3[Mo_5O_{18}H_3] + Nb(OEt)_5 + H_2O \rightarrow (TBA)_3[NbMo_5O_{19}] + 5\ EtOH \qquad (5.22)$$
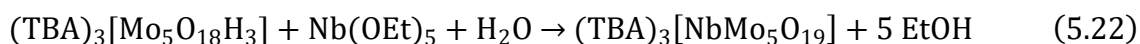
As for the tungsten analogue, there is no obvious sign of a peak corresponding to a terminal Nb=O, which is likely a result of coupling to quadrupolar niobium. The peaks at 892.1 and 882.7 ppm (approx. 4:1 ratio) are characteristic of the two terminal Mo=O environments present in a substituted Lindqvist structure. Formation of the target $(TBA)_3[NbW_5O_{19}]$ is further
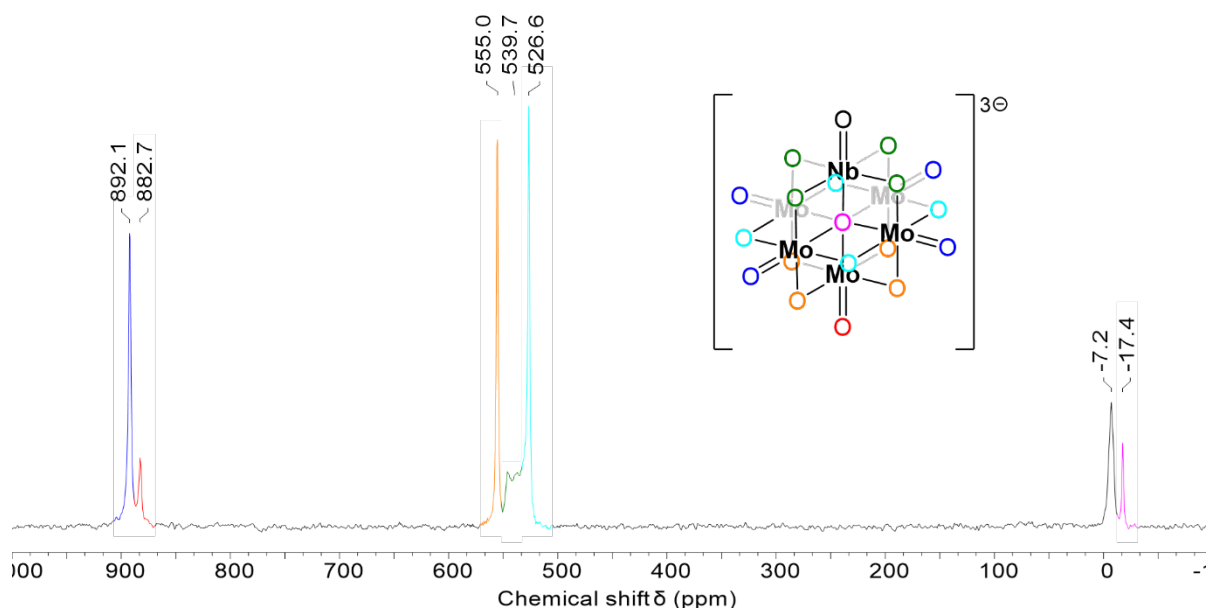
Figure 5.14: ^{17}O NMR spectrum of the product obtained from the reaction of $(TBA)_2[Mo_6O_{19}]$ with TBA(OH), water and $Nb(OEt)_5$. The spectrum is consistent with the formation of $(TBA)_3[NbMo_5O_{19}]$. Spectrum recorded in CD_3CN.

supported by the two sharp peaks at 555.0 and 526.6 ppm (approx. 1:1 ratio) which can be assigned to the oxygen nuclei of the two bridging Mo-O-Mo environments present. There is also an extremely broad feature in this region around 539.7 ppm. This peak can be assigned to the oxygen nuclei of the Nb-O-Mo bridges and is broadened due to coupling to quadrupolar niobium (as was the case for the tungsten analogue). Reacquiring the spectrum while decoupling the ^{93}Nb nucleus should significantly sharpen this peak, and allow observation of the terminal Nb=O, however this would require a specialised triple resonance probe or a dedicated ^{17}O probe with a tuneable broadband channel, neither of which were available. Finally, the peak at −17.4 ppm is in the correct region for the central μ_6-oxo of a Lindqvist-type POM with a 3− charge. The peak at −7.2 ppm is assigned to water.

The ^{93}Nb and ^{95}Mo NMR spectra of the product were also recorded and are shown in **Figure 5.15**. The ^{93}Nb NMR spectrum shows a single peak at −885 ppm. This is very similar to [NbW$_5$O$_{19}$]$^{3-}$, which has a single peak at −883 ppm. The FWHM was only 296 Hz, which is an order of magnitude lower than what was observed for the tungsten analogue. This may be down to differences in concentration and viscosity between the two samples, although the reason for such a large difference between the samples is not fully understood. The ^{95}Mo NMR spectrum is very similar to that obtained for (TBA)$_3$[VMo$_5$O$_{19}$]. The broad peak at 135.1 ppm was assigned to the four equatorial molybdenum nuclei of the Lindqvist unit. The broadness of this peak is attributed to both the low symmetry (C$_1$) and the proximity to the quadrupolar
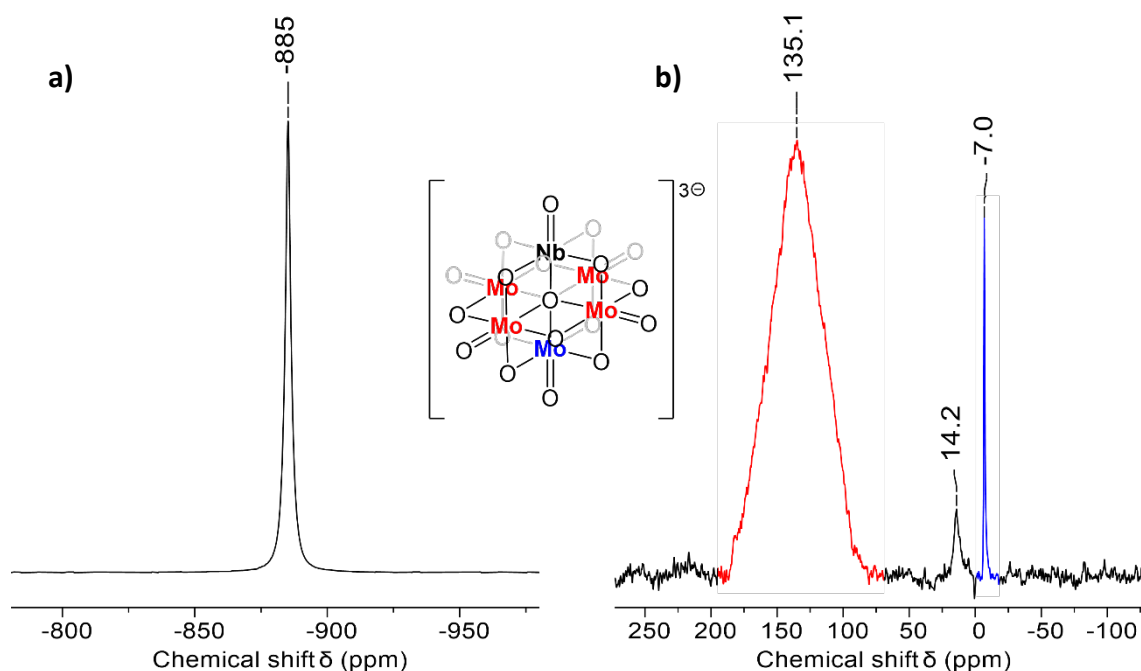
Figure 5.15: **a)** ^{93}Nb NMR spectrum of (TBA)$_3$[NbMo$_5$O$_{19}$] recorded in CD$_3$CN. **b)** ^{95}Mo NMR spectrum of (TBA)$_3$[NbMo$_5$O$_{19}$] recorded in d_6-DMSO.

niobium centre. The peak at −7.0 ppm is substantially sharper and is assigned to the axial (i.e. trans to niobium) molybdenum nucleus. The increased sharpness of this peak is ascribed to the relatively high symmetry at this position and the lack of interaction with niobium. The additional peak at −14.2 ppm is assigned to α-$[Mo_8O_{26}]^{4-}$ as before.

Single-crystal X-ray diffraction quality crystals of $(TBA)_3[NbMo_5O_{19}]$ were obtained by slow evaporation of a saturated solution of the compound in dichloromethane. The obtained structure is shown in **Figure 5.16**. As for the structure of $(TBA)_3[VMo_5O_{19}]$, the heterometal is disordered over all the positions of the Lindqvist structure and therefore the structure was successfully refined with each metal having a 5/6 occupancy of Mo and 1/6 occupancy of Nb. The presence of three cations per Lindqvist unit confirms successful incorporation of a single M(V) into the structure, supporting the conclusions obtained from multinuclear NMR spectroscopy investigations. Unfortunately, as the niobium centre is disordered analysis of specific Nb-O bond lengths cannot be performed.

The multinuclear NMR spectra and crystal structure data presented show that the novel compound $(TBA)_3[NbMo_5O_{19}]$ can be efficiently prepared and purified from $\{Mo_6\}$, TBA(OH) and $Nb(OEt)_5$. Given the success of employing $Nb(OEt)_5$ in this synthesis, efforts were not made to check if the compound is accessible using alternative niobium precursors.
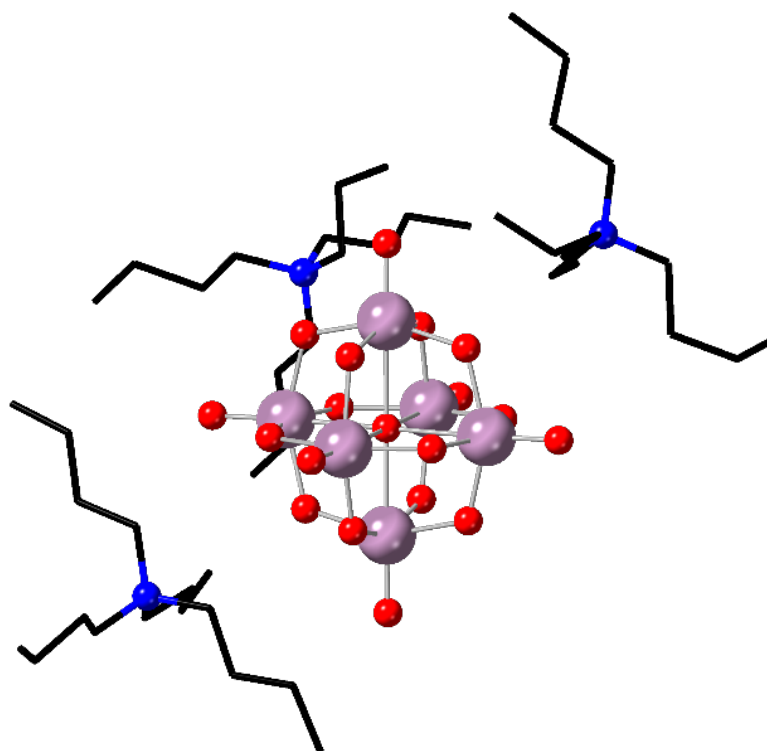
Figure 5.16: Single-crystal X-ray diffraction structure of $(TBA)_3[NbMo_5O_{19}]$. Mo atoms in lilac, the Nb atom is not shown as it is disordered over all metal positions. Cations are shown in skeletal form for clarity and solvent molecules are not shown. Atomic radii set to CSD covalent radii.

5.4.4 Synthesis of (TBA)₃[TaMo₅O₁₉]

After successfully isolating vanadium and niobium substituted Lindqvist-type polyoxomolybdates, attention was turned to the tantalum analogue to complete the series of group(V) containing (TBA)₃[M'M₅O₁₉] compounds, where M = Mo, W and M' = V, Nb, Ta.

Like the niobium substituted polyoxomolybdate just discussed, the synthesis of (TBA)₃[TaMo₅O₁₉] has not been reported in the literature. To attempt to see if the target was accessible using the same methods used for the vanadium and niobium analogues, (TBA)₂[Mo₆O₁₉] was treated with 1.6 equivalents of TBA(OH) and 2.2 equivalents of water to target the virtual precursor "(TBA)₃[Mo₅O₁₈H₃]". This was then reacted directly with neat Ta(OEt)₅ in acetonitrile at room temperature (**Equation 5.23**).

$$(\text{TBA})_3[\text{Mo}_5\text{O}_{18}\text{H}_3] + \text{Ta}(\text{OEt})_5 + \text{H}_2\text{O} \rightarrow (\text{TBA})_3[\text{TaMo}_5\text{O}_{19}] + 5\ \text{EtOH} \qquad (5.23)$$
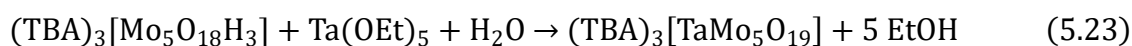
The solvent was removed and the crude material was analysed using ^{17}O NMR spectroscopy. The spectrum obtained is shown in **Figure 5.17**. This spectrum is far more complicated than the other spectra seen so far during attempts to prepare group(V) substituted Lindqvist-type POMs. When considering the ^{17}O NMR spectra presented during investigations into non-aqueous isopolymolybdate speciation (shown in **Figure 5.10**), we can see a lot of familiar signals. Broad peaks at 868.6, 787.1, 498.6, and 399.5 ppm can be assigned to α-[Mo₈O₂₆]⁴⁻, while sharp peaks at 718.4 and 255.4 ppm can be assigned to [Mo₂O₇]²⁻. These species dominate the spectrum and are observed in similar intensities to those in **Figure 5.10b** (Z/Mo
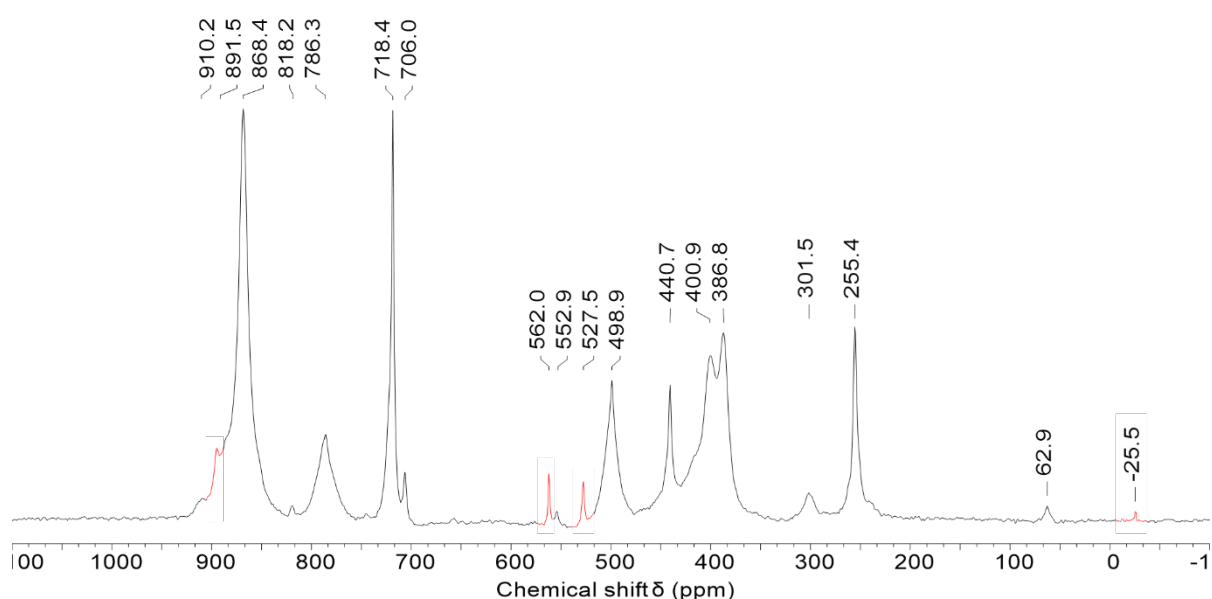
Figure 5.17: ^{17}O NMR spectrum of the crude product obtained from the reaction of (TBA)₂[Mo₆O₁₉] with TBA(OH), water and Ta(OEt)₅. Spectrum recorded in CD₃CN.

= 0.5). The small peaks highlighted in red at 891.5, 562.0, 527.5 and −25.5 ppm were not observed in any of the spectra obtained from reactions of $(TBA)_2[Mo_6O_{19}]$ with different quantities of TBA(OH), and are present in the right regions/relative intensity to suggest formation of $(TBA)_3[TaMo_5O_{19}]$ as a minor product. The fact that these peaks are very small, and that the degradation mixture appears relatively unchanged with respect to what you would expect to see prior to the addition of the heterometal, indicates very minimal interaction between the precursor mixture and the $Ta(OEt)_5$.

One reason for this could be competitive hydrolysis of $Ta(OEt)_5$ by the water in the mixture, leading to the formation of Ta_2O_5 (**Equation 5.24**). If the rate of this process was much faster than the rate of reaction with the POM components of the reaction mixture, then this would inhibit the formation of $(TBA)_3[TaMo_5O_{19}]$. Given the analogous reaction with tungsten proceeds cleanly, we may imply that the precursor solution generated from $\{Mo_6\}$ does not interact as readily with $Ta(OEt)_5$, as we would expect the rate of $Ta(OEt)_5$ hydrolysis to be similar in both systems. Perhaps the known species present in the mixture (i.e. $\{Mo_8\}$ and $\{Mo_2\}$) are more stable with respect to product formation than the degradation products produced from $\{W_6\}$.

$$2\,Ta(OEt)_5 + 5\,H_2O \rightarrow Ta_2O_5 + 10\,EtOH \tag{5.24}$$
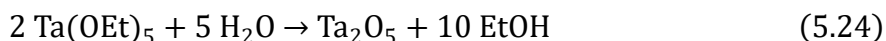
In order to attempt to allow the $Ta(OEt)_5$ to interact with the POM species in the mixture without competitive hydrolysis, a slightly different approach was attempted. As was utilised during our groups attempts to synthesise $(TBA)_3[(RO)TiW_5O_{18}]$, a 1:1 mixture of $(TBA)_4[Mo_8O_{26}]$ and $(TBA)_2[Mo_2O_7]$ can be used, instead of $(TBA)_2[Mo_6O_{19}]$ and 1.6 equivalents of TBA(OH), to target the virtual precursor "$(TBA)_3[Mo_5O_{18}H_3]$". Both mixtures also require the addition of water, however the use of $(TBA)_4[Mo_8O_{26}]/(TBA)_2[Mo_2O_7]$ allows all protons (and water) to be kept out of the reaction until the water is added, whereas use of base leads to hydrolysis of $\{Mo_6\}$ and formation of some water prior to the direct addition of water to the reaction. Therefore, using this approach, the mixture of $(TBA)_4[Mo_8O_{26}]/(TBA)_2[Mo_2O_7]$ can be treated with $Ta(OEt)_5$ and given time to interact without any water present.

This was done by dissolving $(TBA)_4[Mo_8O_{26}]$, $(TBA)_2[Mo_2O_7]$, and $Ta(OEt)_5$ in a 1:1:2 ratio in acetonitrile. The mixture was then stirred at 60 °C overnight. After this period, [17]O enriched water was added and the solution was stirred for a further 24 hours at room temperature.
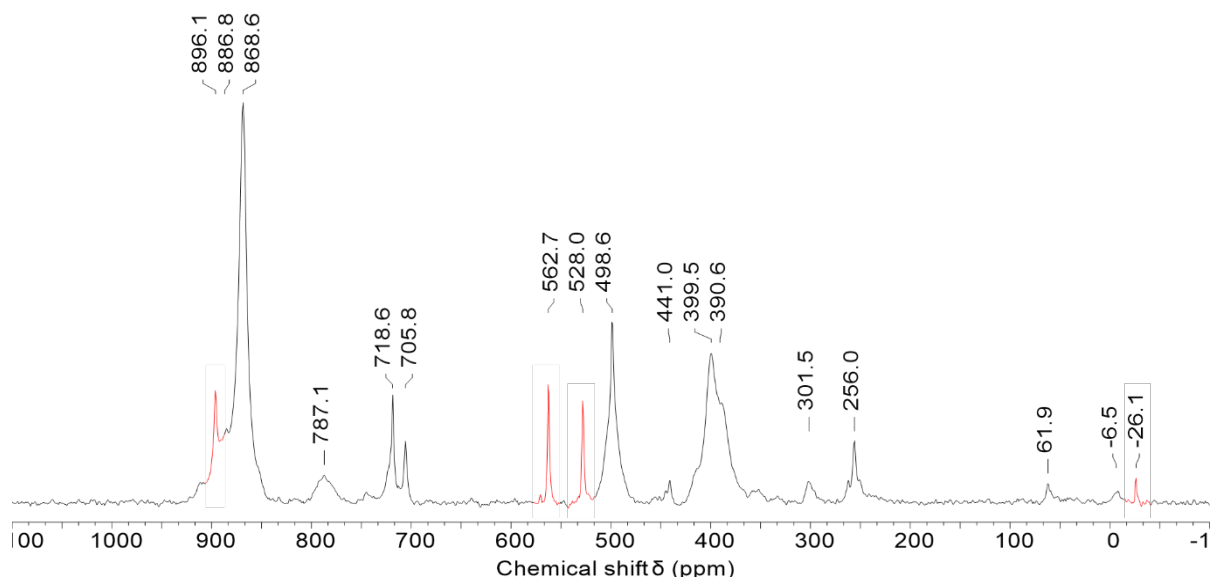
Figure 5.18: ^{17}O NMR spectrum of the crude product obtained from the reaction between $(TBA)_4[Mo_8O_{26}]$, $(TBA)_2[Mo_2O_7]$, $Ta(OEt)_5$, and water. Spectrum recorded in CD_3CN.

Again, the volatiles were removed and the ^{17}O NMR spectrum of the crude material was then recorded. The resulting spectrum is shown in **Figure 5.18**.

Again, the spectrum does not show clean conversion to the target $(TBA)_3[TaMo_5O_{19}]$. The major component of the crude product is $\alpha\text{-}[Mo_8O_{26}]^{4-}$, while the signals at 718.6 and 256.0 assigned to $[Mo_2O_7]^{2-}$ are considerably smaller than those in **Figure 5.17**. The peaks in red, tentatively assigned to $(TBA)_3[TaMo_5O_{19}]$, have increased in intensity suggesting this approach has offered some improvement versus the degradative reassembly approach. However, the conversion still appears to be very low indicating that allowing the POM precursors and $Ta(OEt)_5$ to interact prior to the addition of water has done little to improve the yield of the target product. This suggests that changing the source of molybdenum precursor does little to affect the outcome of the reaction and therefore further attempts to optimise the synthesis of $(TBA)_3[TaMo_5O_{19}]$ from $Ta(OEt)_5$ were not pursued.

Positive results obtained when applying $VOCl_3$ and $NbOCl_3(MeCN)_2$ to the synthesis of the respective heterometal substituted Lindqvist POM could indicate the use of $TaOCl_3$ as a potential alternative source of tantalum to apply to this prep. However, time limitations prevented investigation using this metal salt.

5.5 Examining the redox chemistry

Polyoxometalates are known for their rich redox chemistry, typically centred on reversible reduction of the framework metals which are often present in their highest oxidation states. Given the LUMO (i.e. the orbital populated upon reduction) predominately has metal d-

character, incorporation of one or more heterometal(s) into the cluster can drastically alter the energy (and nature) of the LUMO and in turn the redox properties of the cluster. Furthermore, incorporation of heterometals with different oxidation states (compared to the framework metals they "replace") leads to a change in the overall charge of the cluster. This also has a strong impact on the observed redox properties of the cluster.

5.5.1 Cyclic voltammetry of {MW₅O₁₉}-type POMs (M = W, V, Nb, and Ta)

To examine the redox properties of the series of {MW₅} POMs, whose synthesis was discussed in **Section 5.3**, cyclic voltammetry was performed on the compounds. A 3 mM solution of each POM was prepared in 0.1 M TBA(PF$_6$) (in acetonitrile) and was added to a cell. A standard three electrode setup was employed, using a glassy carbon working electrode, a platinum wire counter electrode and a Ag/Ag(NO$_3$) non-aqueous reference electrode (which is made up of a silver wire immersed in a solution of 0.01 M AgNO$_3$/0.1 M TBA(ClO$_4$) in acetonitrile separated from the cell by a glass frit). Cyclic voltammograms were recorded at a scan rate of 0.1 V/s and are shown in **Figure 5.19**. The integrity of the reference electrode was verified after each experiment by adding a small amount of ferrocene and observing the position of the Fc/Fc$^+$ redox couple, which consistently appeared at +0.11 V.

As reported by Bond and co-workers,[32] the cyclic voltammogram of (TBA)$_2$[W$_6$O$_{19}$] in acetonitrile (shown in black in **Figure 5.19**) features two reversible redox processes, observed here at −1.25 V and −2.21 V respectively. The appearance of these peaks suggests two electrons can be successively added to [W$_6$O$_{19}$]$^{2-}$ to produce [W$_6$O$_{19}$]$^{4-}$. These electrons can then be removed again with no significant structural change.

The substitution of a M(V) centre into the Lindqvist cage leads to a very different picture. The cyclic voltammograms of (TBA)$_3$[VW$_5$O$_{19}$], (TBA)$_3$[NbW$_5$O$_{19}$], and (TBA)$_3$[TaW$_5$O$_{19}$] (shown in orange, blue, and red in **Figure 5.19**) all contain only one reversible redox process at −1.02 V, −2.09 V, and −2.05 V respectively. These processes likely correspond to a one electron reduction of the cluster taking them from [MW$_5$O$_{19}$]$^{3-}$ to [MW$_5$O$_{19}$]$^{4-}$. Addition of a second electron to the POM is not observed. This is probably because addition of a second electron to the now 4− clusters is energetically demanding due to electrostatic repulsion.

The potential required for one electron reduction of (TBA)$_3$[VW$_5$O$_{19}$] is much more positive (i.e. the POM is more easily reduced) than for either (TBA)$_3$[NbW$_5$O$_{19}$] or (TBA)$_3$[TaW$_5$O$_{19}$]. This may be because vanadium, a first-row transition metal, is more easily reduced than either niobium or tantalum as it's empty d-orbitals are lower in energy. This allows localised
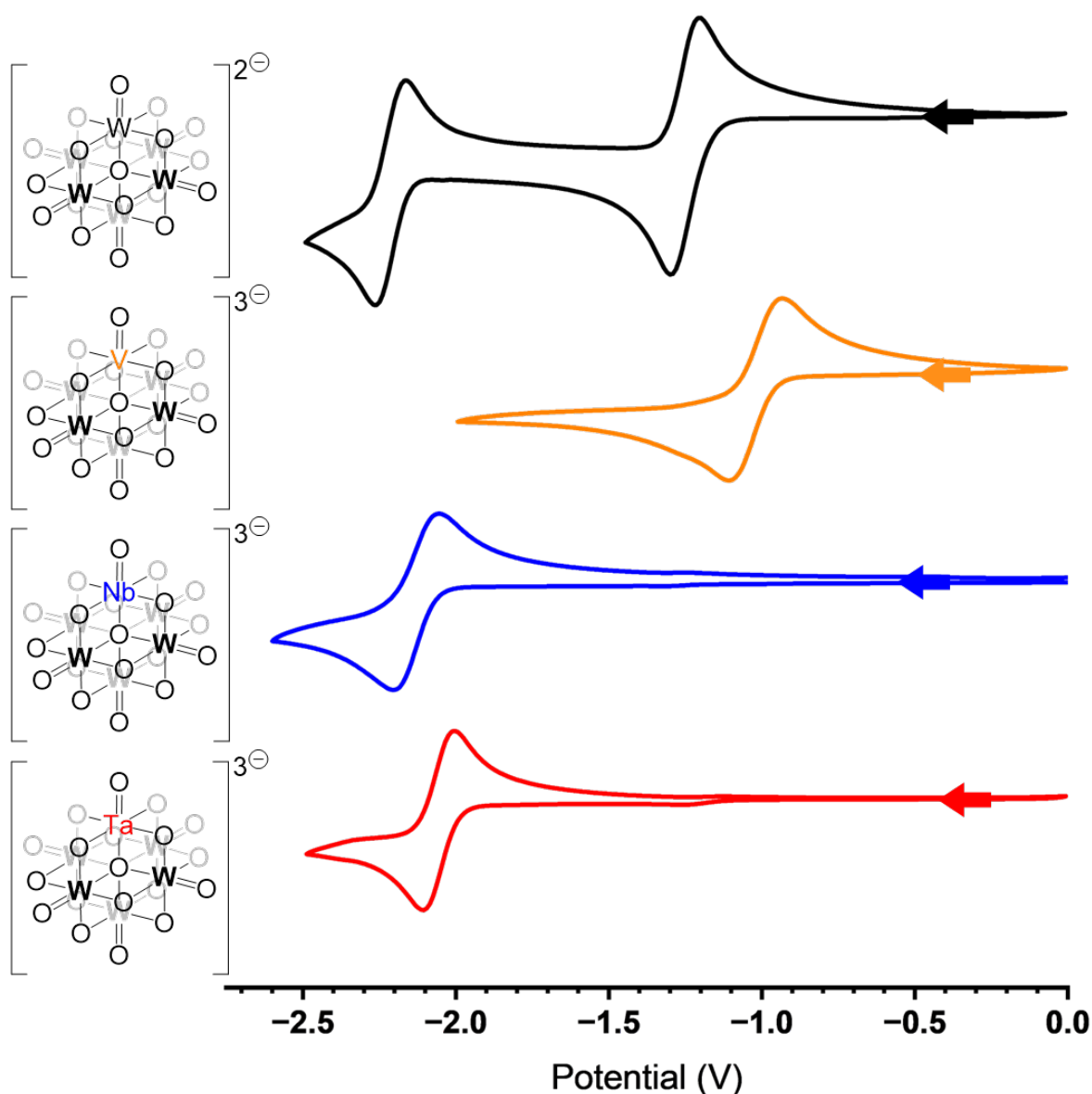
Figure 5.19: Cyclic voltammograms of 3 mM solutions of (TBA)$_x$[MW$_5$O$_{19}$] (M = W, V, Nb, Ta) in 0.1 M TBA(PF$_6$) (In MeCN) obtained with a scan rate = 100 mV s^{-1}.

reduction of vanadium (taking it from V(V) to V(IV)), rather than reduction of the tungsten framework. When the heterometal is not easily reduced, as is the case for niobium or tantalum, reduction of the POM cage occurs. The potential required for this process is approximately the same as the second reduction of {W$_6$} (i.e. taking [W$_6$O$_{19}$]$^{3-}$ to [W$_6$O$_{19}$]$^{4-}$) because the fully oxidised Nb/Ta containing clusters are already 3−. These observations will be further rationalised with the support of Density Functional Theory calculations in **Section 5.5.3**.

5.5.2 Cylic voltammetry of {MMo$_5$O$_{19}$}-type POMs (M = Mo, V, and Nb)

Performing cyclic voltammetry on {MW$_5$O$_{19}$} POMs (M = W, V, Nb, and Ta) showed the effect heterometal incorporation can have on the redox properties of a cluster. Along with variation

of a heterometal, variation of the framework metal can also have a large impact on the redox chemistry observed. In order to explore this for the Lindqvist system, cyclic voltammetry was performed on (TBA)$_2$[Mo$_6$O$_{19}$], (TBA)$_3$[VMo$_5$O$_{19}$], and (TBA)$_3$[NbMo$_5$O$_{19}$]. The results can then be compared to the corresponding tungsten derivatives. The electrochemistry of (TBA)$_3$[TaMo$_5$O$_{19}$] was not explored as the synthesis has not been refined to a point where significant quantities of pure product can be isolated.

The same methodology as described in **Section 5.5.1** was employed, with the [POM] = 3mM and a supporting electrolyte of 0.1 M TBA(PF$_6$) in acetonitrile. The resulting cyclic voltammograms, obtained with a scan rate of 100 mV s^{-1}, of (TBA)$_2$[Mo$_6$O$_{19}$] (grey), (TBA)$_3$[VMo$_5$O$_{19}$] (orange), and (TBA)$_3$[NbMo$_5$O$_{19}$] (blue) are shown in **Figure 5.20**.

The voltammogram of (TBA)$_2$[Mo$_6$O$_{19}$] is reported and is known to contain one reversible redox process around −0.78 V and an irreversible process at −1.62 V (both vs Ag/Ag(NO$_3$)).[31] Our
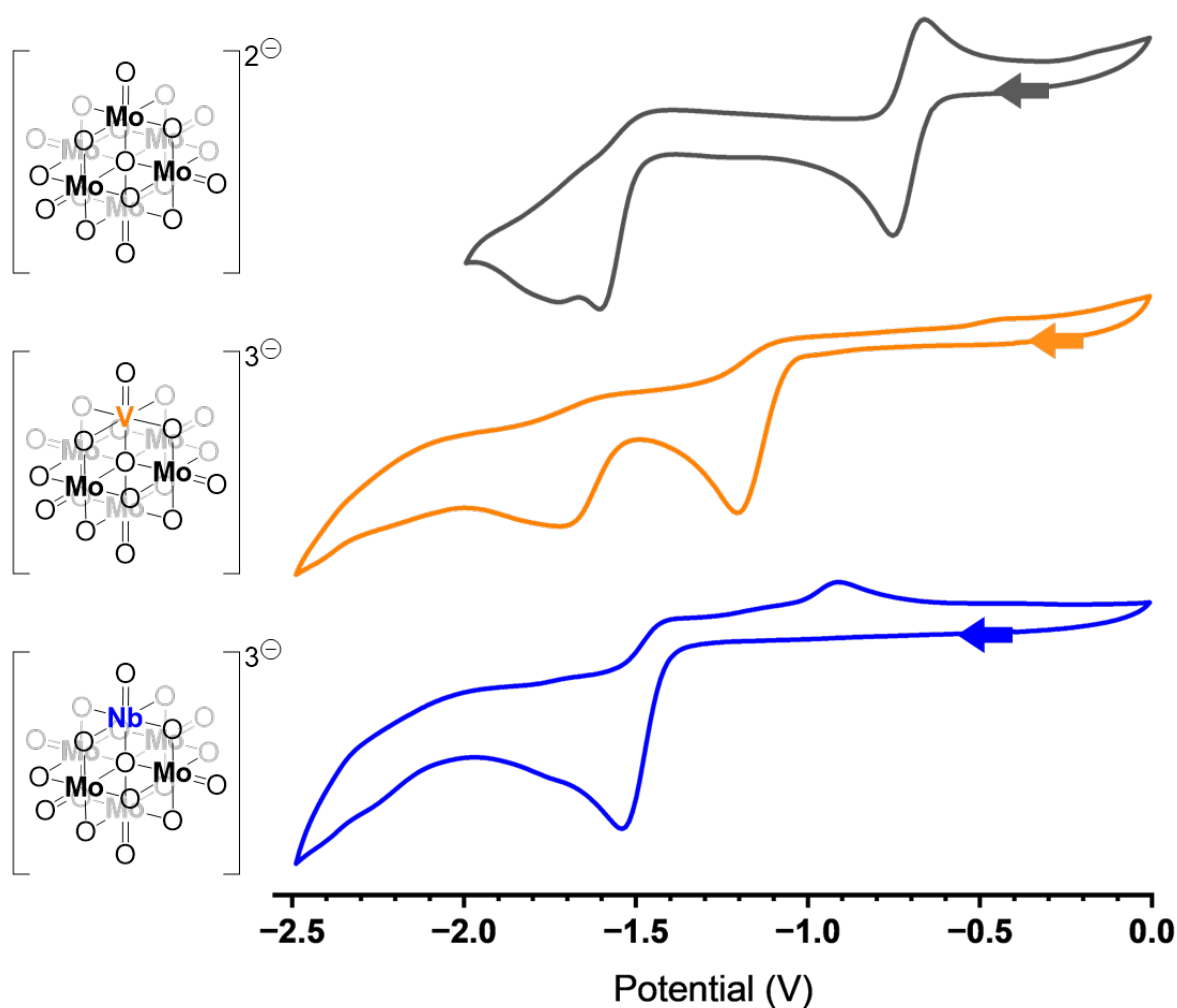
Figure 5.20: Cyclic voltammograms of 3 mM solutions of (TBA)$_x$[MMo$_5$O$_{19}$] (M = Mo, V, Nb, Ta) in 0.1 M TBA(PF$_6$) (In MeCN) obtained with a scan rate = 100 mV s^{-1}.

study shows a very similar picture with a reversible process centred on −0.71 V and an irreversible process at −1.61 V. This behaviour suggests that addition of one electron to $[Mo_6O_{19}]^{2-}$ produces the stable 3− cluster. However, addition of more electrons leads to a chemical change, likely involving rearrangement or decomposition of the Lindqvist framework, and therefore the process is irreversible.

The picture is somewhat similar for the vanadium and niobium substituted analogues. Neither of the substituted derivatives contain a reversible redox process. As was the case for the tungsten derivatives, it is likely that incorporation of the M(V) centre into the framework and the associated increase in negative charge from 2− to 3− limits the ability of the cluster to undergo facile reduction. The effect of this is to essentially "skip" any reversible process associated with taking the cluster from 2− to 3− and instead goes straight to the irreversible process associated with increasing the negative charge from 3− to 4−.

The first irreversible redox process for (TBA)$_3$[VMo$_5$O$_{19}$] is observed at −1.21 V, whereas for (TBA)$_3$[NbMo$_5$O$_{19}$] it is not seen until −1.54 V. This again, is likely a manifestation of the differing LUMO energies of the two systems. The vanadium containing system likely has access to a lower energy empty d-orbital centred on vanadium, whereas the LUMO of the niobium system is more likely to be localised on molybdenum (this will be revisited in **Section 5.5.3**). In either case, addition of this electron must lead to the formation of an unstable $[MMo_5O_{19}]^{4-}$ species, which undergoes conversion/degradation and therefore the corresponding re-oxidation is not observed. The vanadium system shows a second broad irreversible reduction at approximately −1.73 V. It is difficult to hypothesise what this process corresponds to without knowing anything about the previous irreversible redox process. A similar feature is not observed for the niobium analogue. This may indicate the redox chemistry is specific to vanadium, or that the process is shifted to more negative potential and therefore not observed within the electrochemical window examined (which is dictated by the choice of solvent, electrolyte and electrodes).

Though it was not possible to isolate (TBA)$_3$[TaMo$_5$O$_{19}$] and examine its redox properties, comparison of the electrochemistry (TBA)$_3$[NbW$_5$O$_{19}$] and (TBA)$_3$[TaW$_5$O$_{19}$] suggests that the redox properties of (TBA)$_3$[TaMo$_5$O$_{19}$] will be similar to those of (TBA)$_3$[NbMo$_5$O$_{19}$].

5.5.3 Using DFT calculations to rationalise the redox properties of {M'M₅O₁₉}-type POMs (M' = V, Nb, Ta, Mo, W and M = Mo, W)

Cyclic voltammetry experiments presented above show how systematically varying both the heterometal (i.e. the group V metal) and the framework metal leads to changes in the redox properties of the POM. Density functional theory calculations can be used to give insight into the electronic structure of the various POMs to rationalise these changes.

This was done first by optimising the structure of each compound in their fully oxidised form. The B3LYP hybrid functional was applied with a split valence basis set using LANL2DZ (applied to the transition metals) and 6-31G(d,p) (applied to oxygen). Successful minimisation of the structure was verified by performing a frequency calculation and ensuring no imaginary frequencies were present. This was the case for all structures. The results of these calculations allow visualisation of the molecular orbitals. In the context of the redox properties discussed above, the nature of the LUMO is very important as reduction of a POM involves addition of an electron to the LUMO.

The calculated LUMO of each of the series of $[M'M_5O_{19}]^{2/3-}$ (M' = V, Nb, Ta, Mo, W and M = Mo, W) compounds is shown in **Figure 5.21**. There is significant variation in the nature of the LUMO depending on both the heterometal and framework metal present. As expected, the LUMO of $[W_6O_{19}]^{2-}$ is delocalised across all the metals of the cluster, primarily possessing tungsten d_{xy} character. Incorporation of vanadium, a first-row transition metal with lower energy valence 3d orbitals, leads to localisation of a substantial portion of the LUMO on vanadium. This quickly changes as we move to clusters incorporating niobium and tantalum, in which the heterometal contributes less and less to the LUMO. This helps to rationalise the significant difference in the reduction potential of $[VW_5O_{19}]^{3-}$ compared to the niobium and tantalum derivatives. Interestingly, the LUMO of $[NbW_5O_{19}]^{3-}$ contains some Nb d-character but the reduction potential is no higher than that of $[W_6O_{19}]^{3-}$ (i.e. addition of the 2nd electron to {W₆}) or $[TaW_5O_{19}]^{3-}$. This may indicate a diagonal relationship between niobium and tungsten and, in turn, that incorporation of niobium(V) into the cluster produces a cluster with very similar electronic properties to a one electron reduced hexatungstate.

Changing the framework metal from tungsten to molybdenum leads to further changes in electronic structure. Neither $[NbMo_5O_{19}]^{3-}$ or $[TaMo_5O_{19}]^{3-}$ have any significant heterometal contribution to the LUMO. This shows how moving from tungsten to molybdenum, and in turn changing the principal quantum number of the valence orbitals, changes the nature of the
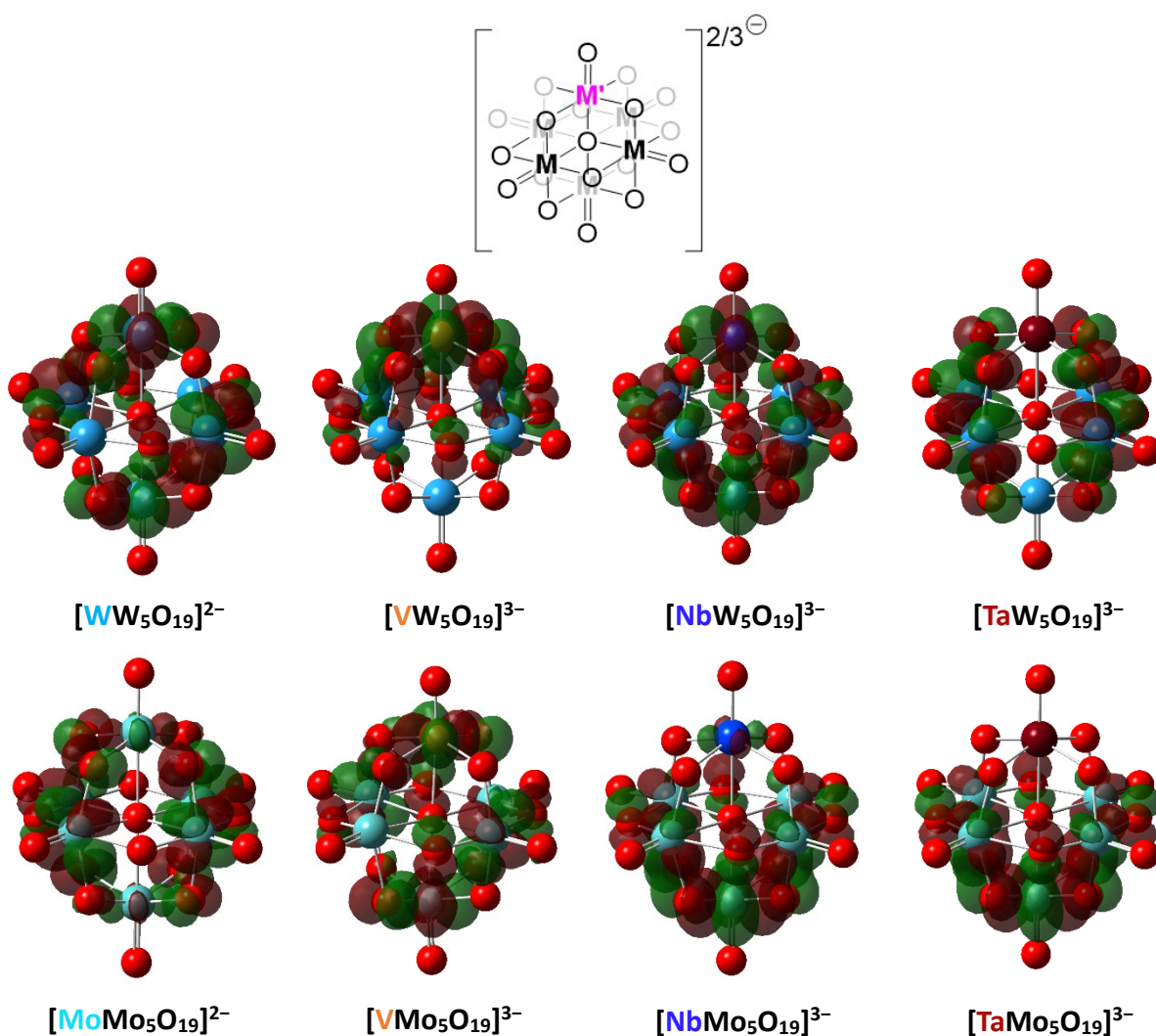
Figure 5.21: LUMO's of series of $[M'M_5O_{19}]^{2/3-}$ (M' = V, Nb, Ta, Mo, W and M = Mo, W) compounds calculated using B3LYP functional with a split valence basis set using LANL2DZ for the transition metals and 6-31-G(d,p) for oxygen. Surfaces shown with an isovalue of 0.003.

LUMO. The lack of heterometal contribution to the LUMO indicates that the empty d-orbitals of the metal(V) centre are too high in energy. This may suggest that the redox properties of $[TaMo_5O_{19}]^{3-}$ would be very similar to $[NbMo_5O_{19}]^{3-}$ if the compound was isolated. $[VMo_5O_{19}]^{3-}$ is very different as it has a LUMO with some vanadium d-character. This implies that these orbitals are comparable in energy to those of molybdenum (again showing a diagonal relation) and thus the LUMO contains contributions from both metals. This helps to rationalise why the reduction of $[VMo_5O_{19}]^{3-}$ occurs at a more positive potential than that of $[NbMo_5O_{19}]^{3-}$.

These findings can be supported further by calculating the spin density of the reduced analogues of the compounds. The optimised geometries of the one electron reduced compounds (i.e. $[M'M_5O_{19}]^{3/4-}$ where M' = V, Nb, Ta, Mo, W and M = Mo, W) were first calculated and successful optimisation was verified as before. Spin density maps were then

generated which show the difference between alpha and beta electron densities. This gives insight into localisation of the additional electron density gained upon reduction.

The obtained spin density maps are shown in **Figure 5.22**. These maps give a clear visual indication in the electronic differences between the respective vanadium and niobium/tantalum containing derivatives. Regardless of framework metal, there is substantial localisation of the additional electron density on vanadium. This is not true for any of the niobium/tantalum derivatives, in which the additional electron prefers to sit predominately on tungsten/molybdenum. This further supports the differences observed in the cyclic voltammetry between the vanadium substituted compounds and the lower group V containing structures. Access to low lying empty d-orbitals on vanadium gives rise to preferential reduction of vanadium, leading to essentially the formation of a $[V(IV)M_5O_{19}]^{4-}$. For the other compounds, the formation of compounds with the general formula $[M'(V)M_5(V/VI)O_{19}]^{4-}$ (M'
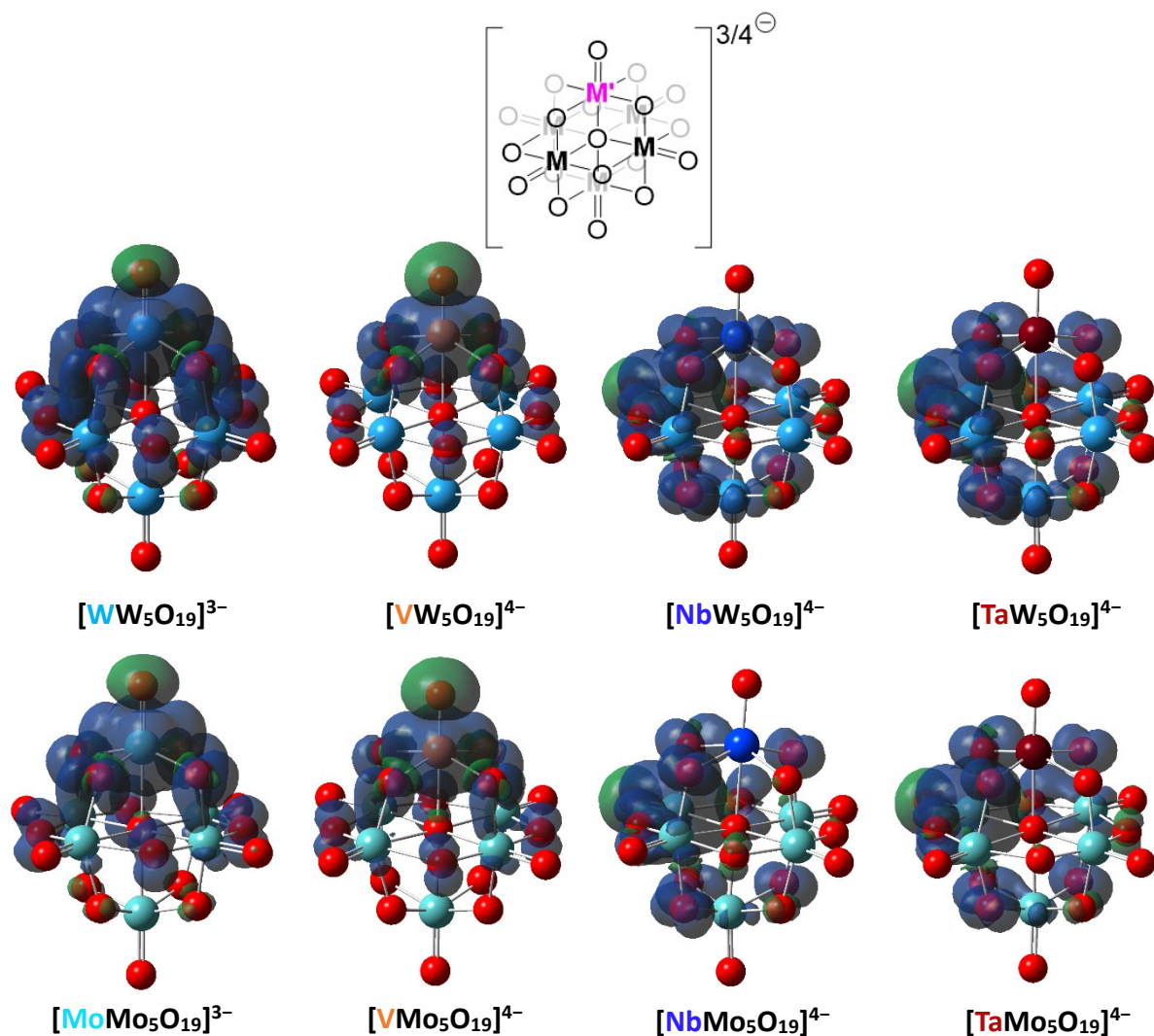
Figure 5.22: Spin density representation for the one electron reduced analogues of the series of $[M'M_5O_{19}]^{3/4-}$ (M' = V, Nb, Ta, Mo, W and M = Mo, W) compounds. The cut-off value used for these surfaces was 0.0004 electron/bohr^3 in atomic units.

= Nb, Ta and M = Mo, W) is supported. These systems appear to show preferential reduction of the framework metal, behaving similar to the one electron reduced parent compounds (i.e. $[Mo_6O_{19}]^{3-}$ and $[W_6O_{19}]^{3-}$). This explains why their first redox event appears at a similar reduction potential to the second redox event of the parent hexametalates.

5.6 Synthesis and chemistry of rhenium substituted hexametalates

The results obtained in this chapter illustrate the ability to incorporate metals in the +5 oxidation state into the Lindqvist architecture using a degradative reassembly approach. Therefore, it may be expected that this methodology can be expanded to elements which can exist in the +5 oxidation state, outside of those within group 5. One such element is rhenium, which can exist anywhere between Re(0) (e.g. $Re_2(CO)_{10}$) to Re(VII) (e.g. $HReO_4$).[33,34]

The understanding of the molecular chemistry of rhenium complexes is extremely relevant. High oxidation state rhenium oxo complexes and Re(VII) oxides have been studied as potential oxidation catalysts.[35,36] Furthermore, the comparative chemistry of rhenium and technetium makes rhenium a perfect non-radioactive surrogate for technetium. This allows the development of systems that may have potential application in the areas of radioactive waste purification (i.e. selective separation of technetium from mixtures of radioactive isotopes) or radio-imaging without handling radioactive technetium until a promising system incorporating rhenium is developed.[37,38]

Several rhenium containing POMs are known, incorporating one or more rhenium centres into the Keggin or Wells-Dawson architecture.[39,40] However, no structures incorporating rhenium into the Lindqvist structure are reported.

5.6.1 Synthesis of ReOCl₃(PPh₃)₂ and [ReO₂(py)₄][Cl]

An important factor in determining the success of syntheses discussed so far in this thesis has been the choice of heterometal source. Given the success of incorporating metals in the +5 oxidation state, a Re(V) precursor was chosen, as oppose to common Re(VII) (e.g. (TBA)[ReO₄]) or Re(VI) (e.g. ReOCl₄) materials. Instead, ReOCl₃(PPh₃)₂ and [ReO₂(py)₄][Cl] (py= pyridine) were identified as promising sources of rhenium as both possess solubility in organic solvents and are air-stable, which is not a universal trait of Re(V) complexes.

ReOCl₃(PPh₃)₂ is commercially available. However, our group was in possession of a significant quantity of rhenium metal and therefore a simple route to ReOCl₃(PPh₃)₂ starting from the metal was developed by adapting a literature procedure.[41] Firstly, rhenium metal was treated

with 30% aqueous hydrogen peroxide. This extremely exothermic reaction led to the oxidation of the Re(0) directly to Re(VII), forming perrhenic acid (HReO$_4$). The solution was then heated at 150 °C to decompose residual hydrogen peroxide. The generated perrhenic acid is soluble in water and therefore was easily separated from any residual traces of metal by dissolution in hot water followed by filtration.

ReOCl$_3$(PPh$_3$)$_2$ is commonly synthesised from KReO$_4$ via the addition of triphenylphosphine (acting as both a reducing agent and ligand) and an excess of hydrochloric acid.[42] Given that the addition of acid likely leads to formation of HReO$_4$ in situ, it was reasoned that the crude perrhenic acid generated from treatment of Re with H$_2$O$_2$ could be used directly in this synthesis. This was done by removing the solvent from the filtrate obtained after extraction and re-dissolving in ethanol. This solution was then treated with PPh$_3$ and aqueous hydrochloric acid, followed by refluxing for one hour under N$_2$. The resulting yellow/green suspension was then cooled and filtered to isolate ReOCl$_3$(PPh$_3$)$_2$ as a yellow solid. The ^{31}P NMR spectrum showed a characteristic peak at −19 ppm which confirmed the formation of the target complex.[42]

[ReO$_2$(py)$_4$][Cl] can be obtained by treating ReOCl$_3$(PPh$_3$)$_2$ with excess pyridine and water in acetone at reflux. This leads to a colour change from yellow to orange and precipitation of [ReO$_2$(py)$_4$][Cl].

5.6.2 Synthesis of (TBA)$_3$[ReW$_5$O$_{19}$]

After the successful synthesis of the desired rhenium containing starting materials, the synthesis of the rhenium substituted Lindqvist-type POM was attempted. Firstly, the use of ReOCl$_3$(PPh$_3$)$_2$ was investigated. As with the previously employed metal oxychlorides, the virtual precursor, "(TBA)$_6$[W$_5$O$_{18}$]", was targeted by treatment of {W$_6$} with 5.2 equivalents of TBA(OH) in acetonitrile. The solvent was then removed, and the crude precursor mixture was dissolved in pyridine, which was the solvent of choice in reactions using VOCl$_3$ and NbOCl$_3$(MeCN)$_2$. This precursor mixture was then treated directly with solid ReOCl$_3$(PPh$_3$)$_2$, following **Equation 5.25**.

$$(TBA)_6[W_5O_{18}] + ReOCl_3(PPh_3)_2 \rightarrow (TBA)_3[ReW_5O_{19}] + 3\,TBA(Cl) + 2\,PPh_3 \quad (5.25)$$
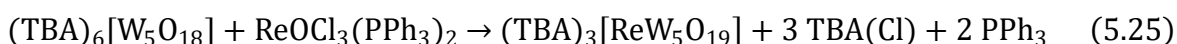
The mixture immediately turned dark red/brown as the solid dissolved and was allowed to stir at room temperature overnight before removing the solvent. The tacky solid was then triturated with toluene, ethyl acetate, and ether to attempt to remove PPh$_3$, TBA(Cl), and
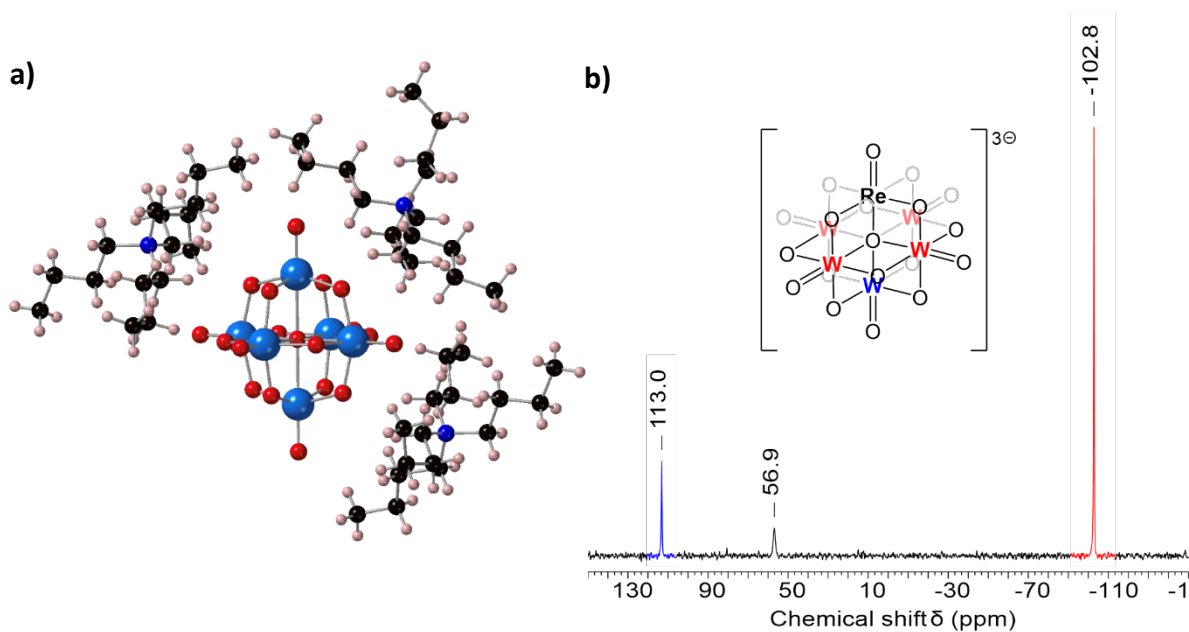
Figure 5.23: a) Single-crystal X-ray diffraction structure of (TBA)₃[ReW₅O₁₉] and b) the [183]W NMR spectrum obtained from dissolution of the same crystals in a mixture of CD₃CN and CH₃CN.

residual solvent. The crude solid was then recrystallized by dissolving in the minimum amount of hot dichloromethane and then cooling to −30 °C overnight.

The obtained crystals were of sufficient quality for analysis by single-crystal X-ray diffraction. The acquired structure is shown in **Figure 5.23a**. Evidence of Re(V) in the structure is given by the presence of three TBA cations per Lindqvist unit, whereas a {W₆} only has two cations per POM (as well as the blue colour of the obtained crystals). As tungsten (Z = 74) and rhenium (Z = 75) have similar electron densities, there is no obvious way to differentiate the metal sites and therefore each site was constrained to an occupancy of 5/6 W and 1/6 Re, though only tungsten atoms are shown in **Figure 5.23a**.

Re(V) is a d^2 metal centre and complexes are often found to be diamagnetic.[43] This allows interrogation using NMR spectroscopy, and in this case [183]W NMR spectroscopy can be used to further verify that the obtained crystals are those of the target compound, (TBA)₃[ReW₅O₁₉]. The acquired spectrum is shown in **Figure 5.23b** and shows two major peaks at 113.0 and −102.8 ppm in a 1:4 ratio. This is consistent with the desired incorporation of a single Re centre into the Lindqvist structure. There is also a minor peak at 56.9 ppm which is consistent with the presence of a small amount of {W₆} present even after recrystallization.

The infrared spectrum of the obtained crystals was recorded and is shown in **Figure 5.24**. The spectrum shows a sharp peak at 951 cm⁻¹ which can be assigned to the terminal W=O stretching mode ($v_{W=O}$). This is very similar to the stretching frequencies observed for
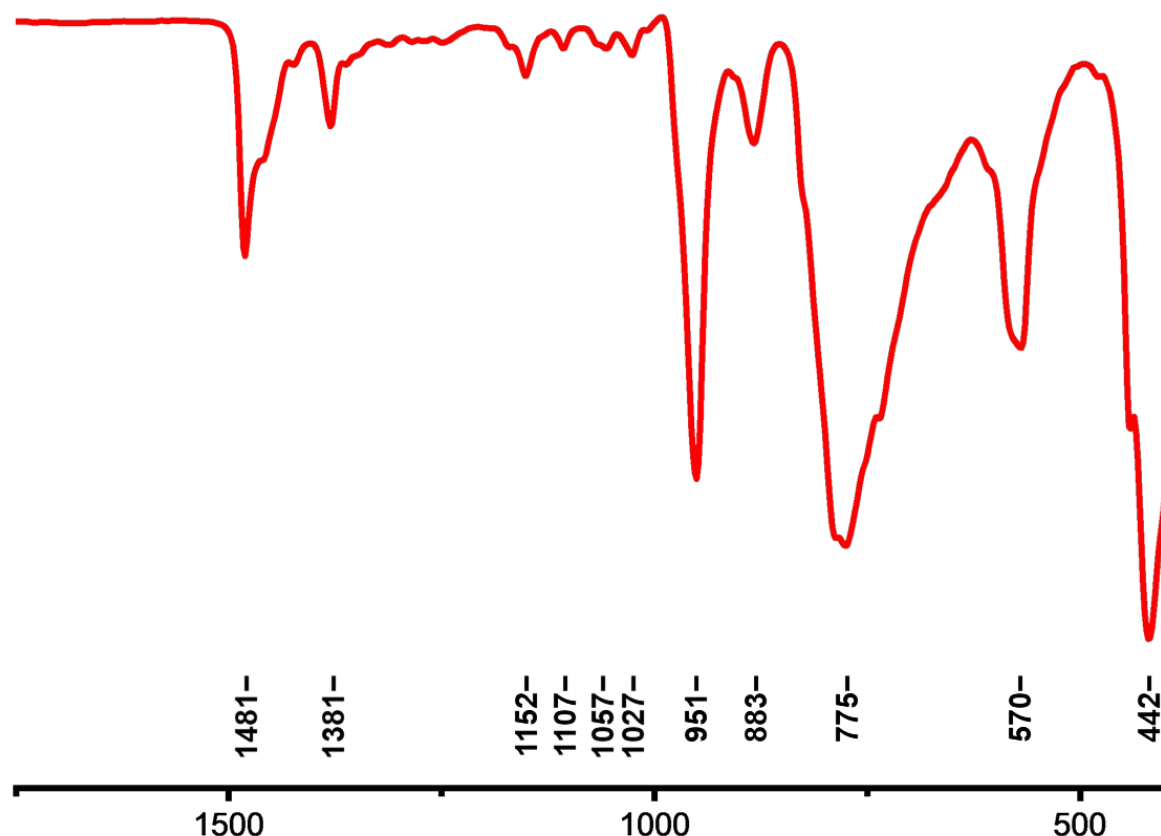
Figure 5.24: ATR FTIR transmittance spectrum of crystalline (TBA)$_3$[ReW$_5$O$_{19}$].

(TBA)$_3$[NbW$_5$O$_{19}$] and (TBA)$_3$[TaW$_5$O$_{19}$] (see experimental **Sections 5.9.9** and **5.9.13**). There is no obvious evidence of a Re=O stretch. The bridging W-O-W region contains a broad peak around 775 cm^{-1}. The simplistic nature of this region is consistent with the formation of a monomeric POM which is consistent with both the X-ray structure and ^{183}W NMR data shown above. Very similar bridging regions are seen for all the (TBA)$_3$[MW$_5$O$_{19}$]-type POMs (M = V, Nb, Ta, and Re). There are also two peaks at 2959 and 2873 cm^{-1}, not shown in **Figure 5.24**, consistent with C-H stretching vibrations of the tetrabutylammonium cations.

After successfully isolating (TBA)$_3$[ReW$_5$O$_{19}$] from ReOCl$_3${PPh$_3$}$_2$, attention was turned to [ReO$_2$(py)$_4$][Cl] to see if it was possible to access the same compound from an alternate rhenium source. The appropriate virtual precursor, "(TBA)$_4$[W$_5$O$_{18}$H$_2$]", was targeted by treatment of {W$_6$} with 2.8 equivalents of TBA(OH) in acetonitrile. The mixture was ^{17}O enriched at this point by adding ^{17}O enriched water and stirring at room temperature overnight. The volatiles were removed and the crude material was re-dissolved in pyridine. The mixture was then treated directly with solid [ReO$_2$(py)$_4$][Cl] following **Equation 5.26**.

$$(TBA)_4[W_5O_{18}H_2] + [ReO_2(py)_4][Cl] \rightarrow (TBA)_3[ReW_5O_{19}] + TBA(Cl) + H_2O \qquad (5.26)$$

An orange suspension formed which showed little change when stirring at room temperature for one hour. It was postulated that the trans-dioxo motif of $[ReO_2(py)_4][Cl]$ may be less reactive towards the degradation mixture than the previously used $ReOCl_3\{PPh_3\}_2$, and therefore the reaction was heated to 60 °C. Within approximately 15 minutes the reaction mixture turned dark red/brown, matching the previous observations from the reaction using $ReOCl_3\{PPh_3\}_2$. The mixture was heated at 60 °C overnight before cooling and concentrating the reaction mixture to isolate crystalline material directly from the reaction mixture. The crystals were analysed using ^{17}O NMR spectroscopy, with the spectrum obtained shown in **Figure 5.25** (the spectrum was recorded in MeCN instead of pyridine as linewidths are lower in this solvent).

The obtained pattern is very familiar to those previously discussed for $(TBA)_3[MW_5O_{19}]$-type POMs. The most downfield peak observed at 997.1 ppm (highlighted in red) is assigned to the terminal Re=O unit. Unlike for vanadium and niobium, this peak is very sharp which can be attributed to the properties of the most abundant rhenium isotopes. Rhenium possesses two spin active isotopes, ^{185}Re (NA = 37.4%, I = 5/2, Q = 2.2 b) and ^{187}Re (NA = 62.6%, I = 5/2, Q = 2.1 b) (NA = natural abundance).[44] Even though both are quadrupolar, the large quadrupole moments (Q) lead to rapid quadrupolar relaxation and consequently decoupling of rhenium from oxygen. This is why the terminal M=O is observable, and the peak is sharp, for the rhenium substituted Lindqvist-type POM. The two peaks at 733.4 and 715.3 ppm respectively, observed in a 4:1 ratio, can be assigned to the two terminal W=O environments. The two peaks
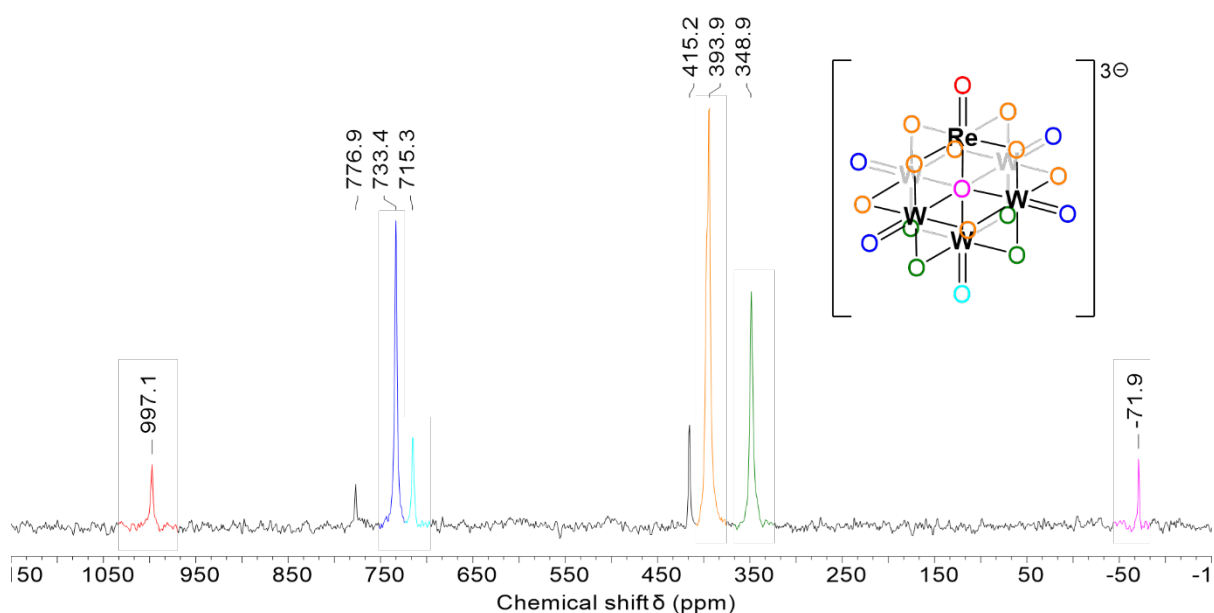
Figure 5.25: ^{17}O NMR spectrum of the crude product obtained from the reaction between $(TBA)_2[W_6O_{19}]$, TBA(OH), and $[ReO_2(py)_4][Cl]$. Spectrum recorded in CD_3CN.

at 393.9 ppm and 348.9 ppm are observed in a 2:1 Ratio. This implies that the three bridging oxygen environments present in $(TBA)_3[ReW_5O_{19}]$ (i.e. Re-O-W and 2 x W-O-W) are contained within these two peaks. When considering the previously discussed ^{17}O NMR spectra of M(V) containing Lindqvist-type POMs, it is likely that the peak at 393.9 ppm (orange) can be assigned to the Re-O-W and one of the W-O-W environments, though definitive assignments of the three bridging oxygen environments cannot be made. The additional peaks at 415.2 and 776.9 ppm are due the presence of a small amount of $(TBA)_2[W_6O_{19}]$.

The data presented conclusively proves the ability to access $(TBA)_3[Re(V)W_5O_{19}]$ using the degradative reassembly approach in combination with an appropriate rhenium(V) starting material, two of which are discussed here.

5.6.3 Oxidation of $(TBA)_3[ReW_5O_{19}]$

Unlike the group V metals discussed in this chapter, rhenium has access to higher oxidation states. After isolating a Keggin structure incorporating Re(V) into the framework, Pope and co-workers showed that stepwise addition of dilute bromine solutions to the compound could be used to isolate structures incorporating Re(VI) and Re(VII).[39]

Exposing dark red/black solutions of $(TBA)_3[ReW_5O_{19}]$ in acetonitrile to air for extended periods leads to a colour change to pale purple, perhaps indicating oxidation of the rhenium centre. In order to verify this observation, a solution of $(TBA)_3[ReW_5O_{19}]$ was treated with Ag(OTf) as shown in **Scheme 5.27**.

$$(TBA)_3[Re(V)W_5O_{19}] + Ag(OTf) \rightarrow (TBA)_2[Re(VI)W_5O_{19}] + Ag(0) + TBA(OTf) \quad (5.27)$$

After stirring at 60 °C overnight, a black/brown suspension had formed. Passing the mixture through a syringe filter allowed separation of a pale purple solution (presumably removing suspended silver metal). The solution was concentrated and pale purple crystals of the product could be isolated by cooling the mixture to −30 °C overnight.

Analysis of the obtained crystals by single-crystal X-ray diffraction gave the structure shown in **Figure 5.26**. Again, the inability to locate rhenium, due to it having an almost identical atomic form factor to tungsten, means the obtained structure is isomorphous with $(TBA)_2[W_6O_{19}]$. This is the expected result but, apart from the colour of the crystals, does not provide direct evidence of the formation of $(TBA)_2[Re(VI)W_5O_{19}]$.
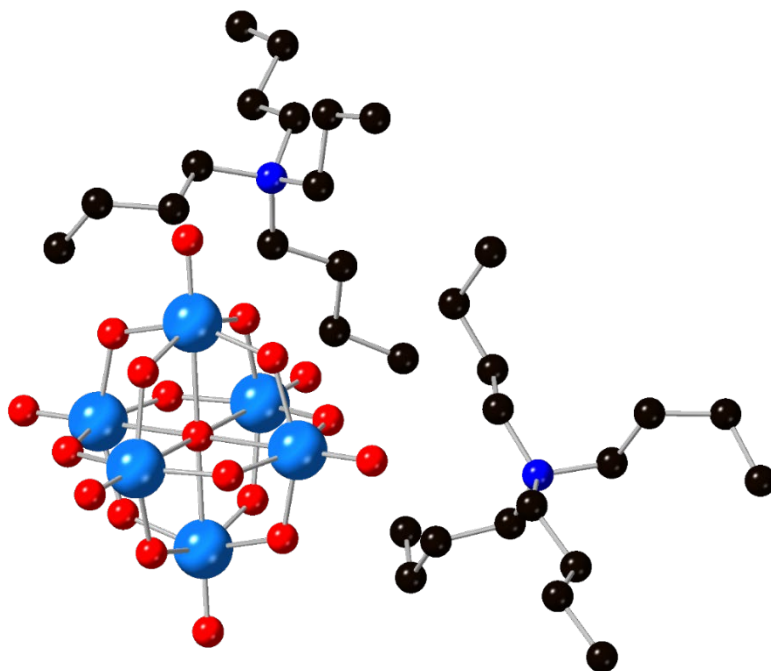
Figure 5.26: Single-crystal X-ray diffraction structure of (TBA)$_2$[Re(VI)W$_5$O$_{19}$] with the cations shown. Some disorder on the tetrabutylammonium cations was masked for clarity. Atomic radii set to CSD covalent radii.

Analysis of the crystals by infrared spectroscopy gave the spectrum shown in **Figure 5.27**. There is a clear shift in the terminal W=O stretching frequency from 951 cm^{-1} in (TBA)$_3$[ReW$_5$O$_{19}$] to 967 cm^{-1} in (TBA)$_2$[Re(VI)W$_5$O$_{19}$]. This is consistent with the reduction in the charge of the cluster from 3– to 2– upon oxidation of the rhenium centre. Furthermore, there is now an additional low intensity peak at 926 cm^{-1}. This may be assignable to a terminal Re(VI)=O stretching vibration. The bridging region is very similar to that of (TBA)$_3$[ReW$_5$O$_{19}$],
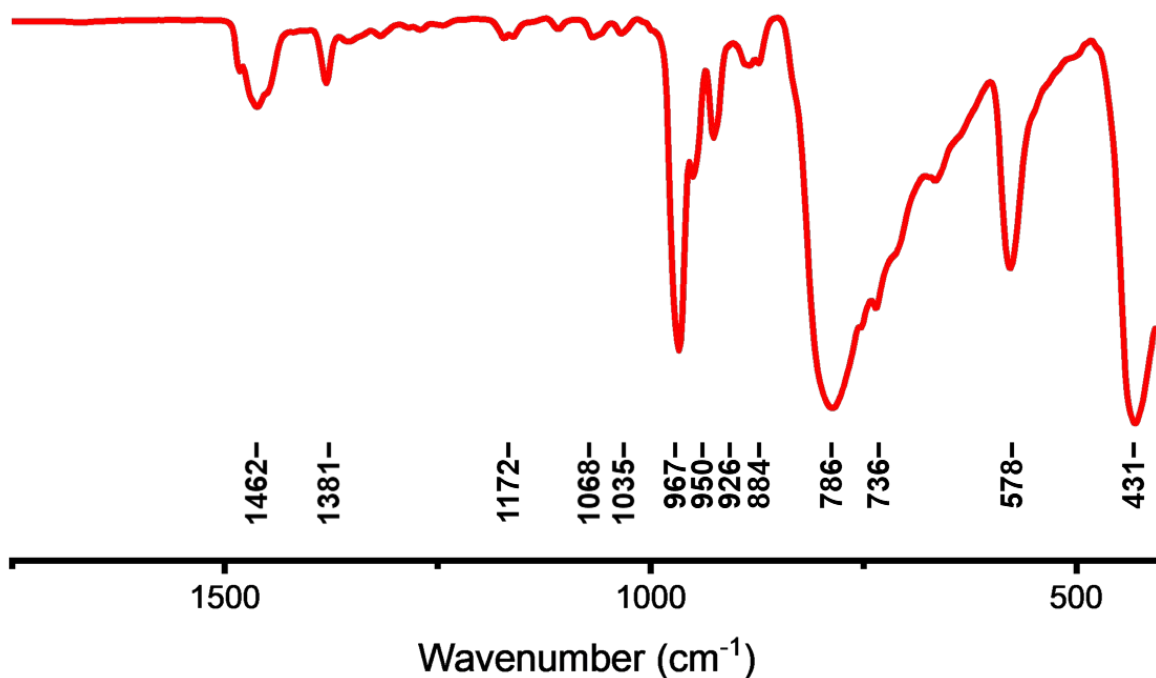
Figure 5.27: ATR FTIR transmittance spectrum of crystalline (TBA)$_2$[ReW$_5$O$_{19}$].

although it has been shifted up from 775 cm^{-1} to 786 cm^{-1}, which again is likely a result of the decreased charge of the cluster.

These results support the isolation of the oxidised compound (TBA)$_2$[Re(VI)W$_5$O$_{19}$]. Additional characterisation including elemental analysis, inductively coupled plasma optical emission spectroscopy (to determine metal ratios), and electron paramagnetic resonance spectroscopy would be desirable to further confirm the formation of (TBA)$_2$[Re(VI)W$_5$O$_{19}$].

5.6.4 Attempted synthesis of (TBA)$_3$[(PhN)ReW$_5$O$_{18}$]

M(V)/M(VI) organoimido complexes are well known.[45] They are often conveniently accessed from the corresponding M=O complex by treatment with isocyanates.[46] This chemistry was expanded to POMs by Matta, who showed that organoimido derivatives of hexamolybdate, with the general formula [(RN)Mo$_6$O$_{18}$]$^{2-}$, could be accessed by refluxing the POM in dry pyridine in the presence of isocyanates.[47,48] Though this chemistry has been around for a long time, it has never been expanded to the [M(V)W$_5$O$_{19}$]$^{3-}$ (M = V, Nb, and Ta) POMs already known in the literature.

After developing a general approach to the synthesis of these metal(V) containing POMs, the formation of the corresponding organoimido complexes was explored. However, several reactions targeting (TBA)$_3$[(RN)VW$_5$O$_{18}$] all failed. These included reactions with isocyanates in pyridine and acetonitrile, reaction with isothiocyanates, and reactions with primary amines in the presence of a dehydrating agent (usually N,N'-dicyclohexylcarbodiimide) both in acetonitrile and DMSO. These results indicated that the V=O unit is apparently unreactive with respect to organoimido formation when placed in the Lindqvist polyoxotungstate environment.

After isolation of (TBA)$_3$[ReW$_5$O$_{19}$], a similar study was performed to ascertain whether the Re=O unit displayed different reactivity to the V=O unit. The compound was dissolved in pyridine and refluxed overnight in the presence of phenyl isocyanate. During this time there was a slight colour change from dark red/black to a dark orange/brown. The solution was allowed to cool to room temperature before the volatiles were removed and the crude residue was dissolved in acetonitrile. Diethyl ether was slowly added to the solution, via vapour diffusion, leading to the formation of crystals. Analysis of these crystals by single-crystal X-ray diffraction gave a disordered structure which gave evidence of the formation of the desired organoimido-containing POM. The {(PhN)ReW$_5$O$_{18}$} unit shown in **Figure 5.28** was accompanied by a disordered Lindqvist-unit. Only two TBA units per Lindqvist unit were
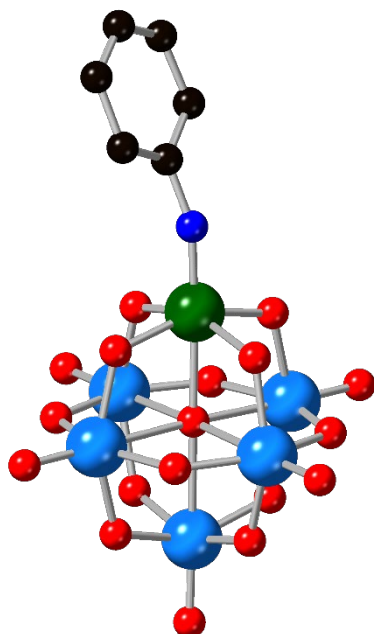
Figure 5.28: {(PhN)ReW$_5$O$_{18}$} unit obtained as part of a disordered structure from single-crystal X-ray diffraction experiments on the crystalline product of the reaction of (TBA)$_3$[ReW$_5$O$_{19}$] and PhNCO. Atomic radii set to CSD covalent radii.

located which may also indicate that the Re(V) centre was oxidised to Re(VI) during the reaction.

These preliminary findings suggest that organoimido derivatives of (TBA)$_3$[ReW$_5$O$_{19}$] are accessible, however further work is required to access pure samples and fully characterise them.

5.7 Conclusion

A single approach has been applied to the synthesis of seven metal(V) containing Lindqvist-type POMs. This approach was based on the basic degradation method developed in **Chapters 2** and **4**. The quantity of base (and water) used was varied to accommodate a range of heterometal sources, showing how robust the methodology is. The method was expanded to substituted polyoxomolybdates, allowing easy access to (TBA)$_3$[VMo$_5$O$_{19}$] and, the previously unknown, (TBA)$_3$[NbMo$_5$O$_{19}$]. Unfortunately, the corresponding tantalum containing compound has not been successfully isolated as of yet. Analysis of the degradation mixtures produced upon treatment of (TBA)$_2$[Mo$_6$O$_{19}$] with base show that the solutions predominately consist of mixtures of α-[Mo$_8$O$_{26}$]$^{4-}$, [Mo$_2$O$_7$]$^{2-}$, and (only at high charge to metal ratios) monomeric [MoO$_4$]$^{2-}$. This implies that the appropriate mixtures of independently prepared tetrabutylammonium salts of these isopolymolybdates may be used as building blocks for substituted Lindqvist-type POMs, in place of the {Mo$_6$}/TBA(OH) mixture.

Electrochemical experiments performed on the obtained POMs show that both the nature of the heterometal and framework metal have a significant impact on the redox properties of the cluster. These observations were largely rationalised with the aid of density functional theory calculations, which show that the nature of the LUMO, and the position of localisation of additional electron density upon reduction, can account for the variation.

5.8 Future work

This chapter has provided a very solid foundation for accessing group V metal containing Lindqvist-type POMs. However, the inability to isolate a pure sample of $(TBA)_3[TaMo_5O_{19}]$ leaves this work incomplete. In order to complete the series, the synthesis of $(TBA)_3[TaMo_5O_{19}]$ from $TaOCl_3$ should be attempted using the same method that was applied when employing $VOCl_3$ and $NbOCl_3(MeCN)_2$ as sources of the heterometal. This could be followed by electrochemical characterisation to see if it behaves similarly to $(TBA)_3[NbMo_5O_{19}]$, as predicted by DFT.

Along similar lines, further characterisation of $(TBA)_3[ReW_5O_{19}]$ by cyclic voltammetry and ICP-OES would give more insight into the electrochemical properties and purity of this compound. Electrochemical characterisation should give some understanding as to whether Re(VII) is accessible within the Lindqvist framework. If this is possible, chemical oxidation with an oxidising agent such as bromine should be attempted, hopefully yielding $(TBA)[Re(VII)W_5O_{19}]$. Characterisation of this (and $(TBA)_2[Re(VI)W_5O_{19}]$) by EPR and SQUID (superconducting quantum interference device) would give vital insight into the number and position of any unpaired electrons (for example proving the isolation of Re(VII) d^0 or checking if the electron in $(TBA)_2[Re(VI)W_5O_{19}]$ is delocalised).

5.9 Experimental

Note: The procedures used to isolate $(TBA)_3[M'M_5O_{19}]$ (M' = V, Nb, Ta and M = Mo, W) from $(TBA)_2[W_6O_{19}]$ or $(TBA)_2[Mo_6O_{19}]$ were often repeated on smaller scales (ca. 100 mg of starting material) using ^{17}O enriched starting materials to produce products with high levels of ^{17}O enrichment, and in turn acquire ^{17}O NMR spectra with good signal/noise ratios. Many of the preparations given below also involve the addition of H_2O and in these cases it is possible to introduce ^{17}O enrichment directly (without the use of pre-enriched materials) via the addition of ^{17}O enriched water, though the enrichment levels are slightly lower.

5.9.1 Synthesis of (TBA)₂[Mo₆O₁₉]

In a 50 mL conical flask, $Na_2MoO_4.2H_2O$ (2.5 g, 10.3 mmol) was dissolved in water (10 mL) with stirring. After complete dissolution, 6 M HCl (2.9 mL, 17.4 mmol) was added to the mixture using a burette over a one-minute period. A solution of TBA(Br) (1.2 g, 3.7 mmol) in water (2 mL) was added with stirring, leading to the immediate formation of a white precipitate. The solution was heated at 80 °C for 45 minutes, during which time the precipitate turns pale yellow. The solution was allowed to cool to room temperature and the solid was isolated using vacuum filtration. The solid was washed with water (3 x 20 mL), ethanol (10 mL), and diethyl ether (2 x 20 mL). The solid was recrystallized by dissolving the crude solid in boiling MeCN followed by slow cooling to −30 °C. Crystals were isolated using vacuum filtration and washed with diethyl ether (3 x 20 mL). The solid is dried in a vacuum oven at 50 °C overnight (1.7 g, 73% yield).

^{95}Mo NMR (32.6 MHz, d_6-DMSO, 353 K) δ (ppm) = 127.7. **^1H NMR** (300 MHz, CD_3CN) δ (ppm) = 0.98 (24 H, t, CH_3), 1.38 (16 H, sext, CH_2), 1.62 (16 H, qu, CH_2), 3.12 (16H, m, CH_2). **^{13}C NMR** (75.5 MHz, CD_3CN) δ (ppm) = 13.4, 20.0, 24.0, 58.9. ν_{max}/cm^{-1} = 2961 (CH), 2931 (CH), 2873 (CH), 1469, 1379, 1175, 1106, 1065, 1029, 950 (vs), 879, 784 (vs), 739, 589, 421 (vs). **ES** m/z = 440.2 [M-Mo_6O_{19}]$^{2-}$.

5.9.2 Synthesis of approx. 7% ¹⁷O enriched (TBA)₂[Mo₆O₁₉]

$(TBA)_2[Mo_6O_{19}]$ (1.0 g, 0.73 mmol) was added to a stainless-steel jar along with two 10 mm stainless steel ball bearings. 40% ^{17}O enriched H_2O (66 µL, 3.7 mmol) was added. The jar was sealed and the reaction mixture was milled at 30 Hz for two hours. The finely divided yellow powder was transferred to a glass sample vial and dried in a vacuum oven overnight at 50 °C. ^{17}O NMR spectrum shows clean enrichment of the starting material and complete removal of

residual water. The powder can be recrystallized from hot MeCN if desired, but it is not required.

^{17}O NMR (67.8 MHz, CD$_3$CN) δ (ppm) = −25.4 (μ_6-O, 1 O), 565.5 (Mo-O-Mo, 12 O), 937.3 (Mo=O, 6 O).

5.9.3 Degradation reactions of ^{17}O enriched (TBA)$_2$[Mo$_6$O$_{19}$] with TBA(OH)

^{17}O enriched (TBA)$_2$[Mo$_6$O$_{19}$] (50 mg, 0.04 mmol) was added to a Schlenk flask and suspended in MeCN (1 mL). The appropriate amount of (TBA)OH (0.25 M in MeCN) was added to the flask. The total volume of the reaction mixture was made up to approx. 3 mL. The solution was stirred at room temperature for 3 days. The solvent was removed and the residual oil was dissolved in CD$_3$CN (0.5 mL). The mixture was transferred to a 5 mm screw top NMR tube for ^{17}O NMR spectroscopy.

5.9.4 Synthesis of VO(O^{t}Bu)$_3$

V$_2$O$_5$ (10 g, 55 mmol) was ground to fine powder using a pestle and mortar and then added to a 500 mL round bottom flask. *Tert*-butanol (250 mL) was added and the suspension was heated at 110 °C with stirring for five days. The mixture was cooled to room temperature and the green/yellow suspension was filtered through Celite. The remaining *tert*-butanol was removed by distillation (hot plate set to 115 °C, still head at 82 °C), leaving a colourless oil that solidifies if left to stand. The crude VO(O^{t}Bu)$_3$ was purified by vacuum distillation (hot plate at 130-140 °C, still head 60-80 °C). It may be required to warm parts of the still head with a heat gun to prevent solid forming in the still head. Again, the distilled oil solidifies at room temperature.

^{51}V NMR (29.9 MHz, CD$_3$CN) δ (ppm) = −672 **^{1}H NMR** (300 MHz, CD$_3$CN) δ (ppm) = 1.44 (s, CH$_3$)

5.9.5 Synthesis of (TBA)$_3$[VW$_5$O$_{19}$] from (TBA)$_2$[W$_6$O$_{19}$] and VO(O^{t}Bu)$_3$

TBA(OH) (1.7 mL, 1.7 mmol, 1 M soln. in MeOH) was added to a Schlenk flask and the solvent removed under vacuum to give a thick oil, which was dissolved in MeCN (2-3 mL) and then the solvent was removed again. This process was repeated twice more to ensure removal of the MeOH. The oil was dissolved in MeCN (20 mL) and (TBA)$_2$[W$_6$O$_{19}$] (2 g, 1.1 mmol) added. The suspension was stirred at room temperature for 60-90 minutes or until all the solid had dissolved. H$_2$O (19.1 µL, 1.1 mmol) was added and solution was stirred overnight. The mixture was transferred via cannula to a separate Schlenk containing VO(O^{t}Bu)$_3$ (0.36 g, 1.3 mmol). The reaction mixture immediately started to turn yellow. The solution was stirred at room temperature overnight. The volatiles were removed, and the crude yellow solid was

recrystallized by dissolving in the minimum amount of hot MeCN followed by cooling to −30 °C in a freezer overnight. The crystals were isolated by vacuum filtration and washed with diethyl ether (2 x 20 mL). The crystals were dried in a vacuum overnight at 50 °C (2.1 g, 83% yield). (Note: solid can also be easily recrystallized by slow evaporation of saturated DCM solutions).

^{51}V NMR (29.9 MHz, CD$_3$CN) δ (ppm) = −508. **^{183}W NMR** (20.8 MHz, d_6-DMSO) δ (ppm) −79.6 ppm (broad). **^{17}O NMR** (40.7 MHz, CD$_3$CN) δ (ppm) = −72.8 (μ$_6$-O, 1 O), 390.8 (W-O-W, 4 O), 397.8 (W-O-W, 4 O), 564.4 (V-O-W, 4 O), 733.4 (W=O, 5 O), 1217.9 (V=O, 1 O). **^{1}H NMR** (300 MHz, CD$_3$CN) δ (ppm) = 0.98 (24 H, t, CH$_3$), 1.40 (16 H, sext, CH$_2$), 1.64 (16 H, qu, CH$_2$), 3.17 (16H, m, CH$_2$). **^{13}C NMR** (75.5 MHz, CD$_3$CN) δ (ppm) = 13.5, 20.0, 24.1, 58.9. **v_{max}/cm^{-1}** = 2958 (CH), 2872 (CH), 1481, 1381, 1151, 1107, 1055, 1026, 989, 963, 949 (vs), 883, 788 (vs), 736, 581, 436 (vs).

5.9.6 Synthesis of (TBA)$_3$[VW$_5$O$_{19}$] from (TBA)$_2$[W$_6$O$_{19}$] and VOCl$_3$

TBA(OH) (5.9 mL, 5.5 mmol, 0.93 M soln. in MeOH) was added to a Schlenk flask and the solvent removed under vacuum to give a thick oil, which was dissolved in MeCN (5 mL) and the solvent was removed again. This process was repeated twice more to ensure complete removal of the MeOH. The oil was dissolved in MeCN (15 mL) and (TBA)$_2$[W$_6$O$_{19}$] (2 g, 1.1 mmol) added. The suspension was stirred at room temperature for 15 minutes or until all the solid had dissolved. The volatiles were removed, and the oil was re-dissolved in MeCN (5 mL). The mixture was pumped dry and this process was repeated. The oil was dissolved in pyridine (15 mL). VOCl$_3$ (0.12 mL, 0.22 g, 1.3 mmol) was added, initially turning the mixture red/brown and then quickly gave way to a green/brown solution. The mixture was stirred at room temperature overnight. Iodine (1-2 crystals) were added which removed the green colour and left a brown solution. The volatiles were removed, and the crude yellow/brown solid was recrystallized by dissolving in the minimum amount of hot MeCN, followed by cooling to −30 °C in a freezer overnight. The crystals were isolated by vacuum filtration and washed with cold dichloromethane (3 x 2 mL) and diethyl ether (2 x 20 mL). The crystals were dried in a vacuum overnight at 50 °C (1.9 g, 75% yield). Identity of the product was confirmed by ^{51}V NMR spectroscopy, which showed a major peak at −508 ppm (CD$_3$CN). Small peaks at −510 and −364 ppm respectively were also observed.

5.9.7 Synthesis of (TBA)₃[VW₅O₁₉] from (TBA)₂[W₆O₁₉] and V₂O₅

TBA(OH) (1.7 mL, 1.7 mmol, 1 M soln. in MeOH) was added to a Schlenk flask and the solvent removed under vacuum to give a thick oil, which was dissolved in MeCN (2-3 mL) and the solvent was removed again. This process was repeated twice more to ensure complete removal of the MeOH. The oil was dissolved in pyridine (15 mL) and $(TBA)_2[W_6O_{19}]$ (2 g, 1.1 mmol) added. The suspension was stirred at room temperature for 60 minutes or until all the solid had dissolved. H_2O (19.1 μL, 1.1 mmol) was added and solution was stirred overnight. The mixture was transferred via cannula to a separate Schlenk containing V_2O_5 (0.12 g, 0.63 mmol). A brown/green suspension formed which was refluxed for two days. While still warm, the mixture was filtered through a bed of Celite. The filter cake was washed with MeCN (2 x 5 mL). The volatiles were removed, and the crude yellow solid was recrystallized by dissolving in the minimum amount of hot MeCN followed by cooling to −30 °C in a freezer overnight. The crystals were isolated by vacuum filtration and washed with diethyl ether (2 x 20 mL). The crystals were dried in a vacuum overnight at 50 °C (1.6 g, 63% yield). Identity of the product was confirmed by ^{51}V NMR spectroscopy which showed a single peak at −508 ppm (CD_3CN).

5.9.8 Synthesis of (TBA)₃[VW₅O₁₉] from WO₃.H₂O and V₂O₅

TBA(OH) (4.8 mL, 4.8 mmol, 1 M soln. in MeOH) was added to a Schlenk flask and the solvent removed under vacuum to give a thick oil, which was dissolved in MeCN (5 mL) and the solvent was removed again. This process was repeated twice more to ensure complete removal of the MeOH. The oil was dissolved in pyridine (20 mL). $WO_3.H_2O$ (2 g, 8.0 mmol) and V_2O_5 (0.15 g, 0.80 mmol) were added. The resulting green/brown suspension was heated at reflux for 2-3 days. While still warm, the mixture was filtered through a bed of celite. The filter cake was washed with MeCN (2 x 5 mL). The volatiles were removed, and the crude yellow solid was recrystallized by dissolving in the minimum amount of hot MeCN followed by cooling to −30 °C in a freezer overnight. The crystals were isolated by vacuum filtration and washed with diethyl ether (2 x 20 mL). The crystals were dried in a vacuum overnight at 50 °C (1.7 g, 53% yield). Identity of the product was confirmed by ^{51}V NMR spectroscopy which showed a single peak at −507 ppm (CD_3CN).

5.9.9 Synthesis of (TBA)₃[NbW₅O₁₉] from (TBA)₂[W₆O₁₉] and Nb(OEt)₅

TBA(OH) (1.7 mL, 1.7 mmol, 1 M soln. in MeOH) was added to a Schlenk flask and the solvent removed under vacuum to give a thick oil, which was dissolved in MeCN (2-3 mL) and the solvent was removed again. This process was repeated twice more to ensure complete

removal of the MeOH. The oil was dissolved in MeCN (20 mL) and (TBA)$_2$[W$_6$O$_{19}$] (2 g, 1.1 mmol) added. The suspension was stirred at room temperature for 60-90 minutes or until all the solid had dissolved. H$_2$O (42.0 μL, 2.3 mmol) was added and solution was stirred overnight. The mixture was transferred via cannula to a separate Schlenk containing Nb(OEt)$_5$ (0.40 g, 1.3 mmol). The colourless solution was stirred at room temperature overnight. The volatiles were removed, and the crude white solid was recrystallized by dissolving in the minimum amount of hot MeCN, followed by cooling to −30 °C in a freezer overnight. The crystals were isolated by vacuum filtration and washed with diethyl ether (2 x 20 mL). The crystals were dried in a vacuum overnight at 50 °C. (2.0 g, 77% yield) (note: solid can also be easily recrystallized by slow evaporation of saturated DCM solutions).

^{93}Nb NMR (122.4 MHz, d_6-DMSO) δ (ppm) = −883 ppm. **^{17}O NMR** (40.7 MHz, CD$_3$CN) δ (ppm) = −64.7 (μ$_6$-O, 1 O), 394.0 (W-O-W, 8 O), 457.6 (Nb-O-W, 4 O), 734.2 (W=O, 5 O), Nb=O not resolved. **^{183}W NMR** (20.8 MHz, d_6-DMSO) δ (ppm) = 29.4 (1W), 74.5 (4W). **^{1}H NMR** (300 MHz, CD$_3$CN) δ (ppm) = 0.98 (24 H, t, CH$_3$), 1.41 (16 H, sext, CH$_2$), 1.65 (16 H, qu, CH$_2$), 3.19 (16H, m, CH$_2$). **^{13}C NMR** (75.5 MHz, CD$_3$CN) δ (ppm) = 13.9, 20.3, 24.5, 59.3. ***v*$_{max}$/cm^{-1}** = 2959 (CH), 2873 (CH), 1482, 1380, 1151, 1107, 1056, 1027, 953 (vs), 915, 885, 789 (Vs), 585, 431 (vs).

5.9.10 Synthesis of NbCl$_5$

Nb$_2$O$_5$.4.33H$_2$O (10.7 g, 31 mmol) was added to a round bottom flask along with thionyl chloride (150 mL) forming a white suspension. The mixture was stirred at room temperature for 72 hours under a stream of N$_2$ (to remove any HCl gas). The nitrogen was bubbled into water after passing through the flask to capture the HCl. The stirring was stopped allowing any residual niobium oxide to settle. The yellow solution was separated via cannula filtration. The volatiles were removed under reduced pressure (note: residual thionyl chloride should be captured in a cold trap and either quenched slowly with ethanol or stored for recycling). The remaining yellow/brown solid was taken into a glovebox and transferred to a sublimation flask. A small layer of glass wool was placed on top of the solid to prevent mixing of the crude and sublimed solid. The crude material was purified by vacuum sublimation at 150 °C leading to the formation of yellow needles on the walls of the flask. (8.9 g, 53% yield based on Nb)

5.9.11 Synthesis of NbOCl$_3$(MeCN)$_2$

NbCl$_5$ (2.2 g, 8.1 mmol) was added to a Schlenk flask with MeCN (15 mL) forming a yellow suspension. In a separate Schlenk flask, hexamethyldisiloxane (1.3 g, 1.7 mL, 8.1 mmol) was dissolved in MeCN (10 mL) and added slowly, via cannula, to the mixture. The yellow solution

was stirred at room temperature for two hours during which time it turned colourless. If required, the solution was filtered to remove any insoluble material and then the solution was concentrated to approximately half the volume under reduced pressure. The solution was cooled to −30 °C in a freezer overnight. The colourless crystals that formed were separated from the mother liquor using cannula filtration and dried under vacuum to leave a white solid (2.0 g, 83% yield).

v_{max}/cm^{-1} = 3000 (CH), 2932 (CH), 2313, 2301, 2284, 2274, 1404, 1364, 1352, 1024, 955 (vs), 945, 930, 792.

5.9.12 Synthesis of (TBA)$_3$[NbW$_5$O$_{19}$] from (TBA)$_2$[W$_6$O$_{19}$] and NbOCl$_3$(MeCN)$_2$

TBA(OH) (1.5 mL, 1.4 mmol, 0.93 M soln. in MeOH) was added to a Schlenk flask and the solvent removed under vacuum to give a thick oil, which was dissolved in MeCN (2-3 mL) and the solvent was removed again. This process was repeated twice more to ensure complete removal of the MeOH. The oil was dissolved in MeCN (5 mL) and (TBA)$_2$[W$_6$O$_{19}$] (0.5 g, 0.26 mmol) added. The suspension was stirred at room temperature for 15 minutes or until all the solid had dissolved. The volatiles were removed, and the oil was re-dissolved in MeCN (5 mL). The mixture was pumped dry and this process was repeated. The oil was dissolved in pyridine (5 mL). Solid NbOCl$_3$(MeCN)$_2$ (94.3 mg, 0.32 mmol) was added. The colourless solution was stirred overnight. The solution was slightly cloudy at this point, and therefore the mixture was passed through a PTFE syringe filter and the volatiles were removed. The crude oil obtained was recrystallized by dissolving in the minimum amount of hot MeCN followed by cooling to −30 °C in a freezer overnight. The colourless crystals that formed were separated from the mother liquor using cannula filtration and dried under vacuum to leave a white solid (0.43 g, 80% yield).

5.9.13 Synthesis of (TBA)$_3$[TaW$_5$O$_{19}$] from (TBA)$_2$[W$_6$O$_{19}$] and Ta(OEt)$_5$

TBA(OH) (1.7 mL, 1.7 mmol, 1 M soln. in MeOH) was added to a Schlenk flask and the solvent removed under vacuum to give a thick oil, which was dissolved in MeCN (2-3 mL) and the solvent was removed again. This process was repeated twice more to ensure complete removal of the MeOH. The oil was dissolved in MeCN (20 mL) and (TBA)$_2$[W$_6$O$_{19}$] (2 g, 1.1 mmol) added. The suspension was stirred at room temperature for 60-90 minutes or until all the solid had dissolved. H$_2$O (42.0 μL, 2.3 mmol) was added and solution was stirred overnight. The mixture was transferred via cannula to a separate Schlenk containing Ta(OEt)$_5$ (0.52 g, 1.3 mmol). The colourless solution was stirred at room temperature overnight. The volatiles were

removed, and the crude white solid was recrystallized by dissolving in the minimum amount of hot MeCN followed by cooling to −30 °C in a freezer overnight. The crystals were isolated by vacuum filtration and washed with diethyl ether (2 x 20 mL). The crystals were dried in a vacuum overnight at 50 °C. (1.9 g, 70% yield) (note: solid can also be easily recrystallized by slow evaporation of saturated DCM solutions).

^{17}O NMR (40.7 MHz, CD$_3$CN) δ (ppm) = −72.7 (μ_6-O, 1 O), 394.8 (W-O-W, 8 O), 421.6 (Ta-O-W, 4 O), 735.8 (W=O, 5 O), Ta=O not resolved. ^{183}W NMR (20.8 MHz, d_6-DMSO) δ (ppm) = 39.7 (1W), 69.7 (4W). ^{1}H NMR (300 MHz, CD$_3$CN) δ (ppm) = 0.98 (24 H, t, CH$_3$), 1.41 (16 H, sext, CH$_2$), 1.65 (16 H, qu, CH$_2$), 3.17 (16H, m, CH$_2$). ^{13}C NMR (75.5 MHz, CD$_3$CN) δ (ppm) = 13.9, 20.3, 24.4, 59.3. v_{max}/cm^{-1} = 2959 (CH), 2873 (CH), 1481, 1381, 1152, 1107, 1054, 1026, 953 (vs), 906, 884, 783 (vs), 574, 496, 426 (vs).

5.9.14 Synthesis of (TBA)$_3$[VMo$_5$O$_{19}$] from (TBA)$_2$[Mo$_6$O$_{19}$] and V$_2$O$_5$

TBA(OH) (2.3 mL, 2.3 mmol, 1 M soln. in MeOH) was added to a Schlenk flask and the solvent removed under vacuum to give a thick oil, which was dissolved in MeCN (2-3 mL) and the solvent was removed again. This process was repeated twice more to ensure complete removal of the MeOH. The oil was dissolved in pyridine (15 mL) and (TBA)$_2$[Mo$_6$O$_{19}$] (2 g, 1.5 mmol) added. The suspension was stirred at room temperature for 60 minutes or until all the solid had dissolved. H$_2$O (26.5 μL, 1.5 mmol) was added and solution was stirred overnight. At this point, the solution was pale brown. The mixture was transferred via cannula to a separate Schlenk containing V$_2$O$_5$ (0.16 g, 0.88 mmol). A brown suspension formed which was refluxed for two days. While still warm, the mixture was filtered through a bed of Celite. The filter cake was washed with MeCN (2 x 5 mL). The volatiles were removed, and the crude yellow solid was recrystallized by dissolving in the minimum amount of hot MeCN followed by cooling to −30 °C in a freezer overnight. The crystals were isolated by vacuum filtration and washed with diethyl ether (2 x 20 mL). The crystals were dried in a vacuum overnight at 50 °C (2.1 g, 76% yield).

^{51}V NMR (29.9 MHz, CD$_3$CN) δ (ppm) = −487. ^{95}Mo NMR (32.6 MHz, d_6-DMSO) δ (ppm) = −6.7, 144.9. ^{17}O NMR (40.7 MHz, CD$_3$CN) δ (ppm) = −23.8 (μ_6-O, 1 O), 532.1 (Mo-O-Mo, 4 O), 541.4 (Mo-O-Mo, 4 O), 667.7 (V-O-Mo, 4 O), 889.5 (Mo=O, 5 O), 1204.0 (V=O, 1 O). ^{1}H NMR (300 MHz, CD$_3$CN) δ (ppm) = 0.97 (24 H, t, CH$_3$), 1.41 (16 H, sext, CH$_2$), 1.65 (16 H, qu, CH$_2$), 3.19 (16H, m, CH$_2$). ^{13}C NMR (75.5 MHz, CD$_3$CN) δ (ppm) = 13.9, 20.3, 24.5, 59.3. v_{max}/cm^{-1} = 2959

(CH), 2872 (CH), 1480, 1424, 1381, 1151, 1106, 1055, 1026, 976, 949, 929 (vs), 883, 853, 782 (vs), 662, 586, 426 (vs).

5.9.15 Synthesis of (TBA)₃[VMo₅O₁₉] from MoO₃ and V₂O₅

TBA(OH) (4.8 mL, 4.8 mmol, 1 M soln. in MeOH) was added to a Schlenk flask and the solvent removed under vacuum to give a thick oil, which was dissolved in MeCN (5 mL) and the solvent was removed again. This process was repeated twice more to ensure complete removal of the MeOH. The oil was dissolved in pyridine (20 mL). MoO_3 (2 g, 13.9 mmol) and V_2O_5 (0.25 g, 1.4 mmol) were added. (Note: the product can be statistically ^{17}O enriched by the addition of 0.5 eq. of 40% ^{17}O enriched H_2O per MoO_3 at this point). The resulting brown suspension was heated at reflux for 2-3 days. While still warm, the mixture was filtered through a bed of Celite. The filter cake was washed with MeCN (2 x 5 mL). The volatiles were removed, and the crude yellow solid was recrystallized by dissolving in the minimum amount of hot MeCN followed by cooling to −30 °C in a freezer overnight. The crystals were isolated by vacuum filtration and washed with diethyl ether (2 x 20 mL). The crystals were dried in a vacuum overnight at 50 °C (2.4 g, 46% yield). Identity of the product was confirmed by ^{51}V NMR spectroscopy, which showed a single peak at −488 ppm (CD₃CN).

5.9.16 Synthesis of (TBA)₃[NbMo₅O₁₉] from (TBA)₂[Mo₆O₁₉] and Nb(OEt)₅

TBA(OH) (2.3 mL, 2.3 mmol, 1 M soln. in MeOH) was added to a Schlenk flask and the solvent removed under vacuum to give a thick oil, which was dissolved in MeCN (2-3 mL) and the solvent was removed again. This process was repeated twice more to ensure complete removal of the MeOH. The oil was dissolved in MeCN (15 mL) and $(TBA)_2[Mo_6O_{19}]$ (2 g, 1.5 mmol) added. The suspension was stirred at room temperature for 60 minutes or until all the solid had dissolved. H_2O (58.1 μL, 3.2 mmol) was added and solution was stirred overnight. At this point the solution was pale brown. The mixture was transferred via cannula to a separate Schlenk containing Nb(OEt)₅ (0.56 g, 1.8 mmol) dissolved in MeCN (10 mL). The solution was stirred overnight during which time the solution becomes pale yellow. The volatiles were removed, and the crude pale-yellow solid was recrystallized by dissolving in the minimum amount of hot MeCN followed by cooling to −30 °C in a freezer overnight. The crystals were isolated by vacuum filtration and washed with diethyl ether (2 x 20 mL). The crystals were dried in a vacuum overnight at 50 °C (1.9 g, 81% yield).

^{93}**Nb NMR** (122.4 MHz, d_6-DMSO) δ (ppm) = −885 ppm. ^{95}**Mo NMR** (32.6 MHz, d_6-DMSO) δ (ppm) = −7.0, 135.1. ^{17}**O NMR** (40.7 MHz, CD₃CN) δ (ppm) = −17.6 (μ₆-O, 1 O), 526.5 (Mo-O-

Mo, 4 O), 545.5 (Nb-O-Mo, 4 O, broad), 555.1 (Mo-O-Mo, 4 O), 882.5 (Mo=O, 1 O), 891.9 (Mo=O, 4 O), Nb=O not resolved. **^{1}H NMR** (300 MHz, CD$_3$CN) δ (ppm) = 0.97 (24 H, t, CH$_3$), 1.40 (16 H, sext, CH$_2$), 1.64 (16 H, qu, CH$_2$), 3.20 (16H, m, CH$_2$). **^{13}C NMR** (75.5 MHz, CD$_3$CN) δ (ppm) = 13.9, 20.3, 24.5, 59.3. **v_{max}/cm^{-1}** = 2958 (CH), 2873 (CH), 1481, 1380, 1151, 1107, 1055, 1026, 964, 933 (vs), 903, 776 (vs), 663, 566, 453 (s).

5.9.17 Attempted synthesis of (TBA)$_3$[TaMo$_5$O$_{19}$] from (TBA)$_2$[Mo$_6$O$_{19}$] and Ta(OEt)$_5$

TBA(OH) (2.3 mL, 2.3 mmol, 1 M soln. in MeOH) was added to a Schlenk flask and the solvent removed under vacuum to give a thick oil, which was dissolved in MeCN (2-3 mL) and the solvent was removed again. This process was repeated twice more to ensure complete removal of the MeOH. The oil was dissolved in MeCN (15 mL) and (TBA)$_2$[Mo$_6$O$_{19}$] (2 g, 1.5 mmol) added. The suspension was stirred at room temperature for 60 minutes or until all the solid had dissolved. H$_2$O (58.1 μL, 3.2 mmol) was added and solution was stirred overnight. At this point the solution was pale brown. The mixture was transferred via cannula to a separate Schlenk containing Ta(OEt)$_5$ (0.71 g, 1.8 mmol) dissolved in MeCN (10 mL). The solution was stirred overnight at 60 °C. The volatiles were removed to leave a brown oil that was re-dissolved in the minimum amount of MeCN. The ^{17}O NMR spectrum was recorded and is shown in **Figure 5.17**. The major peaks correspond to α-[Mo$_8$O$_{26}$]$^{4-}$ and [Mo$_2$O$_7$]$^{2-}$, but there are small peaks at −26.0, 527.5, 562.0 and, 895.0 ppm which could be consistent with the formation of [TaMo$_5$O$_{19}$]$^{3-}$ as a minor product.

5.9.18 Attempted synthesis of (TBA)$_3$[TaMo$_5$O$_{19}$] from (TBA)$_2$[Mo$_2$O$_7$], (TBA)$_4$[Mo$_8$O$_{26}$], and Ta(OEt)$_5$

(TBA)$_2$[Mo$_2$O$_7$] (0.1 g, 0.13 mmol), (TBA)$_4$[Mo$_8$O$_{26}$] (0.27 g, 0.13 mmol) and Ta(OEt)$_5$ (2.5 mL, 0.1 M, 0.25 mmol) were added to a Schlenk flask with acetonitrile (15 mL). The mixture was stirred at 50 °C overnight. The mixture was cooled to room temperature and ^{17}O enriched water (11.4 μL, 0.63 mmol) was added. The mixture was stirred for one day at room temperature. The solvent was removed under reduced pressure, leaving a viscous oil. The oil was re-dissolved in the minimum amount of acetonitrile and the ^{17}O NMR spectrum was recorded (shown in **Figure 5.18**). The major peaks correspond to α-[Mo$_8$O$_{26}$]$^{4-}$ and [Mo$_2$O$_7$]$^{2-}$, but there are small peaks at −26.1, 528.0, 562.7 and, 896.1 ppm which could be consistent with the formation of [TaMo$_5$O$_{19}$]$^{3-}$ as a minor product.

5.9.19 Cyclic voltammetry of (TBA)₃[M'M₅O₁₉] compounds (M' = V, Nb, Ta and M = Mo, W)

Experiments were performed using a small (5 mL) three-electrode cell with a glassy carbon working electrode, a Ag/AgNO₃ non-aqueous reference electrode, and a platinum wire counter electrode. Solutions of the POM (3mM) in a 100 mM solution of TBA(PF₆) in acetonitrile were made up and used for analysis. Solutions were thoroughly degassed by bubbling Ar through the solutions for 10-20 minutes directly before measurement. The headspace of the cell was also purged with Ar through the experiments. Typically a scan rate of 100 mV/s was used.

5.9.20 Density functional theory calculations

Density Functional Theory (DFT) calculations were performed using the Gaussian 09 software package.[49] Geometries were optimised using the B3LYP[50] hybrid functional. A split valence basis set was applied in which oxygen atoms were treated with the 6-31G(d,p)[51-57] basis set and metal atoms were treated with the Lanl2dz[58-61] basis set. Since the compounds are anionic species in solution, the effects of solvent were applied using the Polarizable Continuum Model (PCM), using acetonitrile as the solvent of choice.[62] In order to verify that optimisation calculations had successfully found a minimum, frequency calculations were performed at the same level of theory. The outputs were then checked for the absence of any imaginary frequencies. The xyz co-ordinates of the optimised structures are given in **Appendix B Section B.2**. Reduction potentials (E°₁/₂) were calculated using the differences in Gibbs free energy between the oxidised and reduced forms of the same compounds, as shown in the equations below; where G(Ox) is the Gibbs free energy of the oxidised species, G(red) is the Gibbs free energy of the 1e⁻ reduced species and F is Faraday's constant.[63,64]

$$E°_{1/2} = \frac{G(Ox)-G(red)}{F}$$

$$E°_{1/2}(vs. \ ref) = E°_{1/2} - E°_{abs}(ref \ electrode)$$

$$E°_{abs}(Ag/AgNO_3, MeCN) = 4.727 \ V$$

5.9.21 Synthesis of ReOCl₃(PPh₃)₂

Re (2.01 g, 10.8 mmol) was added to a conical flask. An excess of H₂O₂ (20 mL, 30% w/v in water) was added **DROPWISE INTIALLY AND THEN VERY SLOWLY** with stirring (cooling can be used if necessary as large amounts of heat and effervescence were produced). The resulting solution was stirred at 80 °C for 1 hour, during which the black suspension turned pale brown/clear, and then at 150 °C for 1 hour to decompose any unreacted H₂O₂. The mixture was gravity filtered into a 500 mL rbf and the conical flask and filter paper were washed with

boiling water (50 mL). The solvent was removed on a rotary evaporator to leave an oil (this is usually anywhere from clear to dark green), which was dissolved in EtOH (170 mL). Triphenylphosphine (15.7 g, 60 mmol) was added to give a white suspension, followed by the addition of HCl (12 M, 18.2 mL) and heating under reflux under a stream of N_2 for 1 hour to give a yellow/green suspension. The solution was cooled to approx. 70 °C and vacuum filtered while still warm to give a yellow solid which was washed with boiling EtOH (100 mL), boiling toluene (100 mL) and Et_2O (2 x 20 mL) and dried in a vacuum oven (50 °C) overnight (7.1 g, 79% yield). The identity of the product was confirmed by the single peak in the ^{31}P NMR spectrum at −19 ppm ($CDCl_3$).

5.9.22 Synthesis of [ReO$_2$(Py)$_4$][Cl]

To a solution of $ReOCl_3(PPh_3)_2$ (1.24 g, 1.48 mmol) in acetone (25 mL) was added pyridine (2.5 mL) and water (1.25 mL). The mixture was refluxed for 90 minutes during which time an orange precipitate formed. The solution was allowed to cool and the solid was isolated by vacuum filtration. The solid was washed with toluene (2 x 5 mL) and Et_2O (2 x 5 mL) and dried in a vacuum oven (50 °C) overnight (0.82 g, 97% yield).

5.9.23 Synthesis of (TBA)$_3$[ReW$_5$O$_{19}$] from ReOCl$_3$(PPh$_3$)$_2$

TBA(OH) (5.5 mL, 5.5 mmol, 1M soln. in MeOH) was added to a Schlenk flask and the solvent removed under vacuum to give a thick oil, which was dissolved in MeCN (3-5 mL) and the solvent was removed again. This process was repeated twice more to ensure complete removal of the MeOH. The oil was dissolved in MeCN (10 mL) and $(TBA)_2[W_6O_{19}]$ (2 g, 1.1 mmol) added. The suspension was stirred at room temperature for 30-60 minutes until all of the solid had dissolved. The mixture was pumped dry and re-dissolved in MeCN (10 mL). This process was repeated once more before finally dissolving in pyridine (10 mL). In a separate Schlenk, $ReOCl_3(PPh_3)_2$ was dissolved in pyridine (20 mL) forming a dark green solution. The degradation mixture was added via cannula giving an immediate colour change to olive green and then dark brown/red. The mixture was stirred at room temperature overnight. The volatiles were removed under reduced pressure and the resulting sticky brown solid was triturated with toluene, EtOAc, Et_2O, and hexane to give a free flowing black/brown solid (2.1 g, 77% yield). Single-crystal X-ray diffraction quality crystals obtained by cooling a saturated DCM solution of the crude product.

[183]**W NMR** (20.8 MHz, CD_3CN) δ (ppm) = −102.8 (4W), 113.0 (1W). **^{1}H NMR** (300 MHz, CD_3CN) δ (ppm) = 0.99 (24 H, t, CH_3), 1.41 (16 H, sext, CH_2), 1.66 (16 H, qu, CH_2), 3.20 (16H, m, CH_2).

^{13}C NMR (75.5 MHz, CD$_3$CN) δ (ppm) = 13.9, 20.4, 24.5, 59.3. **ν_{max}/cm^{-1}** = 2960 (CH), 2935 (CH), 2873 (CH), 1481, 1381, 1363, 1152, 1107, 1057, 1027, 951 (vs), 884, 776 (vs), 570, 442 (vs).

5.9.24 Synthesis of (TBA)$_3$[ReW$_5$O$_{19}$] from [ReO$_2$(Py)$_4$][Cl] (non-enriched)

TBA(OH) (3.0 mL, 3 mmol, 1 M soln. in MeOH) was added to a Schlenk flask and the solvent removed under vacuum to give a thick oil, which was dissolved in MeCN (3-5 mL) and the solvent was removed again. This process was repeated twice more to ensure complete removal of the MeOH. The oil was dissolved in pyridine (10 mL) and (TBA)$_2$[W$_6$O$_{19}$] (2 g, 1.1 mmol) added. The suspension was stirred at room temperature for 30-60 minutes until all of the solid had dissolved and then transferred via cannula to a separate Schlenk containing [ReO$_2$(Py)$_4$][Cl] (0.72 g, 1.3 mmol). The orange suspension was stirred overnight at 60 °C to give a red/black solution which was cooled to room temperature, upon which some solid appeared to form. After removal of the solvent under reduced pressure, the resulting sticky black solid was triturated with EtOAc (10 mL) and Et$_2$O (10 mL) in alternation until a free flowing powder was obtained (2.1 g, 77% yield). The solid was recrystallized from a range of solvents including MeCN, DCM and pyridine – the best results in terms of purity were pyridine or pyridine/Et$_2$O.

5.9.25 Preparation of (TBA)$_3$[ReW$_5$O$_{19}$] from [ReO$_2$(Py)$_4$][Cl] by statistical enrichment

TBA(OH) (1.5 mL, 1.5 mmol, 1M soln. in MeOH) was added to a Schlenk flask and the solvent removed under vacuum to give a thick oil, which was dissolved in MeCN (2 mL) and the solvent was removed again. This process was repeated twice more and the oil was dissolved in MeCN (10 mL). (TBA)$_2$[W$_6$O$_{19}$] (1 g, 0.52 mmol) was added and the suspension stirred at room temperature for 30-60 minutes until all of the solid had dissolved.

40% ^{17}O enriched water (52 μL, 2.9 mmol, theoretically giving 6.2% enrichment) was added and the colourless solution was stirred overnight at room temperature. After removal of the solvent under reduced pressure, the resulting oily product was heated under vacuum at 50 °C for 1 hour, dissolved in MeCN (2 mL), and then pumped dry. The dissolution-evaporation process was repeated and pyridine (10 mL) was added to dissolve the resulting oil.

The mixture was transferred via cannula to a separate Schlenk containing [ReO$_2$(Py)$_4$][Cl] (0.36 g, 0.64 mmol) and the orange suspension was stirred overnight at 60 °C to give a red/black solution which was cooled to room temperature. The reaction mixture was concentrated and cooled to crystallize the compound directly from the reaction mixture. Crystals were separated

from the mother liquor by cannula filtration and dried under vacuum. The crystals were dissolved in the minimum amount of CD_3CN and the ^{17}O NMR spectrum was recorded.

^{17}O NMR (40.7 MHz, CD_3CN) δ (ppm) = −71.9 (μ_6-O, 1 O), 348.9 (W-O-W, 4 O), 393.9 (Re-O-W/W-O-W, 8 O), 715.3 (W=O, 1 O), 733.4 (W=O, 4 O), 997.1 (Re=O, 1 O).

5.9.26 Oxidation of (TBA)$_3$[ReW$_5$O$_{19}$] with Ag(OTf)

In a Schlenk flask (TBA)$_3$[ReW$_5$O$_{19}$] (0.5 g, 0.23 mmol) was dissolved in MeCN (6 mL). Ag(OTf) (66 mg, 0.26 mmol, 1.1 eq.) were added to the solution. The solution was heated at 60 °C overnight, giving a black/brown suspension. While the mixture was still hot, the suspension was passed through a PTFE syringe filter. This left a pale purple solution. The solution was allowed to cool to room temperature and slowly evaporate overnight. This led to the formation of pale purple crystals (analysed by SCXRD). The mother liquor was decanted and the crystals were washed with ethyl acetate (2 mL) and diethyl ether (2 mL) before drying under vacuum. (0.21 g, 47% yield)

v_{max}/cm^{-1} = 2963 (CH), 2936 (CH), 2876 (CH), 1462, 1381, 1172, 1068, 1034, 967 (vs), 950, 926, 884, 786 (vs), 735, 578 (s), 431 (vs).

5.9.27 Attempted synthesis of (TBA)$_3$[(RN)ReW$_5$O$_{18}$]

In a Schlenk flask, (TBA)$_3$[ReW$_5$O$_{19}$] (0.57 g, 0.27 mmol) was dissolved in pyridine (5 mL). PhNCO (58 μL, 0.53 mmol, 2 eq.) was added. The flask was sealed and heated at reflux overnight during which time the mixture turned from dark red/black to dark orange/brown. The mixture was allowed to cool to room temperature before the volatiles were removed. The residue was taken up in MeCN (approx. 2 mL). The solution was placed in a thin tube inside a Schlenk flask and surrounded diethyl ether (approx. 15 mL) for vapour diffusion. This led to the formation of crystals over 3 days, which were subsequently analysed by single-crystal X-ray diffraction.

5.10 References

1. R.J. Farrauto and C.H. Bartholomew, *Fundamentals of Industrial Catalytic Processes*, Chapman & Hall, London, 1997, 621–639.

2. I. E. Wachs, *Dalton Trans.*, 2013, **42**, 11762–11769.

3. K.Weissermel and H.-J. Arpe, *Industrial Organic Chemistry – Important Raw Materials and Intermediates*, Verlag Chemie, Weinheim, 1978, 335–339.

4. I. E. Wachs and B.M. Weckhuysen, *Appl. Catal., A*, 1997, 157, 67.

5. M. Ziolek, *Catal. Today*, 2003, **78**, 47–64.

6. Y. Chen, J. L. G. Fierro, T. Tanaka and I. E. Wachs, *J. Phys. Chem. B*, 2003, **107**, 5243–5250.

7. T. Ushikubo, *Catal. Today*, 2000, **57**, 331–338.

8. C. Nico, T. Monteiro and M. P. F. Graça, *Prog. Mater. Sci.*, 2016, **80**, 1–37.

9. C. Chaneliere, J. L. Autran, R. A. B. Devine and B. Balland, *Mater. Sci. Eng. R Reports*, 1998, **22**, 269–322.

10. C. M. J. Flynn and M. T. Pope, *Inorg. Chem.*, 1971, **10**, 2524–2529.

11. P. J. Domaille, *J. Am. Chem. Soc.*, 1984, **106**, 7677–7687.

12. S. Himeno, T. Osakai and A. Saito, *Bull. Chem. Soc. Jpn.*, 1991, **64**, 21–28.

13. M. Filowitz, R. K. C. Ho, W. G. Klemperer and W. Shum, *Inorg. Chem.*, 1979, **18**, 93–103.

14. M. Dabbabi and M. Boyer, *J. Inorg. Nucl. Chem.*, 1976, **38**, 1011–1014.

15. C. Sanchez, J. Livage, J. P. Launay and M. Fournier, *J. Am. Chem. Soc.*, 1983, **105**, 6817–6823.

16. V. W. Day, W. G. Klemperer and D. J. Maltbie, *Organometallics*, 1985, **4**, 104–111.

17. C. J. Besecker, W. G. Klemperer, D. J. Maltbie and D. A. Wright, *Inorg. Chem.*, 1985, **24**, 1027–1032.

18. E. Ishikawa, D. Kihara, Y. Togawa and C. Ookawa, *Eur. J. Inorg. Chem.*, 2019, **2019**, 402–409.

19. K. Bouadjadja-Rohan, C. Lancelot, M. Fournier, A. Bonduelle-Skrzypczak, A. Hugon, O. Mentré and C. Lamonier, *Eur. J. Inorg. Chem.*, 2015, **2015**, 2067–2075.

20. J. Tucher, Y. Wu, L. C. Nye, I. Ivanovic-Burmazovic, M. M. Khusniyarov and C. Streb, *Dalton Trans.*, 2012, **41**, 9938–9943.

21. L.-S. Wang, Y. Wang, C.-L. Lv, C. Guo, F.-Y. Xing, Y.-J. Dong, Z. Xie, S.-Y. Zhou and Y.-G. Wei, *Inorg. Chem. Front.*, 2022, **9**, 4413–4424.

22. W. Clegg, M. R. J. Elsegood, R. J. Errington and J. Havelock, *J. Chem. Soc., Dalton Trans.*, 1996, 681–690.

23. R. J. Errington, S. S. Petkar, P. S. Middleton, W. McFarlane, W. Clegg, R. A. Coxall and R. W. Harrington, *J. Chem. Soc., Dalton Trans.*, 2006, 5211–5222.

24. B. Kandasamy, C. Wills, W. McFarlane, W. Clegg, R. W. Harrington, A. Rodríguez-Fortea, J. M. Poblet, P. G. Bruce and R. J. Errington, *Chem. - A Eur. J.*, 2012, **18**, 59–62.

25. C. Daniel and H. Hartl, *J. Am. Chem. Soc.*, 2009, **131**, 5101–5114.

26. M. A. Fedotov and R. I. Maksimovskaya, *J. Struct. Chem.*, 2006, **47**, 952–978.

27. D. Brown and R. G. Cavell, in *Inorganic Syntheses*, 1967, pp. 88–92.

28. V. C. Gibson, T. P. Kee and A. Shaw, *Polyhedron*, 1988, **7**, 2217–2219.

29. L. Coyle, P. S. Middleton, C. J. Murphy, W. Clegg, R. W. Harrington and R. J. Errington, *Dalton Trans.*, 2012, **41**, 971–981.

30. (Mo) Molybdenum NMR, https://chem.ch.huji.ac.il/nmr/techniques/1d/row5/mo. html (accessed: 10/08/2023).

31. *Y. Huang, J. Zhang, J. Ge, C. Sui, J. Hao, Y. Wei, Chem. Commun., 2017, 53, 2551-2554.*

32. S.-X. Guo, J. Xie, R. Gilbert-Wilson, S. L. Birkett, A. M. Bond and A. G. Wedd, *Dalton Trans.*, 2011, **40**, 356–366.

33. L. S. Crocker, G. L. Gould and D. M. Heinekey, *J. Organomet. Chem.*, 1988, **342**, 243–244.

34. W. Lukas and M. Gaune-Escard, *J. Chem. Thermodyn.*, 1982, **14**, 593–597.

35. W. A. Herrmann, *Angew. Chem. Int. Ed. English*, 1988, **27**, 1297–1313.

36. A. M. Al-Ajlouni and J. H. Espenson, *J. Am. Chem. Soc.*, 1995, **117**, 9243–9250.

37. J. G. Darab and P. A. Smith, *Chem. Mater.*, 1996, **8**, 1004–1021.

38. L. H. Davies, B. B. Kasten, P. D. Benny, R. L. Arrowsmith, H. Ge, S. I. Pascu, S. W. Botchway, W. Clegg, R. W. Harrington and L. J. Higham, *Chem. Commun.*, 2014, **50**, 15503–15505.

39. F. Ortega and M. T. Pope, *Inorg. Chem.*, 1984, **23**, 3292–3297.

40. A. Venturelli, M. J. Nilges, A. Smirnov, R. L. Belford and L. C. Francesconi, *J. Chem. Soc. Dalton Trans.*, 1999, 301–310.

41. N. P. Johnson, C. J. L. Lock, G. Wilkinson, J. L. Booker and R. J. Thompson, in *Inorganic Syntheses*, 1967, pp. 145–148.

42. D. R. Baghurst and D. M. P. Mingos, *J. Organomet. Chem.*, 1990, **384**, C57–C60.

43. A. A. Woolf, *Q. Rev. Chem. Soc.*, 1961, **15**, 372–391.

44. N. J. Stone, *At. Data Nucl. Data Tables*, 2016, **111–112**, 1–28.

45. T. R. Cundari, *J. Am. Chem. Soc.*, 1992, **114**, 7879–7888.

46. G. Horrer, I. Krummenacher, S. Mann, H. Braunschweig and U. Radius, *Dalton Trans.*, 2022, **51**, 11054–11071.

47. J. B. Strong, R. Ostrander, A. L. Rheingold and E. A. Maatta, *J. Am. Chem. Soc.*, 1994, **116**, 3601–3602.

48. J. B. Strong, G. P. A. Yap, R. Ostrander, L. M. Liable-Sands, A. L. Rheingold, R. Thouvenot, P. Gouzerh and E. A. Maatta, *J. Am. Chem. Soc.*, 2000, **122**, 639–649.

49. M. J. Frisch, G. W. Trucks, H. B. Schlegel, G. E. Scuseria, M. A. Robb, J. R. Cheeseman, G. Scalmani, V. Barone, G. A. Petersson, H. Nakatsuji, X. Li, M. Caricato, A. Marenich, J. Bloino, B. G. Janesko, R. Gomperts, B. Mennucci, H. P. Hratchian, J. V. Ortiz, A. F. Izmaylov, J. L. Sonnenberg, D. Williams-Young, F. Ding, F. Lipparini, F. Egidi, J. Goings, B. Peng, A. Petrone, T. Henderson, D. Ranasinghe, V. G. Zakrzewski, J. Gao, N. Rega, G. Zheng, W. Liang, M. Hada, M. Ehara, K. Toyota, R. Fukuda, J. Hasegawa, M. Ishida, T. Nakajima, Y. Honda, O. Kitao, H. Nakai, T. Vreven, K. Throssell, J. A. Montgomery, Jr., J. E. Peralta, F. Ogliaro, M. Bearpark, J. J. Heyd, E. Brothers, K. N. Kudin, V. N. Staroverov, T. Keith, R. Kobayashi, J. Normand, K. Raghavachari, A. Rendell, J. C. Burant, S. S. Iyengar, J. Tomasi, M. Cossi, J. M. Millam, M. Klene, C. Adamo, R. Cammi, J. W. Ochterski, R. L. Martin, K. Morokuma, O. Farkas, J. B. Foresman, and D. J. Fox, 2013, Gaussian 09, Revision D.01, Gaussian, Inc., Wallingford CT.

50. A. D. Becke, *J. Chem. Phys.*, 1993, **98**, 5648–5652.

51. P. C. Hariharan and J. A. Pople, *Theor. Chim. Acta*, 1973, **28**, 213–222.

52. P. C. Hariharan and J. A. Pople, *Mol. Phys.*, 1974, **27**, 209–214.

53. M. M. Francl, W. J. Pietro, W. J. Hehre, J. S. Binkley, M. S. Gordon, D. J. DeFrees and J. A. Pople, *J. Chem. Phys.*, 1982, **77**, 3654–3665.

54. J.-P. Blaudeau, M. P. McGrath, L. A. Curtiss and L. Radom, *J. Chem. Phys.*, 1997, **107**, 5016–5021.

55. V. A. Rassolov, M. A. Ratner, J. A. Pople, P. C. Redfern and L. A. Curtiss, *J. Comput. Chem.*, 2001, **22**, 976–984.

56. R. Ditchfield, W. J. Hehre and J. A. Pople, *J. Chem. Phys.*, 2003, **54**, 724–728.

57. W. J. Hehre, R. Ditchfield and J. A. Pople, *J. Chem. Phys.*, 2003, **56**, 2257–2261.

58. T. H. Dunning Jr. and P. J. Hay, in *Modern Theoretical Chemistry*, Vol. 3 Plenum, New York, 1977, 1-28.

59. P. J. Hay and W. R. Wadt, *J. Chem. Phys.*, 1985, **82**, 270–283.

60. W. R. Wadt and P. J. Hay, *J. Chem. Phys.*, 1985, **82**, 284–298.

61. P. J. Hay and W. R. Wadt, *J. Chem. Phys.*, 1985, **82**, 299–310.

62. J. Tomasi, B. Mennucci and R. Cammi, *Chem. Rev.*, 2005, **105**, 2999–3094.

63. V. V Pavlishchuk and A. W. Addison, *Inorg. Chim. Acta*, 2000, **298**, 97–102.

64. A. A. Isse and A. Gennaro, *J. Phys. Chem. B*, 2010, **114**, 7894–7899.

Appendix A: X-ray diffraction data and bond valance sums

A.1 X-ray diffraction data presented in Chapter 2

A.1.1 (TBA)$_6$[(CoW$_5$O$_{18}$H)$_2$]

Table A.1: Crystal structure data for (TBA)$_6$[(CoW$_5$O$_{18}$H)$_2$]

Empirical formula	$C_{96}H_{216}Co_2N_6O_{36}W_{10}$
Formula weight	3987.1
Temperature/K	150.0(2)
Crystal system	orthorhombic
Space group	$P2_12_12_1$
a/Å	17.0118(2)
b/Å	25.9420(3)
c/Å	31.7819(4)
α/°	90
β/°	90
γ/°	90
Volume/Å^3	14026.0(3)
Z	4
ρ_{calc}g/cm^3	1.888
μ/mm^{-1}	17.013
F(000)	7664
Crystal size/mm^3	0.42 × 0.24 × 0.19
Radiation	Cu Kα (λ = 1.54184)
2Θ range for data collection/°	7.362 to 133.31
Index ranges	-20 ≤ h ≤ 20, -24 ≤ k ≤ 30, -37 ≤ l ≤ 37
Reflections collected	70458
Independent reflections	23743 [R$_{int}$ = 0.0776, R$_{sigma}$ = 0.0739]
Data/restraints/parameters	23743/1982/1395
Goodness-of-fit on F^2	1.021
Final R indexes [I>=2σ (I)]	R$_1$ = 0.0600, wR$_2$ = 0.1516
Final R indexes [all data]	R$_1$ = 0.0710, wR$_2$ = 0.1642
Largest diff. peak/hole / e Å^{-3}	2.42/-2.69
Flack parameter	0.008(8)

Table A.2: Bond valance sums for the oxygen atoms of $(TBA)_6[(CoW_5O_{18}H)_2]$

Atom	W-O bond length (r_{ij})	S_{ij}	Co-O bond length (r_{ij})	S_{ij}	BVS (V or z_j)	No. of H$^+$
O1	1.677	1.913			1.91	0
O2	1.669	1.955			1.95	0
O3	1.720	1.703			1.70	0
O4	1.693	1.832			1.83	0
O5	1.812	1.328	2.189	0.261	2.00	0
			2.024	0.408		
O6	1.888	1.082	2.104	0.328	1.41	**1**
O7	1.886	1.087	2.029	0.402	1.49	**1**
O8	1.760	1.529	2.049	0.381	1.91	0
O9	1.926	0.976			1.89	0
	1.952	0.910				
O10	1.999	0.801			1.91	0
	1.880	1.105				
O11	1.963	0.883			1.99	0
	1.880	1.105				
O12	1.904	1.036			1.81	0
	2.011	0.776				
O13	2.323	0.334	2.264	0.213	1.83	0
	2.329	0.328				
	2.351	0.309				
	2.312	0.344				
	2.355	0.306				
O14	1.890	1.076			1.92	0
	1.978	0.848				
O15	1.890	1.076			1.94	0
	1.972	0.862				
O16	1.923	0.984			1.91	0
	1.944	0.930				
O17	1.831	1.262			1.98	0
	2.041	0.715				
O18	1.670	1.949			1.95	0
O19	1.666	1.971			1.97	0
O20	1.666	1.971			1.97	0
O21	1.725	1.680			1.68	0
O22	1.686	1.867			1.87	0
O23	1.805	1.354	2.040	0.390	2.00	0
			2.202	0.252		
O24	1.796	1.387	2.071	0.359	1.75	0
O25	1.929	0.968	2.057	0.373	1.34	**1**
O26	1.870	1.135	2.104	0.328	1.46	**1**
O27	1.911	1.016			1.85	0
	1.986	0.830				
O28	1.900	1.047			1.96	0
	1.951	0.912				
O29	1.880	1.105			1.93	0
	1.987	0.828				
O30	1.923	0.984			1.96	0
	1.926	0.976				
O31	2.290	0.365	2.256	0.218	1.83	0
	2.349	0.311				
	2.332	0.326				
	2.367	0.296				
	2.343	0.316				
O32	1.957	0.898			1.81	0
	1.950	0.915				

O33	1.922	0.987		1.88	0
	1.960	0.890			
O34	1.865	1.151		1.98	0
	1.988	0.825			
O35	1.854	1.186		1.89	0
	2.047	0.704			
O36	1.667	1.965		1.97	0

A.1.2 (TBA)$_3$[(Py)CoW$_5$O$_{18}$H]

Table A.3: Crystal structure data for (TBA)$_3$[(Py)CoW$_5$O$_{18}$H]

Empirical formula	C$_{53}$H$_{116}$CoN$_4$O$_{19}$W$_5$
Formula weight	2091.67
Temperature/K	150.0(2)
Crystal system	monoclinic
Space group	P2$_1$/n
a/Å	17.0850(3)
b/Å	23.4567(4)
c/Å	17.9363(4)
α/°	90
β/°	90.715(2)
γ/°	90
Volume/Å^3	7187.6(2)
Z	4
ρ$_{calc}$g/cm^3	1.933
μ/mm^{-1}	16.651
F(000)	4044.0
Crystal size/mm^3	0.16 × 0.15 × 0.14
Radiation	Cu Kα (λ = 1.54184)
2Θ range for data collection/°	7.102 to 133.564
Index ranges	-20 ≤ h ≤ 15, -26 ≤ k ≤ 27, -21 ≤ l ≤ 20
Reflections collected	65072
Independent reflections	12651 [R$_{int}$ = 0.0762, R$_{sigma}$ = 0.0524]
Data/restraints/parameters	12651/880/816
Goodness-of-fit on F^2	1.044
Final R indexes [I>=2σ (I)]	R$_1$ = 0.0500, wR$_2$ = 0.1254
Final R indexes [all data]	R$_1$ = 0.0691, wR$_2$ = 0.1412
Largest diff. peak/hole / e Å^{-3}	4.19/-1.87

Table A.4: Bond valance sums for the oxygen atoms of $(TBA)_3[(Py)CoW_5O_{18}H]$

Atom	W-O bond length (r_{ij})	S_{ij}	Co-O bond length (r_{ij})	S_{ij}	BVS (V or z_j)	No. of H^+
O1	1.801	1.368	2.052	0.378	1.75	0
O2	2.008	0.782	2.114	0.320	1.10	1
O3	1.825	1.282	2.093	0.338	1.62	0
O4	1.818	1.307	2.087	0.344	1.65	0
O5	1.706	1.769			1.77	0
O6	1.689	1.852			1.85	0
O7	1.709	1.754			1.75	0
O8	1.694	1.827			1.83	0
O9	1.962	0.885				
	1.906	1.030			1.92	0
O10	1.898	1.053				
	1.976	0.853			1.91	0
O11	1.910	1.019				
	1.931	0.963			1.98	0
O12	1.920	0.992				
	1.971	0.864			1.86	0
O13	2.021	0.755				
	1.863	1.157			1.91	0
O14	1.900	1.047				
	2.002	0.795			1.84	0
O15	2.005	0.788				
	1.877	1.114			1.90	0
O16	2.012	0.774				
	1.883	1.096			1.87	0
O17	1.700	1.798			1.80	0
O18	2.326	0.331	2.226	0.236		
	2.334	0.324				
	2.313	0.343				
	2.372	0.292				
	2.329	0.328			1.85	0

Table A.5: Crystal structure data for (TBA)$_3$[(Quin)CoW$_5$O$_{18}$H]

Empirical formula	C$_{66}$H$_{122}$CoN$_5$O$_{18}$W$_5$
Formula weight	2251.86
Temperature/K	150.0(2)
Crystal system	triclinic
Space group	P-1
a/Å	17.5831(3)
b/Å	17.8329(3)
c/Å	24.8294(4)
α/°	83.9900(10)
β/°	87.5060(10)
γ/°	88.3800(10)
Volume/Å^3	7733.1(2)
Z	4
ρ_{calc}g/cm^3	1.934
μ/mm^{-1}	15.531
F(000)	4376.0
Crystal size/mm^3	0.21 × 0.1 × 0.08
Radiation	Cu Kα (λ = 1.54184)
2Θ range for data collection/°	7.166 to 133.372
Index ranges	-20 ≤ h ≤ 20, -19 ≤ k ≤ 21, -29 ≤ l ≤ 29
Reflections collected	136368
Independent reflections	27050 [R$_{int}$ = 0.0786, R$_{sigma}$ = 0.0548]
Data/restraints/parameters	27050/1880/1849
Goodness-of-fit on F^2	1.059
Final R indexes [I>=2σ (I)]	R$_1$ = 0.0455, wR$_2$ = 0.1117
Final R indexes [all data]	R$_1$ = 0.0587, wR$_2$ = 0.1230
Largest diff. peak/hole / e Å^{-3}	1.66/-2.67

Table A.6: Bond valance sums for the oxygen atoms of $(TBA)_3[(Quin)CoW_5O_{18}H]$

Atom	W-O bond length (r_{ij})	S_{ij}	Co-O bond length (r_{ij})	S_{ij}	BVS (V or z_j)	No. of H$^+$
O1	1.793	1.398	2.097	0.335	1.73	0
O2	2.050	0.698	2.083	0.348	1.05	1
O3	1.782	1.440	2.049	0.381	1.82	0
O4	1.805	1.354	2.095	0.336	1.69	0
O5	1.712	1.740			1.74	0
O6	1.707	1.764			1.76	0
O7	1.715	1.726			1.73	0
O8	1.701	1.793			1.79	0
O9	1.974	0.857				
	1.899	1.050			1.91	0
O10	1.895	1.061				
	1.975	0.855			1.92	0
O11	1.939	0.942				
	1.918	0.997			1.94	0
O12	1.942	0.935				
O13	2.324	0.333	2.229	0.234		
	2.353	0.308				
	2.330	0.328				
	2.352	0.309				
	2.305	0.350			1.86	0
	1.934	0.955			1.89	0
O14	2.030	0.737				
	1.887	1.084			1.82	0
O15	2.032	0.733				
	1.863	1.157			1.89	0
O16	2.004	0.790				
	1.884	1.093			1.88	0
O17	2.045	0.708				
O18	1.717	1.717			1.7	0

A.1.4 (TBA)₃[(AminoPy)CoW₅O₁₈H]

A.1.4 (TBA)$_3$[(AminoPy)CoW$_5$O$_{18}$H]

Table A.7: Crystal structure data for (TBA)$_3$[(AminoPy)CoW$_5$O$_{18}$H]

Empirical formula	C$_{59}$H$_{117}$CoN$_8$O$_{18}$W$_5$
Formula weight	2204.78
Temperature/K	150.0(2)
Crystal system	monoclinic
Space group	P2$_1$/c
a/Å	26.6461(2)
b/Å	18.3003(2)
c/Å	16.58980(10)
α/°	90
β/°	96.1180(10)
γ/°	90
Volume/Å^3	8043.64(12)
Z	4
ρ$_{calc}$g/cm^3	1.821
μ/mm^{-1}	14.925
F(000)	4272.0
Crystal size/mm^3	0.25 × 0.16 × 0.03
Radiation	Cu Kα (λ = 1.54184)
2Θ range for data collection/°	7.214 to 133.222
Index ranges	-31 ≤ h ≤ 31, -21 ≤ k ≤ 21, -18 ≤ l ≤ 19
Reflections collected	153015
Independent reflections	14167 [R$_{int}$ = 0.0834, R$_{sigma}$ = 0.0363]
Data/restraints/parameters	14167/1243/948
Goodness-of-fit on F^2	1.263
Final R indexes [I>=2σ (I)]	R$_1$ = 0.0874, wR$_2$ = 0.1854
Final R indexes [all data]	R$_1$ = 0.0940, wR$_2$ = 0.1887
Largest diff. peak/hole / e Å^{-3}	2.85/-2.95

Table A.8: Bond valance sums for the oxygen atoms of $(TBA)_3[(AminoPy)CoW_5O_{18}H]$

Atom	W-O bond length (r_{ij})	S_{ij}	Co-O bond length (r_{ij})	S_{ij}	BVS (V or z_j)	No. of H^+
O1	1.763	1.516	2.096	0.336	1.85	0
O2	1.780	1.448	2.095	0.336	1.78	0
O3	2.060	0.679	2.149	0.291	0.97	1
O4	1.785	1.429	2.062	0.368	1.80	0
O5	1.708	1.759			1.76	0
O6	1.728	1.667			1.67	0
O7	1.688	1.857			1.86	0
O8	1.673	1.934			1.93	0
O9	1.940	0.940				
	1.943	0.932			1.87	0
O10	1.912	1.014				
	1.947	0.922			1.94	0
O11	2.005	0.788				
	1.854	1.186			1.97	0
O12	1.952	0.910				
	1.915	1.005			1.92	0
O13	2.330	0.328	2.223	0.238		
	2.302	0.353				
	2.362	0.300				
	2.319	0.337				
	2.315	0.341			1.90	0
O14	2.086	0.633				
	1.834	1.251			1.88	0
O15	2.020	0.757				
	1.875	1.120			1.88	0
O16	2.041	0.715				
	1.853	1.189			1.90	0
O17	1.995	0.810				
	1.958	0.895			1.71	0
O18	1.714	1.731			1.73	0

A.1.5 (TBA)$_6$[(4,4'-Bipy)(CoW$_5$O$_{18}$H)$_2$]

Table A.9: Crystal structure data for (TBA)$_6$[(4,4'-Bipy)(CoW$_5$O$_{18}$H)$_2$].2MeCN

Empirical formula	C$_{109.63}$H$_{229.44}$Co$_2$N$_{9.81}$O$_{36}$W$_{10}$
Formula weight	4217.79
Temperature/K	150.0(2)
Crystal system	monoclinic
Space group	P2$_1$/c
a/Å	24.4452(2)
b/Å	19.54690(10)
c/Å	30.7055(2)
α/°	90
β/°	103.5100(10)
γ/°	90
Volume/Å^3	14265.96(18)
Z	4
ρ$_{calc}$g/cm^3	1.964
μ/mm^{-1}	16.780
F(000)	8152.0
Crystal size/mm^3	0.31 × 0.16 × 0.1
Radiation	Cu Kα (λ = 1.54184)
2Θ range for data collection/°	6.942 to 133.236
Index ranges	-29 ≤ h ≤ 28, -22 ≤ k ≤ 23, -30 ≤ l ≤ 35
Reflections collected	125698
Independent reflections	25025 [R$_{int}$ = 0.0704, R$_{sigma}$ = 0.0493]
Data/restraints/parameters	25025/2910/1791
Goodness-of-fit on F^2	1.078
Final R indexes [I>=2σ (I)]	R$_1$ = 0.0508, wR$_2$ = 0.1286
Final R indexes [all data]	R$_1$ = 0.0606, wR$_2$ = 0.1370
Largest diff. peak/hole / e Å^{-3}	2.66/-2.92

Table A.10: Bond valance sums for the oxygen atoms of $(TBA)_6[(4,4'\text{-}$ $Bipy)(CoW_5O_{18}H)_2].2MeCN$

Atom	W-O bond length (r_{ij})	S_{ij}	Co-O bond length (r_{ij})	S_{ij}	BVS (V or z_j)	No. of H^+
O1	1.789	1.413	2.076	0.354	1.8	0
O2	1.850	1.199	2.073	0.357	1.6	0
O3	1.920	0.992	2.084	0.347	1.34	**0.7**
O4	1.875	1.120	2.075	0.355	1.48	**0.5**
O5	1.716	1.722			1.7	0
O6	1.694	1.827			1.8	0
O7	1.699	1.803			1.8	0
O8	1.694	1.827			1.8	0
O9	1.917	1.000				
	1.940	0.940			1.9	0
O10	1.910	1.019				
	1.930	0.965			2.0	0
O11	1.912	1.014				
	1.941	0.937			2.0	0
O12	1.929	0.968				
	1.939	0.942			1.9	0
O13	2.333	0.325	2.223	0.238		
	2.333	0.325				
	2.337	0.321				
	2.317	0.339				
	2.329	0.328			1.9	0
O14	1.872	1.129				
	2.043	0.711			1.8	0
O15	1.989	0.823				
	1.903	1.039			1.9	0
O16	1.937	0.947				
	1.968	0.871			1.8	0
O17	1.980	0.843				
	1.915	1.005			1.8	0
O18	1.701	1.793			1.8	0
O19	1.782	1.440	2.045	0.385	1.8	0
O20	1.798	1.379	2.053	0.377	1.8	0
O21	1.817	1.310	2.086	0.345	1.7	0
O22	2.044	0.709	2.094	0.337	1.05	**1**
O23	1.703	1.783			1.8	0
O24	1.708	1.759			1.8	0
O25	1.711	1.745			1.7	0
O26	1.705	1.774			1.8	0
O27	1.918	0.997				
	1.964	0.881			1.9	0
O28	1.923	0.984				
	1.933	0.958			1.9	0
O29	1.929	0.968				
	1.951	0.912			1.9	0
O30	1.867	1.145				
	2.004	0.790			1.9	0
O31	2.344	0.315	2.223	0.238		
	2.333	0.325				
	2.327	0.330				
	2.306	0.349				
	2.342	0.317			1.9	0
O32	1.887	1.084				
	2.021	0.755			1.8	0

O33	1.848	1.205			
	2.064	0.672		1.9	0
O34	1.903	1.039			
	2.014	0.769		1.8	0
O35	1.854	1.186			
	2.021	0.755		1.9	0
O36	1.703	1.783		1.8	0

A.1.6 (TBA)$_3$[(EtOH)CoW$_5$O$_{18}$H)]

Table A.11: Crystal structure data for (TBA)$_3$[(EtOH)CoW$_5$O$_{18}$H]

Empirical formula	C$_{52}$H$_{113}$CoN$_3$O$_{20}$W$_5$
Formula weight	2078.63
Temperature/K	150.0(2)
Crystal system	orthorhombic
Space group	P2$_1$2$_1$2$_1$
a/Å	16.51580(10)
b/Å	18.07880(10)
c/Å	24.9771(2)
α/°	90
β/°	90
γ/°	90
Volume/Å^3	7457.81(9)
Z	4
ρ$_{calc}$g/cm^3	1.851
μ/mm^{-1}	16.050
F(000)	4012.0
Crystal size/mm^3	0.2 × 0.17 × 0.13
Radiation	Cu Kα (λ = 1.54184)
2Θ range for data collection/°	7.25 to 133.338
Index ranges	-19 ≤ h ≤ 18, -21 ≤ k ≤ 19, -29 ≤ l ≤ 29
Reflections collected	37278
Independent reflections	12782 [R$_{int}$ = 0.0510, R$_{sigma}$ = 0.0504]
Data/restraints/parameters	12782/681/770
Goodness-of-fit on F^2	1.098
Final R indexes [I>=2σ (I)]	R$_1$ = 0.0444, wR$_2$ = 0.1054
Final R indexes [all data]	R$_1$ = 0.0462, wR$_2$ = 0.1073
Largest diff. peak/hole / e Å^{-3}	2.56/-1.33
Flack parameter	0.097(7)

Table A.12: Bond valance sums for the oxygen atoms of $(TBA)_3[(EtOH)CoW_5O_{18}H]$

Atom	W-O bond length (r_{ij})	S_{ij}	Co-O bond length (r_{ij})	S_{ij}	BVS (V or z_j)	No. of H$^+$
O2	1.905	1.033	1.969	0.473	1.51	**0.5**
O3	1.885	1.089	1.933	0.521	1.61	**0.4**
O4	1.847	1.208	1.962	0.482	1.69	**0.3**
O5	1.868	1.142	1.948	0.501	1.64	**0.4**
O6	1.696	1.817			1.82	0
O7	1.703	1.783			1.78	0
O8	1.695	1.822			1.82	0
O9	1.708	1.759			1.76	0
O10	1.940	0.940				
	1.932	0.960			1.90	0
O11	1.936	0.950				
	1.917	1.000			1.95	0
O12	1.942	0.935				
	1.925	0.979			1.91	0
O13	1.906	1.030				
	1.957	0.898			1.93	0
O14	2.313	0.343	2.223	0.238		
	2.308	0.348				
	2.346	0.314				
	2.333	0.325				
	2.316	0.340			1.91	0
O15	1.937	0.947				
	1.928	0.971			1.92	0
O16	1.971	0.864				
	1.931	0.963			1.83	0
O17	1.981	0.841				
	1.900	1.047			1.89	0
O18	1.996	0.808				
	1.895	1.061			1.87	0
O19	1.695	1.822			1.82	0

A.1.7 "H₂Co₄[H₂W₁₂O₄₂].26.4H₂O"

Table A.13: Crystal structure data for "H₂Co₄[H₂W₁₂O₄₂].26.4H₂O"

Empirical formula	Co$_4$H$_{16}$O$_{68.43}$W$_{12}$
Formula weight	3552.93
Temperature/K	150.0(2)
Crystal system	triclinic
Space group	P-1
a/Å	10.8904(4)
b/Å	12.8745(5)
c/Å	13.7962(5)
α/°	76.308(3)
β/°	68.228(3)
γ/°	69.486(3)
Volume/Å^3	1669.74(12)
Z	1
ρ$_{calc}$g/cm^3	3.533
μ/mm^{-1}	45.637
F(000)	1559.0
Crystal size/mm^3	0.18 × 0.09 × 0.03
Radiation	Cu Kα (λ = 1.54184)
2Θ range for data collection/°	6.952 to 133.268
Index ranges	-12 ≤ h ≤ 10, -15 ≤ k ≤ 11, -16 ≤ l ≤ 16
Reflections collected	23203
Independent reflections	5845 [R$_{int}$ = 0.0918, R$_{sigma}$ = 0.0742]
Data/restraints/parameters	5845/476/460
Goodness-of-fit on F^2	1.037
Final R indexes [I>=2σ (I)]	R$_1$ = 0.0595, wR$_2$ = 0.1470
Final R indexes [all data]	R$_1$ = 0.0754, wR$_2$ = 0.1632
Largest diff. peak/hole / e Å^{-3}	3.43/-3.42

A.1.8 Fractional co-ordinates of the partial structure from reaction of (TBA)₆[(CoW₅O₁₈H)₂]

and NaOTf (grown from hot Water/DMSO)

Table A.14: Fractional co-ordinates of atoms in the asymmetric unit

Atom	x	y	z
W1	0.543028	0.235893	0.526228
W2	0.777771	0.249098	0.691632
W3	0.485151	0.110923	0.691172
W4	0.293639	0.03668	0.28065
W5	0.807514	0.172915	0.438932
W6	0.580543	0.173041	0.276961
Co7	0.5	0.5	0.5
Co8	0.5	0	0
Co9	1	0.5	0.5
Na10	1	0	0.5
O11	0.638648	0.213664	0.439193
O12	0.541985	0.000696	0.716057
O13	0.828668	0.201514	0.573682
O14	0.712622	0.128083	0.301019
O15	0.215172	-0.102746	0.301333
O16	0.485945	0.233107	0.642083
O17	0.668377	0.233164	0.766915
O18	0.399552	0.114196	0.440155
O19	0.71756	0.337359	0.636903
O20	0.431069	0.1837	0.293178
O21	0.345895	-0.002385	0.591715
O22	0.24	-0.021058	0.150729
O23	0.589404	0.109769	0.578442
O24	0.905113	0.104586	0.416748
O25	0.430831	0.152164	0.790689
O26	0.902157	0.318744	0.453901
O27	0.197476	0.104586	0.312393
O28	0.526957	0.361447	0.520949
O29	0.535443	0.104255	0.147933
O30	0.649299	0.532427	0.439827
O31	0.619279	0.62071	0.641016
O32	0.662611	0.323366	0.299514
O33	0.6764	0.110455	0.000935
O34	0.917173	0.356368	0.77949
O35	0.429118	0.108079	-0.039035
O38	1.007933	0.112825	0.65575
O39	1.103908	0.502235	0.626286
O41	1.202624	0.134045	0.531612
O42	0.870467	0.514091	0.575697
Na1	0.863681	0.717501	0.587032
O2	0.594483	0.595631	0.276829
O1	0.644949	0.372337	0.128192
Na3	0.844967	0.159684	0.171504
O7	0.983672	0.042686	0.163522
O10	0.97516	0.388295	0.199346
O36	0.469411	0.606246	0.064097
Na2	0.542601	0.486671	0.110525
Na4	1.14767	0.48265	0.859516
O4	1.254695	0.362352	0.902822
O5	1.260839	0.66793	1.020173
Na5	1.14441	0.337614	0.674992
Na6A	0.233972	0.121281	0.041248
O8	0.345161	0.364929	0.089211

O3	0.020925	0.154333	-0.017553
O6	1.090043	0.366391	1.076952
Na6	0.335081	0.210211	0.096757
O9	0.084809	0.139422	0.031751
O4A	1.282253	0.390262	0.827534
Na4A	1.126005	0.418133	0.911081
O5A	1.227945	0.602558	1.050235
O8A	0.435058	0.428579	0.117539
O6A	1.010213	0.376924	1.023137

A.1.9 Fractional co-ordinates of the partial structure from reaction of (TBA)$_6$[(CoW$_5$O$_{18}$H)$_2$] and NaOTf (from nanodrop encapsulation crystallisation)

Table A.15: Fractional co-ordinates of atoms in the asymmetric unit

Atom	x	y	z
W001	0.631868	0.25	0.130823
W002	0.655606	0.325193	0.401727
W00	0.6257	0.403083	0.154973
W004	0.514214	0.325533	0.181351
O0A	0.681677	0.25	0.270534
O0D	0.559161	0.379396	0.075877
O0E	0.682619	0.378806	0.268414
O0F	0.556627	0.25	0.078802
O00G	0.598861	0.459795	0.24938
O00K	0.500109	0.25	0.272954
O00L	0.618314	0.376166	0.490768
O00M	0.49557	0.376586	0.299408
O00O	0.457625	0.323143	0.080127
O00P	0.657838	0.443948	0.039886
O11	0.62296	0.25	0.463015
O12	0.596427	0.319878	0.255931
O16	0.717263	0.318346	0.48379
Co1	0.774026	0.25	0.526826
S6	0.82894	0.118377	0.578562
O15	0.835759	0.18681	0.56705
O3	0.655716	0.184582	0.046279
Na1	0.410509	0.25	-0.02651
C10	0.830884	0.092853	0.425433
H10A	0.828803	0.128188	0.368271
H10B	0.800018	0.06531	0.410009
H10C	0.864938	0.070521	0.410795
C13	0.890933	0.091094	0.624912
H13A	0.919573	0.11098	0.575312
H13B	0.892344	0.046442	0.611736
H13C	0.896451	0.100206	0.714281
O2	0.759214	0.25	0.723861
Na2	0.545398	0.448802	0.429194
Na3	0.856977	0.25	0.787076
O4	0.820368	0.25	0.366356
O1	0.489602	0.532515	0.368431
S5	0.436633	0.523694	0.266114
C8	0.485244	0.515027	0.124625
H8A	0.463978	0.508931	0.047672
H8B	0.507392	0.552341	0.116367
H8C	0.509039	0.479411	0.138016
C25	0.445245	0.608057	0.230766
H25A	0.411276	0.624485	0.196135
H25B	0.474585	0.613505	0.169385
H25C	0.454358	0.630123	0.308367
S2	0.717851	0.231651	0.819201
C1	0.653334	0.26224	0.771955
H1A	0.654836	0.307348	0.773145
H1B	0.625103	0.248017	0.830178
H1C	0.644772	0.248085	0.686699
C24	0.708742	0.151787	0.783617
H24A	0.694806	0.147483	0.69771
H24B	0.682728	0.13373	0.842923
H24C	0.7437	0.130387	0.790719

S1	0.808424	0.229697	0.232766
C14	0.873844	0.22829	0.158952
H14A	0.869871	0.215461	0.071058
H14B	0.889999	0.269529	0.162174
H14C	0.897476	0.19911	0.203214
C44	0.78795	0.150857	0.216119
H44A	0.781126	0.141873	0.127179
H44B	0.816882	0.123867	0.247452
H44C	0.754648	0.143734	0.264625
O1A	0.474723	0.519134	0.381788
S5A	0.484323	0.557989	0.246003
C25A	0.456555	0.489589	0.161744
H25D	0.483812	0.456653	0.16124
H25E	0.44758	0.501004	0.075015
H25F	0.423673	0.475143	0.204671
C8A	0.408613	0.583471	0.233935
H8AA	0.385022	0.547225	0.240426
H8AB	0.402484	0.60385	0.152918
H8AC	0.400212	0.612169	0.302382

A.2 X-ray diffraction data presented in Chapter 3

A.2.1 (TBA)$_5$[W$_7$O$_{24}$H].[W$_6$O$_{19}$].3MeCN

Table A.16: Crystal structure data for (TBA)$_5$[W$_7$O$_{24}$H].[W$_6$O$_{19}$].3MeCN

Empirical formula	C$_{118}$H$_{261}$N$_{10}$O$_{43}$W$_{13}$
Formula weight	4898.40
Temperature/K	150.0(2)
Crystal system	monoclinic
Space group	P2$_1$/c
a/Å	32.1867(8)
b/Å	17.5143(4)
c/Å	28.2674(7)
α/°	90
β/°	90.691(2)
γ/°	90
Volume/Å^3	15934.0(7)
Z	4
ρ_{calc}g/cm^3	2.042
μ/mm^{-1}	9.412
F(000)	9380.0
Crystal size/mm^3	0.39 × 0.14 × 0.05
Radiation	Mo Kα (λ = 0.71073)
2Θ range for data collection/°	6.682 to 57.86
Index ranges	-43 ≤ h ≤ 43, -21 ≤ k ≤ 22, -34 ≤ l ≤ 38
Reflections collected	139244
Independent reflections	36504 [R$_{int}$ = 0.0812, R$_{sigma}$ = 0.0967]
Data/restraints/parameters	36504/2138/1849
Goodness-of-fit on F^2	1.069
Final R indexes [I>=2σ (I)]	R$_1$ = 0.0514, wR$_2$ = 0.0869
Final R indexes [all data]	R$_1$ = 0.1213, wR$_2$ = 0.1119
Largest diff. peak/hole / e Å^{-3}	1.78/-2.61

Table A.17: Bond valance sums for the oxygen atoms of $[W_7O_{24}H]^{5-}$ within

$(TBA)_5[W_7O_{24}H].[W_6O_{19}].3MeCN$

Atom	W-O bond length (r_{ij})	S_{ij}	BVS (V or z_j)	No. of H$^+$
O1	1.734	1.640	1.64	0
O2	1.942	0.935	1.87	0
	1.943	0.932		
O3	1.920	0.992	1.88	0
	1.961	0.888		
O4	2.134	0.556	1.80	0
	1.835	1.248		
O5	1.946	0.925	1.87	0
	1.936	0.950		
O6	1.724	1.685	1.68	0
O7	1.732	1.649	1.65	0
O8	1.726	1.676	1.68	0
O9	1.719	1.708	1.71	0
O10	1.919	0.995	1.98	0
	1.922	0.987		
O11	1.915	1.005	1.97	0
	1.930	0.965		
O12	1.900	1.047	1.98	0
	1.944	0.930		
O13	1.956	0.900	1.93	0
	1.905	1.033		
O14	2.271	0.384	1.76	0
	2.286	0.369		
	2.310	0.346		
	2.338	0.321		
	2.318	0.338		
O15	1.844	1.218	1.95	0
	2.301	0.354		
	2.282	0.373		
O16	1.897	1.056	2.01	
	1.933	0.958		
O17	1.748	1.579	1.58	0
O18	1.903	1.039	2.01	0
	1.929	0.968		
O19	1.732	1.649	1.65	0
O20	2.114	0.587	1.18	1
	2.111	0.592		
O21	1.738	1.622	1.62	0
O22	1.740	1.613	1.61	0
O23	1.950	0.915	1.85	0
	1.942	0.935		
O24	1.731	1.653	1.65	0

A.2.2 (BTMA)$_5$[W$_7$O$_{24}$H].2DMSO.1.71H$_2$O

Table A.18: Crystal structure data for (BTMA)$_5$[W$_7$O$_{24}$H].2DMSO.1.71H$_2$O

Empirical formula	C$_{54}$H$_{92}$N$_5$O$_{27.71}$S$_2$W$_7$
Formula weight	2605.71
Temperature/K	150.0(2)
Crystal system	monoclinic
Space group	P2$_1$/n
a/Å	23.7639(3)
b/Å	10.4977(2)
c/Å	29.5824(4)
α/°	90
β/°	99.2090(10)
γ/°	90
Volume/Å^3	7284.69(19)
Z	4
ρ$_{calc}$g/cm^3	2.376
μ/mm^{-1}	21.044
F(000)	4891.0
Crystal size/mm^3	0.07 × 0.05 × 0.02
Radiation	Cu Kα (λ = 1.54184)
2Θ range for data collection/°	4.438 to 156.782
Index ranges	-29 ≤ h ≤ 30, -10 ≤ k ≤ 12, -37 ≤ l ≤ 35
Reflections collected	49180
Independent reflections	14433 [R$_{int}$ = 0.0434, R$_{sigma}$ = 0.0433]
Data/restraints/parameters	14433/960/922
Goodness-of-fit on F^2	1.016
Final R indexes [I>=2σ (I)]	R$_1$ = 0.0370, wR$_2$ = 0.0889
Final R indexes [all data]	R$_1$ = 0.0492, wR$_2$ = 0.0974
Largest diff. peak/hole / e Å^{-3}	1.15/-2.73

A.3 X-ray diffraction data presented in Chapter 4

A.3.1 (TBA)$_7$[(MnW$_5$O$_{18}$H)$_2$][NO$_3$]

Table A.19: Crystal structure data for (TBA)$_7$[(MnW$_5$O$_{18}$H)$_2$][NO$_3$] (note: nitrate not located in X-ray diffraction experiment)

Empirical formula	C$_{117}$H$_{257}$Mn$_2$N$_8$O$_{36}$W$_{10}$
Formula weight	4300.67
Temperature/K	150.0(2)
Crystal system	monoclinic
Space group	P2$_1$/c
a/Å	17.88960(10)
b/Å	26.6583(2)
c/Å	34.3204(3)
α/°	90
β/°	90.7290(10)
γ/°	90
Volume/Å^3	16366.3(2)
Z	4
ρ$_{calc}$g/cm^3	1.745
μ/mm^{-1}	14.303
F(000)	8372.0
Crystal size/mm^3	0.3 × 0.25 × 0.2
Radiation	Cu Kα (λ = 1.54184)
2Θ range for data collection/°	7.114 to 133.386
Index ranges	-20 ≤ h ≤ 21, -31 ≤ k ≤ 30, -39 ≤ l ≤ 40
Reflections collected	129228
Independent reflections	28097 [R$_{int}$ = 0.0769, R$_{sigma}$ = 0.0559]
Data/restraints/parameters	28097/1577/1598
Goodness-of-fit on F^2	1.072
Final R indexes [I>=2σ (I)]	R$_1$ = 0.0607, wR$_2$ = 0.1453
Final R indexes [all data]	R$_1$ = 0.0791, wR$_2$ = 0.1617
Largest diff. peak/hole / e Å^{-3}	2.71/-2.38

Table A.20: Bond valance sums for the oxygen atoms of $(TBA)_7[(MnW_5O_{18}H)_2][NO_3]$

Atom	W-O bond length (r_{ij})	S_{ij}	Mn-O bond length (r_{ij})	S_{ij}	BVS (V or z_j)	No. of H$^+$
O1	1.808	1.343	2.289	0.251	2.01	0
			2.106	0.412		
O2	1.796	1.387	2.145	0.371	1.76	0
O3	1.931	0.963	2.171	0.346	1.31	1
O4	1.773	1.476	2.152	0.364	1.84	0
O5	1.697	1.812			1.81	0
O6	1.672	1.939			1.94	0
O7	1.691	1.842			1.84	0
O8	1.694	1.827			1.83	0
O9	1.928	0.971			1.96	0
	1.922	0.986				
O10	1.885	1.090			1.99	0
	1.957	0.898				
O11	1.915	1.005			1.97	0
	1.929	0.968				
O12	1.941	0.937			1.92	0
	1.924	0.981				
O13	2.303	0.352	2.432	0.364	2.00	0
	2.335	0.323				
	2.347	0.313				
	2.362	0.300				
	2.308	0.348				
O14	1.887	1.084			1.87	0
	2.006	0.786				
O15	1.944	0.930			1.75	0
	1.989	0.823				
O16	1.893	1.067			1.87	0
	1.998	0.803				
O17	1.875	1.120			1.87	0
	2.023	0.751				
O18	1.696	1.817			1.82	0
O19	1.821	1.296	2.060	0.467	2.04	0
			2.252	0.278		
O20	1.975	0.855	2.157	0.359	1.21	1
O21	1.775	1.468	2.128	0.388	1.86	0
O22	1.766	1.504	2.132	0.384	1.89	0
O23	1.705	1.774			1.77	0
O24	1.678	1.908			1.91	0
O25	1.718	1.712			1.71	0
O26	1.706	1.769			1.77	0
O27	1.915	1.005			1.91	0
	1.956	0.900				
O28	1.914	1.008			1.92	0
	1.951	0.912				
O29	1.910	1.019			1.94	0
	1.949	0.917				
O30	1.915	1.005			1.93	0
	1.945	0.927				
O31	2.309	0.347	2.437	0.366	2.00	0
	2.342	0.317				
	2.338	0.321				
	2.316	0.340				
	2.345	0.315				
O32	1.918	0.997			1.83	0
	1.986	0.830				

O33	1.872	1.129		1.88	0
	2.024	0.749			
O34	1.890	1.076		1.83	0
	2.020	0.757			
O35	1.844	1.218		1.88	0
	2.068	0.665			
O36	1.703	1.783		1.78	0

A.3.2 (TBA)$_3$[(Py)MnW$_5$O$_{18}$H]

Table A.21: Crystal structure data for (TBA)$_3$[(Py)MnW$_5$O$_{18}$H]

Empirical formula	C$_{58}$H$_{115}$MnN$_5$O$_{18}$W$_5$
Formula weight	2144.73
Temperature/K	150.0(2)
Crystal system	orthorhombic
Space group	Aea2
a/Å	24.4872(2)
b/Å	24.5097(3)
c/Å	24.6885(2)
α/°	90
β/°	90
γ/°	90
Volume/Å^3	14817.4(2)
Z	8
ρ_{calc}g/cm^3	1.923
μ/mm^{-1}	15.805
F(000)	8296.0
Crystal size/mm^3	0.25 × 0.23 × 0.16
Radiation	Cu Kα (λ = 1.54184)
2Θ range for data collection/°	7.22 to 134.956
Index ranges	-29 ≤ h ≤ 24, -29 ≤ k ≤ 27, -28 ≤ l ≤ 29
Reflections collected	56496
Independent reflections	12557 [R$_{int}$ = 0.0658, R$_{sigma}$ = 0.0485]
Data/restraints/parameters	12557/1012/874
Goodness-of-fit on F^2	1.063
Final R indexes [I>=2σ (I)]	R$_1$ = 0.0430, wR$_2$ = 0.1066
Final R indexes [all data]	R$_1$ = 0.0460, wR$_2$ = 0.1110
Largest diff. peak/hole / e Å^{-3}	1.02/-2.11
Flack parameter	0.293(18)

Table A.22: Bond valance sums for the oxygen atoms of $(TBA)_3[(Py)MnW_5O_{18}H]$

Atom	W-O bond length (r_{ij})	S_{ij}	Mn-O bond length (r_{ij})	S_{ij}	BVS (V or z_j)	No. of H^+
O1	1.921	0.989	1.929	0.633	1.62	0
O2	1.837	1.241	1.945	0.607	1.85	0
O3	1.801	1.368	1.921	0.647	2.02	0
O4	1.835	1.248	1.934	0.625	1.87	0
O5	1.720	1.703			1.70	0
O6	1.709	1.754			1.75	0
O7	1.715	1.726			1.73	0
O8	1.696	1.817			1.82	0
O9	1.939	0.942				
	1.945	0.927			1.87	0
O10	1.929	0.968				
	1.930	0.965			1.93	0
O11	1.940	0.940				
	1.933	0.958			1.90	0
O12	1.933	0.958				
	1.909	1.022			1.98	0
O13	2.325	0.332	2.199	0.331		
	2.324	0.333				
	2.323	0.334				
	2.322	0.335				
	2.238	0.420			2.08	0
O14	1.983	0.837				
	1.918	0.997			1.83	0
O15	1.981	0.841				
	1.898	1.053			1.89	0
O16	1.956	0.900				
	1.932	0.960			1.86	0
O17	1.975	0.855				
	1.922	0.987			1.84	0
O18	1.697	1.812			1.81	0

A.3.3 Partial structure of (TBA)₃[(Py)FeW₅O₁₈H]

Table A.23: Fractional co-ordinates of atoms in the asymmetric unit

Atom	x	y	z
W001	0.364317	0.536892	-0.367955
W002	0.32399	0.517999	-0.267013
W003	1.051594	0.575388	0.012248
W004	0.498756	0.919834	-0.263603
W005	0.207531	0.44552	-0.411533
W006	0.433054	0.916745	-0.375723
W007	1.025123	0.447676	-0.029601
W008	0.353721	1.042683	-0.374768
W009	0.953061	0.481062	0.060989
W00A	0.413731	1.044098	-0.261796
W00B	0.286793	0.942544	-0.315347
W00C	0.380375	0.411953	-0.324646
W00D	0.175702	0.422178	-0.309802
W00E	0.806916	0.463888	-0.037712
W00F	0.912179	0.552662	-0.087709
Fe0G	0.162667	0.544785	-0.351575
Fe0H	0.55489	1.015853	-0.322931
Fe0I	0.844686	0.583981	0.003305
O00J	0.420594	0.982066	-0.318045
O00K	0.318946	0.395799	-0.385908
O00L	0.931635	0.51728	-0.013038
O00M	0.270414	0.481291	-0.34025
O00N	0.815764	0.499538	-0.093389
O00O	1.104474	0.507809	-0.005778
O00P	0.963705	0.623653	0.02196
O00Q	0.434225	0.473135	-0.351765
O00R	0.150154	0.400522	-0.373471
O00S	1.023763	0.432079	0.031457
O00T	0.370296	0.903471	-0.268736
O00U	0.879291	0.540262	0.066475
O00V	0.368815	0.97779	-0.408373
O00W	0.389679	0.559599	-0.305416
O00X	0.838941	0.60525	-0.066764
O00Y	0.476553	0.984039	-0.230322
O00Z	0.852083	0.443406	0.025512
N010	0.39511	0.724661	-0.299241
O011	1.049262	0.531176	0.065866
O012	0.264875	0.586727	-0.377628
O013	0.529315	1.068499	-0.272223
O014	1.144736	0.613742	0.031851
O015	0.295194	0.501853	-0.421402
O016	0.374529	0.538941	-0.213666
O017	1.013578	0.590919	-0.051983
O018	0.426593	0.868787	-0.416511
O019	0.236688	0.564983	-0.284769
O01A	0.403099	0.453477	-0.27249
O01B	1.09549	0.398728	-0.04285
O01C	0.31754	0.898857	-0.360643
O01D	0.190254	0.917311	-0.311872
O01E	0.592087	0.951676	-0.27459
O01F	0.305121	1.005034	-0.269139
O01G	0.481824	0.878037	-0.319497
O01H	0.294267	0.379044	-0.303063
N01I	0.197447	0.483421	-0.141778

O01J	0.168869	0.417271	-0.462078
O01K	0.126038	0.499643	-0.411137
N01L	0.291183	0.525705	0.138078
O01M	0.970682	0.451114	0.112738
C01N	0.478398	0.75635	-0.268606
N01O	0.050401	0.768889	-0.040769
O01P	0.535013	0.948694	-0.371648
O01Q	0.987991	0.49059	-0.086981
O01R	0.721125	0.423934	-0.058706
N01S	-0.101131	0.448119	-0.518754
O01T	0.102586	0.482011	-0.321501
C01U	0.325282	0.771425	-0.316706
O01V	0.429911	0.578025	-0.390082
O01W	0.751148	0.52346	-0.020556
C01X	0.339464	0.430334	-0.109929
O01Y	0.251123	0.456588	-0.256193
O01Z	0.120213	0.371434	-0.288781
O020	0.471389	1.059809	-0.370857
C021	0.304486	0.478401	0.171368
C022	0.05931	0.531263	-0.190699
O023	0.906703	0.414433	-0.04338
C024	0.329852	0.456889	0.077442
N025	0.062052	0.602836	-0.36109
C026	0.41032	0.694084	-0.339304
N027	0.759987	0.648434	0.01648
C028	0.586984	0.55693	-0.177475
N029	0.283928	0.975558	-0.140802
C02A	-0.06597	0.443217	-0.463045
C02B	0.196405	0.514534	-0.098328
C02C	0.26818	0.499294	0.088196
N02D	0.672649	1.049506	-0.324959
C02E	0.607605	0.424042	-0.213824
C02F	0.248053	0.592648	-0.05044
C02G	0.357783	0.937328	-0.160148
C02H	0.552428	0.71644	-0.25208
O02I	0.89809	0.57339	-0.141513
C02J	0.451191	0.729362	-0.371473
O02K	0.296084	1.083493	-0.415837
C02L	0.34234	0.711926	-0.228121
C02M	0.025498	0.561773	-0.236421
C02N	-0.071031	0.577266	-0.248853
N02O	0.248302	0.222779	-0.349105
C02P	0.221848	0.439532	0.16997
O02Q	0.363431	1.081023	-0.31626
C02R	0.280405	0.673315	-0.213135
C02S	0.254882	0.565547	-0.092329
C02T	0.040965	0.728168	-0.07921
C02U	0.285151	0.463948	-0.145137
C02V	0.628801	0.745336	-0.219413
C02W	0.039391	0.750921	-0.124443
C02X	0.272301	0.248277	-0.306902
C02Y	0.30729	0.978241	-0.088794
C02Z	-0.100486	0.46095	-0.385526
C030	-0.041386	0.802009	-0.048513
C031	0.683978	0.830755	-0.336962
C032	0.247205	0.73935	-0.351104
C033	0.421688	1.006912	-0.014446
C034	0.301404	0.440939	0.031238
C035	-0.048445	0.433317	-0.594867

C036	0.372942	0.603258	0.114803
C037	0.505909	0.45915	-0.44337
C038	-0.111877	0.768041	-0.06456
C039	0.156156	0.517217	-0.184849
C03A	-0.194229	0.370403	-0.533761
N03B	0.475579	0.491524	-0.49261
C03C	0.146312	0.430525	-0.137423
C03D	0.614389	0.502784	-0.26175
C03E	0.364386	0.397851	0.018571
C03F	0.206402	0.558609	0.139911
C03G	0.715323	0.870794	-0.322867
C03I	-0.029777	0.418306	-0.536887
C03J	-0.129097	0.47047	-0.439524
C03K	0.235148	0.394079	0.195934
C03L	-0.106147	0.507734	-0.53195
C03M	0.436155	0.423625	-0.113764
C03N	0.67345	0.556369	-0.269108
C03O	0.498319	1.03307	0.004305
C03P	0.459182	0.702368	-0.414535
C03Q	0.359057	0.682077	-0.269057
C03R	0.220719	0.579432	0.185909
C03S	0.268797	0.830646	-0.035674
C03T	0.711837	0.70772	-0.210555
C03U	0.12214	0.812373	-0.035053
C03V	-0.018228	0.543366	-0.524379
C03W	0.053764	0.773404	0.039302
C03X	0.308639	0.651531	-0.03823
C03Y	0.598729	0.585447	-0.131312
O03Z	0.255814	1.000999	-0.35599
C040	0.777112	0.428139	-0.239228
C041	0.287741	0.583069	-0.540684
C042	0.275668	1.02418	-0.16455
C043	0.391495	1.009201	-0.06932
C044	0.155517	0.350856	0.191292
C045	0.685668	0.618231	-0.337729
C046	0.491273	0.381011	-0.082107
C047	0.599028	0.414616	-0.38362
C048	0.385506	0.554596	0.149121
C04A	0.345455	0.292732	-0.179373
C04B	0.795365	0.70459	0.029359
C04C	0.514654	0.74027	-0.447516
C04D	0.037569	0.414453	-0.602475
O28	0.542949	0.875316	-0.22059
O32	0.410333	1.089063	-0.223348
O33	0.459104	0.365514	-0.316075
N1	0.664288	0.480203	-0.215994
C4	0.067545	0.743982	0.005291
C10	0.644636	0.38906	-0.172191
C11	0.753703	0.46518	-0.20656
C16	0.212932	1.058568	-0.159374
C3	-0.187431	0.423282	-0.537342
C1	0.60732	0.691159	-0.001437
C15	0.67185	0.643355	0.000858
C17	0.258867	0.697411	-0.172125
C13	0.634591	0.57816	-0.317645
C20	0.127997	0.393476	-0.177953
C2	0.67808	1.108154	-0.343148
C5	0.054508	0.635701	-0.329657
C8	0.206346	0.788333	-0.020108

C19	0.58129	0.49462	-0.191437
C6	0.168494	0.796395	-0.347493
C7	0.154443	0.6243	0.183966
C9	0.395897	0.519087	-0.496951
C12	0.582622	0.415926	-0.435058
C14	-0.026712	0.602669	-0.532757
C18	0.348433	0.818215	-0.021049
C24	0.475838	0.684646	0.094783
C21	0.175239	0.941703	-0.209978
C23	0.457488	0.640606	0.123675
C22	0.196189	0.953313	-0.154598
C26	0.447818	0.854545	-0.146826
C29	0.362567	0.227251	-0.381012
C25	0.018035	0.701149	-0.16167
C27	-0.212281	0.800771	-0.071455
C30	0.476388	0.801236	-0.126229
C28	0.381177	0.880523	-0.126593
C35	0.348689	0.38662	-0.51272
C32	-0.026131	0.67793	-0.340127
C31	0.585449	0.344478	-0.174165
C34	0.430877	0.418791	-0.521862
C33	0.129386	0.797995	-0.307403
C37	0.170058	0.586422	-0.681064
C36	0.675254	0.357097	-0.369841
C39	0.075408	0.891072	-0.216125
C40	0.129972	0.760777	0.078934
C38	0.874312	0.406848	-0.241388
C44	-0.293881	0.766973	-0.092565
C43	-0.08896	0.66422	-0.381712
C42	-0.228754	0.348895	-0.502596
C41	0.121805	0.449129	-0.599424
C47	0.642174	0.727017	0.02213
C45	0.781162	1.003069	-0.324894
C46	0.34617	0.542737	-0.545867
C48	0.528045	0.642173	-0.132192
C50	0.145829	0.24232	-0.411394
C49	0.163162	0.190446	-0.33673
C52	0.079202	0.06009	-0.326709
C53	0.375351	0.260205	-0.216533
C51	0.000606	0.604929	-0.396576
C66	-0.138903	0.497825	-0.359448
C67	0.096895	0.338895	-0.169568
C86	0.143269	0.119468	-0.319077
C89	0.321587	0.227505	-0.266376
C54	0.610629	0.304142	-0.206542
C87	0.5508	0.497735	-0.511567
C90	0.01325	0.957128	-0.227414
C96	0.764363	1.13265	-0.3419
C98	-0.268234	0.287305	-0.493538

Table A.24: Bond valance sums for the oxygen atoms of $(TBA)_3[(PyFeW_5O_{18}H]$

Atom	W-O bond length (r_{ij})	S_{ij}	Fe-O bond length (r_{ij})	S_{ij}	BVS (V or z_j)	No. of H^+
O1	1.633	2.155			2.15	0
O2	1.817	1.310				
	2.035	0.727			2.04	0
O3	1.824	1.286				
	2.019	0.759			2.04	0
O4	1.976	0.853				
	1.876	1.117			1.97	0
O5	1.894	1.064				
	2.090	0.627			1.69	0
O6	1.712	1.740			1.74	0
O7	1.929	0.968				
	1.944	0.930			1.90	0
O8	1.681	1.892			1.89	0
O9	1.909	1.022				
	2.001	0.797			1.82	0
O10	1.681	1.892			1.89	0
O11	1.896	1.058				
	2.002	0.795			1.85	0
O12	1.640	2.114			2.11	0
O13	1.934	0.955				
	1.935	0.953			1.91	0
O14	1.817	1.310	2.015	0.468	1.78	0
O15	1.747	1.583	2.110	0.362	1.95	0
O16	1.924	0.981	2.195	0.288	1.27	**1**
O17	1.824	1.286	2.055	0.420	1.71	0
O18	2.335	0.323	2.234	0.259		
	2.331	0.327				
	2.295	0.360				
	2.294	0.361				
	2.398	0.273			1.90	0

A.3.4 Partial strucutre of (TBA)₃[(CH₃CONH₂)FeW₅O₁₈]

Table A.25: Fractional co-ordinates of atoms in the asymmetric unit

Atom	x	y	z
W001	0.252275	0.791574	0.581932
O008	0.319424	0.766336	0.596013
O009	0.18394	0.790057	0.538387
O00A	0.327602	0.834429	0.514304
O00B	0.260051	0.878491	0.551098
O00C	0.311315	0.641285	0.545114
O00D	0.244838	0.682384	0.585672
O00E	0.230478	0.541455	0.540673
O00H	0.396948	0.724123	0.56283
N00I	0.374482	0.525872	0.668293
O00J	0.253713	0.817934	0.642886
C00N	0.375423	0.635779	0.726936
H00A	0.409499	0.64724	0.734367
H00B	0.374252	0.60395	0.754689
C00P	0.429139	0.533823	0.679553
H00C	0.445272	0.553893	0.714848
H00D	0.44269	0.485934	0.679711
N00Q	0.152304	0.504762	0.335037
C00R	0.366296	0.746088	0.777614
H00E	0.399136	0.762278	0.784783
H00F	0.366263	0.715164	0.805865
H00G	0.345579	0.787185	0.775002
C00T	0.346133	0.501146	0.612031
H00H	0.311709	0.498163	0.606542
H00I	0.349226	0.537954	0.588156
C00V	0.441576	0.580498	0.641157
H00J	0.424847	0.626672	0.637
H00K	0.430452	0.557038	0.606763
O00W	0.25	0.75	0.5
C00X	0.49641	0.592848	0.661199
H00L	0.507057	0.618388	0.69478
H00M	0.513032	0.546422	0.667335
C00Y	0.352852	0.598275	0.673604
H00N	0.355545	0.630523	0.646805
H00O	0.318175	0.591389	0.665711
N00Z	0.436197	0.776852	0.442223
C010	0.510928	0.636535	0.622017
H01A	0.502487	0.609886	0.589529
H01B	0.545645	0.645254	0.636875
H01C	0.493783	0.681939	0.615007
C012	0.347253	0.704559	0.725939
H01D	0.348667	0.735666	0.697932
H01E	0.313108	0.692334	0.717423
C013	0.124464	0.5381	0.237541
C014	0.524842	0.765301	0.509882
H01S	0.52002	0.800844	0.533596
H01T	0.517676	0.717801	0.520279
C015	0.371014	0.471148	0.708308
H01F	0.388665	0.490029	0.743705
H01G	0.387299	0.426927	0.704902
C016	0.36159	0.428388	0.596425
C017	0.234421	0.457444	0.333921
C018	0.205783	0.520011	0.345204
C019	0.490561	0.781164	0.453338

H01U	0.497698	0.829392	0.444165
H01V	0.49772	0.747328	0.430087
C01A	0.420864	0.830477	0.475777
H01W	0.385901	0.825033	0.466784
H01X	0.437359	0.817012	0.512747
C01B	0.319272	0.407084	0.749097
H01L	0.338306	0.363436	0.751566
H01M	0.334636	0.434082	0.781797
C01C	0.076218	0.568732	0.33763
C01D	0.12474	0.480361	0.277472
C01E	0.288442	0.47876	0.353631
C01G	0.578038	0.767812	0.514128
H01Y	0.584962	0.815877	0.504453
H	0.581956	0.733813	0.488954
C01H	0.319349	0.452768	0.702622
H01N	0.301189	0.497128	0.700849
H01O	0.303037	0.426381	0.669815
C01I	0.408962	0.793148	0.383258
H01Z	0.418319	0.841198	0.376248
HA	0.420011	0.759085	0.363144
C01J	0.318699	0.421218	0.338326
C01K	0.614595	0.749967	0.568609
H01	0.645402	0.73739	0.566609
HB	0.602789	0.709848	0.582716
HC	0.618966	0.791255	0.591332
C01L	0.147821	0.43926	0.368291
C01M	0.132613	0.573427	0.349375
C01N	0.176526	0.45118	0.430185
C01O	0.267102	0.386536	0.742392
H01P	0.25324	0.354984	0.712372
H01Q	0.247467	0.429517	0.736847
H01R	0.267803	0.362188	0.773742
C01P	0.419374	0.952967	0.509029
H1	0.404675	0.931523	0.530042
C01Q	0.060338	0.639915	0.352071
C01R	0.431066	0.908274	0.470354
H2	0.4654	0.914305	0.476175
HD	0.411548	0.924483	0.434656
C01S	0.095078	0.568174	0.13923
C01T	0.43796	0.640783	0.428753
H3	0.473316	0.640085	0.439397
HE	0.423097	0.646727	0.390563
C01U	0.33139	0.809472	0.306937
H4	0.350056	0.81494	0.286397
C01V	0.423477	0.70161	0.455218
H5	0.439037	0.694631	0.493268
HF	0.388292	0.699249	0.445718
C01W	0.281222	0.819662	0.285571
H6	0.269945	0.821687	0.247615
HG	0.273338	0.864237	0.298591
HH	0.265494	0.780148	0.295649
C01X	0.420487	0.569141	0.444954
H7	0.38494	0.56742	0.429037
HI	0.430164	0.568688	0.483153
C01Y	0.354107	0.789813	0.362906
H8	0.344128	0.741132	0.367636
HJ	0.342574	0.82246	0.383465
C11	0.094087	0.511363	0.182264
C1	0.43002	1.026069	0.514283

H1A	0.440964	1.041124	0.486985
H1B	0.455386	1.035152	0.548401
H1C	0.401109	1.052743	0.511116
C13	0.439861	0.504919	0.429347
H13A	0.423993	0.498299	0.391701
H13B	0.433889	0.463453	0.447221
H13C	0.474528	0.510482	0.438784
W002	0.006693	0.341224	0.31436
W004	0.006788	0.167848	0.315622
O007	-0.06234	0.330609	0.279935
O00F	0	0.253745	0.25
O00G	0	0.39789	0.25
O00K	0.07312	0.317245	0.326352
O00L	0	0.109832	0.25
O3	0.072534	0.187062	0.223348
O2	0.006683	0.253065	0.352848
O6	0.161146	0.265469	0.311466
O1	0.013514	0.405709	0.362792
O4	0.075534	0.190895	0.327258
H01H	0.350319	0.387795	0.611291
H01I	0.39682	0.425224	0.606489
O5	0.013597	0.101391	0.363037
C10	0.333692	0.433957	0.5351
H10A	0.342512	0.478496	0.522111
H10B	0.298559	0.43417	0.526191
Fe3	0.091202	0.26224	0.287767
C8	0.347682	0.369859	0.510066
H8A	0.337216	0.377743	0.472581
H8B	0.332128	0.327156	0.516302
H8C	0.382645	0.363702	0.525312
C9	0.01058	0.646094	0.344849
C2	0.180844	0.36622	0.455358
C20	0.196121	0.384805	0.514504
C14	0.242881	0.251384	0.372478
C15	0.187679	0.244809	0.35014
N19	0.171664	0.22945	0.389877
W006	0.079448	0.252771	0.275655
H01J	0.360446	0.392645	0.621959
H01K	0.395617	0.432712	0.600541
C9A	0.057395	0.69213	0.313789
C20A	0.193828	0.321827	0.445419
C2A	0.160414	0.377629	0.456623
C10A	0.332607	0.397566	0.54048
H10C	0.297704	0.396942	0.532928
H10D	0.343237	0.3487	0.53734
C8A	0.343886	0.448116	0.503362
H8AA	0.322625	0.437456	0.467463
H8AB	0.377417	0.44189	0.507359
H8AC	0.338804	0.497225	0.511603
O4A	0.064474	0.171295	0.317404
O3A	0.059321	0.177413	0.221718
O00M	-0.017513	0.113459	0.235354
O5A	-0.005274	0.097322	0.349181
W0	-0.006574	0.164715	0.304418
O2A	0.00523	0.25341	0.34516
W1	-0.000677	0.347481	0.307886
O7	0.067613	0.337322	0.32121
O1A	-0.000705	0.411615	0.353704
O0	-0.068397	0.325229	0.273203

O8	0	0.25668	0.25
O9	-0.010848	0.400199	0.240851
O6A	0.143254	0.249597	0.300628
Fe1	0.240252	0.619774	0.517053
N5	0.199083	0.556657	0.601744
C6	0.212353	0.512158	0.574632
C7	0.207561	0.429355	0.584637
W005	0.238632	0.64258	0.525153
W003	0.334044	0.734958	0.536315

A.3.5 Partial structure of [(NiW$_5$O$_{18}$H)$_2$]$^{6-}$

Table A.26: Fractional co-ordinates of atoms in the asymmetric unit

Atom	x	y	z
W001	0.372194	0.907161	0.311788
W002	0.510442	0.85959	0.268312
W003	0.623069	0.831397	0.324909
W004	0.441574	0.781651	0.321903
W005	0.484845	0.881082	0.368397
Ni08	0.547205	0.949389	0.314212
O009	0.426368	0.970241	0.309539
O00A	0.401957	0.885005	0.273288
O00B	0.654048	0.908469	0.319268
O00C	0.529739	0.949052	0.359278
O00D	0.606338	0.829654	0.282139
O00E	0.387315	0.906067	0.352653
O00F	0.464072	0.787876	0.282673
O00G	0.497463	0.870511	0.318647
O00H	0.552257	0.92832	0.270393
O00I	0.351592	0.826837	0.318147
O00J	0.558332	0.766099	0.327271
O00K	0.589064	0.850055	0.363731
O00L	0.444745	0.808161	0.361992
O00M	0.515417	0.845877	0.231493
O00N	0.274671	0.927852	0.307795
O00O	0.710647	0.803316	0.331396
O00P	0.473018	0.884341	0.406478
O00Q	0.40378	0.716573	0.325479

Table A.27: Bond valance sums for the oxygen atoms in the asymmetric unit of $[(NiW_5O_{18}H)_2]^{6-}$
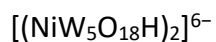
Atom	W-O bond length (r_{ij})	S_{ij}	Ni-O bond length (r_{ij})	S_{ij}	BVS (V or z_j)	No. of H$^+$
O1	1.803	1.361	2.034	0.379	2.04	0
			2.123	0.298		
O2	1.881	1.102	2.100	0.317	1.42	**0.6**
O3	1.980	0.843	2.084	0.331	1.17	**0.8**
O4	1.832	1.258	2.089	0.327	1.58	0
O5	1.739	1.618			1.62	0
O6	1.770	1.488			1.49	**0.5**
O7	1.664	1.981			1.98	0
O8	1.734	1.640			1.64	0
O9	1.903	1.039			2.07	0
	1.907	1.027				
O10	1.936	0.950			1.90	0
	1.937	0.947				
O11	1.994	0.812			1.87	0
	1.895	1.061				
O12	1.956	0.900			1.88	0
	1.925	0.979				
O13	2.320	0.336	2.121	0.300	1.87	0
	2.354	0.307				
	2.348	0.312				
	2.328	0.329				
	2.382	0.285				
O14	2.023	0.751			1.82	0
	1.894	1.064				
O15	1.962	0.885			1.83	0
	1.937	0.947				
O16	2.031	0.735			1.66	0
	1.945	0.927				
O17	2.038	0.721			1.90	0
	1.856	1.179				
O18	1.729	1.662			1.66	0

A.3.6 Partial structure of (TBA)₃[(Py)NiW₅O₁₈H]

Table A.28: Fractional co-ordinates of atoms in the asymmetric unit

Atom	x	y	z
W001	0.517791	0.437499	0.472488
W002	0.546441	0.566733	0.514083
W003	0.450108	0.471671	0.563936
W004	-0.180947	0.505014	0.235762
W005	0.996748	0.407744	0.76429
W006	-0.139152	0.523219	0.134927
W007	0.404167	0.543217	0.414458
W008	0.299905	0.453498	0.465643
W009	1.060673	0.403943	0.876813
W00A	-0.296774	0.431615	0.090008
W00B	-0.33339	0.411171	0.191458
W00C	-0.127219	0.397137	0.178717
W00D	1.209408	0.431651	0.81775
W00E	1.140787	0.530763	0.877936
W00F	1.081075	0.533262	0.764461
Ni0G	-0.335469	0.530631	0.150922
Ni0H	0.342961	0.572838	0.504279
Ni0I	0.946202	0.502238	0.824252
O00J	1.071141	0.468908	0.820167
O00K	0.426419	0.508576	0.48985
O00L	0.462042	0.612726	0.522977
O00M	-0.235399	0.468881	0.16284
O00N	0.519887	0.421639	0.536985
O00O	1.129477	0.39279	0.771159
O00P	0.332342	0.594939	0.43617
O00Q	-0.241813	0.574803	0.127271
O00R	0.543272	0.524545	0.568032
O00S	0.967169	0.554585	0.774732
O00T	1.013741	0.364701	0.819133
O00U	-0.111954	0.542781	0.198407
O00V	0.34708	0.433134	0.531155
O00W	-0.210231	0.483706	0.081618
O00X	1.019551	0.471944	0.73035
O00Y	0.375389	0.533151	0.568445
O00Z	0.509437	0.580059	0.448286
O010	0.64122	0.604717	0.531561
O011	1.127852	0.464039	0.911414
O012	0.596949	0.495573	0.496163
O013	-0.25895	0.445607	0.245076
O014	-0.270047	0.553497	0.216617
O015	0.312746	0.486734	0.410675
O016	0.484297	0.47762	0.415484
O017	-0.357377	0.391157	0.126535
O018	0.245281	0.513398	0.480205
O019	0.902454	0.441786	0.7748
O01A	-0.190948	0.38356	0.116901
N01B	-0.31227	0.469313	0.360413
O01C	-0.376372	0.49112	0.088385
O01D	0.958973	0.438555	0.873239
O01E	0.58308	0.385878	0.46166
O01F	-0.130958	0.527032	0.289096
O01G	0.952163	0.363531	0.722519
O01H	1.189448	0.494273	0.771955
O01I	1.023712	0.55087	0.874644

O01J	-0.070297	0.560762	0.113061
O01K	0.403708	0.406188	0.458525
N01L	-0.102547	0.712119	0.200507
O01M	-0.393087	0.364534	0.21305
N01N	0.259729	0.63526	0.515116
O01O	0.216625	0.409497	0.447989
O01P	1.179944	0.387596	0.861549
O01Q	-0.401051	0.471318	0.178916
N01R	0.451487	0.258532	0.539448
C01S	-0.353557	0.503769	0.317132
N01T	-0.433193	0.58847	0.141493
O01U	-0.101359	0.440932	0.230709
O01V	0.46853	0.443258	0.616272
O01W	-0.220774	0.3663	0.196937
O01X	-0.073051	0.454671	0.149716
O01Y	1.198431	0.573847	0.918957
O01Z	1.065124	0.356765	0.918408
N020	0.788144	0.515598	0.638862
C021	-0.217609	0.456378	0.358206
N022	1.394667	0.436075	0.985751
O023	1.09139	0.579591	0.724157
N024	0.829303	0.536915	0.826788
C025	-0.309602	0.503833	0.403162
C026	-0.480573	0.552238	0.265001
C027	-0.451845	0.5197	0.309975
C028	-0.165678	0.420535	0.394577
N029	0.151413	0.463195	0.286773
C02A	0.761993	0.491042	0.589373
H02I	0.704003	0.473581	0.584281
H02J	0.756525	0.521447	0.567618
C02B	-0.142121	0.67116	0.229028
O02C	1.13508	0.571187	0.821574
O02D	1.240269	0.489614	0.86158
C02E	-0.070416	0.412882	0.389029
C02F	-0.578023	0.564485	0.251071
C02G	-0.019523	0.740607	0.229487
N02H	0.209474	0.459107	0.644501
C02I	-0.252288	0.55499	0.410073
C02J	-0.168453	0.760307	0.183007
C02K	0.792629	0.426686	0.531826
H02K	0.734293	0.410231	0.528376
H02L	0.786419	0.456922	0.509869
C02L	0.8248	0.450107	0.579793
H02M	0.832154	0.419978	0.601908
H02N	0.882329	0.467653	0.583165
C02M	0.853965	0.383514	0.520912
H02O	0.91326	0.398286	0.527234
H02P	0.834283	0.373585	0.489045
H02Q	0.853587	0.351053	0.539476
C02N	0.186975	0.459529	0.592889
C02O	0.539067	0.289617	0.549715
H02E	0.541442	0.315391	0.574796
H02F	0.541995	0.311261	0.522956
C02P	-0.254228	0.584409	0.451958
C02Q	0.084999	0.566778	0.370133
H02A	0.140469	0.587391	0.37878
H02B	0.08816	0.538347	0.393376
C02R	0.08318	0.536932	0.325656
H02C	0.036669	0.508915	0.32012

H02D	0.068336	0.563534	0.300613
C02S	1.426546	0.429348	1.037715
C02T	0.059908	0.701499	0.248573
C02U	1.470131	0.411598	0.967759
C02V	-0.365437	0.418934	0.365015
C02W	0.45141	0.214202	0.576225
H02G	0.395368	0.194221	0.567362
H02H	0.498346	0.187646	0.576031
C02X	0.10159	0.494747	0.571334
C02Y	-0.044848	0.689531	0.084188
C02Z	0.783072	0.353742	0.824312
C030	-0.16044	0.697032	0.272048
C031	-0.190167	0.633462	0.463627
C032	-0.083535	0.682042	0.160976
C033	0.07401	0.4854	0.520362
C034	0.712758	0.555207	0.643507
H03V	0.70415	0.582892	0.619311
H03W	0.658152	0.533837	0.638535
N035	0.819481	0.307958	0.833624
C036	0.26873	0.407638	0.260876
H03A	0.239194	0.373282	0.265361
H03B	0.24478	0.419452	0.229329
C037	0.113293	0.671623	0.501694
C038	0.17628	0.629581	0.501263
C039	0.099705	0.410225	0.288271
H03C	0.100065	0.388449	0.261201
H03D	0.038358	0.42029	0.286166
C03A	1.394938	0.438883	1.114888
C03B	0.110574	0.488626	0.239833
H03E	0.109863	0.460488	0.216635
H03F	0.049243	0.498334	0.238127
C03C	-0.015624	0.373609	0.42407
C03D	1.365564	0.455707	1.063246
C03E	0.463733	0.234483	0.624287
H03N	0.507806	0.264011	0.630555
H03O	0.408069	0.249584	0.627921
C03F	0.156492	0.53907	0.228337
H03G	0.140047	0.569914	0.245275
H03H	0.219842	0.533155	0.240755
C03G	0.140995	0.732444	0.277015
C03H	0.38028	0.302645	0.538131
H03P	0.387677	0.317686	0.56876
H03Q	0.38855	0.332909	0.518295
C03I	0.79781	0.471468	0.674602
H03X	0.847861	0.447865	0.673489
H03Y	0.811152	0.488996	0.704602
C03J	0.433247	0.22998	0.493067
H03R	0.475109	0.199544	0.495026
H03S	0.37392	0.21408	0.486069
C03K	-0.21969	0.662134	0.292857
C03L	1.21524	0.731751	0.796832
C03M	0.296527	0.68186	0.536544
C03N	0.219469	0.515868	0.667212
C03O	0.620591	0.250438	0.562708
H03T	0.621529	0.230957	0.591033
H03U	0.617374	0.223	0.538701
C03P	0.163069	0.511527	0.325638
H03I	0.188474	0.495281	0.355617
H03J	0.204289	0.539456	0.320193

C03Q	0.380391	0.348793	0.226683
H03K	0.419724	0.319588	0.241341
H03L	0.405758	0.367651	0.204956
H03M	0.323965	0.333095	0.211022
C03R	-0.376613	0.376533	0.324646
C03S	0.089542	0.384283	0.116969
C03T	0.729661	0.380919	0.696489
H03Z	0.777957	0.360876	0.688695
H	0.749813	0.390533	0.728767
C03U	0.668324	0.58496	0.827898
C03V	0.96799	0.669991	0.590298
H03	0.934205	0.702196	0.594377
HA	0.943284	0.654428	0.560387
HB	1.028704	0.680582	0.593116
C03W	-0.256371	0.739411	0.147951
C03X	0.133007	0.423624	0.658949
C03Y	0.716958	0.43595	0.66914
H1	0.694379	0.427117	0.636823
HC	0.671693	0.457697	0.678202
C03Z	1.383926	0.49575	0.974597
C040	-0.043768	0.716094	0.129365
C041	1.305169	0.407099	0.966692
C042	1.537169	0.394609	0.897115
C043	0.003616	0.722266	0.053743
C044	0.121184	0.295752	0.517246
H04E	0.108929	0.287918	0.484985
H04F	0.080268	0.323428	0.522448
H04G	0.114565	0.262283	0.533499
C045	0.221116	0.692618	0.292091
C046	0.877976	0.589602	0.612047
H04L	0.825652	0.612964	0.608161
H04M	0.875533	0.571912	0.582806
C047	0.289589	0.280813	0.521559
H04H	0.286878	0.243834	0.534119
H04I	0.275083	0.277576	0.488376
C049	0.702556	0.284651	0.568597
H04J	0.702458	0.302651	0.539763
H04K	0.703495	0.313448	0.591302
C04A	0.294481	0.550011	0.659402
C04B	1.444619	0.413998	0.914526
C04C	0.249859	0.451816	0.292852
H04A	0.275773	0.440258	0.324294
H04B	0.278813	0.486168	0.28779
C04D	1.465644	0.53352	0.983985
C04E	0.655111	0.341592	0.691595
H04N	0.60551	0.360327	0.698462
H04O	0.673214	0.311031	0.71246
H04P	0.638006	0.327778	0.660673
C04F	0.87659	0.544611	0.647982
H04Q	0.922659	0.517377	0.647918
H04R	0.889736	0.5616	0.678187
C04G	0.434714	0.408203	0.728154
C04H	0.295646	0.42481	0.656635
C04I	-0.001528	0.448064	0.057203
C04J	0.146972	0.714543	0.526486
C04K	-0.009936	0.52092	0.494585
C04L	0.162849	0.341823	0.1283
C04M	0.759234	0.506217	0.807183
C04N	-0.433225	0.62649	0.172954

C04O	0.132133	0.373025	0.330255
H04C	0.193712	0.362898	0.33309
H04D	0.129621	0.39366	0.357573
O1	-0.335097	0.403592	0.037653
O2	1.309086	0.407479	0.814271
O3	0.389305	0.564967	0.360283
O4	-0.047971	0.349055	0.190028
C8	0.439871	0.266718	0.455248
H8A	0.501919	0.275502	0.457989
H8B	0.408797	0.301307	0.457231
C16	0.49399	0.187006	0.658145
H16A	0.449502	0.15772	0.652162
H16B	0.549192	0.171543	0.654193
C17	-0.506627	0.580172	0.112834
C18	0.396645	0.237216	0.4048
H18A	0.432405	0.258409	0.38872
H18B	0.429629	0.202701	0.412334
C20	-0.564802	0.661647	0.137533
C3	0.220332	0.318351	0.535167
H3A	0.223672	0.355391	0.522839
H3B	0.234903	0.321379	0.568364
C4	-0.23791	0.689467	0.333296
C5	0.17814	0.601093	0.165777
H5A	0.219386	0.588558	0.149054
H5B	0.20849	0.624644	0.190633
H5C	0.130993	0.621669	0.145613
C1	0.96451	0.627356	0.626325
H1A	0.965643	0.64623	0.654935
H1B	1.016839	0.603794	0.631476
C9	0.726995	0.583926	0.687124
C12	0.645551	0.612989	0.691465
C13	0.241524	0.726329	0.541586
C14	0.660401	0.532348	0.806884
C15	0.102002	0.367777	0.629153
C6	0.012247	0.60633	0.373706
H6A	-0.042988	0.586423	0.368625
H6B	0.006851	0.635098	0.35102
H6C	0.026365	0.622759	0.403758
C19	0.14422	0.557262	0.18247
H19A	0.160661	0.525473	0.16654
H19B	0.080297	0.561166	0.170746
C2	1.350464	0.471981	1.143516
C11	0.316189	0.409805	0.707849
C22	0.080162	0.3236	0.327506
C10	1.25986	0.332244	1.006146
C21	0.162627	0.15413	0.24462
H21A	0.134739	0.184642	0.225727
H21B	0.117896	0.131634	0.252711
H21C	0.195211	0.1319	0.228021
C7	1.30329	0.35075	0.971539
N3	-0.035145	0.467573	0.006839
C30	-0.083764	0.410185	-0.026015
C25	0.068088	0.400531	0.067831
C31	-0.191071	0.326018	-0.039788
C28	-0.109345	0.510591	0.007185
C29	-0.163492	0.523613	-0.041357
C24	0.825378	0.590881	0.843349
C26	0.045823	0.489758	-0.01188
C27	0.111275	0.527784	0.016272

C23	-0.337445	0.782594	0.146119
C34	0.181492	0.607561	0.027474
C39	-0.422607	0.322299	0.332347
C33	-0.493331	0.666972	0.171718
C32	0.364957	0.397382	0.26909
H32A	0.388683	0.382217	0.299626
H32B	0.395788	0.431947	0.266696
C38	1.603939	0.435355	0.91129
C37	1.43903	0.590945	0.973737
C36	0.782381	0.249543	0.58345
H36A	0.770704	0.219787	0.602381
H36B	0.83102	0.271673	0.600668
H36C	0.797499	0.234265	0.556991
C42	0.689162	0.260932	0.834916
C40	0.685414	0.356221	0.819399
C43	0.506634	0.205923	0.702703
H43A	0.45029	0.216106	0.707882
H43B	0.545148	0.237834	0.707416
H43C	0.533241	0.176962	0.723746
C41	0.647598	0.305644	0.820132
C44	0.735764	0.618472	0.84482
C46	0.02248	0.288719	0.624395
C45	0.280444	0.6084	0.671357
C49	-0.156398	0.380579	-0.013397
N1	1.2626	0.710548	0.84394
C52	1.161486	0.701707	0.871473
C50	1.306518	0.6532	0.84348
C54	1.156479	0.780303	0.700244
C55	1.403825	0.562068	0.82812
C51	1.363395	0.62602	0.81514
C53	1.216336	0.735324	0.75482
C57	0.767905	0.257051	0.841897
C56	1.231369	0.272879	1.015645
C58	1.273017	0.709187	0.646193
C48	1.605914	0.733619	0.877993
C66	0.051747	0.338368	0.649307
C65	-0.239438	0.598262	-0.015702
C67	1.535272	0.619006	0.97445
C69	1.566022	0.754352	0.844015
C59	1.508856	0.781901	0.878947
C71	0.415179	0.354088	0.705631
C60	1.426409	0.783543	0.944478
C35	1.319761	0.749713	0.921953
C62	-0.047074	0.207515	0.088087
C63	-0.578269	0.620493	0.109756
H22A	0.018168	0.3343	0.322127
H22B	0.097083	0.305007	0.357056
C47	-0.366406	0.783263	0.190304
C61	0.087797	0.28243	0.291136
H61A	0.050433	0.250866	0.292174
H61B	0.069351	0.299749	0.261488
H61C	0.148484	0.270375	0.296513
C70	0.561281	0.579653	0.673676
H22C	0.081611	0.302892	0.300063
H22D	0.018786	0.333266	0.325727
C68	0.117069	0.288367	0.369333
H68A	0.082181	0.25505	0.367565
H68B	0.177619	0.278635	0.370771
H68C	0.114969	0.308924	0.396363

C47A	-0.395716	0.757399	0.102474
C70A	0.663451	0.661572	0.724451

Table A.29: Bond valance sums for the oxygen atoms of one of the "$[(Py)NiW_5O_{18}H]^{3-}$" units present in the partial structure

Atom	W-O bond length (r_{ij})	S_{ij}	Ni-O bond length (r_{ij})	S_{ij}	BVS (V or z_j)	No. of H^+
O1	1.686	1.867			1.87	0
O2	1.872	1.129				
	2.029	0.739			1.87	0
O3	1.932	0.960				
	1.972	0.862			1.82	0
O4	1.875	1.120				
	2.011	0.776			1.90	0
O5	1.921	0.989				
	2.003	0.793			1.78	0
O6	1.649	2.063			2.06	0
O7	1.893	1.067				
	1.982	0.839			1.91	0
O8	1.674	1.929			1.93	0
O9	1.906	1.030				
	1.927	0.973			2.00	0
O10	1.697	1.812			1.81	0
O11	1.909	1.022				
	1.944	0.930			1.95	0
O12	1.672	1.939			1.94	0
O13	1.895	1.061				
	1.946	0.925			1.99	0
O14	1.781	1.444	2.074	0.340	1.78	0
O15	1.904	1.036	2.097	0.320	1.36	**0.6**
O16	1.787	1.421	2.031	0.382	1.80	0
O17	1.895	1.061	2.085	0.330	1.39	**0.6**
O18	2.363	0.300	2.131	0.292		
	2.326	0.331				
	2.360	0.302				
	2.341	0.318				
	2.294	0.361			1.90	0

A.3.7 Partial structure of (TBA)₆[(ZnW₅O₁₈H)₂]

Table A.30: Fractional co-ordinates of atoms in the asymmetric unit

Atom	x	y	z
W001	0.166111	0.293026	0.227958
W002	0.502983	0.312476	0.185312
W003	-0.015754	0.253729	0.209554
W004	0.340769	0.209496	0.063668
W005	0.005056	0.189917	0.106072
W006	0.522486	0.248711	0.081651
W007	0.479366	0.204462	0.188648
W008	0.027427	0.29786	0.102498
W009	0.37019	0.316598	0.05759
W00A	0.137839	0.186338	0.234083
Zn0B	0.177013	0.226178	0.123556
Zn0C	0.331376	0.27638	0.168606
O00D	0.428159	0.261493	0.123119
O00E	0.53126	0.255895	0.22785
O00F	0.395468	0.173935	0.132475
O00G	0.414656	0.316745	0.212757
O00H	0.042811	0.206487	0.257218
O00I	0.066914	0.293882	0.251219
O00J	-0.062598	0.213462	0.15139
O00K	0.111646	0.281809	0.077258
O00L	0.544908	0.204825	0.141515
O00M	0.10074	0.326867	0.166031
O00N	-0.045407	0.296961	0.149347
O00O	0.08454	0.185154	0.0834
O00P	0.185787	0.238622	0.271564
O00Q	-0.020492	0.244015	0.073788
O00R	0.572143	0.350697	0.227318
O00S	0.565835	0.291822	0.135369
O00T	0.449705	0.348143	0.121536
O00U	0.218049	0.332193	0.274594
O00V	0.314989	0.265433	0.022403
O00W	0.296637	0.318475	0.099494
O00X	0.593035	0.238314	0.047476
O00Y	0.438449	0.207962	0.046365
C00Z	0.536951	0.311316	0.360168
O010	0.276896	0.224556	0.103158
O011	0.209472	0.184144	0.191295
O012	0.057653	0.155903	0.176571
O013	0.384117	0.22044	0.21569
O014	0.517349	0.162522	0.237666
O015	-0.01858	0.338247	0.056572
O016	0.286521	0.169566	0.018769
O017	0.086078	0.242057	0.167773
O018	0.457315	0.295784	0.037453
O019	0.232588	0.278213	0.188554
O01A	0.336844	0.358358	0.007342
O01B	-0.062603	0.152932	0.065273
O01C	0.174365	0.147988	0.286863
N01D	0.05738	0.24789	-0.085876
O01E	-0.091161	0.262905	0.241043
N01F	0.44549	0.24912	0.377689
C01G	0.043264	0.218652	-0.042332
C01H	0.06957	0.217606	-0.133607
N01I	-0.247639	0.356418	0.091787

C01J	-0.056857	0.305754	-0.083476
C01K	0.528373	0.221452	0.410235
C01L	-0.240106	0.306975	0.083606
H01A	-0.196989	0.296417	0.115956
H01B	-0.288552	0.293392	0.085782
C01M	-0.256595	0.366719	0.146918
H01C	-0.265636	0.398202	0.147789
H01D	-0.304687	0.352243	0.148334
C01N	-0.006738	0.277003	-0.118332
C01O	0.379466	0.220981	0.344606
C01P	0.744438	0.191923	0.229801
C01Q	-0.217907	0.243396	0.03876
H01E	-0.263489	0.230028	0.045837
H01F	-0.170135	0.235476	0.069336
N01R	0.766123	0.138563	0.164884
C01S	0.545187	0.190265	0.371414
N01T	0.247046	0.066663	0.125499
C01U	0.76038	0.185208	0.17533
N01V	0.248063	0.435363	0.158565
C01W	-0.226687	0.290084	0.034427
H01G	-0.178917	0.303182	0.030375
H01H	-0.271192	0.297597	0.00118
C01X	-0.211096	0.225612	-0.027729
H01I	-0.263552	0.219947	-0.053419
H01J	-0.179927	0.199129	-0.022426
H01K	-0.186145	0.24819	-0.043114
C01Y	-0.193624	0.35548	0.198242
H01L	-0.145419	0.370405	0.197881
H01M	-0.183881	0.324038	0.197921
C01Z	-0.463946	0.385046	-0.007896
H01N	-0.511523	0.367313	-0.023414
H01O	-0.445447	0.393742	-0.03896
C020	0.166528	0.30654	-0.090976
C022	-0.399454	0.357124	0.03423
H02A	-0.410816	0.355623	0.069725
H02B	-0.40189	0.327369	0.019543
C024	0.740813	0.245102	0.248638
C025	0.424909	0.275108	0.41984
C026	0.203887	0.404536	0.108263
C027	0.372173	0.309853	0.40006
C028	0.357934	0.185719	0.379655
C029	0.123409	0.277119	-0.054589
C02A	0.73701	0.248955	0.307773
C02B	0.682295	0.118065	0.155268
C02C	-0.317767	0.374381	0.045438
H02C	-0.319915	0.405729	0.052443
H02D	-0.305419	0.371424	0.010435
C02D	0.306145	0.4072	0.202081
C02G	0.297146	0.034244	0.100817
C02H	0.289881	0.473859	0.134445
C02I	0.189119	0.463793	0.185682
C02K	0.821565	0.107653	0.200084
C02M	0.188623	0.092239	0.081793
C02N	0.298821	0.09443	0.166921
C02O	0.341376	0.451107	0.105581
C02Q	0.474853	0.278813	0.338835
C20	-0.174287	0.373916	0.089299
C26	-0.208488	0.366681	0.252472
H26A	-0.222042	0.397711	0.251448

H26B	-0.254672	0.350171	0.253841
C30	0.378553	0.10732	0.275196
C31	0.787204	0.137446	0.111793
C32	0.118909	0.396807	0.011205
C36	0.35487	0.076251	0.220837
C39	0.413874	0.39937	0.29887
C40	0.15803	0.189237	-0.106516
C42	0.35584	0.43203	0.252948
C43	0.139657	0.430959	0.208383
C48	-0.142451	0.358144	0.305712
H48A	-0.095393	0.350145	0.296903
H48B	-0.157032	0.33451	0.326012
H48C	-0.132189	0.384253	0.328681
C49	0.133524	0.429577	0.067162
C50	0.125213	0.067331	0.026258
C51	0.093154	0.456703	0.245283
C54	0.393016	0.495761	0.08799
C56	0.33809	0.060646	0.071582
C57	0.79764	0.092044	0.057269
C58	0.634732	0.129124	0.078284
C59	-0.48586	0.428268	0.020823
H59A	-0.490797	0.42074	0.056937
H59B	-0.535395	0.440141	-0.003206
H59C	-0.444528	0.44984	0.025959
C61	0.891865	0.132702	0.237887
C63	0.43683	0.084935	0.321854
C67	0.066758	0.020017	0.186344
C68	0.521014	0.106167	0.038131
C73	0.198446	0.03104	0.158666
C78	0.472295	0.427627	0.350817
C79	0.066304	0.097594	-0.016595
C83	0.056377	0.42935	0.268246
C85	0.535594	0.14126	-0.000971
C89	0.414571	0.022383	0.067621
C96	0.054843	0.411187	-0.038487
C114	0.9474	0.096682	0.295321
C116	0.360342	0.003589	0.018553
C119	0.026905	0.069386	-0.060182
C128	0.13991	0.013167	0.233807
C131	0.329264	0.506904	0.041313
C183	0.131597	0.05644	0.179085
C34	-0.047827	0.189903	-0.069464
C24	0.258415	0.079591	0.398793
C1	0.28833	0.034941	0.395639
N41	0.312218	-0.000524	0.387795
C02L	-0.153578	0.41997	0.1185
H02E	-0.125539	0.416476	0.158663
H02F	-0.201791	0.436775	0.113887
H20A	-0.177115	0.37658	0.049935
H20B	-0.131744	0.353423	0.10746
C60	-0.07898	0.50378	0.115782
H60A	-0.046508	0.522609	0.101325
H60B	-0.131062	0.516476	0.107571
H60C	-0.055036	0.500709	0.156023
C3	-0.087244	0.449543	0.082284
H3A	-0.112557	0.451296	0.041588
H3B	-0.035731	0.435363	0.09055
H20C	-0.165389	0.361666	0.055909
H20D	-0.132313	0.362663	0.121865

C4	-0.162602	0.424992	0.087683
H4A	-0.201461	0.440125	0.100912
H4B	-0.169479	0.434539	0.049275
C3A	-0.056447	0.438236	0.136232
H3AA	-0.019096	0.415096	0.135405
H3AB	-0.054681	0.443386	0.175008
C60A	-0.037939	0.488916	0.102268
H60D	0.014377	0.499795	0.122377
H60E	-0.041657	0.482739	0.063742
H60F	-0.076857	0.510724	0.102918

Table A.31: Bond valance sums for the oxygen atoms of $(TBA)_6[(ZnW_5O_{18}H)_2]$

Atom	W-O bond length (r_{ij})	S_{ij}	Zn-O bond length (r_{ij})	S_{ij}	BVS (V or z_j)	No. of H^+
O1	1.783	1.436	1.995	0.455	2.12	0
			2.248	0.230		
O2	2.068	0.665	2.104	0.339	1.00	**1.0**
O3	1.905	1.033	1.961	0.499	1.53	**0.5**
O4	1.917	1.000	2.073	0.369	1.37	**0.6**
O5	1.719	1.708			1.71	0
O6	1.743	1.600			1.60	0
O7	1.766	1.504			1.50	0
O8	1.746	1.588			1.59	0
O9	1.921	0.989			1.80	0
	1.994	0.812				
O10	1.913	1.011			1.82	0
	1.995	0.810				
O11	1.904	1.036			1.83	0
	2.000	0.799				
O12	1.893	1.067			1.95	0
	1.961	0.888				
O13	2.333	0.325	2.385	0.159	1.82	0
	2.288	0.367				
	2.385	0.282				
	2.368	0.296				
	2.265	0.390				
O14	1.916	1.003			2.00	0
	1.918	0.997				
O15	1.901	1.044			1.97	0
	1.944	0.930				
O16	1.853	1.189			1.95	0
	2.020	0.757				
O17	1.881	1.102			2.04	0
	1.942	0.935				
O18	1.754	1.554			1.55	0
O19	1.817	1.310	2.250	0.279	2.18	0
			1.970	0.595		
O20	1.905	1.033	2.046	0.485	1.52	**0.5**
O21	1.685	1.872	2.045	0.486	2.36	0
O22	1.863	1.157	2.160	0.356	1.51	0
O23	1.710	1.750			1.75	0
O24	1.720	1.703			1.70	0
O25	1.717	1.717			1.72	0
O26	1.696	1.817			1.82	0
O27	1.898	1.053			1.98	0
	1.945	0.927				
O28	1.902	1.041			1.86	0
	1.992	0.817				
O29	1.820	1.300			2.42	0
	1.874	1.123				
O30	1.905	1.033			2.05	0
	1.910	1.019				
O31	2.347	0.313	2.279	0.246	1.83	0
	2.384	0.283				
	2.348	0.312				
	2.336	0.322				
	2.299	0.356				
O32	1.932	0.960			1.71	0
	2.022	0.753				

O33	1.937	0.947	1.66	0
	2.043	0.711		
O34	1.874	1.123	1.87	0
	2.025	0.747		
O35	1.935	0.953	1.75	0
	2.001	0.797		
O36	1.777	1.460	1.46	**0.5**

A.3.8 (TBA)$_3$[(Py)ZnW$_5$O$_{18}$H]

Table A.32: Crystal structure data for (TBA)$_3$[(Py)ZnW$_5$O$_{18}$H]

Empirical formula	C$_{53}$H$_{113}$N$_4$O$_{18}$W$_5$Zn
Formula weight	2079.09
Temperature/K	150.0(2)
Crystal system	monoclinic
Space group	P2$_1$/c
a/Å	18.2097(2)
b/Å	16.4169(2)
c/Å	23.5493(2)
α/°	90
β/°	94.7880(10)
γ/°	90
Volume/Å^3	7015.42(13)
Z	4
ρ_{calc}g/cm^3	1.968
μ/mm^{-1}	15.611
F(000)	4012.0
Crystal size/mm^3	0.23 × 0.15 × 0.15
Radiation	Cu Kα (λ = 1.54184)
2Θ range for data collection/°	7.262 to 133.134
Index ranges	-21 ≤ h ≤ 19, -17 ≤ k ≤ 19, -28 ≤ l ≤ 26
Reflections collected	58837
Independent reflections	12301 [R$_{int}$ = 0.0573, R$_{sigma}$ = 0.0406]
Data/restraints/parameters	12301/1602/982
Goodness-of-fit on F^2	1.050
Final R indexes [I>=2σ (I)]	R$_1$ = 0.0445, wR$_2$ = 0.1117
Final R indexes [all data]	R$_1$ = 0.0584, wR$_2$ = 0.1260
Largest diff. peak/hole / e Å^{-3}	1.70/-2.16

Table A.33: Bond valance sums for the oxygen atoms of $(TBA)_3[(Py)ZnW_5O_{18}H]$

Atom	W-O bond length (r_{ij})	S_{ij}	Zn-O bond length (r_{ij})	S_{ij}	BVS (V or z_j)	No. of H^+
O1	1.921	0.989	2.075	0.367	1.36	1
O2	1.837	1.241	2.080	0.362	1.60	0
O3	1.801	1.368	2.072	0.370	1.74	0
O4	1.835	1.248	2.078	0.364	1.61	0
O5	1.709	1.754			1.75	0
O6	1.698	1.807			1.81	0
O7	1.701	1.793			1.79	0
O8	1.699	1.803			1.80	0
O9	1.896	1.058				
	1.942	0.935			1.99	0
O10	1.915	1.005				
	1.935	0.953			1.96	0
O11	1.938	0.945				
	1.922	0.987			1.93	0
O12	1.946	0.925				
	1.919	0.995			1.92	0
O13	1.967	0.874				
	1.977	0.850			1.72	0
O14	2.010	0.778				
	1.919	0.995			1.77	0
O15	2.025	0.747				
	1.867	1.145			1.89	0
O16	2.008	0.782				
	1.902	1.041			1.82	0
O17	1.725	1.680			1.68	0
O18	2.315	0.341	2.330	0.184		
	2.326	0.331				
	2.334	0.324				
	2.320	0.336				
	2.288	0.367			1.88	0

A.3.9 (TBA)$_6$[(MgW$_5$O$_{18}$H)$_2$]

Table A.34: Crystal structure data for (TBA)$_6$[(MgW$_5$O$_{18}$H)$_2$]

Empirical formula	C$_{111}$H$_{231}$Mg$_2$N$_9$O$_{36}$W$_{10}$
Formula weight	4155.15
Temperature/K	150.0(2)
Crystal system	monoclinic
Space group	P2$_1$
a/Å	16.7733(2)
b/Å	25.6436(2)
c/Å	17.5127(2)
α/°	90
β/°	108.1950(10)
γ/°	90
Volume/Å^3	7156.06(14)
Z	2
ρ$_{calc}$g/cm^3	1.928
μ/mm^{-1}	15.060
F(000)	4024.0
Crystal size/mm^3	0.18 × 0.09 × 0.06
Radiation	CuKα (λ = 1.54184)
2Θ range for data collection/°	5.312 to 149.576
Index ranges	-19 ≤ h ≤ 20, -31 ≤ k ≤ 31, -21 ≤ l ≤ 21
Reflections collected	91642
Independent reflections	28030 [R$_{int}$ = 0.0405, R$_{sigma}$ = 0.0376]
Data/restraints/parameters	28030/2282/1730
Goodness-of-fit on F^2	1.045
Final R indexes [I>=2σ (I)]	R$_1$ = 0.0310, wR$_2$ = 0.0772
Final R indexes [all data]	R$_1$ = 0.0332, wR$_2$ = 0.0789
Largest diff. peak/hole / e Å^{-3}	1.14/-1.02
Flack parameter	-0.026(7)

Table A.35: Bond valance sums for the oxygen atoms of $(TBA)_6[(MgW_5O_{18}H)_2]$

Atom	W-O bond length (r_{ij})	S_{ij}	Mg-O bond length (r_{ij})	S_{ij}	BVS (V or z_j)	No. of H^+
O1	1.821	1.296	2.184	0.273	1.57	0
O2	1.786	1.425	2.053	0.389	1.81	0
O3	1.969	0.869	2.053	0.389	1.26	1
O4	1.864	1.154	2.060	0.382	1.54	0
O5	1.714	1.731			1.73	0
O6	1.727	1.671			1.67	0
O7	1.717	1.717			1.72	0
O8	1.711	1.745			1.75	0
O9	1.909	1.022				
	1.956	0.900			1.92	0
O10	1.940	0.940				
	1.932	0.960			1.90	0
O11	1.906	1.030				
	1.965	0.878			1.91	0
O12	1.913	1.011				
	1.948	0.920			1.93	0
O13	2.336	0.322	1.996	0.454		
	2.301	0.354				
	2.355	0.306				
	2.320	0.336				
	2.344	0.315			2.09	0
O14	2.017	0.763				
	1.879	1.108			1.87	0
O15	2.046	0.706				
	1.870	1.135			1.84	0
O16	1.923	0.984				
	1.985	0.832			1.82	0
O17	1.963	0.883				
	1.936	0.950			1.83	0
O18	1.722	1.694			1.69	0
O19	1.831	1.262	2.154	0.296	1.56	0
O20	1.950	0.915	2.069	0.373	1.29	1
O21	1.845	1.215	2.064	0.378	1.59	0
O22	1.792	1.402	2.059	0.383	1.79	0
O23	1.716	1.722			1.72	0
O24	1.714	1.731			1.73	0
O25	1.724	1.685			1.68	0
O26	1.722	1.694			1.69	0
O27	1.973	0.860				
	1.906	1.030			1.89	0
O28	1.936	0.950				
	1.943	0.932			1.88	0
O29	1.934	0.955				
	1.919	0.995			1.95	0
O30	1.952	0.910				
	1.909	1.022			1.93	0
O31	2.323	0.334	2.264	0.220		
	2.327	0.330				
	2.324	0.333				
	2.333	0.325				
	2.353	0.308			1.85	0
O32	1.983	0.837				
	1.899	1.050			1.89	0
O33	1.913	1.011				
	1.982	0.839			1.85	0

O34	1.997	0.806			
	1.920	0.992		1.80	0
O35	2.055	0.689			
	1.851	1.195		1.88	0
O36	1.730	1.658		1.66	0

A.4 X-ray diffraction data presented in Chapter 5

A.4.1 (TBA)$_3$[VMo$_5$O$_{19}$]

Table A.36: Crystal structure data for (TBA)$_3$[VMo$_5$O$_{19}$].2CH$_2$Cl$_2$

Empirical formula	C$_{50}$H$_{112}$Cl$_4$Mo$_5$N$_3$O$_{19}$V
Formula weight	1731.86
Temperature/K	150.0(2)
Crystal system	monoclinic
Space group	P2$_1$/c
a/Å	24.1764(5)
b/Å	17.2594(3)
c/Å	17.7172(3)
α/°	90
β/°	103.7237(17)
γ/°	90
Volume/Å^3	7181.8(2)
Z	4
ρ$_{calc}$g/cm^3	1.602
μ/mm^{-1}	9.876
F(000)	3544.0
Crystal size/mm^3	0.16 × 0.1 × 0.05
Radiation	CuKα (λ = 1.54184)
2Θ range for data collection/°	6.356 to 157.426
Index ranges	-29 ≤ h ≤ 29, -21 ≤ k ≤ 7, -20 ≤ l ≤ 21
Reflections collected	51738
Independent reflections	14280 [R$_{int}$ = 0.0348, R$_{sigma}$ = 0.0338]
Data/restraints/parameters	14280/713/807
Goodness-of-fit on F^2	1.066
Final R indexes [I>=2σ (I)]	R$_1$ = 0.0386, wR$_2$ = 0.1056
Final R indexes [all data]	R$_1$ = 0.0552, wR$_2$ = 0.1199
Largest diff. peak/hole / e Å^{-3}	1.12/-1.17

A.4.2 (TBA)$_3$[NbMo$_5$O$_{19}$]

Table A.37: Crystal structure data for (TBA)$_3$[NbMo$_5$O$_{19}$]

Empirical formula	C$_{50}$H$_{113}$Mo$_5$N$_3$NbO$_{19.5}$
Formula weight	1641.04
Temperature/K	150.0(2)
Crystal system	monoclinic
Space group	C2/c
a/Å	29.8149(5)
b/Å	18.4920(3)
c/Å	27.1454(4)
α/°	90
β/°	112.965(2)
γ/°	90
Volume/Å^3	13780.1(4)
Z	8
ρ_{calc}g/cm^3	1.582
μ/mm^{-1}	9.075
F(000)	6728.0
Crystal size/mm^3	0.151 × 0.124 × 0.065
Radiation	CuKα (λ = 1.54184)
2Θ range for data collection/°	5.762 to 142.89
Index ranges	-27 ≤ h ≤ 36, -22 ≤ k ≤ 21, -33 ≤ l ≤ 31
Reflections collected	39973
Independent reflections	12883 [R$_{int}$ = 0.0275, R$_{sigma}$ = 0.0272]
Data/restraints/parameters	12883/886/839
Goodness-of-fit on F^2	1.032
Final R indexes [I>=2σ (I)]	R$_1$ = 0.0312, wR$_2$ = 0.0804
Final R indexes [all data]	R$_1$ = 0.0363, wR$_2$ = 0.0848
Largest diff. peak/hole / e Å^{-3}	0.95/-1.27

A.4.3 (TBA)$_3$[ReW$_5$O$_{19}$]

Table A.38: Crystal structure data for (TBA)$_3$[ReW$_5$O$_{19}$].2CH$_2$Cl$_2$

Empirical formula	C$_{50}$H$_{112}$Cl$_4$N$_3$O$_{19}$ReW$_5$
Formula weight	2306.67
Temperature/K	150.0(2)
Crystal system	monoclinic
Space group	P2$_1$/c
a/Å	24.2318(6)
b/Å	17.3311(4)
c/Å	17.7224(4)
α/°	90
β/°	103.528(2)
γ/°	90
Volume/Å^3	7236.3(3)
Z	4
ρ_{calc}g/cm^3	2.117
μ/mm^{-1}	9.791
F(000)	4392.0
Crystal size/mm^3	0.38 × 0.19 × 0.03
Radiation	Mo Kα (λ = 0.71073)
2Θ range for data collection/°	4.386 to 61.292
Index ranges	-34 ≤ h ≤ 31, -22 ≤ k ≤ 24, -25 ≤ l ≤ 22
Reflections collected	63405
Independent reflections	17816 [R$_{int}$ = 0.0459, R$_{sigma}$ = 0.0515]
Data/restraints/parameters	17816/806/809
Goodness-of-fit on F^2	1.019
Final R indexes [I>=2σ (I)]	R$_1$ = 0.0378, wR$_2$ = 0.0741
Final R indexes [all data]	R$_1$ = 0.0804, wR$_2$ = 0.0883
Largest diff. peak/hole / e Å^{-3}	1.67/-1.59

A.4.4 (TBA)$_2$[ReW$_5$O$_{19}$]

Table A.39: Crystal structure data for (TBA)$_2$[ReW$_5$O$_{19}$]

Empirical formula	C$_{32}$H$_{72}$N$_2$O$_{19}$ReW$_5$
Formula weight	1894.36
Temperature/K	150.0(2)
Crystal system	triclinic
Space group	P-1
a/Å	11.6149(2)
b/Å	12.6123(3)
c/Å	19.0685(3)
α/°	78.811(2)
β/°	74.4420(10)
γ/°	62.769(2)
Volume/Å^3	2384.45(9)
Z	2
ρ_{calc}g/cm^3	2.638
μ/mm^{-1}	14.609
F(000)	1750.0
Crystal size/mm^3	0.28 × 0.16 × 0.14
Radiation	Mo Kα (λ = 0.71073)
2Θ range for data collection/°	4.108 to 61.494
Index ranges	-14 ≤ h ≤ 16, -17 ≤ k ≤ 15, -26 ≤ l ≤ 27
Reflections collected	39958
Independent reflections	11854 [R$_{int}$ = 0.0391, R$_{sigma}$ = 0.0395]
Data/restraints/parameters	11854/580/573
Goodness-of-fit on F^2	0.989
Final R indexes [I>=2σ (I)]	R$_1$ = 0.0236, wR$_2$ = 0.0458
Final R indexes [all data]	R$_1$ = 0.0305, wR$_2$ = 0.0476
Largest diff. peak/hole / e Å^{-3}	0.97/-1.03

A.4.5 Partial structure of (TBA)₃[(PhN)ReW₅O₁₈]

Table A.40: Fractional co-ordinates of atoms in the asymmetric unit

Atom	x	y	z
W002	0.874871	0.863242	0.300922
W003	0.749578	0.964288	0.261424
W005	0.864538	0.976189	0.381543
W006	0.707207	0.829181	0.293569
Re00	0.821235	0.843106	0.411593
W008	0.697049	0.942598	0.373924
O00E	0.828799	0.920791	0.24829
O00F	0.920182	0.9305	0.343216
O00H	0.685342	0.983656	0.306001
O00I	0.887779	0.821857	0.368559
O00J	0.820798	1.009488	0.311919
O00L	0.793522	0.812573	0.271961
O00N	0.695096	0.894406	0.242264
O00P	0.65107	0.876064	0.329891
O00R	0.777033	0.994541	0.401196
O00S	0.877875	0.913406	0.434262
O00T	0.939303	0.834546	0.272518
O00U	0.722772	1.007649	0.20549
O00W	0.742178	0.88539	0.42774
O00X	0.749446	0.795437	0.362153
O010	0.922383	1.02946	0.413005
O011	0.648352	0.775894	0.260904
O014	0.630513	0.970638	0.399196
N018	0.866106	0.970653	0.59812
N019	0.626564	0.455914	0.395358
O01A	0.78721	0.901426	0.339281
N01D	0.415159	0.830646	0.286272
N01F	0.586998	1.148244	0.21314
C01G	0.975068	0.824298	0.608517
C01I	0.878684	1.055893	0.668779
N01J	0.847847	0.795094	0.46604
C01K	0.567321	0.554299	0.265972
C01L	0.521718	1.110482	0.283196
C01N	0.375573	0.85544	0.325802
C01O	0.581597	0.479798	0.34038
C01P	0.906981	0.995927	0.652434
C01Q	0.610241	0.540569	0.324685
C01R	0.486896	0.869193	0.221532
C01S	0.333612	0.811745	0.350479
C01T	0.853161	1.017796	0.553403
C01U	0.482494	1.172721	0.131267
C01V	0.640821	0.501161	0.439298
C01W	0.909238	0.921638	0.582066
C01X	0.917609	0.866616	0.619578
C01Y	0.923072	1.071503	0.726867
C01Z	0.583933	0.404694	0.411832
C020	0.626021	1.122527	0.173204
C021	0.365649	0.797763	0.2402
C022	0.667592	1.167415	0.148851
C023	0.92168	1.05149	0.548507
C024	0.450546	0.883786	0.266204
C025	0.521224	0.803152	0.366578
C026	0.897721	1.108205	0.515838
C027	0.98579	0.770138	0.645507

C028	0.574044	0.534774	0.448075
C029	0.553285	1.096401	0.235705
C02A	0.575894	0.35089	0.374375
C02B	0.303669	0.835	0.207579
C02C	0.490884	1.051078	0.300802
C02D	0.530771	1.19526	0.186042
C02E	0.470632	0.783985	0.314179
C02F	0.637282	1.183834	0.2582
C02G	0.520592	0.307153	0.389562
C02H	0.79306	0.948618	0.603068
C02I	0.698619	1.146737	0.291608
C02J	0.963098	1.143982	0.510356
C02K	0.519832	0.930001	0.207782
C02L	0.463099	1.060515	0.350401
C02M	0.57308	0.751702	0.386787
C02N	0.533084	0.627681	0.487264
C02O	0.429868	1.224332	0.10988
C02P	0.897615	1.133115	0.74268
C02Q	0.74786	1.188461	0.332418
C02R	0.293956	0.848692	0.38594
C02S	0.747723	0.920858	0.552537
C02T	0.699019	0.434865	0.387234
C02U	0.258187	0.791514	0.167037
C02V	0.597895	0.591862	0.480576
C02W	0.193844	0.82389	0.1285
C02X	0.809724	1.155288	0.369296
C02Y	0.593182	0.615011	0.249198
C02Z	0.553993	0.921444	0.159479
C030	0.622301	0.76657	0.444339
C031	0.509252	0.252232	0.354062
C032	0.676878	0.898279	0.56391
C033	0.701972	1.121846	0.106359
C034	0.684954	0.847097	0.600594
C035	0.862535	0.741995	0.494926
C036	0.381503	1.206752	0.054064
C037	0.748156	0.408112	0.439372
C038	0.816896	0.387309	0.424661
C039	0.943884	0.658265	0.52889
C03A	0.929355	0.713895	0.498704
C03B	0.814625	0.719062	0.523641
C03D	0.835525	0.664781	0.552976
C23	0.898199	0.638506	0.555337
C24	0.803103	0.330436	0.389072
C7	0.248892	0.810351	0.410304
C12	0.751475	1.160077	0.094087
W001	0.364826	0.621215	0.293986
W004	0.197224	0.651404	0.29501
W009	0.238652	0.520038	0.257483
W00A	0.321782	0.636709	0.409982
W00B	0.358966	0.50388	0.372361
W00C	0.195866	0.538062	0.373435
O00D	0.282646	0.669037	0.269918
O00G	0.382145	0.658789	0.363287
O00K	0.183771	0.591339	0.242009
O00M	0.31682	0.564083	0.242857
O00O	0.413375	0.552757	0.336174
O00Q	0.423398	0.649617	0.26087
O00V	0.250294	0.684227	0.364439
O00Y	0.148016	0.604502	0.336224

O00Z	0.137742	0.704687	0.263307
O012	0.176502	0.498501	0.305752
O013	0.31147	0.472047	0.304422
O015	0.275788	0.483895	0.39835
O016	0.378154	0.567034	0.427283
O017	0.245903	0.592152	0.429043
O01B	0.280796	0.576578	0.335848
O01C	0.208299	0.477184	0.200662
O01E	0.418574	0.449442	0.401904
N01H	0.349911	0.680619	0.466482
O01M	0.133706	0.509712	0.40328
C66	0.436044	0.840347	0.524998
C48	0.384028	0.860373	0.549582
C41	0.323657	0.826356	0.547002
C63	0.315302	0.772313	0.519837
C35	0.367319	0.752287	0.495253
C30	0.42769	0.786303	0.497833
O01N	0.144142	0.708847	0.272412
W0	0.355195	0.495999	0.360515
O1	0.37188	0.550817	0.417168
O2	0.269163	0.473101	0.379654
O3	0.407058	0.544306	0.323906
O4	0.304501	0.468833	0.286466
O5	0.413824	0.439537	0.384865
O6	0.27327	0.571863	0.323522
W1	0.315715	0.624107	0.40766
W2	0.189843	0.525905	0.360084
W3	0.363777	0.615159	0.291413
W4	0.234377	0.520723	0.243776
W00D	0.201941	0.65235	0.291352
O7	0.377887	0.64635	0.36441
O8	0.237186	0.575917	0.417557
O9	0.245446	0.674745	0.363858
O00{	0.349404	0.661949	0.468326
O0	0.174414	0.49269	0.288679
O10	0.143538	0.59758	0.323151
N01I	0.123953	0.493676	0.385189
O11	0.2842	0.673318	0.271247
O12	0.312373	0.567394	0.231706
O01D	0.430781	0.649707	0.270071
O13	0.181444	0.594895	0.231498
O01F	0.205465	0.484893	0.182367
C35A	0.080825	0.503892	0.440764
C63A	0.008645	0.515596	0.421876
C41A	-0.034868	0.515191	0.457773
C48A	-0.006201	0.503082	0.512559
C66A	0.065979	0.491378	0.531448
C30A	0.109493	0.491783	0.495551
C14	0.374615	0.891302	0.524164
C15	0.414072	0.840618	0.521054
C21	0.470271	0.843076	0.49637
C20	0.487013	0.896218	0.474797
C18	0.447557	0.946903	0.477908
C1	0.391358	0.944446	0.502591
C2	0.317268	0.889778	0.550758

Appendix B: Optimised geometries from Density Functional Theory calculations

B.1 XYZ co-ordinates of optimised structure discussed in Chapter 3

B.1.1 [W₇O₂₄H]⁵⁻

O	2.026992000	-1.561976000	0.558394000
O	1.095016000	0.102449000	2.422638000
O	0.785218000	-3.899591000	-0.115066000
O	-1.232505000	-0.302464000	3.869409000
O	0.787007000	-1.598567000	-1.911462000
O	-0.478444000	-1.958496000	1.661875000
O	0.000000000	0.000000000	0.000000000
O	-1.129143000	0.248039000	-2.740587000
O	-1.503878000	-2.551721000	-0.788809000
O	-2.602858000	-0.171055000	1.421698000
O	-3.200820000	-0.581354000	-1.197412000
O	-5.356262000	-0.236542000	0.724185000
O	-3.700686000	0.245103000	-3.943135000
W	2.156664000	0.285195000	0.790987000
W	0.142052000	-2.270435000	-0.178692000
W	-0.827096000	-0.142171000	2.184635000
O	3.783461000	0.541371000	1.392527000
O	1.453259000	2.105559000	0.725787000
O	2.359269000	0.462280000	-1.145730000
O	-0.539666000	4.103003000	0.224778000
O	1.471000000	0.468145000	-3.769605000
O	-0.890397000	1.770567000	1.878284000
O	0.364294000	2.126231000	-1.669616000
O	-2.049418000	1.807895000	-0.541693000
O	-4.186752000	2.187710000	1.302044000
O	-2.577686000	2.651741000	-3.208525000
O	-4.419011000	1.465213000	-1.420975000
W	-0.406681000	2.366554000	0.096075000

```
W      0.727939000     0.300105000     -2.205004000
W     -3.938489000     0.730636000      0.340845000
W     -2.897753000     1.031487000     -2.590800000
H     -2.459576000    -1.218845000     -0.998855000
```

B.2 XYZ co-ordinates of optimised structures discussed in Chapter 5

B.2.1 [W₆O₁₉]²⁻

W	-0.209621000	-0.111679000	-2.336789000
O	0.448081000	2.611189000	-0.165422000
O	-3.306315000	-2.325435000	0.406702000
O	-1.359273000	-0.986018000	2.055530000
O	0.362060000	0.195060000	4.041037000
O	-1.245968000	1.446384000	-1.843999000
O	1.246183000	-1.446479000	1.844179000
O	-0.000180000	-0.000166000	-0.000274000
O	2.605127000	-0.460407000	-0.211140000
O	3.306297000	2.325398000	-0.406946000
O	1.359410000	0.986183000	-2.055708000
O	2.334329000	-3.324381000	-0.049931000
O	-0.911374000	1.624757000	1.890021000
O	-2.334247000	3.324514000	0.049525000
O	-2.605261000	0.460461000	0.211131000
O	-1.694020000	-1.165165000	-1.678758000
O	1.693903000	1.165190000	1.678792000
O	-0.448153000	-2.611390000	0.165360000
O	0.911310000	-1.624591000	-1.889978000
W	-1.911032000	-1.346272000	0.235816000
W	-1.350743000	1.922156000	0.029283000
W	1.911024000	1.346241000	-0.236070000
W	1.350614000	-1.922197000	-0.029042000
W	0.209763000	0.111737000	2.336891000
O	-0.361956000	-0.194986000	-4.040929000

B.2.2 [W₆O₁₉]^{3−}

W	-2.366125000	-0.101879000	0.157725000
O	0.113626000	1.726411000	2.038034000
O	0.188725000	-4.055405000	-0.354457000
O	1.953867000	-1.781499000	-0.287463000
O	4.065032000	0.175305000	-0.273284000
O	-1.703042000	-0.239922000	2.050699000
O	1.753834000	0.235948000	-1.985775000
O	-0.013253000	-0.000772000	0.000019000
O	-0.149933000	2.040864000	-1.718920000
O	-0.113776000	4.058712000	0.348256000
O	-1.911623000	1.851658000	0.289451000
O	-0.247798000	0.342308000	-4.052814000
O	2.016152000	-0.075011000	1.734397000
O	0.322226000	-0.338652000	4.047793000
O	0.254939000	-2.037490000	1.713735000
O	-1.766287000	-2.010382000	-0.043192000
O	1.814703000	1.945013000	0.033922000
O	-0.009329000	-1.722048000	-2.045620000
O	-1.975962000	0.081527000	-1.804929000
W	0.078902000	-2.342299000	-0.203325000
W	0.156240000	-0.198698000	2.338521000
W	-0.096944000	2.341609000	0.205160000
W	-0.174527000	0.196839000	-2.337200000
W	2.346916000	0.102194000	-0.156814000
O	-4.078374000	-0.175909000	0.272537000

B.2.3 [W₆O₁₉]⁴⁻ (triplet)

W	1.866985000	-1.469941000	-0.017334000
O	-1.193058000	-1.436639000	-1.941294000
O	0.019101000	0.023889000	4.084388000
O	-1.458048000	1.203846000	1.893618000
O	-3.188754000	2.570439000	0.030339000
O	0.320670000	-2.688862000	-0.013563000
O	-0.316462000	2.654984000	0.013365000
O	0.001716000	-0.013286000	0.000166000
O	1.132143000	1.531905000	-1.880030000
O	-0.028326000	0.061021000	-4.083811000
O	1.477047000	-1.117706000	-1.954469000
O	2.497546000	3.245568000	0.000289000
O	-2.683876000	-0.233234000	0.013031000
O	-2.581354000	-3.191144000	0.000325000
O	-1.171637000	-1.452868000	1.942112000
O	1.499385000	-1.135526000	1.927992000
O	-1.479510000	1.220437000	-1.866311000
O	1.152993000	1.514988000	1.880431000
O	2.663469000	0.404215000	-0.013048000
W	0.016485000	-0.034231000	2.352502000
W	-1.469113000	-1.866863000	0.000021000
W	-0.010903000	-0.012796000	-2.352702000
W	1.463441000	1.853775000	-0.000131000
W	-1.858371000	1.458201000	0.017329000
O	3.258111000	-2.497363000	-0.030610000

B.2.4 [VW₅O₁₉]³⁻

V	0.000078000	0.001275000	-2.502779000
O	-1.968309000	1.805386000	-0.191583000
O	0.169808000	-4.049604000	-0.244685000
O	0.083390000	-1.879256000	1.675319000
O	-0.000334000	0.002181000	3.852216000
O	-1.838464000	-0.083697000	-2.058421000
O	1.879987000	0.085833000	1.673435000
O	-0.000212000	-0.000029000	-0.145259000
O	1.805472000	1.968026000	-0.191572000
O	-0.169827000	4.049590000	-0.247735000
O	-0.081586000	1.835911000	-2.059076000
O	4.049839000	0.169417000	-0.246012000
O	-1.880291000	-0.081038000	1.673377000
O	-4.049700000	-0.170170000	-0.246404000
O	-1.805414000	-1.968179000	-0.186955000
O	0.081722000	-1.839274000	-2.056843000
O	-0.083517000	1.882225000	1.671730000
O	1.968066000	-1.805271000	-0.186903000
O	1.838807000	0.079605000	-2.058354000
W	0.096971000	-2.326652000	-0.237632000
W	-2.326775000	-0.097142000	-0.238262000
W	-0.097056000	2.326659000	-0.236793000
W	2.326921000	0.096869000	-0.238127000
W	-0.000054000	-0.000306000	2.125270000
O	0.000273000	-0.000036000	-4.094512000

B.2.5 [VW₅O₁₈]⁴⁻

V	0.000643000	-0.000478000	-2.553285000
O	2.646107000	-0.440212000	-0.146967000
O	-2.368260000	3.308491000	-0.189022000
O	-1.087350000	1.526599000	1.688104000
O	-0.000050000	0.000163000	3.873454000
O	1.570183000	1.120129000	-2.042766000
O	-1.526091000	-1.086790000	1.689069000
O	0.000351000	-0.000576000	-0.170180000
O	-0.440310000	-2.645840000	-0.147526000
O	2.367500000	-3.308174000	-0.189221000
O	1.120373000	-1.569774000	-2.042703000
O	-3.308016000	-2.368218000	-0.189247000
O	1.526145000	1.086772000	1.688967000
O	3.308580000	2.367591000	-0.188972000
O	0.440293000	2.646274000	-0.146876000
O	-1.119506000	1.569490000	-2.042032000
O	1.086843000	-1.526642000	1.689565000
O	-2.646539000	0.439936000	-0.147186000
O	-1.569543000	-1.120207000	-2.042937000
W	-1.359155000	1.897792000	-0.248050000
W	1.897620000	1.359053000	-0.248776000
W	1.358696000	-1.897394000	-0.248268000
W	-1.897716000	-1.358683000	-0.248973000
W	0.000261000	-0.000533000	2.135847000
O	0.000164000	0.000181000	-4.164289000

B.2.6 [NbW₅O₁₉]³⁻

Nb	0.001213000	-0.001225000	-2.554167000
O	2.659048000	-0.187625000	-0.101443000
O	-2.668062000	3.071027000	-0.086289000
O	-1.227906000	1.418144000	1.760144000
O	-0.001250000	0.000903000	3.942452000
O	1.477697000	1.281055000	-1.989981000
O	-1.418565000	-1.227641000	1.760756000
O	-0.000242000	0.000529000	-0.102281000
O	-0.187932000	-2.659077000	-0.101720000
O	2.668204000	-3.071261000	-0.084251000
O	1.281558000	-1.477652000	-1.989026000
O	-3.071176000	-2.667968000	-0.085444000
O	1.418296000	1.226985000	1.761133000
O	3.071243000	2.668029000	-0.084633000
O	0.187857000	2.658945000	-0.100761000
O	-1.280698000	1.477297000	-1.990916000
O	1.226771000	-1.418396000	1.760983000
O	-2.659241000	0.187978000	-0.101393000
O	-1.476884000	-1.281078000	-1.990035000
W	-1.539210000	1.770938000	-0.144516000
W	1.771152000	1.539236000	-0.142825000
W	1.539283000	-1.771106000	-0.141486000
W	-1.771053000	-1.539142000	-0.142685000
W	-0.000898000	0.001109000	2.217057000
O	0.001783000	-0.003505000	-4.308475000

B.2.7 [NbW₅O₁₉]⁴⁻

Nb	0.000351000	0.041943000	-2.547787000
O	1.823354000	-1.953012000	-0.100800000
O	0.120203000	4.092395000	-0.063120000
O	0.052948000	1.844254000	1.831454000
O	-0.001241000	-0.051977000	3.956037000
O	1.975653000	-0.117756000	-2.005082000
O	-1.887415000	0.008784000	1.769446000
O	0.000906000	0.015833000	-0.104638000
O	-1.933591000	-1.844556000	-0.101250000
O	-0.118863000	-4.083590000	-0.099063000
O	-0.056434000	-1.958584000	-1.989608000
O	-4.085191000	0.079733000	-0.083329000
O	1.884991000	-0.099940000	1.770320000
O	4.082424000	-0.158187000	-0.083892000
O	2.004091000	1.796711000	-0.115331000
O	0.055535000	1.927601000	-2.057421000
O	-0.054760000	-1.890722000	1.751699000
O	-1.896224000	1.909958000	-0.115707000
O	-1.978738000	-0.003734000	-2.003896000
W	0.068957000	2.365935000	-0.123919000
W	2.353010000	-0.059930000	-0.150121000
W	-0.068784000	-2.351258000	-0.153740000
W	-2.352957000	0.077181000	-0.148137000
W	0.001124000	-0.002362000	2.221008000
O	-0.001932000	-0.001658000	-4.315500000

B.2.8 [TaW₅O₁₉]³⁻

Ta	2.381445000	0.108369000	-0.004554000
O	0.055283000	-1.967905000	-1.795334000
O	-0.047535000	0.185833000	4.067041000
O	-1.888167000	0.000470000	1.874152000
O	-4.071065000	-0.183386000	0.007002000
O	1.944845000	-1.859790000	0.087248000
O	-1.973129000	1.782877000	-0.083608000
O	-0.007525000	-0.000557000	0.000085000
O	-0.116925000	1.792029000	-1.968003000
O	-0.044495000	-0.189750000	-4.067035000
O	1.855954000	-0.004687000	-1.949754000
O	-0.232071000	4.060860000	-0.187367000
O	-1.802266000	-1.955334000	0.089772000
O	0.140133000	-4.065082000	0.187979000
O	0.053722000	-1.795147000	1.968699000
O	1.854556000	0.174636000	1.942384000
O	-1.887318000	-0.172722000	-1.867830000
O	-0.118704000	1.965403000	1.795676000
O	1.767076000	2.029027000	-0.092014000
W	0.009273000	0.108900000	2.347459000
W	0.117568000	-2.344823000	0.108573000
W	0.010809000	-0.108001000	-2.347614000
W	-0.096828000	2.345829000	-0.108127000
W	-2.349049000	-0.107000000	0.003975000
O	4.138033000	0.186479000	-0.007006000

B.2.9 [TaW₅O₁₉]⁴⁻

Ta	1.684193000	-0.086289000	1.679369000
O	-1.332449000	1.870648000	1.360965000
O	2.879344000	0.012827000	-2.918935000
O	-0.056779000	0.074870000	-2.686325000
O	-2.897073000	0.149852000	-2.881169000
O	1.316202000	1.893965000	1.433149000
O	-1.407456000	-1.815110000	-1.373349000
O	0.004045000	0.001149000	-0.016194000
O	-1.423807000	-1.879901000	1.254901000
O	-2.948553000	-0.010522000	2.837032000
O	-0.099574000	-0.073042000	2.693312000
O	-0.154613000	-4.082158000	-0.117594000
O	-1.318521000	1.952908000	-1.267682000
O	0.036417000	4.085696000	0.111205000
O	1.357564000	1.952828000	-1.252644000
O	2.719166000	-0.066281000	0.028958000
O	-2.667985000	0.064881000	-0.019034000
O	1.267741000	-1.941028000	-1.358464000
O	1.220792000	-2.029679000	1.325002000
W	1.692542000	0.006492000	-1.663472000
W	0.073172000	2.353890000	0.071404000
W	-1.674829000	-0.007605000	1.662001000
W	-0.037990000	-2.354625000	-0.060404000
W	-1.647910000	0.085847000	-1.680141000
O	2.891168000	-0.151518000	2.975799000

B.2.10 [Mo₆O₁₉]²⁻

Mo	1.936383000	0.747337000	1.132905000
O	-1.263566000	-0.312863000	2.337354000
O	0.333826000	2.974490000	-2.750648000
O	-1.384739000	0.669471000	-2.192894000
O	-3.268253000	-1.449182000	-1.943796000
O	0.355661000	1.790783000	1.966218000
O	-0.355616000	-1.791252000	-1.966756000
O	0.000216000	-0.000153000	-0.000153000
O	1.086221000	-2.435539000	0.266436000
O	-0.334007000	-2.974488000	2.750554000
O	1.384757000	-0.669865000	2.193117000
O	2.414994000	-2.375044000	-2.251747000
O	-2.659482000	0.316027000	0.201070000
O	-2.414707000	2.375679000	2.251730000
O	-1.086058000	2.435357000	-0.266529000
O	1.580355000	2.140716000	-0.331817000
O	-1.580081000	-2.140415000	0.331618000
O	1.263569000	0.312983000	-2.337617000
O	2.659625000	-0.315834000	-0.200782000
Mo	0.291274000	1.711601000	-1.598686000
Mo	-1.335325000	1.456481000	1.295912000
Mo	-0.290876000	-1.711468000	1.598780000
Mo	1.334899000	-1.456573000	-1.296000000
Mo	-1.936494000	-0.747430000	-1.132771000
O	3.268012000	1.449401000	1.943905000

B.2.11 [Mo₆O₁₉]³⁻

Mo	-1.651864000	-1.730452000	-0.013526000
O	-1.263777000	1.496296000	-1.833567000
O	0.002805000	0.007292000	4.043980000
O	1.445212000	1.205215000	1.856514000
O	3.006872000	2.792276000	0.033497000
O	-2.779007000	0.180751000	0.053555000
O	2.778864000	-0.179224000	0.049133000
O	-0.001634000	-0.000760000	-0.029255000
O	1.260299000	-1.502816000	-1.828484000
O	-0.002871000	-0.009063000	-4.049798000
O	-1.501085000	-1.265627000	-1.827918000
O	2.792149000	-3.006610000	0.043913000
O	0.179895000	2.778222000	0.045912000
O	-2.790492000	3.007611000	0.037037000
O	-1.200824000	1.447442000	1.858882000
O	-1.442398000	-1.199284000	1.863750000
O	1.498294000	1.258015000	-1.833971000
O	1.203613000	-1.440157000	1.861284000
O	-0.180342000	-2.779632000	0.056518000
Mo	0.000275000	0.005176000	2.323080000
Mo	-1.730248000	1.652339000	-0.020625000
Mo	-0.001375000	-0.004892000	-2.337906000
Mo	1.730594000	-1.652345000	-0.014817000
Mo	1.653011000	1.730173000	-0.021636000
O	-3.007631000	-2.789939000	0.047530000

B.2.12 [Mo₆O₁₉]⁴⁻ (triplet)

Mo	-2.365170000	-0.178988000	0.063823000
O	0.020586000	-0.034209000	2.726867000
O	0.299415000	-2.803231000	-2.975005000
O	2.014649000	-1.029922000	-1.386481000
O	4.075780000	0.423930000	-0.063466000
O	-1.784465000	-1.556965000	1.260061000
O	1.731769000	1.596215000	-1.392604000
O	0.001102000	-0.000839000	0.033936000
O	-0.349042000	2.675079000	-0.055631000
O	-0.250314000	2.896863000	2.879041000
O	-2.113313000	1.122313000	1.383655000
O	-0.339066000	2.877083000	-2.900114000
O	2.132831000	-1.156666000	1.326630000
O	0.287805000	-2.969728000	2.799897000
O	0.348223000	-2.673080000	-0.127737000
O	-1.750686000	-1.561037000	-1.407926000
O	1.801723000	1.525462000	1.274709000
O	-0.019169000	0.033562000	-2.663478000
O	-2.031720000	1.063804000	-1.331727000
Mo	0.084437000	-1.661132000	-1.690072000
Mo	0.175366000	-1.685313000	1.657007000
Mo	-0.152659000	1.643243000	1.701216000
Mo	-0.106962000	1.703330000	-1.646981000
Mo	2.365190000	0.177507000	0.036674000
O	-4.077172000	-0.421526000	-0.019377000

B.2.13 [VMo$_5$O$_{19}$]$^{3-}$

V	0.137806000	0.093996000	2.374235000
O	1.903713000	-1.930019000	0.248346000
O	-4.085283000	0.120798000	0.123409000
O	-1.892391000	-0.079917000	-1.856365000
O	0.047407000	-0.144916000	-3.944137000
O	-0.058147000	-1.767384000	2.018264000
O	0.068854000	1.799651000	-1.825495000
O	-0.009002000	0.003515000	0.082898000
O	1.952578000	1.886864000	0.104223000
O	4.092980000	-0.115640000	0.145234000
O	1.848050000	0.083861000	2.007215000
O	0.095260000	4.049462000	0.007954000
O	0.087773000	-1.925223000	-1.686255000
O	-0.118614000	-4.037001000	0.270681000
O	-1.957521000	-1.868427000	0.081199000
O	-1.940733000	0.062448000	1.969149000
O	1.969733000	-0.051588000	-1.738590000
O	-1.890656000	1.921717000	-0.053130000
O	-0.071311000	1.913893000	1.899440000
Mo	-2.365498000	0.156480000	0.222834000
Mo	-0.162654000	-2.316739000	0.226904000
Mo	2.375232000	-0.160513000	0.051594000
Mo	0.159562000	2.330810000	0.079579000
Mo	-0.099941000	-0.075152000	-2.228721000
O	0.050943000	0.149517000	3.971043000

B.2.14 [VMo₅O₁₉]⁴⁻

V	-0.001237000	-0.001258000	2.370234000
O	2.058723000	1.904512000	0.057069000
O	-0.259473000	-4.095962000	0.080607000
O	-0.024979000	-1.875342000	-1.750005000
O	0.001752000	0.003790000	-3.936414000
O	1.948609000	-0.043790000	1.927153000
O	-1.876811000	0.027681000	-1.749345000
O	0.000181000	-0.000002000	0.126537000
O	-1.904847000	2.057531000	0.055713000
O	0.258874000	4.095751000	0.084942000
O	0.040731000	1.947218000	1.927364000
O	-4.096242000	0.258325000	0.081625000
O	1.877424000	-0.023360000	-1.747254000
O	4.095526000	-0.260022000	0.083475000
O	1.903224000	-2.057848000	0.051668000
O	-0.042691000	-1.950240000	1.925453000
O	0.026138000	1.879082000	-1.745447000
O	-2.056825000	-1.903113000	0.051503000
O	-1.950063000	0.040602000	1.926247000
Mo	-0.306660000	-2.364029000	0.156417000
Mo	2.363530000	-0.307367000	0.158264000
Mo	0.307852000	2.363663000	0.158726000
Mo	-2.364226000	0.306944000	0.157151000
Mo	0.000554000	0.001129000	-2.202749000
O	-0.001205000	-0.002983000	3.988689000

B.2.15 [NbMo₅O₁₉]³⁻

Nb	0.001071000	0.002823000	-2.358513000
O	2.582491000	-0.981758000	0.027777000
O	-1.777430000	3.694942000	0.056005000
O	-0.722204000	1.737778000	1.861396000
O	-0.002382000	-0.003705000	4.038411000
O	1.821720000	0.762583000	-1.844828000
O	-1.740075000	-0.722468000	1.859264000
O	0.000560000	-0.000044000	-0.009534000
O	-0.981320000	-2.581968000	0.024522000
O	1.776691000	-3.695234000	0.051190000
O	0.762931000	-1.818890000	-1.847167000
O	-3.695180000	-1.777466000	0.049567000
O	1.737925000	0.720367000	1.862221000
O	3.695231000	1.776647000	0.057371000
O	0.981562000	2.582415000	0.028266000
O	-0.761122000	1.821416000	-1.844796000
O	0.720431000	-1.740241000	1.860276000
O	-2.582270000	0.980797000	0.025694000
O	-1.819075000	-0.760640000	-1.847976000
Mo	-1.151689000	2.093883000	-0.015364000
Mo	2.093939000	1.151703000	-0.015541000
Mo	1.151663000	-2.093885000	-0.019316000
Mo	-2.094181000	-1.151445000	-0.019671000
Mo	-0.000934000	-0.002817000	2.317413000
O	0.002342000	0.004439000	-4.119764000

B.2.16 [NbMo₅O₁₉]⁴⁻

Nb	0.744326000	2.273159000	0.031537000
O	-1.923218000	0.420327000	1.770960000
O	0.123125000	-0.013101000	-4.078177000
O	-0.396245000	-1.877330000	-1.884153000
O	-1.139739000	-3.935423000	-0.058728000
O	-1.399517000	2.424346000	0.016582000
O	1.332816000	-2.320784000	0.084999000
O	-0.015038000	0.004666000	-0.029199000
O	1.723181000	-0.544555000	2.014951000
O	-0.215841000	-0.113052000	4.078704000
O	0.347295000	1.776241000	2.015278000
O	3.926555000	-1.209283000	0.185921000
O	-2.405353000	-1.378090000	-0.122533000
O	-3.939563000	1.133812000	-0.111999000
O	-1.806649000	0.531636000	-1.908552000
O	0.602551000	1.903245000	-1.881675000
O	-0.593757000	-1.846452000	1.815958000
O	2.002446000	-0.478578000	-1.808505000
O	2.410405000	1.242176000	0.222276000
Mo	0.095153000	0.038878000	-2.357588000
Mo	-2.243337000	0.788755000	-0.074281000
Mo	-0.040440000	-0.027545000	2.358666000
Mo	2.274290000	-0.722749000	0.025415000
Mo	-0.787501000	-2.238191000	-0.071883000
O	1.236516000	3.974737000	0.144526000

B.2.17 [TaMo₅O₁₉]³⁻

Ta	-2.151495000	-0.005582000	0.003710000
O	0.194221000	1.380258000	2.399332000
O	0.227302000	-3.932359000	-1.180303000
O	2.030238000	-1.821540000	-0.442857000
O	4.201967000	0.014914000	-0.008514000
O	-1.671893000	-0.476167000	1.913367000
O	2.017474000	0.447045000	-1.833058000
O	0.137282000	-0.000016000	0.000451000
O	0.181680000	2.399468000	-1.379580000
O	0.203817000	3.933854000	1.178580000
O	-1.684467000	1.903214000	0.471540000
O	0.204328000	1.179809000	-3.933505000
O	2.028883000	-0.429732000	1.825317000
O	0.228548000	-1.178505000	3.932446000
O	0.209974000	-2.399088000	1.378688000
O	-1.671093000	-1.916753000	-0.463310000
O	2.016137000	1.837141000	0.434312000
O	0.196303000	-1.378374000	-2.398886000
O	-1.683485000	0.459369000	-1.906846000
Mo	0.155071000	-2.253567000	-0.815074000
Mo	0.156819000	-0.815007000	2.253263000
Mo	0.144662000	2.254199000	0.815098000
Mo	0.142796000	0.815435000	-2.254119000
Mo	2.483132000	0.006978000	-0.004499000
O	-3.917846000	-0.013794000	0.006967000

B.2.18 [TaMo₅O₁₉]⁴⁻

Ta	-2.177804000	0.025312000	0.000962000
O	0.128973000	-1.787677000	2.047648000
O	0.209548000	-0.166549000	-4.089264000
O	2.103996000	-0.216755000	-1.851416000
O	4.257048000	-0.126026000	0.012970000
O	-1.748164000	-1.904506000	0.202137000
O	2.188246000	1.845013000	-0.104719000
O	0.141505000	-0.000709000	-0.024044000
O	0.310439000	1.980083000	1.752295000
O	0.265316000	0.214884000	4.090198000
O	-1.664456000	0.224288000	1.978218000
O	0.306217000	4.097255000	-0.158183000
O	1.961591000	-1.960115000	0.148462000
O	0.108125000	-4.101660000	0.233333000
O	0.060102000	-2.081751000	-1.797696000
O	-1.789927000	-0.026777000	-1.914653000
O	2.067902000	0.032255000	1.858682000
O	0.243819000	1.854613000	-1.931794000
O	-1.696802000	2.046016000	-0.050814000
Mo	0.136035000	-0.104262000	-2.371565000
Mo	0.132529000	-2.383483000	0.040995000
Mo	0.174438000	0.044266000	2.370739000
Mo	0.141801000	2.376648000	-0.099544000
Mo	2.533909000	0.025416000	-0.034212000
O	-3.954256000	0.064576000	0.081186000

B.2.19 Calculated redox potentials vs. Ag/Ag(NO₃)

Table B.1: Redox potentials for calculated from the difference in free energies between the optimised structures of the oxidised and reduced compounds vs. experimental findings.

Reduction reaction	Calc. E(1/2) vs. Ag/Ag(NO₃) (V)	Exp. E(1/2) vs. Ag/Ag(NO₃) (V)
$[W_6O_{19}]^{2-} + e^- \rightarrow [W_6O_{19}]^{3-}$	−1.29	−1.25
$[W_6O_{19}]^{3-} + e^- \rightarrow [W_6O_{19}]^{4-}$	−2.23	−2.21
$[VW_5O_{19}]^{3-} + e^- \rightarrow [VW_5O_{19}]^{4-}$	−0.79	−1.02
$[NbW_5O_{19}]^{3-} + e^- \rightarrow [NbW_5O_{19}]^{4-}$	−2.10	−2.09
$[TaW_5O_{19}]^{3-} + e^- \rightarrow [TaW_5O_{19}]^{4-}$	−2.07	−2.05
$[Mo_6O_{19}]^{2-} + e^- \rightarrow [Mo_6O_{19}]^{3-}$	−0.48	−0.71
$[Mo_6O_{19}]^{3-} + e^- \rightarrow [Mo_6O_{19}]^{4-}$	−1.55	−1.61
$[VMo_5O_{19}]^{3-} + e^- \rightarrow [VMo_5O_{19}]^{4-}$	−0.87	−1.21
$[NbMo_5O_{19}]^{3-} + e^- \rightarrow [NbMo_5O_{19}]^{4-}$	−1.36	−1.54
$[TaMo_5O_{19}]^{3-} + e^- \rightarrow [TaMo_5O_{19}]^{4-}$	−1.32	N/A